AUSTRALIA

AGSO
AUSTRALIAN GEOLOGICAL SURVEY ORGANISATION

BULLETIN 239

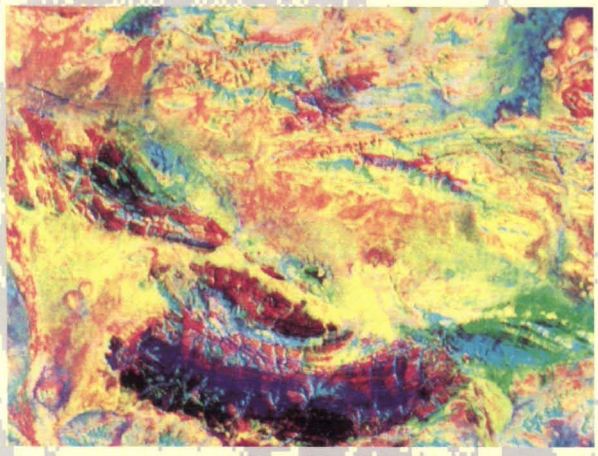

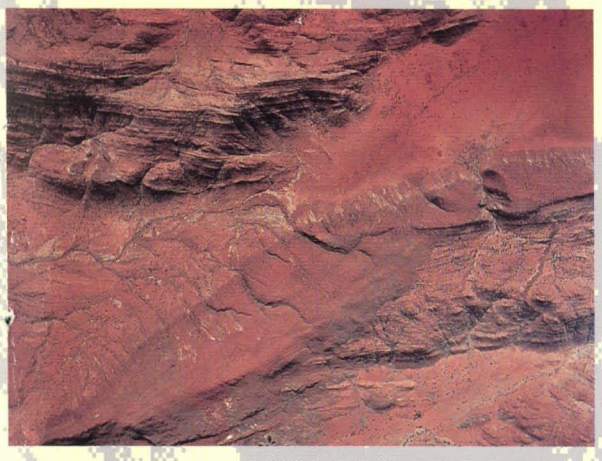

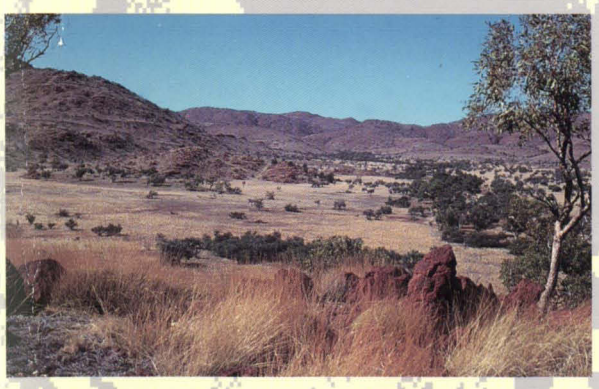

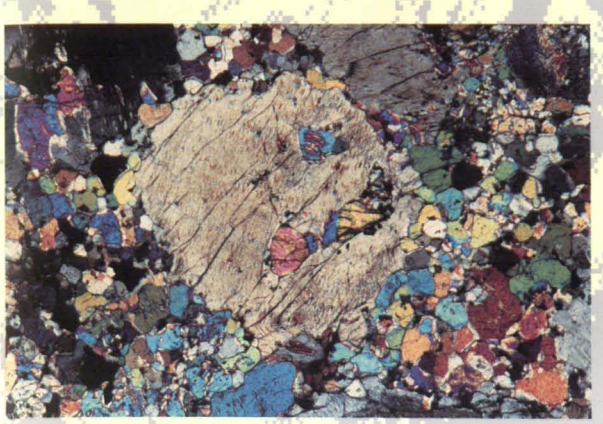

GEOLOGY of the western Musgrave Block, central Australia, with particular reference to the mafic–ultramafic Giles Complex

A. Y. Glikson, A.J. Stewart, C.G. Ballhaus, G.L. Clarke, E.H.J. Feeken, J.H. Leven, J.W. Sheraton & S-S. Sun

AUSTRALIAN GEOLOGICAL SURVEY ORGANISATION
DEPARTMENT OF PRIMARY INDUSTRIES AND ENERGY

BULLETIN 239

Geology of the western Musgrave Block, central Australia, with particular reference to the mafic–ultramafic Giles Complex

A.Y. GLIKSON[1], A.J. STEWART[1], C.G. BALLHAUS[2], G.L. CLARKE[3], E.H.J. FEEKEN[4], J.H. LEVEN[1], J.W. SHERATON[1] & S-S. SUN[1]

[1] *Minerals Division, AGSO*
[2] *Max-Planck-Institut für Chemie, Abt. Kosmochemie, Postfach 3060, 55020 Mainz, Germany*
[3] *Department of Geology & Geophysics, University of Sydney, NSW 2006*
[4] *Newington Road, Sutton, NSW 2620*

AUSTRALIAN GOVERNMENT PUBLISHING SERVICE
CANBERRA

ISSN 0084–7089

ISBN 0 644 36263 4

Editors: Marjorie Curtis and John Sheraton
Cover design and figures prepared by AGSO Cartographic Services Unit unless otherwise indicated
Prepared for publication by Lin Kay

Printed in Australia by National Capital Printing, 22 Pirie Street, Fyshwick ACT 2609

AUSTRALIAN GOVERNMENT PUBLISHING SERVICE CANBERRA 1996

***Front-cover illustration*:**

Views of the Ewarara pyroxenite intrusion, north of Kalka, South Australia: Landsat-5 Thematic Mapper directed principal components/band ratio pc2(4/3;5/7):5/4:4/3 RGB image, showing the Ewarara (left of top centre), Kalka (left of centre), and Mount Davies (bottom centre) intrusions; aerial photograph, showing the Ewarara intrusion emplaced concordantly to discordantly into layered granulite-facies felsic gneiss (top left and bottom right); Ewarara Creek and hills, looking west; photomicrograph of spinel–olivine websterite (sample 91985001E), containing large orthopyroxene grains, with olivine and clinopyroxene inclusions, in a partly recrystallised matrix of orthopyroxene, clinopyroxene, olivine, and minor spirel, biotite, and plagioclase.

Contents

Tables

Figures

Plates: Geology of the Giles Complex and environs, western Musgrave Block.

Frontispiece. Dulgunja Hill, near Kalka, consisting of outcrops of the Kalka norite/pyroxenite intrusion; looking east from the Hinckley Range.

Abstract

The western Musgrave Block in the Tomkinson Ranges, which straddle the South Australian–Western Australian border, contains the most extensive outcrops of the c. 1080 Ma layered mafic–ultramafic intrusions of the Giles Complex. Detailed to semi-detailed geological, petrological, and structural mapping of many of these bodies, and of their granulite-facies country rocks (Mount Aloysius Complex) was carried out. The Giles Complex consists of at least 17 intrusions and/or faulted segments of intrusions, of several types: (1) large (10–40 km along strike) clinopyroxene–orthopyroxene–plagioclase gabbro and olivine–clinopyroxene–plagioclase troctolite bodies, locally magnetite-rich, with little or no ultramafic component (Jameson Range, Blackstone Range, Cavenagh Range, Bell Rock, Hinckley Range); (2) large gabbroic bodies with a significant ultramafic component (Michael Hills, Mount Davies, Kalka); (3) medium-sized (<10 km) layered gabbro–pyroxenite intrusions (Murray Range, The Wart, Wingellina Hills, Claude Hills); (4) small (<5 km) bodies of pyroxenite and minor melagabbro (Gosse Pile, Ewarara); and (5) stratiform lenses and tongues of anorthosite emplaced into felsic granulite near Teizi. Some of these bodies, e.g., Blackstone Range–Bell Rock, The Wart–Bell Rock, and Kalka–Gosse Pile, may have originally been continuous, but most appear to be discrete sill-like bodies, rather than tectonic slices of a single Bushveld-type lopolith.

The various intrusions cannot be related to a single liquid line of descent of a single continuously fractionating parent magma, but crystallised from separate batches of variably fractionated parent melts. Phase equilibrium considerations show that at least three parent magmas (primitive, gabbroic, and troctolitic), related to a primitive mantle-derived parental liquid or liquids by various degrees of polybaric pyroxene±olivine fractionation, were involved. The Wingellina Hills, Murray Range, and The Wart intrusions were derived from near-primitive (i.e., little-fractionated) olivine-normative tholeiitic melts; the Bell Rock, Jameson Range, and Blackstone Range troctolitic bodies were derived from strongly fractionated, relatively silica-undersaturated melts with olivine and plagioclase as liquidus phases; the Hinckley Range gabbronorite falls between these extremes, having crystallised from a moderately fractionated, near silica-saturated melt. The geographical distribution of the intrusions appears to reflect vertical stacking of individual magma chambers within the Mesoproterozoic crust controlled by magma density. The ratio of mafic to ultramafic components in the intrusions increases south-southwestwards, implying decreasing density with progressively shallower crustal levels, from peridotite and pyroxenite-dominated intrusions along the northeastern Tomkinson Ranges, through gabbro-dominated intrusions with significant to minor pyroxenite, to troctolitic intrusions in the southern and western parts of the western Musgrave Block.

The following sequence of events is proposed for the western Musgrave Block:

- c. 1550 Ma and c. 1300 Ma felsic igneous rocks, including some which probably represent new felsic crust, together with subordinate sedimentary and mafic igneous rocks, form protoliths of the high-grade metamorphic Mount Aloysius Complex.

- Granulite-facies metamorphism and deformation about 1200 Ma ago involved mostly penetrative pure shear during D_1 and D_2 at >750°C and 5±1 kb. Metamorphism was associated with emplacement of post-D_1, pre-D_2 orthopyroxene granites ('charnockites') and post-D_2 granitoids, including rapakivi types (1188±4 Ma) and syenites. Leuconorite was emplaced at 1176±5 Ma.

- Emplacement of voluminous mafic–ultramafic magmas of the Giles Complex occurred 1078±3 Ma ago, with near-isobaric cooling from 1150° to 750°C at 6±1 kb for the Wingellina Hills intrusion and lower pressures (about 4 kb) for troctolitic bodies in the southwestern part of the area. Pervasive granite veining, probably representing back intrusion of crustal melts, was associated with recrystallisation to mafic granulite of marginal parts of the Giles Complex (during D_3), particularly in the western Hinckley Range. Extrusion of the bimodal Tollu Group volcanic rocks onto an uplifted and eroded basement of amphibolite-facies granitic gneisses was coeval with the Giles magmatism. The basement was apparently metamorphosed at shallower crustal levels than the granulite-facies gneisses into which the Giles Complex was emplaced, and may, in part, represent younger felsic crust. Some associated dolerite dykes may well be feeders to Giles Complex intrusions.

- Penetrative simple shear deformation (D_3) produced near-vertical high-strain zones, apparently under high-pressure conditions (650–700°C, ~11 kb). This may reflect increased lithostatic pressures associated with emplacement of the thick (>10 km in total) sills and lopoliths of the Giles Complex. It was apparently followed by near-isothermal decompression, associated with major uplift and erosion of more than 12 km of crust, to about 4 to 5 kb.

- Post-D_3 type C olivine dolerite dykes were emplaced about 1000 Ma ago, although their age is not well constrained. They are chemically and isotopically similar to the slightly older (~1080 Ma) Kulgera (eastern Musgrave Block) and Stuart (Arunta Block) dyke swarms.

- Type B quartz dolerite dykes were emplaced about 800 Ma ago. They are chemically and isotopically equivalent to the Amata dykes (eastern Musgrave Block) and the Gairdner dyke swarm (Gawler Craton), and so form part of a very extensive swarm.

- At least four phases of mylonite and ultramylonite zone formation (D_{4-7}) post-date type B dykes. The c. 550 Ma east–west-trending D_6 ultramylonite–pseudotachylite zones are the largest, and were formed during major northward thrusting of the Giles Complex and host gneisses in the Petermann Ranges orogeny. They are best developed in the Bates 1:100 000 sheet area, where they form the western extension of the Woodroffe Thrust, and formed at elevated pressures (>750°C, 14.0±1.1 kb) along the sole of the thrust; sub-eclogite-facies garnet–clinopyroxene-bearing assemblages were formed. Other major thrusts include the marginal thrust of the Officer Basin and the Bell Rock–Blackstone Range thrust fault, which led to the erosional removal of the Tollu Group volcanic rocks from the Tomkinson Ranges and eastern parts of the Musgrave Block.

The Giles Complex, together with coeval mafic volcanic rocks of the Tollu Group (Mummawarrawarra Basalt) and mafic dykes, was derived by melting of an enriched source, probably involving subcontinental lithospheric mantle. A major thermal perturbation, perhaps resulting from lithospheric thinning associated with crustal extension, and/or mantle plume activity, was clearly necessary to account for the scale of melting involved. The emplacement of voluminous mafic–ultramafic magma with associated felsic plutonic and volcanic activity is a classic example of a coeval mafic magmatism and crustal anatexis in pre-existing sialic crust.

Introduction

The Giles Complex consists of a suite of massive, partly deformed and recrystallised, layered mafic–ultramafic intrusions emplaced within the southern granulite-facies zone of the Mesoproterozoic Musgrave Block (Fig. 1). Part of this zone occupies an approximately 200x40 km east–west-trending belt in the western part of the Musgrave Block, and includes the Tomkinson Ranges, Blackstone Range, Cavenagh Range, Jameson Range, and smaller groups of hills (Fig. 2; Plates 1–3). The layered intrusions of the Giles Complex represent the most extensive mafic igneous activity recognised in exposed deep levels of the continental crust in Australia and even world wide (Nesbitt et al. 1970; Daniels 1974; Ballhaus & Glikson 1989, 1995; Ballhaus & Berry 1991; Ballhaus 1993). As such, they are of outstanding geological interest, as well as having economic potential for both platinum-group elements (PGE) and base metals, such as Ni. This Bulletin, and the accompanying maps, reports, and datasets, are the principal results of AGSO's Musgrave Project, initiated in 1987 as a specialised study of the Giles Complex and continued in 1990 within the framework of the National Geoscience Mapping Accord (NGMA).

The western Musgrave Block high-grade metamorphic terrane is included within the Mann (South Australia) and Cooper and Scott (Western Australia) 1:250 000 sheet areas, about the Surveyor General's Corner of these states and Northern Territory (Fig. 2). Early geological observations in this area (Sprigg & Wilson 1959) were followed by regional geological mapping by Daniels (1970, 1971a, b, 1972, 1974), Thomson (1965a, 1975, 1980) and Thomson et al. (1962). Detailed mapping and petrological studies of layered intrusions of the Giles Complex in South Australia were conducted by University of Adelaide researchers (Nesbitt & Kleeman 1964; Nesbitt & Talbot 1966; Goode & Krieg 1967; Nesbitt et al. 1970; Goode & Moore 1975; Goode 1975, 1976, 1977, 1978; Moore 1971a, b). Geochemical studies of the granulite-facies metamorphic rocks were conducted by Wilson et al. (1960), and Gray (1977), and isotopic studies by Compston & Nesbitt (1967), Arriens & Lambert (1969), Gray & Oversby (1972), Gray (1978), Gray & Compston (1978), Gray & Goode (1981, 1989), Webb (1985), and Maboko et al. (1991).

Some of the more significant suggestions made during these studies of the Musgrave Block, mainly in the South Australian part of the Tomkinson Ranges, include (1) an interpretation of the Giles Complex as tectonic slices of an originally continuous lopolith (Nesbitt et al. 1970), (2) a view of the latitudinal Hinckley Fault as a lineament separating a high-pressure terrane to the north from a younger, lower-pressure terrane to the south (Nesbitt et al. 1970; Gray 1978), (3) metamorphism of the northern terrane at very high pressures of about 10–12 kb (Goode & Moore 1975), and (4) increased differentiation with higher stratigraphic levels in some Giles Complex intrusions (Ballhaus 1993). However, there remained a number of major questions relating, in particular, to the origin of the Giles Complex, such as (1) the conditions under which the mafic–ultramafic intrusions were emplaced, including the pressure–temperature (P–T) history of the country rocks, (2) the original spatial relationships between individual mafic–ultramafic bodies, (3) the age(s) of emplacement, (4) the effects of emplacement on the granulite-facies country rocks and possible genetic relations between the Giles Complex and spatially associated granitoids, (5) the relations between the Giles Complex and associated mafic dykes, including identification of feeders of the layered intrusions, (6) the deformation history of the Giles Complex and associated

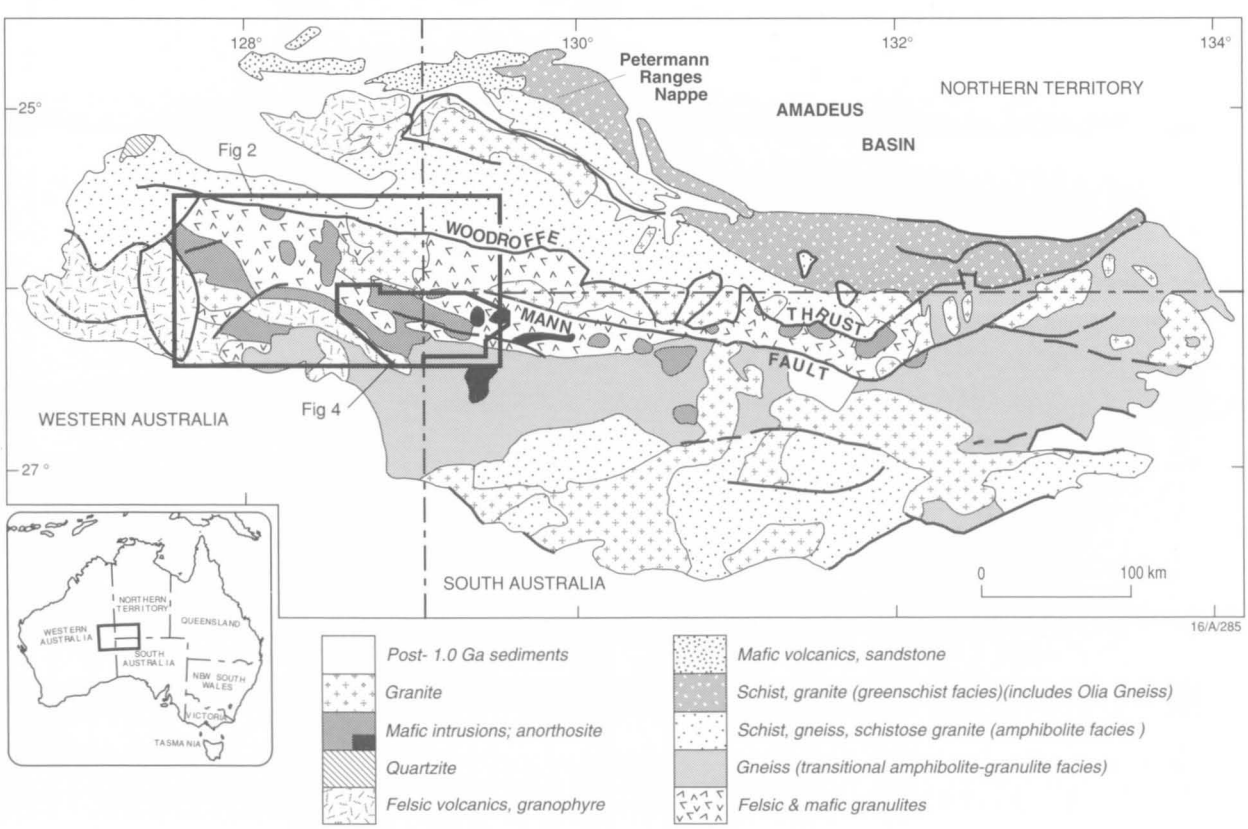

Figure 1. Generalised geological map of the Musgrave Block.

rocks, and (7) the origin of the mafic igneous activity and its possible lateral extent across central Australian Precambrian terranes. This Bulletin addresses these questions using the results of detailed studies of the field relationships, structure, petrology, and geochemistry of the principal rock suites in the Tomkinson Ranges–Blackstone Range region.

Field mapping in the western Musgrave Range was facilitated by 1:20 000 colour aerial photographs, acquired by AUSLIG in 1987 and designed to cover the better-exposed parts of the western Musgrave Block, including the Tomkinson

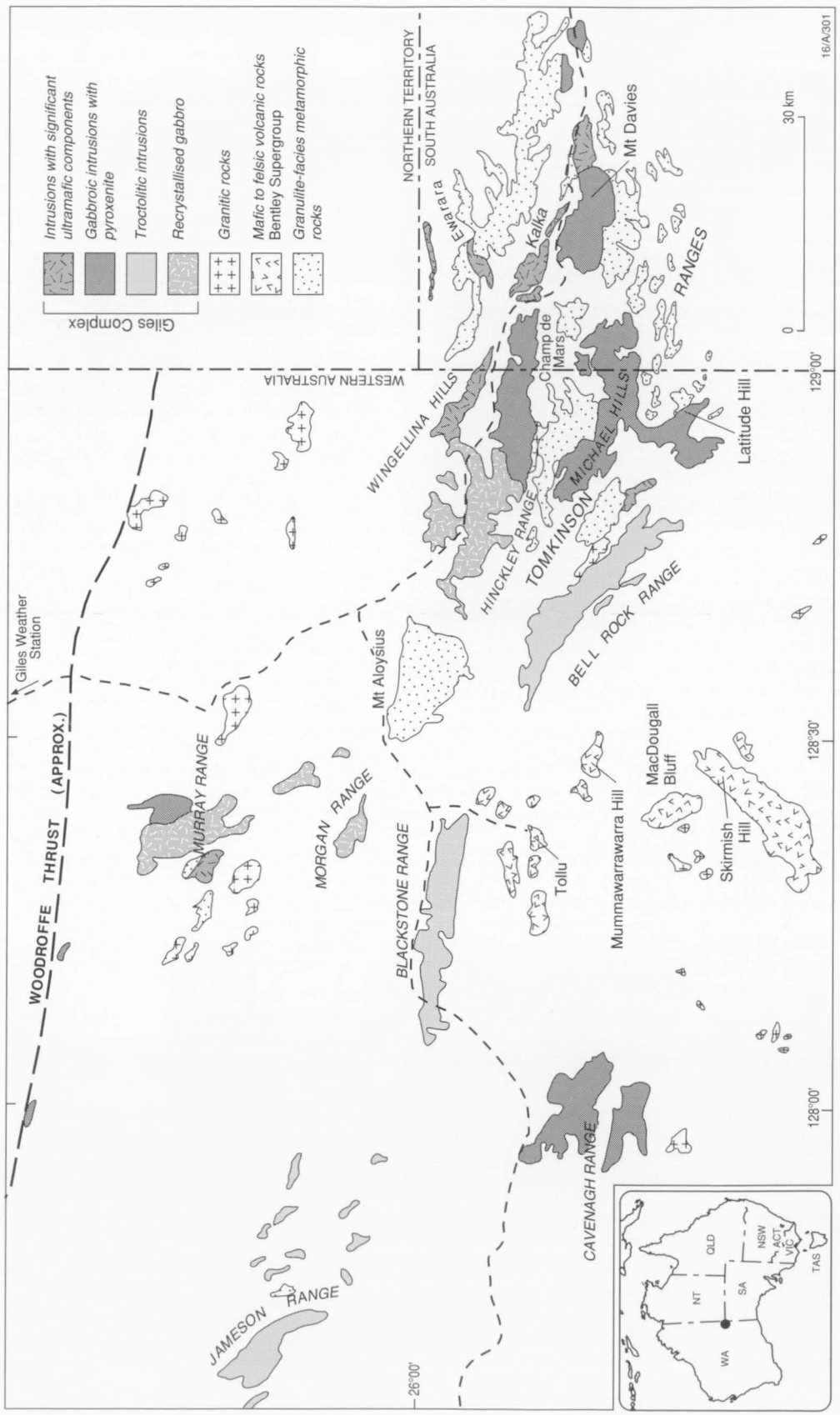

Figure 2. Geological map of the Tomkinson Ranges–Blackstone Range–Jameson Range region, western Musgrave Block.

Ranges, Blackstone Range, Cavenagh Range, Murray Range, and Jameson Range. Image processing of Landsat-5 Thematic Mapper (TM) and of Geoscan Mark-I airborne multispectral scanner (AMSS) data were conducted by C.J. Simpson (unpublished data), Glikson (1993, 1994), and Glikson & Creasey (1995). Total magnetic intensity (TMI) data are based on north–south-oriented 1600 metre-spaced AGSO aerial surveys.

The survey reported here proceeded in the following stages:

1987 Studies of the field relationships of, and systematic sampling traverses across, layered intrusions of the Giles Complex (Bell Rock, Hinckley Range, and Michael Hills) by A.Y. Glikson and C.G. Ballhaus. Detailed mapping of the Wingellina Hills layered intrusion by C.G. Ballhaus and A.Y. Glikson. Correlations of remotely sensed data by C.J. Simpson.

1988 Continued studies and systematic sampling of Giles Complex intrusions (Latitude Hill, The Wart, Bell Rock, Blackstone Range, Murray Range, Morgan Range, Cavenagh Range, and Jameson Range) by A.Y. Glikson and C.G. Ballhaus. Structural synthesis by T.C. Pharaoh.

1990 Redefinition of the Giles Project as the Musgrave NGMA Project. Field mapping conducted in the Davies (South Australia) and Bell Rock (Western Australia) 1:100 000 sheet areas by A.Y. Glikson and A.J. Stewart, including detailed mapping of the Champ de Mars area, the western part of the Ewarara area, and Mount Aloysius by A.J. Stewart, and mapping of the Ewarara–Teizi and Mount West areas by A.Y. Glikson.

1991 Completion of field mapping in accessible parts of the Bell Rock, Bates, Blackstone, Holt, and Finlayson 1:100 000 sheet areas by A.Y. Glikson and A.J. Stewart. Detailed mapping of Mount Aloysius by A.J. Stewart. Detailed structural studies in the western Hinckley Range and Champ de Mars areas by G.L. Clarke. Rock sampling for geochemical and isotopic studies by J.W. Sheraton and S-S. Sun.

Other reports and papers based on the present project include Ballhaus (1993), Ballhaus & Berry (1991), Ballhaus & Glikson (1989, 1992, 1995), Clarke (1992), Clarke & Powell (1991), Clarke et al. (1992, 1993, 1995a, b), Feeken (1992), Feeken et al. (1991), Glikson (1993, 1994), Glikson & Ballhaus (1989), Glikson & Creasey (1995), Glikson & Mernagh (1990), Glikson & Stewart (1992), Glikson et al. (1990a, b, 1991, 1995), Pharaoh (1990), Sheraton & Sun (1995, in press), Stewart (1993, 1995a, b), Stewart & Glikson (1991), Sun & Sheraton (1992), and Sun et al. (1996a, b). Some of these appear in a special issue of the AGSO Journal of Australian Geology and Geophysics (volume 16, numbers 1 & 2, 1995). This Bulletin is accompanied by the 1:100 000 (with 1:50 000 insets) Geological Map of the Giles Complex and Environs, Western Musgrave Block, Central Australia (Plates 1–3).

Terms used in this Bulletin follow the Glossary of Geology (Bates & Jackson 1987). The classification of Streckeisen (1976) and LeMaitre (1989) is used for igneous rocks and, where appropriate, their metamorphosed equivalents. Felsic granulite has a mafic mineral content of less than 15 percent, intermediate granulite 15 to 35 percent, and mafic granulite more than 35 percent. Anorthite (An) contents of plagioclase were mostly optically estimated from albite twinning. Grain-size terms are: fine, less than 1 mm; medium, 1 to 5 mm; and coarse, more than 5 mm. Terms used to describe thickness of igneous or metamorphic layering are: thin-layered, less than 5 cm; medium-layered, 5 cm to 2 m; and thick-layered, more than 2 m. The fold terminology follows Fleuty (1964), and the cumulate terminology used in descriptions of the Giles Complex is that of Irvine (1982).

Microprobe analyses of minerals from Giles Complex intrusions were carried out by C.G. Ballhaus on a Cameca SX50 Camebax electron microprobe in the Central Science Laboratory of the University of Tasmania. Analyses of minerals appropriate to constraining the P–T history of the western Musgrave Block were made by G.L. Clarke on the University of Sydney ETEC autoprobe and the University of Melbourne Cameca SX50 Camebax microprobe, both operated with an accelerating voltage of 15 kV and a beam width of 1–10 nm. Data were reduced using ZAF (Sydney) and PAP (Melbourne) matrix corrections.

Almost 600 whole-rock chemical analyses were carried out as part of the project. These comprise: (1) about 120 analyses of high-grade metamorphic rocks, mostly felsic orthogneisses, but including some paragneisses and mafic granulites; (2) about 150 syn to post-metamorphic granitic rocks; (3) about 240 analyses of Giles Complex mafic–ultramafic rocks, mostly from the Bell Rock, Blackstone Range, and Jameson Range troctolite/gabbro intrusions and the Murray Range pyroxenite/peridotite/gabbro intrusion; (4) about 50 analyses of dolerite and metadolerite dykes; and (5) about 50 analyses of mafic to felsic volcanic rocks from the Tollu Group. These analyses are stored in the AGSO ROCKCHEM database, and may be purchased separately or as part of the complete database. Most elements were determined by X-ray fluorescence spectrometry (XRF), major elements on glass fusion discs, using the method of Norrish & Hutton (1969), and trace elements on pressed powder pellets, using the method of Norrish & Chappell (1977). FeO was determined volumetrically, H_2O and CO_2 gravimetrically, and Li, Be, and Ag by atomic absorption spectrophotometry. Further details of methods and accuracy are given by Cruickshank & Pyke (1993). Details of the analysed samples are given in Appendixes II and III.

Mapping and remote sensing methodology

Mapping of high-grade metamorphic terranes

Outcrop-scale to meso-scale (up to a few hundred metres) lithological interleaving, penetrative deformation, and a scarcity of marker units are characteristic of high-grade metamorphic terranes, complicating regional-scale mapping (Glikson & Stewart 1992). The resolution of primary lithological relationships generally requires mapping of the least-deformed structural windows. In the Musgrave Block, the size of the terrane and limits on the time available for field work dictated that mapping proceeded in the following stages: (1) numerous detailed observations in relatively well-exposed creek bed and waterfall localities, (2) less detailed mapping of less well-exposed areas, and (3) interpolations between ground observations, utilising aerial photographs and multispectral images. While all the recorded information is digitally stored on Intergraph and Arc/Info systems, hard copy presentation is best achieved on a variety of scales, including (1) a 1:100 000 scale map (Plate 1), (2) 1:50 000 scale insets (Plates 2 & 3), and (3) small-scale figures presented with the text of reports. On 1:100 000 and 1:50 000 maps, lithological units which are less than 100 m thick could not be polygonised and are therefore represented as line units on Plates 1 to 3.

The pixel sizes for airborne magnetic and radiometric data flown at 1500 m line spacing are an order of magnitude larger than are necessary to resolve lithological units in high-grade metamorphic terranes. On the other hand, remotely sensed multispectral 10 m and 30 m pixel data have proved successful in providing targets for field mapping of features otherwise difficult to chart in the field. The generally excellent outcrop and the dry climatic conditions of the western Musgrave Block result in the accentuation of lithological differences on thin weathering crusts, whose clay/iron oxide/silica ratios correlate with the primary lithologies and are amenable to colour aerial photo and remotely sensed correlations. Examples in the present study include:

1. Discrimination between gabbro and ferrogabbro, due to the more clay-rich weathering crusts on gabbro, relative to more iron oxide-rich weathering crusts on ferrogabbro, e.g., in the Bell Rock (Fig. 89) and Blackstone Range intrusions (Fig. 108).
2. Discrimination between felsic granulite and calc-silicate and/or anorthosite units interlayered on a small scale, due to the more clay-rich weathering crusts on anorthosite, and more quartz-rich nature of weathered felsic granulite, e.g., in the Teizi area (Fig. 53).
3. Discrimination between gabbro and gabbro-derived mafic granulite, due to the silica-rich surfaces on the felsic vein-intruded mafic granulite, e.g., in the western Hinckley Range (Fig. 79) and northern Michael Hills (Fig. 71).
4. Discrimination between interlayered gabbro and pyroxenite, due to the more iron oxide-rich weathering surfaces on pyroxenite (although discrimination between pyroxenite of various types and ferrogabbro requires close ground control), e.g., in the Michael Hills and Kalka intrusions (Fig. 50).
5. Estimation of the degree of lateritisation of bedrock types, due to differences in the degree of iron oxide enrichment of weathered surfaces, e.g., pyroxenite along the northern flank of the Kalka intrusion (Fig. 50).
6. The use of composition of alluvial deposits as fingerprints allowing identification of their source terranes, e.g., clay-rich rings around isolated outcrops of felsic granulite and iron oxide-rich material shed from outcrops of mafic rocks (Fig. 50).

The remote sensing methods used in the present study (Glikson 1993, 1994; Glikson & Creasey 1995) are described below, and in more detail in Appendix I.

Multispectral analysis

A study of Landsat-5 Thematic Mapper (TM) multispectral image data (6 bands with a 30x30 m pixel size, and a seventh thermal band with 120x120 m pixel size) was conducted in conjunction with the detailed geological mapping of the Tomkinson Ranges (Glikson 1993, 1994; Glikson & Creasey 1995). Remotely sensed data available for the Tomkinson Ranges include the Landsat-5 TM 180 x 180 km scene path 105, row 78 (scanning date 27 October 1986). Statistical data for the image, sub-image, and relatively lithologically homogeneous test areas are given in the above references. The Landsat data are affected by the additive atmospheric radiance (path radiance or multiple atmospheric scatter) and by multiplicative factors (including atmospheric transmittance of solar radiation, solar illumination variations, reflected radiation at specific solar zenith and satellite nadir view angles, and sensor gains), and require calibration. This involves removal of the atmospheric influences, sensor gains, and sensor offsets from the scanned data. Ideally, direct comparisons should be made between the remotely sensed data and field or laboratory spectral measurements. For this purpose, relatively homogeneous pixels are selected (e.g., water, uniform green vegetation cover, open cuts of lithologically uniform material of known composition), and are compared with available mineral or rock spectra. Potential test pixels were examined in the Tomkinson Ranges by C.J. Simpson in 1987, but no homogeneous pixels consisting of a single component could be identified. Chrysoprase open cuts in silcrete near the Wingellina and Kalka settlements show high reflectance, as well as spectral features suggestive of contamination with iron oxide and clay. A eucalypt and grass-rich patch at the Wingellina school grounds provides a relatively homogeneous green vegetation pixel.

Image processing methods applied in the present study, following warping to the Australian Metric Grid (AMG) co-ordinates, included: (1) single band dark pixel correction; (2) band ratioing; (3) logarithmic residual (Green & Craig 1985), in which individual band digital number (DN) values are normalised through division by the within-pixel band mean, the resulting value being further normalised through division by the pixel array bands mean; (4) principal component analysis of single bands; (5) directed principal component analysis of band ratios: pc2(4/3;5/7), displayed as red, green, and blue (RGB) (Fraser & Green 1987); (6) pixel unmixing analysis, applying radiance correction for atmospheric scatter and resolving the proportions of individual end members (Bierwirth 1990); (7) devegetation of single band images, subtracting the vegetation end members resolved by the pixel unmixing analysis of Bierwirth (1990); and (8) unsupervised classification (Appendix I).

Significant correlations were found between images which emphasise iron oxide and clay–carbonate-dominated weathering surfaces and primary rock types. Discrimination of iron oxide is facilitated by several methods, including (1) log residuals of bands 5 and 7, (2) the 5/4 band ratio, and (3) the iron oxide end member of pixel-unmixed images. Discrimination of iron oxide, as shown by the 3/1 band ratio, is

partly masked by vegetation. Separation of goethite from haematite on Landsat-5 TM images was found to be difficult. Discrimination of clay and/or carbonate is facilitated by the following methods: (1) a high 5/7 band ratio, (2) the clay end member of pixel-unmixed images, (3) pc2(4/3;5/7) RGB images, and (4) indirectly by band 4, which highlights green vegetation, commonly implying clay-rich soils. Method 3 was found to be particularly effective in resolving clay from vegetation. Discrimination between carbonate and clay is difficult, but calcrete banks along creeks are characterised by a high albedo relative to clay. Discrimination of quartz and silica-rich weathering crusts is allowed by the combined high reflectance of bands 1 and 7, but this may be partly masked by clay or iron oxide coatings. This effect is particularly pronounced for deposits containing abraded quartz (e.g., dunes), as represented by the bands 1+7 component, e.g., the pc2(4/3;5/7) : 5/4 : 1+7 RGB image type that corresponds to devegetated clay : iron oxide : quartz–silica ratios (Figs 27, 50, 60, 71, 101).

Effective discrimination between a wide range of materials is allowed by (1) RGB images, which combine principal components of mineral and vegetation ratios with band ratios, (2) log residual images (Green & Craig 1985), and (3) pixel unmixing images, which allow resolution of some individual end members in composite pixels according to the method of Bierwirth (1990). A combination of the various image processing methods with a sound field knowledge of the petrological, structural, and morphological characteristics of the terrane allows discrimination of several surface types (Glikson 1994), including: (1) peridotite (partly magnesite covered); (2) orthopyroxenite (iron oxide-rich weathering); (3) clinopyroxenite (weaker iron oxide weathering); (4) gabbro (clay and carbonate-dominated weathering); (4) ferrogabbro (iron oxide-rich weathering); (5) anorthosite (high albedo carbonate-rich weathering); (6) mafic granulite (iron oxide and silica-rich crusts); (7) felsic granulite and granite (clay and silica-rich crusts), commonly crossed by lineaments representing the iron oxide-rich weathering of mafic dykes; (8) laterite (iron oxide-rich); (9) calcrete (high-albedo, common along creeks); (10) silcrete (very high albedo); (11) mafic source-derived alluvium (iron oxide-dominated); (12) felsic source-derived alluvium (clay and quartz-dominated); and (13) clay pans and silty (in places ferruginous) dry lake (playa) deposits. Discrimination of the composition of small isolated bedrock outcrops (inselbergs) is facilitated by their associated haloes of derived detritus, namely iron oxide-rich detritus around mafic outcrops and clay+quartz-rich detritus around felsic outcrops. Discrimination between old vegetation and fireburn varies between mafic terranes, where the increase in albedo in burnt areas is small and is highest in band 4, and felsic terranes, which show a stronger increase in albedo with a maximum in band 5. Burnt dune areas are brightest in band 4, signifying regrowth of green vegetation.

Preliminary image processing of two 5 km-wide strips of Geoscan Mark-I (13 bands, 10x10 metre pixel) airborne scanner imagery of the Tomkinson Ranges shows the superior spatial resolution and the significance of the thermal bands of this imagery (Honey & Daniels 1985, 1986). Quartz and silcrete-rich areas are expressed by a high 11/10 band ratio. Logarithmic residual images, for example RGB log residual bands 9:4:1, effectively resolve detailed lithological contrasts on a scale close to that of individual outcrops. An example is the Wingellina lateritic nickel deposit, where logarithmic residual images are capable of outlining areas underlain by fresh to weakly weathered gabbro from areas underlain by lateritised mafic and ultramafic rocks.

From the above, and as documented in more detail in Appendix I, the remotely sensed data allow discrimination of the following rock types:

Bedrock

1. layered to massive felsic to intermediate granulite.
2. massive to foliated granitoids associated with felsic granulite.
3. mafic granulite of two types: (1) associated with felsic granulite, and (2) recrystallised gabbro of the Giles Complex.
4. gabbro, gabbronorite, and norite of the Giles Complex.
5. anorthosite of the Giles Complex.
6. pyroxenite of the Giles Complex.
7. peridotite of the Giles Complex.
8. mafic–ultramafic plugs.
9. mafic, intermediate, and felsic volcanic rocks

Duricrust

10. calcrete and magnesite.
11. ferricrete and laterite.
12. silcrete.

Surface deposits

13. colluvium (coarse-grained arenite and conglomerate associated with pediments).
14. mafic source-derived alluvium, including plains and creek terrace deposits.
15. felsic source-derived alluvium, including plains and creek terrace deposits.
16. mixed source-derived alluvium, including plains and creek terrace deposits.
17. clay pans of clay or iron oxide-rich signature.

Good correspondence is observed between these groupings as mapped in the field and as observed on Landsat imagery, e.g., compare Plates 1 to 3 with Figures 27, 50, 53, 60, 71, 79, 89, 101, and 108.

Morphology and surface deposits

Geography and history of exploration

The Tomkinson Ranges–Blackstone Range–Jameson Range region straddles the Western Australia–South Australia–Northern Territory borders around Surveyor General's Corner (129°00'E 26°00'S), forming a 200x50 km west-northwest-trending belt (Fig. 2). The region includes four permanent Aboriginal settlements: Irrunytju (Wingellina), Pipalyatjara (Mount Davies), Blackstone, and Monte Maru (Jameson), as well as several outstations. Chief access tracks connect with Amata (east along the Gun Barrel Highway), Giles weather station (north along the Gun Barrel Highway), and Docker River and Warburton (west). Average daily summer temperatures range between 21°C and 36°C, and winter temperatures between 3°C and 18°C. Median annual rainfall is between 150 and 200 mm, with an average of 20 rainy days per year, principally during the summer months. Average annual moisture evaporation is about 3500 mm, resulting in arid conditions. Except for a few soaks or springs in creek beds, no permanent surface water exists in the area, and Aboriginal communities obtain water from bores, some of which contain dangerously high concentrations of nitrate.

A number of exploring parties travelled through the region in the late 19th and early 20th centuries. Ernest Giles and William C. Gosse traversed the area south of the Hinckley Range in separate exploratory parties in 1873. John Forrest traversed the country on his journey from Perth to the overland telegraph line in 1874. S.G. Hubbe travelled south of the Hinckley Range in search of a stock route to the west in 1895. R.T. Maurice, exploring a route from Fowlers Bay to the Rawlinson Range for the South Australian Department of Mines, passed through the Tomkinson Ranges in 1901. L.A. Wells went on a prospecting journey to the northwest of South Australia, which included the Tomkinson Ranges, in 1903. Frank Hann carried out investigations in the southern Tomkinson Ranges in 1907. Further details of the exploration of the area are given by Daniels (1974) and Feeken (1992).

A comprehensive geographical account of the Cooper, Scott, Bentley, and Talbot 1:250 000 sheet areas was given by Daniels (1974), who provided information on the flora and fauna of the Tomkinson Ranges. Laut (1977) reported on the Tomkinson Ranges in a report for the CSIRO Division of Land Use. Laws (1982) provided hydrological information for Aboriginal communities in the Blackstone region. The Southwestern Mining Company (unpublished reports, Mines Department, Western Australia) added some environmental information based on regional mapping and prospecting for lateritic nickel in the western Musgrave region. The surface deposits and vegetation of the Tomkinson Ranges were discussed by Feeken (1991, 1992).

Morphology

The Tomkinson Ranges–Blackstone Range–Jameson Range region consists of a series of ridges (Fig. 3A) and inselbergs, separated by alluvial flats and valleys (Fig. 3B) and dune-covered plains (Feeken 1991, 1992). Most outcrops are strongly dissected, reaching elevations of about 1000 m above sea level in the Hinckley Range (1014 m; Fig. 77A), Mount Davies (1053 m), Ewarara (1018 m), Dulgunja Hill, near Kalka (1009 m; Frontispiece; Fig. 3A), Teizi hills (871 m), Mount Aloysius (982 m; Fig. 3C), Bell Rock Range (874 m; Fig. 87A), Michael Hills (838 m), and Mount West (858 m). Duricrusts form low rises above valley floors and plains.

Elevated morphological units in the Tomkinson Ranges consist of mafic and, to a lesser extent, ultramafic rocks. These include the Hinckley Range, Bell Rock, Kalka, Mount Davies, Michael Hills, and The Wart (southern Mount West) intrusions, which weather to typical jagged ridge profiles (Figs 3A, E, F). Other elevated units consist of felsic granulite and granitic gneiss, including Mount Aloysius, Mount West, Ewarara, and numerous scattered outcrops. Ridges of gabbro or pyroxenite display jagged skylines and may contain prominent rock piles of slumped subangular boulders several metres across with little soil or vegetation in between. Examples of such boulder piles are common in the Bell Rock Range (Fig. 87A), where they consist largely of gabbro, and on the Kalka and Ewarara (Fig. 3E) intrusions, where the boulders consist mainly of pyroxenite. Boulder piles are formed where removal rates of fine grained inter-boulder material from steep rock falls exceed the erosional rates of resistant, little-weathered boulders of dolerite, gabbro, or pyroxenite. Where weathering of the gabbro is more advanced, the rocks display onion-like exfoliation features. No boulder piles are developed in mafic granulite which was formed by recrystallisation of gabbro, e.g., in the western Hinckley Range and Wingellina Hills. Mafic granulite is usually less resistant to erosion than gabbro, and forms more subdued morphological features. Mafic dykes which cut gabbro outcrops are commonly less resistant and thus tend to form local depressions (Fig. 87A). In contrast, mafic dykes cutting mafic granulite stand out as narrow ridges, as is common in the Wingellina Hills.

Felsic metamorphic and igneous rocks display relatively rounded, turtleback or inselberg morphological features, readily distinguished from the jagged mafic rock outcrops. Granite gneiss forms oval domes and tors in several areas, e.g., Champ de Mars (3G, H), and inselbergs surrounded by dunes, e.g., north of the Blackstone Range and west of the Bell Rock Range. Outcrops of felsic granulite, including quartz-rich metasedimentary units, may display transposed sedimentary layering, imparted by relict quartzite units, with good examples at Mount Aloysius and in the Ewarara–Teizi area. Mafic dyke swarms which intrude felsic rock commonly stand out as narrow knife-like ridges (Fig. 138A, B). Granitic veins intruding mafic granulite are generally more resistant to weathering than the latter, and form light-coloured bouldery ridges.

Surface deposits

Bedrock ridges are commonly engulfed by colluvial deposits, e.g., along the southeastern margin of the Hinckley Range and around the base of the Michael Hills. Elsewhere, notably at the base of Mount Davies and large parts of Ewarara–Teizi range, colluvium forms isolated occurrences. Pediments are associated with colluvium or are interspersed with alluvial fans, jutting out into the plains.

Intermontane valleys and intersecting plains in the Tomkinson Ranges show a general decrease in elevation towards the southwest, expressed by a southward-stepping decline from about 700 m above sea level in the northeast (Ewarara–Teizi area) to about 550 m in the south and southwest (south of Michael Hills), each step involving a fall of about 50 m. Plains and valleys are covered by lithic materials, which grade from gravel in parts of the flood plains and alluvial plains, through coarse sand in alluvial fans, to clayey red to red-brown soil at the centres of alluvial plains.

Sandy plains and dunes are widespread in the northwest, north, northeast, and south of the study area. Some dunes, particularly those near the northeastern edge of the Hinckley Range, contain interbeds of fine magnetite grains. Individual

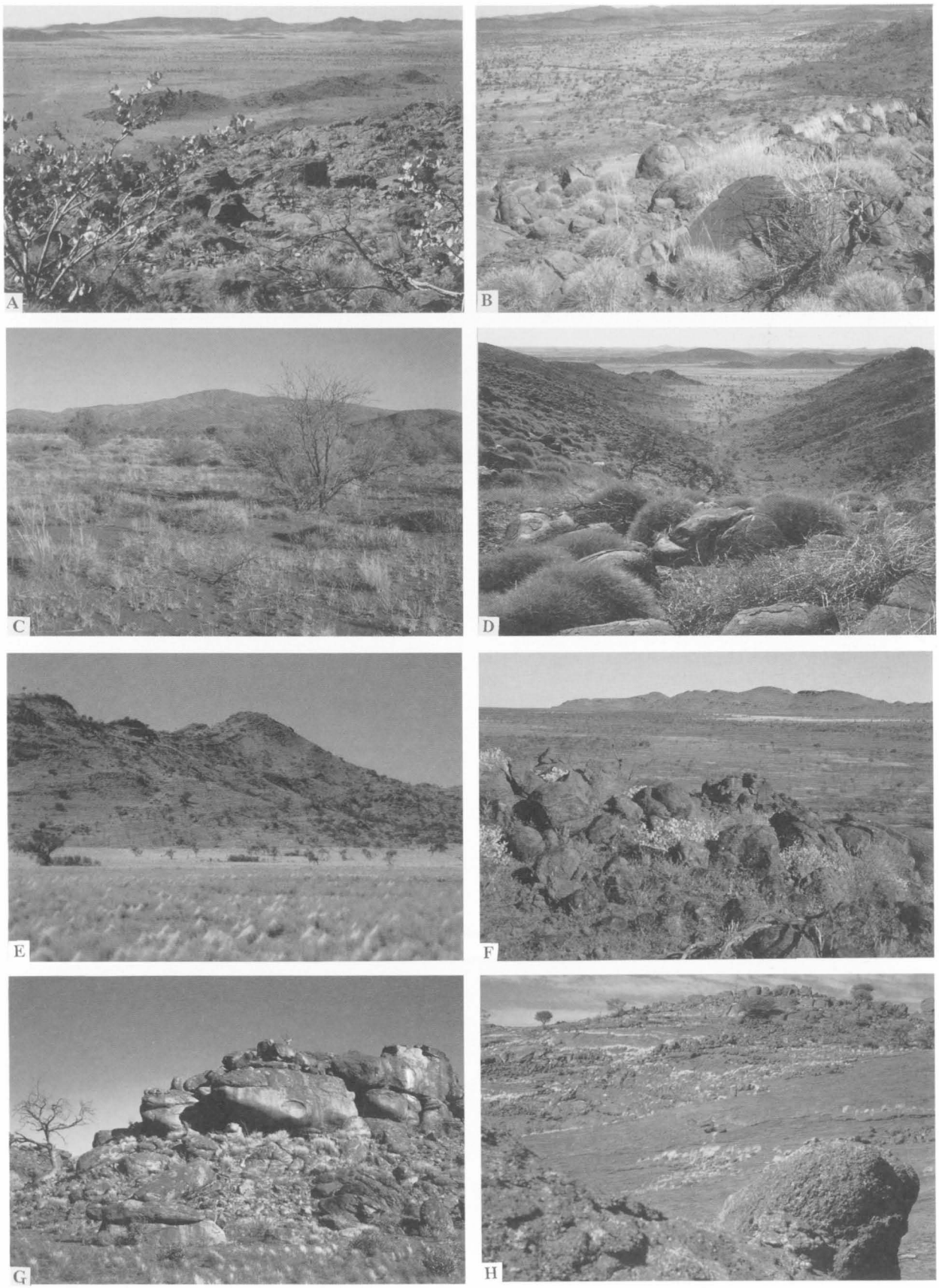

Figure 3. Morphological features of the Tomkinson Ranges. (A) Dulgunja Hill, near Kalka from the Hinckley Range. (B) Part of the Champ de Mars valley, between the Hinckley Range and Michael Hills. (C) Mount Aloysius from the south. (D) Valley in the western Hinckley Range. (E) Ewarara hills from the south. (F) Jameson Range from the southeast. (G) Granite tors, Carruthers Creek. (H) Granite tors, Champ de Mars valley.

dunes average 10 m in height, and are of several types. Network dune patterns display gradational changes to broad-crested linear dunes, some chain-forming, e.g., southwest of Mount Aloysius and northwest of the Bell Rock Range. Other sets of dunes are irregular and widely spaced. South of Mount Davies, a parallel system of narrow, single-crested dunes trends consistently southeast for many kilometres. Another type of dune occurs in groups or as isolated rises, which mostly fringe the northern, wind shadow, margins of small outcrops and inselbergs, e.g., west of the Hinckley Range, at Wandu Hill, and north and south of Mount Davies.

Drainage patterns, well defined within ridge areas, become diffuse and are rapidly lost once they enter the plains. The catchment areas of southward-directed drainage are larger than those of northward-directed drainage areas, a pattern clearly related to the general southward decrease in plain elevation. Consequently, northward-flowing streams are short, while the longest southward-running stream beds — Carruthers Creek and Pidgingadinga Creek — are a little over 25 km long and terminate in large floodplains. Sporadic intense downpours result in high-level debris along creeks, with the level of flood waters indicated by vegetation debris caught above creek banks and in trees.

Calcrete duricrusts are common along creeks and in the vicinity of mafic and ultramafic rock outcrops, but are less common or absent around felsic rock outcrops. Ferricrete outcrops occur mainly, but not exclusively, above ultramafic rocks, e.g., north of Wingellina, north of Dulgunja Hill, and at Mount Davies. Relict lateritic profiles also occur above felsic rocks, e.g., west of Teizi bore. Silcrete duricrusts may form part of relict lateritic profiles, e.g., 4 km east of Wingellina and along the southern flank of Dulgunja Hill. Silcrete is commonly interlayered with calcrete along creek beds.

Vegetation patterns

The distribution of vegetation in the Tomkinson Ranges is correlated with surface deposits. The floral habitat is dominated by mulga, spinifex, and annual and perennial grasses. Mulga can occur on plains, on outcrops, or among dunes, with or without other vegetation. An inverse relationship is seen between mulga and spinifex, i.e., mulga decreases or is totally absent where heavy spinifex growth occurs. In some areas, mulga has died back extensively in the recent past, as in parts of the valley between the Wingellina Hills and northern Hinckley Range, and the plains around Poonawarra, south of Michael Hills. In these areas, over 70 percent of the mulga has died, and little regeneration is evident. This decline is not obviously correlated with burning or with the rabbit population, and may suggest the effects of disease or long term climatic change. Spinifex tussocks dominate mafic and ultramafic rock outcrops, but are also common over some felsic rock terrains, as at Mount West, as well as in plains. Bunch grasses dominate on the plains and are also important on felsic granulite and granitic outcrops. Corkwood trees (*Hakea* sp) are locally prominent and commonly occupy margins of outcrops, including pediments and alluvial fans. Two species of *Grevillea* are prominent in dune fields on or near dune crests, and dense interdunal desert heath (*Thryptomene*) is associated with species of native fuchsia, and cassia.

Geological and geophysical framework

Stratigraphy of igneous and metamorphic units

The geology and bedrock stratigraphy of the Giles Complex and associated rock units, as determined by field relationships and isotopic age studies (Table 14) are summarised in Figures 2, 4, and 5, and Plate 1. The following stratigraphic sequence has been established:

MAFIC DYKES:

DB Type B quartz dolerite dykes: post-D_3, unmetamorphosed.

DC Type C olivine dolerite dykes: post-D_3, unmetamorphosed.

DA Type A intergranular dolerite dykes: post-D_2, pre-D_3, commonly metamorphosed.

BENTLEY SUPERGROUP (BS):

Tollu Group (TG):

BTH Hogarth Formation: mafic volcanic rocks.

BTS Smoke Hill Felsic Volcanics: rhyolite.

BTM Mummawarrawarra Basalt: amygdaloidal basalt and tuff.

BTD MacDougall Formation: basal quartz-pebble conglomerate, interbedded with cross-bedded arkose and sandstone

GRANITIC ROCKS:

GT Felsite, granophyre, granite (including rapakivi types), and pegmatite veins and dykes: syn to post-Giles Complex, post-D_2, pre-D_3.

GP Porphyritic and rapakivi granite stocks and associated felsite, granite, and pegmatite veins: pre-Giles Complex, post-D_2, pre-D_3.

GCH Orthopyroxene granite gneiss (charnockite) pods in felsic granulite: post-D_1, pre-D_2.

GILES COMPLEX MAFIC–ULTRMAFIC INTRUSIONS (GC):

HRG Hinckley Range gabbronorite intrusion (<6000 m): olivine gabbro, gabbronorite, troctolite, anorthosite, pyroxenite, marginal microgabbro, olivine–spinel mafic dykes; the western part of the HRG is extensively recrystallised to mafic granulite, intruded by felsic dykes.

BRTG Bell Rock troctolite/gabbro intrusion (c. 3800 m): troctolite, gabbroic troctolite, anorthosite, gabbro, microgabbro, minor dunite, magnetite-rich troctolite, and pods and lenses of cumulus magnetite.

TWGP The Wart gabbro/pyroxenite intrusion (c. 1900 m): feldspathic clinopyroxenite, clinopyroxenite, wehrlite, peridotite, olivine melagabbro, mafic dykes; possibly a basal segment of the Bell Rock troctolite/gabbro.

MHG Michael Hills gabbro intrusion (<8000 m): gabbro, orthopyroxenite, olivine-bearing ultramafic cumulates, abundant late sills of microgabbro.

LHGP Latitude Hill gabbro/pyroxenite intrusion (c. 8000 m): dolerite-textured gabbronorite, pyroxenite, feldspathic peridotite, gabbro, anorthosite, marginal microgabbro; a segment of the Michael Hills gabbro intrusion.

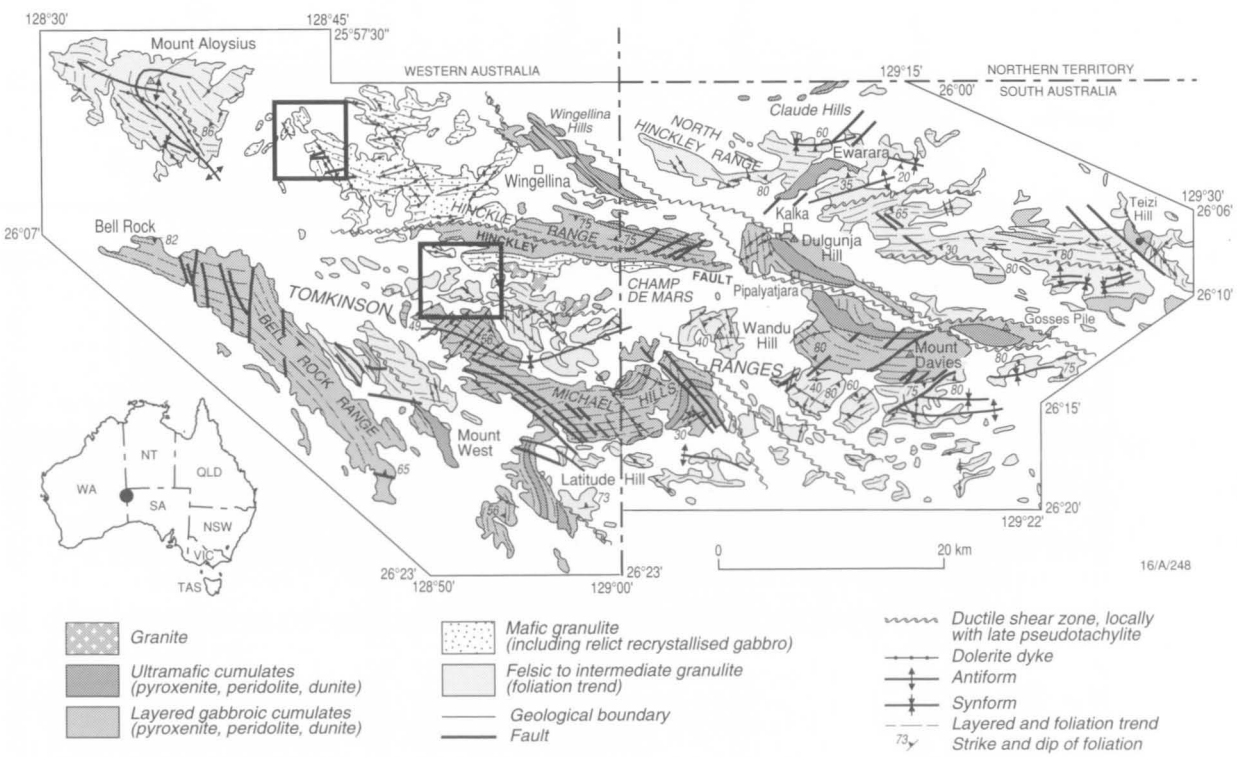

Figure 4. Geological map of the Tomkinson Ranges, showing locations of Figures 153 (top left) and 154.

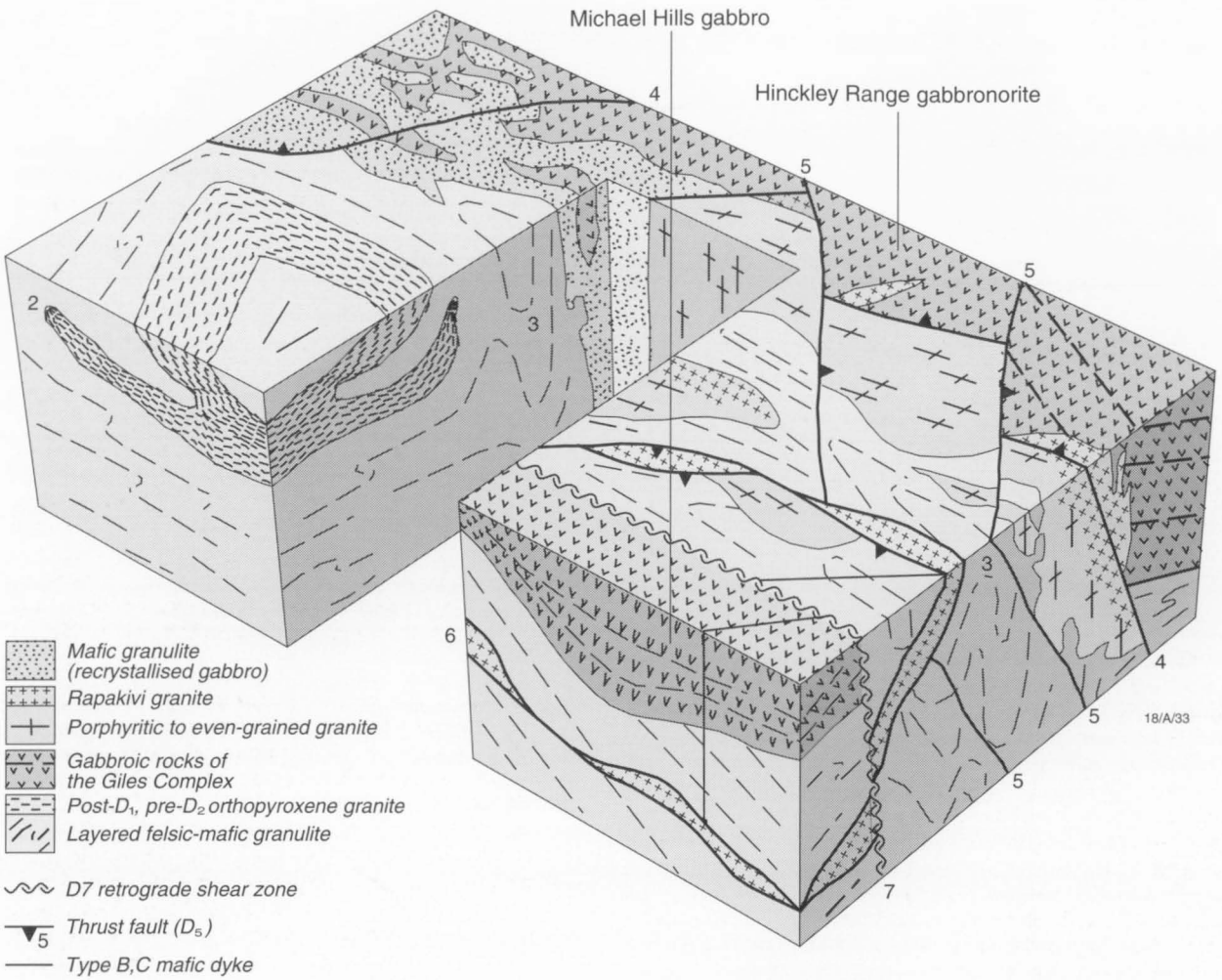

Figure 5. Block diagram showing relationships between geological units and structural elements in the Hinckley Range area (after Clarke 1992).

MDGP Mount Davies gabbro/pyroxenite intrusion (>7000 m): gabbro, gabbronorite, pyroxenite, peridotite.

KNP Kalka norite/pyroxenite intrusion (>5000 m): norite, anorthosite, olivine gabbro, olivine websterite, peridotite.

GPP Gosse Pile pyroxenite intrusion (>2000 m): orthopyroxenite, olivine orthopyroxenite, websterite, peridotite, norite.

EWP Ewarara pyroxenite intrusion (>500 m): bronzitite, harzburgite, pyroxenite, melagabbro.

WGP Wingellina Hills gabbro/pyroxenite intrusion (>1600 m): gabbro, gabbronorite, olivine gabbro, clinopyroxenite, wehrlite, minor peridotite.

CHPG Claude Hills peridotite/gabbro intrusion: a thin poorly exposed sliver of altered peridotite, pyroxenite, and gabbro.

MPG Murray Range pyroxenite/peridotite/gabbro intrusion (c. 2600 m): pyroxenite, peridotite, harzburgite, dunite, gabbro, gabbronorite.

UP Ultramafic plugs and stocks of pyroxenite, peridotite, and dunite; mainly in the Ewarara area and probably related to the Ewarara pyroxenite.

BTG Blackstone Range troctolite/gabbro intrusion (c. 3600 m): troctolite, olivine gabbro, anorthosite.

CG Cavenagh Range gabbro intrusion: flat-lying gabbro and gabbronorite, intruded by a dense (10–100 m) network of mafic dykes.

JTG Jameson Range troctolite/gabbro intrusion (c. 2500 m): troctolite, gabbroic troctolite, anorthosite, monomineralic vanadiferous magnetite units.

GRANULITE-FACIES PARAGNEISS AND ORTHOGNEISS:

MAC Mount Aloysius Complex: granulite-facies felsic gneiss, intermediate gneiss, and minor mafic granulite, interlayered on scales ranging from centimetres to hundreds of metres; the granulites are intruded by a few small bodies of granite, syenite, and pegmatite, and include garnet and sillimanite-bearing metasedimentary varieties and quartzite units; lithological types include *fns, fg, fna, fnm, fn, fnk, fnq, fni, fnv, fns,* and *mn* (see Plates 1–3); deformed by at least three deformation phases (D_{1-3}) and intruded by mafic dykes.

Units included in the MAC:

MWG Gneiss at Mount West: dominated by granitic orthogneiss and including units or enclaves of paragneiss and minor mica schist.

ETG Granulite of the Ewarara–Teizi area: dominated by paragneiss, including interlayered felsic granulite, por-

phyroblastic orthogneiss, and minor mafic granulite, anorthosite, quartzite, garnet and sillimanite-bearing granulite, and marble.

WIG Granulite at Wandu–Ilitjata: dominated by layered felsic granulite, including minor quartz-rich granulite, garnet–sillimanite granulite, and mafic granulite.

Regional structure

The regional structure of the western Musgrave Block is reflected by the total magnetic intensity (TMI) map (Tarlowski & Simonis 1992), shown in Figures 6 and 95. In the central Musgrave Block, west-northwest-trending magnetic lineaments are associated with the Mann Fault and Davenport Shear, which juxtapose blocks of granulite-facies gneiss with blocks of amphibolite-facies gneiss (Forman 1972; Collerson et al. 1972). In the western Musgrave Block, the Hinckley Fault follows a similar trend, but separates granulite-facies rocks to both the north and south. The trace of the Woodroffe Thrust Fault is less well defined, due to the low dip (20–30°) of this structure. The edge of the Musgrave Block is clearly defined by the contrast between the low frequency anomalies associated with areas of Neoproterozoic to Palaeozoic sediments of the Officer Basin in the south, and the high frequency anomalies associated with the Musgrave Block. At the western end of the block, distinctive magnetic anomalies associated with the Tollu Group volcanic rocks of the Bentley Supergroup persist for some distance to the west, indicating only a thin sedimentary cover in this area.

Several lineaments with north-northwest or northwest trends cut across the western end of the Musgrave Block, intersecting the west-northwest-trending structures (Figs 6, 95). One major lineament, which runs from Baggaley Hill to the Murray Range, west of the Bell Rock Range, appears to be associated with significant displacement at the margins of the Musgrave Block. Bending of the high-frequency anomalies associated with the Giles Complex bodies suggests that this zone has a dextral displacement of about 30 km. This lineament could be the cause of the re-orientation of structures in the northwest-trending zone from Mount West to Mount Aloysius and the reason for the major re-entrant in the anomaly pattern in the southern part of the block. Daniels (1974) inferred that the Tollu Group occupies large cauldron-subsidence structures above a contiguous layered mafic lopolith which includes the Bell Rock, Blackstone Range, and Cavenagh Range bodies. TMI data strongly suggest the existence of a 15 km diameter circular structure in the Tollu area, south of the Bell Rock Range (Fig. 95), but this is cut off from the Bell Rock and Blackstone Range intrusions by major faults.

Comparisons between the TMI (Fig. 6) and Bouguer anomaly (Fig. 7) maps with the geological maps of the Tomkinson Ranges and environs (Figs 4, 8; Plates 1–3) indicate the following features:

1. TMI highs may coincide with layered intrusions of the Giles Complex, notably the Bell Rock intrusion, or may coincide with felsic granulite terranes, such as Mount Aloysius, Kunatjara, and much of the Ewarara–Teizi area.

2. TMI lows may also coincide with layered intrusions of the Giles Complex, e.g., the Hinckley Range, Mount Davies, Gosse Pile, Ewarara, and Kalka intrusions.

3. Some intrusions include both high-TMI and low-TMI zones, e.g., the Michael Hills and Kalka intrusions. This suggests that remagnetisation of the high-grade terrane during metamorphism and shearing overprinted primary magnetisation patterns (Mutton et al. 1983).

4. Boundaries between TMI highs and lows commonly coincide with major fault lineaments, principal examples being (1) the fault-bounded western and eastern margins of the Bell Rock intrusion, (2) the northeastern boundary of the Bell Rock intrusion, which may signify a western extension of the Hinckley Fault, and (3) part of the Numbunja Fault (Figs 4, 6, 8). However, anomaly boundaries are more commonly displaced from, although they may parallel, major faults, e.g., the Champ de Mars Fault, much of the Hinckley Fault, the Wingellina Fault, and part of the Numbunja Fault (Figs 4, 6, 8). This suggests that the major faults dip at shallow to moderate angles, rather than being near-vertical.

5. A close coincidence exists between Bouger anomaly highs and the central parts of layered intrusions of the Giles Complex, including the Bell Rock, Michael Hills, Hinckley Range, and Mount Davies intrusions (Fig. 7). Conversely, Bouger anomaly lows coincide with felsic granulite–granite terranes, e.g., Mount West, Champ de Mars, and Wandu Hill. The Mount Aloysius felsic granulite massif and the Ewarara–Teizi felsic granulite ridges are marked by steep northward-dipping gradients. Steep gradients also mark the fault boundary between the Bell Rock intrusion and the granitic basement and overlying Tollu Group volcanic rocks to the southwest (Fig. 7).

Large-scale structures in the western part of the Musgrave Block are dominated by east–west-trending open concentric folds with steeply plunging fold axes, represented by flexuring of segments of the Giles Complex, e.g., the synformal flexure of the Michael Hills and antiformal flexures of Latitude Hill and Mount Davies (Fig. 4). These folds are in places related to movements along shear zones, e.g., the Champ de Mars and Numbunja Faults, reflecting adpression of the folds during ductile deformation. Most of these zones have an east–west trend, but on Mount Aloysius, the trend of the folds and limb attenuation zones is northwest. The east–west-trending deformation zones transect the felsic granulite and may continue into, or define the margins of, truncated layered intrusions of the Giles Complex.

Field and age relationships

The tectonic, metamorphic, and igneous evolution of the western Musgrave Block is summarised in Table 14 and Figure 5, and described in more detail in the sections on the Mount Aloysius Complex (Tables 1–4) and on the metamorphic and structural history. Hence, only a brief outline is given here in order to set the context for later sections of this Bulletin which deal with specific aspects of the geological history.

The oldest components identified in the Tomkinson Ranges are interlayered granulite-facies gneisses of both sedimentary and igneous origin. Metasedimentary rocks (paragneiss) include widespread, but volumetrically minor, orthoquartzite, calc-silicate granulite, and garnet±sillimanite-bearing gneiss. Metaigneous rocks are predominantly granitic (*s.l.*) orthogneiss, with minor mafic granulite. Protoliths of felsic orthogneisses appear to have been emplaced about 1550 and 1300 Ma ago, on the basis of Rb–Sr isochron ages (Gray 1978) and U–Pb zircon and Sm–Nd data (Sun et al. 1996a). High-grade metamorphism is estimated to have occurred at 1198±6 Ma (the U–Pb zircon age of syn-metamorphic granite gneiss, Sun & Sheraton 1992; Sun et al. 1996a), consistent with a Rb–Sr isochron age of 1204±17 (Gray 1978).

Evidence for two early deformation events (D_1 and D_2), which accompanied granulite-facies metamorphism, is preserved (Figs 31, 32). Except for F_2 hinges, S_1 has been rotated into parallelism with S_2, and only rarely can isoclinal F_1 folds

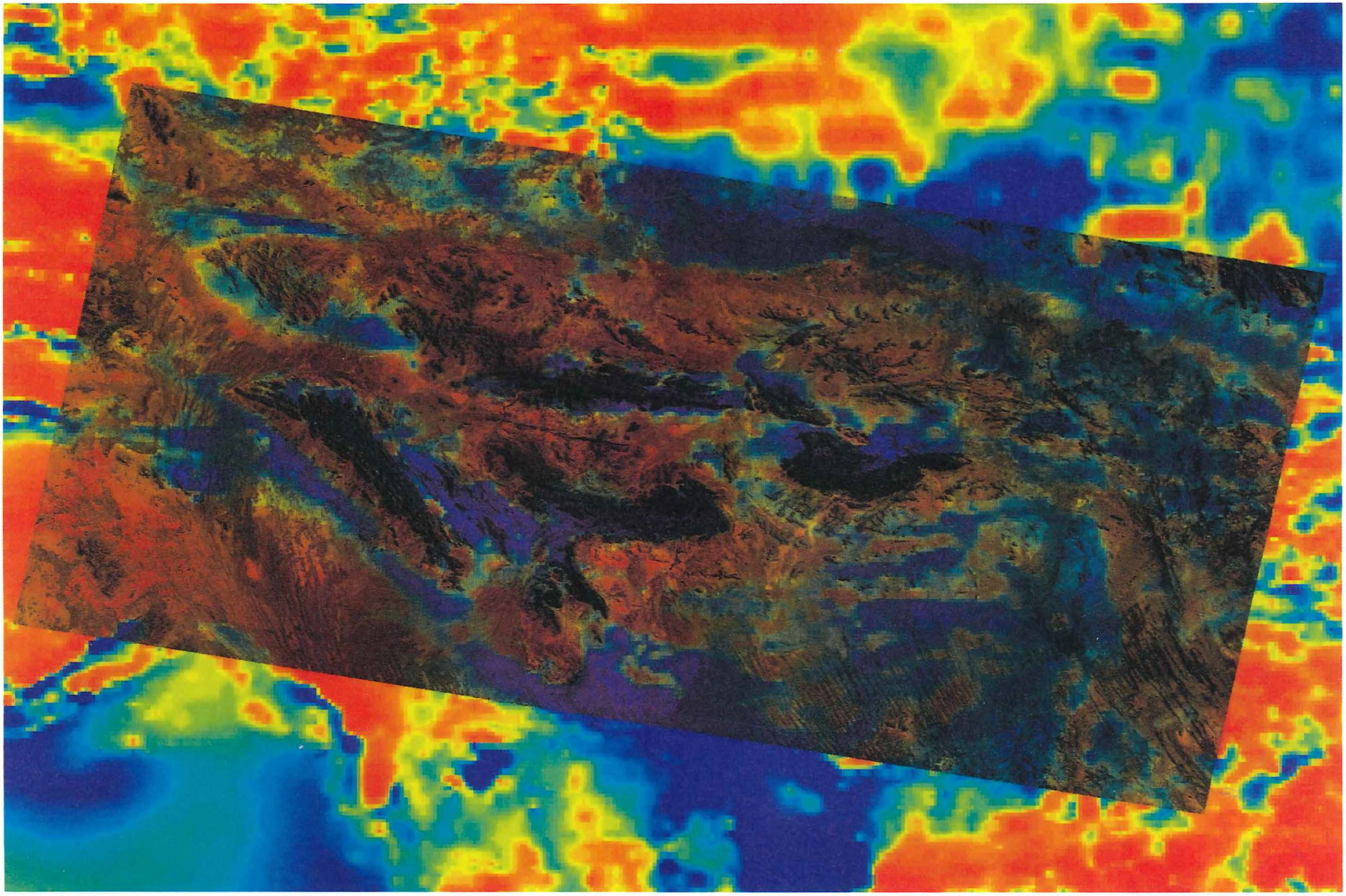

Figure 6. Total magnetic intensity (TMI) images of the Tomkinson Ranges; lighter areas are more positive. (A) TMI north gradient pixel map merged with Landsat-5 TM band 5 image. (B, top of facing page) TMI contour map showing magnetic highs (H) and lows (L), and interpreted geological boundaries from Figure 8.

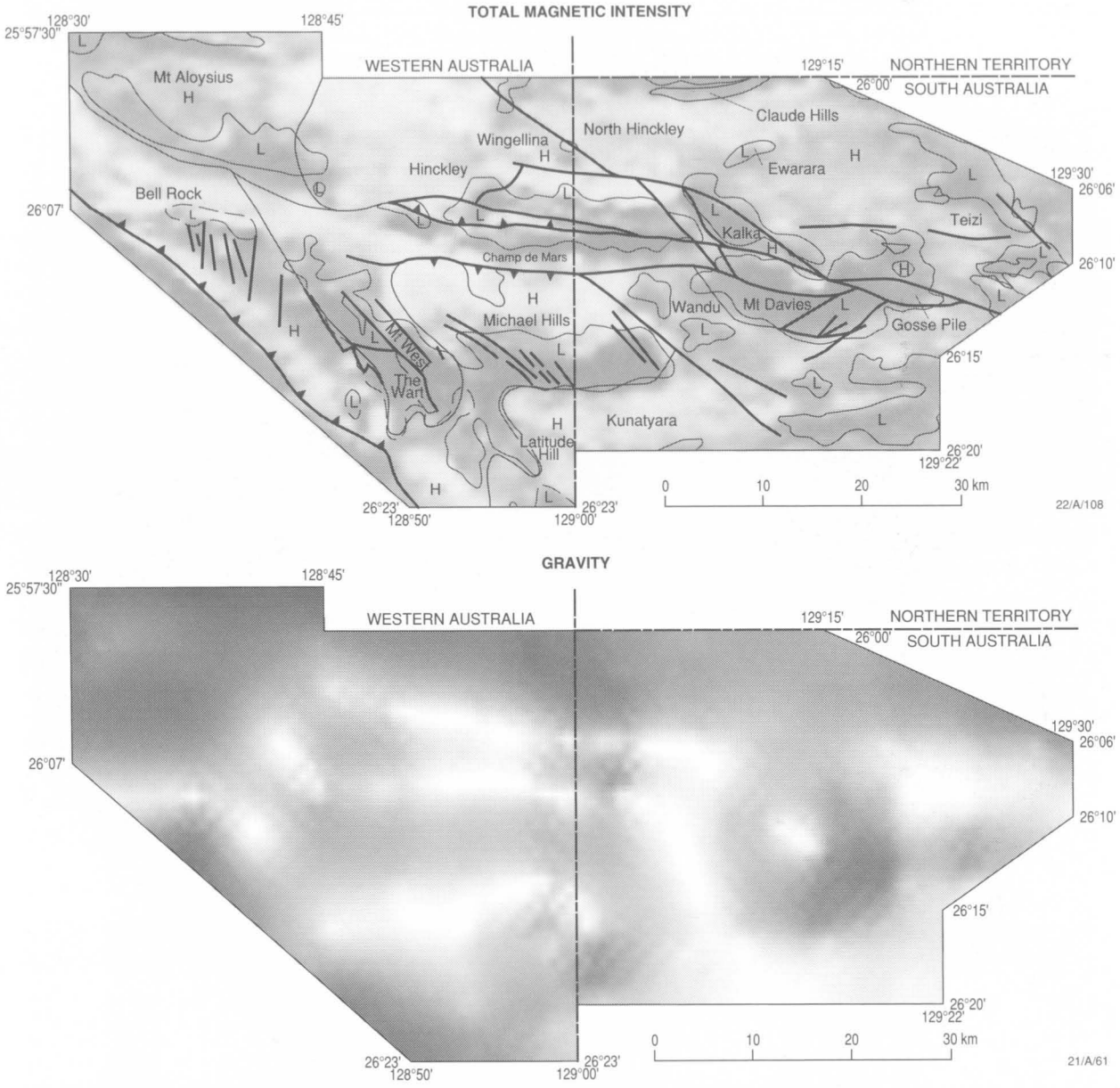

Figure 7. Bouguer gravity anomaly image of the Tomkinson Ranges; lighter areas are more positive.

be identified. D_2 produced mesoscopic to macroscopic isoclinal reclined F_2 folds, with an axial planar foliation (S_2) which is the pervasive gneissosity in the granulites (Clarke 1992; Clarke et al. 1995a). D_2 involved mostly pure shear, and resulted in a shallowly dipping reclined or recumbent terrane. Syn-metamorphic orthopyroxene granitoids ('charnockites') were emplaced between S_1 and S_2, and form pods and lenses of orthogneiss.

The field relations of the Giles Complex are commonly difficult to interpret, because, in most cases, the contacts are either unexposed or faulted (Fig. 4; Plates 1, 2). However, cross-cutting contacts with felsic granulite at the western tip of the Hinckley Range intrusion (Fig. 158D) indicate that its emplacement postdated S_2, although the contacts have been largely disrupted by later deformation (D_3 and younger events). Well-exposed intrusive contacts are seen along the northern basal contact of the Kalka intrusion (Fig. 49), the southern upper contact of the Mount Davies body (Fig. 55; Nesbitt et al., 1970), and in The Wart intrusion.

In some places, notably the western and southern parts of the Hinckley Range gabbronorite intrusion, marginal gabbroic rocks are extensively intruded by veins of K-feldspar megacrystic granite, locally with rapakivi textures, and microgranite, in places containing xenoliths of mafic granulite and amphibolite. Such felsic veins are interpreted as back intrusions generated by partial melting of felsic country rocks (Figs 77E, F, 87G, H). This is suported by U–Pb zircon dating, which indicates that at least some granitic veins are about 1050–1080 Ma old, very similar to the age of both the Giles Complex (1078±3 Ma) and the coeval Tollu Group volcanic rocks (1078±5 Ma, Sun et al. 1996a, b). However, some petrographically similar granitic rocks, also including K-feldspar megacrystic varieties, are considerably older (1188±4 Ma, Sun et al. 1996a). Contact effects generally die out rapidly into the interior of the mafic bodies.

The metamorphic country rocks and the Giles Complex are intruded by at least three generations of mafic dyke. The oldest, defined as type A and consisting mostly of northwest, or, less commonly, northeast and north-trending intergranular dolerites, is deformed by the next major phase of deformation

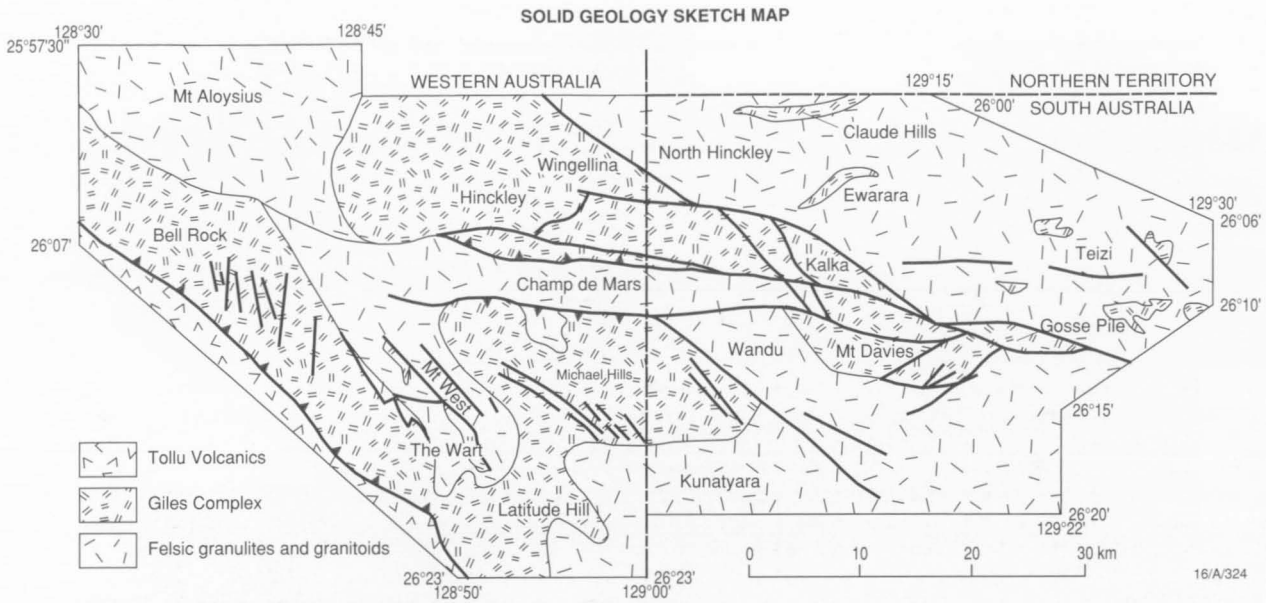

Figure 8. Interpreted solid geological map of the Tomkinson Ranges, based on geological mapping and TMI data.

(D_3). This produced the near-vertical, southeast-trending granulite-facies S_3 mylonitic foliation present throughout much of the western Musgrave Block. Much of the marginal recrystallisation of Giles Complex gabbroic rocks to mafic granulite, which was particularly extensive in the western Hinckley Range, was associated with D_3. D_3 structures comprise upright to reclined, tight to isoclinal, mesoscopic F_3 folds, with a steeply south-dipping S_3 axial plane mylonitic foliation (Fig. 30). A steeply plunging southwest-trending L_3 stretching lineation suggests southwest-directed compression and recrystallisation under dominantly simple (rotational) shear.

In general, D_3 is difficult to detect in massive gabbro. However, in felsic vein-injected recrystallised gabbro (mafic granulite), S_3–L_3 fabrics are dominant, and include penetrative rodding of felsic stringers related to simple shear rotation. Apart from those in the western Hinckley Range, deformation zones intruded by granitic veins, and probably also of D_3 age, occur in (1) the eastern fault margin of the Bell Rock intrusion (Fig. 87G, H), (2) the eastern faulted margin of The Wart intrusion (Fig. 64C), (3) a granite vein-rich zone of recrystallised gabbro south of the Wingellina Fault, and (4) the southern fault-bounded annealed portion of the Gosse Pile intrusion (Moore 1971a, b).

Type A dykes display marginal to complete recrystallisation of primary igneous textures to granulite-facies S_3 assemblages; their trend results from F_3 folding and is mostly aligned with the southeast-trending S_3 foliation. Mostly northeast-trending (rarely northwest-trending) type C olivine dolerite dykes, commonly fine grained and pyrite bearing, cross-cut S_3 fabrics and therefore postdate D_3. Northeast-trending type B quartz dolerite dykes, represent the youngest mafic intrusions in the area. Both dyke types are pre-D_4 (Clarke et al. 1995a).

The Hinckley Range and Kalka layered intrusions are bounded to the south by mainly east–west shear zones (D_4), consisting of mylonite and ultramylonite, which define the Hinckley Fault of Goode (1978) and its offshoots (Figs 4, 78). West of Dulgunja Hill, the Hinckley Fault splits into a number of west to northwest-trending mylonite zones which transect the mafic rocks of the Hinckley Range gabbronorite. The mylonitic D_4 deformation resulted in zones of intense recrystallisation, 10 to 100 m wide, with throws up to about 100 m estimated from mafic dyke displacements. Southeast-directed transport is indicated by S_4–L_4 geometry, including augen in deformed rapakivi granite in the Champ de Mars valley.

Many of the Giles Complex intrusions are cut and separated from each other by major mylonitic shear zones, which form an anastomosing pattern associated, in part, with faulted felsic granulite–granite core zones. The latter occupy intermediate positions between the layered intrusions and commonly formed loci of granitoid emplacement, the principal examples being the Champ de Mars and Mount West felsic core complexes (Fig. 4; Plates 1–3). The tops of the layered intrusions are invariably truncated by the shear zones, which cannot always be unequivocally assigned to a particular deformation event; the main examples are (1) Champ de Mars–north Mount Davies Fault, which truncates the tops of the north-younging Michael Hills and Mount Davies intrusions (Fig. 55), (2) the Wingellina–Kalka Fault, which truncates the tops of the Wingellina Hills and Kalka intrusions (Figs 49, 59), (3) the Mount Davies–Numbunja Creek Fault, which truncates the tops of the Mount Davies and Gosse Pile intrusions (Figs 52, 55), and (4) the Bell Rock–Blackstone magnetic lineament, which truncates the tops of the Bell Rock and Blackstone Range bodies, considered by Daniels (1974) to be parts of the same intrusion (Figs 4, 88, 107). Fault zones developed along the bases of mafic–ultramafic intrusions include the D_4 Hinckley Fault (Fig. 78), and the Mount West shear zones, which underlie the Bell Rock intrusion (Fig. 88).

In the Hinckley Range area, the dominantly east–west D_4 mylonitic shear zones are offset by mainly north-trending D_5 ultramylonite zones, which dip steeply east and show evidence for southwest-directed transport, with reverse throws of a few hundred metres (Clarke 1992; Clarke et al. 1995a). Broad east–west-trending D_6 ultramylonite zones are the most prominent of the shear zones, and it is probable that, in at least some cases, they overprint earlier (e.g., D_4) mylonite zones. The D_6 structures include major faults, such as the Champ de Mars Fault (Figs 4, 5) and the Woodroffe Thrust (Forman 1965) and its western extension in the Bates 1:100 000 sheet area (Stewart 1995b). The Champ de Mars fault is a zone of pervasive D_6 recrystallisation up to 500 m wide in felsic rocks, and up to 150 m wide in gabbro, where it is imprinted by extensive pseudotachylite (Glikson & Mernagh, 1990). The Woodroffe Thrust and related faults were involved in northward thrusting of the Musgrave Block over the Amadeus

Basin during the c. 550 Ma Neoproterozoic to Cambrian Petermann Ranges orogeny (Collerson et al. 1972; Forman & Shaw 1973; Glikson et al. 1990a; Clarke et al. 1995b), which resulted in the easterly trend of the Musgrave Block. This event produced high-pressure garnet+clinopyroxene-bearing assemblages in ultramylonite zones adjacent to the Woodroffe Thrust in the Bates 1:100 000 sheet area (Stewart 1995b). The final deformation recognised in the western Tomkinson Ranges comprises poorly exposed east-trending D_7 retrograde shear zones that dip north and show a reverse sense of movement.

It has not been possible to distinguish between the D_{4-7} events at Mount Aloysius (see next section), either because they are not represented there and the mylonites are of different generations, because their orientations are highly varied, or, quite probably, both. In either case, regional correlations are difficult. Northeast-trending sub-vertical brittle faults, discordant to the strike of the Giles Complex and mostly with a sinistral sense, e.g., at Mount Davies and the eastern end of the Hinckley Range, are clearly post-D_4. Northwest-trending faults displace layering in the Michael Hills intrusion with a dextral sense, and some are co-planar with the axial traces of northwest-trending cross folds. These conjugate fault sets may reflect north–south-directed compression, and may therefore have formed during D_6. The northwest and northeast trends of the brittle fracture systems are subparallel to those of two older (pre-D_4) mafic dyke swarms. The dominant northwest-trending swarm (probably type B) has an en-echelon pattern and is compatible with north-northwest compression, whereas the orthogonal northeast-trending set in the Michael Hills and western Hinckley Ranges (probably type C) indicates northeast-directed compression. In contrast, some mylonite zones are pre-D_4, as at Mount Aloysius where both syn-D_2 and, in particular, syn-D_3 mylonites are present (Stewart 1995a).

Northern boundary of the granulite-facies sector of the Musgrave Block: the Woodroffe Thrust Fault

The Woodroffe Thrust is part of a major system of south-dipping D_6 thrust faults that bound the southern margin of the Amadeus Basin, central Australia (Fig. 9). In the Musgrave Ranges, the Woodroffe Thrust dips south at 20–30° and separates high-grade metamorphic rocks in the south (the Fregon subdomain of Major & Conor 1993) from medium-grade metamorphic rocks in the north (the Mulga Park subdomain of Major & Conor 1993). In the present study, the Woodroffe Thrust zone has been traced into the Bates 1:100 000 sheet area north of the Tomkinson Ranges by Stewart (1995b) (Fig. 10), some 120 km farther west than recognised by earlier mapping, and as predicted from airborne TMI data. In this area, the thrust separates sub-eclogite-facies metamorphic rocks and granite in the south from deformed amphibolite-facies

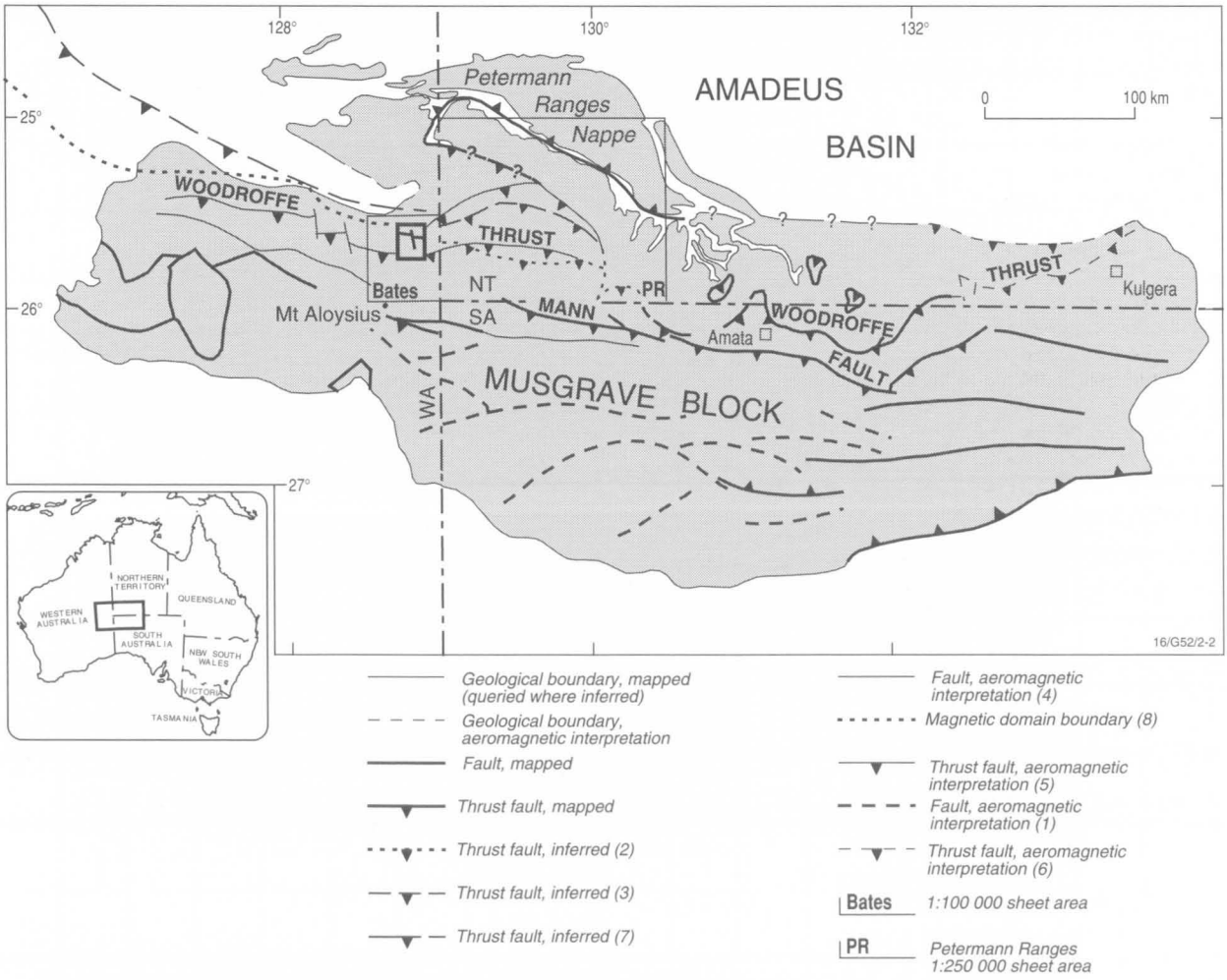

Figure 9. Structural map of the Musgrave Block showing major faults, locations of Petermann Ranges (PR) 1:250 000 and Bates 1:100 000 sheet areas, and area of Figure 11. [1]A.J. Stewart, AGSO, unpublished data; [2]Forman 1972; [3]D'Addario et al. 1976; [4,5]Pharaoh 1990; [6]Edgoose et al. 1993; [7]Myers 1990; [8]Shaw et al. 1995.

Figure 10. Largest exposure of the Woodroffe Thrust in Bates 1:100 000 sheet area, GR 827632, looking southwest. Entire hill is mylonite, with the most intense zone arrowed. Striped rock face at centre is location of Figure 13.

granite in the north (Fig. 11). The thrust dips gently south, and is marked by isolated exposures of mylonite derived from the granite north of the thrust. Lineations in the mylonite, and in the northern and southern terranes, are subhorizontal to gently plunging and east-northeast-trending, oblique to the strike of the thrust.

In the Bates 1:100 000 sheet area, the Woodroffe Thrust is defined by a mylonite zone that is about 1 km wide (Fig. 11). It separates granulite-facies garnet ± orthopyroxene ± clinopyroxene ± hornblende granite, patchily recrystallised to subeclogite facies (Clarke et al. 1995a), which was thrust over amphibolite-facies schistose biotite ± hornblende granite to the north. South of the mylonite zone, garnet granite has been patchily recrystallised to a groundmass of fine-grained quartz, plagioclase, garnet, and hornblende, enclosing large relict grains of K-feldspar. One kilometre south of the mylonite zone, garnet granite is cut by seams of mylonite up to about 1 m thick. North of the mylonite zone, schistose granite shows effects of the faulting over a much wider area than does the garnet granite south of the mylonite. The schistose granite is generally mylonitic and cut by mylonite seams; in places, however, it is recrystallised to a fine-grained mosaic. Four kilometres north of the mylonite zone, generally massive fine-grained recrystallised quartz veins occur throughout a northwest-trending belt 5 km long (Fig. 11). In some places, the quartz veins have a relict mylonitic lineation, but elsewhere are massively brecciated or sheared to quartz augen wrapped by secondary limonite.

The mylonite zone was derived from the schistose granite, and displays a transition in rock type, as follows:

- Along the northern and southern margins of the mylonite zone, the schistose granite is cut by numerous anastomosing extensional shear bands; these are a few centimetres thick and 10–20 cm apart (Fig. 12) in the north, and a few metres thick and several metres apart in the south.
- Near the centre of the zone, friable fine-grained schistose mylonite with small feldspar augen is intensely foliated and lineated.
- In the centre of the mylonite zone, the most intensely deformed rock comprises either thin gently south-dipping alternating layers of black aphanitic ultramylonite and pale mylonitic schistose granite (Fig. 13), or gently folded pods of mylonitic granite in ultramylonite. Steeply dipping extensional shear zones of mylonite cross-cut the gently dipping mylonite and schistose granite (Fig. 13).

All the granitic mylonitic rocks consist, in various proportions, of angular bent porphyroclasts of K-feldspar, sericitised plagioclase, and hornblende (in some samples), in a streaky groundmass of ribbon quartz and microcrystalline K-feldspar and uniformly oriented biotite aggregates (Fig. 14). A mafic dyke with relict garnet is metamorphosed in the mylonite zone to actinolite, bleached biotite, and sericitised plagioclase.

The mylonite zone is cut by a north-striking cross or tear fault which also has mylonite along it (Fig. 15) and is similar in grade to that along the east–west fault, suggesting that the two faults could have formed at the same time.

Foliation trends throughout the northern (Fig. 16A) and southern (Fig. 16B) terranes are at large angles to the east–west mylonite zone (Fig. 11), which dips gently to moderately south (Fig. 16C). Lineations in the two terranes are subhorizontal to gently plunging and mostly east-trending (Fig. 16D–F) and indicate a west-southwest–east-northeast movement direction. This coincidence of lineation orientation strongly suggests a common origin during the c. 550 Ma Petermann Ranges orogeny. Kinematic indicators are rare, and were observed in only five exposures at four locations (Fig. 17); three indicate movement of the top block to the east (Fig. 17A, C, D), and two indicate movement of the top block to the

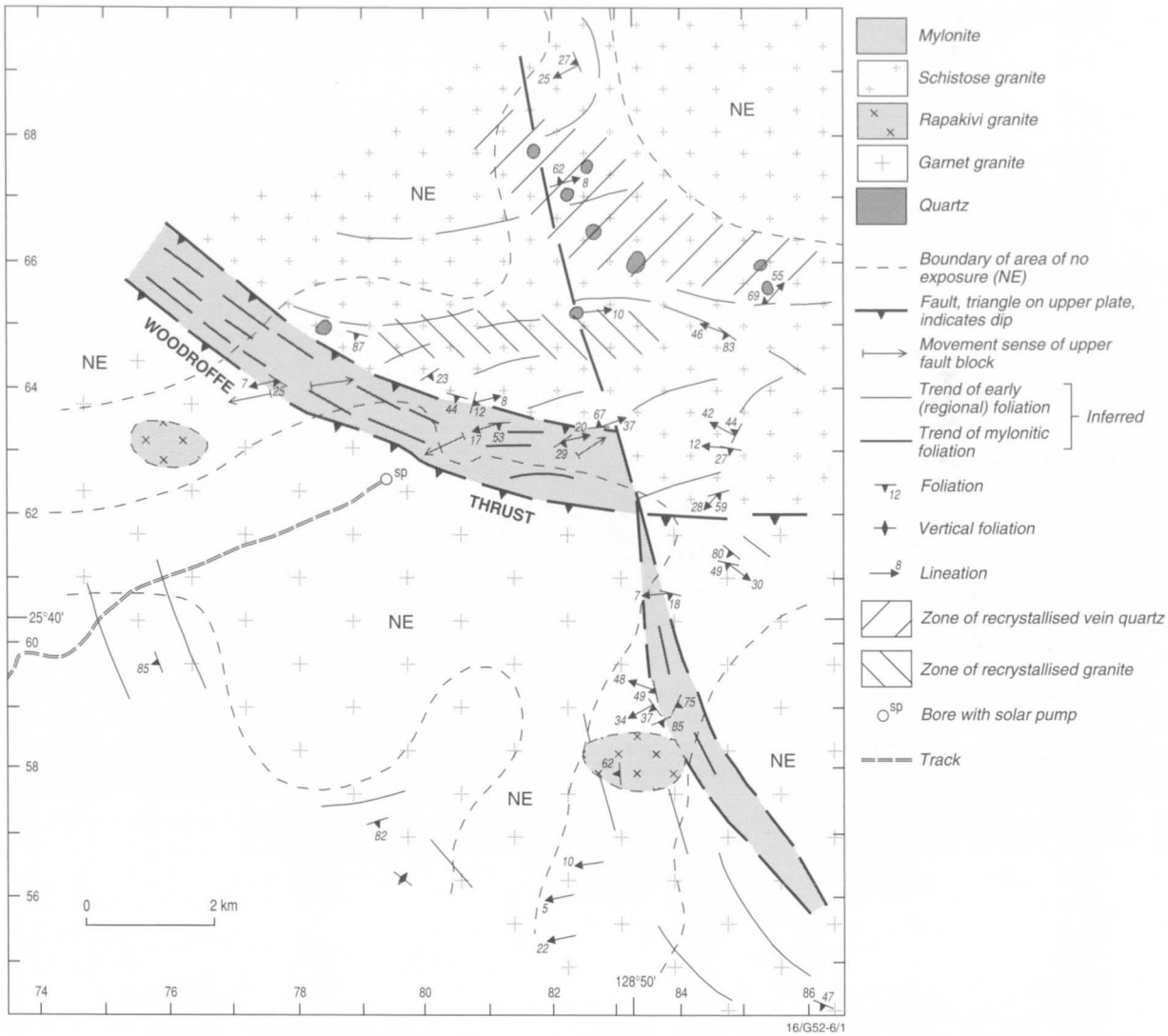

Figure 11. Geological map of mylonite zone, Bates 1:100 000 sheet area. Numbered ticks are 1 km intervals of Australian Map Grid (AMG), Zone 52.

west (Fig. 17B, E). The scarcity of shear indicators suggests that the fabric is not markedly asymmetrical, implying that large strain produced almost parallel shearing and flattening planes.

The Woodroffe Thrust has been interpreted as the root zone of the Petermann Ranges Nappe at the southwest margin of the Amadeus Basin (Fig. 9). In the Amata and Kulgera areas, northward movement on the thrust is well documented (Collerson et al. 1972; Bell 1978; Edgoose et al. 1993). Both the Woodroffe Thrust and Redbank Thrust Zone (Goleby et al. 1988; Shaw & Black 1991; Lambeck & Burgess 1992) formed in response to north–south compression of the Australian plate, which transmitted stress from the plate margins to the continental interior (Shaw 1991).

Southern boundary of the Musgrave Block: the Musgrave–Officer Basin Thrust Fault

The southern boundary of the Musgrave Block forms a major arcuate feature strongly expressed on Bouguer gravity and TMI images of Australia. It is manifested by an abrupt gravity gradient of up to 20 ns^{-2}, and by a TMI change from a short high-frequency wavelength magnetic variation characteristic of the Musgrave Block to a relatively subdued low-frequency magnetic signature over the Officer Basin. This boundary is important in understanding the structure and evolution of the central Australian region, but until now geophysical investigations of the feature have been hampered by logistic and access problems.

A major reflection seismic survey of the central Officer Basin recorded five regional lines, including a traverse across the southern boundary of the Musgrave Block (line 93AGS01, Fig. 18; Leven & Lindsay, 1995). These data show a series of pervasive, north-dipping reflection events within the Musgrave Block, which extend from at or near the surface to a two-way time (TWT) of around 10 seconds (about 30 km depth), with a northerly dip of around 30°. About 200 km south of the boundary, deep seismic data (line 93AGS05; Fig. 18) show a similar series of roughly parallel north-dipping basement structures which terminate at the base of the Officer Basin succession without disrupting the basin sediments. This suggests that they were truncated by an erosional event before deposition of the regionally extensive Willouran basal units of the Officer Basin (Pindyin Sandstone and Alinya Formation on Fig. 19).

Twenty kilometres north of the boundary of the Officer Basin, line 93AGS01 shows a set of prominent north-dipping

Figure 12. Schistose mylonitic granite sliced by extensional shear zones, northern margin of the Woodroffe Thrust, looking south. Rock consists of small angular porphyroclasts of strained microcline and oligoclase in a groundmass of recrystallised granuloblastic microcline, quartz ribbons, strings of broken hornblende grains, and anastomosing aggregates of small strongly aligned ragged flakes of biotite. Scale in centimetres and millimetres. Same locality as Figure 17E, AMG grid reference (GR) 812635.

Figure 13. Interlayered ultramylonite (dark grey) and mylonite (white) in most intense zone of the Woodroffe Thrust (striped rock face at centre of Fig. 10), looking southwest. Mylonitic foliation displaced by extensional shear zones (top block down to left, i.e., east-northeast), one zone 2.5 cm to right of scale, another 9 cm to left of scale. Ultramylonite comprises clasts of fractured and subrounded hornblende, nearly strain-free quartz, subrounded plagioclase, pink fractured garnet, rutile, and titanite in a streaky brown groundmass of very fine-grained biotite, opaque grains, and cryptocrystalline quartz and/or feldspar. Scale 15 cm long. GR 826630.

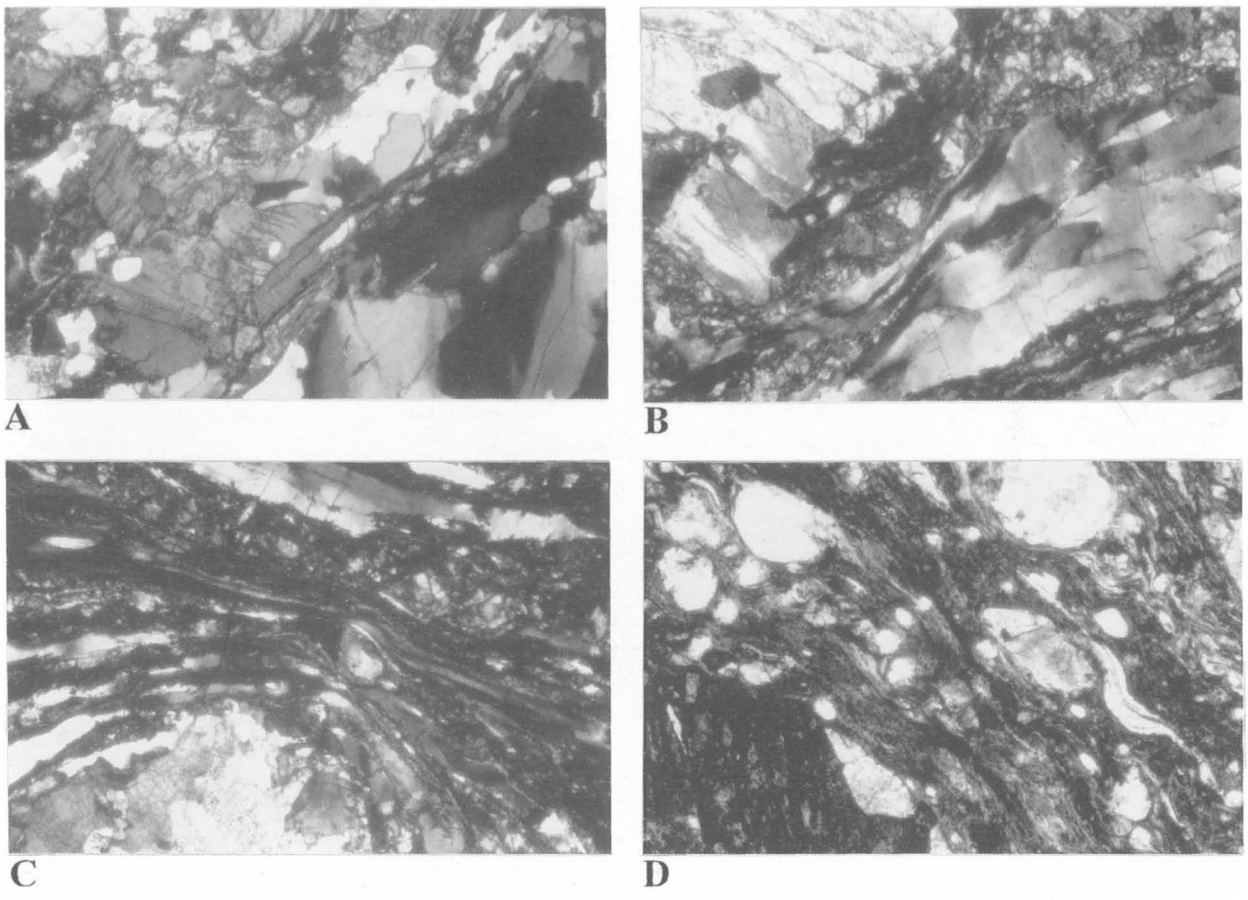

Figure 14. Granitic mylonitic rocks associated with the Woodroffe Thrust, all with crossed polarisers. Longer side of all photos 2 mm. (A) Tonalite at margin of mylonite zone, showing broken oligoclase (left), strained quartz (three large grains, right) and round titanite grain (centre of top edge); sample 91989421; GR 802643. (B) Granite mylonite at centre of mylonite zone, showing broken microcline porphyroclasts (top left), large lenticle of flattened elongated quartz (right), and granulated oligoclase (middle); 91989423A; GR 813635. (C) Granite mylonite at centre of mylonite zone, showing laminae of recrystallised platy quartz (white, left), extremely flattened little-recrystallised quartz (white, top), unresolvable biotite (black), and granulated microcline and oligoclase bent around large microcline porphyroclast (bottom); 91989423A; GR 813635. (D) Granite ultramylonite at centre of mylonite zone comprising round porphyroclasts of nearly strain-free quartz (white), subrounded plagioclase (grey, right of centre), and large broken porphyroclast of hornblende (bottom left) in a dark streaky groundmass of unresolvable biotite and opaque grains, and small, bent, highly flattened lenses of cryptocrystalline quartz and/or feldspar; 91989425E, GR 826630.

basement structures which bifurcate at a branch point around 3 seconds TWT (about 7.5 km depth) beneath CMP 3300 (Fig. 20). The lower branch of this bifurcation forms a basal decollement which soles into the evaporitic Alinya Formation near the base of the sedimentary succession as a blind thrust. The upper branch of this bifurcated thrust flattens at depths of less than 2 km. Its surface expression has not been mapped because of the blanket cover of Pleistocene sand dunes. However, its surface location corresponds to a significant topographic ridge, with surface elevation decreasing southwards by 40 m over 2.5 km, which can be inferred to indicate recent thrust movement on this fault zone.

Near the northern margin of the Officer Basin, these basement features are genetically related to the steep northern margin of the basin. Figure 21 shows that at the present northern margin, Palaeozoic strata have been folded into a homocline. Farther east in the eastern Officer Basin, foreland basin sediments of Devonian age indicate movement of this fault system during the Alice Springs orogeny. The margin is thus erosional, and the original northerly extent of the basin is unknown. South of this structure (Fig. 21), sediments of the central Officer Basin have suffered relatively little disruption, in spite of their proximity to this major thrust boundary.

Figure 21 shows the detailed structure of the northern margin of the Officer Basin, and the structure of the thrusts in the Musgrave Block. Only the upper succession of the Officer Basin strata has been folded into the homoclinal upturn at this margin. The lower succession, interpreted to include part of the Alinya Formation and the Pindyin Sandstone, has been abruptly truncated beneath CMP 4520. North of this, portions of stratigraphic units with a similar reflection character to this lower succession are evident, suggesting that, in this region, the lower succession has failed by thrust faulting, rather than being folded into a homoclinal upturn. A complex set of faults has been interpreted in this disrupted zone beneath the homocline, but these faults do not penetrate into the upper succession.

South of the thrust margin, the lower succession has been compressed into several broad kinks over a distance of 30 km (Fig. 22). These kinks have an amplitude of around 150 m and are unconformable with the more gently folded strata of the upper succession. They represent a net shortening of the lower succession relative to the upper succession, and are interpreted to have formed by flowage within the Alinya Formation (an evaporitic unit) in response to the compression of the Officer Basin sediments during the southward thrusting

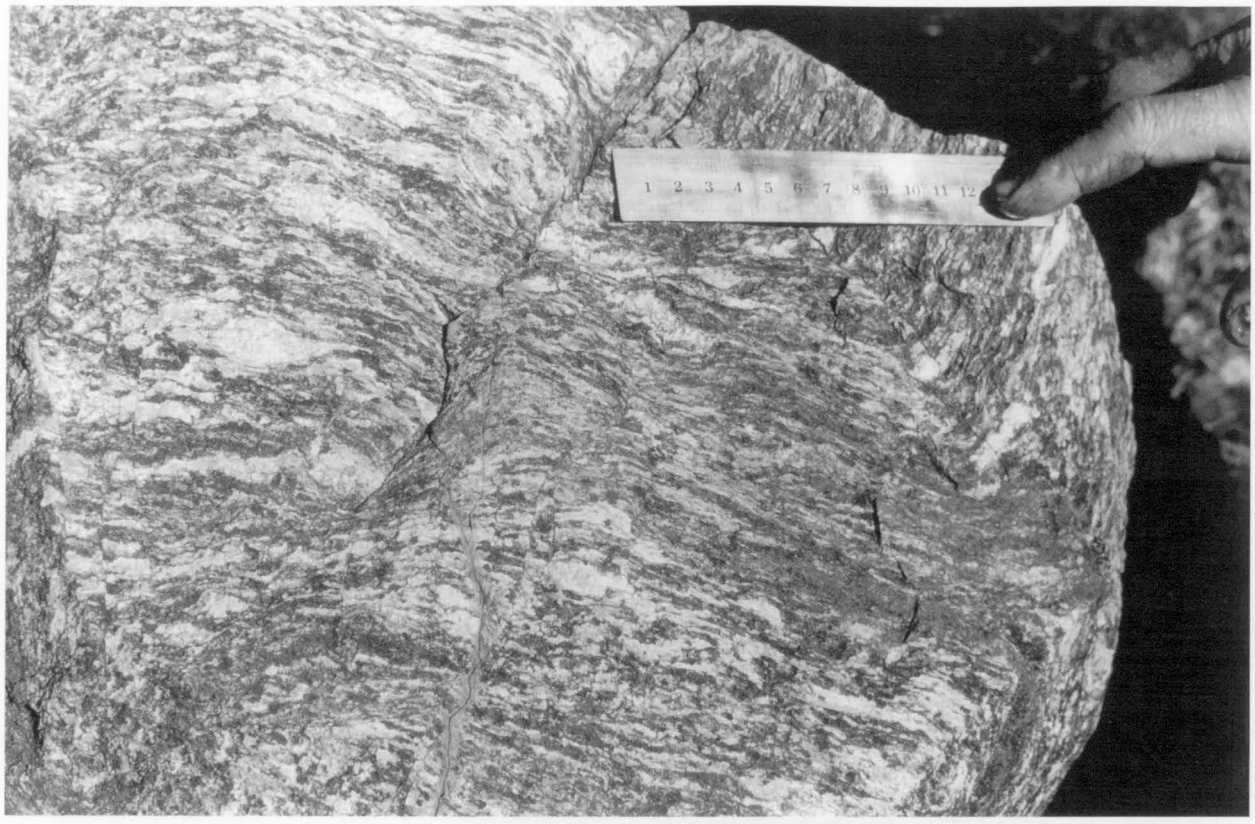

Figure 15. Garnet granite mylonite in tear fault crossing the Woodroffe Thrust. Augen and lenticles of fine-grained recrystallised K-feldspar (white), deformed and recrystallised lenticles of quartz (pale grey), and broken and cracked garnet, in a dark grey groundmass of cryptocrystalline quartz, feldspar, garnet microclasts, hornblende grains, opaque grains, and unresolvable microcrystalline biotite. Scale 15 cm long; GR 838593.

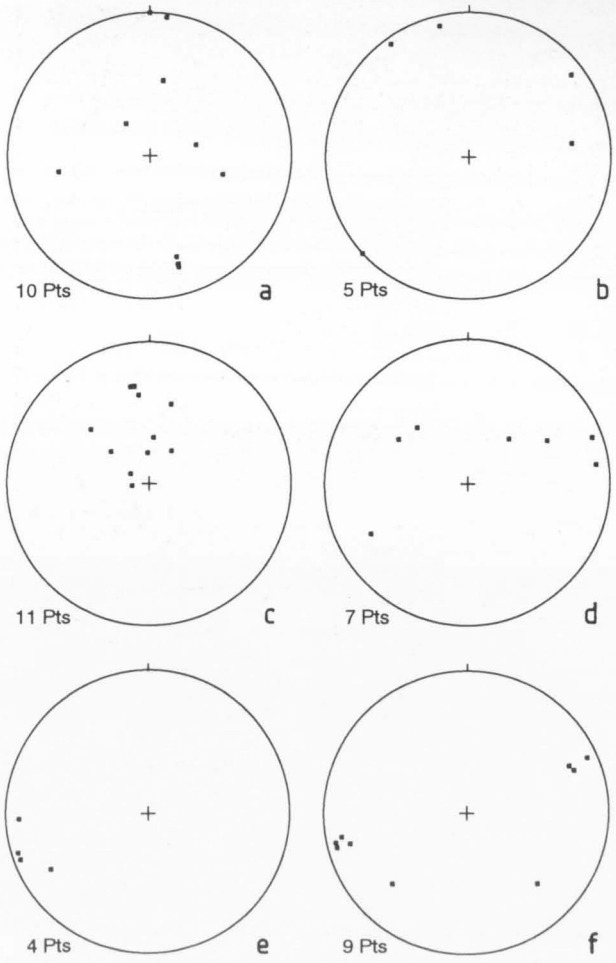

Figure 16. Stereograms of foliations and lineations in and near the Woodroffe Thrust. (a) Poles to foliation in schistose granite of northern terrane. (b) Poles to foliation in garnet granite of southern terrane. (c) Poles to foliation in main and subsidiary mylonite zones. (d) Lineations in northern terrane. (e) Lineations in southern terrane. (f) Lineations in main and subsidiary mylonite zones. Equal-area plots on lower hemisphere. Stereograms plotted using GEORIENT program devised by R. Holcombe, University of Queensland.

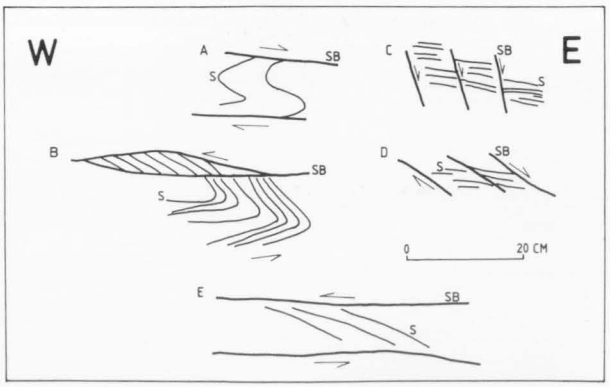

Figure 17. Sketches of shear indicators in granitic mylonite, Woodroffe Thrust. (S) Mylonitic foliation. (SB) shear bands interpreted as extensional because of observed extensional offsets, large angle to foliation, and paucity of bending of foliation near shear bands. (A,B) Northern margin of Woodroffe Thrust. (C,D) Southern margin of thrust. (E) Northern margin of thrust, same locality as Figure 12.

of the Musgrave Block. As this lower succession is not deformed by the homoclinal structure, its shortening has been accommodated by kinking and ductile flow within the evaporitic units south of CMP 4300, and by imbrication and extensive brecciation north of CMP 4300, forming a triangle zone.

In contrast, the clastic upper succession responded to the compression by slippage along a bedding plane separating the two successions, and back-thrusting over the imbricated and brecciated lower succession in the triangle zone (Fig. 23). This back-thrusting of the upper succession must have post-dated formation of the adjacent brecciated lower succession in the triangle zone, as faults in this zone do not penetrate into the homocline. We interpret this structure to be the result of bedding-plane slippage on a surface within the Alinya

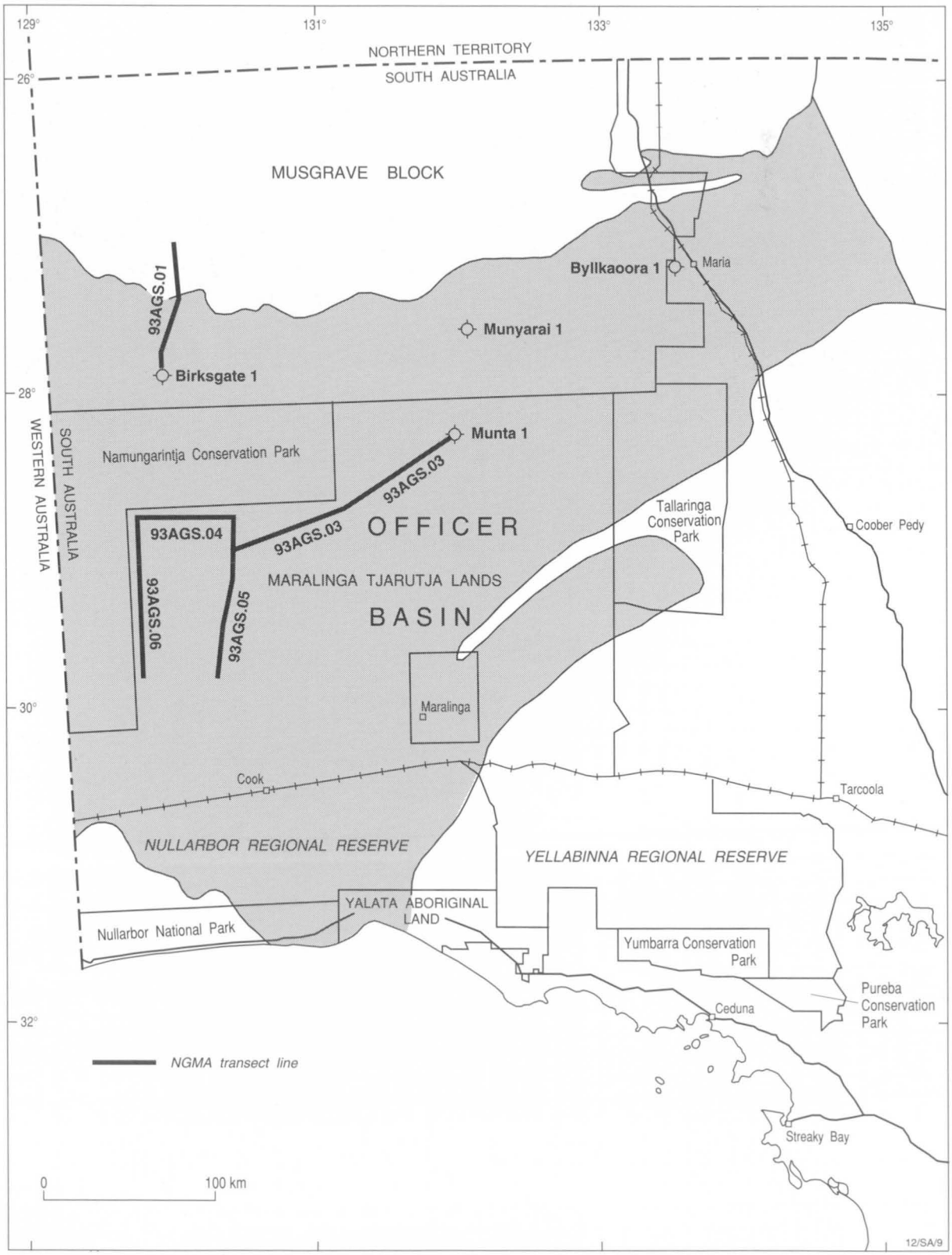

Figure 18. Map of the Musgrave Block and the Officer Basin (shaded grey) and surrounding regions of western South Australia, showing location of the five NGMA seismic reflection traverses.

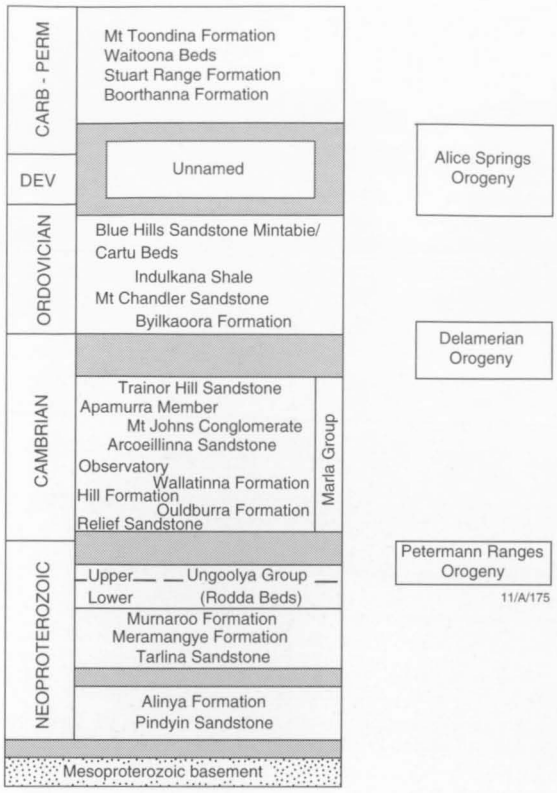

Figure 19. Simplified stratigraphic succession of the central Officer Basin.

Formation, which accommodated different mechanical responses to compression in the two successions.

The TMI image (Fig. 24) gives a clear picture of the structure of the Musgrave Block, and provides structural information over an area of the Officer Basin where the geology is generally obscured by sand dunes. The image illustrates the changing nature of the Musgrave Block's southern margin along strike. To the west, the TMI image suggests that this margin is a relatively sharp feature, involving a single thrust fault or a narrow fault zone, whereas to the east of meridian 130°30′E, the margin gives the appearance of having a stepped structure, suggesting the presence of multiple thrust sheets of basement.

This difference in character along the southern margin of the Musgrave Block corresponds to a change in boundary structure associated with the thrusting. West of 130°30'E, this boundary appears to have a relatively simple structure, with tectonic disturbance of the basin sediments constrained to a narrow region close to the edge of the Musgrave Block. In this central region, the Musgrave Block appears to have encountered little impediment to its southward thrust-sense movement. In contrast, the structure east of 130°30′E in the eastern Officer Basin is relatively complicated, as evidenced by basement-involved thrusting extending a considerable distance southwards into the basin (Lindsay 1995). Here, movement of the Musgrave Block was obstructed by the Gawler Craton to the southeast, and the Officer Basin sequence was deformed in the confined space between the Musgrave Block and Gawler Craton.

Aeromagnetic TMI data were collected along the seismic lines after seismic acquisition. TMI data along line 93AGS01 have long-wavelength characters south of CMP 4100, and a short-wavelength ('high frequency') response characteristic of

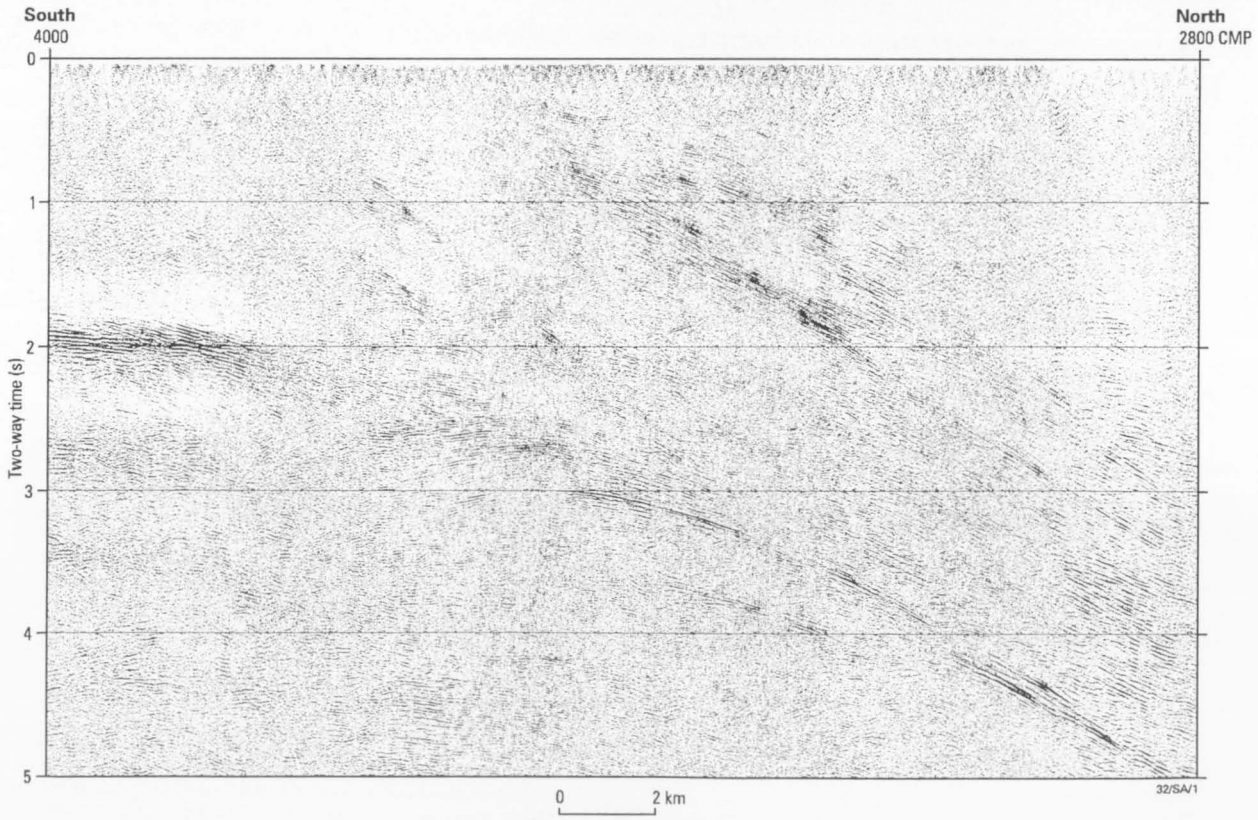

Figure 20. Portion of the seismic traverse 93AGS01 between CMP 2800 and 4000, showing the top 5 seconds two-way time (TWT) of the upper crustal structure beneath the southern boundary of the Musgrave Block. A prominent series of north-dipping structures is imaged, the lower set bifurcating around 3 s TWT (about 7.5 km depth) beneath CMP 3300. This lower branch flattens and soles into the base of the sedimentary succession farther south.

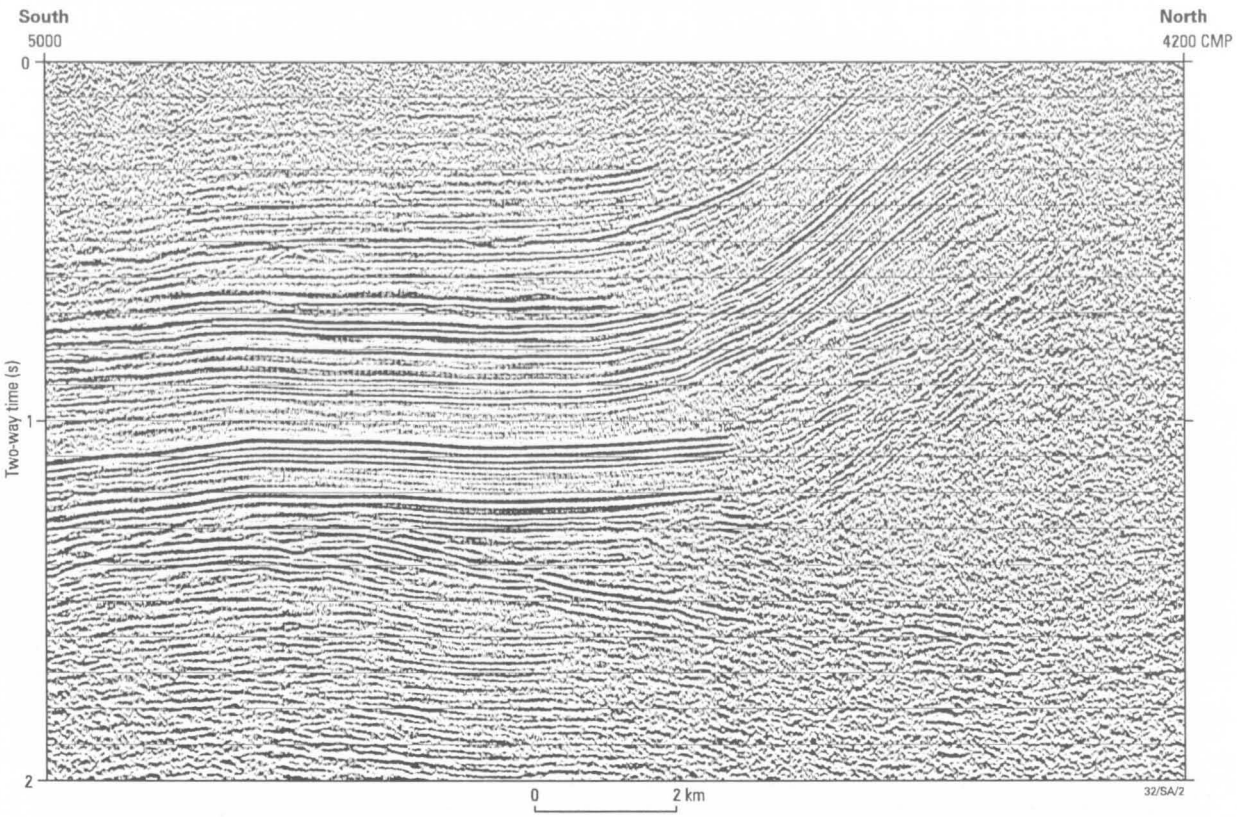

Figure 21. Portion of the seismic traverse 93AGS01 between CMP 4200 and 5000 (2 s TWT), showing the sedimentary structure at the northern margin of the Officer Basin. The sedimentary strata are divided into two successions, the upper succession folded into a homocline, and the lower succession abruptly truncated beneath CMP 4520. A prominent north-dipping structure soles into the base of the sedimentary succession at 1.4 s beneath CMP 4800.

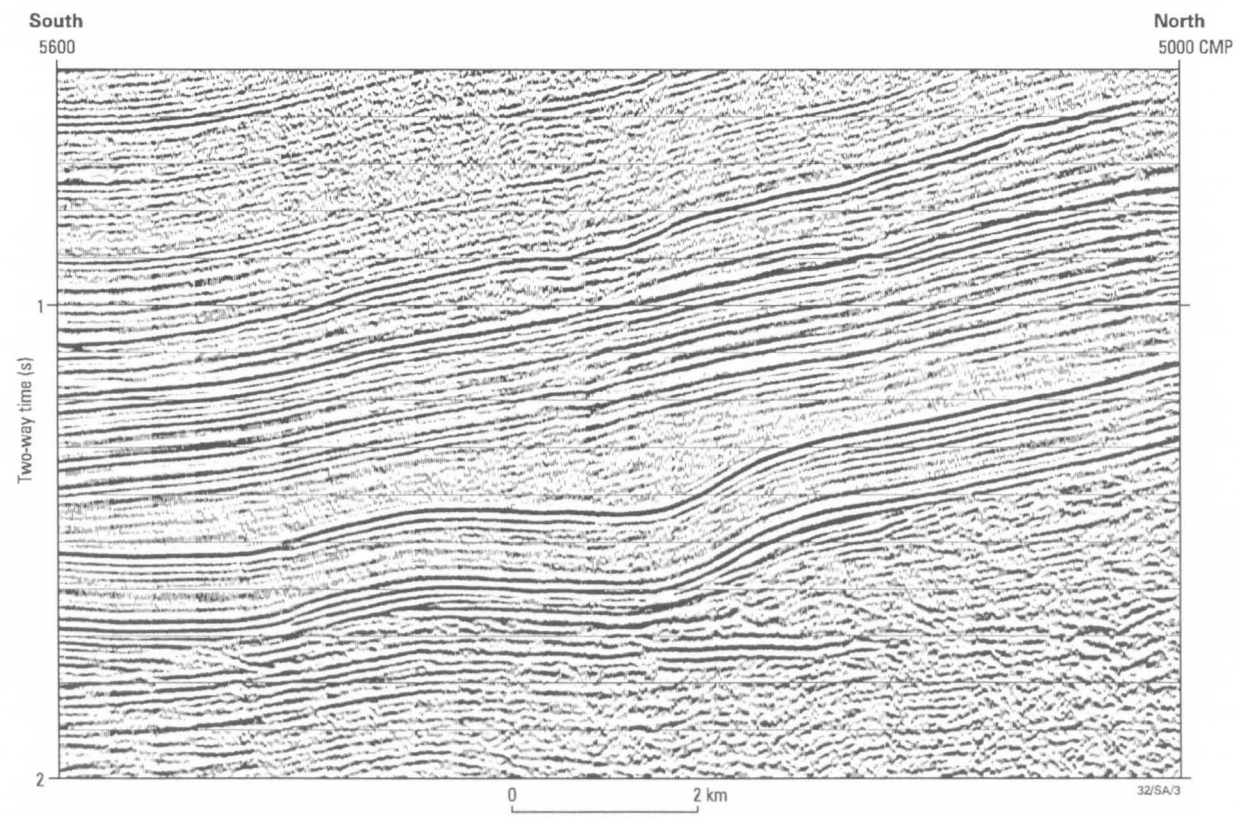

Figure 22. Portion of the seismic traverse 93AGS01 between CMP 5000 and 5600 (2 s TWT), showing the sedimentary structure south of the northern margin of the Officer Basin. The sedimentary strata are divided into two successions which are unconformable. The upper succession is gently folded, whereas the lower succession has been folded into additional kink structures evident beneath CMP 5500 and 5280.

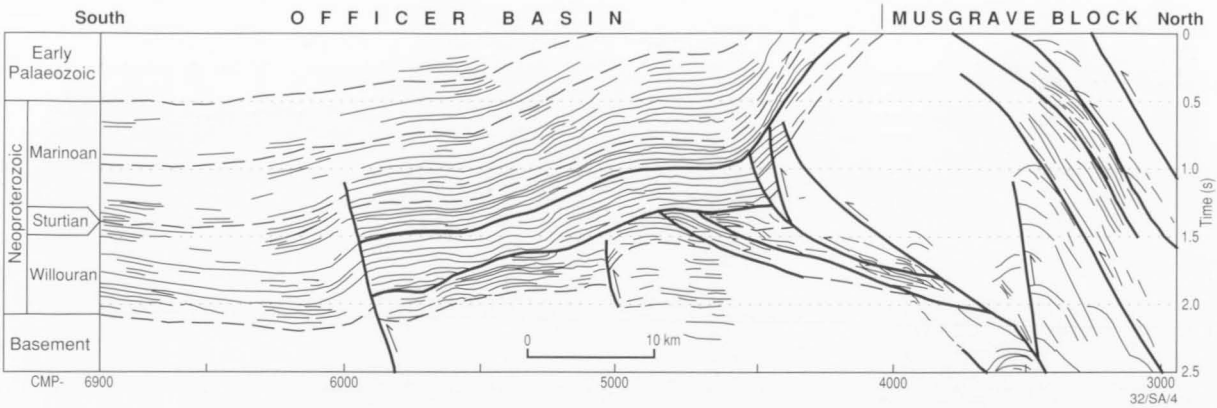

Figure 23. Line diagram of the structure of reflection events at the northern margin of the Officer Basin, showing the Officer Basin succession folded and back-thrust over a non-reflective triangle zone which underlies the main thrust zone at the southern margin of the Musgrave Block.

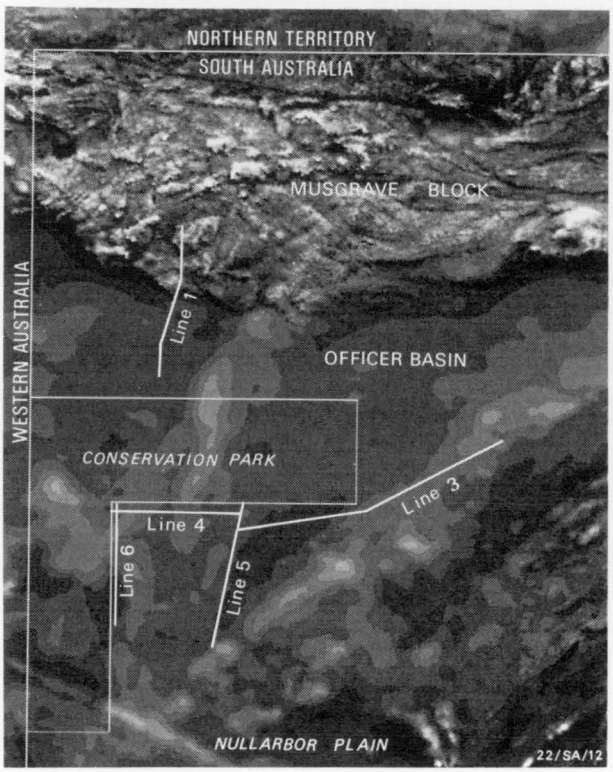

Figure 24. TMI image of the Musgrave Block and the northern Officer Basin, showing the locations of the NMGA seismic traverses.

the Musgrave Block north of this point. Interpretation of the TMI data indicates that the thin edge of the Musgrave Block thrust sheet starts at CMP 4100. Seismic data do not image this portion of the thrust clearly in the top 200 milliseconds, although the upper branch of the bifurcated thrust structure appears to flatten near the surface in agreement with the magnetic interpretation.

Gravity observations were made along the seismic traverses during seismic acquisition, and the reduced Bouguer gravity profile along line 93AGS01 is shown in Figure 25. It is noteworthy that the major inflection in Bouguer gravity does not correspond to the location of the homoclinal fold in basin sediments near CMP 4400, but is displaced to the north. These data require a causative density contrast to be located north of this homoclinal fold. This observation is reconciled in the gravity model by proposing that the upper branch of the bifurcating thrust is the major thrust zone associated with the southern margin of the Musgrave Block thrust sheet, as is also required by the TMI data. The triangle zone between the Musgrave Block thrust zone and the homocline is proposed to be a zone of brecciated and disrupted Officer Basin sediments. The trapezoidal volume above the basal decollement therefore has a density appropriate to sediments.

Figure 25 shows a model of the density variation which is consistent with the seismic, TMI, and gravity observations along seismic line 93AGS01. Like the model of Milton & Parker (1973), displacement of the major inflection in the Bouguer gravity profile approximately 20 km north of the homoclinal fold zone can be explained by a wedge of disrupted lower density sediments beneath the basement thrust sheet. The upper succession of Officer Basin sediments, which forms the homoclinal structure, appears to have been folded by back-thrusting over the brecciated and disrupted sediments in the triangle zone.

In summary, interpretation of these data in conjunction with gravity and magnetic data indicate that:

1. The region is underlain by a series of pervasive north-dipping structures which predate formation of the Officer Basin.

2. Reactivation of some of these older (pre-Willouran) structures produced a major thrust zone which forms the Officer Basin's northern margin.

3. This thrust fault zone bifurcates beneath the Musgrave Block. The lower branch of this bifurcated thrust zone forms a basal decollement which soles into the base of the Officer Basin sedimentary succession. The upper branch flattens near the surface.

4. A trapezoidal wedge or triangle zone of disrupted sediments was formed in front of the thrust zone.

5. An upper portion of the sedimentary section was excised by this wedge and has been back thrust into a homoclinal fold structure.

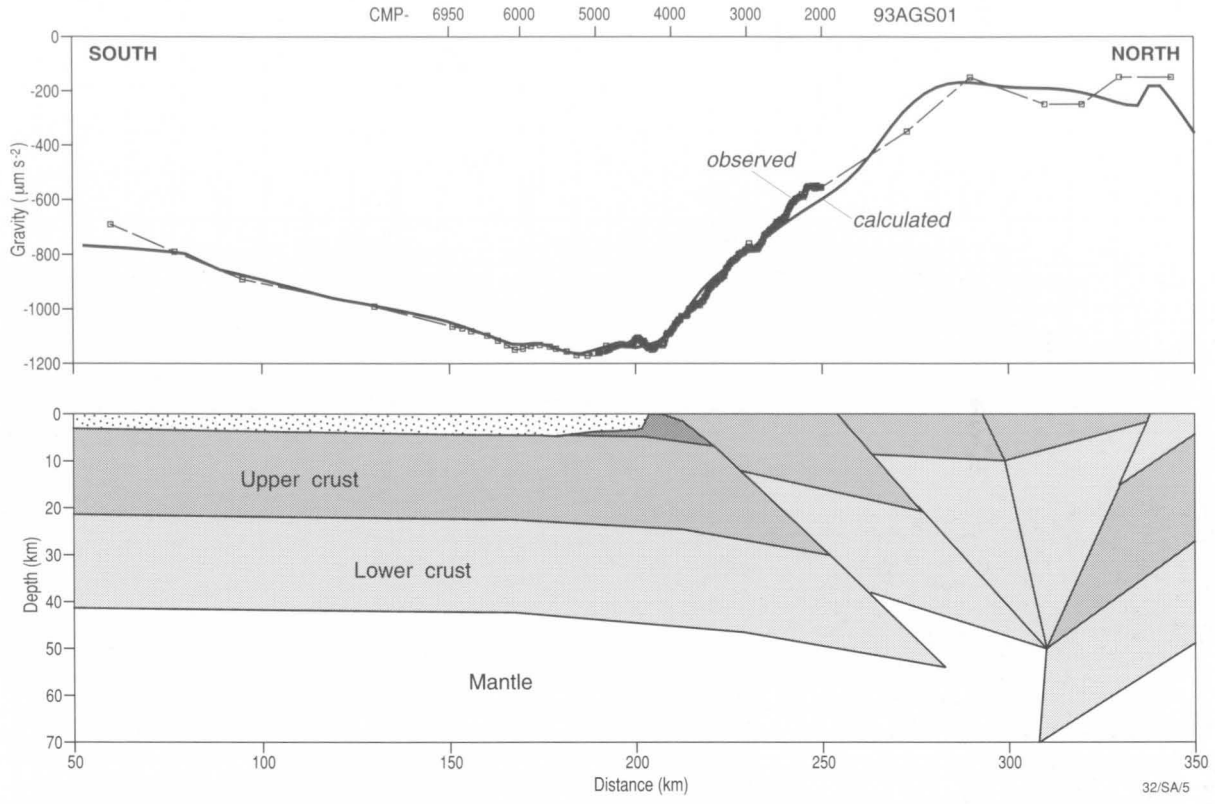

Figure 25. Bouguer gravity data measured with a station spacing of 250 m along seismic traverse 93AGS01 were extended to the north and south with regional gravity data to produce the observed gravity profile. The modelled gravity profile was calculated from the proposed gravity model, which is consistent with both the seismic data from 93AGS01 and the southern edge of the Musgrave Block as defined by the magnetic data. The model was adapted from that of Lambeck & Burgess (1992).

Felsic granulite terranes

The Mount Aloysius Complex and equivalents

The host rocks of the mafic–ultramafic intrusions of the Giles Complex consist of massive to layered, mostly felsic, granulite-facies metamorphic rocks. They crop out as elevated terrains, e.g., Mount Aloysius (Fig. 3C), northern Hinckley Range, Ewarara–Teizi area, Wandu Hill, Mount West, and isolated inselbergs around the Tomkinson Ranges (Figs 3G, H, 4). Daniels (1974) divided these rocks into two types: (1) well-layered granulite that is characterised by compositional variations on a centimetre to metre scale, inferred to be transposed sedimentary bedding, and (2) poorly-layered felsic granulite, which includes orthopyroxene-bearing ('charnockitic') gneiss, inferred to be orthogneiss. Felsic granulite, derived from igneous protoliths is dominant and is interlayerd with minor mafic granulite layers and lenses (Gray 1977, 1978). A variety of metasedimentary rocks, including quartzite, metapelite, and calc-silicate granulite, are commonly intercalated with the orthogneiss.

The layered granulite, including both the meta-igneous (orthogneiss) and metasedimentary (paragneiss) components, predates the Giles Complex, as shown by intrusive contacts of the latter (Nesbitt et al. 1970; Glikson et al. 1995), the presence of older D_1 and D_2 structural fabrics in the granulite (Clarke 1992; Clarke et al. 1995a), and isotopic age data. The granulite also contains massive pods and lenses of granitic gneiss, foliated orthopyroxene granitoids (charnockites), porphyritic and rapakivi hornblende–biotite granitoids, and syenite, all of which predate the Giles Complex. Protoliths of high-grade orthogneisses were apparently emplaced about 1550 and 1300 Ma ago, on the basis of Rb–Sr isochron ages (Gray 1978) and U–Pb zircon and Sm–Nd data (Sun et al. 1996a, b). High-grade metamorphism is estimated to have occurred at 1198±6 Ma (the U–Pb zircon age of syn-metamorphic granite gneiss at Minno, near Mount Davies, Sun & Sheraton 1992; Sun et al. 1996a). This age is consistent with a Rb–Sr isochron age of 1204±17 reported by Gray (1978).

The granulite-facies metamorphic rocks of the western Musgrave Block are collectively termed the Mount Aloysius Complex (MAC), which is defined in Appendix IV. The Mount Aloysius Complex comprises all such units throughout the area, including those referred to on Plate 1 as gneiss at Mount West (MWG), granulite of the Ewarara–Teizi area (ETG), and granulites at Wandu–Ilitjata (WIG). In this section, detailed descriptions of the geology of the type area at Mount Aloysius, as well as the Ewarara area, are given. The geochemistry and petrogenesis of the felsic gneiss are also discussed.

The Mount Aloysius type area

Geological framework

The Mount Aloysius massif forms a roughly triangular range of hills rising to 982 m at Mount Aloysius, 400 m above the surrounding plain (Fig. 26; Stewart 1995a). Daniels (1974) mapped the massif as a single unit of layered granulite cut by dolerite dykes. Gray (1977, 1978) mapped the central part of the massif, and delineated units of massive granulite, garnet granulite, layered granulite, and sillimanite granulite. Detailed mapping of the whole massif by A.J. Stewart in 1990–91 used 1:20 000 colour air photographs supported by Landsat imagery (Fig. 27). The rock types which crop out at Mount Aloysius is summarised in Table 1.

The Mount Aloysius massif comprises felsic, intermediate, and mafic granulite interlayered on scales ranging from centimetres to hundreds of metres (Fig. 28). The granulite is intruded by a few small bodies of granite, syenite, and pegmatite, and by abundant dolerite dykes. Layering (S_{1a}) is compositional and is imparted by changes in mineral proportions and grain size. Thin layers commonly narrow, widen, bifurcate, or lens out along strike distances of less than a few metres, and in places cross-cut each other at low angles. Some mafic layers have even more mafic selvedges. Hence, the layering is regarded as being of metamorphic differentiation origin. On the other hand, compositional variations which occur on a scale of hundreds of metres probably represent original sedimentary, volcanic, or intrusive units, e.g., units of felsic garnet granulite and sillimanite–garnet granulite in the centre of the massif and mafic granulite in the northwest are probably original sedimentary and volcanic units, respectively. The metamorphic layering is broadly parallel to these macroscopic layers, and may reflect transposed bedding in rocks of sedimentary composition. Stratigraphic younging directions were nowhere recognised.

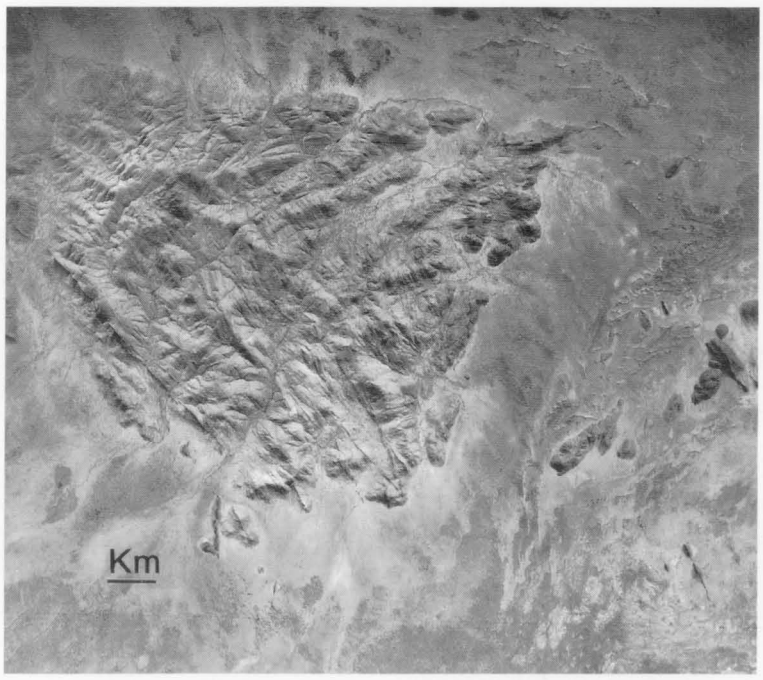

Figure 26. Aerial photograph of Mount Aloysius.

The following map units are defined in the Mount Aloysius Complex:

fns. Felsic sillimanite–garnet granulite of sedimentary origin crops out only in the centre of the massif. It is fine to medium-grained, discontinuously thin layered, and prominently jointed.

fg. Felsic garnet granulite forms a well-defined unit in the centre of the Mount Aloysius massif, and thin layers in the north and south of the massif. The rock is massive to weakly layered, and coarse to very coarse grained.

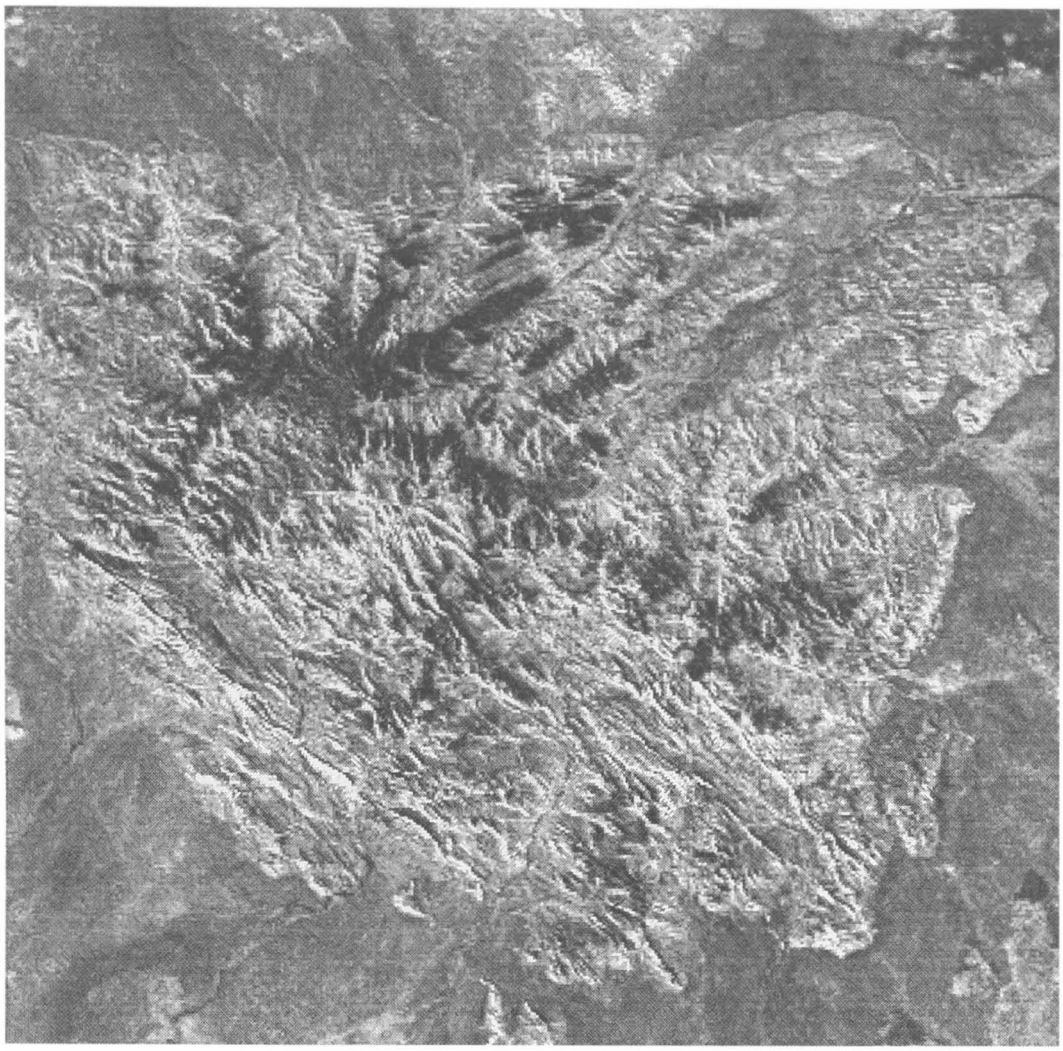

Figure 27. Landsat-5 TM 5/4 band ratio image of Mount Aloysius showing distribution of iron oxide on weathering surfaces (light areas), with northwest-trending dolerite dykes being clearly shown (compare with Fig. 29).

fna. This unit is confined to the east, and is composed of intermediate granulite and felsic granulite which are weakly layered. The layering is inconspicuous, poorly defined, commonly interrupted, and lithological differences between layers are slight. The rock is medium to coarse grained, and in places agmatitic. Its boundaries cross-cut the layering in the adjoining unit *fn,mn*, and it is interpreted as a mobilised, locally intrusive unit of orthogneiss.

fn,mn. This composite unit, shown at Mount Aloysius on Plates 1 and 2, consists of thin to thick layered felsic granulite (mainly orthogneiss), with numerous mafic granulite interlayers and rare intermediate granulite. Calc-silicate and quartzite layers are present in places.

fn. Felsic granulite forms a prominent disrupted layer in the south of the Mount Aloysius massif, and another layer in the north. The granulite is a coarse-grained, leucocratic, homogeneous orthogneiss.

mn. Mafic granulite, with rare interlayers of intermediate and felsic granulite, forms mappable units in the northwest, as well as thin to thick layers and lenses in the felsic granulite units.

fnk. Leucofelsic granulite (orthogneiss), with minor mafic granulite, forms discrete bodies concentrated around the margins of the Mount Aloysius massif. It is weakly layered to massive, medium to coarse grained, and blue–green where fresh. The outcrops centred at AMG grid references (GR) 577263 and 555265 in the north of the massif are of very weakly layered quartz syenite composition (91989056). Layering in the *fn,mn* layered granulite unit diverges around the eastern outcrop, and the body appears to be a syn-tectonic or late-tectonic intrusion. This is supported by the occurrence of a dyke of syenite 500 m to the south at GR 578249, which has intruded obliquely across the granulite layering of unit *fn,mn*.

Other units, not present at Mount Aloysius, are:

fni. Intermediate granulite (orthogneiss), a widespread, but volumetricaly minor, unit which is interlayered with massive felsic granulite (*fn*).

fnm. Homogeneous intermediate to mafic granulite, which commonly forms discrete layers, e.g., near Ewarara.

fnq. Quartz-rich felsic granulite, a minor metasedimentary unit which crops out near Teizi Hill and Mount West.

fnv. Garnetiferous granulite, another minor unit, probably in part of sedimentary orign, which crops out near the Gosse Pile intrusion.

Table 1. Rock types of the Mount Aloysius massif.

Unit and map symbol	*Lithology*	*Remarks*
Type B quartz dolerite dykes	Subophitic; clinopyroxene + plagioclase + Fe–Ti oxides	Strike NW; 820 Ma
Type C olivine dolerite dykes	Subophitic to aphanitic, rarely mgr; olivine–plagioclase-phyric; pyrite-bearing	Strike NNE to NE; 1000 Ma
Type A intergranular dolerite dykes, commonly metamorphosed	Orthopyroxene + clinopyroxene + plagioclase; commonly plagioclase-phyric	(Sub)parallel to, and folded with, layering of host granulite
Meta-anorthosite sheets	Plagioclase 88–97%; grade into metadolerite towards ends of sheets	In NE; few 10s m long; possibly related to type A dolerite dykes
Pegmatite dykes	Granodiorite to granite	Small, rare, cross-cutting; confined to unit *fna*
Syenite, *sy*	Bluish-green to yellowish-green, cgr, massive to weakly foliated	Small intrusive bodies in S
Granite, *g*	Creamy white to pale brown, m–cgr, foliated alkali feldspar granite	Small bodies in NW, S, and NE; distinctive corestones
Leucofelsic granulite with minor mafic granulite, *fnk*	Weakly layered to massive, m–cgr, blue–green; orthogneiss: leucotonalite, quartz alkali feldspar syenite	Discrete pre- or syntectonic bodies around margins of massif
Mafic granulite, rare interlayers of intermediate and felsic granulite, *mn*	Grey to black, f–mgr, massive to weakly foliated	Thick units in NW, thin elsewhere
Felsic granulite, *fn*	Cgr, leucocratic, homogeneous orthogneiss: tonalite, leucotonalite, leucogranite, alkali feldspar granite	Prominent disrupted layers in S and N
Felsic granulite with numerous mafic and rare intermediate granulite layers, *fn,mn*	Thin to thick-layered; mainly orthogneiss with calc-silicate and quartzite layers in places	The most distinctly layered unit, forming most of the massif
Intermediate and felsic granulite, interlayered, *fna*	Massive to weakly layered, m–cgr, in places agmatitic; orthogniss: leuconorite, leuco-quartz monzogabbro, leucotonalite, alkali feldspar granite	In E; layering poorly defined and commonly interrupted
Felsic garnet granulite, *fg*	Massive to weakly layered, c–vcgr	In centre, N, and S
Felsic sillimanite–garnet granulite, *fns*	Discontinuously thin-layered, f–mgr; metasedimentary	In centre; prominently jointed

Abbreviations: fgr, fine-grained; mgr, medium-grained; cgr, coarse-grained; vcgr, very coarse-grained.

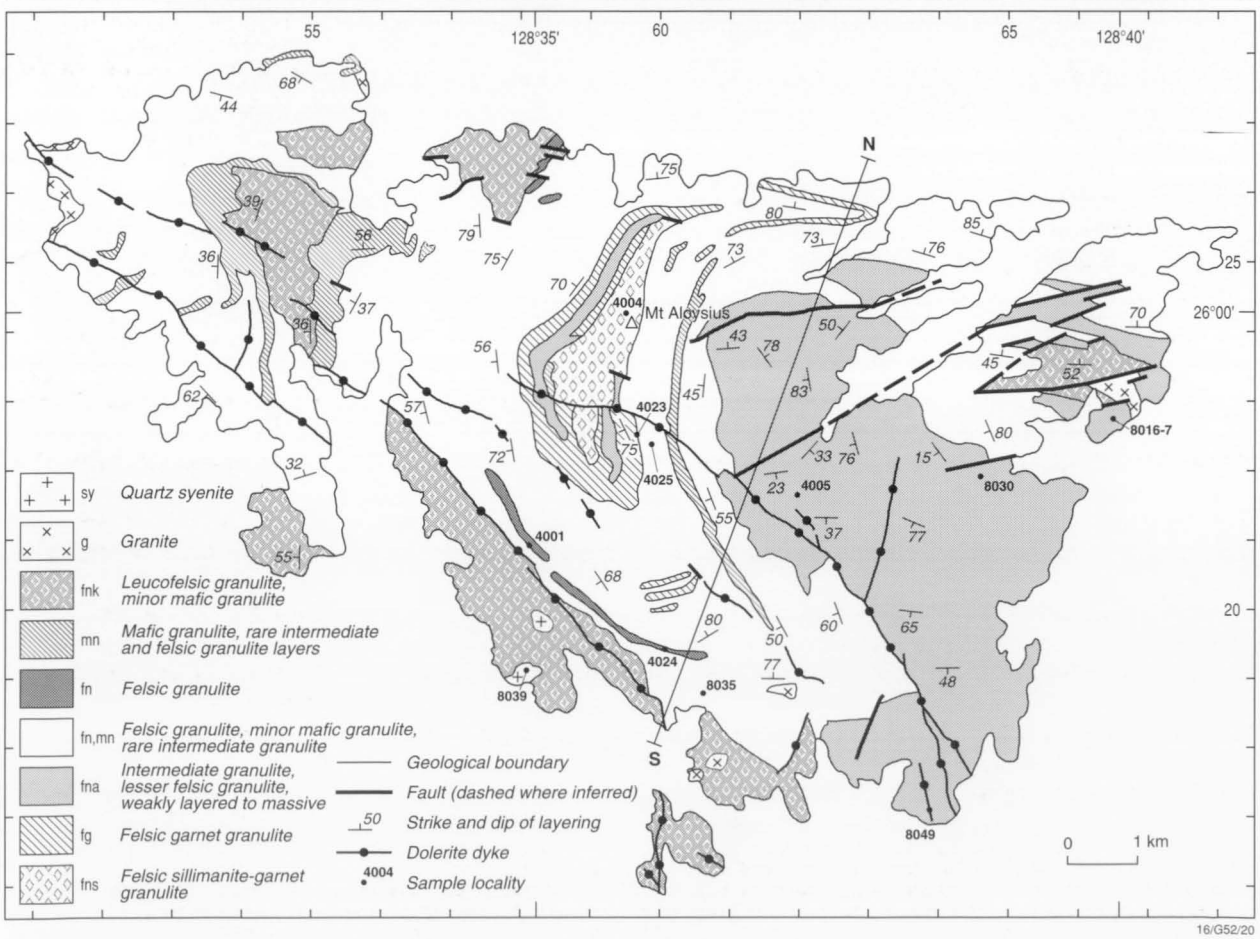

Figure 28. Generalised geological map of the Mount Aloysius massif, based on mapping by A.J. Stewart, except for boundaries of units forming fold closure around Mount Aloysius by Gray (1971). N–S is position of cross-section in Figure 37. Locations of zircon U–Pb dated samples are shown; sample numbers starting with '4' are prefixed '9098', those starting with '8' are prefixed '9198'. Numbered ticks at margins of this and similar diagrams are 1 km intervals of the AMG, Zone 52.

Lithological units

The principal lithological features and mineral assemblages of the Mount Aloysius Complex are summarised in Table 2:

Mafic granulite. Mafic granulite is dark grey to black, fine to medium grained, massive to weakly foliated, and generally homogeneous, but in many places includes a few thin lenses of felsic and/or intermediate granulite. The rock is generally of gabbronorite composition, ranging to norite, leuconorite, and rarely melagabbronorite. Texture is usually granulo- or granoblastic, less commonly cataclastic or mylonitic; one sample (90984107) is allotriomorphic with minor granoblastic patches, indicating an igneous protolith for the granulite. The granulite consists chiefly of plagioclase (bytownite–andesine, An_{71-40}), orthopyroxene, and lesser clinopyroxene, opaque grains, hornblende, biotite or phlogopite, rare quartz, and traces of apatite, titanite, and secondary muscovite. Garnet forms symplectite coronas around opaque grains in some samples (91989082, 91989060), and discrete orange grains in others (91989059).

Felsic granulite. Felsic granulite is the most abundant rock type. It is white, pale grey or grey–brown, thin to thick layered, or elsewhere pod or bleb-like, and medium to coarse grained; the textute is generally granulo- to granoblastic, or, less commonly, cataclastic to mylonitic. Migmatitic to agmatitic structure is present in a few places. Most felsic granulite is of igneous composition, and represented in the major map units as follows:

- *fn*: tonalite, leucotonalite, leucogranite, alkali feldspar granite;
- *fna*: leuconorite, leuco-quartz monzogabbro, leucotonalite, alkali feldspar granite;
- *fnk*: leucotonalite, quartz alkali feldspar syenite.

These rocks are composed chiefly of plagioclase (labradorite–andesine, An_{68-40}), quartz, mesoperthitic alkali feldspar, orthopyroxene, and opaque grains (magnetite). Garnet, biotite, spinel, and zircon occur in some samples, as do trace amounts of secondary epidote, clinozoisite, and muscovite.

Two felsic granulite samples are clearly of sedimentary origin. Sample 91989070 (a psammo-pelite) consists of quartz (73%), garnet (15%), sillimanite (8%), andesine (2%), orthoclase (1%), and biotite (1%). 91989059 (a calc-silicate) comprises thin interlayers respectively composed of (A) quartz (89%), labradorite (5%), garnet (5%), and zircon (1%), and (B) labradorite (42%), garnet (27%), clinozoisite (18%), quartz (10%), amphibole (2%, rimmed with garnet), and muscovite (1%).

Many other felsic layers contain relatively calcic plagioclase (labradorite). Sample 91989102B from a boudinaged layer is symmetrically zoned as follows:

Table 2. Petrography of the Mount Aloysius massif.

Rock type and composition	*Texture*	*Mineral assemblage**
Felsic granulite. White to grey–brown, thin to thick-layered, pod or bleb-like, migmatitic to agmatitic in places. Orthogneiss: tonalite, leucotonalite, leuconorite, leuco-quartz monzogabbro, leucogranite, alkali feldspar granite, quartz alkali feldspar syenite. Rare metasediments: metapelite, calc-silicate granulite (5 layers)	M–cgr, generally grano- to granuloblastic, less commonly cataclastic to mylonitic	**Ess:** Pl (An_{68-40}), Qz, Kfs (meso), Opx, Opq. **In some samples:** Gt, Bt, Sp. **Tr:** Zir, Ap, Ep, Clz, Ms. **Metapelite:** Qz, Gt, Si, And, Kfs, Bt. **Calc-silicates:** 1. Qz, Lab, Gt, Zir. 2. Lab, Gt, Clz, Qz, Am, Ms. 3. Kfs, Qz, Lab, Opx. 4. Qz, Lab, Opx, Opq 5. And, Opx, Opq.
Intermediate granulite. *Unit fna.* Unevenly and indistinctly thin to thick-layered, mostly homogeneous, elsewhere agmatitic. Leucogabbronorite, quartz leu- conorite, quartz anorthosite.	Mgr, grano- to granuloblastic or cataclastic	**Ess:** Lab (An_{68-54}), Opx, Opq. **In some samples:** Qz, Cpx. **Acc:** Bt, Ap. **Sec:** Ep, Chl, Cc, Ms.
Unit fn,mn. Rare thin layers of calc-silicate, locally interlayered with mafic granulite	Mgr	1. Byt, Opx, Gt, Bt, Opq. 2. Lab, Qz, Di, Tit, Opq, Clz.
Mafic granulite. Gabbronorite, norite, leuconorite, melagabbronorite	F–mgr, grano- to granuloblastic, less commonly cataclastic to mylonitic, rarely relict allotriomorphic	**Ess:** Pl (An_{71-40}), Opx, Cpx, Opq, Hbl, Bt/Phl, Qz. **Tr:** Ap, Tit. **Sec:** Gt, Ms.
Granite. Alkali feldspar granite	Mgr, granoblastic	**Ess:** Kfs (meso), Qz. **Tr:** Bt, Opq, Gt, Opx, Ap, Zir, All.
Pegmatite.	Patchily recrystallised	**Ess:** Kfs, Qz, sodic Pl. **Acc:** Opq.
Meta-anorthosite. Pale grey, massive	F–mgr, allotriomorphic to granoblastic	**Ess:** Pl (An_{80-66}). **Tr:** Hbl, Opq, ±Opx, ±Cpx, ±Rut, ±Ap.
Garnet anorthosite. Core of zoned metadolerite		**Ess:** Lab (An_{62}), Gt. **Tr:** Kfs, Hbl, Opq.
Type A dolerite dykes.	Intergranular to granuloblastic, locally cataclastic	**Ess:** Lab (An_{64}), Opx, Cpx, Opq, Bt; Ol in one sample
Type C olivine dolerite dykes.	Subophitic to porphyritic, locally cataclastic; one with quenched variolitic margin	**Ess:** Ol, Pl (An_{68-46}), Cpx, Bt, Opq; rare Sp.
Type B quartz dolerite dykes.	Subophitic, locally granoblastic to cataclastic	**Ess:** Lab (An_{62}), Cpx, Opq. **Tr:** Qz, Bt, Am; rare Opx.

* Anorthite (An) contents of plagioclase are optically estimated from albite twinning.
Abbreviations: Acc, accessory; Ess, essential; Sec, secondary; Tr, trace; All, allanite; Am, amphibole; An, anorthite; And, andesine; Ap, apatite; Bt, biotite; Byt, bytownite; Cc, calcite; Chl, chlorite; Clz, clinozoisite; Cpx, clinopyroxene; Di, diopside; Ep, epidote; Fl, fluorite; Gt, garnet; Hbl, hornblende; Kfs, K-feldspar; Ky, kyanite; Lab, labradorite; Meso, mesoperthite; Ms, muscovite; Mt, magnetite; Ol, olivine; Opq, opaque mineral(s); Opx, orthopyroxene; Parg, pargasite; Phl, phlogopite; Pl, plagioclase; Qz, quartz; Rut, rutile; Si, sillimanite; Sp, spinel; Tit, titanite; Zir, zircon.

- A core (2 cm thick) of alkali feldspar (40%), quartz (30%), labradorite (25%), and orthopyroxene (5%);
- An intermediate zone (1 cm) of quartz (50%), labradorite (44%), orthopyroxene (5%), and opaque grains (1%);
- An outer zone (1 cm) of andesine (50%), orthopyroxene (45%), and opaque grains (5%).

This rock appears to be a metamorphosed and boudinaged calcareous sediment. Other labradorite-bearing leucocratic layers may also be calcareous metasediments. Such calc-silicate granulite, although volumetrically minor, is quite widespread in the Mount Aloysius Complex (e.g., near Ewarara, Latitude Hill, and Mount Fanny, as well as Mount Aloysius itself). It typically contains clinopyroxene, calcic plagioclase, and various amounts of quartz, orthopyroxene, garnet, titanite, allanite, and, less commonly, clinozoisite or epidote.

Apart from the relatively few demonstrably metasedimentary rocks, the granitic (*s.l.*) compositions of most felsic granulites suggest an origin by metamorphism of felsic volcanic or intrusive rocks, associated with minor mafic igneous rocks (possibly volcanic rocks and/or dykes). The thin and intimate layering is probably the result of strong deformation and metamorphic differentiation.

Intermediate granulite. Intermediate granulite in unit *fna* is unevenly and indistinctly thin to thick layered, and nearly homogeneous in many places. Elsewhere, it is agmatitic, with quartzo-feldspathic streaks, swirls, blebs, and bulbous veinlets. The rock is medium grained, grano- or granuloblastic to cataclastic, and ranges in composition from leucogabbronorite, through quartz leuconorite, to quartz anorthosite. The rock consists essentially of plagioclase (60-80%; labradorite, An_{68-54}), orthopyroxene (5–20%), and opaque grains (1–5%), with quartz (5–15%) and clinopyroxene (5–10%) in some samples, and accessory biotite and apatite. Secondary epidote, chlorite, calcite, and muscovite are rare. This granulite type was probably mainly derived by metamorphism of intermediate to mafic volcanic or intrusive rocks, although some may be of sedimentary origin.

Intermediate granulite in unit *mn* forms rare thin medium-grained layers, which are commonly tightly folded and in places interlayered with mafic granulite. Two rock types are present. 91989117, of uncertain origin, consists of bytownite (An_{71}), orthopyroxene with garnet rims, garnet with symplectitic coronas of secondary orthopyroxene+plagioclase+opaques, biotite, and opaque grains. The second type (91989075, 91989106), calc-silicate granulite, consists of labradorite (10–65%), quartz (80–10%), diopside (5–20%), titanite, opaque grains, and clinozoisite.

Granite. Granite forms small stocks and bosses in the northwest, south, and northeast. It is creamy white to pale brown, homogeneous, evenly medium or coarse grained, non-layered, schistose, and forms distinctive round corestones. The texture (90984103) is granoblastic as a result of recrystallisation. Most rocks are alkali feldspar granite, and consist of mesoperthite (80%), quartz (20%), and trace amounts of biotite, garnet, orthopyroxene mantled with opaque material, opaque grains, and allanite.

Syenite. Syenite forms small intrusive bodies in the south of the Mount Aloysius massif. The rock is bluish green to yellowish green, coarse grained, massive to weakly schistose, and contains clinopyroxene with exsolved blebs and lamellae of orthopyroxene (possibly after pigeonite: ~5%), fayalite (~1%), and minor orthopyroxene, greenish-brown hornblende, and biotite. Orthopyroxene also occurs as granular rims (with clinopyroxene) around primary clinopyroxene. Abundant accessory minerals include Fe–Ti oxides, apatite, zircon, ?chevkinite, and fluorite, and K-feldspar is strongly perthitic.

Pegmatite. Rare cross-cutting pegmatite dykes in unit *fna* consist of orthoclase, quartz, sodic plagioclase, and accessory opaque grains. The rock ranges from granodiorite to granite in composition, and is weakly deformed and patchily recrystallised.

Meta-anorthosite sheets. Sheets or sill-like layers of meta-anorthosite are present in the northeast of the Mount Aloysius massif. The rock is pale grey, fine to medium grained, massive, and allotriomorphic to granoblastic. It is composed of plagioclase (88–97%; bytownite–labradorite, An_{80-66}), hornblende (1%), and opaque grains (1%), with or without orthopyroxene (up to 1%), clinopyroxene (up to 2%), rutile (up to 1%), and apatite. Both pyroxenes form relict cores in hornblende. The anorthosite bodies are about 8 m thick and several tens of metres long. They grade into metadolerite towards the ends, and may therefore be related to the type A dykes. One metadolerite is zoned, with a central core of granoblastic 'garnet anorthosite', composed of labradorite (78%; An_{62}), orange garnet, commonly with cores of hornblende (20%), orthoclase (1%), and opaque grains (1%); multicrystalline clots of hornblende are rimmed with garnet.

In unit *mn* in the northeast of the Mount Aloysius massif, mafic granulite is bordered to the south by white massive medium-grained clinozoisite rock (90984093; clinozoisite (90%), quartz (7%), titanite (2%), garnet (1%), opaque grains (up to 1%)) which is presumably a metamorphosed quartz anorthosite.

Mafic dykes. Mafic dykes are ubiquitous throughout the Mount Aloysius massif, and range from a few centimetres to several tens of metres thick. They are of at least three generations (Fig. 29):

Type A dolerite dykes (Clarke et al. 1992; Sheraton & Sun in press) were intruded before large-scale D_3 folding of the granulites, and are characterised by extensive high-grade metamorphic effects. The dykes strike northwest on the southwest limb of the major D_3 antiform that trends west-northwest through the Mount Aloysius massif, and east to east-northeast on the northern limb. Textures are blastophitic to granoblastic or cataclastic. Type A dykes consist of labradorite (10–70%; An_{64}), poikilitic orthopyroxene (5–40%), clinopyroxene (17–58%), opaque grains (5–8%), and biotite (1–5%); olivine is present in one sample (90984102). Clinopyroxene is largely recrystallised to fine-grained aggregates which include rare large relics of original igneous clinopyroxene.

Type C olivine dolerite dykes were emplaced after D_3 folding, and are characterised by the presence of abundant pyrite. The dykes strike north-northeast to northeast across the axial plane of the major D_3 antiform through the Mount Aloysius massif (Fig. 29). The largest dyke (90984100) forms a depression in the surrounding granulite, in contrast to the ridges of type B dykes nearby. The rocks are commonly aphanitic, but some are medium grained. Textures are ophitic, some are porphyritic, and one (91989112) has a very fine-grained chilled margin with variolitic texture. Type C dykes consist of olivine (1–20%), rimmed with iddingsite or amphibole, plagioclase (25–55%; labradorite–andesine, An_{68-46}), clinopyroxene (17–40%), opaque grains (5–25%), and rare biotite and spinel.

Type B quartz dolerite dykes were intruded long after D_3 folding, and are generally olivine free. They are large dykes, parallel or subparallel to the axial plane of the major northwest-trending D_3 antiform in the Mount Aloysius massif, with a few offshoots striking north. Textures are blastophitic to granoblastic, and rarely cataclastic. These dykes are composed of labradorite (45–50%; An_{62}), commonly partly to substantially recrystallised to a fine-grained mosaic, clinopyroxene (10–50%), rimmed by pale green amphibole (2–8%), and opaque

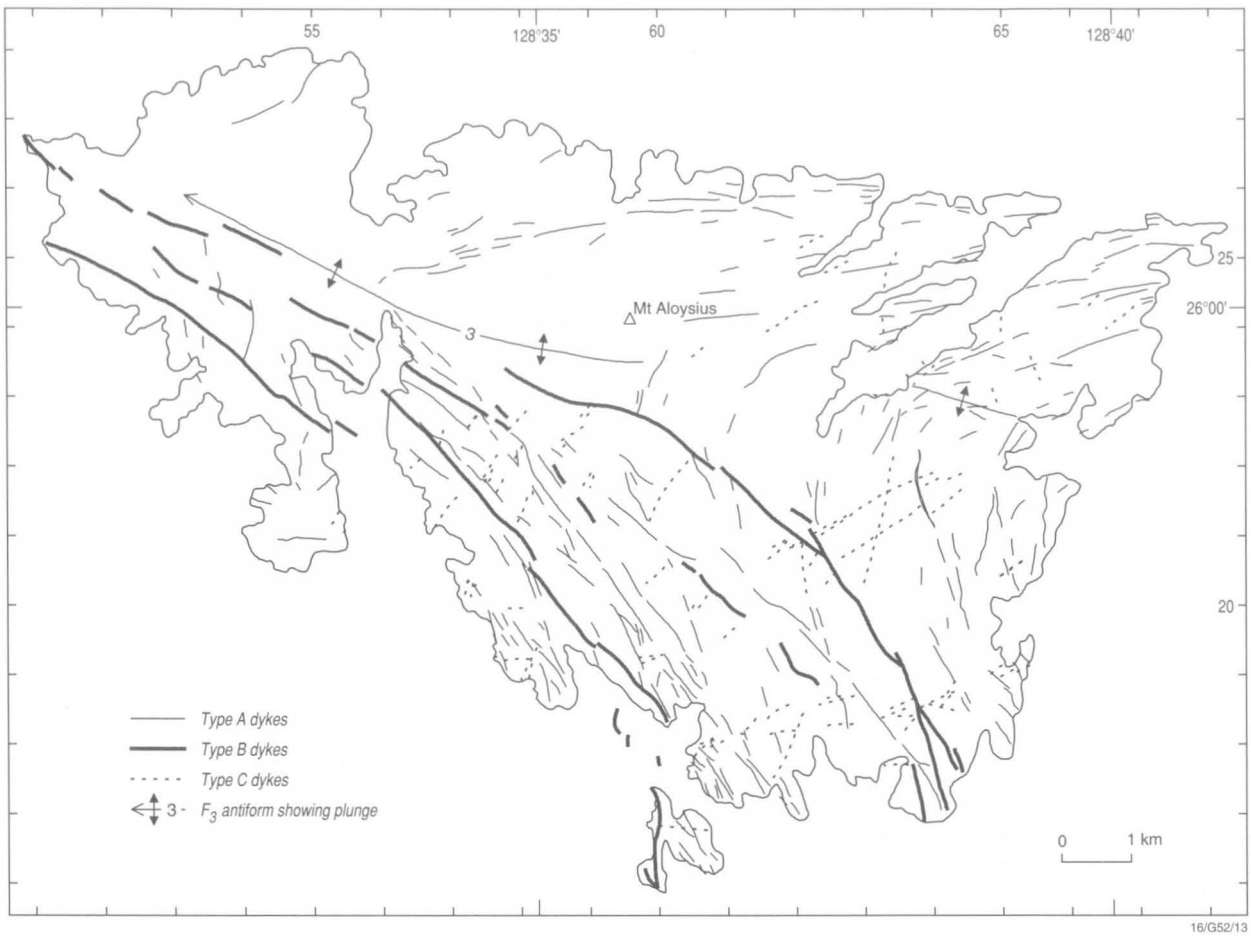

Figure 29. Map of Mount Aloysius, showing types A, B, and C mafic dykes. Type A dykes are folded around an F_3 antiform, type B are subparallel to axial plane of the F_3 antiform, and type C cross-cut the F_3 antiform.

grains (2–15%). Orthopyroxene (up to 30%), rimmed by amphibole, is present in some samples (90984105, 91989068), and biotite (10%) and olivine (2%) in one sample each.

Structure

The most recent accounts of structural relationships in the Tomkinson Ranges are by Clarke (1992) and Clarke et al. (1995a), who recognised seven episodes of deformation (D_{1-7}) in the Champ de Mars–Hinckley Range area, 30 km east of Mount Aloysius. The structural, igneous, and metamorphic events recognised in the Mount Aloysius massif are set out in Table 3. The rocks were affected by an additional episode of mesoscopic folding between D_3 and D_4 of Clarke (1992) and Clarke et al. (1995a), denoted as D_{4*} in Table 3. The four generations of mylonite–ultramylonite and retrogade shear zone formation (D_{4-7}) of Clarke et al. (1995a) have not been positively recognised in the Mount Aloysius massif, although other mylonite zones, which cannot be directly correlated, are present.

D_1. D_1 formed the S_{1a} layering in the granulites, which is shown on the map as airphoto trends (Fig. 30). As discussed above, S_{1a} is regarded as mainly a product of metamorphic differentiation superimposed on original igneous or sedimentary layering, and normally has a massive granuloblastic texture. In places in the west (GR 538229–540240), however, there is a tectonic foliation parallel to the layering, shown principally by flattening of quartz grains, boudins of mafic granulite or coarsely crystalline quartz, or ellipsoidal garnet aggregates. Weakly or non-layered granulites also show this grain-flattening foliation parallel to nearby layering.

F_{1b} folds (Figs 31, 32A–D) affect S_{1a} layering and so formed after the initiation of S_{1a}. The folds are observed only in widely separated parts of the massif, and are characterised by an absence of axial-plane foliation. In the northeast (Fig. 31A, B) and south (Fig. 31C), the folds are close to isoclinal (Fig. 32A–C), reclined, and are preserved in the hinge regions of large-scale F_2 folds, the axial planes of the F_{1b} folds being at right angles to the S_2 axial-plane foliation. In places, F_{1b} folds are transected by S_2 (Figs 31B, 32B, C). In the west, around GR 567225, several exposures of tight southwest-plunging upright folds (Figs 31E, F, 32D) are assigned to F_{1b} because they trend southwest at right angles to a nearby large-scale F_2 fold, and have no axial-plane foliation; some are transected by an S_2 axial-plane foliation (Fig. 31F).

D_2. D_2 formed large-scale upright north to north-northwest-trending F_2 folds in the centre and southeast in unit *fna*, and, to the west, an overturned (west-inclined) antiform–synform pair in units *fg*, *fns*, and *fn,mn* (Fig. 30). The antiform and synform are steeply plunging, but this is a D_3 effect, and the D_2 plunges would have been gentle. Both folds are tight to isoclinal, and have southwest-dipping axial planes in the south of the massif, which are bent around large-scale F_3 axes to a northwest, and eventually north, dip in the north of the massif (Fig. 30). Similarly, the antiform and synform plunge west to southwest in the south, and northwest in the north.

In unit *fna* (Fig. 28), F_2 folds are outlined by weak S_{1a} layering trends. They are tight to isoclinal, and plunge 40–50° north-northwest in the north, whereas in the south they are open and plunge 27–70° south. A northeast-striking fault separates the two areas, and an east-striking fault forms the

Table 3. Sequence of events in the Mount Aloysius massif.

Event	*Age (Ma)*	*This Bulletin*	*Clarke (1992)*
Mylonitisation	550?	Post-D_{4*} mylonite	D_{4-7}
Mafic intrusion	820[2]	Type B dolerite dykes; NW strike, subophitic	Type C dykes
D_{4*}		F_{4*} upright gentle to open folds, NNE trend and S_{4*} axial plane foliation; local greenschist-facies retrogression	
Mafic intrusion	c.1000[2]	Type C dolerite dykes; aphanitic to porphyritic, NE to NNE strike	Type B dykes
D_3		F_3 upright gentle to tight folds, NW to WNW plunge; S_3 axial-plane cataclastic to mylonitic foliation strikes SE to E; granulite-facies metamorphism and partial melting	D_3
Mafic intrusion	1050–1080[2]	Type A intergranular dolerite dykes; commonly metamorphosed, subparallel to and folded with S_{1a}	Type A dykes
Felsic intrusion	c.1180[2]	Syenite plugs	
D_2	1200[1,2]	F_2 upright to W-inclined close to isoclinal NNW-trending folds (where not refolded) with S_2 granoblastic axial-plane foliation; granulite-facies metamorphism; syn-D_2 mylonites	D_2
Felsic intrusion	1200[1,2]	Granite bodies	Charnockite
D_1		S_{1a} layering, granoblastic, with foliation parallel to layering in south; F_{1b} reclined (originally recumbent) close to isoclinal folds, no axial-plane foliation; granulite-facies metamorphism	D_1
Sedimentation; emplacement of intrusive and volcanic rocks	c.1550[1,2]	Protoliths of felsic orthogneiss; ages of protoliths of mafic granulite and calcareous and quartzitic metasediments unknown	Protoliths of ortho- and paragneiss

[1] Rb–Sr whole-rock isochron ages (Gray 1978); [2]U–Pb zircon ages (Sun & Sheraton 1992; Sun et al. 1996a, b; S-S. Sun unpublished data).

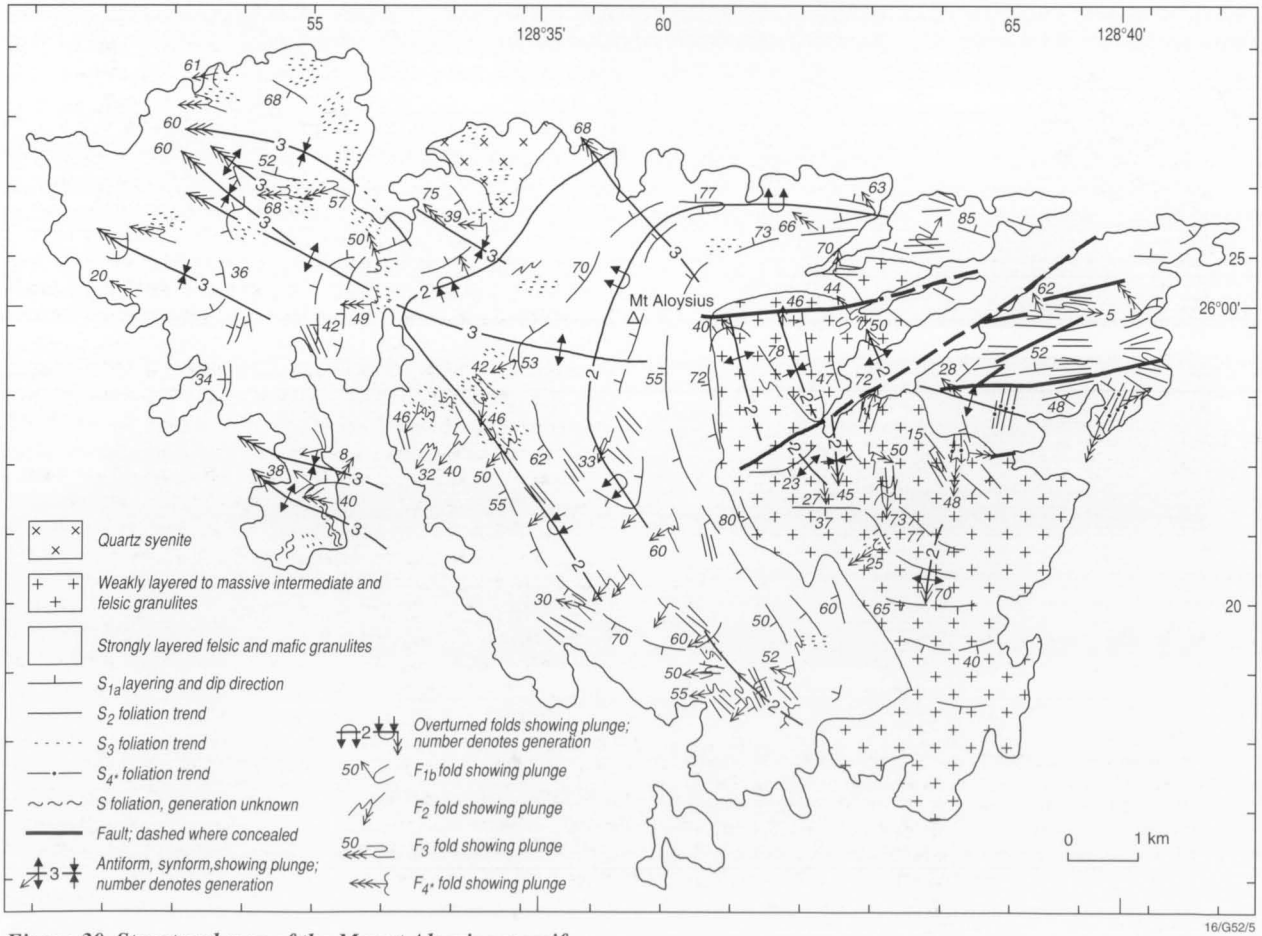

Figure 30. Structural map of the Mount Aloysius massif.

northern margin of the northern area.

The closed map pattern of units *fns*, *fg*, and *fna* (Figs 28, 30) outlines the major north-trending F_2 antiform that passes through Mount Aloysius itself. At two localities (GRs 593220 and 596225) on the eastern limb, an axial-plane foliation S_2 dips at a lower angle than S_{1a} layering, and at GRs 577234 and 581247 on the western limb, parasitic F_2 folds verge southeast and northeast, respectively; these observations (Fig. 33) confirm the antiformal nature of the fold.

Mesoscopic F_2 folds are close to isoclinal, asymmetric (Figs 32E, F, 34C), and parasitic on the limbs of large-scale F_2 folds. They typically have thickened hinges and a weak to strong S_2 axial-plane foliation, which cuts S_{1a} layering at a low angle on both limbs of the folds (Fig. 35A–D). Rarely, S_2 parallels the longer limb and cuts the shorter limb obliquely (Fig. 35C). S_2 is generally defined by flattening of quartz grains and development of a granoblastic texture. Elongation of grains or mineral clots or ellipsoidal garnet aggregates defines an L_2 lineation, but is rare. In the hinge of the antiform at GR 592237, L_2 lineation parallels the axes of gently north-plunging F_2 folds in S_2, and has obliterated layering in unit *fns*. Leucofelsic granulite around GR 567225 has a strong lineation imparted by rod-shaped quartz grains parallel to the southwesterly fold plunge. Mafic rocks are only weakly foliated. Rarely (91989102B, GR 580248), S_2 is cataclastic to mylonitic, with kinked orthopyroxene, flattened plagioclase, and lenticular strained quartz.

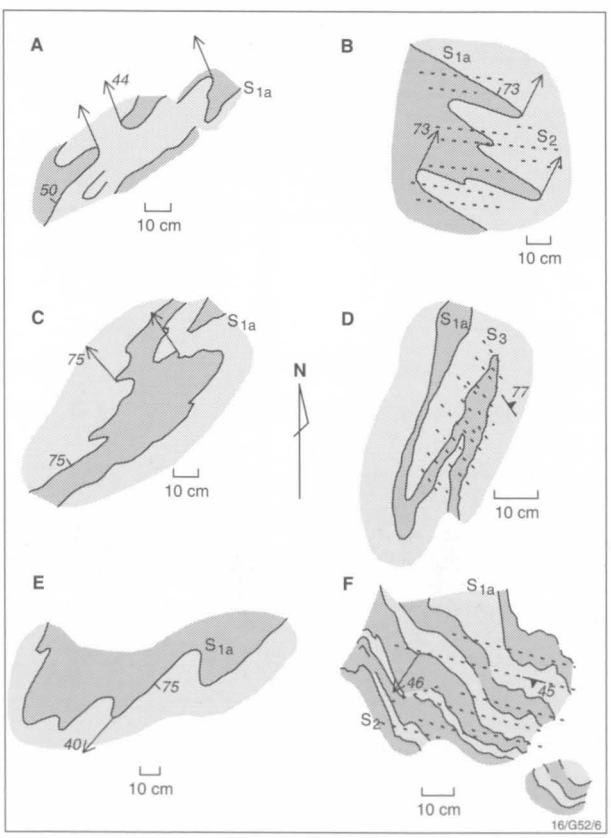

Figure 31. Sketches of mesoscopic F_{1b} folds at Mount Aloysius. (A) Tight to isoclinal reclined folds in weakly layered felsic granulite of unit fna, GR 626239. (B) Tight reclined folds transected by S_2 foliation in weakly layered leucofelsic granulite of unit fn,mn, GR 636251. (C) Tight reclined folds in felsic granulite with mafic interlayers, unit fn,mn, GR 615187. (D) Tight fold in quartz layer in felsic granulite of unit fn,mn transected by S_3 foliation, GR 531284; same locality as Figure 32C. (E) Close to tight upright folds in thinly interlayered mafic and felsic granulites of unit fn,mn, GR 571223. (F) Open upright folds transected by S_2 foliation in thinly interlayered mafic and felsic granulites of unit fn,mn, GR 565227; same locality as Fig. 32D.

In places, F_2 folds are transected by S_3 foliation, which cuts undeviated through both F_2 limbs (Fig. 35E–G). L_2 is also folded by F_3 (Fig. 36D).

D_3. D_3 formed the major west to west-northwest-trending upright F_3 folds in the centre and northwest (Fig. 30). The folds are open in the northwest, but close in the centre and east. They are outlined by layering trends in unit *fn,mn* (Fig. 30) and by the map pattern of units *fg* and *mn* in the northwest (Fig. 28). Plunges range from 28° northwest in the east to 60° northwest in the west and 68° northwest in the central north. Folding during D_3 of the major isoclinal F_2 antiform produced its present shape, with plunges of 63–65° northwest in the north of the massif, and 60° west-southwest in the south (Fig. 30).

Numerous east-striking faults in the east are interpreted as contractional, and the result of the space problem in the hinge of the largest F_3 antiform. The two faults bounding the group of three tight to isoclinal F_2 folds in the north of the intermediate to felsic granulite unit *fna* (Fig. 30) are similarly interpreted as contractional, and bound a block that moved down from the hinge region of the antiform to the more spacious lower region of the fold (Fig. 37).

Mesoscopic F_3 folds occur mostly in the northwest. The folds are upright, and range from gentle in the east (Fig. 36A–C) to tight in the northwest (Figs 34D, 36D, E). Plunges are steep, reflecting the pre-existing steep attitude of layering resulting from D_2 folding. Tight folds in the northwest are asymmetric and parasitic on the large-scale F_3 limbs. Many folds have a steep axial-plane S_3 foliation which cross-cuts S_{1a} layering and in places transects F_{1b} and F_2 folds. In the east and southeast, S_3 is a spaced cleavage with a weak cataclastic texture. In the northwest, S_3 is a strong grain-flattening penetrative foliation with rare grain elongation forming a lineation. S_3 texture is cataclastic to mylonitic, and characterised by twisted, kinked, bent, and broken plagioclase with recrystallised grain boundaries, flat lenses of recrystallised mosaic quartz, strained K-feldspar augen, cracked or marginally recrystallised garnet, orthopyroxene with sutured boundaries, and fine-grained aggregates of recrystallised clinopyroxene. In places, a relict S_2 granoblastic texture is preserved. Type A dolerite dykes and granite pegmatites have a weak S_3 foliation. At GR 529255, S_3 is a spaced crenulation cleavage with parallel partial melt stringers along the cleavage, and crenulates the S_{1a} layering (Fig. 36F). In unit *fna* in the east, disrupted blocks of granulite with gentle to isoclinal F_2 folds are enclosed in massive leucosome (Fig. 34A, B), which is also interpreted as a D_3 melt. At GR 609250, S_3 is a finely spaced cleavage with small offsets of the layering.

In the northeast, bending of the F_2 inclined antiform into parallelism with the northern limb of the major F_3 antiform means that S_2 and S_3, where both are present, are also parallel. The existence of tight to isoclinal F_2 folds with an axial-plane foliation implies that the foliation is S_2, and the east-striking foliation in this area is identical with S_2 in texture, being generally granulo- to granoblastic, rather than cataclastic to mylonitic, which is more typical of S_3.

L_3 lineation is found only in the northwest, and arises from grain elongation parallel to F_3 fold axes.

Large-scale interference patterns of F_2 and F_3 folds are well displayed by the distribution of units *fg*, *fns*, and *fn,mn* on the geological map (Fig. 28), the isoclinal F_2 antiform and synform being folded to their present Type 2 (Ramsay 1967) irregular arcuate shapes (Fig. 38A). The axes of the major antiformal closure plunge 63–65° northwest in the north and 60° southwest in the south (Fig. 30). If the F_3 folds are unfolded, the closure reverts to a north-trending west-inclined

doubly plunging F_2 antiform with an axis bending through about 90° in the axial plane (Fig. 38B). The 90° bend probably formed early in D_3, the strain increasing an originally gentle plunge at each F_2 hinge to its presently steep attitude, forming a Type 1 (Ramsay 1967) elongated isoclinal antiform. An alternative process, large-scale D_2 shear of the antiform to form an F_2 sheath fold, the crest of which the F_2 antiform resembles, is less likely, because of the lack of an intense L_2 stretching lineation, and because the axes at each hinge are far from parallel, as a sheath fold shape requires.

F_{1b}–F_2 and F_2–F_3 interference patterns are well displayed on a mesoscopic scale in the south, forming Type 1 domes, saddles, and basins, and Type 2 crescents in thinly interlayered felsic and mafic granulites (Figs 34E, 39).

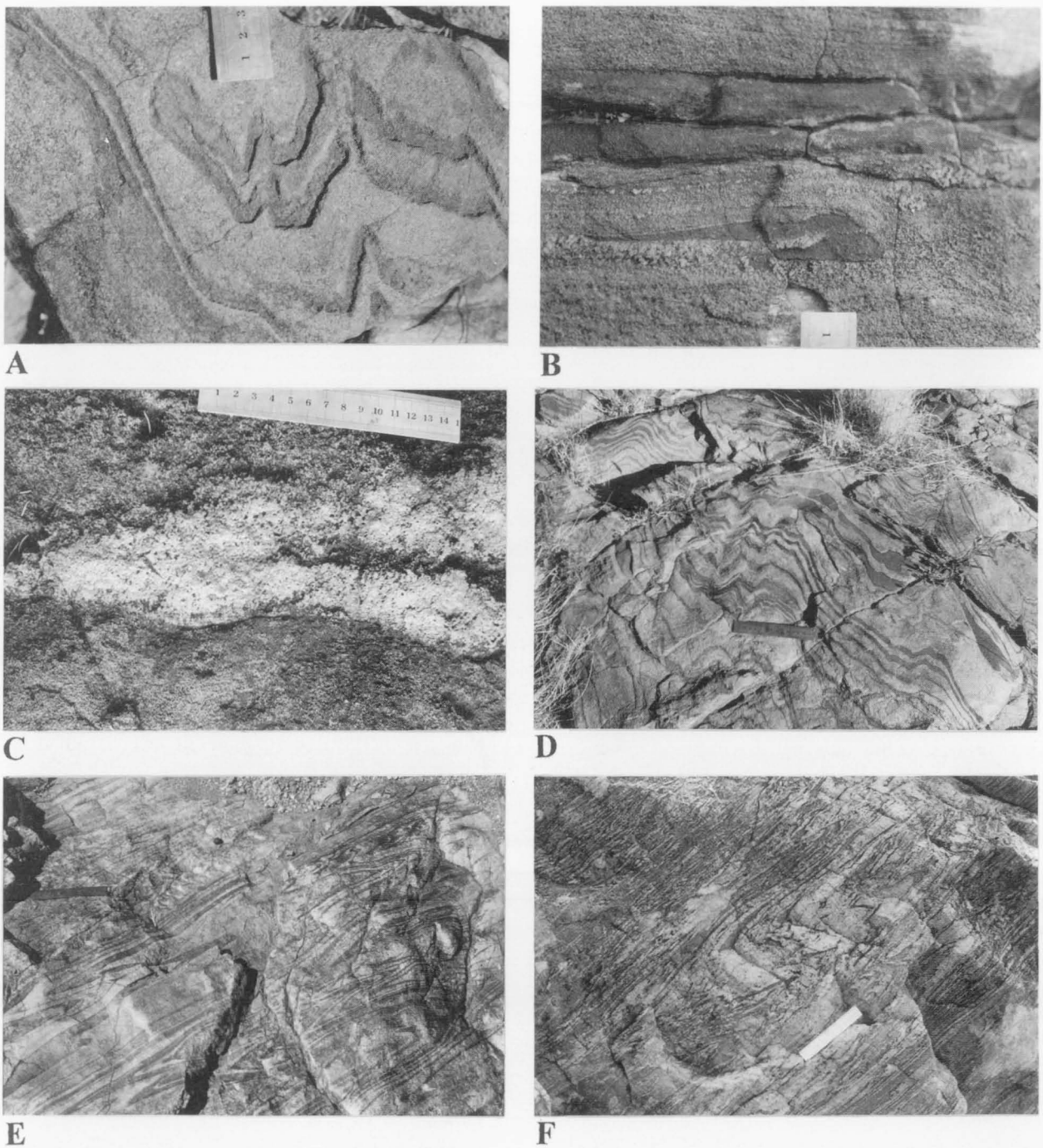

Figure 32. Mesoscopic F_{1b} and F_2 folds at Mount Aloysius. (A) Isoclinal F_{1b} fold in interlayered felsic and mafic granulites of unit fn,mn, folded into Type 2 crescent and partly disrupted by tight upright F_2 folds; scale in cm and mm; GR 608188. (B) Isoclinal F_{1b} fold in mafic and felsic granulites of unit fn,mn, transected by S_3 foliation well shown in coarse-grained leucocratic layers; scale in cm and mm; GR 549277. (C) Tight to isoclinal F_{1b} fold in quartz layer in felsic granulite of unit fn,mn, obliquely transected by S_3 foliation; scale 15 cm; GR 531284, same locality as Figure 31D. (D) Open upright F_{1b} folds in thinly interlayered felsic and mafic granulites of unit fn,mn; scale 15 cm; GR 565227, same locality as Figure 31F. (E) Tight F_2 folds in thinly interlayered felsic and mafic granulites of unit fn,mn; scale 15 cm; GR 577222. (F) Tight F_2 folds in thin-layered (S_{1a}) calc-silicate granulite (modal percentages: labradorite 64, diopside 20, quartz 10, titanite 5, opaque grains 1) of unit fn,mn; scale 15 cm; GR 577234.

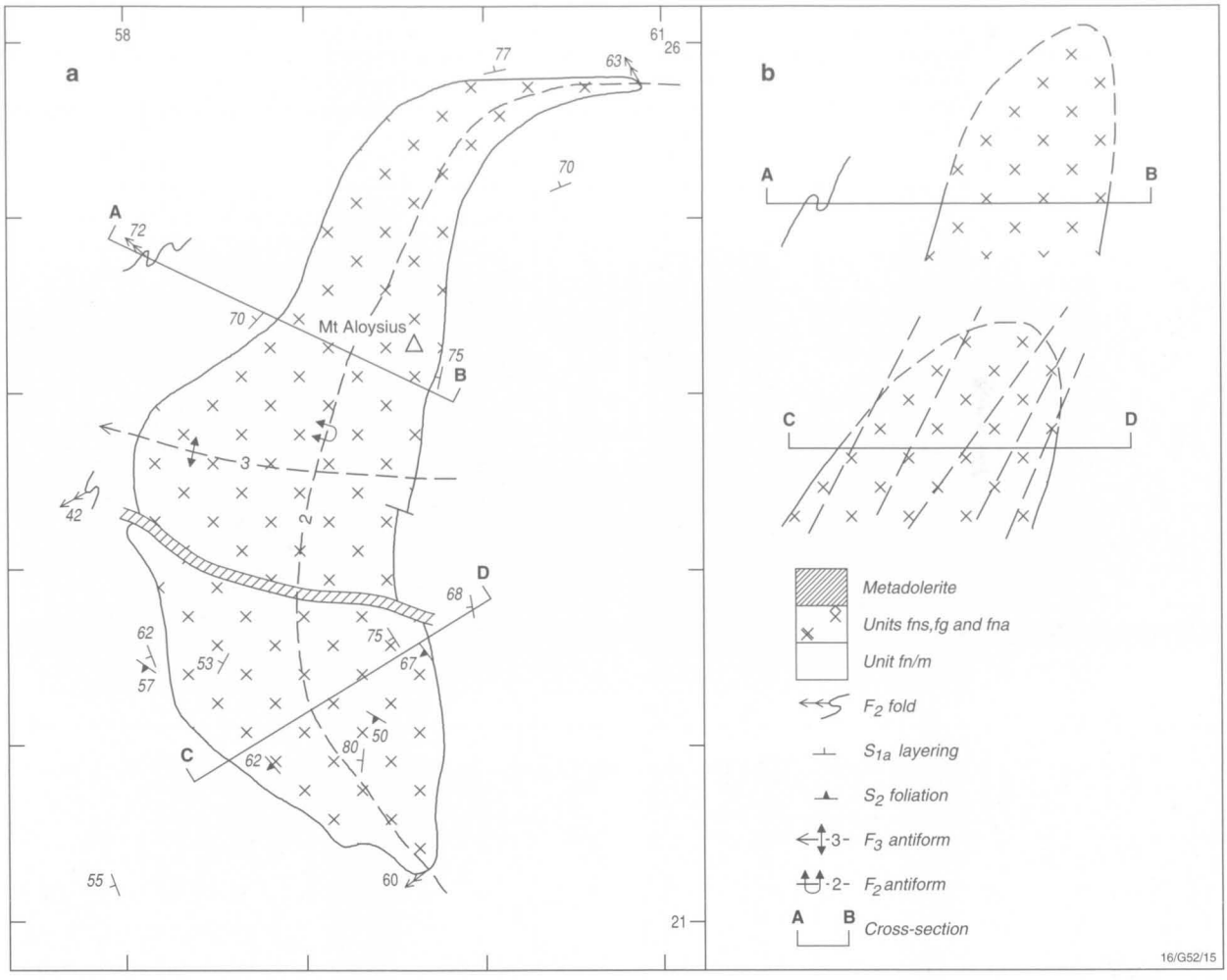

Figure 33. (A) Geological map and (B) cross-sections of central part of Mount Aloysius, showing S_2 foliation dipping less steeply than S_{1a} layering on eastern limb of F_2 fold, and parasitic folds with easterly component of vergence on western limb, indicating antiformal orientation of the F_2 fold.

D_{4*}. D_{4*} effects are mesoscopic only, and of restricted, though widely scattered, extent. F_{4*} folds (Fig. 40) are upright, gentle to open, and have a north-northeast-striking axial-plane cleavage, ranging from spaced cleavage seams 10 cm apart to a mild flattening of quartz and K-feldspar (Fig. 34F), with growth of new grains at their margins. Texture is granulo- to granoblastic. Scattered epidote, abundant disseminated calcite, and chlorite rims around opaque grains have formed in the northeast (90984085, GR 665226).

Mylonite zones. Seventeen mesoscopic mylonite zones were mapped in the Mount Aloysius massif (Fig. 41). The zones are a few metres wide and all consist of strongly foliated and lineated granulite-facies fine-grained gneiss (less commonly augen gneiss), with extreme elongation of quartz to ribbons. The mylonites are assigned to the various deformation events based on their effects (or lack of) on mafic dykes, or, where there is no such relationship, on their orientation and distribution with respect to major fold axes and foliations. Mylonitisation took place at syn-D_2, syn-D_3, and post-D_{4*} times. Mesoscopic kinematic information was observed in only seven of the mylonites, despite careful search, and in all cases indicated contractional movement, ranging from reverse dip slip, through oblique slip, to strike slip in a few places. Where kinematic information is lacking, the mylonites are presumed to have a reverse movement sense, and are so depicted in Figure 41. Examples of mylonite zones and pseudotachylite veins in the Hinckley Range area are shown in Figures 156 and 157.

Three syn-D_2 mylonite zones were found; they have no effect on, and are therefore older than, adjoining type A dykes. They have an easterly strike, moderately steep dips (>60°), and a shallow to steep lineation, indicating strike slip to dip slip. Data are too few to allow any kinematic conclusions.

Ten syn-D_3 mylonite zones were noted. They affect type A dolerites, as well as the host granulite, but the effects on the former, such as microjointing, spaced cleavage, and marginal mylonitic foliation, are weaker than in the adjoining mylonitised granulite. The mylonites strike easterly, dips are moderate to steep (33–78°), and lineations plunge from 5° to steeply down dip. All but one of the mylonites on the northern limb of the major F_3 antiform dip north and, similarly, those on the southern limb dip south (Fig. 41). In both limbs, the mylonites dip more gently than the granulite layering. The mylonites are interpreted as conjugate shears that helped to accommodate the space problem in the core of the F_3 antiform, allowing the core rocks to move out and down from the hinge region (Fig. 37).

Four post-D_{4*} mylonite zones were observed. Two cut granulite and have bordering veinlets of ultramylonite. Two coincide with and brecciate or cleave type C dolerite dykes. The mylonites strike north, through northeast, to east, and dip from from 45° to vertical. Data are too few to allow any

kinematic conclusions to be drawn. The post-D_{4*} mylonites cannot be directly correlated with the D_4 mylonites of Clarke (1992) in the Champ de Mars area, as the latter are an order of magnitude larger in thickness and throw, and differ significantly in orientation and metamorphic facies (amphibolite-facies) from those at Mount Aloysius.

Felsic granulite of the Ewarara area

The Ewarara intrusion is located in the north–central part of the Tomkinson Ranges 1:100 000 sheet area, about 3 km north of Kalka. The intrusion and surrounding granulite were mapped and studied in detail by Goode & Krieg (1967), Goode & Moore (1975), and Moore & Goode (1978). The felsic granulite (ETG) surrounding the Ewarara intrusion is part of the same granulite sequence found throughout the

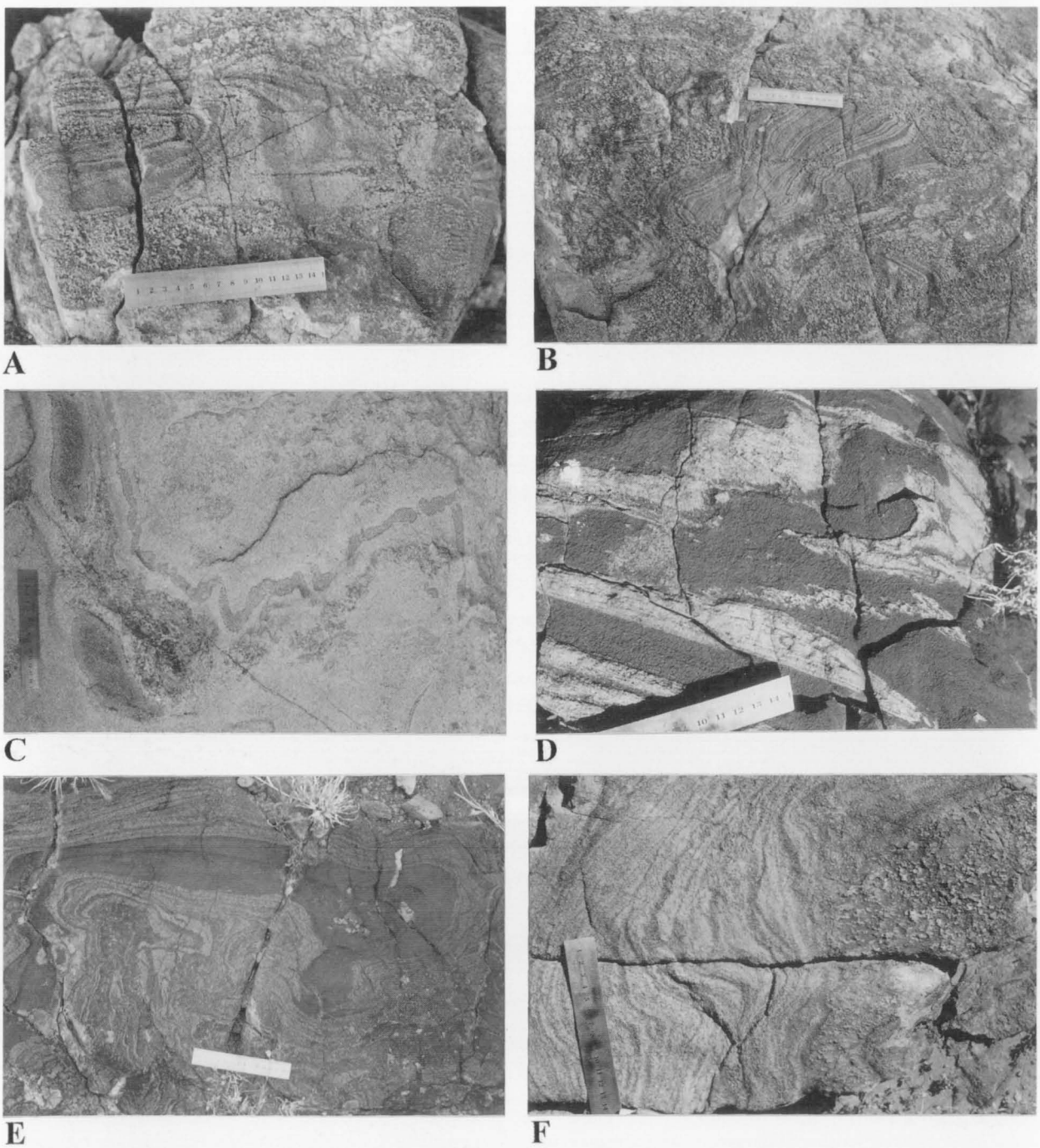

Figure 34. Mesoscopic F_2, F_3, and F_{4*} folds at Mount Aloysius. (A, B) Blocks of thin-layered felsic garnet granulite: (A) with isoclinal F_2 fold enclosed in massive very coarse-grained garnet leucosome of unit fna; scale 15 cm; GR 641219. (C) Open to close F_2 folds in interlayered felsic and boudinaged mafic granulites of unit fn,mn; scale 15 cm; GR 608188. (D) Open to tight F_3 folds in felsic granulite melt patches in mafic granulite of unit mn; scale in cm and mm; GR 558251. (E) Interference folds in interlayered felsic and mafic granulites of unit fn,mn; scale 15 cm; GR 613187; explanatory sketch shown in Figure 39. (F) Gentle to open F_{4*} fold in weakly layered felsic granulite of unit fna, with axial-plane foliation visible in coarse-grained granulite (right); scale in cm and mm; GR 666227.

Tomkinson Ranges, and classified as the Mount Aloysius Complex. The rocks are mostly well layered, the layering being of metamorphic differentiation origin, superimposed on igneous and/or sedimentary layering (Moore & Goode 1978). No stratigraphic facing was recognised. The sequence dips generally north at low to moderate angles, and so the oldest units are presumed to be those in the south of the area. The Ewarara intrusion and small mafic dykes and plugs (the

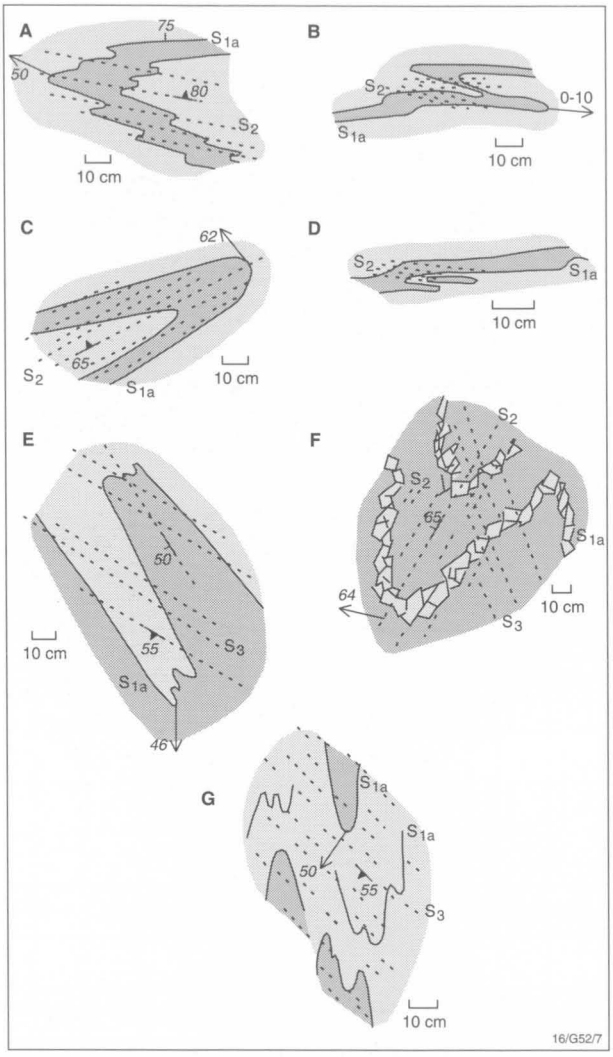

Figure 35. Sketches of mesoscopic F_2 folds at Mount Aloysius. (A, B) Tight upright folds with axial-plane foliation in thin-layered felsic granulite of unit fna; GR 658242. (C) Tight reclined fold with S_2 foliation parallel to one limb and oblique to the other limb in leucofelsic granulite of unit fn,mn; GR 653240. (D) Isoclinal folds in laminated to thin-layered felsic granulite of unit fna; GR 656241. (E) Tight folds transected by S_3 foliation in thin-layered felsic granulite of unit fn,mn; GR 574229. (F) Close reclined fold with S_2 axial-plane foliation transected by S_3 foliation in felsic garnet granulite with very coarse-grained quartz laminae S_{1a}, unit fn,mn; GR 607192. (G) Tight inclined folds transected by S_3 foliation in thinly layered felsic granulite with mafic to intermediate layers; GR 576222.

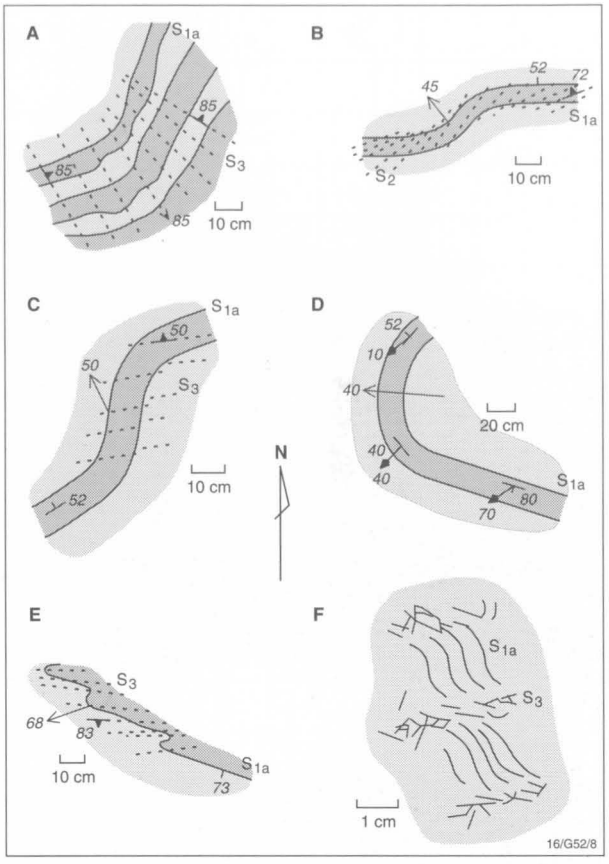

Figure 36. Sketches of mesoscopic F_3 folds at Mount Aloysius. (A) Gentle upright fold with axial-plane foliation in medium-grained compositionally layered felsic granulite of unit fna; GR 643221. (B) Gentle upright fold which bends S_{1a} layering and S_2 foliation in leucofelsic granulite of unit fn,mn; GR 669241. (C) Gentle reclined fold with axial-plane foliation in thin to medium-layered felsic granulite of unit fn,mn; GR 560249. (D) Close upright fold which folds L_2 lineation in medium-layered felsic granulite of unit fn,mn; GR 551217. (E) Tight upright folds with axial-plane foliation in weakly layered leucofelsic granulite of unit fnk; GR 548259. (F) Spaced crenulation cleavage S_3 with partial melt quartzo-feldspathic stringers parallel to S_3 and crenulating earlier S_{1a} layering in felsic garnet granulite of unit fn,mn; GR 529256.

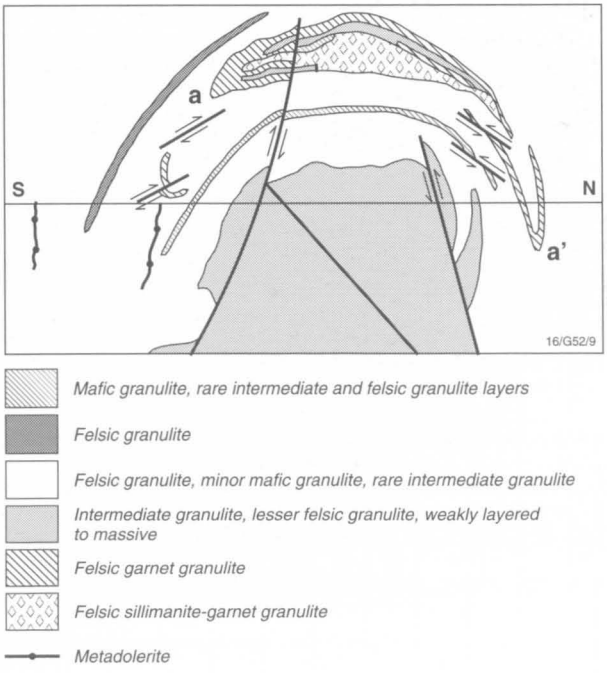

Figure 37. North–south vertical cross section through the Mount Aloysius massif, showing major F_2 and F_3 antiforms, block displaced down from hinge region of F_3 antiform, and schematic syn-D_3 mylonite zones on limbs of F_3. At a and a', F_2 antiform has a synformal orientation because of rotation on limbs of F_3 antiform. Same lithological patterns as Figure 28; vertical and horizontal scales equal.

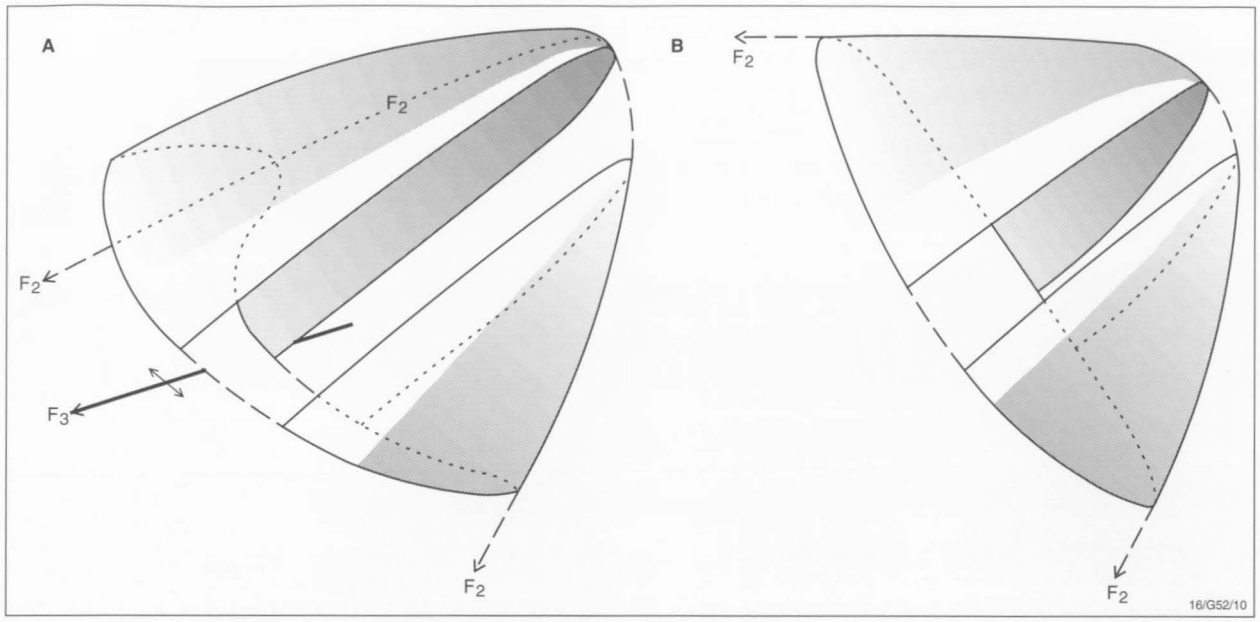

Figure 38. (A) Sketch of F_2–F_3 interference antiform folded into Type 2 arc late in D_3. (B) Sketch of Type 1 steeply doubly plunging isoclinal F_2–F_3 interference antiform formed early in D_3.

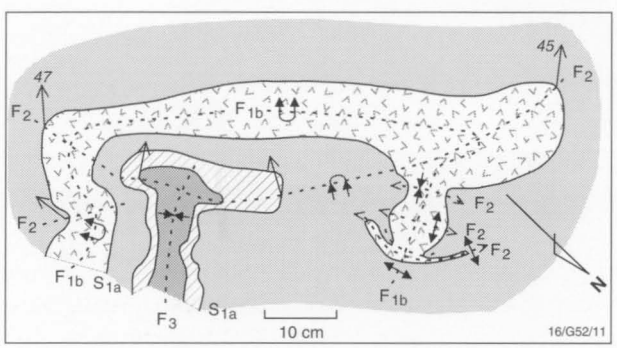

Figure 39. Explatory sketch of interference folds shown in Figure 34E. F_{1b} is an isoclinal antiform bent into Type 2 crescents (Ramsay 1967) by F_2 reclined folds (at left and right of Figure) and squashed into Type 1 domes and saddles by F_2 (right) and into a Type 1 basin by F_3 (slightly left of centre). GR 613187.

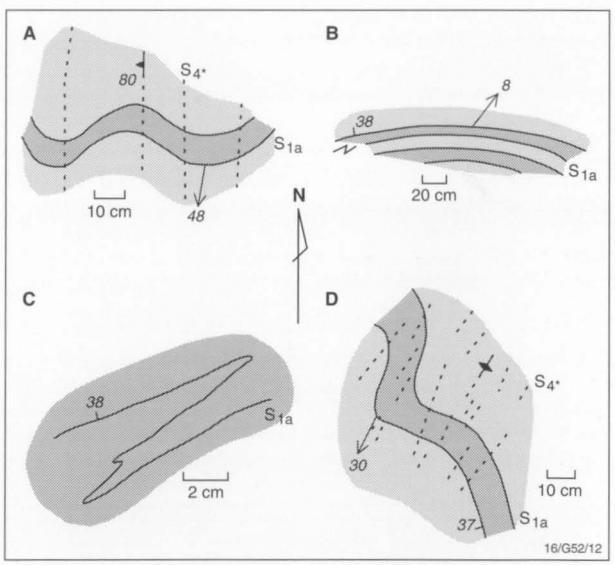

Figure 40. Sketches of mesoscopic F_{4*} folds at Mount Aloysius. (A) Open upright fold with spaced axial-plane cleavage in thin-layered weathered granulite (magnetite–goethite–quartz) of unit fna; GR 642219. (B) Gentle inclined fold with F_{1b} reclined fold preserved in left limb in thinly interlayered felsic granulite (massive medium-grained leucocratic layers and coarse-grained leucocratic layers) of unit fn,mn; GR 551216. (C) Enlargement of F_{1b} fold at left of (B). (D) Open upright fold with axial-plane cleavage in felsic magnetite granulite of unit fna; GR 663224.

'transgressive picrite suite' of Goode 1975) intrude the granulite.

Map units

fn. Felsic granulite (mostly orthogneiss) with minor mafic granulite crops out in four separate areas: southwest of the Ewarara intrusion, at the western end of the intrusion, around the eastern end of the intrusion, and in the extreme east of the area. The unit includes rare layers or boudins of intermediate and mafic granulite, up to 1 m thick (*fnm*).

fg. Garnet-bearing felsic granulite forms a small body in the south of the area, and also crops out at the northern margin of the Ewarara intrusion.

fna. Massive to weakly layered felsic granulite (orthogneiss) crops out along the eastern and western sides of the Ewarara intrusion, and at its southwestern end, where it is interlayered with intermediate granulite.

fni. Intermediate granulite of probable igneous origin is interlayered with massive to weakly layered granulite in the southwest of the area.

fnk. Leucofelsic granulite (orthogneiss) crops out in the far southeast and northwest of the area, but was not studied in detail.

mn. Mafic granulite layers of probable mafic igneous origin crop out throughout the area.

Rock units

Felsic granulite. Felsic granulite of various types makes up more than 90 percent of the granulite surrounding the Ewarara intrusion. It is prominently to indistinctly and dis-

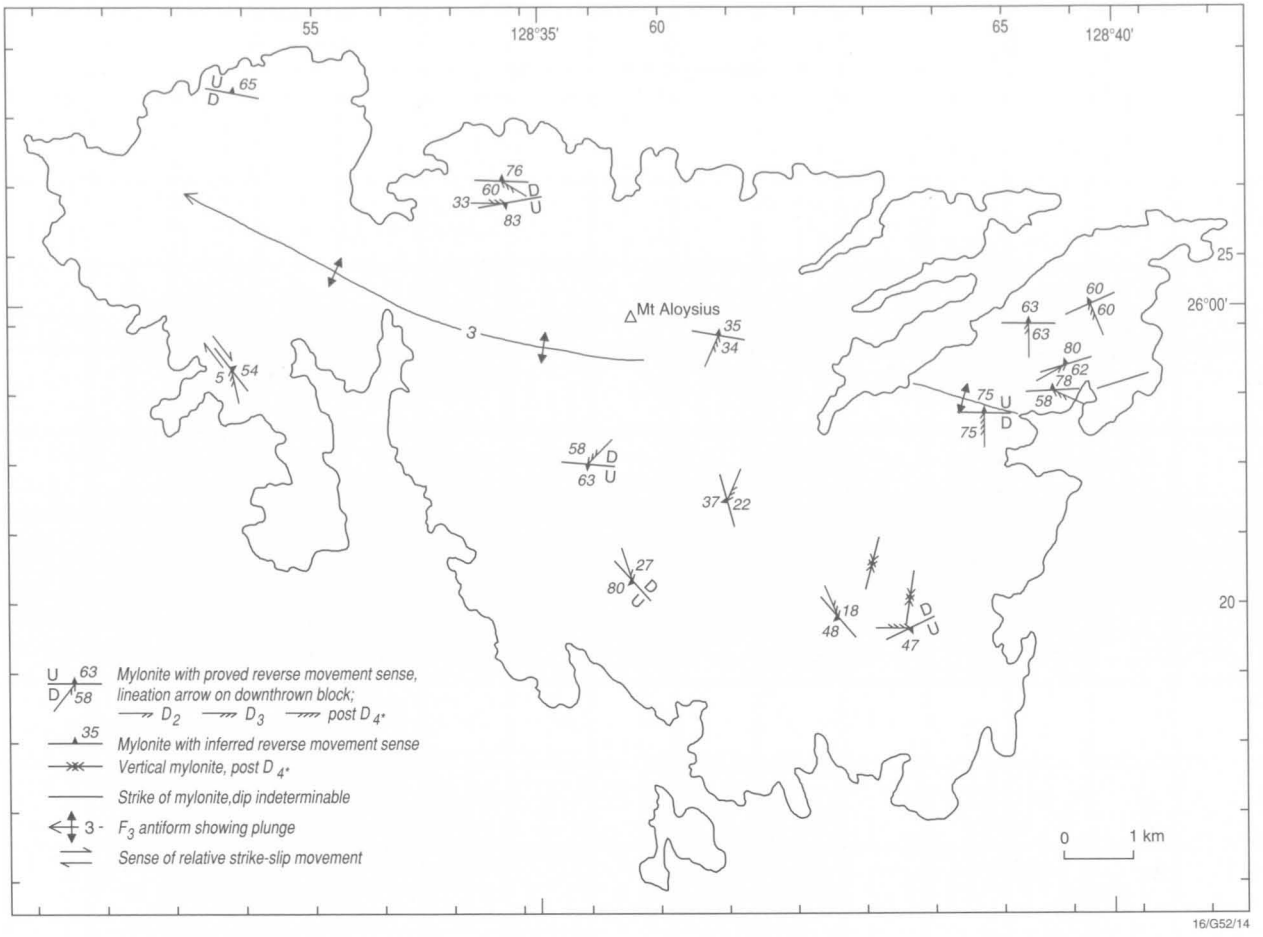

Figure 41. Distribution and attitudes of mesoscopic mylonite zones at Mount Aloysius.

continuously thinly to (rarely) thickly layered, but in a few places is non layered. Layers range from massive to foliated, the foliation arising from flattening of, mainly, quartz grains. Grain size is generally even within a layer, and ranges from fine to coarse in different layers; a few layers contain plagioclase or K-feldspar augen. Texture is generally granoblastic to lepidoblastic or blastomylonitic. Essential minerals are quartz and mesoperthitic alkali feldspar, together with various amounts of plagioclase, magnetite, green spinel, orthopyroxene, and garnet enclosing rare orthopyroxene remnants. The granulite at one locality (GR 188168) has abundant disseminated pyrite.

Relatively quartz-poor, feldspar-rich varieties with orthopyroxene are probably of felsic igneous origin, derived from either intrusive or extrusive rocks. Thick layers of felsic augen gneiss are characteristic of the massive to weakly layered felsic granulite unit (*fna*), and probably represent strongly deformed granitic intrusive rocks. In the southwestern area, the granulite comprises augen up to 2 cm long of K-feldspar, commonly with multicrystalline plagioclase mantles, in a fine to coarse-grained groundmass of discontinuously thin to thick-layered (or in places non-layered) felsic magnetite±garnet granulite. The plagioclase mantles range in shape from annular ovoid rims to long thin lenses. In some places, the augen consist only of plagioclase, and the rock is quartz-rich and coarse grained. The layering wraps around the augen.

Some felsic granulite has a metasedimentary appearance and composition. These characteristics include a very even grain size, giving an arenitic appearance, and high quartz, garnet, and magnetite contents, in places in alternating quartz-rich and magnetite and/or garnet-rich layers. Elsewhere magnetite-bearing felsic granulite grades across strike into magnetite quartzite or quartz-rich granulite. Quartzite, with less than 5 percent feldspar and garnet is also present. Some granulite, consisting only of quartz and feldspar, resembles meta-arkose. At GR 188141, banded iron formation is composed of magnetite (70%), quartz (13%), garnet (10%), orthopyroxene (2%), clinopyroxene (1%), and apatite (trace). Such compositions indicate that these granulites were derived from sedimentary protoliths.

Intermediate granulite. This is characteristically a medium-grained, two-pyroxene granulite, which is massive to indistinctly layered and forms layers up to 45 m thick interlayered with felsic augen gneiss. The rock commonly has a leuconoritic composition. It is granoblastic, and consists of labradorite, orthopyroxene, clinopyroxene, opaque grains, and minor biotite and hornblende.

Mafic granulite. Mafic granulite forms layers and boudins up to 1 m thick in felsic granulite. It is fine to medium grained, granuloblastic to weakly cataclastic, and of gabbronoritic to mela-gabbronoritic composition. It comprises labradorite, orthopyroxene, clinopyroxene, hornblende, and, locally, garnet, opaque grains, and spinel. Boudins of mafic granulite in the southwest of the area consist of clinopyroxene, andesine, and orthopyroxene.

Mafic dykes. As found elsewhere in the Tomkinson Ranges, three generations of mafic dykes intrude the felsic granulites around the Ewarara intrusion. Type A metadolerites have only been recognised in the northeast (GRs 182165 and 187164) where they dip 15° east and are boudinaged. They are fine-grained and recrystallised to a massive granuloblastic texture. Straight, northeast-striking, steeply dipping dolerite dykes are

common throughout the area, and their orientation suggests that they are mainly of type C. They are commonly cleaved (cleavage planes 4–20 cm apart), fractured and, in places, brecciated, with pseudotachylite along their margins and forming the matrix of the breccia.

Structure

Felsic granulite around the Ewarara intrusion dips uniformly north at 20–50°, except for a localised northeast-trending antiform–synform pair. The intrusion occupies the site of the former synform, the antiform being preserved along its northwestern margin. Two dextral strike-slip faults displace the granulite east of the intrusion, and an east-striking crush zone separates the northern and southern lobes of the intrusion. Numerous dolerite dykes strike parallel to the axial planes of the F_3 folds, and cut S_{1a} layering in the F_3 hinges.

D1. The layering in the granulite, as in the Mount Aloysius area, is mainly a product of metamorphic differentiation superimposed on original sedimentary and igneous layering, and is denoted S_{1a}. It is shown as trend lines on the Tomkinson Ranges 1:100 000 map. There is commonly a tectonic flattening of mineral grains and rare mafic boudins parallel to the layering. F_{1b} folds which affect the layering were found at only one locality (GR 195155), and consist of small intrafolial isoclinal detached fold hinges of mafic granulite about 1 cm thick, enclosed in felsic granulite.

D2. Only one possible D_2 structure was recognised in the Ewarara area, a mesoscopic gentle upright fold transected by S_3 foliation at GR 158165. The fold plunges 21° east-northeast, parallel to the F_3 folds described below, and with which it appears identical, so it may be a local early F_3 fold.

D3. D_3 formed the gentle macroscopic F_3 antiform on the northern side of the Ewarara intrusion, and the two dextral strike-slip faults to the east. A synform complementing the antiform appears to have been largely displaced by the intrusion, although its age relationships are by no means unequivocal, particularly as the antiform is preserved in only one area (GR 142153), about 700 m west of the intrusion. The antiform plunges 23° northeast, and is accompanied in most places by a near-vertical axial-plane foliation S_3. Northwest of the intrusion, S_3 ranges from a set of microfractures concentrated in quartz grains or in coarse-grained garnet-rich layers, to a flattening of quartz and feldspar grains. Elongation of the grains produces a mineral-stretching lineation (L_3), which plunges steeply down dip at a large angle to mesoscopic F_3 fold axes. S_3 generally diverges around the axial plane in the direction of fold closure, but, in a few places, converges. Between the intrusion and the western strike-slip fault, S_3 is weaker, and is defined by a set of microfractures, microcracks, or a closely spaced (mm scale) cleavage.

Mesoscopic F_3 folds are abundant northwest of the Ewarara intrusion. They are gentle to open, upright, plunge gently east-northeast, and parallel the macroscopic F_3 fold. Two dextral strike-slip faults cut the granulites southeast of the Ewarara intrusion, and are assigned to D_3 because their dextral sense of shear is the same as that of the macroscopic F_3 antiform–synform pair northwest of the intrusion. Displacement on the western fault is about 1.5 km, and on the eastern fault about 300 m. The eastern fault is filled with a dolerite dyke.

Mylonite zones. Four mylonite and ultramylonite zones were noted in the area northwest of the Ewarara intrusion. They are generally less than 1 m thick. The zones strike north-northeast and dip steeply northwest or southeast. Lineation in three is horizontal, and steep in only one, suggesting that the mylonites are coeval with the D_3 strike-slip faults east of the intrusion. No mesoscopic kinematic information was obtained from the mylonites. North and southeast of the intrusion, pseudotachylite forms veinlets and breccia matrix, and because of its brittle-fracture connotation is assigned to a younger episode in the deformation sequence.

The geological history of the Ewarara area is given in Table 4, together with episodes recognised by Clarke et al. (1995a) in the Champ de Mars–Hinckley Range area, 20 km to the west, and by Pharaoh (1990) in the Ewarara area for comparison.

Petrography and geochemistry of felsic gneiss

Orthopyroxene-bearing felsic gneiss is widespread in the western Musgrave Block. It commonly contains up to 4 percent of strongly pleochroic orthopyroxene, as well as quartz, K-feldspar, plagioclase (typically calcic oligoclase or andesine), and accessory zircon, apatite, and opaque minerals. Clinopyroxene occurs in some layers, particularly the more mafic ones. Most such gneiss has a granitic (*s.s.*) composition; granodiorite is less common, and tonalite, quartz monzodiorite, and diorite are rare. K-feldspar is commonly strongly perthitic, plagioclase is antiperthitic, and in some rocks mesoperthite is the only feldspar. However, many gneisses are partly or wholly recrystallised and some have mylonitic textures. Reddish-brown biotite and, less commonly, brownish-green hornblende are present in many of these deformed rocks, and appear to be mostly of retrograde origin, replacing pyroxene.

Garnet-bearing gneiss is also common and, apart from the presence of garnet (up to about 6%), rather than orthopyroxene, is petrographically similar to the orthopyroxene gneiss. A few gneisses contain both garnet and orthopyroxene, but the former does not appear to coexist with either clinopyroxene or hornblende, except in secondary assemblages formed during later deformations. Some garnet leucogneiss is thought to be of igneous origin (see below), although in some places (e.g., Mount Aloysius) more garnet-rich paragneiss is interlayered with other metasedimentary rocks (garnet+sillimanite-bearing metapelites, quartzite, and calc-silicate granulite).

The widespread occurrence of mesoperthite indicates crystallisation of the original feldspar at high temperatures and very low water pressures. Calcic alkali feldspar cannot form at high water pressures, because the temperature of the alkali feldspar solvus crest rises steeply with increasing An content, and would intersect the feldspar solidus, which is lowered with increasing P_{H2O} (Morse 1968). Low P_{H2O} is consistent with the essentially anhydrous assemblages present in most undeformed felsic gneiss.

Chemical data (Table 5; Fig. 42), mainly for rocks from the western Hinckley Range area, are consistent with a felsic igneous origin for most orthopyroxene-bearing gneisses, which are metaluminous or only slightly peraluminous. ASI (alumina-saturation index: molecular $Al_2O_3/(CaO-3.33P_2O_5+Na_2O+K_2O)$ values are less than 1.1 (Fig. 43), so they are equivalent to I-type (derived by partial melting of igneous precursors) granitoids on the classification of Chappell & White (1974). However, it is unclear whether they represent metamorphosed intrusive or extrusive rocks. More massive orthogneisses may well be intrusive, whereas many of those interlayered with metasedimentary rocks could be of volcanic origin.

Many orthopyroxene-bearing gneisses (mostly granodioritic to granitic) belong to the Y (and heavy rare-earth elements: HREE) depleted suite of Sheraton & Black (1983) (Fig. 44), which is thought to represent new (i.e., primary) continental crust derived by partial melting of a hornblende±garnet-bearing, but feldspar-poor, mafic source (such as subducted hydrated oceanic crust or a mafic underplate). Y-depleted gneisses tend to have high Sr and Ce/Y (Fig. 45), and spidergrams show little or no Sr depletion (Fig. 46), because plagioclase was

Table 4. Sequence of events in the Ewarara area.

Event	*Age (Ma)*	*This Bulletin*	*Clarke (1992)*	*Pharaoh (1990)*
Brecciation, faulting	550?	Spaced cleavage, breccia, pseudotachylite	D_{4-7}	Pseudotachylyte veining
Mafic intrusion	820[2]	Type B dolerite dykes	Type C dykes	Olivine dolerite dykes
Mafic intrusion		?Ewarara intrusion (relationships to D_3 uncertain), type C dolerite dykes	Type B dykes	Emplacement of Ewarara intrusion
D_3		F_3 upright gentle folds, ENE trend, S_3 axial-plane foliation; strike-slip faults; granulite-facies metamorphism		D_2, F_{2F}
Mafic intrusion	1050–1080[2]	Type A dykes, commonly metamorphosed	Giles Complex, type A dykes	Early recrystallised dykes, early bodies of Giles Complex
D_2	1200[1,2]	One F_2 fold observed, transected by S_3; granulite-facies metamorphism	D_2	D_1, F_{1F}, S_{1F} composite layering
D_1		S_{1a} layering, F_{1b} isoclinal intrafolial folds; granulite-facies metamorphism	D_1	Early gneissose fabric (if tectonic)
Sedimentation; emplacement of intrusive and volcanic rocks	c.1550[1,2]	Protoliths of felsic orthogneiss; ages of protoliths of mafic rocks and calcareous and quartzitic metasediments unknown	Protoliths of ortho- and paragneiss	Protoliths of banded series, early gneissose fabric (if sedimentary)

[1] Rb–Sr whole rock isochron ages (Gray, 1978); [2]U–Pb zircon ages (Sun & Sheraton 1992; Sun et al. 1996a, b; S-S. Sun unpublished data).

not a major residual (nor presumably a fractionating) phase; some show marked positive Sr anomalies. Zircons from one such gneiss from Mount Aloysius indicate a protolith age of about 1530 Ma and metamorphic age of about 1200 Ma (U–Pb ion-microprobe data, Sun & Sheraton 1992).

In contrast, many, mostly granitic, gneisses are not depleted in Y (nor presumably HREE) (Fig. 44), and these probably mainly represent partial melts of predominantly felsic crustal rocks. They tend to have low Sr and Ce/Y (Fig. 45), and spidergrams, particularly for the more fractionated siliceous granites, have significant negative Sr anomalies (Fig. 46), consistent with residual plagioclase and/or plagioclase fractionation. However, two high-Sr gneisses, which have quartz monzodioritic and dioritic compositions without significant Sr anomalies, may have been derived by melting of a mantle source, with subsequent fractionation. An Y-undepleted granitic gneiss from north of Mount Davies has given zircon U–Pb ion-microprobe ages of 1305±8 Ma and 1223±7 Ma, attributed to those of the igneous protolith and high-grade metamorphism, respectively (Sun & Sheraton 1992).

Many garnet-bearing gneisses also have near-minimum melt (i.e., granitic, *s.s.*) compositions (Fig. 42), suggesting that, like the orthopyroxene gneisses, they are orthogneisses. This is supported by their only slightly peraluminous compositions (ASI 1.0-1.1: Fig. 43). However, other garnet gneisses are more strongly peraluminous and some are relatively quartz-rich, more consistent with a sedimentary origin. Most analysed garnet gneisses have relatively high Y, but low Sr and Ce/Y (Figs 44, 45), typical of both felsic igneous rocks formed by intracrustal melting and clastic sedimentary rocks derived therefrom (Tarney et al. 1987); spidergrams show marked negative Sr anomalies (Fig. 46).

Unlike many other granulite terranes, which appear to have undergone depletion in large-ion lithophile elements

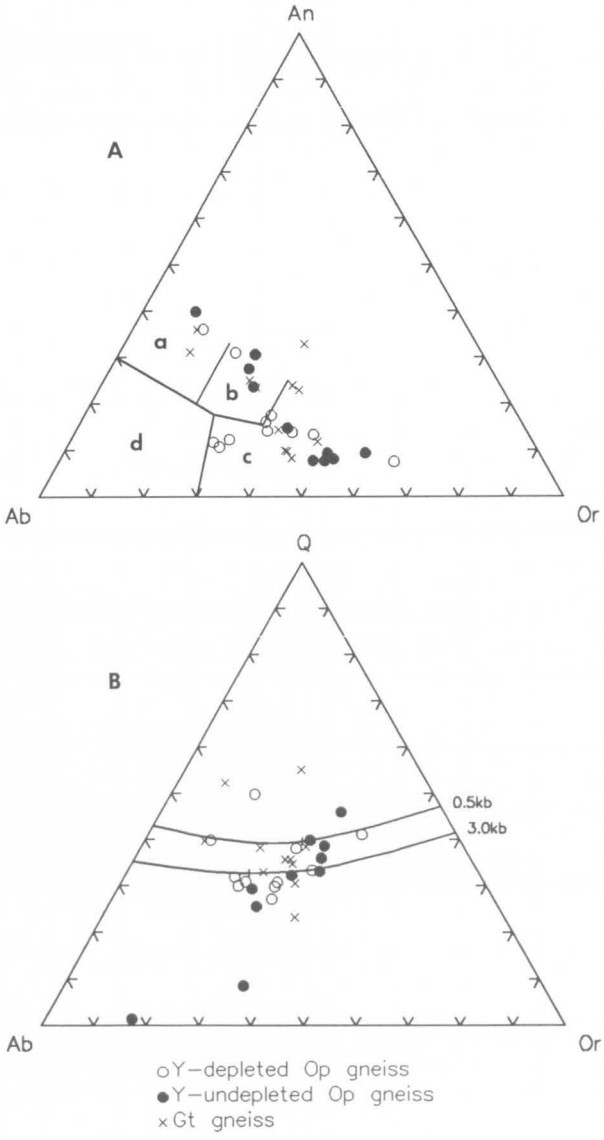

Figure 42. (A) Normative Ab–Or–An diagram for felsic gneisses from the western Tomkinson Ranges, showing the a, tonalite; b, granodiorite; c, granite; and d, trondhjemite fields of Barker (1979). (B) Normative Q–Ab–Or diagram showing quartz–feldspar field boundaries and positions of quaternary isobaric minima at 0.5 and 3.0 kb P_{H2O} (after Tuttle & Bowen 1958).

Table 5. Chemical analyses of representative felsic orthogneisses from the western Musgrave Block.

Sample no.	*90984005*	*91988087*	*91989009*	*90984007*	*90984057*	*91988015*	*90984019*	*91988033*
Locality	*Mount Aloysius (central)*	*Western Champ de Mars*	*Murray Range*	*Western Champ de Mars*	*Western Champ de Mars*	*Mount Aloysius (east)*	*Mount Aloysius (central)*	*Mount Aloysius (south)*
Lithology	*Op-Kf-Qz-Pl gneiss*	*Bt-Op-Pl-Qz-Kf gneiss*	*Bt-Op-Mp gneiss*	*Bt-Hb-Op-Qz-Kf-Pl gneiss*	*Bt-Hb-Op-Qz-Mp gneiss*	*Op-Cp-Qz-Kf-Pl gneiss*	*Op-Gt-Pl-Qz-Kf gneiss*	*Bt-Gt-Qz-Mp gneiss*
Group	*Y-dep.*	*Y-dep.*	*Y-dep.*	*Y-undep.*	*Y-undep.*	*Y-undep.*	*Y-undep.*	*Y-undep.*
SiO_2	65.14	73.37	69.45	64.97	74.28	56.01	68.79	74.00
TiO_2	0.55	0.42	0.52	0.67	0.37	0.90	0.53	0.15
Al_2O_3	15.86	13.30	15.05	16.36	13.10	17.07	15.71	13.90
Fe_2O_3	1.51	0.85	1.35	2.22	0.78	2.92	0.88	0.66
FeO	4.57	0.76	1.10	2.19	0.47	4.63	2.42	0.46
MnO	0.10	0.03	0.08	0.11	0.03	0.13	0.04	0.03
MgO	2.45	0.62	0.78	1.43	0.47	4.35	1.03	0.16
CaO	4.29	1.86	2.13	4.16	1.41	5.61	3.18	1.34
Na_2O	3.45	3.29	3.98	3.73	3.04	3.58	3.42	3.70
K_2O	1.32	4.36	4.21	3.06	5.44	3.09	2.88	4.71
P_2O_5	0.07	0.08	0.14	0.16	0.10	0.38	0.07	0.03
LOI	0.51	0.34	0.29	0.45	0.40	0.52	0.44	0.31
Rest	0.20	0.15	0.26	0.31	0.20	0.52	0.27	0.16
Total	**100.02**	**99.43**	**99.34**	**99.82**	**100.09**	**99.71**	**99.66**	**99.61**
	C.I.P.W. norms							
Q	24.45	32.85	24.77	20.54	32.41	4.58	28.40	31.38
C	1.12	–	0.41	—	–	–	1.35	0.35
Or	7.80	25.76	24.88	18.08	32.15	18.26	17.02	27.83
Ab	29.19	27.84	33.68	31.56	25.72	30.29	28.94	31.31
An	20.83	8.65	9.65	18.86	6.03	21.38	15.32	6.45
Di	–	0.05	–	0.59	0.24	3.20	–	–
Hy	12.52	1.58	2.14	4.56	1.06	14.12	5.47	0.51
Mt	2.19	1.23	1.96	3.22	0.54	4.23	1.28	0.96
Il	1.04	0.80	0.99	1.27	0.70	1.71	1.01	0.28
Ap	0.17	0.19	0.33	0.38	0.24	0.90	0.17	0.07
mg	48.9	59.3	55.8	53.8	64.1	62.6	43.1	38.3
	Trace elements in parts per million							
Ba	614	694	1135	1391	862	2565	1258	474
Li	15	11	33	11	6	8	11	12
Rb	18	116	137	100	171	99	82	326
Sr	383	138	282	407	176	827	345	121
Pb	13	28	38	30	37	21	31	72
Th	<2	<2	7	8	21	7	<2	31
U	0.5	<0.5	<0.5	<0.5	<0.5	<0.5	1.0	10
Zr	140	112	241	228	145	160	175	92
Hf	2	4	7	6	5	8	4	5
Nb	4	<2	5	7	8	8	12	8
Y	18	6	5	28	25	28	17	20
La	30	15	47	38	35	62	33	31
Ce	62	15	85	62	53	135	60	44
Nd	24	3	26	24	18	48	23	15
Pr	4	<2	10	8	6	15	<2	<2
Sc	20	6	7	15	7	18	11	3
V	107	22	16	60	11	130	61	7
Cr	31	7	3	14	4	62	73	1
Ni	10	6	3	6	3	28	17	2
Cu	5	2	<1	4	<1	20	7	<1
Zn	66	29	51	67	20	85	63	35
Sn	<2	3	8	4	3	2	<2	5
Ga	16	13	16	18	14	20	21	21
S	<100	100	20	100	70	100	<100	10
Be	1	<1	2	3	1	4	1	2

mg, atomic 100Mg/(Mg+Fe^{2+}); LOI, loss on ignition.
Bt, biotite; Cp, clinopyroxene; Fl, fluorite; Gt, garnet; Kf, K-feldspar; Mp, mesoperthite; Op, orthopyroxene; Pl, plagioclase; Qz, quartz.

(LILE: K, Rb, Th, U, etc.) during metamorphism (Tarney et al. 1972), K/Rb ratios are not particularly high (mostly 200–300), implying little loss of Rb relative to K. However, this may reflect the rarity of K-feldspar-free rocks (e.g., tonalitic gneiss) which, because they do not contain a phase capable of retaining much Rb, are the most susceptible to such depletion (Tarney & Windley 1977). The only analysed tonalitic orthogneiss has a K/Rb ratio of 609. On the other hand, as pointed out by Gray (1977), Th/U ratios are much higher (up to about 80) than the estimated crustal average (~3.8: Taylor & McLennan 1985), consistent with metamorphic depletion of U, possibly during dehydration.

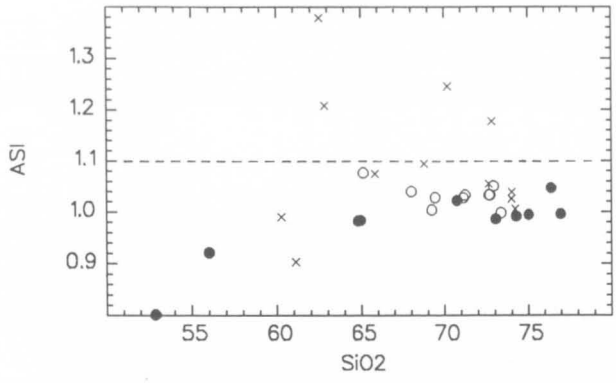

Figure 43. Plot of alumina saturation index (ASI = molecular $Al_2O_3/(Na_2O+K_2O+CaO-3.33P_2O_5)$) against SiO_2 for felsic gneisses. The dashed line separates the fields of I-type (igneous-derived) (lower) and S-type (sedimentary-derived) granitoids of Chappell & White (1974). Some garnet-bearing gneisses are markedly peraluminous. Symbols as in Figure 42.

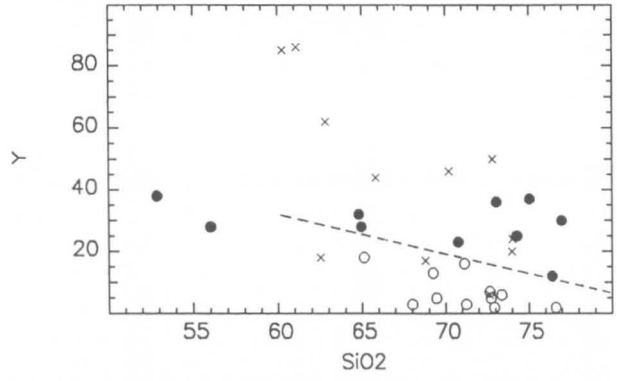

Figure 44. Plot of Y against SiO_2 for felsic gneisses. Dashed line indicates the approximate boundary between fields of Y-depleted (lower) and Y-undepleted felsic orthogneisses of the Archaean Napier Complex, Enderby Land, Antarctica (after Sheraton & Black 1983). Symbols as in Figure 42.

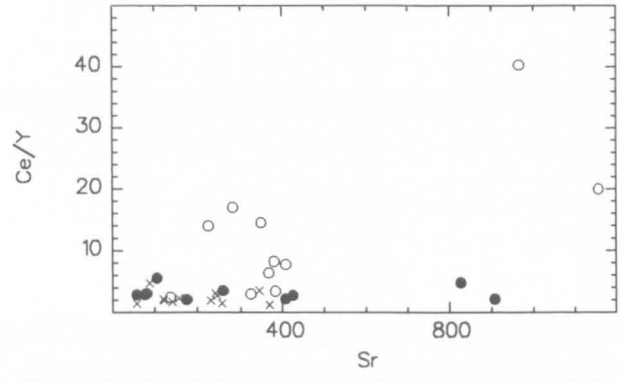

Figure 45. Plot of Ce/Y against Sr for felsic gneisses. Y-depleted orthogneisses commonly have high Sr and Ce/Y, consistent with derivation by partial melting of a hornblende± garnet-bearing mafic source. Symbols as in Figure 42.

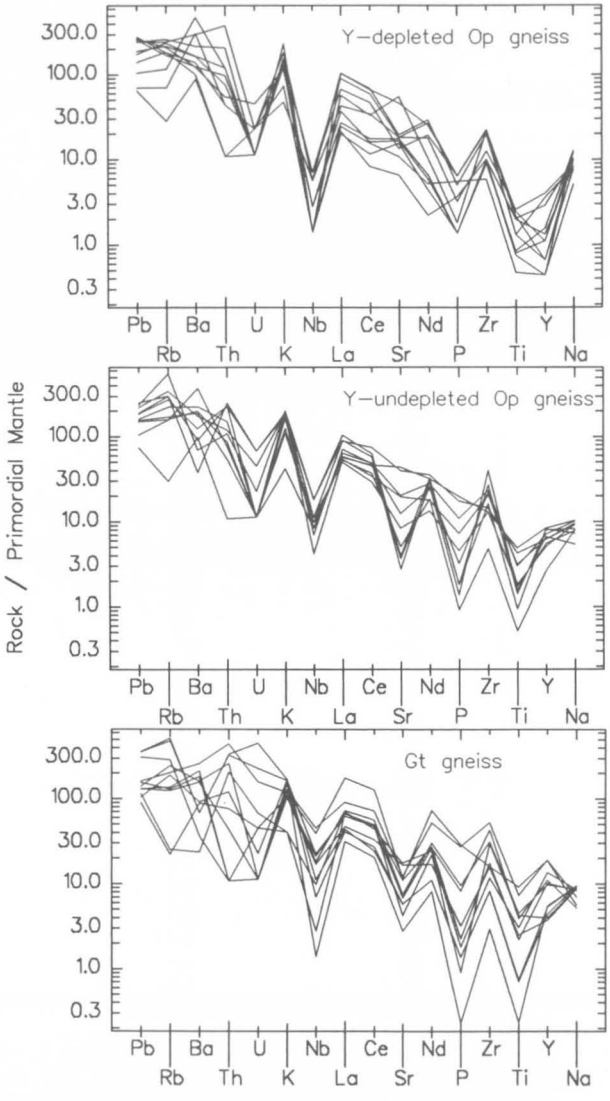

Figure 46. Primordial mantle-normalised incompatible element abundance diagrams (spidergrams) for felsic gneisses. Normalising values (Pb, 0.20; Rb, 0.63; Ba, 6.91; Th, 0.092; U, 0.022; K, 230; Nb, 0.71; La, 0.70; Ce, 1.81; Sr, 20.9; Nd, 1.35; P, 95; Zr, 11.1; Ti, 1270; Y, 4.52; Na, 2890 ppm) after Sun & McDonough (1989). Most Y-depleted orthogneisses do not have significant Sr anomalies, whereas Y-undepleted orthogneisses have marked negative Sr anomalies, consistent with partial melting of felsic crustal rocks.

The Giles Complex 1: Tomkinson Ranges

Regional geological framework

In the western Musgrave Block, the Giles Complex consists of 17 exposed intrusions and faulted segments of intrusions confined to the granulite-facies felsic to mafic granulite terrane bounded to the north by the Woodroffe Thrust Fault. The extension of the latter north of the Mann and Tomkinson Ranges is delineated by well-defined magnetic and gravity lineaments (Figs 95, 96). Mapping in the Bates 1:100 000 sheet area, north of the Tomkinson Ranges (Fig. 1), has identified a northwest-trending mylonitic shear zone (Fig. 9), which probably represents the extension of the Woodroffe Thrust in this area (Stewart 1993, 1995b). This zone is up to 3 km wide and has moved upper amphibolite-facies garnet–hornblende granite and rapakivi granite in the south over middle amphibolite-facies granitic gneiss in the north. The southern block is cut by dolerite dykes containing metamorphic garnet–clinopyroxene assemblages, which indicate pressures of 14.0±1.1 kb for T = 750°C (Clarke et al. 1995a), suggesting that the sole of the thrust in this area represents the deepest structural level so far seen in the western Musgrave Block. As indicated below, progressively shallower crustal levels south of the Woodroffe Thrust are indicated by the transition from ultramafic-dominated intrusions (e.g., Murray Range, Wingellina Hills, Claude Hills, Ewarara, Kalka, Gosse Pile) to gabbroic (e.g., Hinckley Range, Michael Hills, Mount Davies) and, ultimately, troctolite-dominated intrusions (Blackstone Range, Bell Rock, Jameson Range). Further P–T studies of the host felsic granulites are required to confirm shallower crustal levels in this direction.

The Giles Complex within the Tomkinson Ranges and ranges to the west includes the following bodies (from east to west): Teizi anorthositic suite (at least six discrete bodies and numerous recrystallised tongues), Claude Hills, Ewarara, Kalka, Gosse Pile, Mount Davies, Wingellina Hills, Hinckley Range, Michael Hills, The Wart, Bell Rock, Blackstone Range, Cavenagh Range, Morgan Range, Murray Range (two bodies), and Jameson Range (Fig. 47; Plates 1–3). Some of these bodies are believed to have originally been continuous, for example Blackstone–Bell Rock (Daniels 1974), The Wart–Bell Rock, Kalka–Gosse Pile (Moore 1971a, b) and possibly Michael Hills–Mount Davies. Several of these intrusions, including the Kalka, Ewarara, Gosse Pile, Mount Davies, and Teizi intrusions within South Australia, have been the subject of detailed investigations by staff and students of the University of Adelaide (Nesbitt & Kleeman 1964; Nesbitt & Talbot 1966; Goode & Krieg 1967; Goode 1970, 1976, 1977, 1978; Nesbitt et al. 1970; Moore 1971a, b; Goode & Moore 1975). For this reason, only the principal features of these bodies are summarised below, whereas the layered intrusions in Western Australia are described in more detail. Sampling traverses were made across seven of these intrusions (The Wart, Latitude Hill, Hinckley Range, Bell Rock, Murray Range, Blackstone Range, and Jameson Range: Fig. 47), and the petrography of individual samples is listed in Appendix II.

The mafic–ultramafic intrusions are mostly oriented subparallel to foliation in granulite-facies gneiss, which in the northern Hinckley Range–Ewarara–Teizi area trends broadly east–west, with strike deflections near Mount West, Wandu Hill, and south of Mount Davies (Figs 4, 47; Plates 1, 2). The most notable discordances between the strike of mafic–ultramafic intrusions and the foliation of country rock gneiss are around the Ewarara (Fig. 48), Mount Davies (Figs 50, 55), and Murray Range (Figs 99–101) layered intrusions.

The degree of deformation of layered intrusions tends to decrease from east to west: the eastern bodies are mostly steeply dipping, cut by mylonitic shears, and contain pervasive pseudotachylite vein–breccia systems (e.g., Kalka, Mount Davies, Hinckley Range, Wingellina Hills; Glikson & Mernagh 1990). The western intrusions are commonly little deformed to flat lying (e.g., Bell Rock, Blackstone Range, Jameson Range, Cavenagh Range). Preliminary estimates suggest pressures of about 6 kb for emplacement of the Wingellina Hills body and lower pressures for the Blackstone Range and Jameson Range intrusions (Ballhaus & Berry 1991; Ballhaus & Glikson 1995). The density of mafic dykes varies widely in the western intrusions, for example, dykes form about one quarter of the outcrop in the Cavenagh Range intrusion.

The layered intrusions in South Australia also display a general north to south progression from ultramafic-dominated bodies south of the Woodroffe Thrust, such as Claude Hills, Ewarara (Goode & Krieg 1967), and Gosse Pile (Moore 1971a, b), to interlayered ultramafic–mafic intrusions, such as Kalka (Goode 1970, 1976, 1977, 1978), and Mount Davies (Nesbitt & Kleeman 1964). For a review of these intrusions see Nesbitt et al. (1970).

The best estimate of the age of the Giles Complex is 1078±3 Ma for granophyre from the Bell Rock intrusion (Sun et al. 1996a, b), considerably younger than the age range of 1200 to 1185 Ma, suggested by Sun & Sheraton (1992) on the basis of preliminary data for apparently associated granitoids.

Claude Hills peridotite/gabbro intrusion

This body is poorly exposed along an east-northeast-trending, roughly 3 km long range of low hills, about 12 km north of Kalka. Most outcrops consist of weakly layered peridotite and pyroxenite, with minor melagabbro. The rocks are deeply weathered, including magnesite and laterite crusts. No detailed study of this body was undertaken during the present survey.

Ewarara pyroxenite intrusion

This body, although relatively small (>500 m thick, 6 km along strike), is the most completely preserved layered intrusion of the Giles Complex (Goode & Krieg 1967). It consists of a lower zone of olivine bronzitite (or harzburgite) and an upper zone of pyroxenite and melagabbro. The body is keel shaped (Cover; Figs 3E, 48), as shown by structural attitudes and a gravity profile, and is discordantly intruded into, and in places intertongued with, layered felsic granulite, which includes augen gneiss (see previous section). Well-defined chilled to hybrid contacts against felsic granulite are characterised by sharp decreases in the pyroxene/plagioclase ratio, abundant biotite and rare felsic xenoliths. A steepening of igneous layering along the southeastern lobe is interpreted as a possible feeder zone. There is some evidence that the Ewarara intrusion may be post-D_3, although this is by no means certain (see previous section).

Kalka norite/pyroxenite intrusion

This body, at least 5000 m thick and 11 km along strike (Frontispiece; Figs 49–51), consists of (1) a basal pyroxenite zone, consisting of orthopyroxenite and websterite; (2) a thick norite zone, consisting of norite, minor pyroxenite, gabbro, anorthosite, olivine-bearing norite, and olivine websterite (Goode 1970, 1976, 1977, 1978). Phase layering and centimetre-scale pyroxene–plagioclase layering, which is grada-

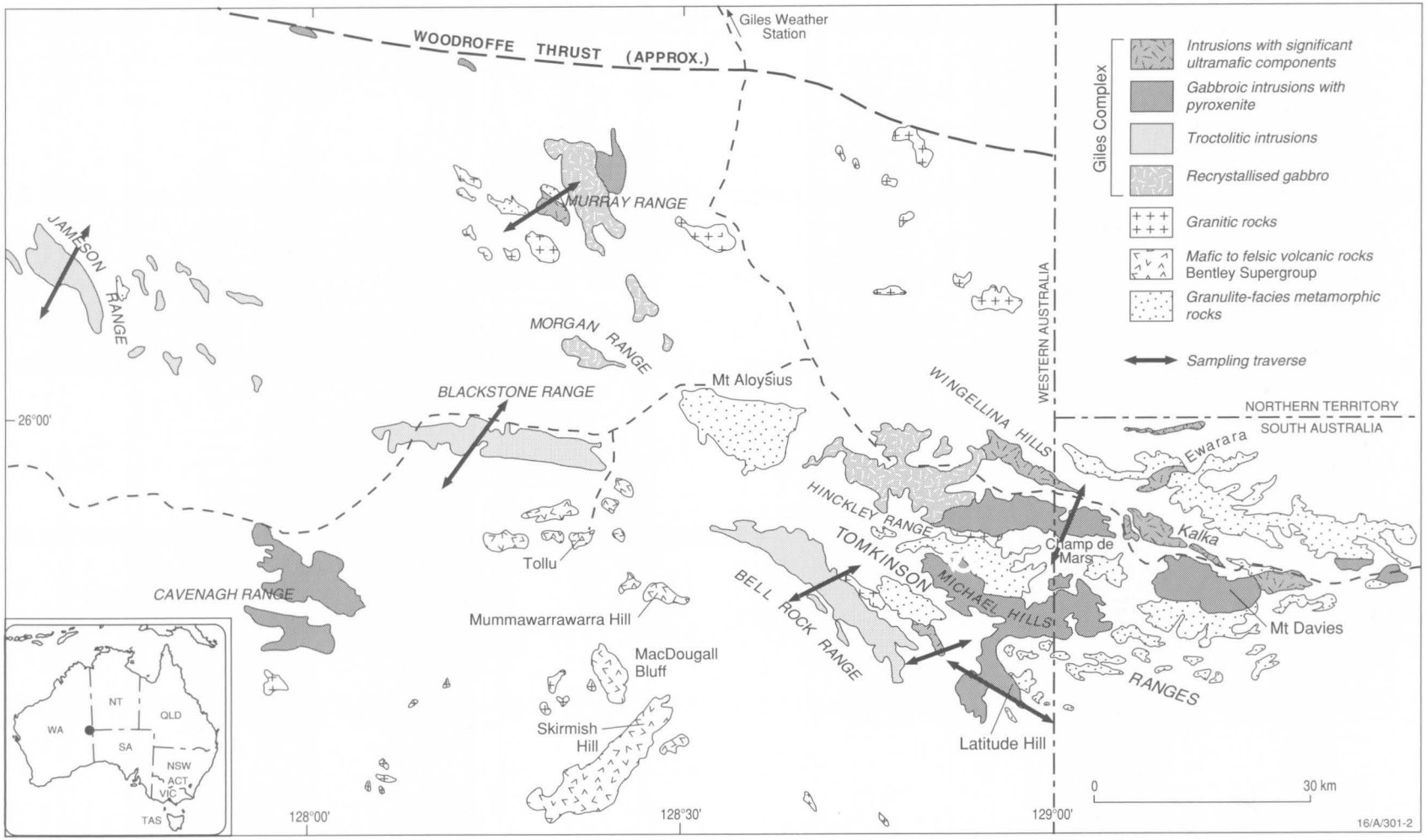

Figure 47. Geological map of the Tomkinson Ranges–Blackstone Range–Jameson Range region, western Musgrave Block, showing the major Giles Complex mafic–ultramafic intrusions and locations of sampling traverses.

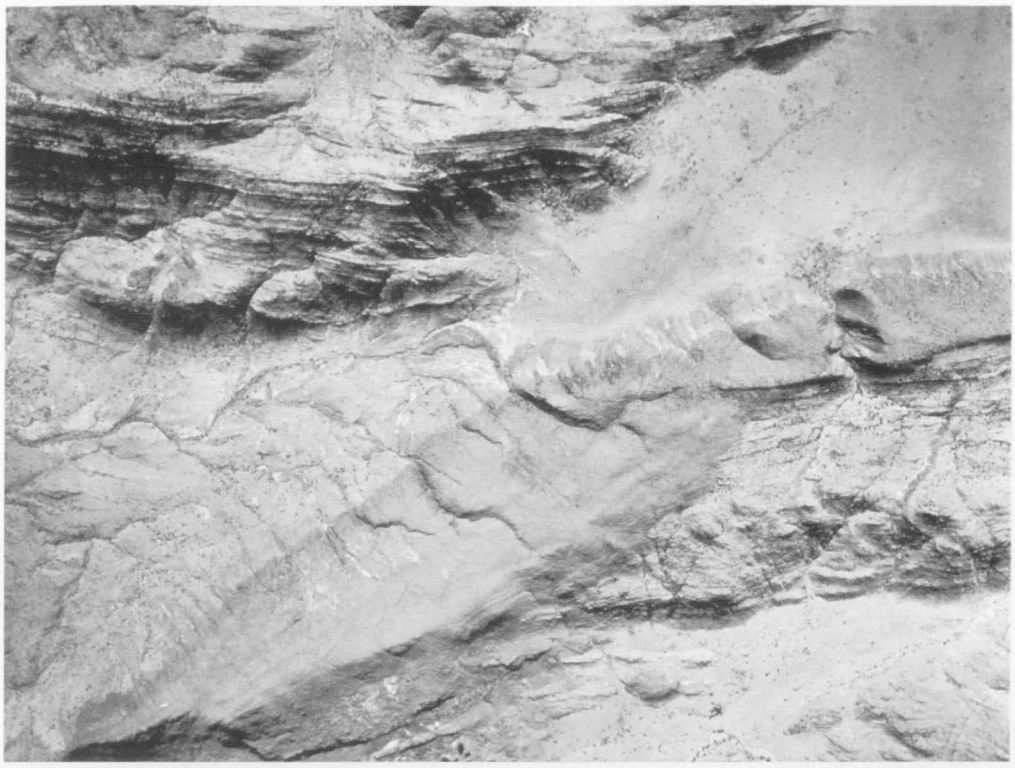

Figure 48. Aerial photograph of the Ewarara pyroxenite intrusion, showing discordant contact with layered felsic granulite.

Figure 49. Aerial photograph of the northern part of the Kalka norite/pyroxenite intrusion.

tional or sharply bounded, occurs locally; (3) a lens of harzburgite occurs within the norite zone, occupying a marked topographic depression; (4) an olivine gabbro zone, up to 600 m thick and 6.5 km along strike, within the norite zone, including minor orthopyroxene-bearing cumulates, clinopyroxenite and olivine-bearing pyroxenite. Centimetre-scale graded layering and isomodal sharp-bounded layering are present, especially in an upper 5 metre-thick horizon, which extends over a strike length of about 3 km (Johnson member, Goode 1976); and (5) an anorthosite zone, which forms low hills at the western end of the intrusion. This unit includes locally finely banded leucogabbro and anorthositic gabbro, with olivine and magnetite as minor phases, and local magnetite–ilmenite-rich layers.

Gosse Pile pyroxenite intrusion

This Gosse Pile intrusion, at least 2000 m thick and 7 km along strike (Figs 52–54), consists of a near-vertically dipping sequence of pyroxenite-dominated cumulates (Moore 1971a, b),

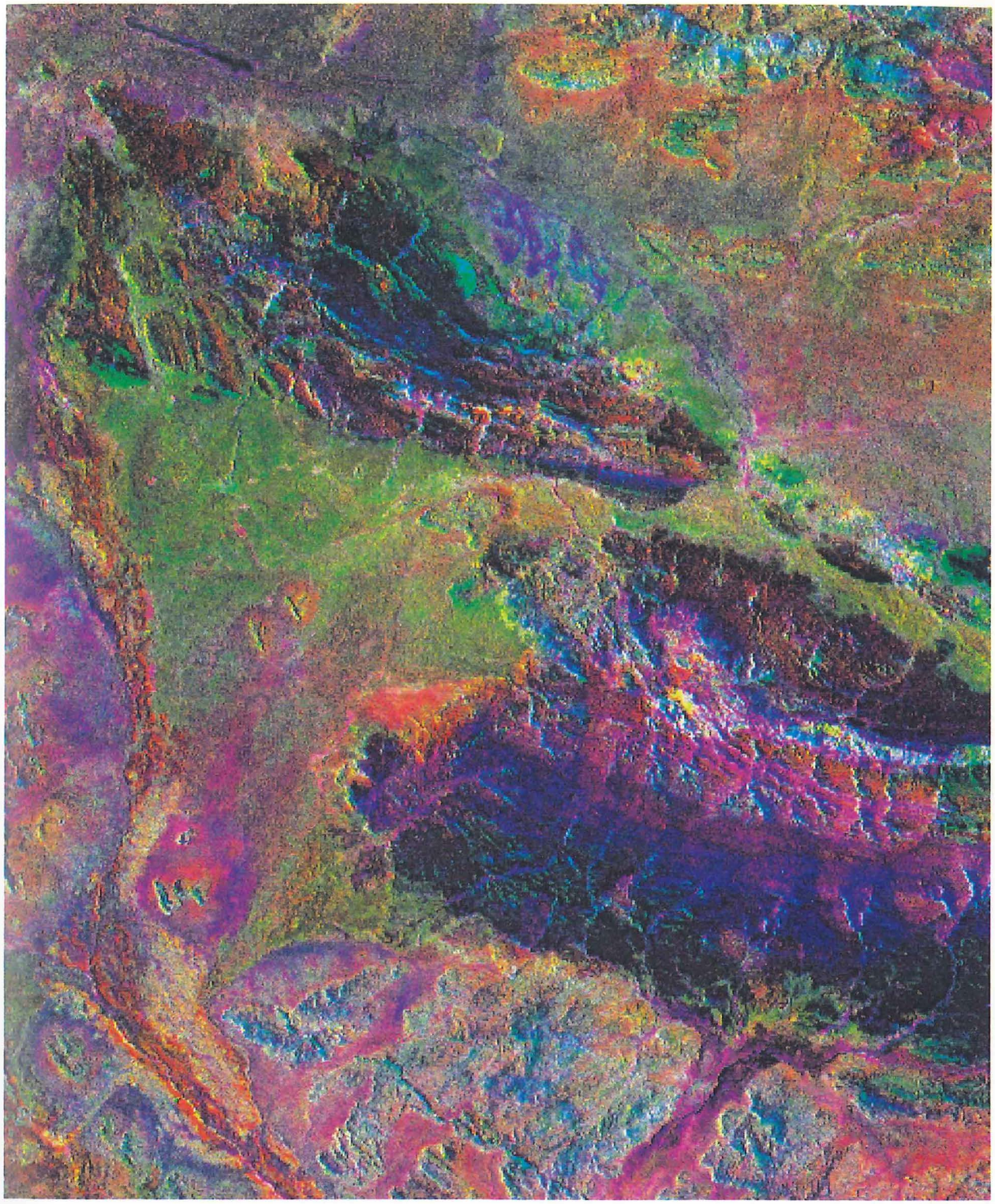

Figure 50. Landsat-5 TM pc2(4/3;5/7):5/4:4/3 RGB image of the western Mount Davies and Kalka layered intrusions. Basal pyroxenite units (Px) and olivine gabbro (Og) of the Kalka intrusion are depicted in deep azure blue, reflecting their iron oxide-rich weathering crusts. Gabbro (Gb) displays in red, representing clay-dominated weathering crusts covered by dry spinifex vegetation. Anorthosite (An) shows in orange, representing clay–carbonate-dominated weathering crusts. The lower gabbroic zone of the Mount Davies intrusion (displaying in red, representing clay-rich weathering and dry vegetation) is overlain by a large depression-forming peridotite lens (Pd) capped by magnesite–calcrete, which shows in mottled yellow–white–red patterns. Pyroxenite intercalations (Px) form narrow strike-parallel valleys showing in green (iron oxide-rich) and blue (green vegetation-rich). Felsic granulite (Fg), intruded by the Mount Davies body, shows greenish-yellow, signifying mixed iron oxide–clay high-albedo (quartz-rich) weathering surfaces. They are cut by northwest-trending mafic dykes (Md), which show in blue-green, due to their iron oxide-rich weathering surfaces and thicker vegetation. Outcrops of felsic rocks are surrounded by red to purple zones (Fc), representing clay-rich alluvial material derived from the felsic rocks. A zone of nickel-bearing laterite (L), east of the Kalka intrusion, shows in apple green. Alluvial material derived from the layered mafic intrusions are dominated by iron oxide (Fg). Thick calcrete (Ca) duricrusts along Pidingadinga Creek show in deep orange. The southern slopes (Ss) of Mount Davies are covered by thick green vegetation (Gv), that shows in blue, especially along gullies, and at lower levels feature a major burnout (B) of dark brown low albedo. The southern Hinckley Fault-bounded escarpment of Kalka and the southern slope of a felsic granulites ridge (Fg) at the northeastern corner of the area also show strong green vegetation effects. A geological overlay for the area is shown in Figure 51.

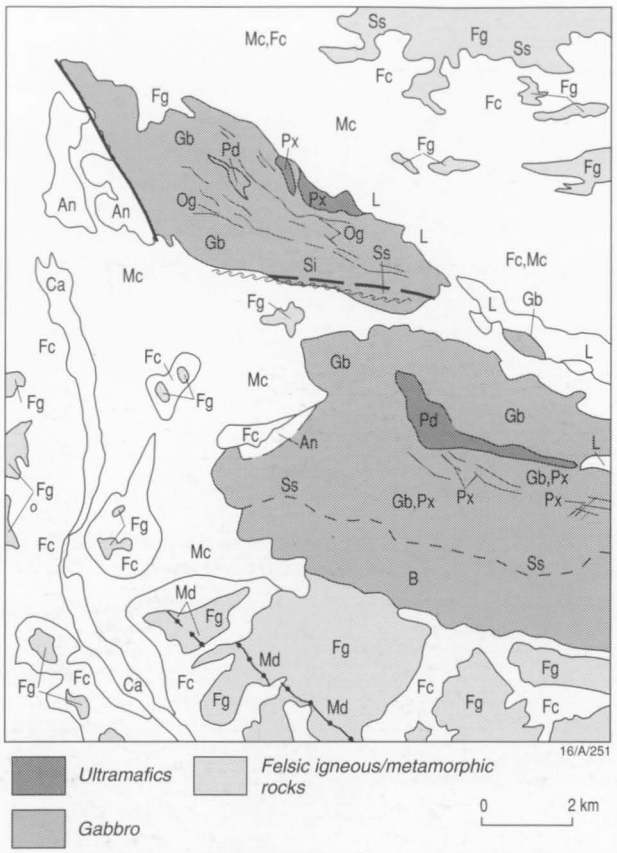

Figure 51. Geological overlay for the western Mount Davies–Kalka area. Symbols for this and Figures 54, 80, 90, and 109: Pd, peridotite; Px, pyroxenite; Og, olivine gabbro; Gb, gabbro; Gf, ferrogabbro; An, anorthosite; Mn, mafic granulite; Md, mafic dyke; V, volcanic rocks; Fg, felsic granulite and granitic gneiss; L, laterite; Ca, calcrete; Si, silcrete; Fc, felsic alluvial collar; Mc, mafic alluvial collar; Dv, dry vegetation; Gv, green vegetation; Ss, southern slopes (normally densely vegetated); B, fireburn.

separated by a major fault from the Mount Davies intrusion. Thin noritic intrusives at the base of the body are interdigitated with felsic granulite. These are overlain by a discrete, deeply weathered and valley-forming body of serpentinised peridotite, consisting of poikilitic pyroxene and finer-grained olivine and plagioclase. A fine-grained marginal facies contains xenoliths of olivine pyroxenite. The overlying layered sequence consists of orthopyroxenite, olivine orthopyroxenite, websterite, and norite, and includes a distinct layer of gabbro. The southern part of the intrusion consists of sheared and recrystallised derivatives of these rock types. Moore (1971a, b) suggested the presence of three magmatic cycles whose feldspar-dominated tops have mostly been removed, and correlated Gosse Pile with the lower ultramafic section of the Kalka intrusion to the northwest.

Mount Davies gabbro/pyroxenite intrusion

The Mount Davies gabbro/pyroxenite (Nesbitt & Kleeman 1964) is the second largest layered mafic–ultramafic body of the Giles Complex, at least 7000 m thick and 15 km along strike (Figs 55, 56). It consists of (1) a thick lower gabbroic zone, which discordantly intrudes felsic granulite and features a hybrid transition zone, several hundred metres wide; (2) a zone of pyroxenite and olivine gabbro intercalations within gabbro; (3) a central valley-forming serpentinised peridotite unit; and (4) an upper gabbro zone with pyroxenite intercalations. The body is cut by numerous faults, including the near-strike Greenwood Fault. In the present study, only the westernmost part of the body was accessible, and was sampled in detail across the strike.

Wingellina Hills gabbro/pyroxenite intrusion

This intrusion consists of a 1600 metre-thick succession of olivine gabbro and gabbronorite, which contains lenticular stratabound intercalations of pyroxenite and peridotite (Figs 57–61). It was described in detail by Ballhaus & Glikson (1989). The ultramafic cyclic units are underlain by hybrid footwall zones, representing basal mixing of ultramafic increments with the resident gabbro (Fig. 62, and see section on petrogenesis of the Giles Complex). Olivine compositions

Figure 52. Aerial photograph of the Gosse Pile pyroxenite intrusion.

range from Fo_{89} to Fo_{77}, below which olivine is replaced by cumulus orthopyroxene (Fig. 63). Clinopyroxene *mg* values (atomic 100Mg/(Mg+Fe^{2+})) of 91–77 are higher than those of coexisting orthopyroxene and olivine. The *mg* values correlate with the An (atomic 100Ca/(Ca+Na)) content of plagioclase. Highly calcic antiperthite ($An_{65}Ab_{15}Or_{20}$), signifying crystallisation of the original feldspar under high-temperature anhydrous conditions, occurs as an interstitial constituent of pyroxenite. Systematic variations in *mg* values of gabbro with stratigraphic level indicate weak Fe enrichment upwards,

Figure 53. Landsat-5 TM pc2(4/3;5/7):5/4:4/3 RGB image of the Gosse Pile–Teizi bore area. The image includes part of the Gosse Pile pyroxenite intrusion (bottom left). Pyroxenite units (Px) are dominated by iron oxide-rich weathering crusts, and the different shades of green reflect the importance of this component; clinopyroxene–plagioclase-rich rocks have higher clay contents in their weathering crust and thus include a red component, giving a yellow signature. The deeply weathered serpentinised peridotite strike depression is characterised by calcrete–magnesite crusts showing in red and white. Shed iron oxide-rich alluvial material shows in deep apple green (Mc). Shaded southern slopes (Ss) display green vegetation superposed on pyroxenite bedrock, resulting in deep azure blue. The Teizi anorthosite suite includes several massive bodies (An) and numerous thin recrystallised tongues intercalated with felsic granulite (Fg). Anorthosite shows in red, representing clay–carbonate-dominated weathering, and felsic granulite in green and yellow tones, representing iron oxide–clay mixtures. Landsat discrimination of thin recrystallised anorthosite units is much more efficient than time-consuming field work. The sequence is cut by west to northwest-striking mafic dykes (Md). Alluvium derived from felsic granulite is typically clay-rich (Fc), showing in red or purple where supporting green vegetation.

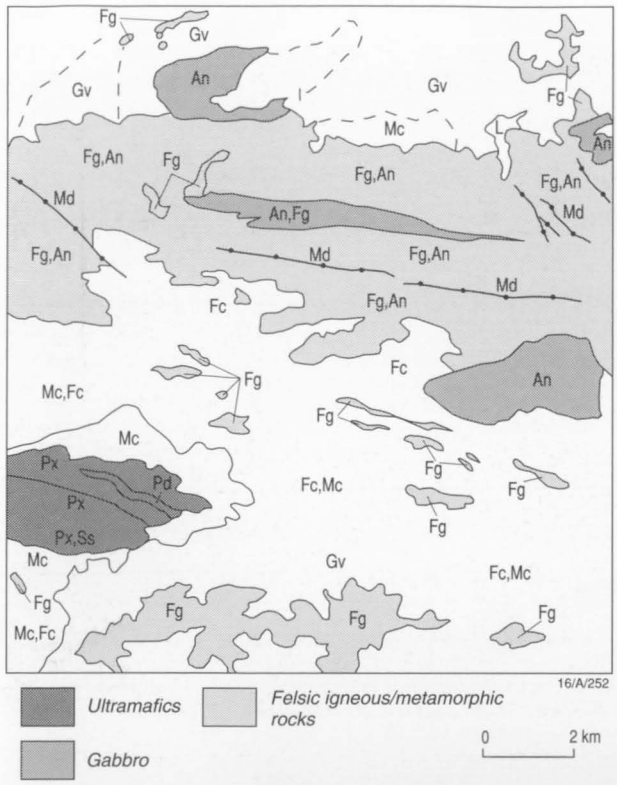

whereas ultramafic units display sharp compositional reversals. The origin of this composite body is interpreted in terms of continuous fractionation of a resident olivine–clinopyroxene–plagioclase-saturated magma, periodically replenished by increments of olivine-saturated ultramafic melts which resulted in formation of peridotite, wehrlite, clinopyroxenite, and olivine gabbro. Orthopyroxene-rich cumulates formed by mixing of ultramafic increments with resident, more siliceous gabbro. The temperature difference between the host gabbro and the ultramafic pulses resulted in rapid quench crystallisation of the latter.

The Wart gabbro/pyroxenite intrusion

The Wart intrusion, which probably includes the sequence along strike to the northwest near Mount West, forms a sliver of interlayered gabbro and pyroxenite, overlain by more massive gabbro. It is separated by the Poonawarra valley from the Bell Rock intrusion to which it may be related as a basal

Figure 54. Geological overlay for the Gosse Pile–Teizi area (Fig. 53). Symbols as in Figure 51.

Figure 55. Aerial photograph of the western Mount Davies and Kalka layered intrusions.

Figure 56. Landsat-5 TM 5/4 band ratio image of the Mount Davies–Kalka area. Light areas represent iron oxide-rich laterite and iron oxide-rich weathering surfaces of pyroxenite and felsic granulite. Compare with Figure 50.

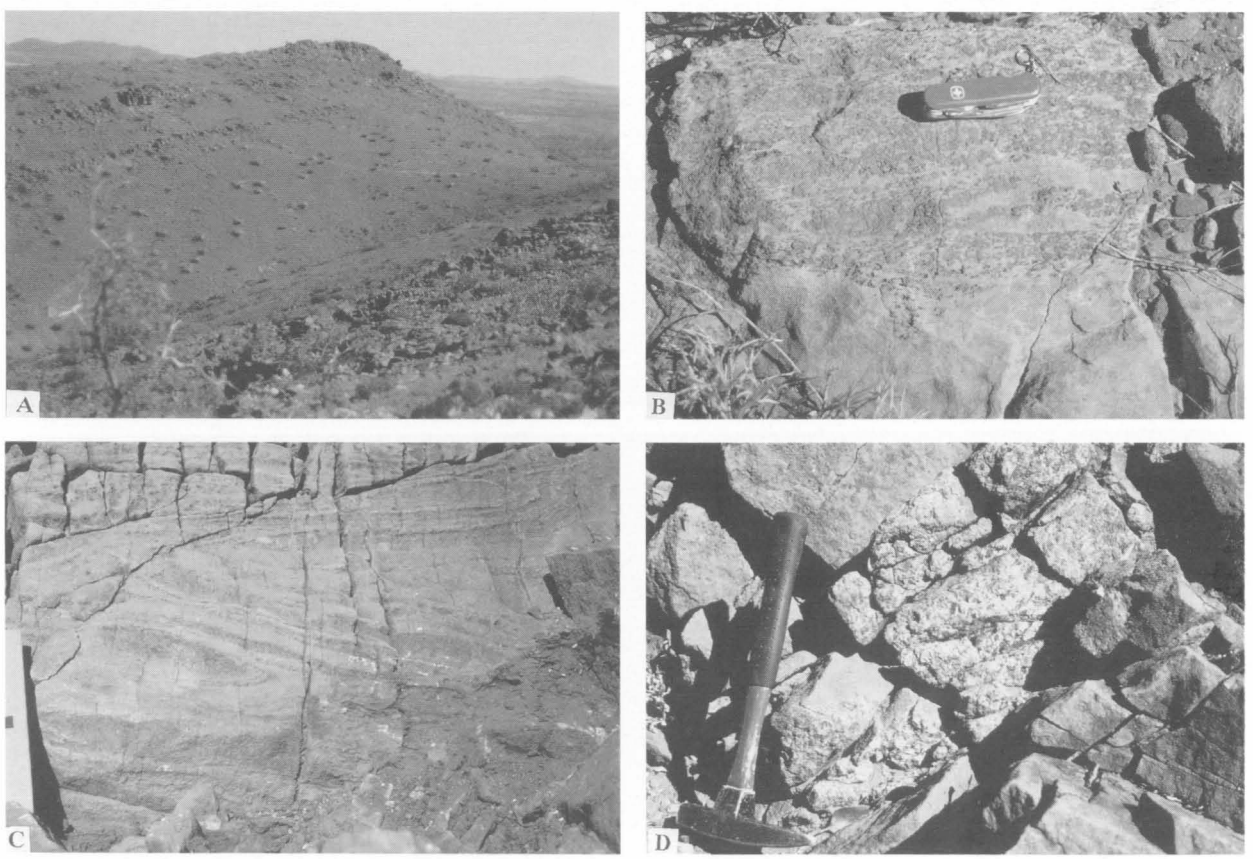

Figure 57. Outcrops of the Wingellina Hills gabbro/pyroxenite intrusion. (A) Valley section of gabbro (smooth slope) and pyroxenite (dark outcrop banks). (B) Mixed zone of gabbronorite and pyroxenite. (C) Folded flow-segregated gabbronorite. (D) Pegmatoid pyroxenite unit, with chromitite pods.

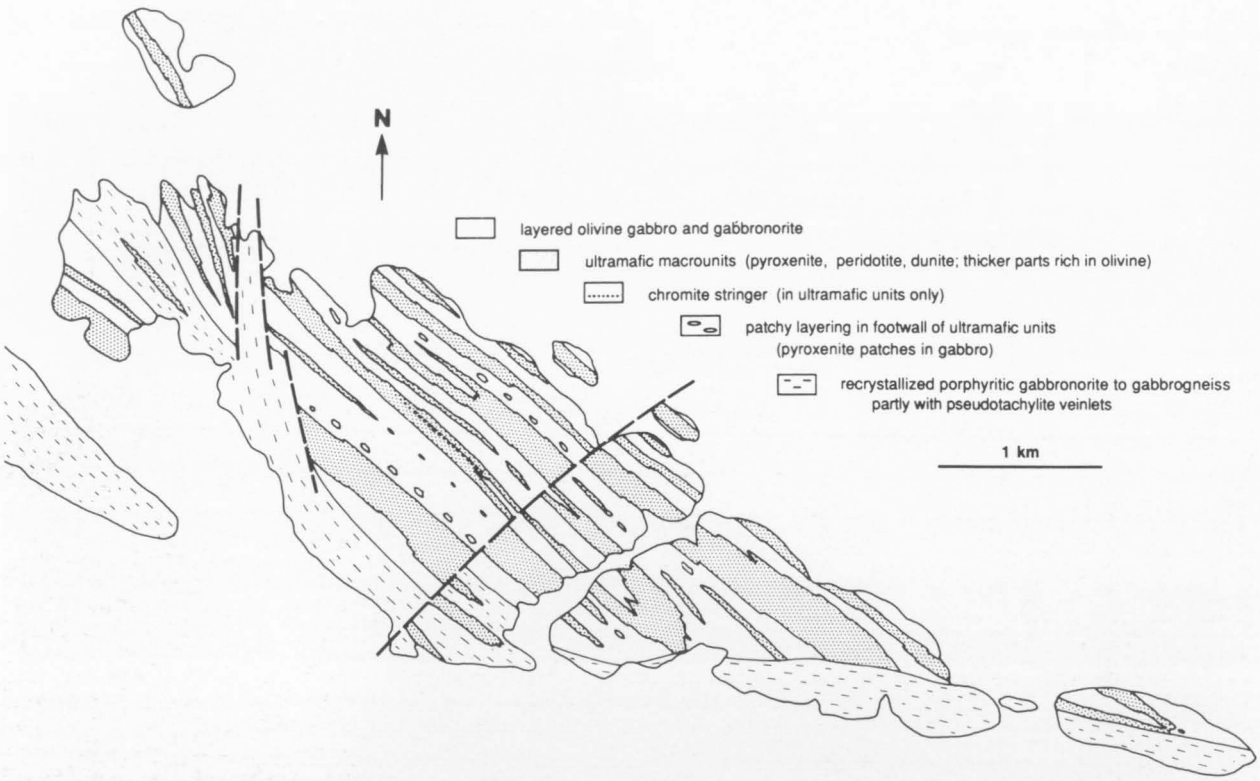

Figure 58. Geological map of the Wingellina Hills intrusion (after Ballhaus & Glikson 1989).

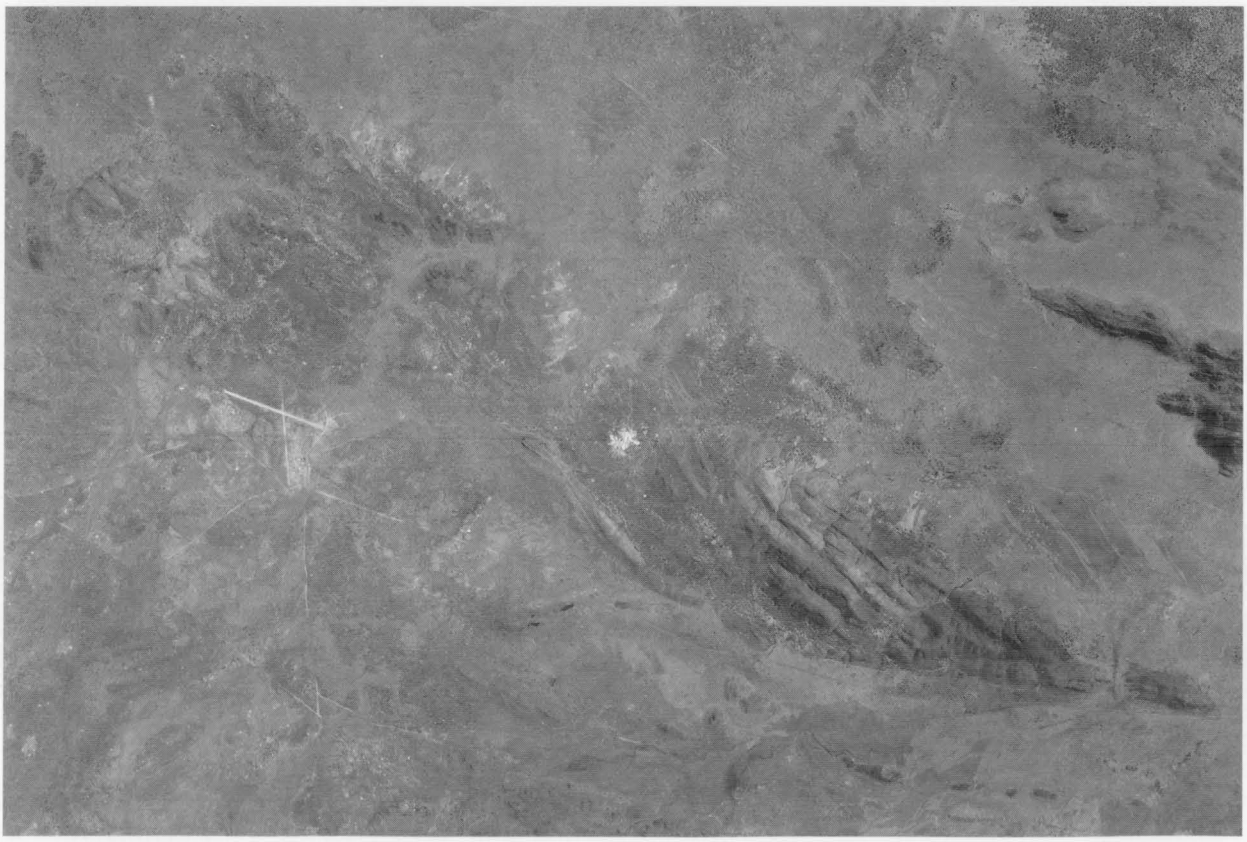

Figure 59. Aerial photograph of the Wingellina Hills intrusion.

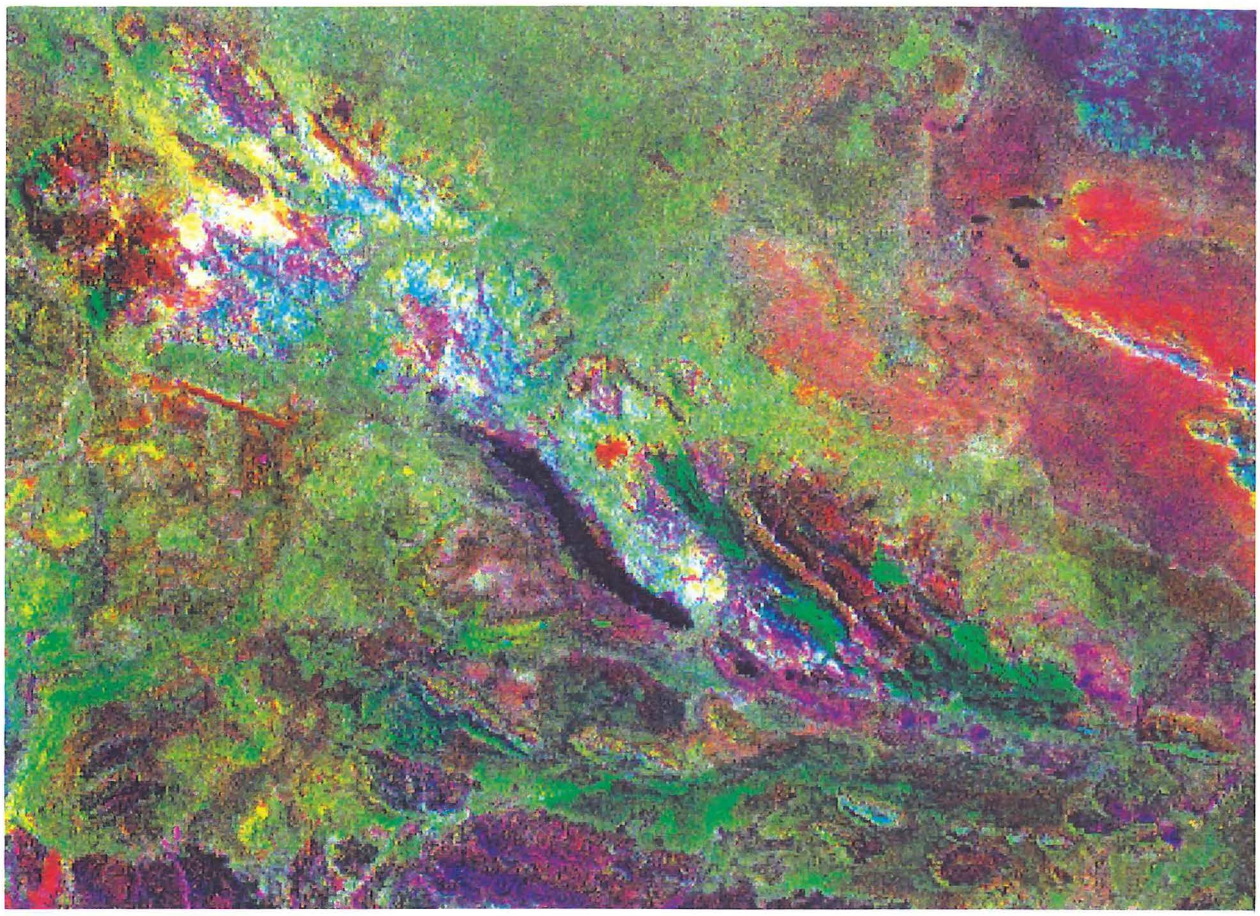

Figure 60. Landsat-5 TM pc2(4/3;5/7):5/4:4/3 RGB image of the Wingellina Hills intrusion and surrounding area. Outcrops of gabbro dominated by clay weathering appear in red, outcrops of pyroxenite and lateritised ultramafic rocks, dominated by iron oxide, are green, and heavily vegetated laterite north and east of Wingellina show in bluish green. The west-northwest-trending trace of the Wingellina Fault is clearly shown south of the Wingellina Hills intrusion. Note the strong clay signature (red) of the alluvial girdle around felsic granulite of the northern Hinckley Range (near the eastern edge of the image). Compare with Plate 2.

mafic–ultramafic segment (Figs 64, 65). Both the mafic–ultramafic and mafic sequences young to the west. The Wart sequence is at least 1900 m thick and dips range from 50 to 90°. The northeastern margin displays a sheared intrusive contact with felsic granulite, with mesoscale felsic apophyses intruding the gabbro. As along the northeastern contact of the Bell Rock intrusion, these veins may well be back-intruded felsic melts. The northern margin of the gabbro intrudes a contact-recrystallised facies of the felsic granulite.

The mafic–ultramafic sequence consists of a well-layered suite of clinopyroxenite to melagabbro mesocumulates to adcumulates, intercalated with abundant (several tens) lenticular wehrlite to peridotite orthocumulate units and some olivine melagabbro, overlying a sequence of gabbroic cumulates (Figs 66, 68; Ballhaus 1993). There are numerous microgabbro sills with textural transitions from rapidly chilled rocks to genuine cumulate layers. The pyroxenite is very poor in plagioclase compared with other intrusions. The most fractionated units exposed are olivine-bearing melagabbro with less than 40 percent calcic plagioclase. The Wart sequence includes transitions between pyroxenite, wehrlite, peridotite, and melagabbro, sometimes as multiple variations within a few metres, and is thus one of the most variable intrusions in terms of modal mineralogy, texture, and cumulate porosity. There is evidence in some horizons for rapid cooling. In some cumulate layers, cumulus clinopyroxene is present in a distinctly bimodal grain size distribution.

The main rock types are as follows:

Feldspathic clinopyroxenite orthocumulates. Brown clinopyroxene, rich in exsolved spinel, is the main cumulus phase, and may be accompanied by rounded cumulus olivine (Fig. 66A). Rarely, orthopyroxene grades into a late-magmatic intercumulus phase. Intercumulus plagioclase is locally abundant and attains a near-cumulus status. Minor orthopyroxene occurs as columnar rims around olivine where the latter is in contact with plagioclase.

Clinopyroxenite adcumulates. Clinopyroxene and, in places, minor olivine are closely packed cumulus phases, but are generally annealed, obliterating primary magmatic textures. Grain boundaries between clinopyroxene grains are equilibrated and locally outlined by small brownish spinel neoblasts (Fig. 66B). Orthopyroxene is extremely rare. Isolated occurrences of interstitial plagioclase are mostly antiperthitic, with minute exsolution rodlets of K-feldspar in a matrix of bytownite (~An_{80}).

Wehrlite and peridotite. Cumulus olivine and clinopyroxene are set in interstitial plagioclase (Fig. 66D, E). In peridotite orthocumulates, clinopyroxene may be poikilitic and very rich in exsolved spinel. Orthopyroxene is rare. The parental magma must have been saturated with olivine and, in some cases, clinopyroxene. Unlike peridotite units of the Murray Range or Wingellina Hills intrusions, cumulus spinel appears to be absent.

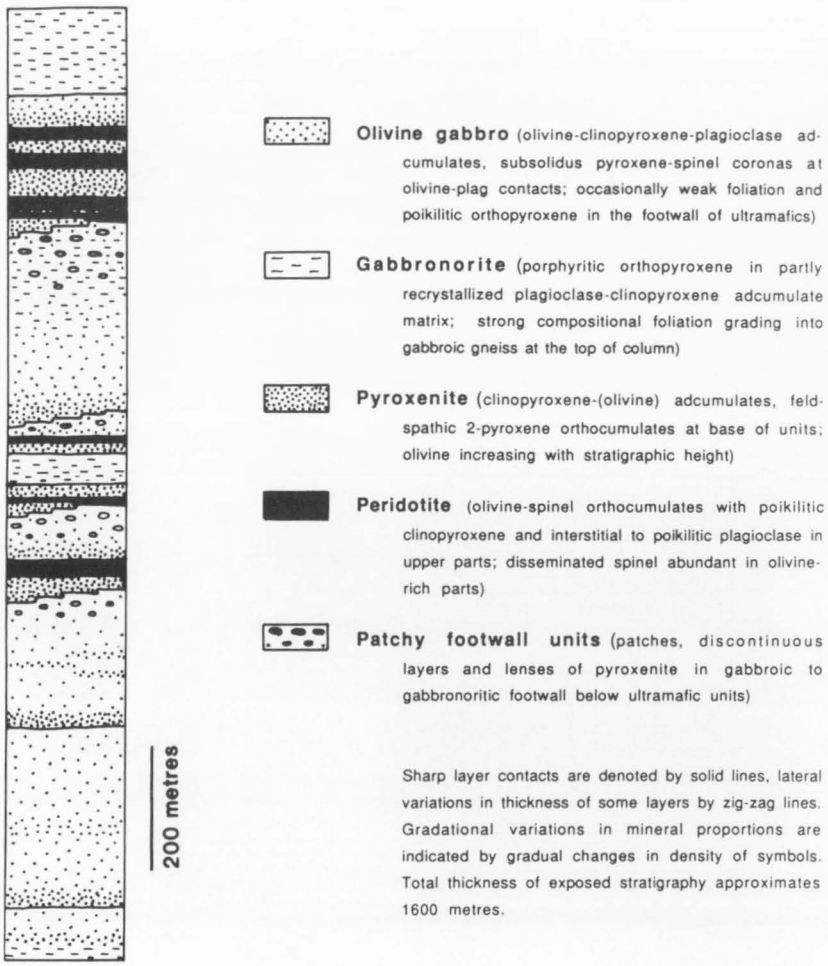

Figure 61. Stratigraphy of the central part of the Wingellina Hills intrusion (after Ballhaus & Glikson 1989).

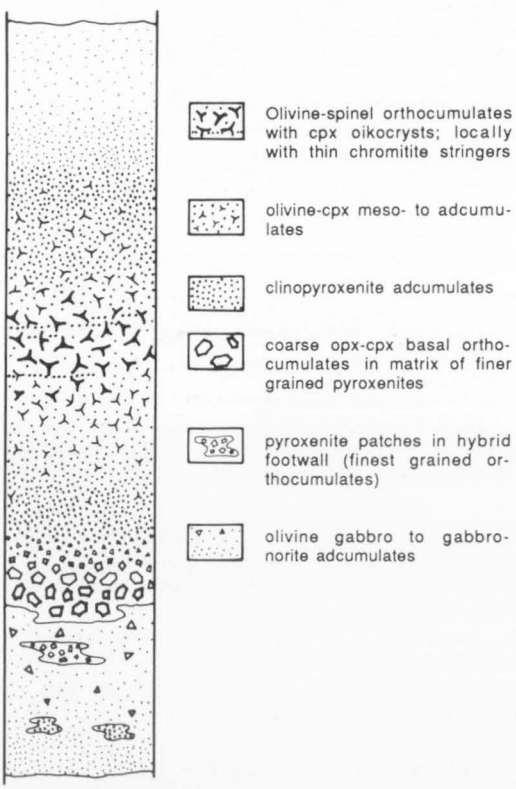

Figure 62. Stratigraphic section through an ultramafic cyclic unit and its hybrid footwall in the Wingellina Hills intrusion. The total thickness of ultramafic units ranges from 50 to 200 m. Size of pyroxenite patches in the hybrid footwall and thickness of basal pyroxenite orthocumulates are exaggerated for clarity (after Ballhaus & Glikson 1989).

Olivine melagabbro. These contain clinopyroxene, plagioclase, and olivine as cumulus phases (Fig. 66F). Plagioclase commonly grades from a cumulus phase to a nearly interstitial phase, especially in the melanocratic rocks. All textural transitions exist between clinopyroxenite orthocumulates and olivine melagabbro, particularly in units where textures suggest rapid cooling.

The Wart sequence is cut by at least three generations of mafic dyke with different phenocryst populations (Fig. 67). The most common type carries subhedral clinopyroxene and elongated plagioclase laths as phenocrysts, embedded in a fine-grained oxide-rich groundmass (Fig. 67A). Another common 'troctolitic' generation carries rounded olivine and elongated plagioclase phenocrysts, set in a hydrated biotite-rich groundmass (Fig. 67B). These troctolitic dykes cannot be related to any of the cumulates observed in The Wart sequence, but may represent a parent melt to the more fractionated troctolitic cumulates, such as the Bell Rock and Blackstone Range intrusions. One dyke contains elongated euhedral, peripherally resorbed orthopyroxene as the only phenocryst phase, apart from some plagioclase microphenocrysts. Orthopyroxene may be of pre-emplacement, high-pressure crystallisation, and this dyke type qualifies as a possible feeder to some of the Giles Complex layered intrusions (Fig. 67C, D).

In terms of phase compositions (Figs 68, 69), The Wart intrusion is nearly as primitive as the Murray Range and Wingellina Hills sequences (Ballhaus & Glikson 1989). Olivine ranges in composition from Fo_{87} to Fo_{78}, below which it is replaced by orthopyroxene. Coexisting orthopyroxene has slightly higher *mg* values. In comparison with the Murray Range sequence, orthopyroxene is much rarer and clinopyroxene is more fractionated, with Cr/(Cr+Al) ratios not ex-

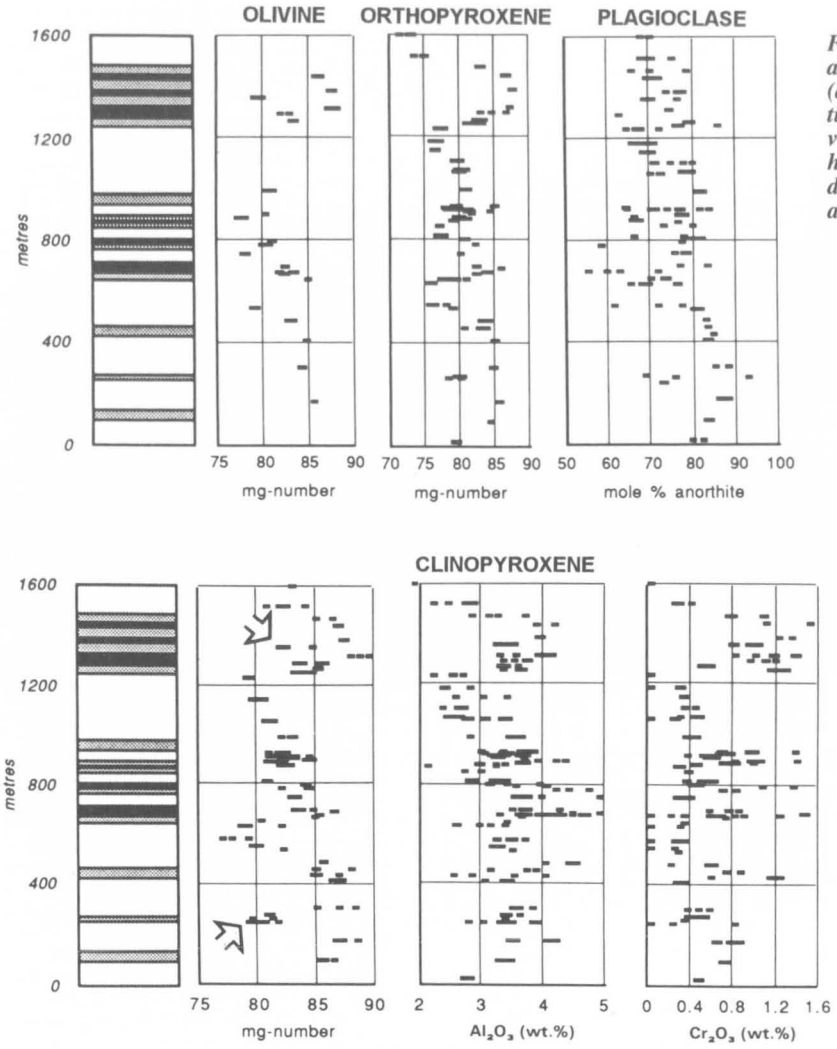

Figure 63. Mineral compositional variations in the Wingellina Hills intrusion (after Ballhaus & Glikson 1989). The stratigraphic sections at left are schematic versions of Figure 61. Some pyroxenite horizons which fall outside the general differentiation trend are indicated by arrows.

ceeding 0.16. No cumulus spinel is present, probably because the magma was depleted in Cr by extensive clinopyroxene crystallisation. Plagioclase is, for a given olivine composition, far more calcic (An_{95-55}) than that in the Murray Range intrusion.

The cryptic modal layering in The Wart sequence arises from the intrusion of numerous small to medium-sized batches of primitive parent magma into a continuously differentiating body of somewhat more fractionated resident melt. From stratigraphic relationships, it is suggested that this layered sequence youngs to the southwest and could, therefore, form the base of the Bell Rock intrusion. Most ultramafic units commence with a sharp modal change to olivine-rich orthocumulates, followed by an upward gradation to wehrlite and then pyroxenite. This cyclic pattern is likely to have resulted when olivine-rich liquid ponded on the magma chamber floor and gradually mixed with the overlying cooler resident melt. The lower northeastern half of the sequence, up to the 1050 m stratigraphic level, signifies a period of multiple magma addition, whereas the upper half indicates chemically more stagnant conditions, with fewer magmatic replenishment events.

The parent magma characteristics are similar to those of the Murray Range intrusion, namely a near-primitive, olivine-normative melt. The common lack of orthopyroxene and spinel indicates that silica activity and Cr contents may have been slightly lower than in the Murray Range magma, possibly because the magma experienced some pyroxene fractionation prior to emplacement into the crustal magma chamber. The magma was close to clinopyroxene saturation. Its crystallisation sequence, best reflected in the most primitive orthocumulate units, is believed to have been (1) olivine + clinopyroxene, (2) clinopyroxene + olivine, and (3) clinopyroxene + plagioclase + olivine.

Michael Hills gabbro and Latitude Hill gabbro/pyroxenite intrusions

The Michael Hills gabbro intrusion forms the most extensive member of the Giles Complex in Western Australian, with one of the thickest cumulate sequences (Figs 70, 71). It consists of a low-angle north-dipping to near flat-lying sequence of gabbro, containing locally abundant thin (1–20 m) pyroxenite layers. The intrusion has been deformed, probably in conjunction with late faulting, into a northward-concave steep axial flexure. The Latitude Hill sequence appears to be a tectonic segment of the Michael Hills gabbro, and has a pyroxenite-rich section at its base (Fig. 72). It is up to 8000 m thick, north–south striking, and dips at 80–90°. Because detailed sampling was confined to the Latitude Hill intrusion, the following discussion applies mainly to that body, but is probably also relevant to the Michael Hills intrusion.

The Latitude Hill sequence is dominated by gabbro and pyroxenite and consists of two steeply dipping (80–90°), uniform, olivine gabbro units with numerous layers and lenses of olivine-bearing pyroxenite and rare peridotite, totalling about 8000 m in thickness (Fig. 75). However, these two

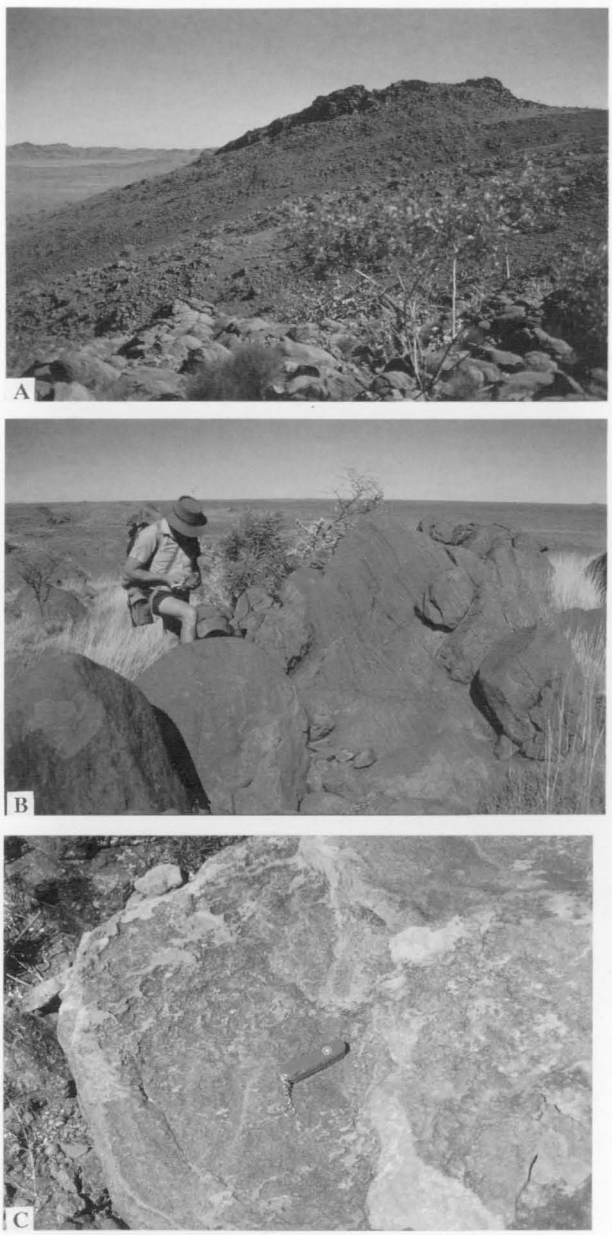

Figure 64. Outcrops of The Wart gabbro/pyroxenite intrusion. (A) Layered gabbro and pyroxenite capped by massive gabbro. (B) Layered melagabbro and pyroxenite, north of Mount West. (C) Granitoid vein-injected eastern margin of The Wart intrusion.

magmatic units are separated in the central part of the intrusion (2900–4250 m) by a zone of altered, highly strained, recrystallised gabbro, cut by pseudotachylite veins (Figs 72, 74, 75), which is also more fractionated than the enclosing cumulates. Hence, the structural continuity of the latter is uncertain. In addition to the highly deformed central unit, the Latitude Hill sequence includes a few localised shear zones in which cataclastic deformation predominates over ductile deformation styles, suggesting relatively low deformation temperatures (Fig. 74A–C). The magmatic rocks of the Latitude Hill intrusion feature several unusually fine-grained 'doleritic-textured' (subophitic) units, which Ballhaus (1993) interpreted as intraplutonic chill zones.

The Latitude Hill gabbro/pyroxenite is one of the few cumulate sequences of the Giles Complex with demonstrably intrusive contacts with felsic granulite along its eastern margin. The marginal facies consists of fine-grained microgabbro where distinctly euhedral plagioclase laths, rounded clinopyroxene, and orthopyroxene are cumulus phases. The rocks contain coarser-grained enclaves with euhedral cumulus grains and quartz–orthoclase myrmekite (Fig. 73H), probably derived by partial melting of the felsic granulite and back-intrusion of the melt.

The main components of the Latitude Hill intrusion are as follows:

Gabbroic rocks. Gabbroic rocks are dominated by olivine, clinopyroxene, orthopyroxene, and plagioclase, coexisting as cumulus phases. Monomineralic units are rare. There is a transition between quenched dykes and sills, enclaves of microgabbro with chilled margins, and mature cumulates. Olivine-bearing doleritic-textured gabbronorite consists of about 50 percent large elongated plagioclase laths and smaller rounded grains of cumulus clinopyroxene (Fig. 73A–D). Orthopyroxene, where present, is texturally younger than clinopyroxene. It tends to form poikilitic grains surrounding cumulus olivine and clinopyroxene aggregates. Plagioclase laths contain submicroscopic brownish inclusions, especially near their centres.

Pyroxenite. Orthopyroxene and clinopyroxene cumulus phases are accompanied by a few slightly altered olivine grains (Fig. 73E, F). The size distribution of pyroxene is bimodal, with orthopyroxene forming elongated laths considerably coarser grained than clinopyroxene. Olivine locally occurs as a minor cumulus phase coexisting with cumulus orthopyroxene grains. Plagioclase contents are highly variable, between 2 and 40 modal percent, in adcumulates. Feldspathic orthocumulates grade into melagabbro. Pyroxenite adcumulates contain finer-grained feldspathic orthocumulate pockets in which abundant plagioclase forms a near-cumulus phase. Both plagioclase and pyroxene commonly contain submicroscopic opaque inclusions.

Feldspathic peridotite. Peridotite cumulates occur near the 600 m stratigraphic level. Olivine, orthopyroxene, clinopyroxene, and chromite form cumulus phases, while highly altered zoned sodic plagioclase is interstitial. The peridotitic cumulates are not as primitive as in the Murray Range and Wingellina Hills intrusions, where olivine and chromite are commonly the only cumulus phases.

Gabbro and anorthosite of the central section. These rocks differ markedly from gabbro of the lower and upper sections. Major components include fractionated oxide-bearing gabbro and anorthosite, mostly highly deformed and veined by pseudotachylite (Fig. 73G, H). Plagioclase is the most abundant cumulus phase, followed by cumulus to intercumulus clinopyroxene and, less commonly, orthopyroxene. Where the original cumulus texture is preserved, iron-rich clinopyroxene contains exsolved opaque oxides. The sequence comprises anorthositic units with total pyroxene contents up to 10 percent, altered gabbroic rocks and units intruded by granitic to aplitic veins.

Mineral compositions are displayed in Figures 75 and 76. The Latitude Hill intrusion is significantly more fractionated than the primitive Murray Range or The Wart sequences. Olivine occurs only in a series of thin peridotite layers at the 610 m level and in olivine gabbro and olivine-bearing pyroxenite of the central section. It ranges in composition from Fo_{83} to Fo_{67}. Orthopyroxene is slightly more magnesian than coexisting olivine, with *mg* values ranging from 85 in the most primitive ultramafic units to about 58 in the central deformed granulitic zone. Orthopyroxene replaces olivine at Fo_{68}. Cr/(Cr+Al) in clinopyroxene varies sympathetically with

mg value of orthopyroxene and rarely exceeds 0.1. Plagioclase An contents range from about 50 to 85, and vary coherently with *mg* of olivine and orthopyroxene.

The stratigraphic orientation of the sequence, as shown in Figure 72, is arbitrary, as there is no textural indication of where the bottom and top contacts are situated, nor does the shape of the cryptic fractionation patterns (Fig. 75) provide any clue. The two magmatic piles on either side of the central deformed zone feature a major chemical reversal followed by a similarly extensive period of normal fractionation. Abrupt

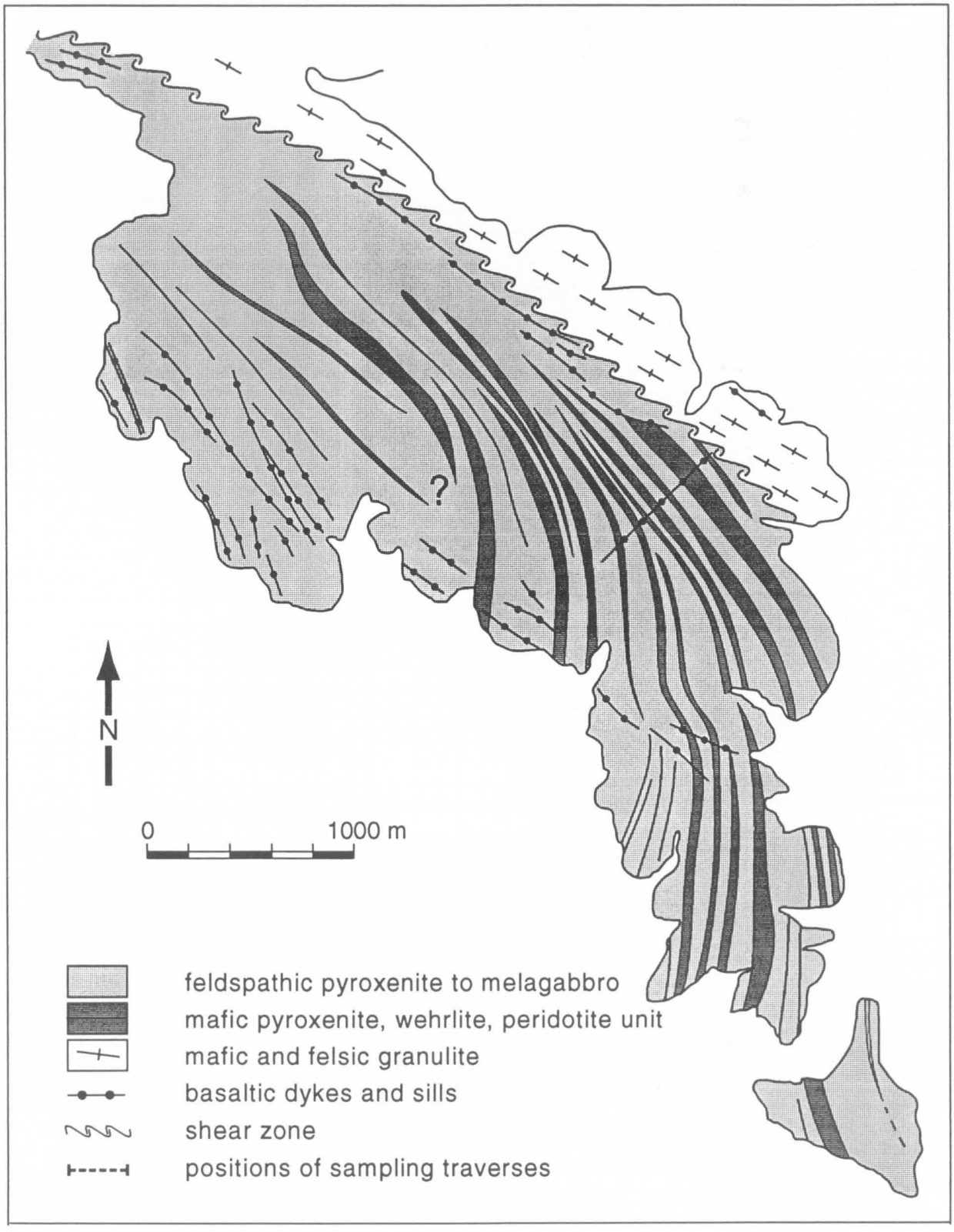

Figure 65. Geological map of The Wart intrusion.

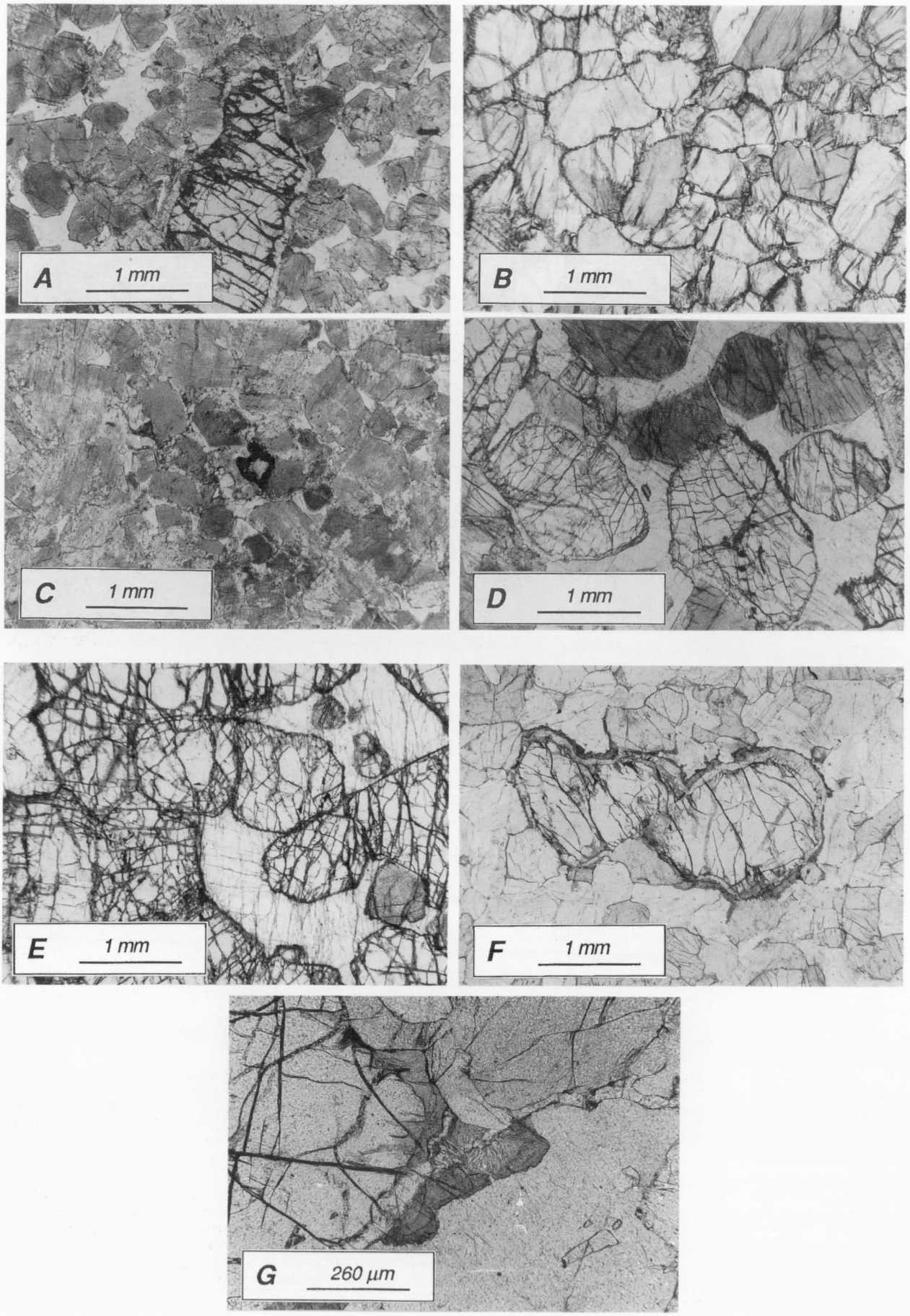
A
1 mm
B
1 mm
C
1 mm
D
1 mm
E
1 mm
F
1 mm
G
260 µm

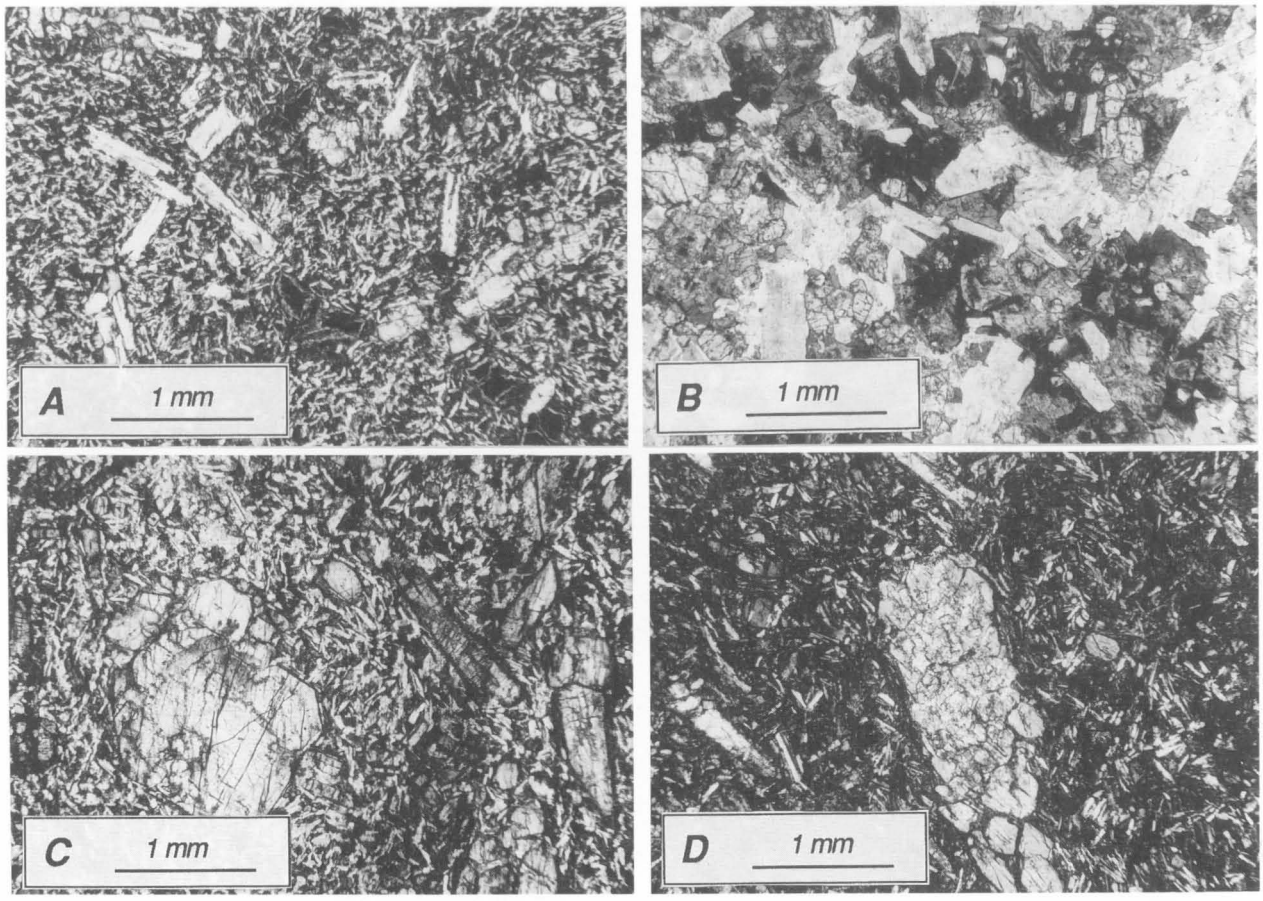

Figure 67. Mafic dykes cutting The Wart intrusion. (A) Fine-grained clinopyroxene–plagioclase-phyric dyke (88981037). Elongated plagioclase and subhedral clinopyroxene phenocrysts are set in an oxide-rich groundmass. (B) Coarse-grained olivine–plagioclase-phyric dyke (88981036). Large euhedral plagioclase laths and smaller rounded olivine grains (with cracks) form phenocrysts, in a brownish biotite-rich hydrated groundmass. This dyke composition is probably unrelated to the host layered sequence. (C) Orthopyroxene-phyric high-pressure basaltic dyke (88981045). Possible intratelluric orthopyroxene phenocrysts are set in a groundmass rich in plagioclase, orthopyroxene and Ti-augite microphenocrysts, and opaque oxides. Several generations of orthopyroxene include the equant grain in the centre, overgrown by a zoned rim, and smaller elongated phenocrysts at right. (D) Same sample as C, showing a skeletal, optically homogeneous augite phenocryst intergrown with plagioclase, possibly a rapid-growth texture.

changes in modal mineralogy and megascale layering are rarer and less obvious than in the more primitive Murray Range and The Wart cumulate sequences.

The parent magma of the Latitude Hill sequence was close to multiple saturation with olivine, pyroxene, and plagioclase. As a result, megascale layering is poorly developed, because new magma pulses did not lead to major changes in the crystallisation sequence. The suggested crystallisation sequence is: (1) olivine + orthopyroxene, (2) orthopyroxene + clinopyroxene, and (3) orthopyroxene + clinopyroxene + plagioclase. Cr/(Cr+Al) in clinopyroxene and the *mg* value at which olivine was replaced by orthopyroxene are lower than in the ultramafic sequences. This indicates that the Latitude Hill liquids were more fractionated and had a lower silica activity than the melts of the ultramafic intrusions, probably owing to pyroxene fractionation before emplacement.

Figure 66. Cumulate and subsolidus textures in The Wart intrusion. (A) Feldspathic olivine-bearing clinopyroxenite orthocumulate (sample 88981033). The rock consists of large rounded olivine, smaller roundish clinopyroxene, rich in exsolved spinel, and colourless interstitial plagioclase. Olivine is surrounded by a columnar orthopyroxene rim. (B) Annealed clinopyroxenite adcumulate (88981043), with spinel-free clinopyroxene and minor antiperthitic plagioclase. (C) Olivine-bearing clinopyroxenite mesocumulate (88981029). This contains altered relict olivine (dark), cumulus clinopyroxene, with abundant exsolved spinel, and interstitial plagioclase. Olivine is partly replaced by columnar orthopyroxene. (D) Feldspathic wehrlite orthocumulate (88981030). Rounded olivine and subhedral brownish exsolved spinel-rich clinopyroxene are cumulus phases, with interstitial altered zoned plagioclase. (E) Feldspathic peridotite orthocumulate (88981044), containing rounded cumulus olivine, cumulus to poikilitic clinopyroxene (with brown exsolved spinel), and interstitial zoned altered plagioclase. (F) Olivine gabbro to melagabbro (88981049). Rounded olivine has an inner rim of clear orthopyroxene and an outer clinopyroxene–orthopyroxene–spinel symplectite rim. Exsolved spinel-free clinopyroxene is cumulus, and colourless plagioclase cumulus to locally interstitial. (G) Olivine gabbro (88981039), showing subsolidus re-equilibration textures. Cumulus olivine grains in contact with plagioclase are surrounded by an inner rim of columnar orthopyroxene and an outer discontinuous rim of 'cauliflower' orthopyroxene–clinopyroxene–spinel symplectite.

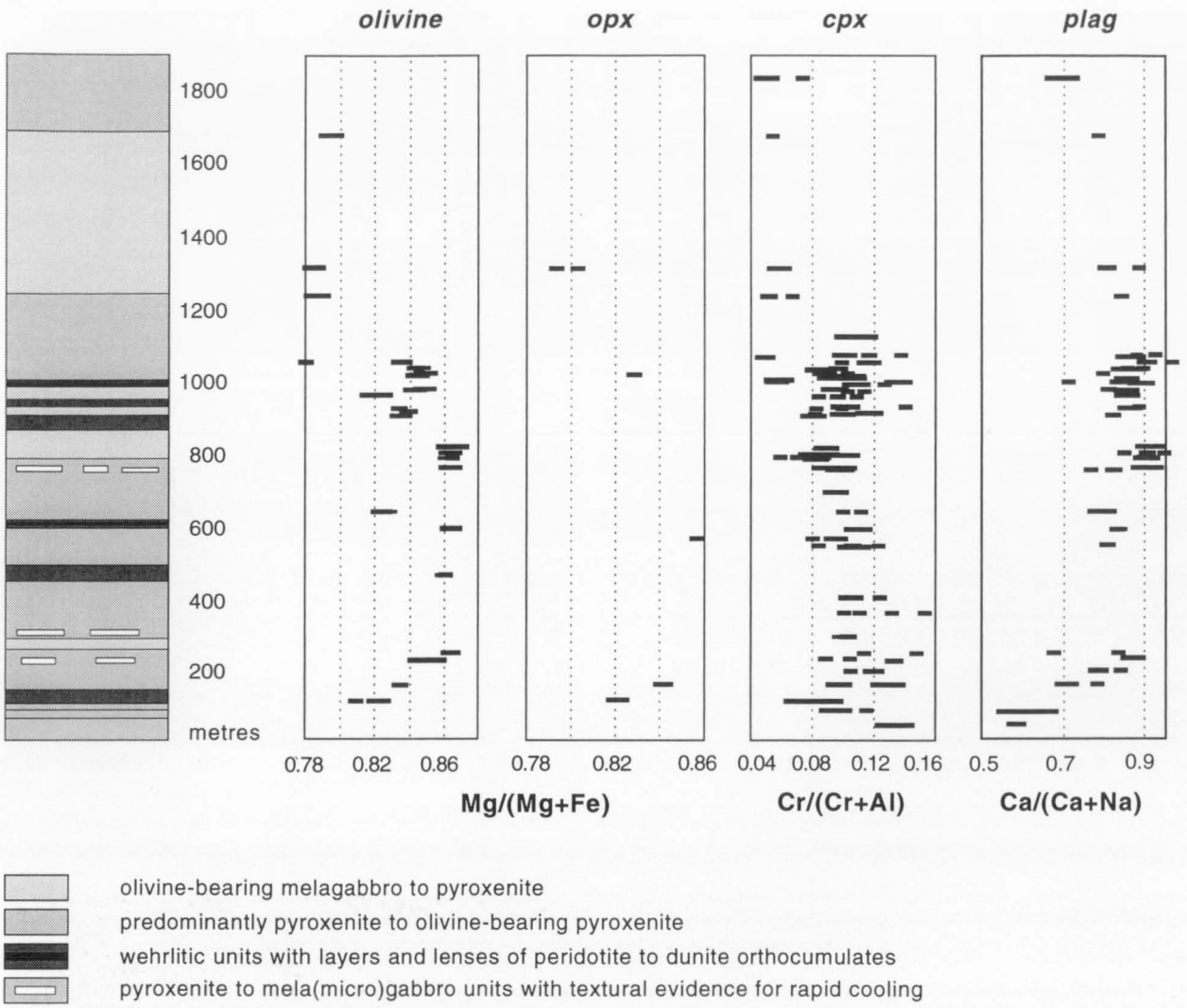

Figure 68. Stratigraphy and mineral chemistry of The Wart intrusion.

Hinckley Range gabbronorite intrusion

The Hinckley Range intrusion is one of the largest and most deformed intrusions of the Giles Complex. It forms a 38 km-long meridional ridge, up to 12 km wide, and the magmatic sequence is approximately 5800 m thick and dips north at 70–80° (Figs 77–80). Its western and northwestern parts are affected by a pervasive metamorphic overprint, which produced mafic granulite, extensively intruded by granitic veins, mainly during D_3 deformation (Stewart & Glikson 1991; Clarke 1992; Clarke et al. 1995a). Cumulate textures and magmatic layering are poorly preserved. The eastern (magmatic) part of the intrusion is well layered and has largely escaped the metamorphic overprint evident in the west. Intrusive contacts are only rarely preserved, because of later deformation, but can be seen in a few places (Fig. 158D).

The Hinckley Range intrusion is dominantly gabbroic, with the most common cumulates being gabbroic troctolite, troctolitic gabbro, gabbronorite, anorthosite, and locally minor pyroxenite (Figs 81, 85). The most common rock types in the eastern part include troctolite, gabbronorite, olivine gabbro, anorthosite, and their deformed equivalents. These rocks are intruded by thin (~5 m) layers and pods of finer-grained microgabbro back-intruded by the coarser-grained host gabbro, suggesting that the sills were emplaced at a late magmatic stage while the host gabbro was still mobile. Multiple intraplutonic chill zones, i.e., multiple repetitions of fine-grained 'marginal' layered microgabbro and subophitic gabbroic sills are also common (Ballhaus 1993). Phenocryst populations and crystallisation sequences in these finer-grained units closely resemble those in the host cumulates.

Olivine and plagioclase are the principal cumulus phases in troctolite and gabbroic troctolite, and are followed in the crystallisation sequence by subhedral poikilitic oxide-rich clinopyroxene and younger anhedral intercumulus orthopyroxene (Fig. 81A–C). Orthopyroxene forms wide, optically continuous reaction rims around olivine and may have formed as a result of a peritectic olivine–melt reaction. In places, orthopyroxene grades into oikocrysts and irregular orthopyroxene–magnetite symplectites. Plagioclase is commonly elongated and euhedral, and impregnated by submicroscopic opaque inclusions (Fig. 81B), possibly exsolved iron oxide impurities incorporated in the plagioclase lattice during high-temperature crystallisation. Olivine in contact with plagioclase may be rimmed by a columnar orthopyroxene moat formed during the subsolidus stage, in contrast to wider optically continuous orthopyroxene rims that commonly grade into poikilitic grains. Clinopyroxene is commonly strain-recrystallised to a granular mosaic of clinopyroxene neoblasts and rounded opaque oxides.

All transitions exist between troctolitic rocks with interstitial clinopyroxene and clinopyroxene-dominated gabbroic rocks.

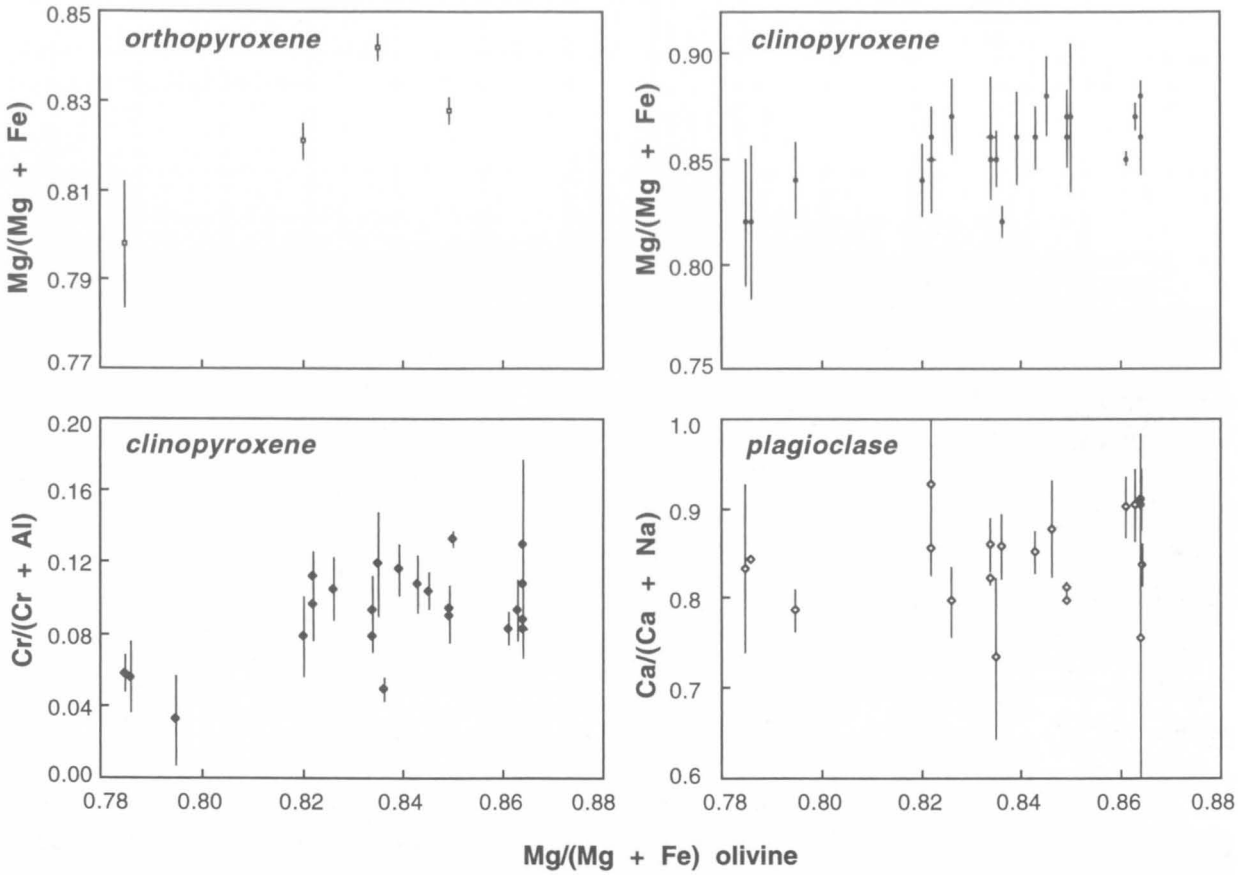

Figure 69. Average mineral compositions of The Wart intrusion (error bars are two standard deviations).

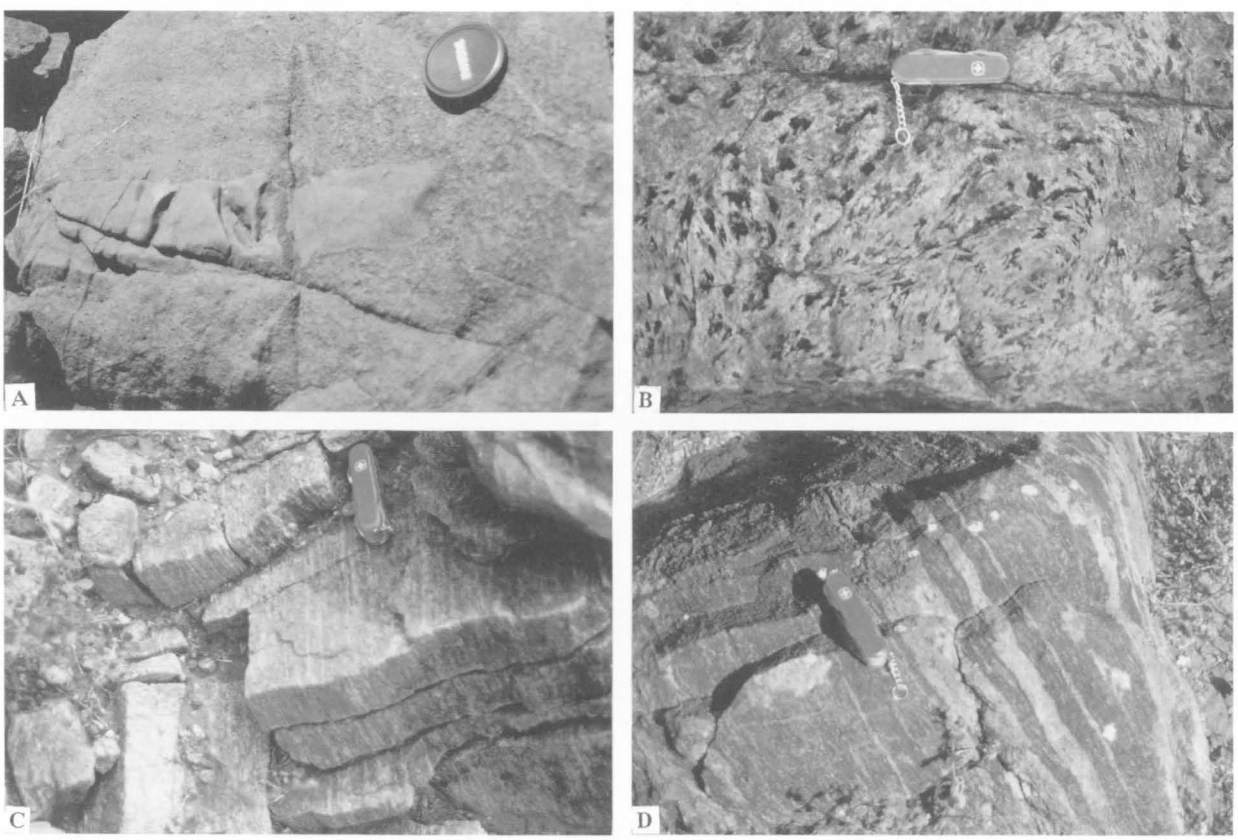

Figure 70. Outcrops of the Michael Hills gabbro and Latitude Hill gabbro/pyroxenite intrusions. (A) Truncated sill of microgabbro in coarse-grained gabbro, into which the sill was emplaced at a late magmatic stage. (B) Very coarse-grained to pegmatitic flow-textured gabbro, south of the Champ de Mars Fault. (C) Mylonitised gabbro, Latitude Hill. (D) Recrystallised gabbro intruded by felsic veins, Latitude Hill.

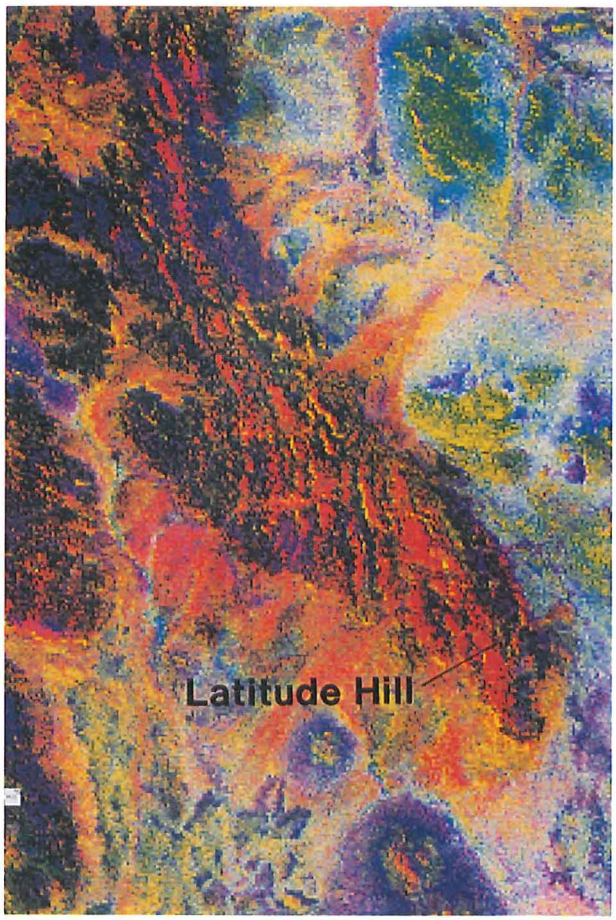

Figure 71. Landsat-5 TM log residual bands 7:5:4 RGB image of the Latitude Hill intrusion, a tectonic sliver of the Michael Hills intrusion, showing intercalated pyroxenite (red, iron oxide-rich weathering crusts) and gabbro (blue–black, clay-rich weathering crusts).

Olivine gabbro contains plagioclase, large clinopyroxene grains, rich in exsolved opaque oxides, and sparse olivine as cumulus phases, whereas orthopyroxene forms later peritectic rims around olivine and clinopyroxene. In the most fractionated samples near the northern margin of the intrusion, olivine is progressively replaced by orthopyroxene, resulting in gabbronorite. Late-magmatic brownish-green amphibole forms narrow rims around all ferromagnesian minerals. The most fractionated samples are anorthositic, with plagioclase as the only cumulus phase, sparse clinopyroxene, and interstitial orthopyroxene and oxides locally recrystallised to neoblastic grains (Fig. 81C).

The southern basal part of the sequence is characterised by finer-grained rocks, showing transitions between porphyritic fine-grained sills and subophitic troctolitic to anorthositic cumulates intermediate between cumulates and rapidly chilled microgabbro equivalents. These rocks contain elongated inclusion-rich euhedral zoned plagioclase and some rounded olivine as phenocryst phases, and intergranular clinopyroxene and opaque oxides.

The western and northern parts of the intrusion consist of mafic granulite and abundant gabbroic relics, which generally produce a lower relief than the little-recrystallised and little-deformed gabbro of the central and eastern sections. The mafic granulite is intruded by numerous granite, aplite, and pegmatite veins. Deformation is manifested by transitions from slightly deformed cumulates with incipient recrystallisation of clinopyroxene, through fine-grained granoblastic two pyroxene–plagioclase–oxide granulite, to mylonite (Fig. 83). The sequence is cut by several prominent east–west-trending mylonite zones with abundant pseudotachylite veins, mostly subparallel to the magmatic layering. These mylonite zones are mostly related to, and branch from, the Hinckley Fault (Goode 1978), where superimposed pseudotachylite vein systems reach over 50 m in thickness (Glikson & Mernagh 1990). Alteration of cumulates is represented by amphibole rims around ferromagnesian phases.

The Hinckley Range sequence also includes a few rather enigmatic fine-grained marginal gabbroic rocks, which are neither clearly of primary magmatic origin, nor clearly formed during high-temperature recrystallisation (mafic granulite). Some fine-grained marginal rocks contain coarse-grained cumulate-textured clinopyroxene–plagioclase enclaves in a fine-grained granular clinopyroxene–orthopyroxene–plagioclase–oxide neoblastic matrix (Fig. 82A, B). Plagioclase in some is euhedral, consistent with a magmatic origin (Fig. 82D). Thus, at least some primary magmatic chilled margins may have survived a post-emplacement metamorphic overprint.

The sequence is cut by several generations of mafic dyke (Fig. 84). These include a primitive olivine–spinel-phyric type which may be similar to a parental melt of ultramafic olivine-rich units in the Wingellina Hills, Murray Range, and Kalka intrusions (Fig. 84C). Olivine–plagioclase-phyric dykes are also widespread.

Mineral compositional trends are summarised in Figures 85 and 86. Olivine ranges from Fo_{75} to Fo_{69}, below which it is replaced by orthopyroxene. Orthopyroxene *mg* values vary sympathetically with olivine from about 82 to 71, and range down to about 59. Cr/(Cr+Al) in clinopyroxene is low, reflecting significant fractionation of the melt prior to emplacement. Plagioclase composition is highly variable, both in single samples and single grains, especially in the more recrystallised cumulates, ranging from $An_{82–59}$. With protracted fractionation, there is a poorly defined trend toward more sodic average plagioclase compositions. The marginal cumulates depart from the overall fractionation trend, with *mg* values of ferromagnesian phases being intermediate relative to the range of the cumulates, whereas plagioclase has variable An contents.

The morphology of the cryptic layering profiles and graded and cross-layering features suggest that the Hinckley Range gabbro youngs towards its northern contact, i.e., in the opposite direction to the Wingellina Hills intrusion (Ballhaus & Glikson 1989). This correlates with a normal fractionation trend in the same direction, although there is a poorly defined reversal above the 2000 m level (Fig. 85). With protracted fractionation upward in the sequence there is a steady increase in modal orthopyroxene and clinopyroxene at the expense of olivine.

The parent magma of the Hinckley Range intrusion was clearly more fractionated than that of the Murray Range sequence, but more primitive than the parent melts that gave rise to the Blackstone Range and Jameson Range sequences. Orthopyroxene is more abundant than in the latter intrusions. At the time of emplacement, the magma was multiply saturated with olivine and plagioclase, but slightly undersaturated in clinopyroxene. The increase in orthopyroxene and clinopyroxene upwards at the expense of olivine indicates that the fractionating phase assemblages were, mostly, lower in bulk SiO_2 content than the parent melt, so that the fractionating liquid became SiO_2-saturated. In contrast, the Blackstone Range and Jameson Range magmas were so SiO_2-undersaturated that olivine persisted to the most fractionated derivative liquids. The sequence shows a relatively sudden increase in modal clinopyroxene above the 2500 m level, where troctolitic cumulates give way to predominantly gabbroic rocks. This change in modal mineralogy nearly coincides with a poorly defined reversal in cryptic layering patterns. It appears there was a slight change in parent magma composition towards a

melt with higher normative clinopyroxene and higher silica activity. Such a change during the intrusive period of an intrusion is not unreasonable in view of the wide ranges of parental melt compositions identified in the Giles Complex intrusions and the dyke suites of the Tomkinson Ranges.

Bell Rock troctolite/gabbro intrusion

The Bell Rock intrusion hosts one of the most fractionated magmatic sequences of the whole Giles Complex and belongs to the troctolitic suite. Total exposed thickness is about 3800 m

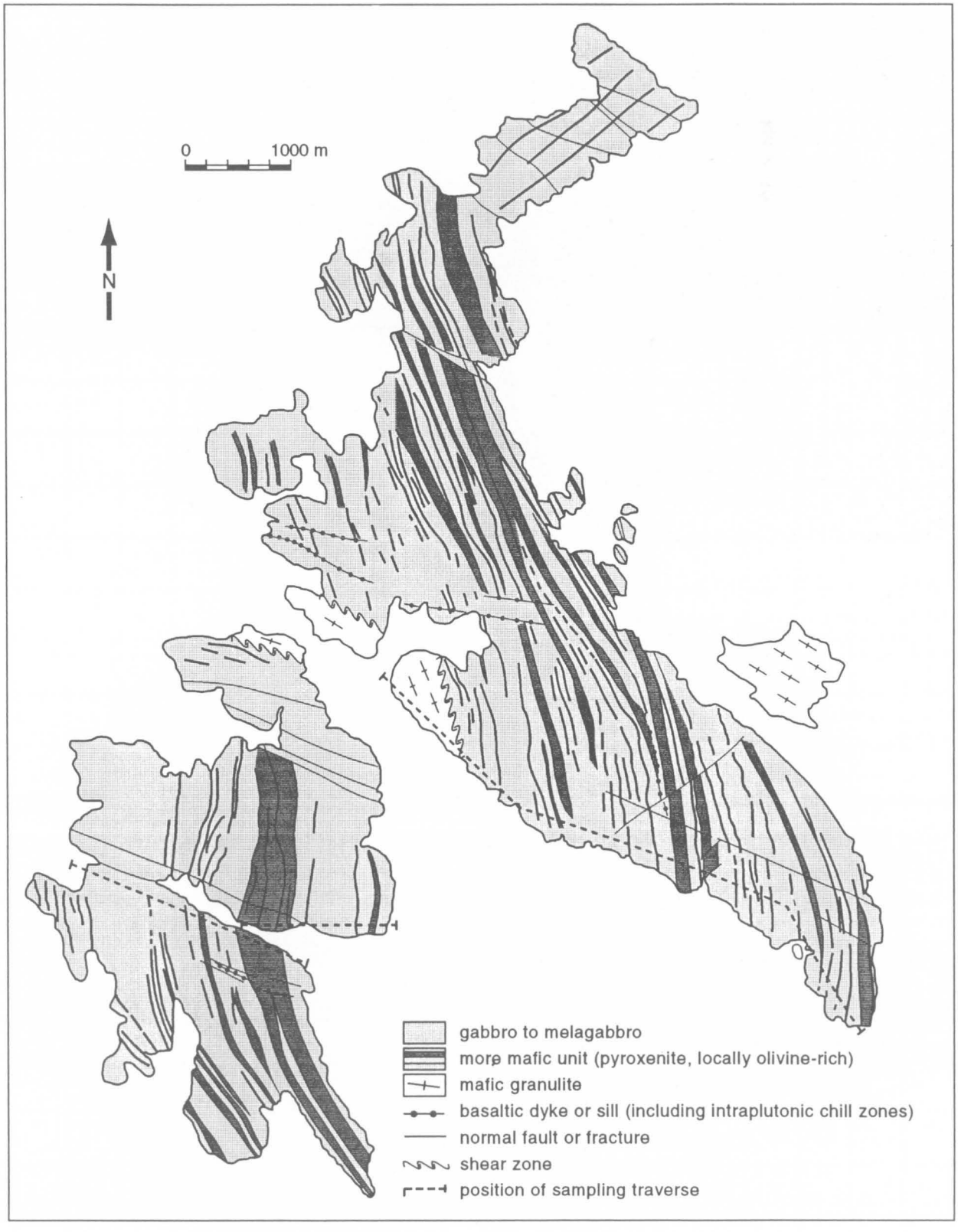

Figure 72. Geological map of the Latitude Hill intrusion.

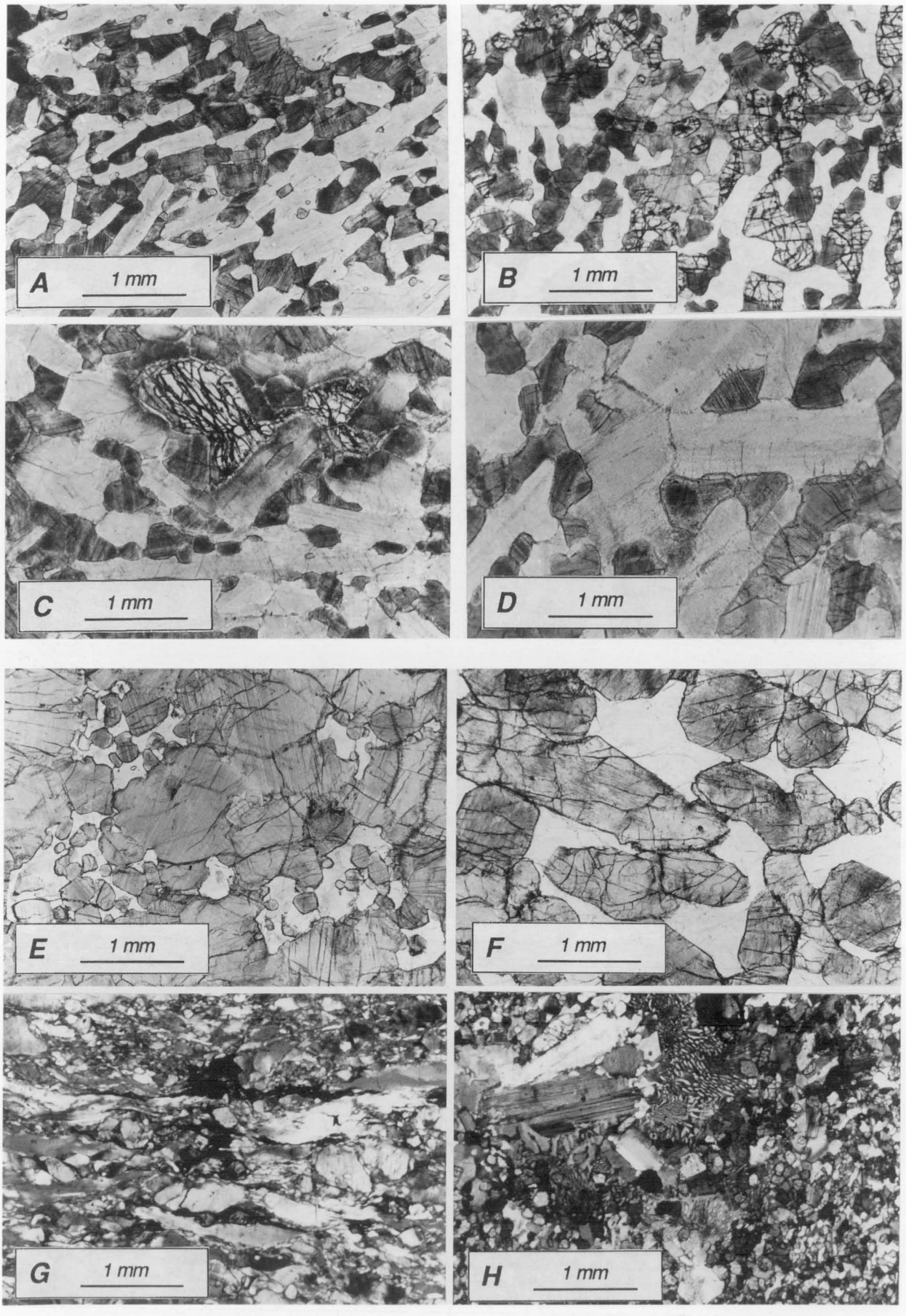
A
1 mm
B
1 mm
C
1 mm
D
1 mm
E
1 mm
F
1 mm
G
1 mm
H
1 mm

and the layering dips at about 70° southwest (Figs 87–90). The intrusion consists of a massive, laterally continuous sequence of troctolite, gabbroic troctolite, and anorthosite, each being several hundred metres thick (Figs 91–93). Units of magnetite-rich ferrogabbro, thin massive magnetite horizons, and dunite cumulates are intercalated with the gabbroic rocks. Most contacts with country rocks are hidden by alluvium. The lower quarter of the intrusion consists of gabbroic troctolite, olivine gabbro, gabbronorite, and microgabbro. The remainder of the sequence is dominated by oxide-bearing troctolite, anorthosite, pyroxene-cumuloblastic gabbro, and thin dunite layers. Further up the sequence, magnetite changes from

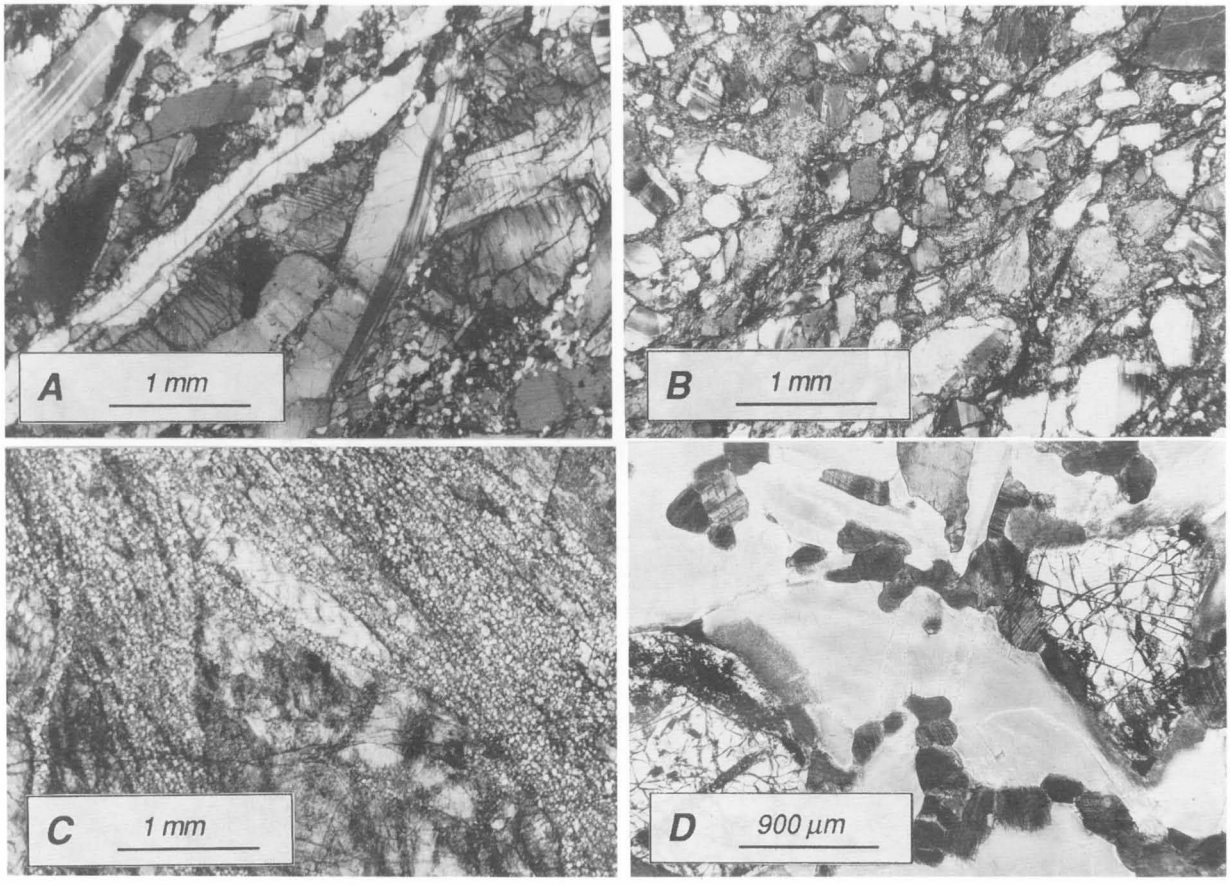

Figure 74. Deformation and subsolidus textures in the Latitude Hill intrusion. (A) Sheared gabbronorite with proto-mylonitic texture (88983061). Plagioclase grain boundaries show incipient granulation, and clinopyroxene is largely broken or recrystallised to neoblasts. (B) Gabbroic cataclasite (88983005). Angular fragments of plagioclase are set in matrix of actinolitic amphibole (probably replacing clinopyroxene fragments). (C) Mylonitised pyroxenite (88983066C). Relict cumulus pyroxene porphyroclasts occur in a matrix of small clinopyroxene neoblasts and fragments. (D) Reaction texture between olivine and plagiodase in doleritic-textured olivine gabbronorite (88983008). Plagioclase in contact with olivine contains clinopyroxene inclusions that coarsen and become more abundant towards the olivine, probably reflecting subsolidus Fe–Mg diffusion from olivine to react with Ca in plagioclase. Primary magmatic clinopyroxene forms rounded grains along clouded plagioclase grain boundaries.

Figure 73. Cumulate and deformation textures in the Latitude Hill intrusion. (A) Fine-grained laminated doleritic-textured olivine-bearing gabbronorite (88983021). Elongated plagioclase laths contain submicron-sized opaque inclusions, probably reflecting exsolution of impurities (e.g., Fe oxide) trapped in the lattice of rapidly growing plagioclase. Pyroxene tends to be interstitial, and is also dusted with very fine-grained opaque inclusions and exsolutions. (B) Doleritic-textured olivine gabbronorite (88983023). Olivine (dark cracks) and clouded plagioclase are cumulus, whereas pyroxene is cumulus to poikolitic. Clinopyroxene is much darker than orthopyroxene, due to the presence of abundant sub-microscopic impurities. (C) Coarser-grained doleritic-textured olivine gabbro (88983013). Plagioclase is clouded with impurities, and, where in contact with olivine, contains small greenish inclusions, probably clinopyroxene, as a result of diffusion and reaction of Fe and Mg with anorthite in plagioclase. Pyroxene is largely interstitial. (D) Coarse-grained doleritic-textured gabbronorite (88983008). Euhedral plagioclase laths contain impurities that recrystallise along grain boundaries as small clinopyroxene neoblasts. Primary magmatic clinopyroxene and orthopyroxene are largely interstitial, clinopyroxene being darker than orthopyroxene (richer in opaque inclusions). (E) Mature pyroxenite adcumulate with feldspathic orthocumulate pockets, giving a mottled appearance in the field (88983015B). Both orthopyroxene and clinopyroxene are cumulus phases. (F) Feldspathic pyroxenite orthocumulate, locally olivine-bearing (88983051). Orthopyroxene (slightly porphyritic) and clinopyroxene are cumulus, whereas plagioclase is interstitial. In such mature cumulates, plagioclase is virtually free of impurities, probably a consequence of lower cooling rates. (G) Gabbroic mylonite to proto-mylonite (88983035). Relict plagioclase and clinopyroxene porphyroclasts are set in an altered matrix of plagioclase fragments, infiltrated by pseudotachylite. (H) Marginal microgabbro, possibly a chilled margin (88983041A), containing small euhedral plagioclase, orthopyroxene, and clinopyroxene. Myrmekitic intergrowths of quartz and K-feldspar may be due to incorporation of granitic melts from partially melted felsic country rocks.

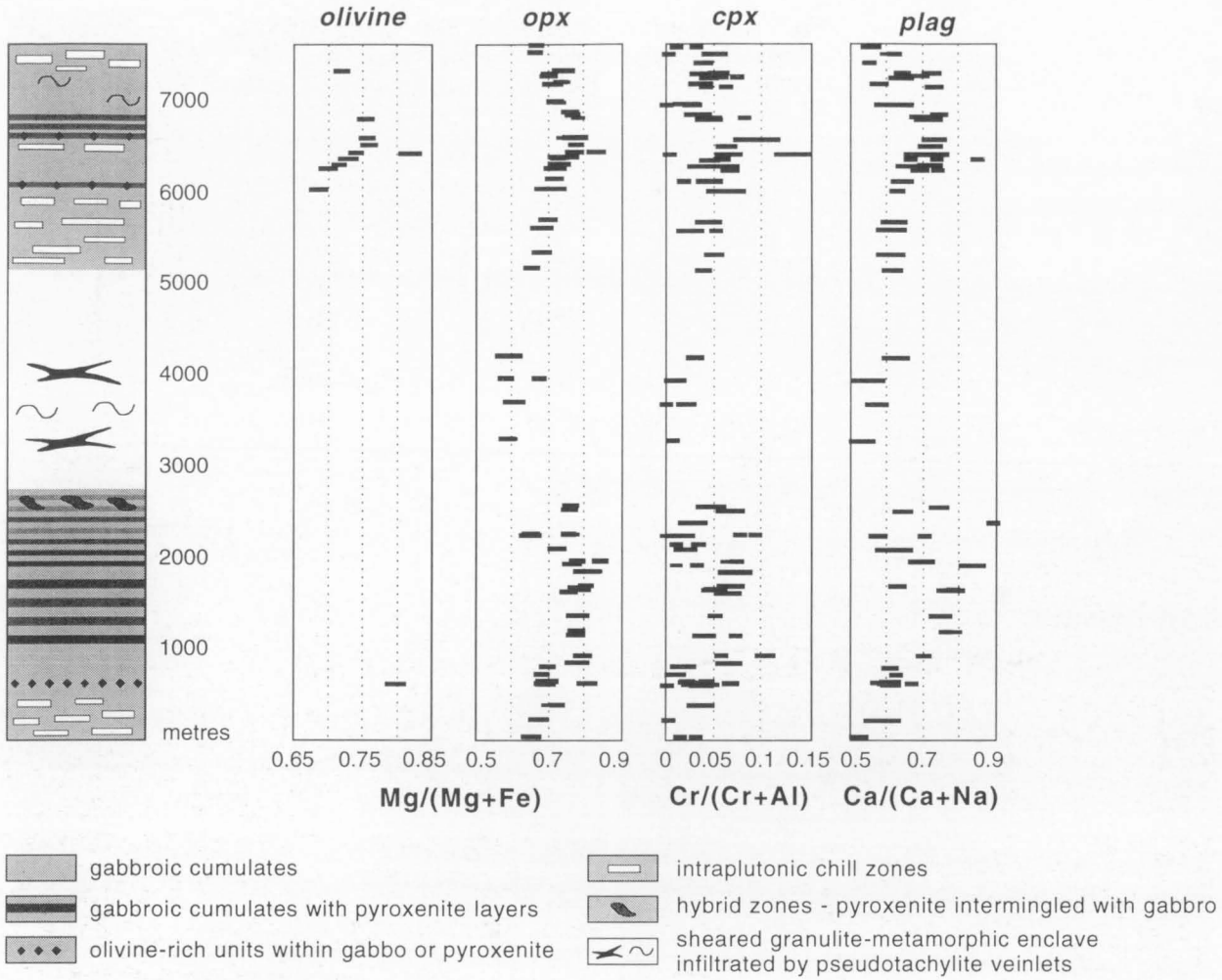

Figure 75. Stratigraphy and mineral chemistry of the Latitude Hill intrusion.

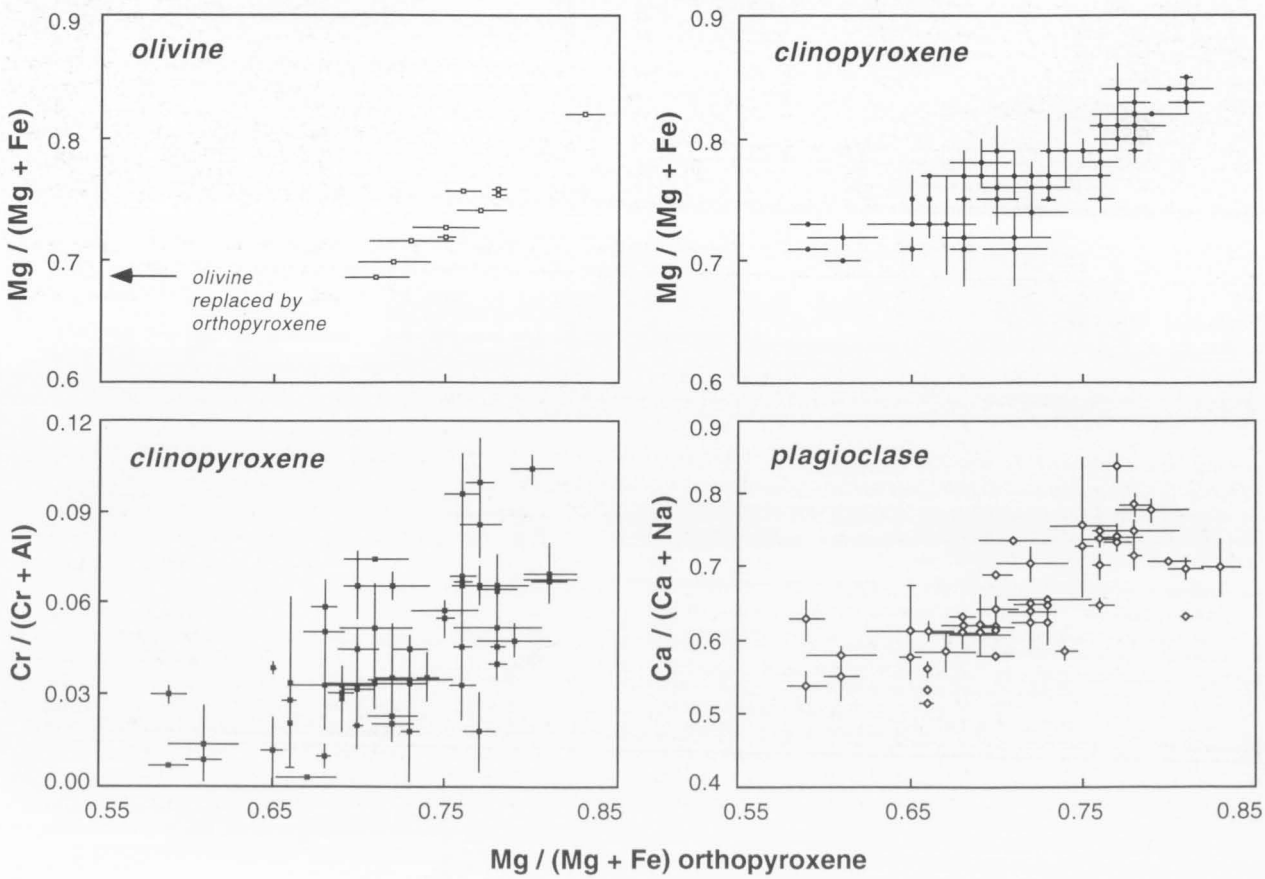

Figure 76. Average mineral compositions of the Latitude Hill intrusion (error bars are two standard deviations).

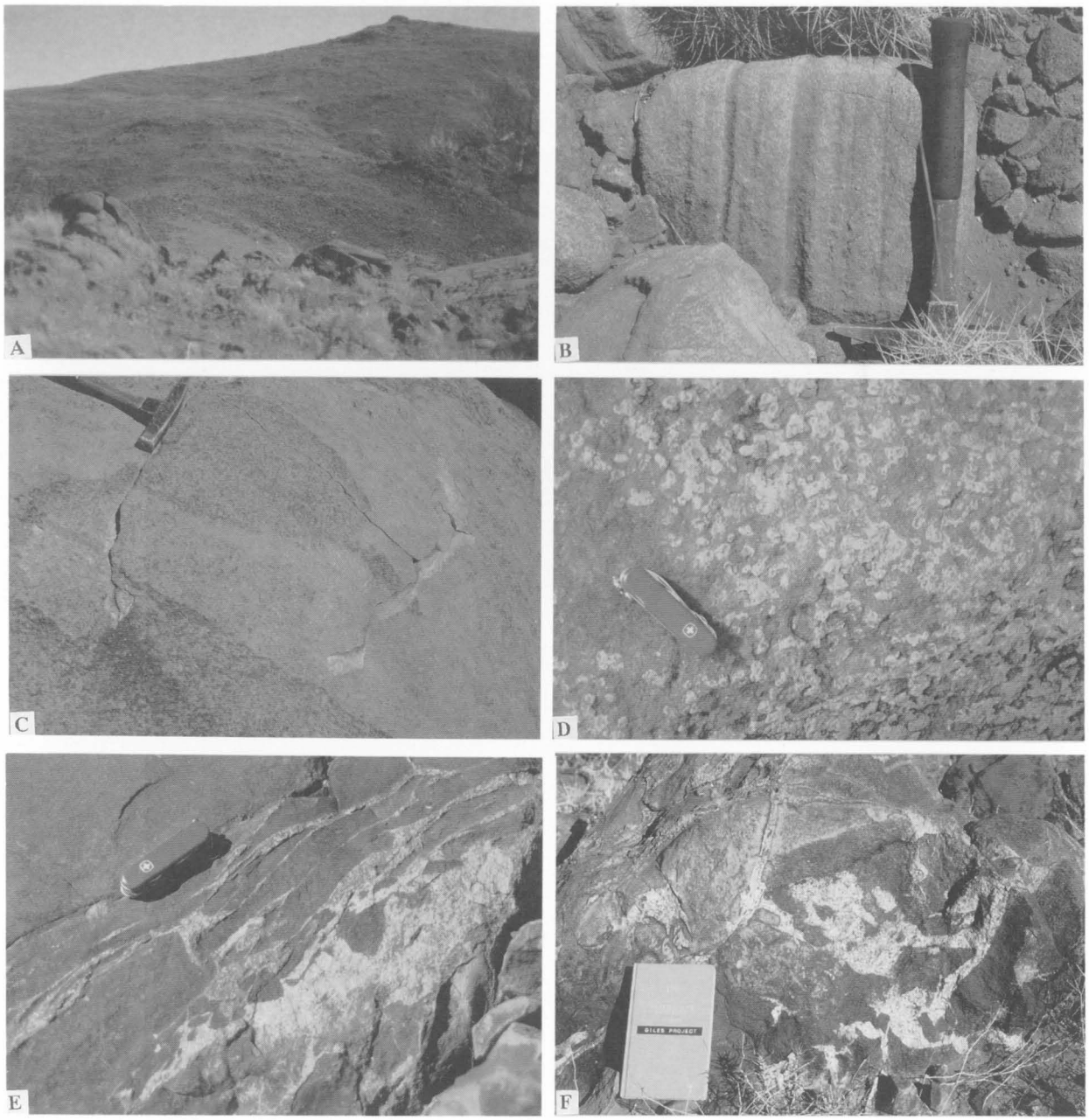

Figure 77. Outcrops of the Hinckley Range gabbronorite intrusion. (A) Southern slopes of Mount Hinckley. (B) Layered and graded gabbro. (C) Interlayered coarse-grained gabbro and microgabbro. (D) Altered plagioclase-phyric gabbro. (E) Mafic granulite (recrystallised gabbro) veined by microgranite, western Hinckley Range. (F) Remnants of mafic granulite in granitic veins, western Hinckley Range.

intercumulus to cumulus, culminating in the deposition of several 10 cm-thick massive magnetite layers. This uppermost iron-rich unit forms a consistent marker along the Bell Rock intrusion, well expressed on aerial photographs and multispectral images. Apart from the magnetite and dunite units, monomineralic rocks are rare.

Magmatic layering is mainly developed only on a small (cm to m) scale (cf. Boudreau 1987), and the megascale cyclicity, so typical of the more mafic intrusions of the Giles Complex, is poorly developed. Part of the sequence contains numerous stratiform repetitions of microgabbro sills, which may be chilled equivalents of the coarser-grained cumulates (Fig. 87E). The phenocryst mineralogy of cross-cutting dykes is similar to the cumulus mineralogy and crystallisation sequence in the layered cumulates. The magmatic stratigraphy, mineralogy, style of magmatic layering, and degree of fractionation of the Bell Rock intrusion are strikingly similar to those of the Blackstone Range intrusion.

Most cumulate types show well-preserved primary magmatic textures, whereas advanced recrystallisation is apparent in the near-monomineralic dunite, anorthosite, and magnetite layers, in which post-magmatic annealing has produced equilibrated granular–mosaic textures with triple grain boundaries. More advanced deformation to mylonite occurs along shear zones, which are particularly prominent below the stratigraphically low dunite horizons.

The principal types of cumulate in the Bell Rock intrusion (Figs 91, 92) comprise:

Troctolite. Rounded olivine and, in places, euhedral plagioclase laths are the principal cumulus phases, accompanied in the upper parts of the sequence by sparse cumulus magnetite. In the more mafic troctolite, olivine is concentrated in aggre-

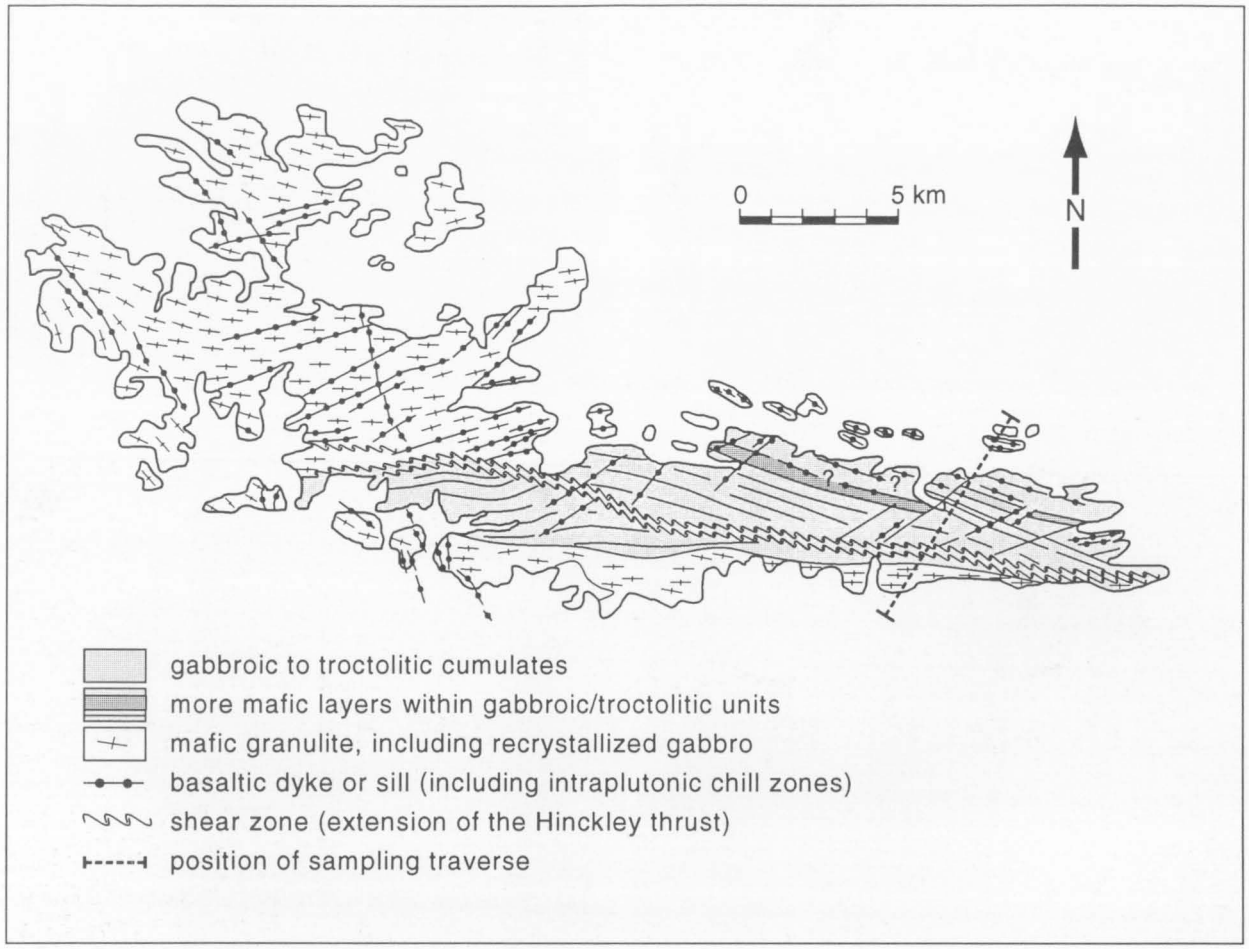

Figure 78. Geological map of the Hinckley Range intrusion.

gates and rimmed by columnar orthopyroxene. In troctolite with lower olivine/plagioclase modal ratios, orthopyroxene becomes more abundant and may form large oikocrysts. Clinopyroxene is invariably younger than olivine and plagioclase and slightly younger than orthopyroxene. Opaque oxides are intercumulus, but tend to become cumulus phases near the massive magnetite layers above the 1970 m level. Post-magmatic biotite and rare amphibole are associated with oxide grains.

Anorthosite. Plagioclase is the sole cumulus phase, whereas olivine and clinopyroxene are minor intercumulus phases. Orthopyroxene forms large poikilitic grains and is more abundant than both olivine and clinopyroxene. Troctolite, anorthosite, and a complete range of transitional rocks are commonly interlayered in a rhythmic pattern.

Dunite. Dunite is confined to a narrow, rhythmically layered stratigraphic interval at about 1580 m where layers alternate with troctolite and anorthosite. Olivine is the only cumulus phase and plagioclase a minor intercumulus mineral, partly replaced by greenish actinolitic amphibole. The dunite displays adcumulate textures recrystallised to a well-equilibrated equigranular fabric with triple grain boundaries.

Gabbroic cumulates. Olivine and plagioclase are cumulus phases, orthopyroxene is interstitial and less common than in troctolitic cumulates, and clinopyroxene, rich in exsolved opaque oxides, forms large subhedral to near-euhedral poikilitic grains which may grade into cumulus textures. Opaque oxides are interstitial or form rounded neoblasts exsolved from clinopyroxene. Post-magmatic phases include red biotite and greenish-brown amphibole, commonly associated with magmatic oxides.

Microgabbro units. Microgabbro units occur as fine-grained cumulates at the margins of the intrusion or form stratiform sills interleaved with, and intruded by, coarser-grained cumulates. Cross-cutting mafic dykes may represent feeders of these units and/or younger intrusions (Fig. 92B, C). Complete gradations occur between coarse-grained slightly immature cumulate textures, finer-grained subophitic microgabbro, and quenched basaltic melts. Phenocrysts in the latter units are similar in composition to cumulus phases in the layered sequence.

Mineral compositional ranges are shown in Figures 93 and 94. Olivine ranges from Fo_{68} to about Fo_{56}. No textural evidence was found to indicate that olivine was replaced by orthopyroxene (i.e., no peritectic reaction relationship with the melt); for example, modal orthopyroxene does not increase with falling *mg* value upward in the sequence, in contrast to the gabbroic and ultramafic intrusions. Relative to olivine, orthopyroxene has higher *mg*, ranging from 72 to 62. Clinopyroxene shows no systematic compositional trend, probably because it is a late intercumulus phase. Clinopyroxene *mg* values are poor indicators of magmatic differentiation, because clinopyroxene becomes more magnesian as it exsolves orthopyroxene during subsolidus equilibration. Plagioclase An contents are highly variable (85 to 55), and show little systematic variation with coexisting olivine compositions.

The stratigraphic orientation of the Bell Rock Range sequence (Figs 88, 93) remains ambiguous, as the morphology of the cryptic layering pattern can be interpreted either way.

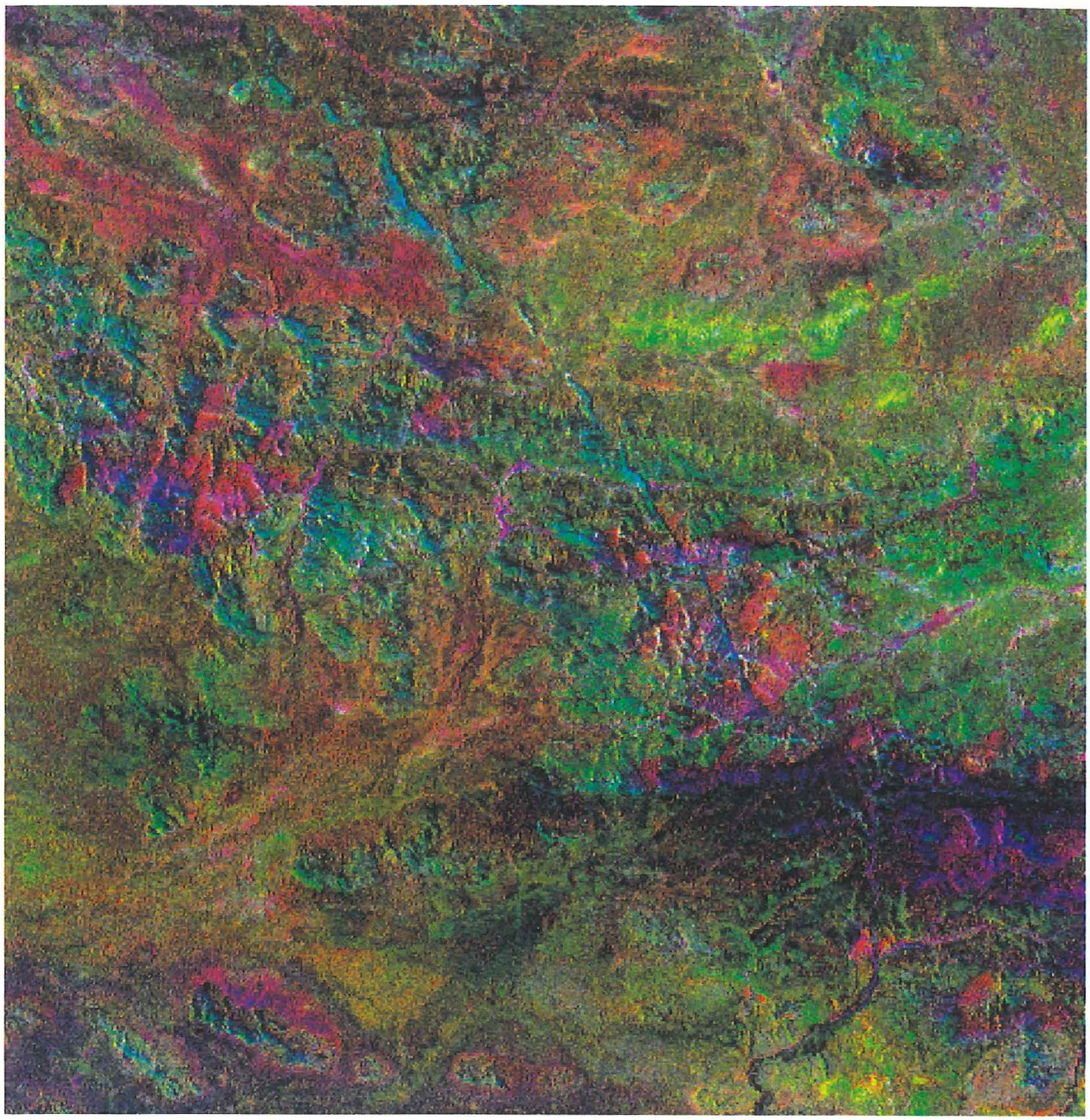

Figure 79. Landsat-5 TM pc2(4/3;5/7):5/4:4/3 RGB image of the western part of the Hinckley Range intrusion, which has been extensively recrystallised to mafic granulite, with abundant gabbroic relics, and intruded by numerous granitic veins. The sequence is cut by several generations of dolerite dykes (Md). Effective discrimination of gabbro from mafic granulite in the field is made difficult by their similar appearance and irregular dimensions and borders. However, in Landsat images, clay-weathered relict gabbro (Gb), which shows in red, can readily be discriminated from mafic granulite (Mn), which shows in yellow to green, due to iron oxide and silica-rich weathering crusts. The presence of thin silica crusts on mafic granulite is related to the abundance of granite and aplite veins. Thus, despite the overall similarities in the chemistry and mineralogy of the gabbro and mafic granulite, the reflectance characteristics of the latter are more like that of felsic granulite.

However, unless it is overturned, the general dip of the cumulate sequence suggests that it youngs to the southwest. Grading and cross-layering structures also suggest southwestward younging, and there is a tendency for modal magnetite to increase in the same direction.

The parent magma must have been highly fractionated and saturated with olivine and plagioclase (and possibly also clinopyroxene and magnetite) at the time of emplacement. As a direct consequence, there is no departure from olivine–plagioclase co-precipitation even at stratigraphic levels where chemical reversals signify influxes of fresh melt. Silica activity does not seem to increase with protracted fractionation, i.e., there is no increase in modal orthopyroxene upward in the sequence, probably because the fractionating phase assemblages were at all times richer in SiO_2 than the equilibrium melt. Magnetite saturation presumably resulted from Fe enrichment and an increase in oxygen fugacity in the derivative liquids. The correlation between the Bell Rock and Blackstone Range intrusions (Daniels 1974) is based on (1) the occurrence of stratigraphically low dunite layers in both intrusions, (2) the occurrence of closely spaced magnetite units above the dunites in both sequences, and (3) the normal fractionation

trend between 2700 and 3600 m in the Bell Rock sequence resembles a similar trend in the Blackstone Range sequence between 1800 and 2500 m.

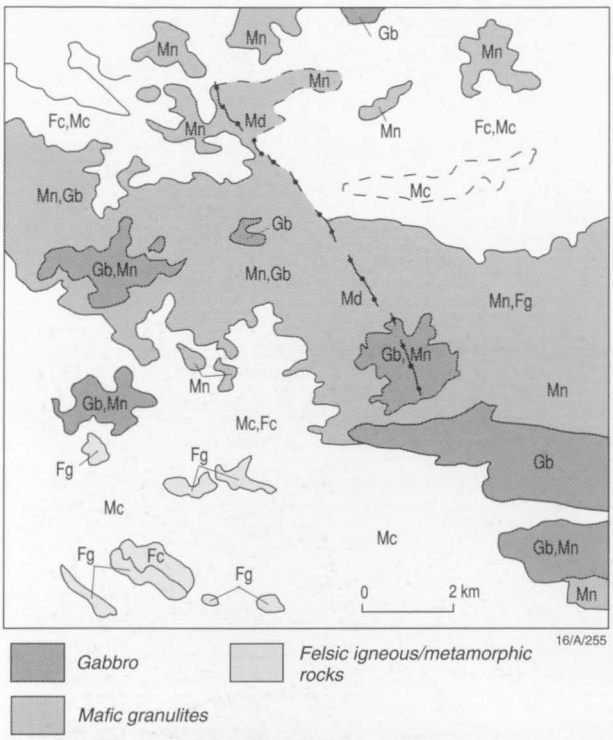

Figure 80. Geological overlay for the western part of the Hinckley Range intrusion (Fig. 79). Symbols as in Figure 51.

Teizi anorthosites

The felsic granulite sequence of the Ewarara–Teizi area, between north of Gosse Pile and the Teizi bore, is extensively intruded by lenses of little-deformed, coarse-grained, magmatically textured to gneissose anorthosite, and by numerous sills of recrystallised fine-grained granoblastic meta-anorthosite. Discrimination between fine-grained granoblastic anorthosite and feldspathic felsic granulite is difficult in outcrop, but the former is quartz-free and displays a more clay-rich weathering crust due to the lower stability of calcic plagioclase. Accurate depiction of these units by the clay indicators of

Figure 81. Cumulate textures in the eastern (magmatic) part of the Hinckley Range intrusion. (A) Typical olivine-bearing gabbronorite (87980003). Olivine (clear grains with cracks), brownish clinopyroxene (with exsolved oxide), lighter orthopyroxene (partly with magnetite symplectites), and euhedral plagioclase laths are the main constituents. The grey clouding of plagioclase is due to minute dark grains, possibly Fe oxide impurities incorporated into the lattice during high-temperature crystallisation that exsolved on cooling. (B) Gabbroic cumulate (87980023B). Plagioclase, forming laths dusted with small inclusions, is the main cumulus phase, whereas clinopyroxene is cumulus to intercumulus. This rock is interpreted as an immature cumulate that may have formed by comparatively rapid crystallisation. (C) Anorthositic gabbronorite cumulate (87980001). Elongated euhedral plagioclase is cumulus, whereas clinopyroxene is largely intercumulus and recrystallised to small clinopyroxene–oxide neoblasts. The texture is similar to that of some sills or dykes with subophitic to intergranular textures, which contain plagioclase phenocrysts and granular clinopyroxene and opaque oxides in the groundmass. Such textures suggest relatively rapid cooling and crystallisation. This is one of the most fractionated cumulates sampled in the Hinckley Range intrusion.

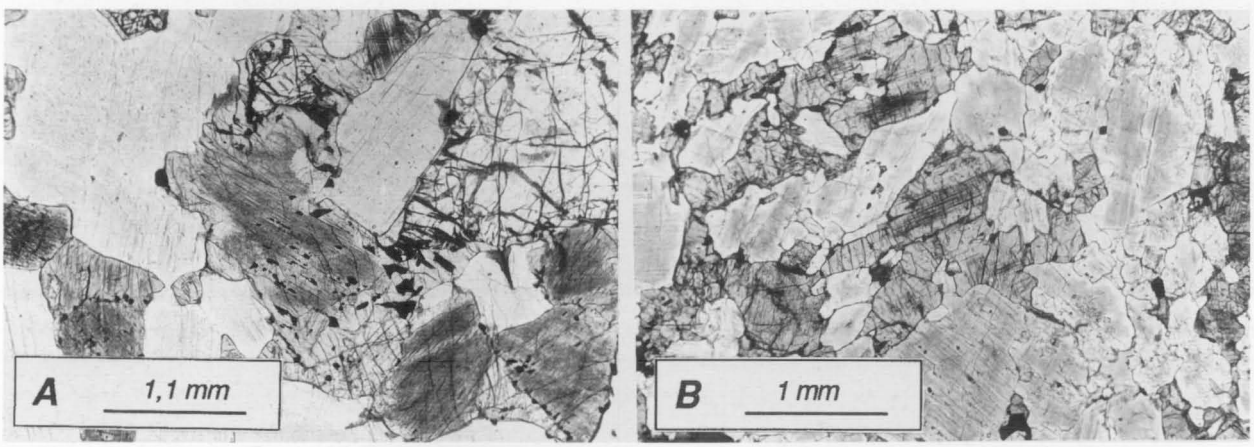

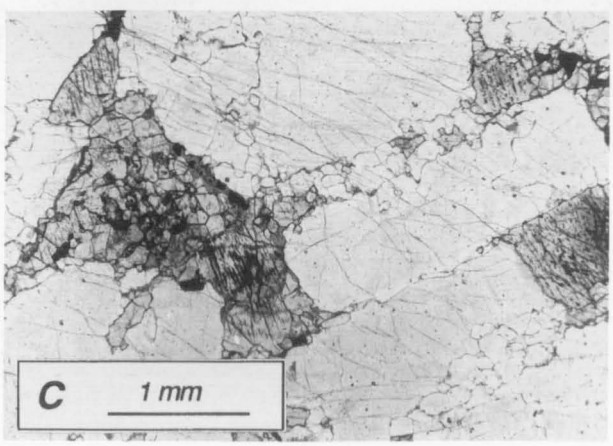

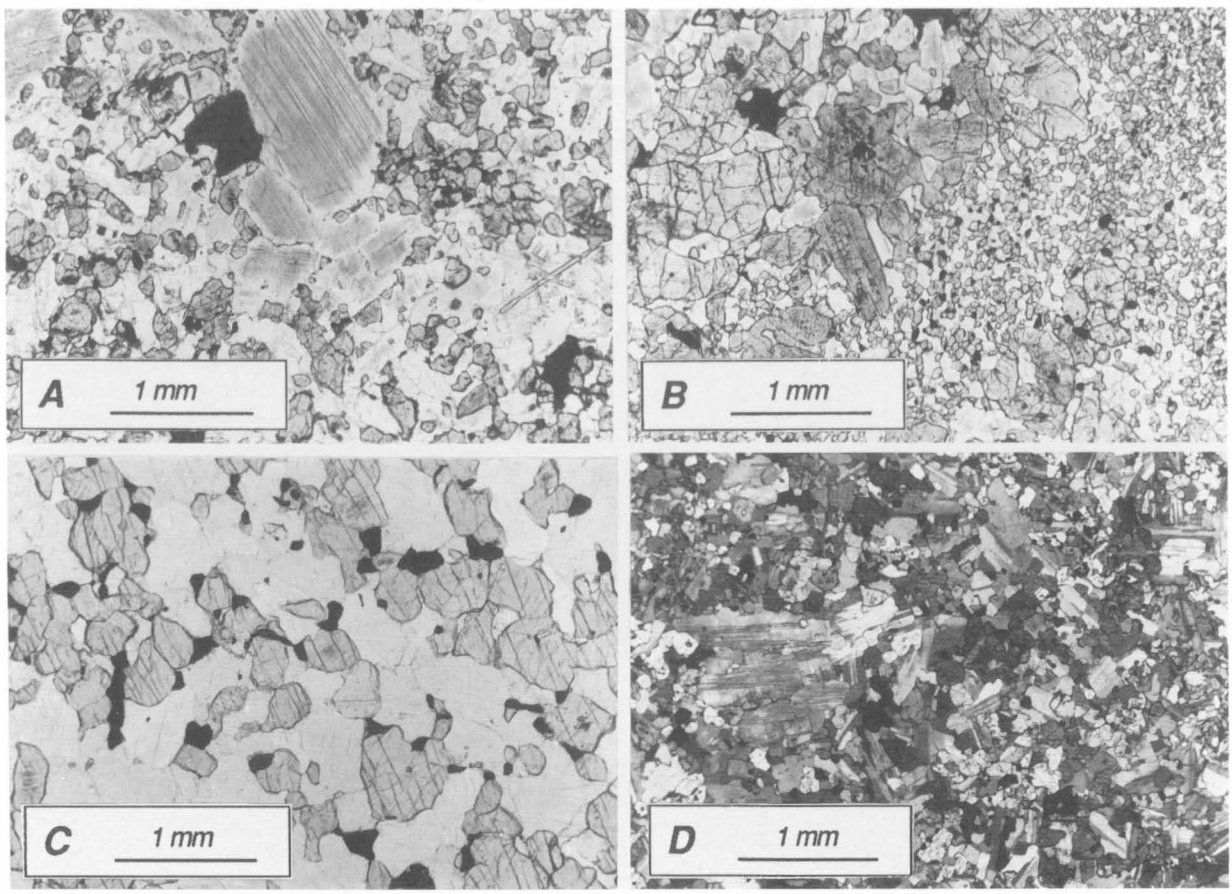

Figure 82. Fine-grained marginal rocks in the Hinckley Range intrusion. (A) Fine-grained sample from the southern margin of the intrusion (87980017). This may be a rapidly quenched gabbroic rock that formed under highly varied cooling rates and/or amounts of strain, or may have lost a fluid phase during crystallisation, thus allowing rapid growth of fine-grained material. Plagioclase is typically crowded with minute opaque inclusions, suggesting rapid growth. (B) Fine-grained marginal gabbroic rock with coarse-grained cumulate-textured enclaves (87980021A). It is not clear whether this is a primary magmatic texture (a chilled margin, formed with highly varied cooling rates, amount of strain, or fluid pressures) or a secondary metamorphic texture (subsolidus high-temperature shearing, followed by static recrystallisation). (C) Gabbroic granulite (87980016), with equigranular plagioclase, clinopyroxene, and subordinate opaque oxides and orthopyroxene. Phlogopite is a common minor phase. The modal ratio of clinopyroxene to oxide neoblasts is about the same as in primary clinopyroxene with exsolved oxide, consistent with a gabbroic precursor. (D) Fine-grained, possibly chilled marginal rock (87980021B), with small euhedral to subhedral twinned plagioclase laths and granular clinopyroxene and orthopyroxene. Plagioclase morphology suggests that this is a primary magmatic texture. Crossed polarisers.

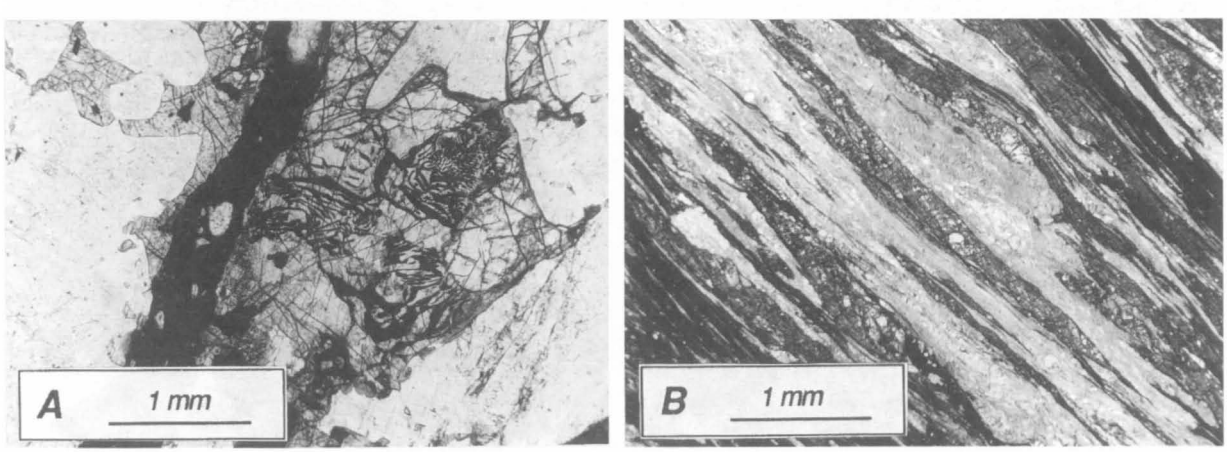

Figure 83. Deformation textures in the Hinckley Range intrusion. (A) Altered troctolite cut by opaque pseudotachylite veinlet (87980002). Olivine is surrounded by thin green symplectitic rims of orthopyroxene and magnetite, possibly representing an oxidation reaction. (B) Gabbroic mylonite (87980032). Deformed clinopyroxene relics are partly replaced by amphibole (medium-gray layers), and altered plagioclase is largely replaced by amphibole (light layers); near-opaque pseudotachylite is black. The sample is from near the Hinckley Fault.

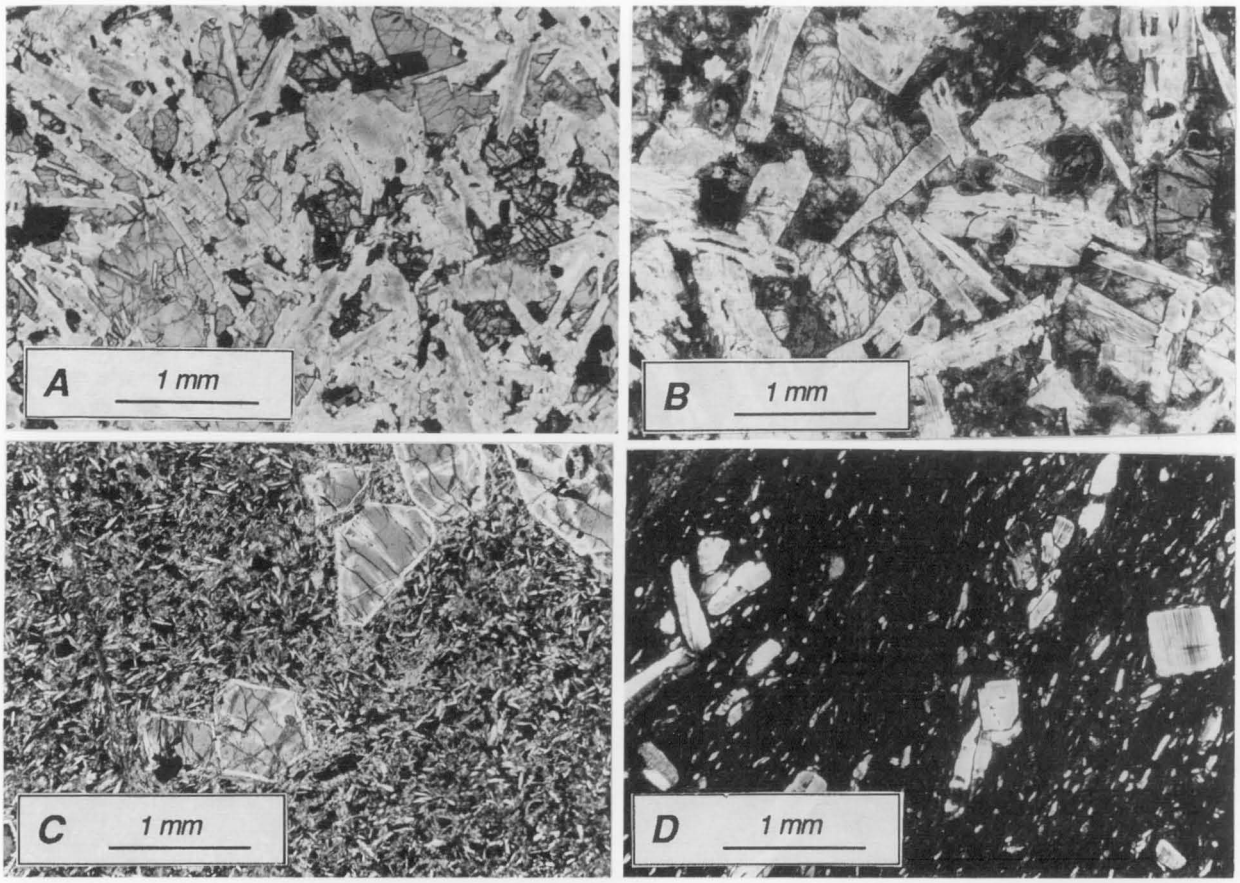

Figure 84. Mafic sills and dykes in the Hinckley Range intrusion. (A) Coarse-grained olivine–plagioclase-phyric dyke (87980007). Elongated brownish-clouded plagioclase laths and rounded olivine grains are phenocrysts, with interstitial clinopyroxene. There are close textural similarities with immature doleritic-textured cumulates (cf. Fig. 81C). (B) Plagioclase–olivine-phyric sill or chilled margin (87980019). Rounded olivine and lath-shaped plagioclase phenocrysts are set in a 'dirty' oxide-rich clinopyroxene-bearing groundmass. Fine-grained spinel-bearing symplectites in the groundmass reflect reaction between olivine and plagioclase. (C) Primitive olivine–spinel-phyric dyke (87980024B). Euhedral olivine phenocrysts, with euhedral Cr–Al spinel inclusions, are set in a plagioclase–clinopyroxene–oxide-rich groundmass. Such a composition is a possible parent magma to the Wingellina Hills–Murray Range ultramafic intrusions. (D) Extremely fine-grained flow-textured dyke (87980023A). Zoned plagioclase phenocrysts are set in dark groundmass. This rock is either a dyke or a thick pseudotachylite vein, the euhedral plagioclase grains probably being more consistent with the former.

Landsat-5 TM, e.g., the pc2(4/3;5/7) index, is very useful in the mapping of these units (Figs 53, 54).

The Teizi anorthosites have been described in detail by Gray (1967). They consist of anorthosite (nearly 100% plagioclase), orthopyroxene–plagioclase gneiss, and rare orthopyroxene rocks. The total thickness of the sequence is about 1500 m, and nine mappable lithological units can be distinguished, which define an antiformal structure. The core of the antiform consists of even-grained gabbroic anorthosite, comprising interlocking antiperthitic plagioclase (~85%) and interstitial orthopyroxene (~15%). Contacts between the anorthosite and country rock felsic granulite are poorly defined and not well exposed. However, there is a transitional contact unit of mafic orthopyroxene–clinopyroxene–plagioclase–garnet granulite. The major component of the Teizi anorthosites is coarse-grained blue-grey anorthosite, with pyroxene rarely exceeding 10 percent. Antiperthitic plagioclase occurs as serrated interlocking grains, forming a metamorphic texture. Pyroxene locally forms foliated aggregates and augen-shaped clots. The unit includes a sheared recrystallised fine-grained equivalent of the anorthosite, containing relict coarse-grained anorthosite. This variety dominates the narrow, strongy sheared and recrystallised, fine-grained anorthositic sills to the north and west of Teizi bore (Fig. 53). Pegmatitic units consist of very coarse-grained orthopyroxene.

Deformation has produced complex interlayering, with gradational contacts between pyroxene–plagioclase gneiss, foliated gabbroic anorthosite, and pure anorthosite. Such layered anorthositic units within massive anorthosite form useful structural markers. The layering, on a centimetre to metre scale, is defined by various pyroxene–plagioclase proportions. Mineral assemblages include garnet and hornblende, and plagioclase in such units is not antiperthitic; the texture is granoblastic. Advanced to cataclastic deformation of anorthosite is marked by a general decrease in twinning and bending of relict twinning, undulose extinction, shearing, areas of granulation, and grain alignment with long axes parallel. Alteration was associated with development of carbonate.

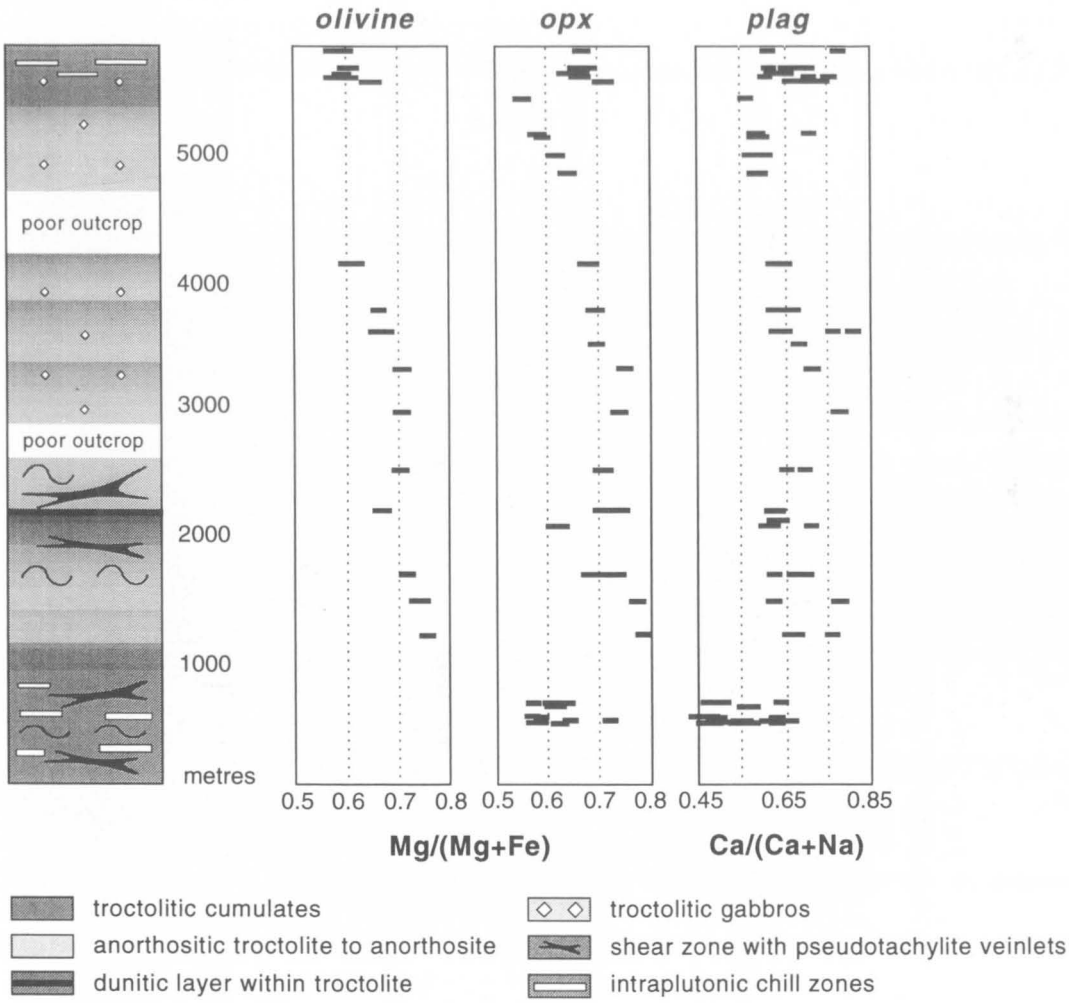

Figure 85. Stratigraphy and mineral chemistry of the Hinckley Range intrusion.

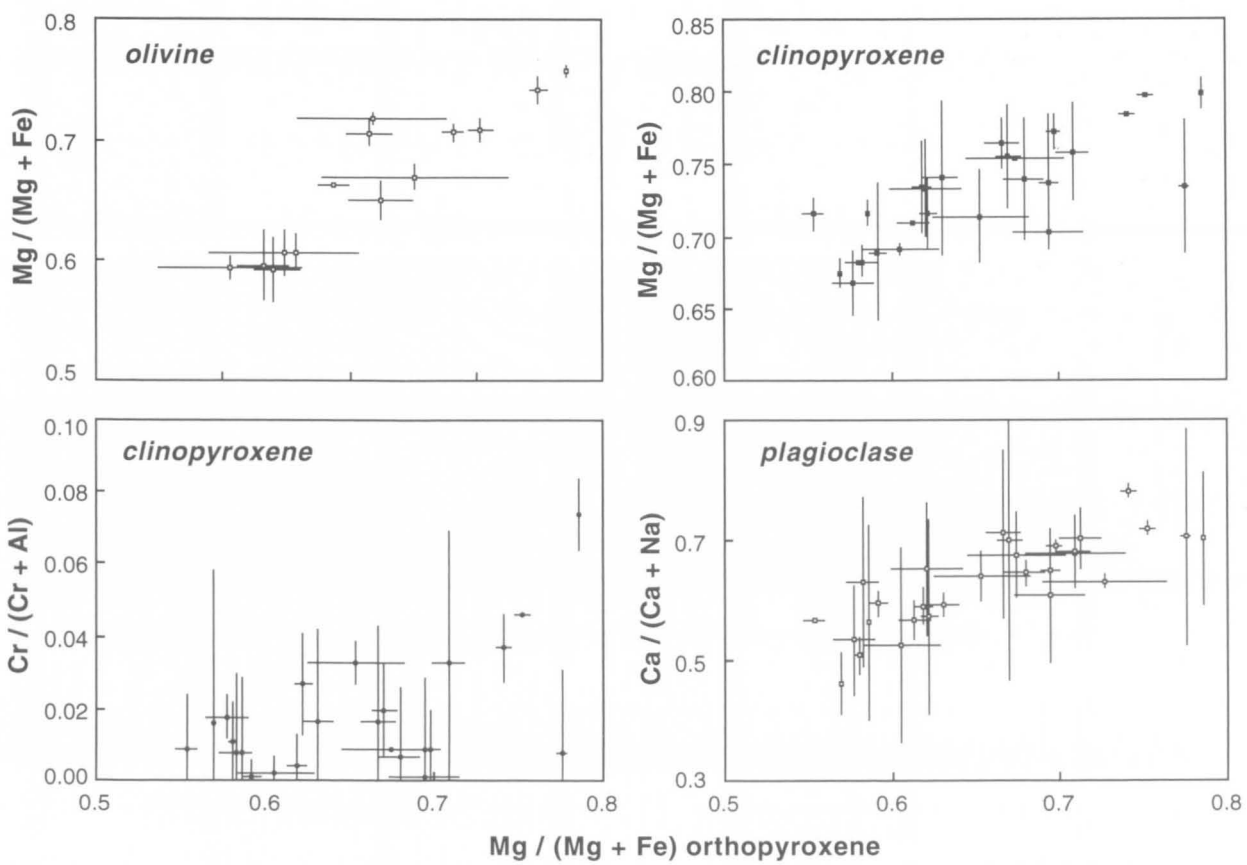

Figure 86. Average mineral compositions of the Hinckley Range intrusion (error bars are two standard deviations).

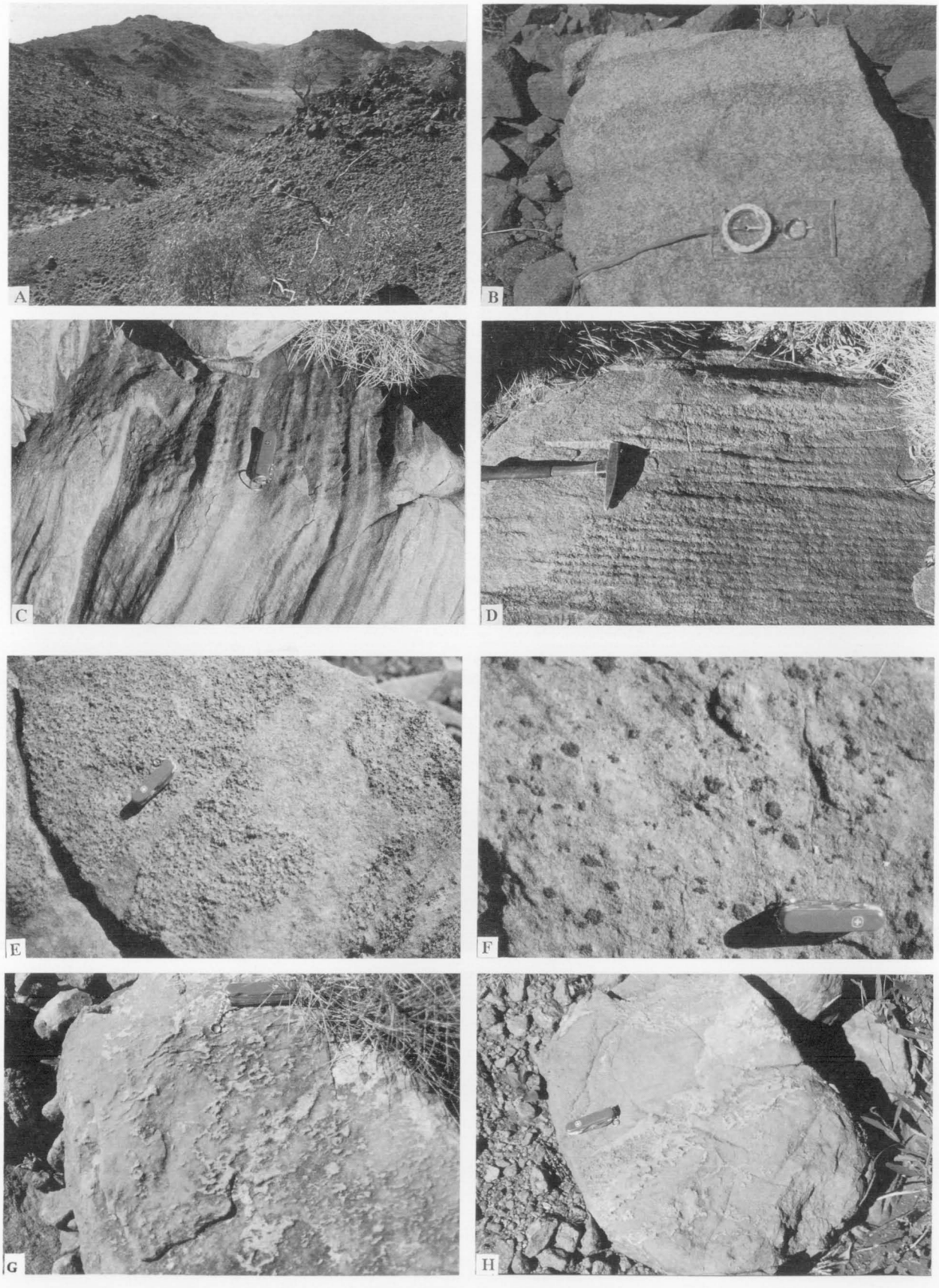

Figure 87. Outcrops of the Bell Rock troctolite/gabbro intrusion. (A) Outcrops of gabbro, cut by a mafic dyke, northern Bell Rock Range. (B) Cross-layered gabbro. (C, D) Rhythmically layered gabbro. (E) Intermingled coarse-grained and medium-grained gabbro. (F) Cumuloblasts of pyroxene in gabbro. (G, H) Microgranite-veined contact with felsic orthogneiss.

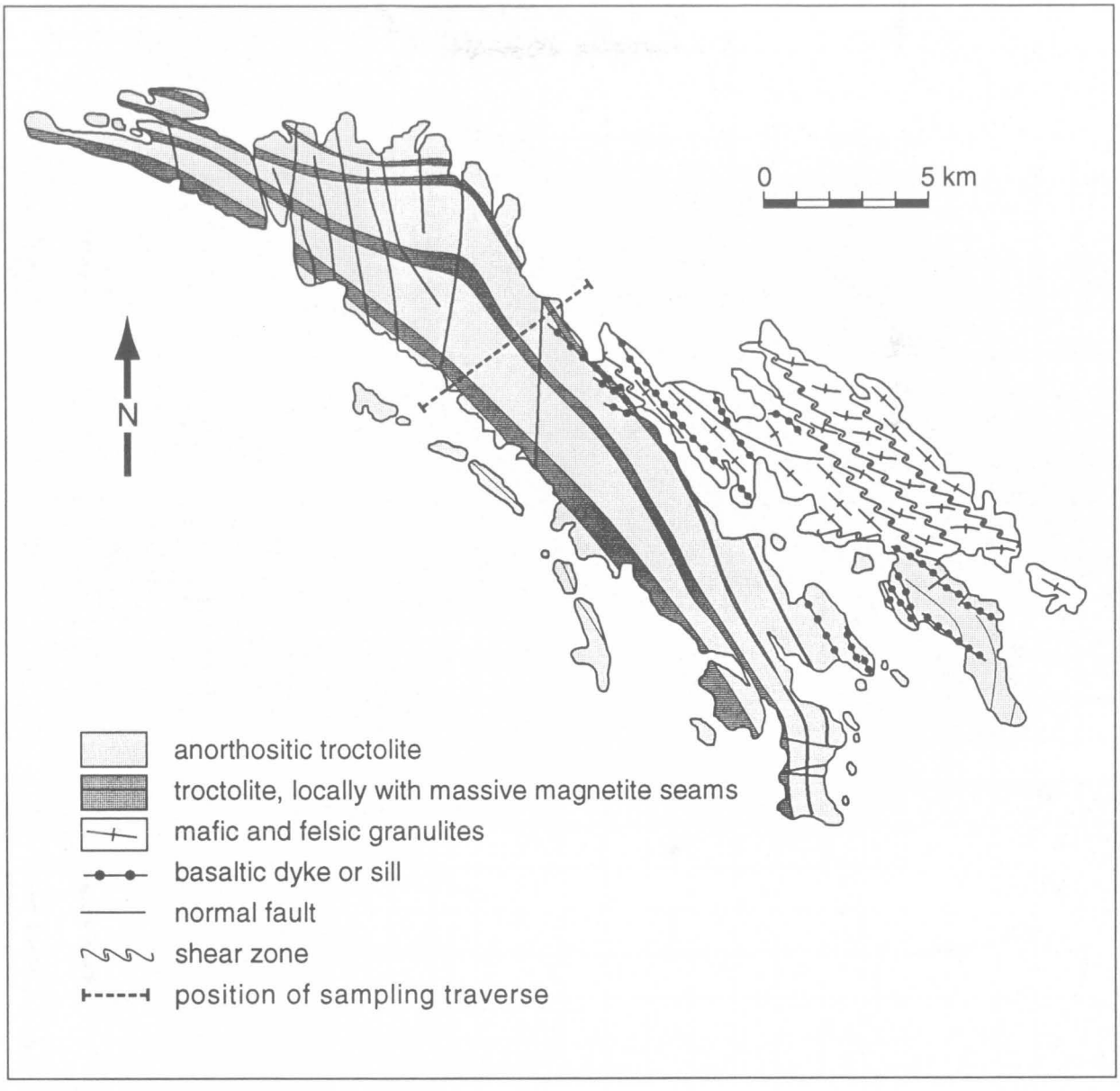

Figure 88. Geological map of the Bell Rock intrusion.

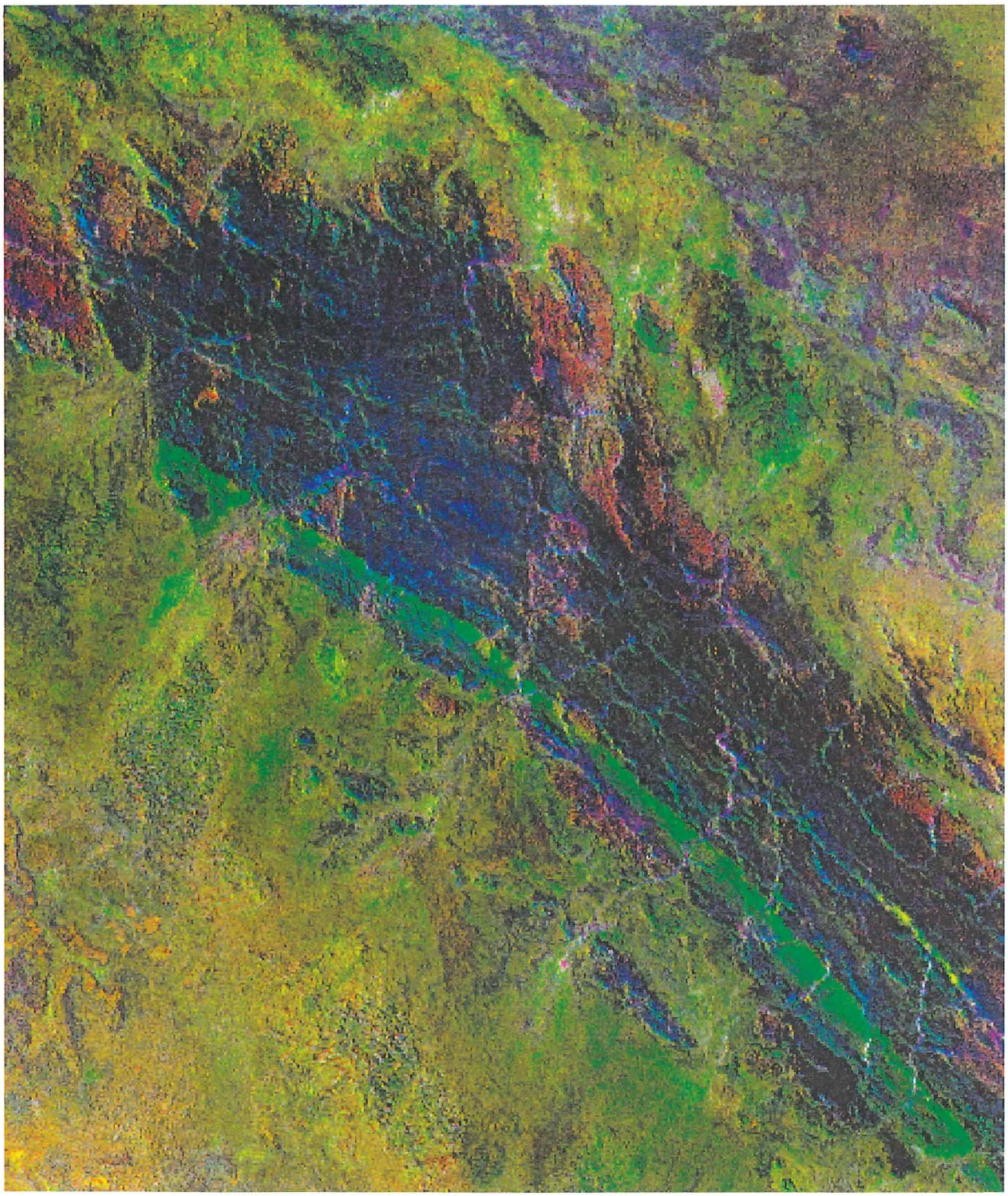

Figure 89. Landsat-5 TM pc2(4/3;5/7):5/4:4/3 RGB image of the northwestern part of the Bell Rock intrusion. Extensive fireburns in the area result in excellent exposure of the layered mafic rocks. Unburnt areas show the typical clay-like red reflectance of dry vegetation. Whereas gabbro (Gb) in burnt areas reflects in low-albedo dark brown colours, units of ferrogabbro (Gf) and mafic dykes, characterised by abundant magnetite and its weathering products, show in bright green. The high resolution of these units makes their discrimination more straightforward than is allowed by field and aerial photograph mapping.

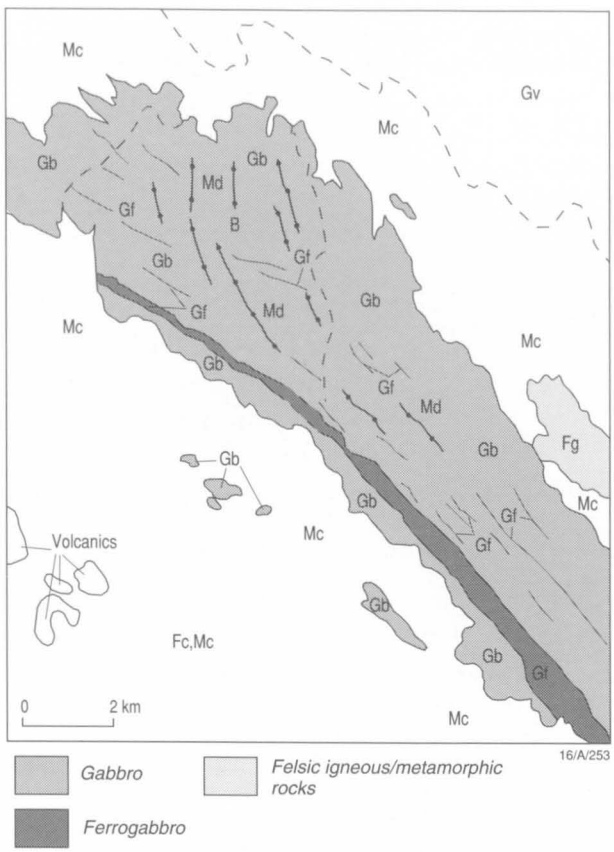

Figure 90. Geological overlay for the northwestern part of the Bell Rock intrusion (Fig. 89). Symbols as in Figure 51.

Figure 91. Cumulate textures in the Bell Rock intrusion. (A) Troctolite (88982012). Olivine (dark cracks) and plagioclase are cumulus phases, clinopyroxene, rich in exsolved oxide, is interstitial to poikilitic, and there is minor orthopyroxene around olivine. Plagioclase is clouded with dark very fine-grained inclusions. (B) Gabbroic troctolite (88982014). Olivine and clouded plagioclase are cumulus minerals, and clinopyroxene (at left) is poikilitic. (C) Troctolite (88982013). Olivine is locally surrounded by columnar orthopyroxene overgrowths and plagioclase is clouded with minute oxide inclusions. (D) Anorthosite (88982015), consisting of cumulus plagioclase, minor interstitial clinopyroxene, and rare euhedral opaque oxide grains.

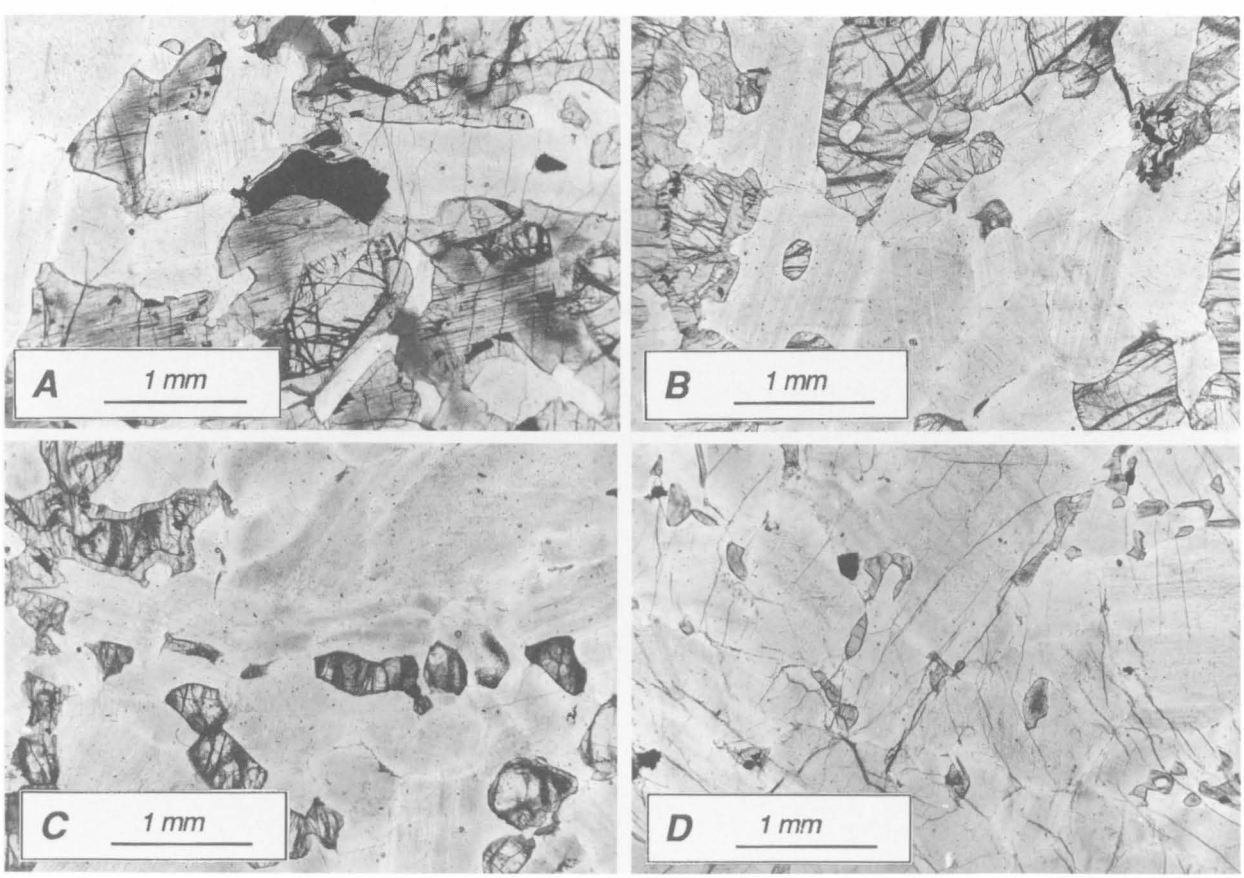

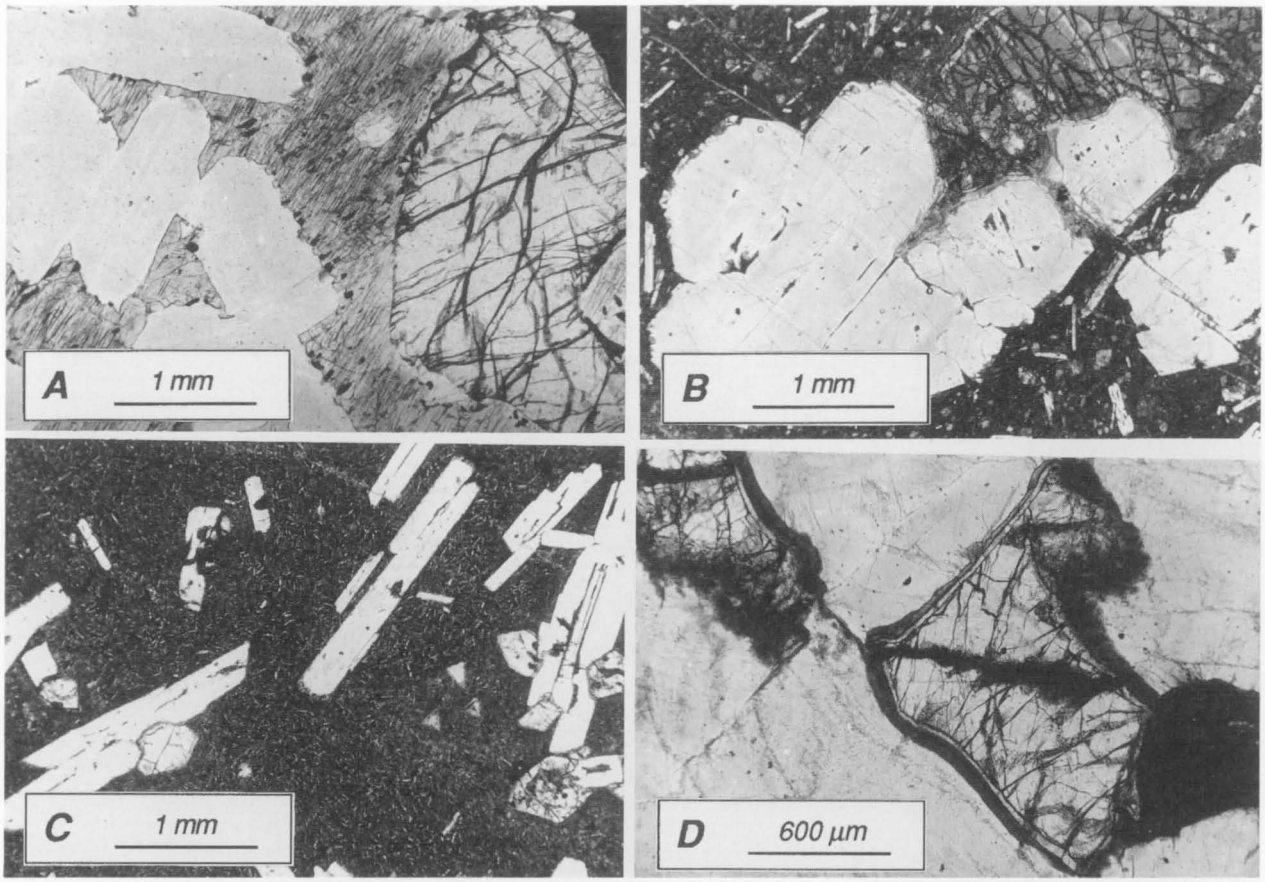

Figure 92. Cumulate textures and mafic dykes and sills in the Bell Rock intrusion. (A) Gabbroic troctolite (88982019A). Olivine and clouded euhedral plagioclase are cumulus phases, whereas exsolved oxide-rich clinopyroxene is interstitial. The texture is thought to indicate higher than normal cooling rates. (B) Olivine–plagioclase-phyric dyke (88982007). Rounded olivine and euhedral plagioclase phenocrysts are set in a very fine-grained quenched groundmass. The phenocryst population resembles in detail the cumulus phases predominating in the host cumulates (cf. Fig. 92A). (C) Fine-grained olivine–plagioclase-phyric sill (88982010B). Euhedral olivine and elongated euhedral plagioclase phenocrysts occur in a very fine-grained groundmass. In contrast to stratabound microgabbro units, the sill, although conformable with the magmatic layering, is younger than the cumulates. (D) Altered deformed troctolite (88982010A). Olivine (dark cracks) in contact with plagioclase is surrounded by a narrow clear inner rim of columnar orthopyroxene, followed by an extremely fine-grained greenish symplectitic outer rim. Such a reaction is common to most Giles Complex intrusions where there has been fluid infiltration.

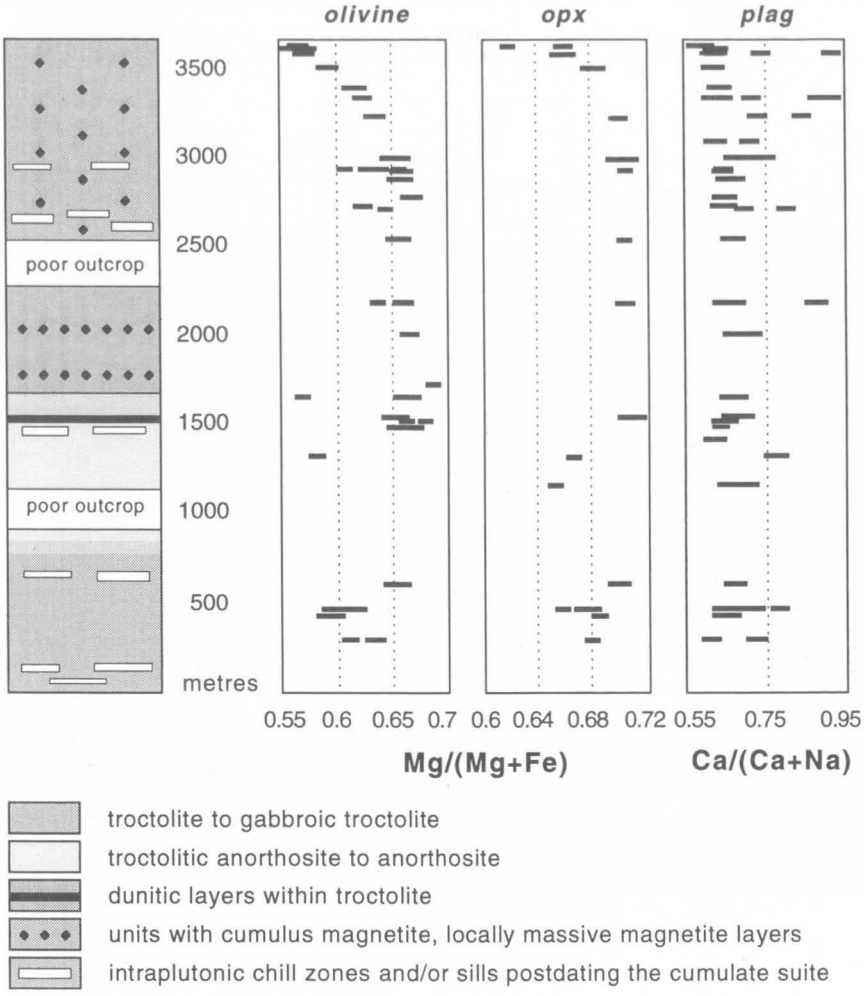

Figure 93. Stratigraphy and mineral chemistry of the Bell Rock intrusion.

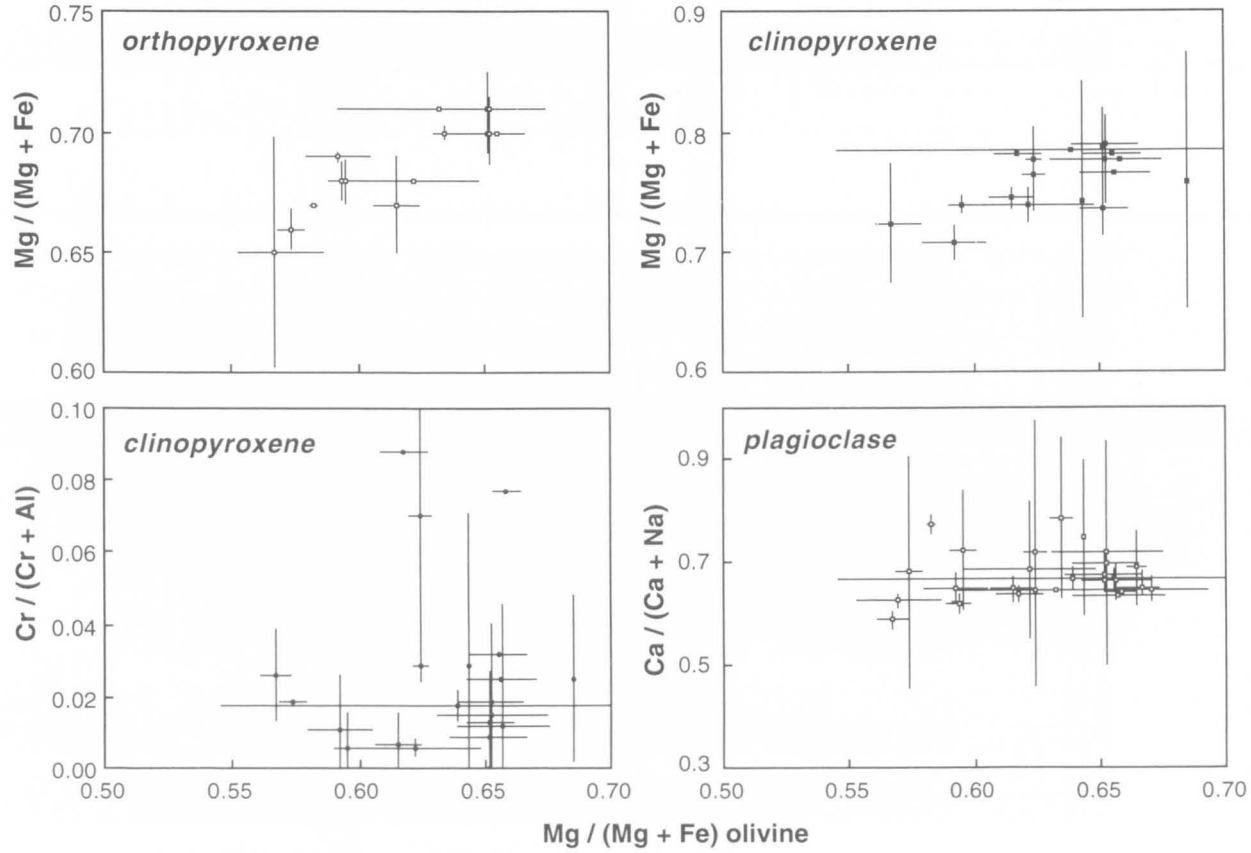

Figure 94. Average mineral compositions of the Bell Rock intrusion (error bars are two standard deviations).

The Giles Complex 2: Blackstone–Jameson region

Regional geological framework

The region west of the Tomkinson Ranges, from 127° 00′ to 128° 30′E and 25° 00′ to 26° 20′S (Figs 1, 47), contains numerous outliers of the Giles Complex, which commonly form elevated ridges, interspersed with dune areas and alluvial plains containing scattered hills of gneiss and Tollu Group volcanic rocks. This area, referred to here as the Blackstone–Jameson region and mapped by Daniels (1974), was investigated in the present study principally with regard to the mafic–ultramafic intrusions of the Giles Complex, which include the Blackstone Range troctolite/gabbro, Cavenagh Range gabbro, Murray Range pyroxenite/peridotite/gabbro, Jameson Range troctolite/gabbro, and the smaller Morgan Range gabbro intrusions. Systematic sampling cross-sections and petrological studies were conducted on the Blackstone Range, Murray Range, and Jameson Range bodies. Most of the Cavenagh Range and large parts of the Jameson Range bodies, and intervening gneiss and volcanic terranes, were inaccessible due to their status as Aboriginal sacred areas. For this reason, field mapping of the terranes within the Blackstone, Cooper, Holt, and Finlayson 1:100 000 sheets remains incomplete, and this section is based on mapping of accessible areas, petrology of the mafic–ultramafic intrusions, and interpretation of Landsat-5 TM and airborne TMI data flown at 1500 m intervals.

The broad structural features of the Blackstone–Jameson region are outlined by the airborne TMI map (Fig. 95), which displays the layered mafic–ultramafic intrusions as blocks characterised by strongly disturbed positive and negative anomalies. Thus the latitudinal 33x4 km steeply dipping Blackstone Range body is marked by a line of magnetic lows fringed by magnetic highs to the north and south. The sharp southern boundary of this intrusion suggests a major fault, extending westward from the fault which bounds the Bell Rock intrusion and delimiting the downfaulted Tollu Group volcanic rocks and underlying granitic basement to the south (Figs 47, 95). The fault is nowhere exposed, and may be a west-directed thrust fault. The flat-lying Cavenagh Range gabbro is likewise marked by several roughly circular magnetic lows over an area of 22x18 km. This intrusion has been interpreted as a flat-lying segment of a lopolith comprising the Bell Rock and Blackstone Range intrusions, and possibly

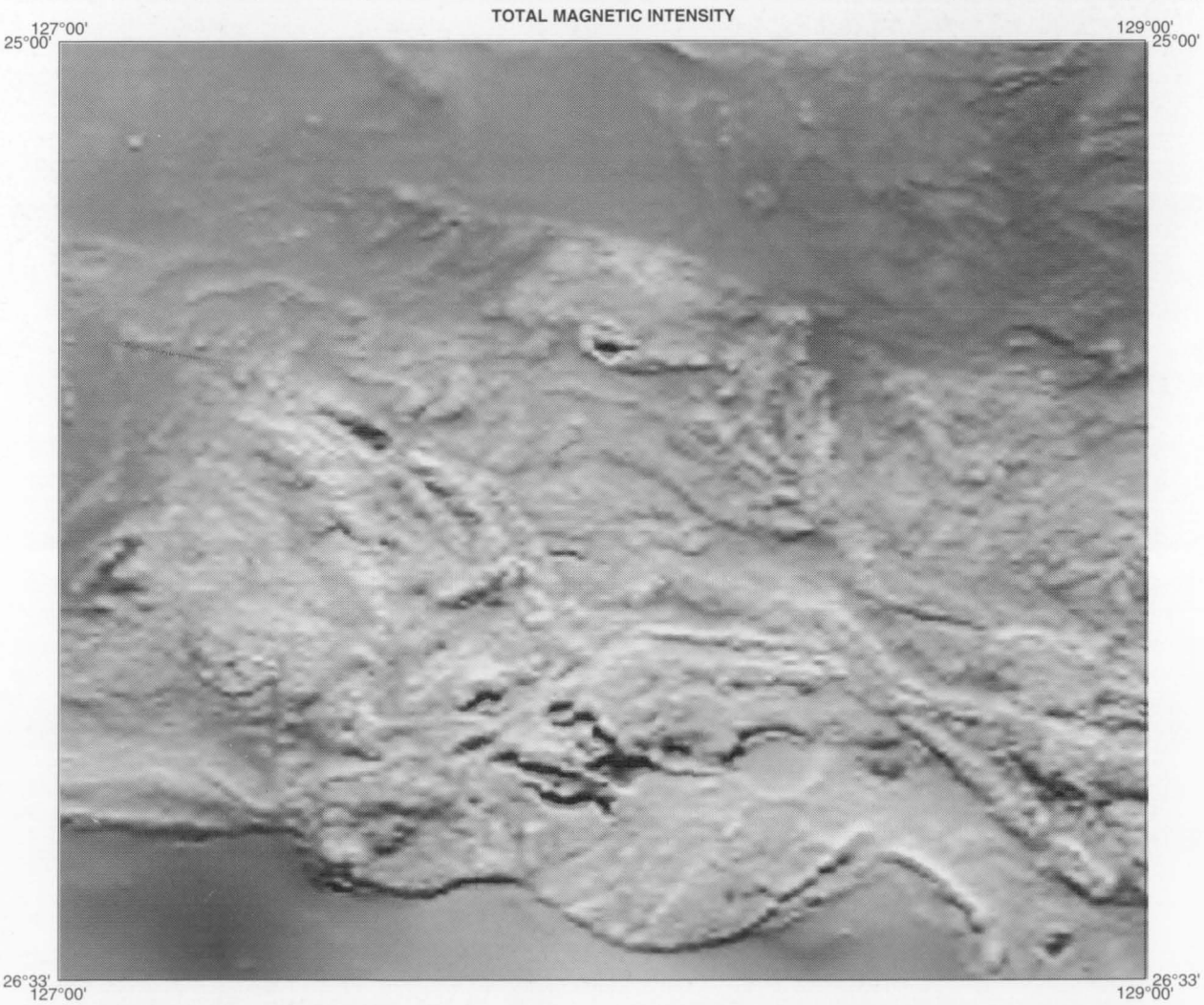

Figure 95. TMI image of the western Musgrave Block. Lighter areas are more positive. See Figure 97 and Plate 3 for correlations with the principal geological features. The traces of the Officer Basin Thrust Fault to the south and the Woodroffe Thrust Fault to the north are well represented. Outlines of many of the major Giles Complex intrusions (e.g., Bell Rock, western Michael Hills, Hinckley Range, Blackstone Range, and Jameson Range) are also well shown.

coeval with the Tollu Group (Nesbitt et al. 1970; Daniels 1974).

Negative magnetic anomalies are also associated with mafic volcanic rocks of the Tollu Group, in particular at MacDougall Bluff and Mummawarrawarra Hill, and also along strike of interlayered felsic to mafic volcanic units south of the Blackstone Range intrusion. South of this terrane, the major thrust faults which divide the Musgrave Block from the Officer Basin are indicated by a conspicuous 2–4 km-wide arcuate zone, delineated by a line of magnetic lows, in places coupled with a line of magnetic highs to their north. This coupling is interpreted in terms of thrusting of volcanic rocks of the Bentley Supergroup, together with granitic basement rocks, over the Townsend Quartzite to the south.

A major northwest-trending magnetically disturbed zone, about 75 km long and up to 15 km wide, marks a major mafic intrusion which includes the troctolite–gabbro outcrops of the Jameson and Finlay Ranges in the Finlayson and Bentley 1:100 000 sheet areas (Fig. 95). The peak anomaly of 7400 nT occurs over an unexposed area to the north of the Jameson Range. A smaller, possibly separate, mafic body is marked by gabbro outcrops associated with a magnetic high about 33 km north-northwest of Jameson community (Fig. 95). The most northwesterly outcrops of the Finlay Range–Jameson Range intrusion occur near 127° 28′E, 25° 40′S (near the eastern boundary of the Bentley 1:100 000 sheet), but the extension of the disturbed magnetic zone suggests that the underlying mafic body extends a further 20 km to the northwest. Isolated outcrops, representing the northernmost exposures of the Giles Complex, have been reported from Diorite Hill (Fig. 97), where they are associated with a magnetic anomaly (Daniels 1974). The isolated mafic–ultramafic outcrops of the Murray Range, Lehmann Hill, and Mount Muir are also marked by magnetic anomalies (Fig. 95).

The distribution of mafic–ultramafic bodies of the Giles Complex is apparent on Landsat-5 TM images where they are overlain by thin alluvial cover which in part includes their decomposed products. The clay-dominated weathering crusts of the gabbro associated with iron oxide-rich streaks derived from magnetite-rich gabbro and monomineralic magnetite layers outline the shallow subsurface distribution of the Jameson–Finlay Range troctolite/gabbro and Cavenagh Range gabbro. The close match between the Landsat-5 TM patterns and the magnetically disturbed zone allows an accurate delineation of the boundaries of otherwise poorly exposed mafic bodies manifested by TMI (Fig. 95) and Bouguer gravity (Fig. 96) anomalies, so that the bedrock geology can be delineated with a reasonable degree of confidence (Fig. 97). Iron oxide-rich alluvial deposits, shed from monomineralic magnetite seams within the Jameson Range intrusion, show clearly on the images, due to high 5/4 ratios, expressed as green lineaments and strings of alluvial depressions on pc2(4/3;5/7):5/4:4/3 RGB images. Such images are useful in delineating magnetite-rich gabbro units, for example in the Blackstone Range (Fig. 108) and Murray Range intrusions (Fig. 101).

Murray Range pyroxenite/peridotite/gabbro intrusion

Most of the Murray Range is made up of gabbroic rocks, which, in the central part of the range, are extensively recrystallised to mafic granulite and contain relict layers of felsic

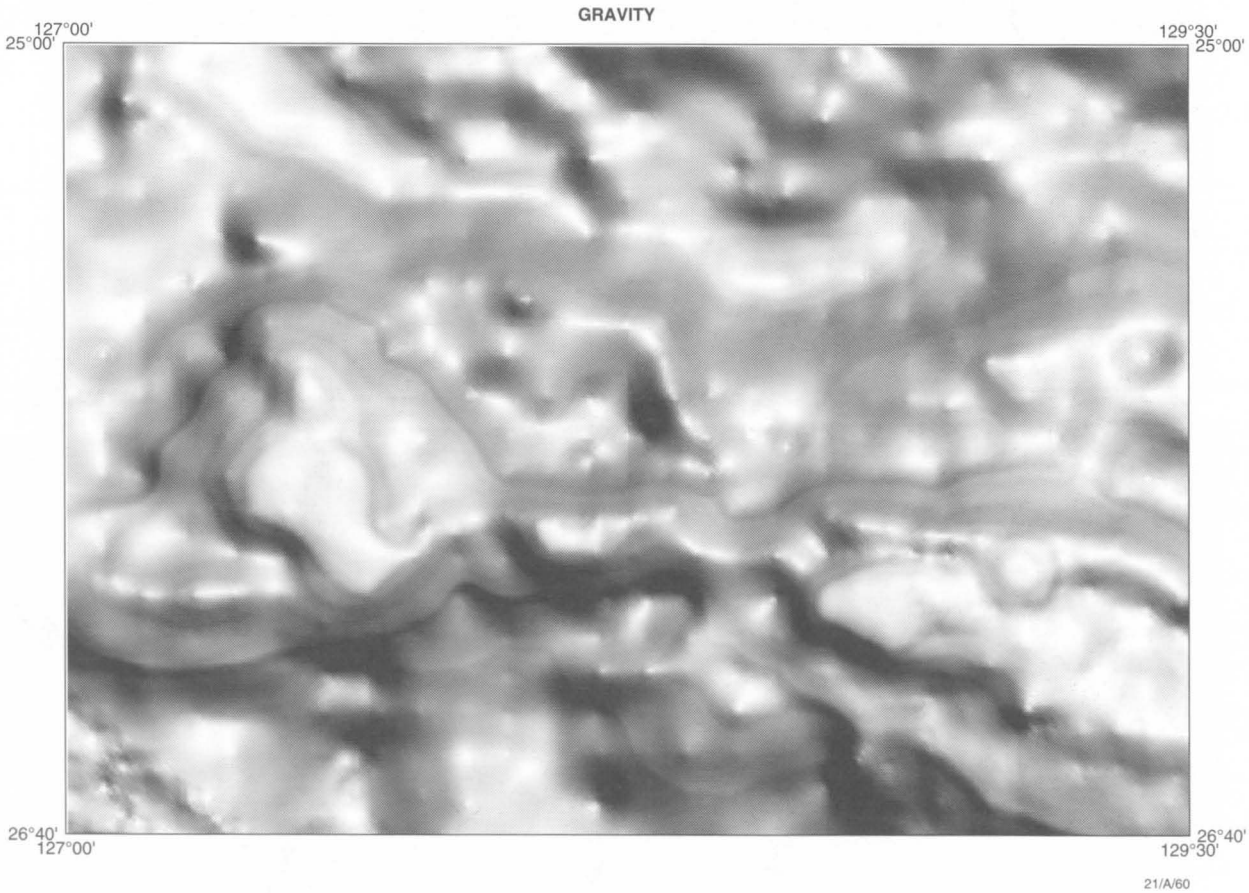

Figure 96. Bouguer gravity anomaly image of the western Musgrave Block, outlining the traces of the Officer Basin and Woodroffe Thrust Faults and anomalies associated with mafic–ultramafic intrusions of the Giles Complex. Lighter areas are more positive.

granulite and granitic gneiss (Daniels 1972). These rocks have not been studied in detail due to difficulties of access. The western Murray Range intrusion is an isolated well-layered body surrounded by felsic to mafic granulite and granite gneiss (Figs 98–101; Plate 3). This western succession is continuous for about 2600 m and the layering strikes northwest and dips steeply between 80 and 90°. The magmatic sequence is well layered from centimetre-scale to megascale, and consists mainly of pyroxenite, peridotite, harzburgite, and dunite, with subordinate gabbro and gabbronorite (Fig. 104). It has the highest proportion of peridotite and the most primitive cumulates observed in the Giles Complex, with some similarities to the Wingellina Hills, Kalka, and Ewarara intrusions to the east (Ballhaus & Glikson 1995). Intrusive contacts with the country rock granulites are obliterated by faulting or covered by alluvium, and no chilled margins have been found.

No clear way-up criteria have been observed, but the unit interpreted as the first 500 m of the sequence consists of massive, poorly layered uniform pyroxenite. This is followed by an exceptionally well-layered sequence of gabbroic to gabbronoritic units, alternating with wehrlite and peridotite layers (600 m to at least 1500 m). Stratigraphically higher units consist of coarse-grained orthopyroxenite, harzburgite (Fig. 98B), and subordinate dunite orthocumulates. Plagioclase in the upper part of the sequence is exclusively intercumulus and rarely exceeds 5 percent. The sequence is cut by concordant shear zones, associated with mylonitisation and hydrous alteration of the cumulates and, locally, by granitic and aplitic veins.

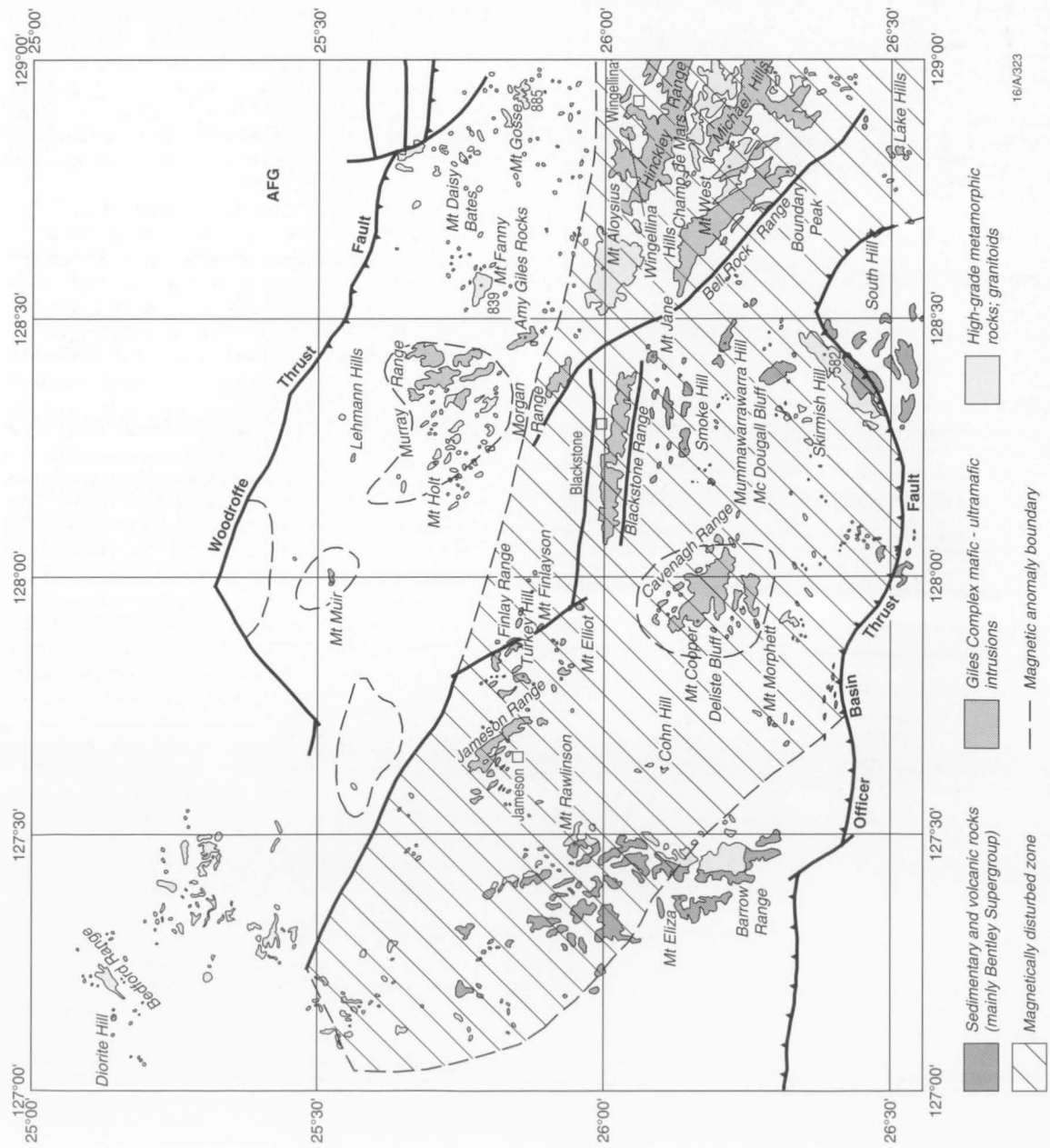

Figure 97. Interpreted solid geological map of the western Musgrave Block, based on field geology (including Daniels 1970, 1971a, b, 1972), TMI, and Landsat-5 TM imagery. The extensive magnetically disturbed zone is indicated, as are the principal faults and main outcrop areas of the Giles Complex and Bentley Supergroup (compare with Figs 95, 96, and Plate 3).

Figure 98. Outcrops of the Murray Range pyroxenite/peridotite/gabbro intrusion. (A) Layered gabbro, recrystallised gabbro, pyroxenite, and peridotite, looking northeast. (B) Layered peridotite.

The major cumulate units are as follows:

Orthopyroxenite adcumulates to orthocumulates. Orthopyroxene is commonly the only cumulus phase and occurs as both an early generation of large elongated euhedral phenocrysts (Fig. 102A, B), and a later generation of smaller equant grains. Clinopyroxene is less abundant, particularly as a cumulus phase, and is mostly poikilitic, with abundant exsolved brownish spinel. Clinopyroxenite is only found in the lower half of the sequence. Plagioclase is interstitial and commonly antiperthitic (Fig. 102C), notably in pyroxenite adcumulates with low modal plagioclase contents. Some orthopyroxenite contains modal plagioclase in excess of 35 to 40 percent (Fig. 102D). The most primitive pyroxenite carries minor cumulus olivine, coexisting with cumulus orthopyroxene (Fig. 102E). Orthopyroxene shows a bimodal distribution in pyroxenite orthocumulates (Fig. 102A, B) towards the top of the sequence, a feature explained by the crystal growth rate exceeding nucleation rate under rapid undercooling conditions, followed by a decrease in cooling rates (Campbell 1987; Marsh 1988). Such intraplutonic quenching may have occurred where hot primitive magma mixed with cooler resident melt.

Feldspathic peridotite and dunite orthocumulates. These rocks consist of cumulus olivine and accessory chromite, with poikilitic orthopyroxene and clinopyroxene (Fig. 102F, G). Transitions occur to dunite (Fig. 102G), wehrlite, and pyroxenite. Where total modal pyroxene exceeds about 25 percent, it may grade into cumulus grains (Fig. 102H). Clinopyroxene, and to a lesser extent, orthopyroxene are exceptionally rich in exsolved brownish spinel (Fig. 102F). Olivine is completely altered to a characteristic intergrowth of silicified serpentine with impregnations of magnetite and brown limonite. Chromite varies according to textural occurrence and host mineral from near opaque and distinctly euhedral, where included in pyroxene, to greenish translucent and irregularly shaped, where included in olivine. Chromite in contact with plagioclase has locally reacted to form pyroxene–amphibole–biotite intergrowths. Plagioclase is invariably intercumulus, and may be altered and zoned as a result of subsolidus reactions.

Gabbronorite. Plagioclase and large orthopyroxene grains are the main cumulus phases. Clinopyroxene is rich in exsolved orthopyroxene and opaque oxides, and ranges from cumulus to intercumulus (Fiug. 102J). Gabbronorite is commonly strongly deformed, to the extent that magmatic exsolved clinopyroxene grains are recrystallised to small clinopyroxene neoblasts coexisting with rounded opaque oxide grains (recrystallised exsolved opaque minerals).

The effects of late or post-magmatic processes are widespread. Cumulus dark brown spinel grains in contact with plagioclase are commonly overgrown by symplectites of clinopyroxene and light green spinel (Fig. 103E). Plagioclase in contact with reacted spinel is optically zoned and depleted in An adjacent to spinel. These clinopyroxene–spinel symplectites are attributed to net transfer of Al from plagioclase to spinel during high-pressure cooling. In some samples, ferromagnesian silicates in contact with plagioclase are rimmed by poorly developed fine-grained spinel–amphibole symplectites. It appears that symplectites of this type were formed where deformation and post-magmatic fluid infiltration occurred, lowering kinetic barriers during subsolidus equilibration.

Plagioclase commonly contains micron-scale euhedral light green clinopyroxene inclusions, especially in deformed cumulates. Compositionally, these inclusions resemble coarser-grained equilibrated clinopyroxene groundmass neoblasts. It is likely that they represent recrystallisation of submicron impurities in plagioclase. Clinopyroxene and orthopyroxene in the most primitive cumulate units may be exceptionally rich in exsolved brown spinel grains (Fig. 103F). Spinel is commonly cleared from the rims of pyroxene grains by granule exsolution, but forms small recrystallised blebs along grain boundaries (Fig. 103F).

The sequence includes several stratabound layers and lenses of amphibolite, mostly in the vicinity of shear zones. The amphibole/plagioclase ratio reflects the pyroxene+olivine/plagioclase ratio of their magmatic protoliths. The main phases are greenish-blue coarse-grained euhedral tremolitic amphibole (Fig. 103A) and sodic plagioclase. The latter is locally preserved as deformed magmatic cumulus relics. Relict clinopyroxene is rare and partly replaced by amphibole. As these rocks are commonly little deformed, they presumably relect hydration associated with introduction of volatiles along the shear zones or faults.

In zones of mylonite and cataclasite development (Fig. 103B–D), magmatic clinopyroxene tends to recrystallise to aggregates of equant neoblastic grains, rarely intergrown with rounded opaque oxides, probably magnetite–ilmenite lamellae exsolved from clinopyroxene. Such deformed cumulates also show granulation along plagioclase grain boundaries, but orthopyroxene is the most resistant phase to recrystallisation. Thus, ultramylonites have large porphyroclasts of kinked orthopyroxene in a flow-textured matrix of plagioclase and uralitised clinopyroxene. In places, proto-cataclasite predominates over proto-mylonite, possibly due to variations in deformation temperature and/or the subsolidus fluid regime.

The range of mineral compositions is summarised in Figures 104 and 105. Olivine ranges from about Fo_{88} to Fo_{77}, the most magnesian olivine in the well-layerd ultramafic sequence around the 2000 m level being close to equilibrium with a primitive mantle-derived melt. Orthopyroxene replaces

olivine on the liquidus at about Fo_{78}. Orthopyroxene *mg* values range from about 88 to 67 and vary coherently with olivine. Clinopyroxene is significantly more magnesian than coexisting orthopyroxene. Cr/(Cr+Al) in clinopyroxene is a very sensitive to chemical fractionation, because Cr partitions far more strongly into pyroxene than does Al. Up to 0.25 in the most primitive peridotitic units, it decreases to about 0.05 in the most fractionated gabbronorite. In clinopyroxene coexisting with cumulus spinel, Cr/(Cr+Al) varies coherently. Plagioclase An contents range from about 80 to 20, but show little correlation with olivine composition. For a given *mg* value of coexisting olivine or orthopyroxene, plagioclase is comparatively sodic, at least in comparison with other ultramafic intrusions of the Giles Complex such as the Wingellina Hills intrusion (Ballhaus & Glikson 1989). This may be due to the interstitial nature of plagioclase in most Murray Range cumulates, but could also reflect higher crystallisation pressures (Green & Hibberson 1970).

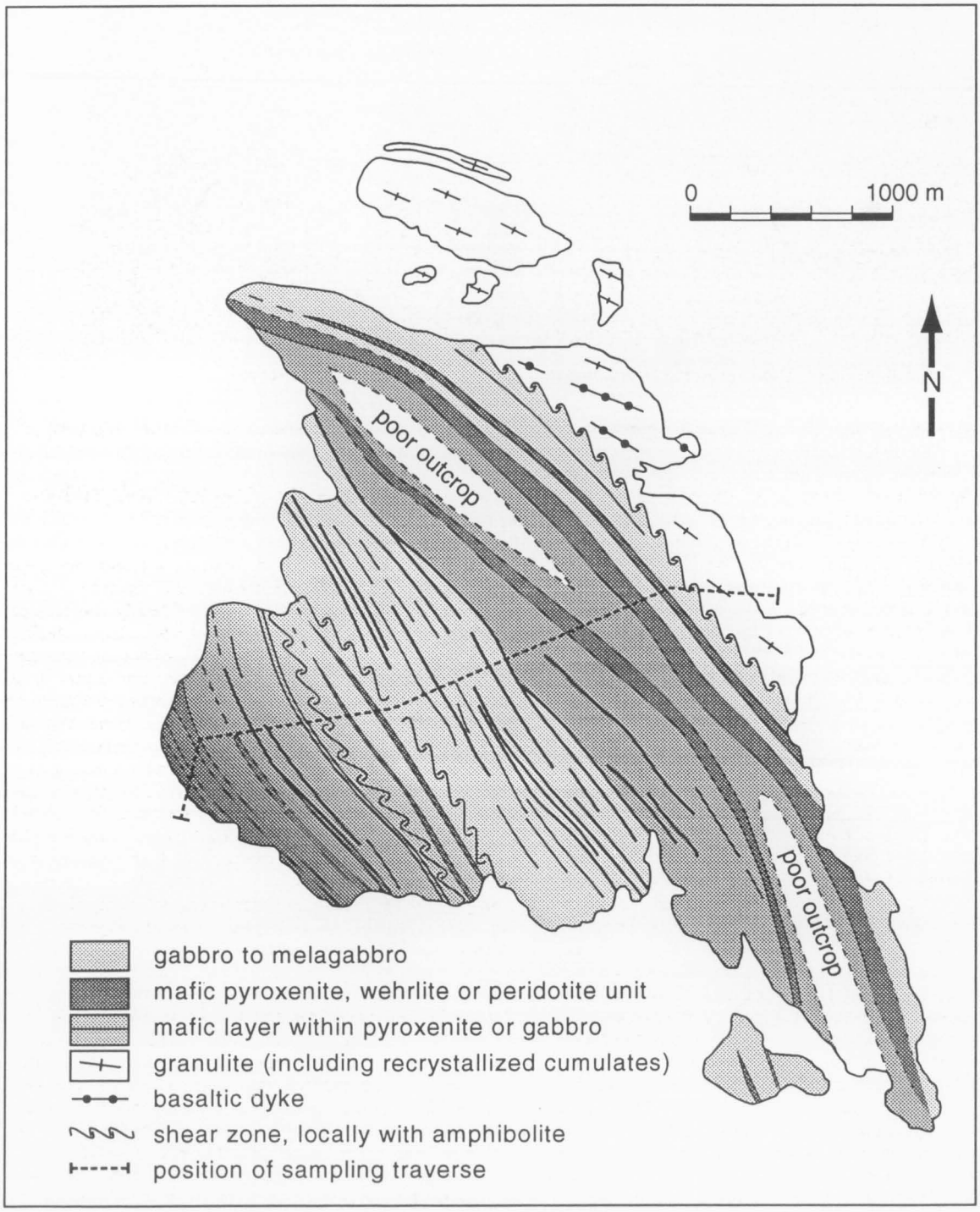

Figure 99. Geological map of the Murray Range intrusion.

Figure 100. Aerial photograph of the southern part of the southwestern Murray Range intrusion.

The Murray Range sequence is an example of a multiply replenished magma chamber (cf. Irvine 1980). The cryptic layering pattern (Fig. 104) reveals two gradual chemical reversals (near the basal contact and 1100 m level) towards more primitive (i.e., more Mg and Ca-rich) mineral compositions, each followed by extended periods of normal fractionation. These reversals are reflected in changes in *mg* in orthopyroxene and Cr/(Cr+Al) in clinopyroxene. The lack of overall chemical differentiation makes it difficult to decide which way the sequence is younging. We believe that the southern contact marks the bottom of the intrusion, for three reasons: (1) the chemical reversals are broadly situated where the sequence changes from predominantly gabbroic to predominantly ultramafic lithologies, (2) the bases of ultramafic cycles are typically orthocumulates, suggesting that they formed in a high thermal gradient (Campbell 1987; Ballhaus & Glikson 1989), and (3) several ultramafic intercalations are preceded by hybrid zones in which patches and schlieren of ultramafic cumulate material occur intermingled with more fractionated gabbroic material (Ballhaus & Glikson 1989). Such hybrid zones may form when the first batches of a major pulse collect on the magma chamber floor and freeze before they can homogenise with the cooler resident melt. As such, they must define the footwall contact of an ultramafic unit. Hence, the stratigraphic sequence of the Murray Range intrusion probably youngs towards the northeast.

Crystallisation sequences and mineral compositions in the most mafic units suggest that the parental melt of the Murray Range intrusion was saturated with olivine and an aluminous spinel, and was near-primitive with respect to MgO content. The crystallisation sequence was (1) olivine±aluminous spinel, (2) olivine(orthopyroxene)–clinopyroxene, and (3) (olivine)–orthopyroxene–clinopyroxene–plagioclase. The megascale layering is a direct consequence of the undersaturated nature of the replenished melt. Any pulse of a liquid saturated only in olivine into multiply saturated resident melt must have resulted in the loss of at least one liquidus phase, and commonly two, with a corresponding change in the cumulate mineralogy.

Blackstone Range troctolite/gabbro intrusion

The Blackstone Range intrusion is a major troctolitic magmatic sequence, similar to the Bell Rock troctolite/gabbro (Daniels 1974). It consists of at least 3600 m of highly fractionated, commonly rhythmically layered troctolite, olivine gabbro, anorthosite, rare dunite layers, and monomineralic magnetite layers (Figs 106–109, 112). The cumulates are largely undeformed except along the top and bottom margins, but intrusive contacts with granulite-facies country rocks are not exposed. Near the northern margin, the cumulates are recrystallised to massive, fine-grained phlogopite-bearing mafic granulite, possibly incorporating former chilled margins. The southern contact is faulted against Tollu Group volcanic rocks (Daniels 1974). The fault shows as a marked lineament on the TMI map (Fig. 95), but is not exposed. With the exception of dunite and magnetite layers, megascale phase layering is poorly developed, although olivine–plagioclase layering on a cm scale is common. The magmatic layering dips relatively steeply (70–75°) to the south.

The principal cumulate types (Fig. 110) comprise:

Troctolite, gabbroic troctolite, and troctolitic gabbro. Olivine and plagioclase are the main cumulus phases, locally accompanied by minor cumulus clinopyroxene (Fig. 110A, B). Greenish clinopyroxene with exsolved opaque oxide is a later poikilitic phase. Orthopyroxene forms narrow irregular moats around olivine, grading in places into larger irregular orthopyroxene–magnetite symplectites (Fig. 110A) and poikilitic orthopyroxene grains. Opaque oxides include titaniferous magnetite and rounded green hercynite–pleonaste inclusions. Adjacent to massive magnetite layers, magnetite grades from intercumulus to cumulus with increasing abundance. Accessory

phases include post-magmatic biotite flakes around magmatic oxides, rare brownish amphibole moats around intercumulus magnetite, and rare greenish actinolitic amphibole. Primary magmatic phases are usually fresh and undeformed, except near shear zones and pseudotachylite veinlets.

Anorthosite. Anorthosite is common in well-laminated parts of the magmatic sequence. Olivine-bearing anorthosite cumulates contain up to 10 percent modal olivine and little or no interstitial clinopyroxene. In rocks with very low olivine contents, the olivine is interstitial (Fig. 110B). In some anorthosite layers, plagioclase is the only cumulus phase and olivine and clinopyroxene are absent. Interstitial ferromagnesian phases in anorthosite are commonly replaced by actinolitic amphibole.

Dunite. Rare dunite shows tightly packed adcumulate to mesocumulate textures (Fig. 110E). Dunite and other near-monomineralic cumulates (anorthosite and massive magnetite layers) commonly display advanced annealed textures, where primary cumulus textures are replaced by granular mosaic fabrics with 120° triple grain boundaries. No primary interstitial phases were observed in dunite, having been replaced by greenish actinolitic amphibole. However, cumulus olivine was not affected by hydrous alteration, suggesting that it must have taken place above the thermal stability limit of serpentine.

Quenched equivalents of cumulates. The upper part of the sequence includes a stratigraphic interval near 2850 m with several fine-grained layers, interpreted as mafic sills that intruded later than the layered cumulates, or as late-magmatic liquid quenched against much cooler resident melt. Elongated euhedral plagioclase and opaque oxide-rich aggregates (olivine pseudomorphs?) are phenocryst phases. Granular clinopyroxene and oxides form interstitial aggregates between the plagioclase laths (Fig. 110F). From the phenocryst populations,

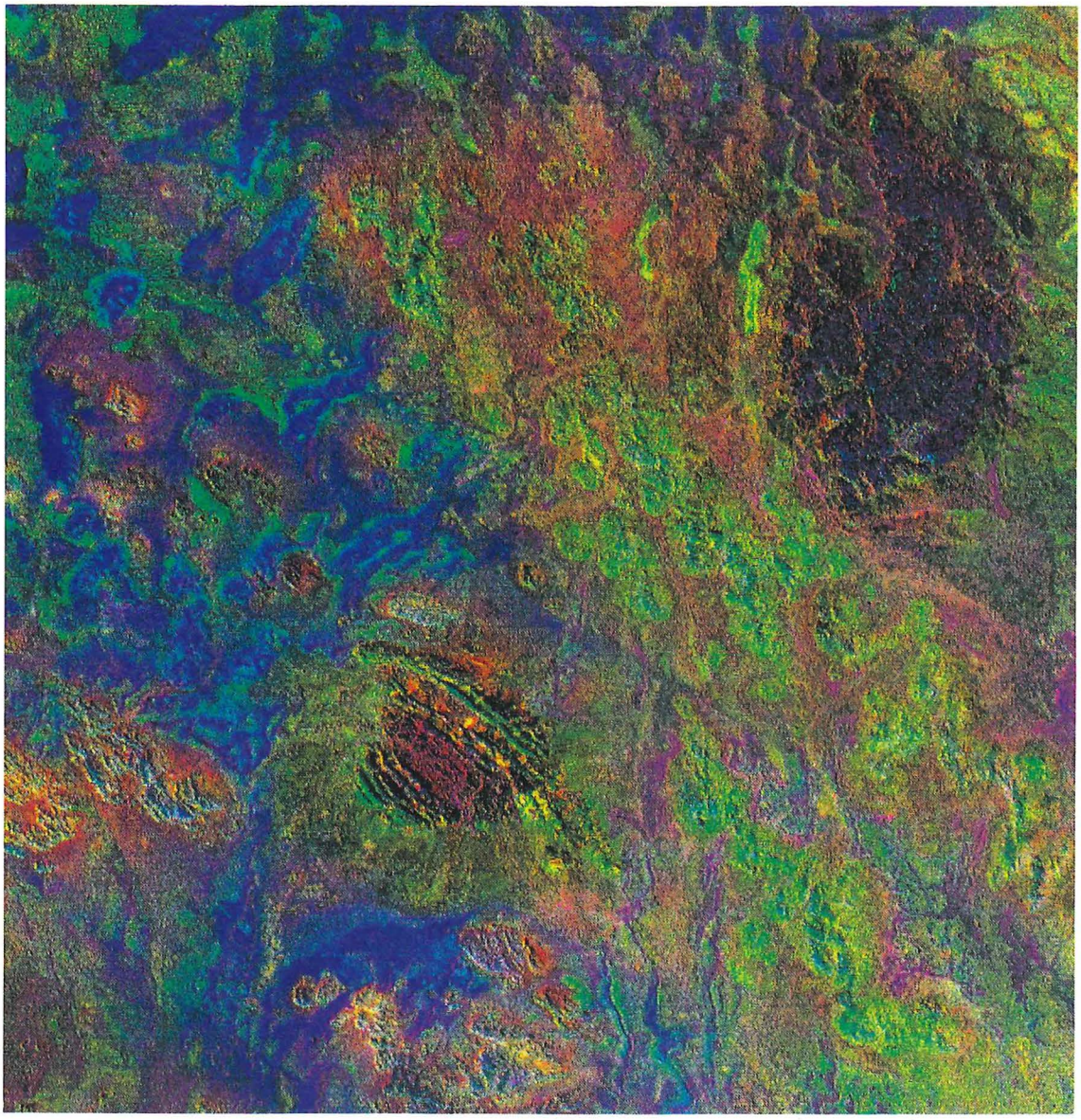

Figure 101. Landsat-5 TM pc2(4/3;5/7):5/4:4/3 RGB image of the Murray Range area. The western Murray Range pyroxenite/peridotite/gabbro intrusion (lower left of centre) shows carbonate alteration of ultramafic rocks (red) and iron oxide-coated pyroxenite ridges (green). The northeastern gabbroic body (near Illurpa Bore, top right) has a predominantly red clay-weathering signature. Mafic granulite and felsic orthogneiss of the central Murray Range (northwest–southeast-trending belt) have a green iron oxide-weathering signature. Vegetated alluvial valleys appear as blue (high 4/3 band ratio). Compare with the geological map on Plate 3.

these rock types may be equivalent to parent melts of the host cumulates. Underlying and overlying this fine-grained zone are several intervals dominated by orthocumulates, with cumulus plagioclase and olivine (Fig. 110C, G).

Recrystallised cumulates. Most cumulates show little deformation, but are locally cut by mylonitic shear zones associated with hydrous alteration. Granophyre veins occur locally. In some samples, olivine in contact with plagioclase is surrounded by greenish symplectitic coronas of grain sizes below the resolution of optical microscope and microprobe. Such symplectites probably consist mainly of hydrous phases as they are confined to altered deformed cumulates near mylonite zones. Gabbroic cumulates along the margins of the intrusion show various degrees of recrystallisation. Primary clinopyroxene with exsolved oxide tends to recrystallise to granoblastic aggregates of clinopyroxene and rounded opaque oxide neoblasts (Fig. 110H). Olivine is much less common in the recrystallised zones, suggesting that recrystallisation was accompanied by the introduction of alkali-bearing fluids to form phlogopite. Some extensively recrystallised rocks contain relict coarse-grained gabbroic micro-enclaves with euhedral plagioclase (Fig. 111A), whereas others are completely recrystallised to mafic granulite (Fig. 111B).

Mineral compositional variations are shown in Figures 112 and 113. Olivine ranges from Fo_{67} to Fo_{40}, the latter being the most fractionated olivine reported from the Giles Complex, and *mg* values of coexisting orthopyroxene range from about 70 to 55. Cr contents of clinopyroxene are close to the detection limit and show no systematic stratigraphic trend. Clinopyroxene *mg* values probably do not reflect primary magmatic cryptic layering trends due to equilibration at lower temperatures. Plagioclase An contents range from more than 80 to about 50, and vary sympathetically with *mg* of olivine and orthopyroxene. The cryptic layering pattern suggests at least two major magma pulses, one starting at the assumed bottom contact of the intrusion and a second above the 2500 m level.

The cryptic layering pattern strikingly resembles that of the Bell Rock intrusion (cf. Figs 93 and 112). It is suggested that the minimum *mg* value at the 2400 m level is equivalent to a similar minimum at the 3600 m level in the Bell Rock sequence. Likewise, the dunite layers in the 400–450 m sequence of the Blackstone Range intrusion may correlate with a similar sequence near the 1500 m level at Bell Rock. There is again no clear indication as to which way chemical fractionation was directed and where the bottom and top contacts may have been situated. However, unless the sequence is overturned, it youngs toward the south. We concur with Daniels (1974) that the Bell Rock and Blackstone Range sequences originally formed one continuous intrusion.

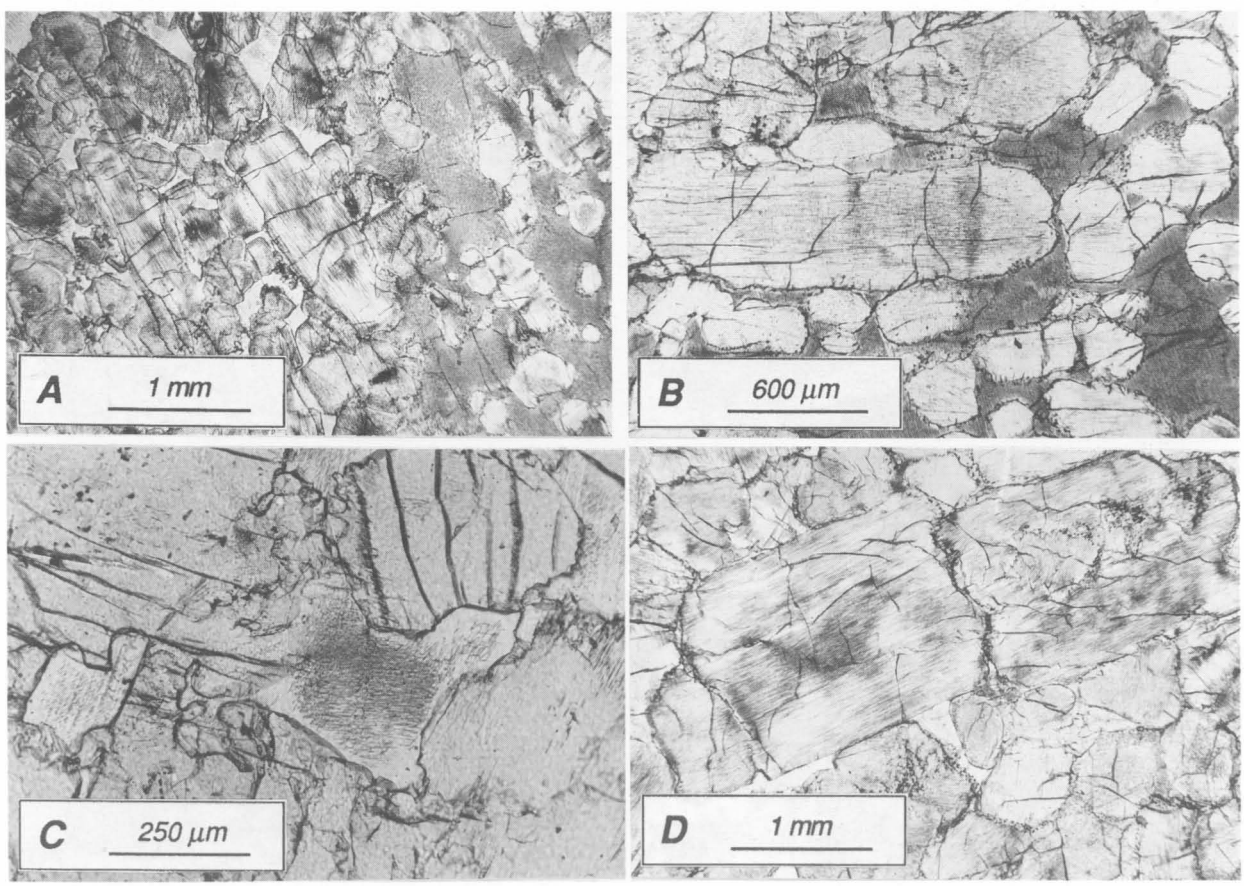

Figure 102. Cumulate textures in the Murray Range intrusion. (A) Orthopyroxenite orthocumulate (88980012). Orthopyroxene occurs both as porphyritic grains, with minor exsolved spinel, and as a second generation of smaller rounded grains. Brownish clinopyroxene is poikilitic and much richer in exsolved spinel than orthopyroxene. Plagioclase is colourless and interstitial. Elongated grains and bimodal size distributions are thought to reflect rapid cooling rates. (B) Orthopyroxenite orthocumulate (88980017). Elongated porphyritic orthopyroxene, with exsolved spinel and spinel granules at grain margins, and a later generation of rounded orthopyroxene are all included in brownish poikilitic clinopyroxene, rich in exsolved spinel. (C) Annealed pyroxenite adcumulate with rare plagioclase (88980001). Both orthopyroxene and clinopyroxene are cumulus. Plagioclase (centre) is antiperthitic and rich in exsolved K-feldspar rodlets that tend to be concentrated near grain centres. (D) Orthopyroxene orthocumulate (88980022). Orthopyroxene forms euhedral, slightly elongated phenocrysts in a matrix of interstitial plagioclase. The modal plagioclase content (about 40 vol. %) is normally much too high for an intercumulus phase.

Jameson Range troctolite/gabbro intrusion

The Jameson Range intrusion is composed of approximately 2500 m of layered Fe-rich troctolite, gabbroic troctolite, and anorthosite adcumulates, with various proportions of disseminated magnetite (Figs 114, 116). The outcrops represent part of a 75x15 northwest-trending mafic body defined by TMI

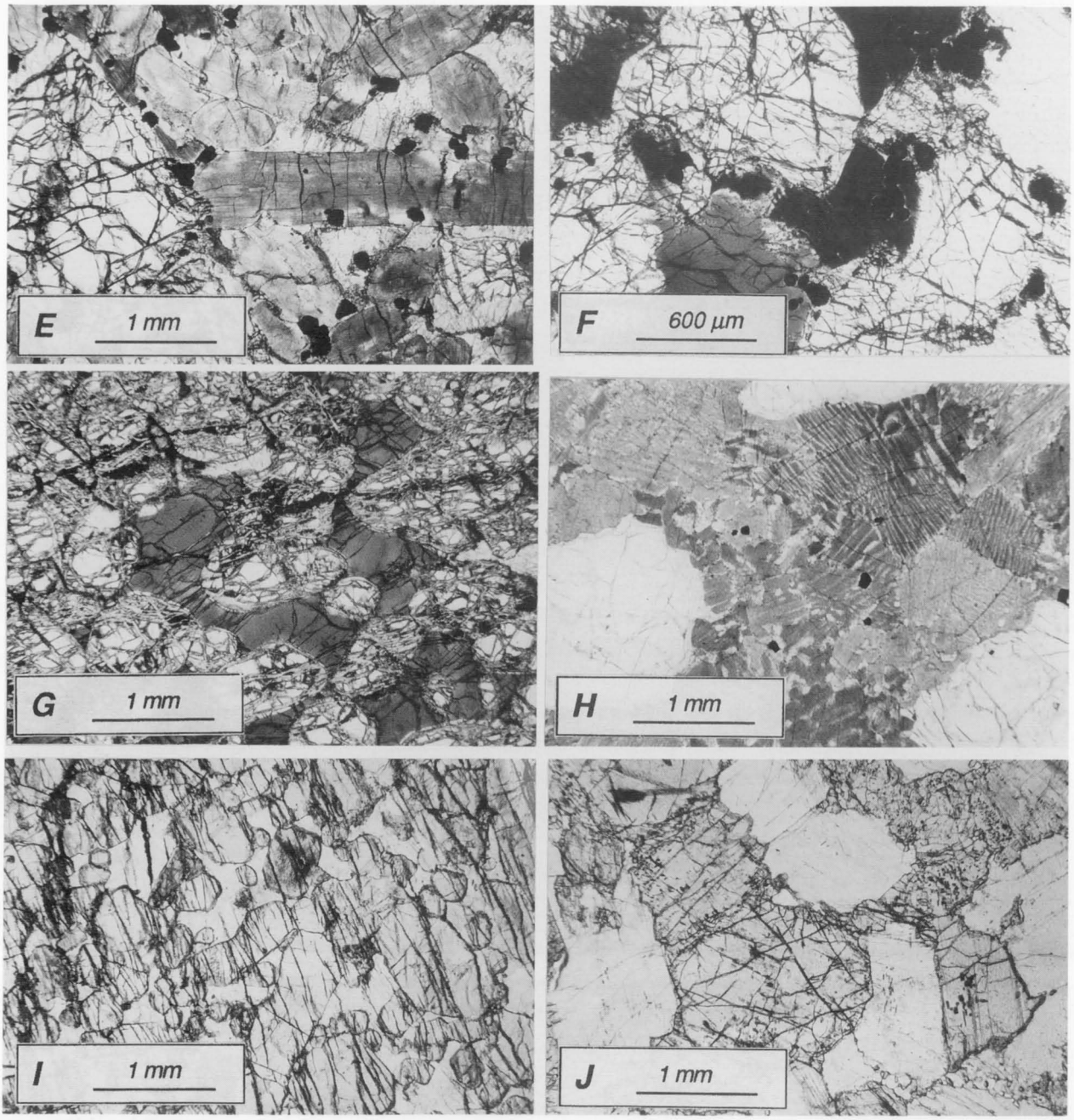

Figure 102 (cont.). (E) Olivine-bearing orthopyroxenite to harzburgite orthocumulate (88980010). This consists of rounded cumulus olivine (clear cracked grains at left), elongated porphyritic orthopyroxene (with brown exsolved spinel), a second generation of rounded orthopyroxene with much less exsolved spinel, dark rounded cumulus clinopyroxene grains, and opaque euhedral cumulus chromite. Clear plagioclase between rounded orthopyroxene grains is interstitial. (F) Peridotite orthocumulate (88980002). The main phases are rounded cracked olivine, brownish poikilitic orthopyroxene, dark brown poikilitic to interstitial clinopyroxene, and small opaque rounded cumulus chromite grains. Exsolved spinel in clinopyroxene is so abundant as to mask the birefringence colours; such clinopyroxene contains more than 6.5 weight percent Al_2O_3 and about 1 percent Cr_2O_3. (G) Dunite orthocumulate (88980011), containing rounded olivine with characteristic serpentine mesh, poikilitic exsolved spinel-rich clinopyroxene, rare altered colourless plagioclase (to right of photograph), and clear orthopyroxene rims around some olivine grains. (H) Annealed wehrlite adcumulate (88980036), with rounded colourless olivine in a matrix of annealed clinopyroxene, rich in fine-grained exsolved spinel and vermicular exsolved blebs of orthopyroxene. A few opaque euhedral chromite grains are present. (I) Fine-grained feldspathic orthopyroxene orthocumulate 'pocket' in a matrix of strongly annealed feldspar-free orthopyroxenite adcumulate (88980004). Patches of orthocumulate are up to several cm across. The origin of the texture and patchy distribution of orthocumulate pockets is uncertain. (J) Typical gabbronorite adcumulate (88980005), containing orthopyroxene, with some exsolved ilmenite plates, smaller clinopyroxene grains, and colourless plagioclase.

anomalies (Fig. 95), Bouguer gravity anomalies (Fig. 96), and by Landsat-5 TM images. About two-thirds of the magmatic sequence is covered by alluvium. The top and bottom contacts of the intrusion are not exposed and the nature of the contacts with the country rocks is unknown.

Lithological variations are largely controlled by variations in the olivine/plagioclase modal ratio, mostly on a centimetre to metre scale (Fig. 115A–C). Plagioclase and Fe-rich olivine are the dominant cumulus phases. Clinopyroxene with opaque exsolution lamellae (Fig. 115D) is usually a minor phase and is poikilitic or interstitial relative to olivine and plagioclase. Orthopyroxene is also minor, and forms narrow moats around olivine. Magnetite is a common accessory intercumulus phase, grading into cumulus in the vicinity of massive magnetite

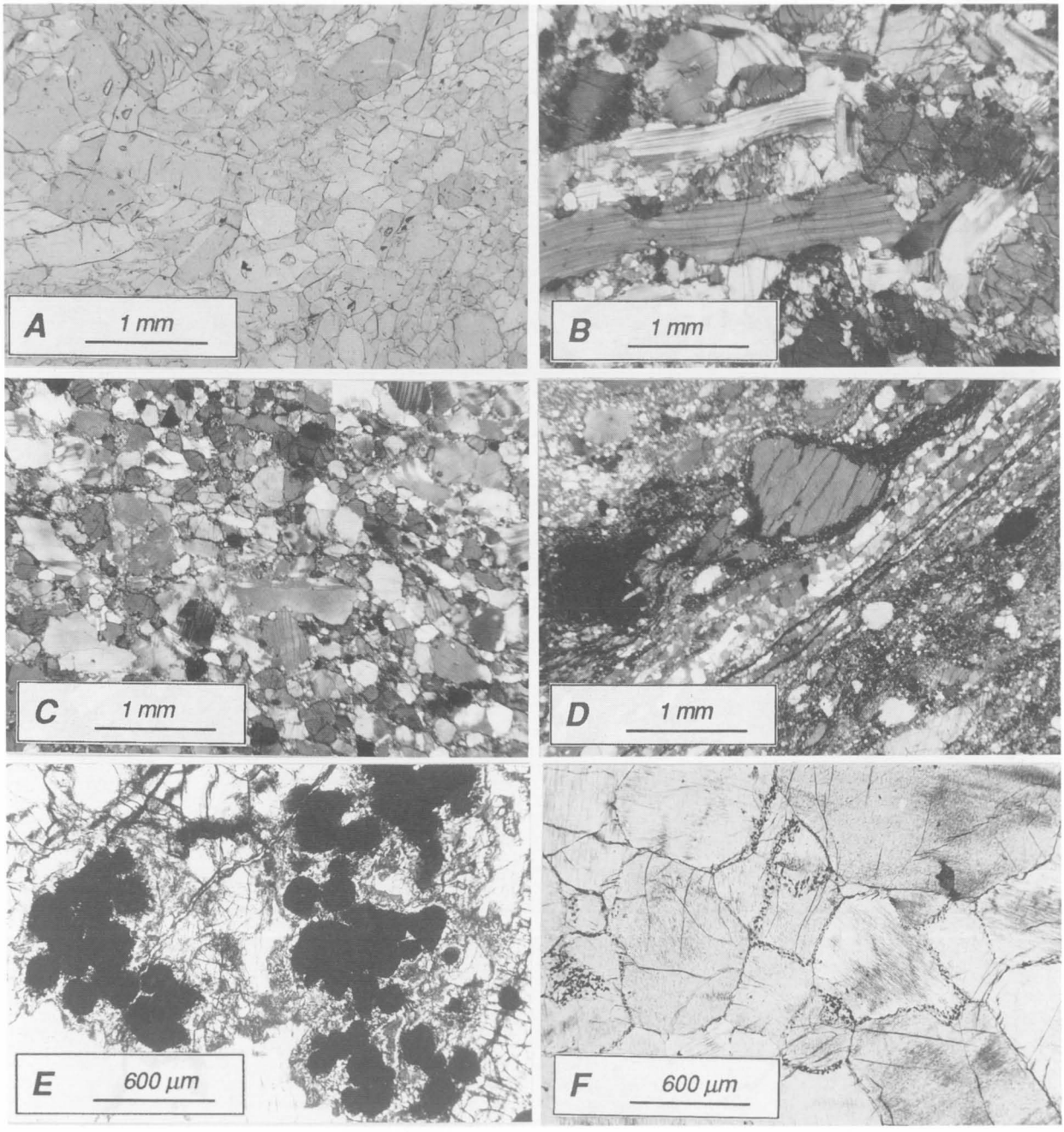

Figure 103. Deformation and subsolidus textures in the Murray Range intrusion. (A) Amphibolite (uralitised pyroxenite or peridotite cumulate, 88980037), consisting of greenish actinolitic amphibole, without plagioclase. Such amphibolites are mostly undeformed, but occur in close spatial relationships with mylonite zones and can replace entire cumulate sequences. (B) Strongly deformed gabbro to gabbronorite with proto-mylonite or proto-cataclasite texture (88980054). Rounded relict cumulus orthopyroxene and large deformed plagioclase laths occur in a granular matrix of clinopyroxene, orthopyroxene, and plagioclase. No primary clinopyroxene is preserved. (C) Strongly sheared gabbronorite (cataclasite, 88980058), with orthopyroxene and plagioclase fragments in a fine-grained matrix of plagioclase, clinopyroxene, and some hydrous phases. (D) Uralitised gabbroic mylonite to cataclasite (88980060C). Relict magmatic clinopyroxene porphyroclasts and coarse-grained amphibole occur in a fine-grained fragmented matrix of plagioclase and secondary amphibole. The rock is cut by rare felsic veins (centre). (E) Opaque relict cumulus chromite grains, in contact with olivine (fragmented grains) and plagioclase (clear grains), in peridotite orthocumulate (88980002). Spinel grains are surrounded by clinopyroxene–spinel–amphibole symplectites. (F) Granule exsolution of spinel in orthopyroxenite adcumulate (88980023). Exsolved spinel in cumulus orthopyroxene grains is largely absent from grain rims, being concentrated in small brownish spinel granules around grain boundaries.

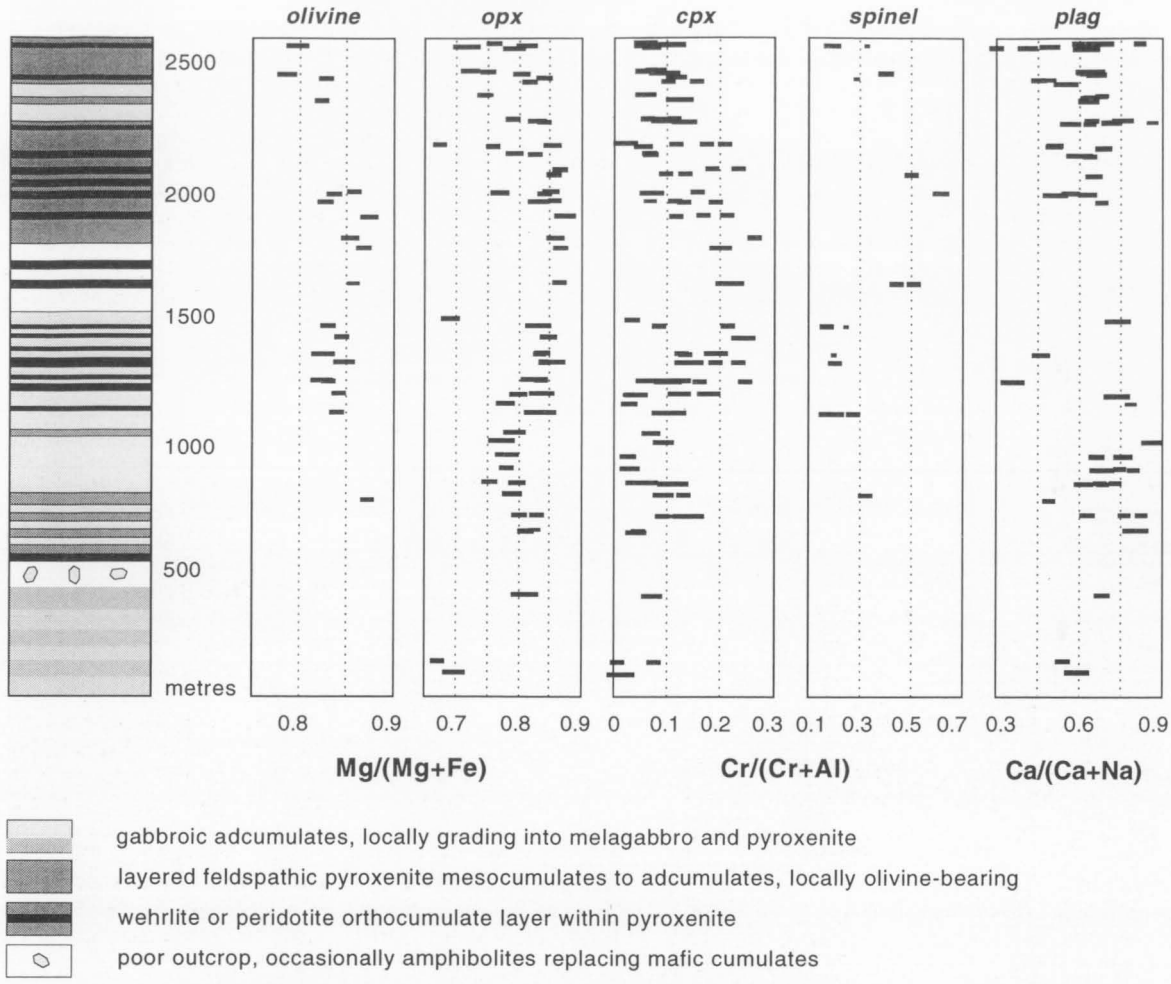

Figure 104. Stratigraphy and mineral chemistry of the Murray Range intrusion.

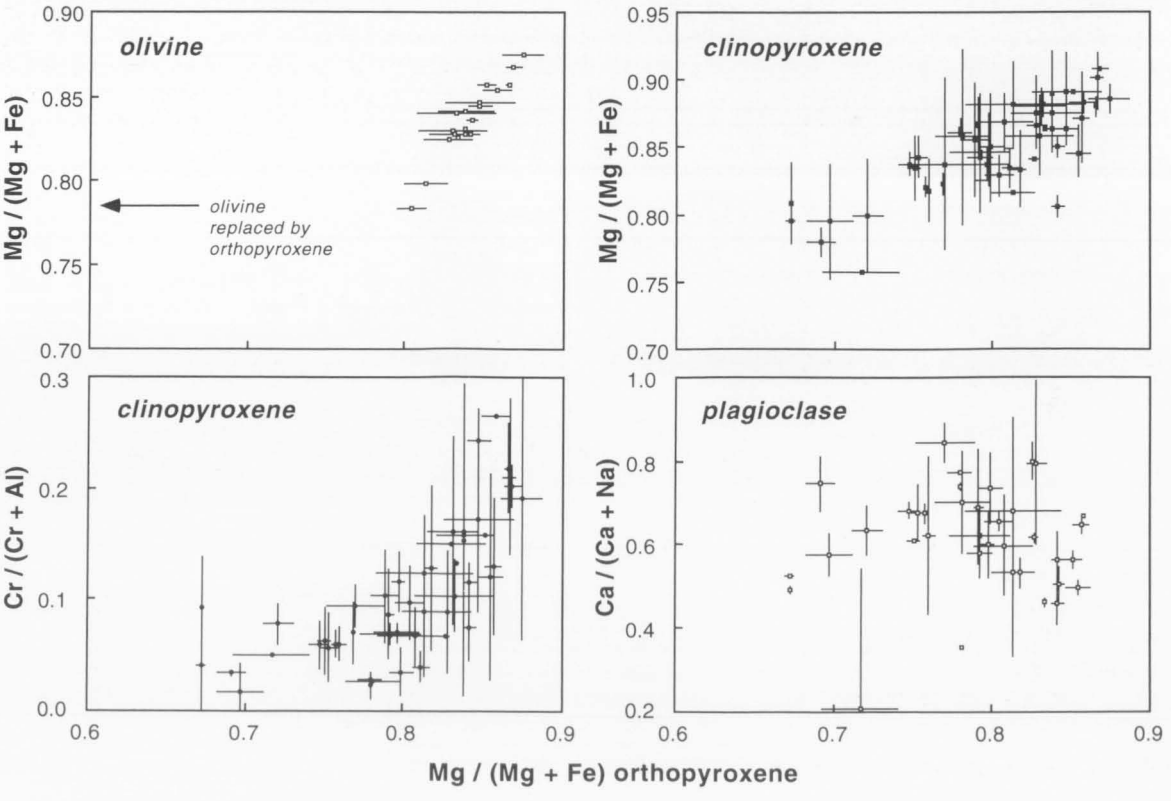

Figure 105. Average mineral compositions in the Murray Range intrusion (error bars are two standard deviations).

layers. Late or post-magmatic accessory minerals include red Ti-rich biotite (Fig. 115E) and thin brownish amphibole rims, both generally near magnetite grains. Recrystallised rocks contain secondary olivine, clinopyroxene, and orthopyroxene neoblasts of similar composition to cumulus phases. These neoblasts commonly coexist with rounded post-magmatic opaque oxides (Ti-magnetite) that probably resulted from granule exsolution from primary magmatic clinopyroxene (Fig. 115D). Plagioclase–olivine-phyric dykes (Fig. 115F), with a phenocryst mineralogy resembling the crystallisation sequence inferred for the gabbroic cumulates, may represent feeders of the cumulate sequence.

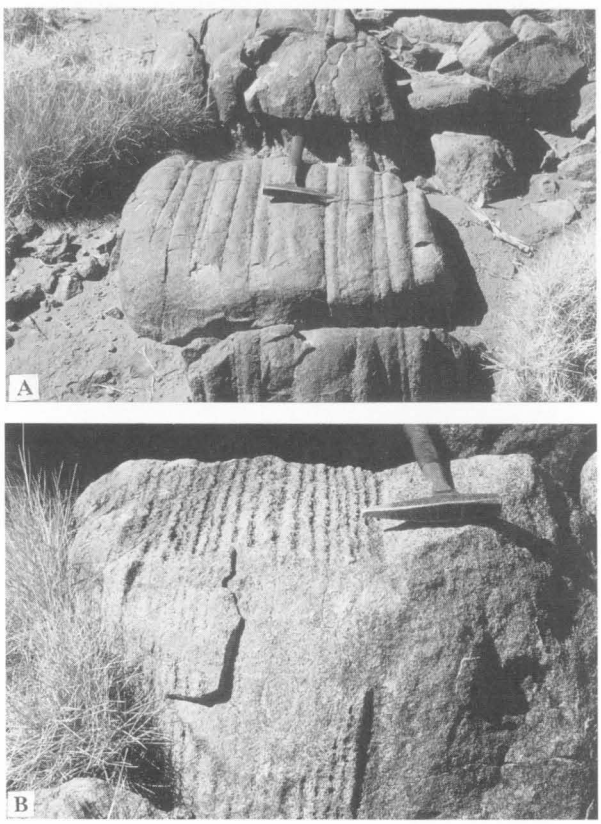

Figure 106. Outcrops of the Blackstone Range troctolite/gabbro intrusion. (A, B) Rhythmically layered troctolite.

The Jameson Range intrusion includes some of the most fractionated cumulates of the Giles Complex (Figs 116, 117). Extreme chemical differentiation in the upper part of the sequence led to the formation of several layers of massive titaniferous and vanadiferous magnetite (Fig. 114D), which contain from 1.06 to 1.30 percent V_2O_5. Olivine ranges from about Fo_{65} to Fo_{51}, and *mg* values of coexisting orthopyroxene from 72 to 62. There is no indication of a peritectic relationship between olivine and orthopyroxene, nor does modal orthopyroxene increase with increasing degree of fractionation. Clinopyroxene is significantly more magnesian than orthopyroxene and Cr is near the detection limit. Plagioclase An contents vary randomly from 75 to 49, sometimes with a 20 percent variation within single grains. This can be attributed to incomplete equilibriation during subsolidus recrystallisation.

Sampling density across strike is insufficient to identify any clear cryptic variation pattern (Fig. 116), nor can abrupt changes in cumulus mineralogy or any megascale layering be identified, except where massive magnetite seams occur in a zone of magnetite-bearing troctolite between the 1200 and 1700 m levels. Phase layering is particularly prominent where the magma became enriched in iron under conditions of high oxygen fugacity, triggering magnetite precipitation and formation of magnetite layers. There is no obvious stratigraphic variation in modal olivine/orthopyroxene ratio nor any correlation of that ratio with chemical fractionation, implying that the magma was too Fe-rich for olivine to react with its equilibrium melt. There is no clear geochemical evidence to indicate the younging direction, but the shallow southwesterly dip of the magmatic layers makes it likely that the sequence youngs to the southwest. This is consistent with the distribution of disseminated magnetite within the troctolite, namely a change from intercumulus to cumulus magnetite upwards towards the monomineralic seams.

Cavenagh Range gabbro intrusion

The Cavenagh Range gabbro consists of nearly flat-lying sheets of gabbro and gabbronorite cut by dense swarms of subvertical dolerite dykes on a variety of scales. In places, dykes are spaced every 10 to 100 m or so. The body forms a dissected plateau and a group of low table-top hills which occupy an area of about 10x10 km. As most of the body

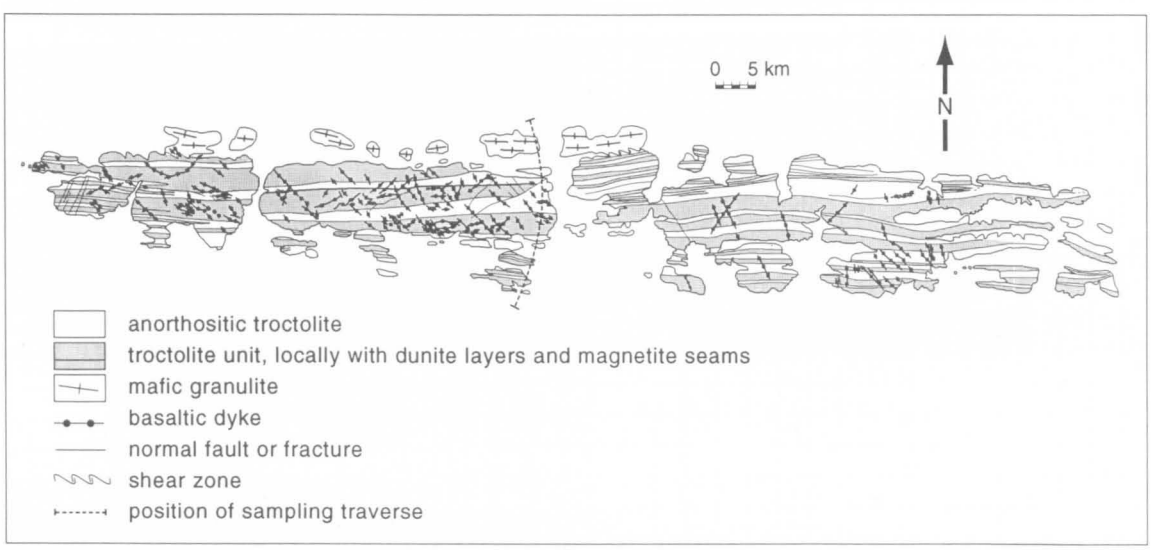

Figure 107. Geological map of the Blackstone Range intrusion.

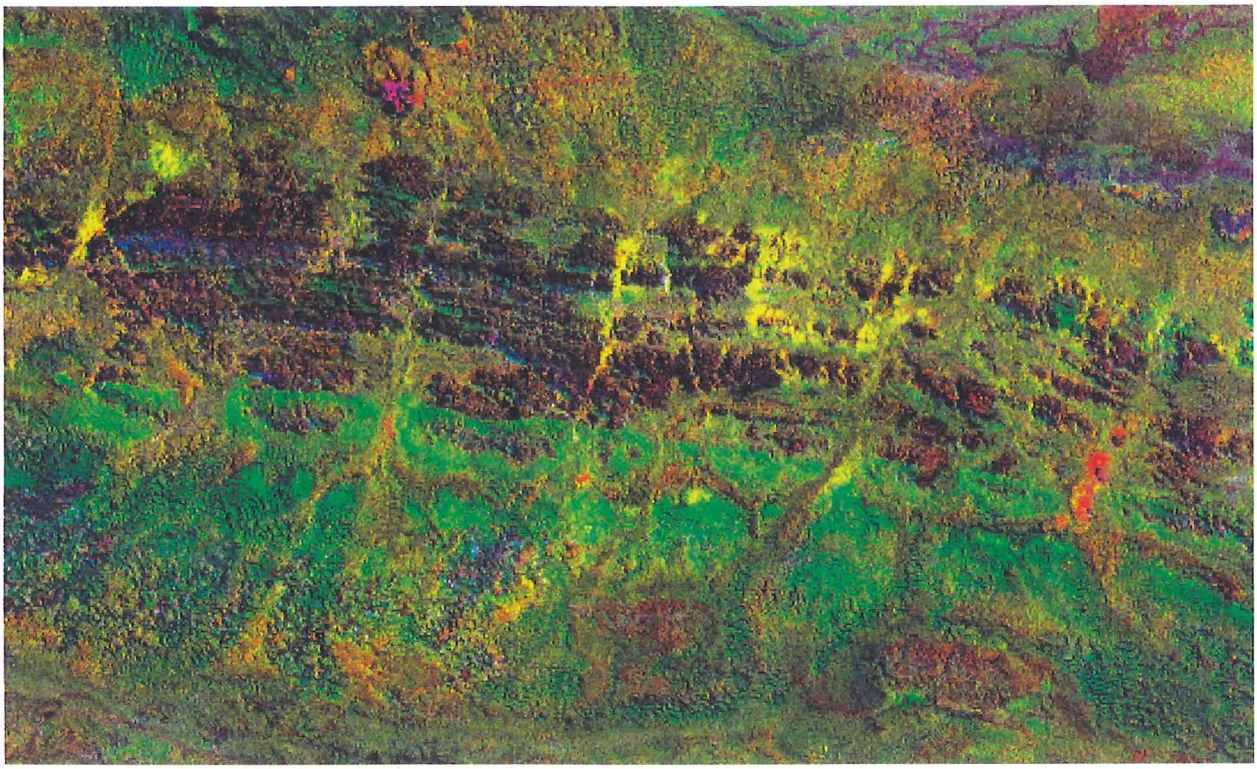

Figure 108. Landsat-5 TM 5/4 pc2(4/3;5/7):5/4:4/3 RGB image of the eastern part of the Blackstone Range intrusion. The image allows effective discrimination of thin magnetite-rich gabbro units (Gf), otherwise difficult to map in the field, which show as green lineaments along strike, between clay-weathered gabbro zones. The iron oxide-rich alluvial material shed from the intrusion is deep apple green. Creeks appear yellow, representing mixtures of iron oxide and clay.

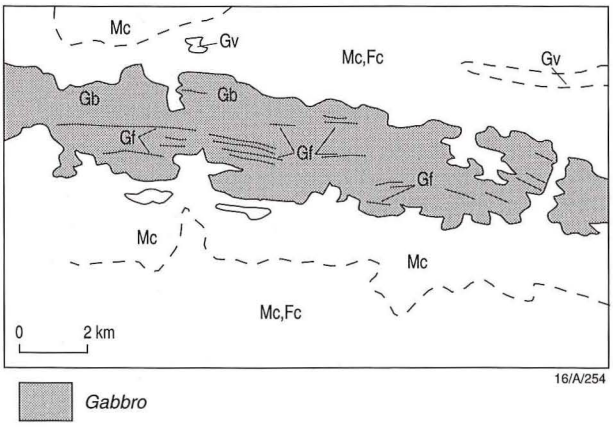

Figure 109. Geological overlay for the eastern part of the Blackstone Range intrusion (Fig. 108). Symbols as in Figure 51.

Figure 110. Cumulate and quenched textures in the Blackstone Range intrusion. (A) Coarse-grained troctolite (90987505). This contains rounded, locally interstitial olivine grains (cracked), interstitial opaque oxides partly rimmed by amphibole, and an orthopyroxene–magnetite symplectite adjacent to orthopyroxene rims around oxide grains. The colourless matrix is plagioclase. (B) Troctolite to troctolitic anorthosite (90980178). Irregular cracked olivine, clinopyroxene, and magnetite occur in a matrix of cumulus plagioclase. Olivine becomes interstitial in the most leucocratic troctolites. (C) Marginal olivine gabbro (90980148). Elongated euhedral plagioclase laths and irregular olivine are cumulus, and clinopyroxene is an early intercumulus phase. This is interpreted as a rapid crystallisation texture, similar to those in porphyritic dykes. (D) Poikilitic clinopyroxene with exsolved opaque oxide in a gabbroic troctolite (90980166). An olivine grain is at lower right. Euhedral plagioclase appears to penetrate clinopyroxene, suggesting rapid cooling. (E) Dunitic adcumulate (90980167), containing rounded olivine grains, with former interstitial phases (plagioclase and/or clinopyroxene?) replaced by actinolitic amphibole. (F) Coarse-grained plagioclase-phyric sill in the upper part of the Blackstone Range sequence, possibly a chilled margin (90980143). The rock contains elongated plagioclase phenocrysts, and the dark oxide-rich aggregates may represent pseudomorphs after olivine. The groundmass contains opaque oxides and clinopyroxene. Partly crossed polarisers. (G) Gabbroic troctolite cumulate with a subophitic texture like that of coarse-grained dykes (90980166). Cumulus olivine (clear rounded cracked grains), elongated cumulus plagioclase laths, and poikilitic clinopyroxene, with interstitial opaque oxides are the main constituents. The sample is from near the southern margin of the intrusion. (H) Poikilitic exsolution-rich clinopyroxene, partly recrystallised to smaller rounded clinopyroxene and opaque oxide neoblasts, in troctolitic anorthosite (90987505).

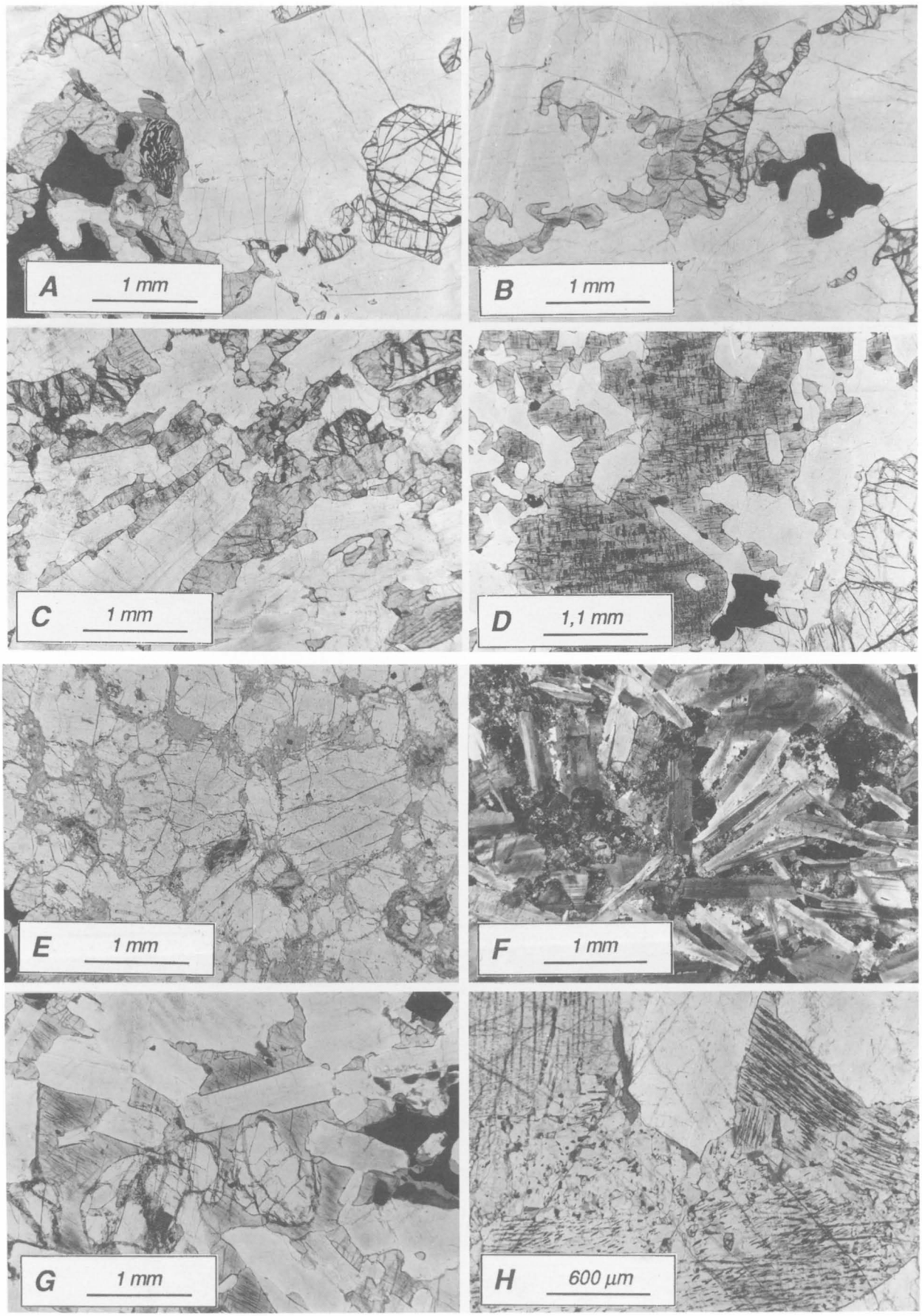
A
1 mm
B
1 mm
C
1 mm
D
1,1 mm
E
1 mm
F
1 mm
G
1 mm
H
600 µm

occurs within Aboriginal sacred ground, only the northernmost part was examined and the intrusion remains a subject for future work.

Morgan Range gabbro intrusion

This 5 km long, northwest-trending body consists mainly of intensely recrystallised gabbro and mafic granulite intruded by pegmatite and granite veins and cut by both northwest and northeast-trending mafic dykes. The extensive recrystallisation has resulted in obliteration of most primary magmatic structures and textures.

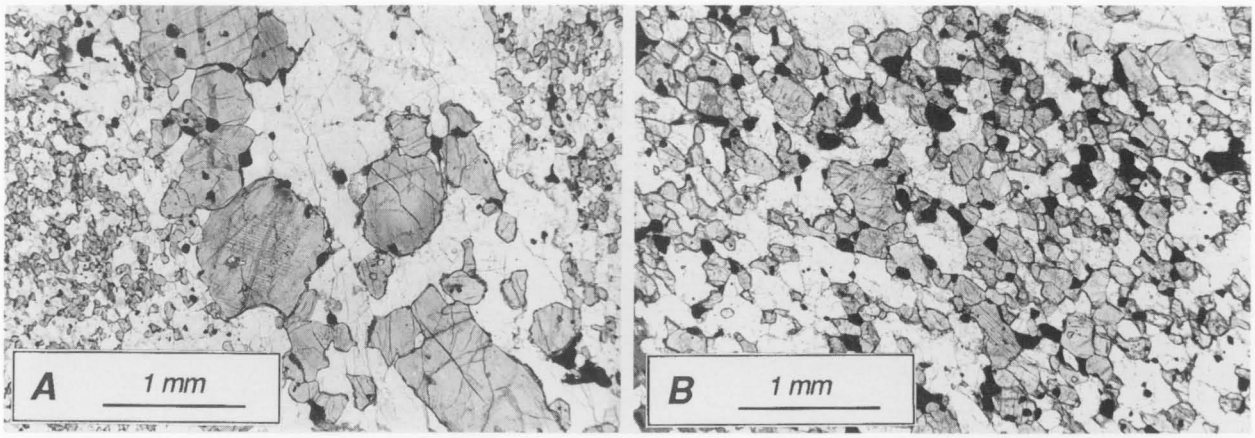

Figure 111. Marginal rocks in the Blackstone Range intrusion. (A) Gabbroic granulite or rapidly chilled marginal rock (90980151). Coarse-grained gabbroic clinopyroxene–plagioclase enclaves with relict cumulus texture occur in a fine-grained granular (?recrystallised) matrix of clinopyroxene, plagioclase, and opaque oxide neoblasts. It is not clear whether this is a primary-magmatic or a secondary metamorphic texture. (B) Fine-grained recrystallised marginal gabbro (90980147), consisting of clinopyroxene, orthopyroxene, plagioclase, and oxide neoblasts, with minor phlogopite. Olivine is absent from these marginal recrystallised gabbroic rocks.

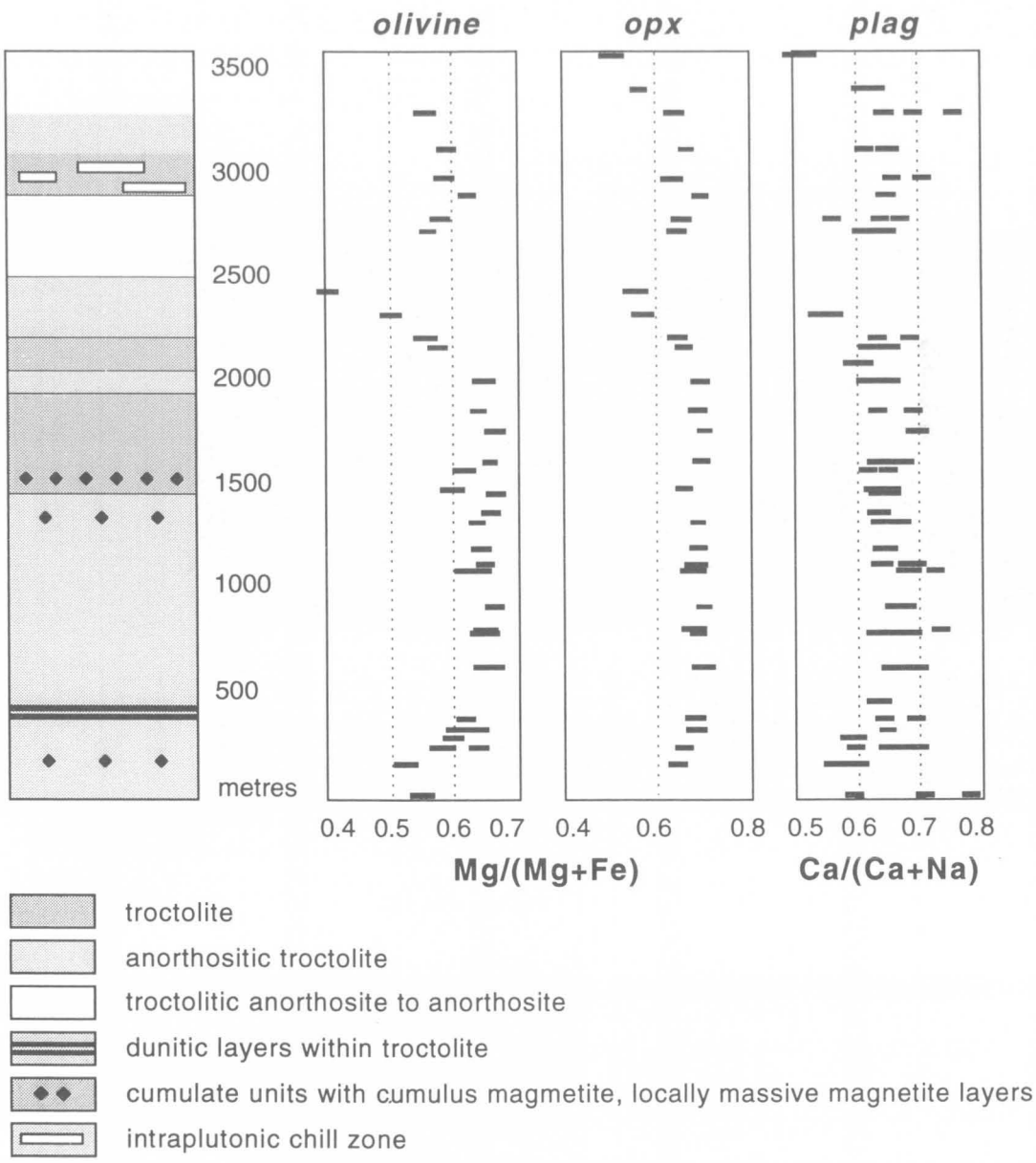

Figure 112. Stratigraphy and mineral chemistry of the Blackstone Range intrusion.

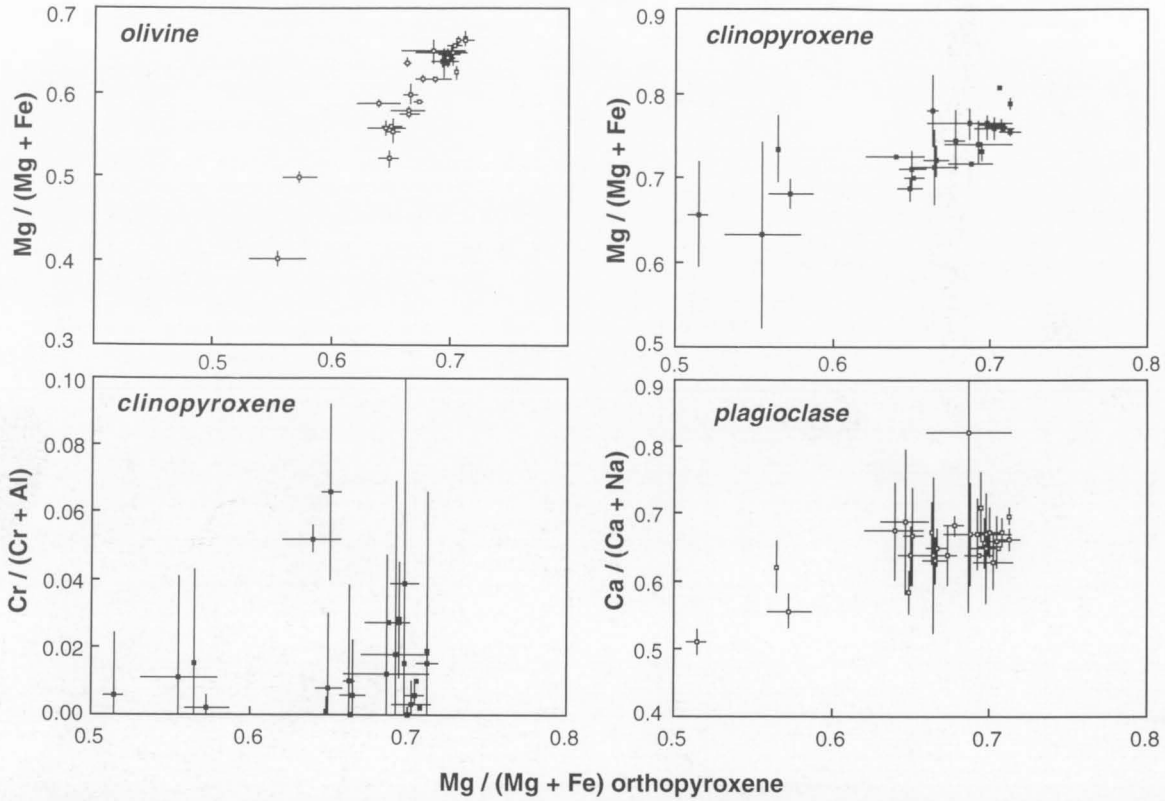

Figure 113. Average mineral compositions in the Blackstone Range intrusion (error bars are two standard deviations).

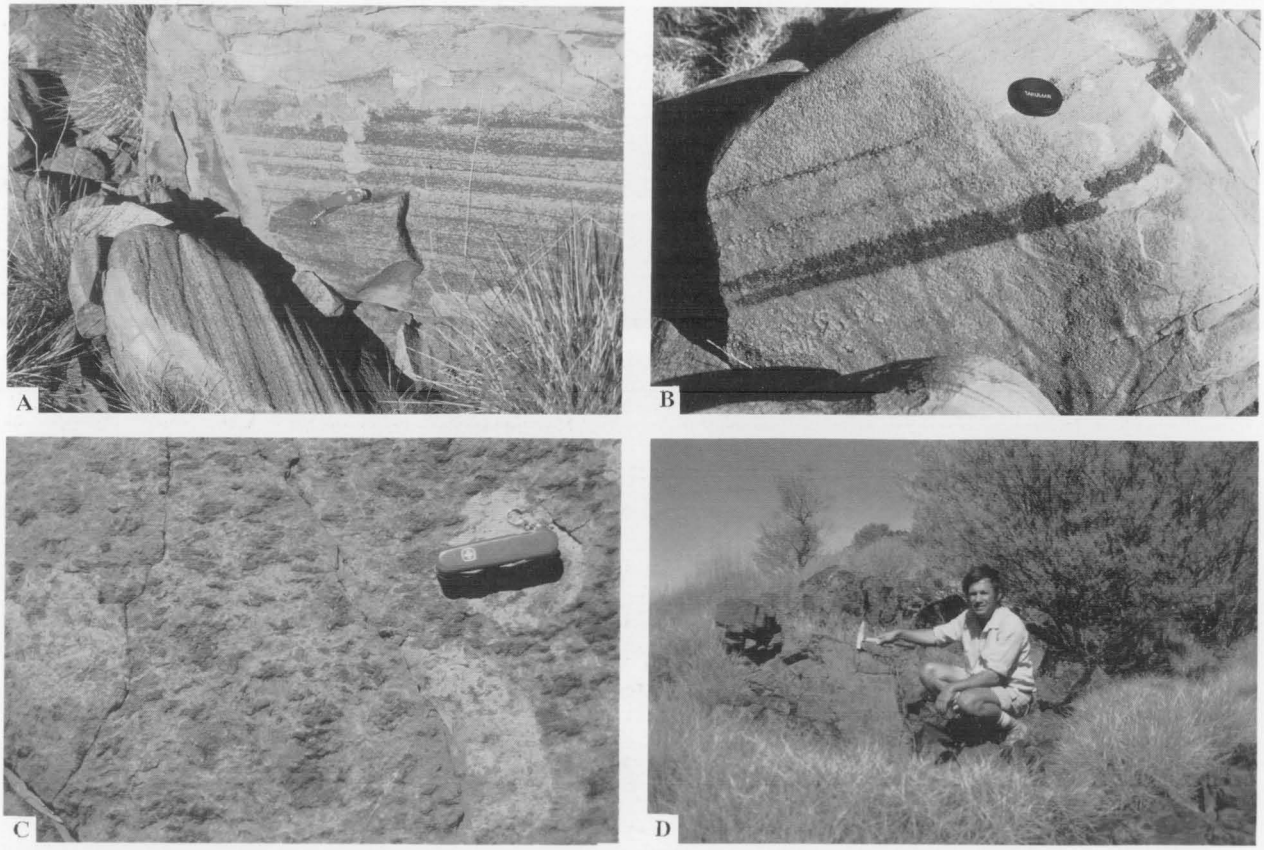

Figure 114. Outcrops of the Jameson Range troctolite/gabbro intrusion. (A) Layered troctolite. (B) Olivine and clinopyroxene-rich layers in troctolite. (C) Cumuloblastic blebs of olivine and clinopyroxene in troctolite. (D) Outcrops of 5 metre-thick magnetite unit in troctolite.

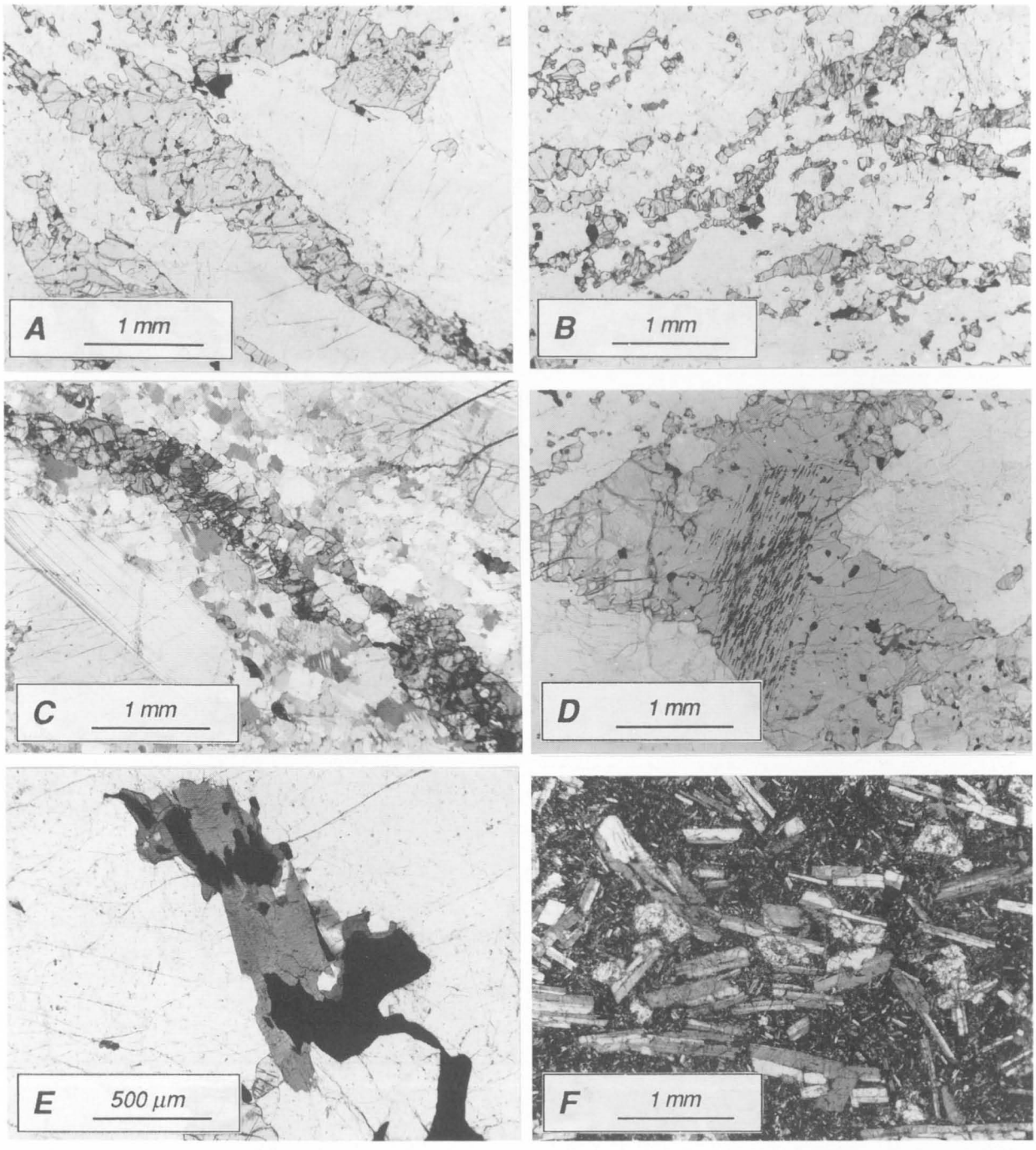

Figure 115. Cumulate textures in the Jameson Range intrusion. (A) Laminated troctolitic anorthosite (90980023). Small olivine and clinopyroxene grains form layers and lenses in a plagioclase-dominated matrix. A few rounded oxide grains represent granule exsolution of oxide lamellae in magmatic clinopyroxene. A magmatic clinopyroxene grain with exsolved opaque oxides is at upper right. (B). Finely layered recrystallised leucotroctolite to anorthosite (90980019). Small olivine and clinopyroxene neoblasts occur in a matrix of highly deformed granoblastic plagioclase. (C) Olivine-rich layer in a strongly deformed and recrystallised troctolitic anorthosite (90980022). There are a few large deformed plagioclase relics within a neoblastic matrix of plagioclase. Partly crossed polarisers accentuate the degree of deformation of plagioclase. (D) Recrystallised gabbroic troctolite (90980039). A large relict magmatic clinopyroxene grain has abundant exsolved opaque oxides near its centre. It is recrystallised to clinopyroxene–opaque oxide neoblasts near the grain margins. (E) Coarse-grained anorthosite (90980042) has reddish biotite flakes attached to a late-magmatic intercumulus magnetite grain. (F) Small olivine–plagioclase-phyric dyke cutting the layered sequence (90980032). The dyke has elongated plagioclase and euhedral olivine phenocrysts in a fine-grained plagioclase–oxide-rich groundmass. Such dykes have phenocryst populations that resemble the cumulus phases in the troctolitic intrusions, and may therefore represent derivative parental melts to the host intrusion.

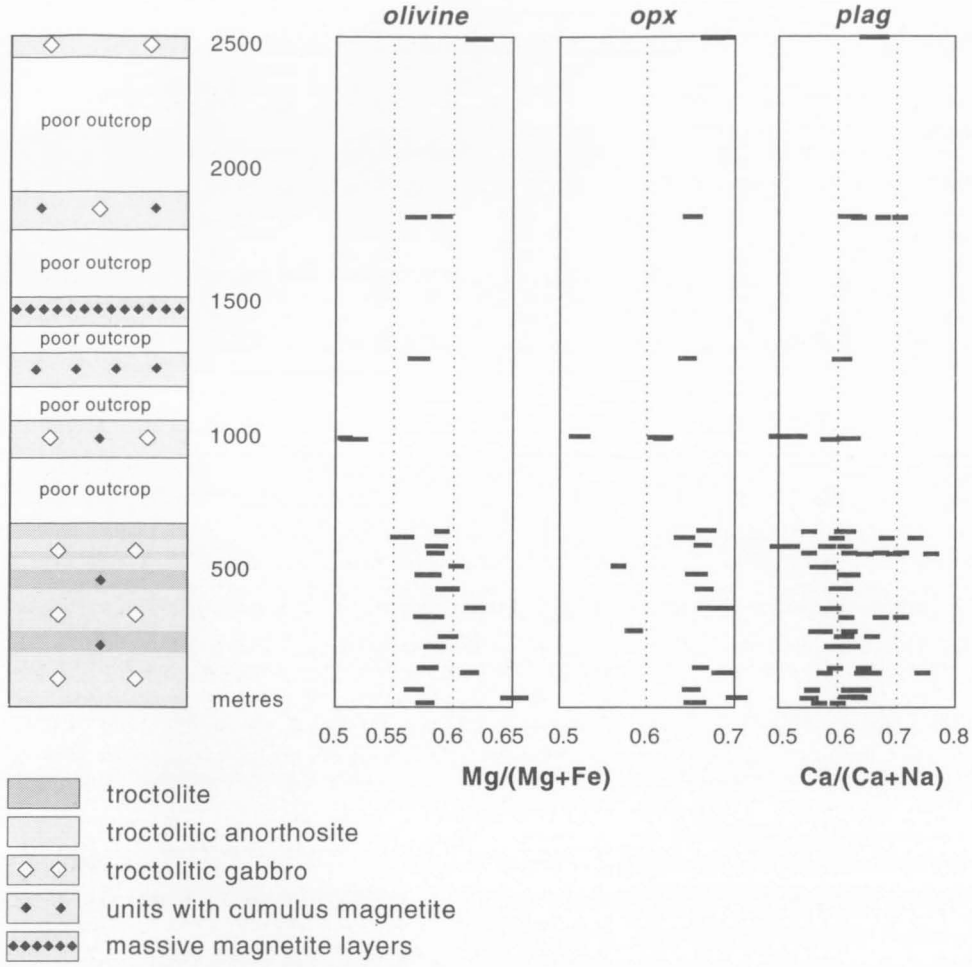

Figure 116. Stratigraphy and mineral chemistry of the Jameson Range intrusion.

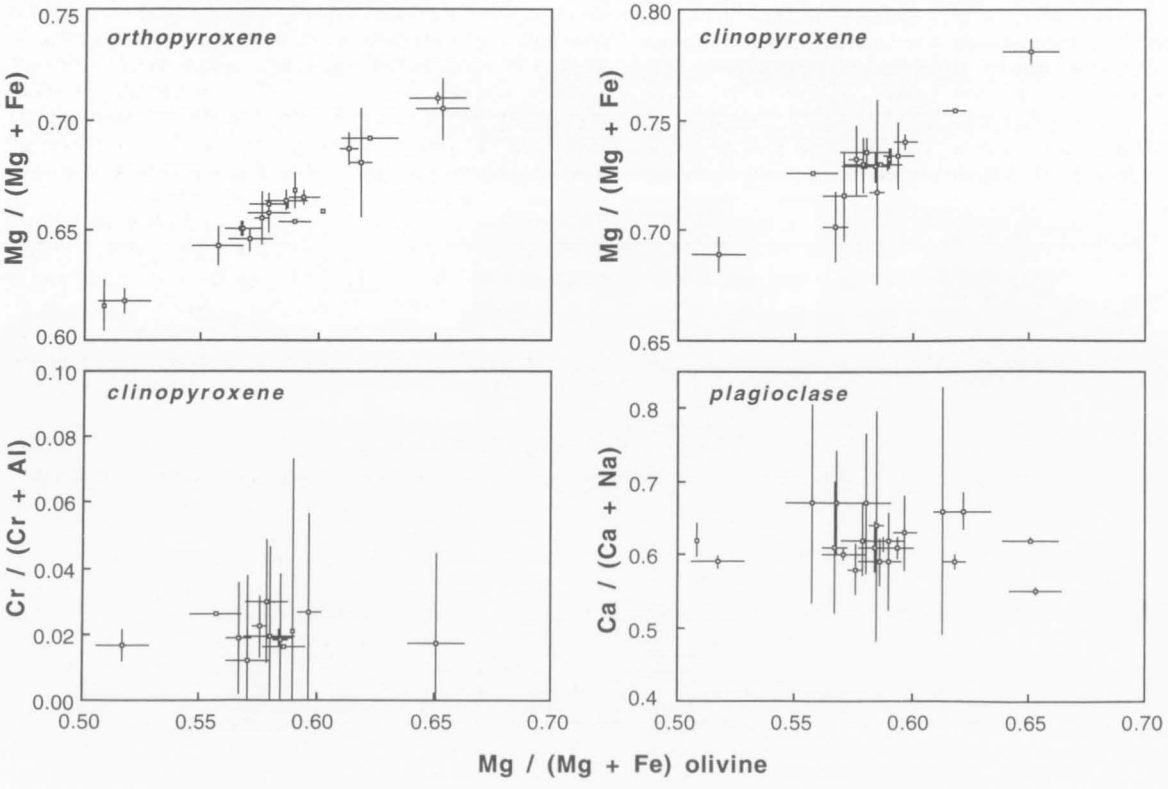

Figure 117. Average mineral compositions in the Jameson Range intrusion (error bars are two standard deviations).

The Giles Complex 3: petrogenesis

A comprehensive electron microprobe study of the Giles Complex intrusions, including analyses of about 300 samples, was conducted by Ballhaus (1993). The Giles Complex consists of three major types of cumulate: primitive (producing ultramafic cumulates), gabbroic, and troctolitic. In the following section we identify, in broad terms, the parent magma compositions that gave rise to these cumulates and discuss how they may be related. The study indicates that the magma types which form the various intrusions of the Giles Complex cannot be related to a single liquid line of descent from a unique parent magma. Several crystallisation sequences are distinguished, including (1) ultramafic olivine–clinopyroxene-rich cumulate sequences, (2) mafic clinopyroxene–plagioclase-rich sequences, and (3) evolved troctolitic olivine–plagioclase±magnetite-rich sequences. These sequences were derived from at least three discrete parent magmas: (1) a near-primitive olivine±clinopyroxene-saturated melt, (2) a more fractionated olivine–(orthopyroxene)–clinopyroxene–plagioclase-saturated melt, and (3) a strongly fractionated olivine–plagioclase±magnetite-saturated melt. These magmas represent derivatives of a parental liquid (or liquids) that experienced various degrees of polybaric orthopyroxene–clinopyroxene±olivine fractionation at significantly greater depths than those at which the Giles Complex was subsequently emplaced. The layered bodies are intruded by several generations of mafic dyke, the phenocryst assemblages of at least some of which resemble the crystallisation sequences in the host cumulates.

Parental magmas of the Giles Complex

Although chilled margins occur locally (e.g., Kalka, Mount Davies), their contaminated state requires estimation of parent melt compositions from crystallisation sequences and phase compositions of the most primitive cumulates in each intrusion. Implicit in this is that the crystallisation sequences in the cumulates reflect the liquidus relations of the parent melts. On this basis we identify three major types of parental magma: (1) a primitive, olivine-normative, olivine–spinel-saturated liquid, (2) a moderately fractionated, near silica-saturated (only slightly olivine-normative), pyroxene–plagioclase-saturated gabbroic melt, and (3) a highly evolved, but relatively silica-undersaturared (only slightly hypersthene-normative), olivine–plagioclase±magnetite-saturated troctolitic melt.

Primitive parental melts

Examples of cumulate sequences derived from a primitive melt are the Murray Range, The Wart, and Wingellina Hills (Ballhaus & Glikson 1989) intrusions, and possibly the Kalka and Ewarara intrusions (Goode & Krieg 1967; Goode & Moore 1975), for which systematic phase compositions are not available. The following criteria allow characterisation of the parent melt:

- Olivine was replaced on the liquidus at about Fo_{78} (Figs 105, 118). This, in combination with the observation that dunite cumulates are volumetrically minor in all Giles Complex ultramafic intrusions, suggests that the normative olivine content of the melt could not have been particularly high.
- The most primitive cumulates (Murray Range and Wingellina Hills intrusions) are dunitic orthocumulates in which the most magnesian olivine is $Fo_{88–89}$. Assuming that total Fe as FeO in the melt was about 10 weight percent (reasonable for continental tholeiitic melts), the MgO content of the melt would be about 12 percent (Roeder & Emslie 1970).
- Typical Ni content in the most primitive olivine is about 2500 ppm. Available partition coefficient data constrain Ni in the equilibrium melt to about 200 ppm (Henderson 1982; Hirschmann & Ghiorso 1994).
- The maximum Cr content of the texturally earliest cumulus clinopyroxene ranges from 1800 to 2200 ppm, suggesting a Cr content in the equilibrium melt of about 150–200 ppm (e.g., Philpotts 1990).
- Every reversal in the cryptic layering patterns of the ultramafic intrusions is matched in the cumulate sequence by loss of at least one cumulus phase, and commonly two (clinopyroxene and plagioclase). This suggests that, at the pressure of emplacement, the primitive magma was only saturated with olivine (+ spinel).

The above points summarise the chemical characteristics of a relatively low-pressure mafic melt in near equilibrium with mantle assemblages (cf. Green & Ringwood 1967a; Jaques & Green 1980). We conclude that the parent melt of the ultramafic intrusions of the Giles Complex was broadly tholeiitic and only moderately olivine normative. It experienced little phase fractionation or contamination prior to emplacement into the crustal magma chambers.

Gabbroic parental melts

The cumulate series of the gabbroic intrusions (e.g., Hinckley Range and Latitude Hill) formed from multiply saturated parental melts significantly more evolved than the parent liquids of the ultramafic intrusions. The melts must have been saturated with olivine–(orthopyroxene), clinopyroxene, and plagioclase at the time of emplacement. As a direct result there is little change in cumulus mineralogy, even where reversals in mineral composition signify a major influx of new magma into the magma chamber. A new melt pulse can only change cumulate mineralogy (and initiate megascale layering) if it is compositionally far removed from a cotectic. In cases where a melt is close to multiple phase saturation, a modal change will only result if the mass ratio of added (more primitive) to resident (more fractionated) melt is high.

Overall, the gabbroic parent magma must have experienced appreciable pyroxene and olivine fractionation prior to emplacement. The most primitive olivine compositions encountered are Fo_{83} at Latitude Hill and Fo_{75} in the Hinckley Range sequence, and these were replaced by orthopyroxene when olivine had evolved to Fo_{67} and Fo_{56}, respectively. Cr in the gabbroic parental melt was also severely depleted. Cr/(Cr+Al) in clinopyroxene of the Latitude Hill sequence is less than 0.15, and in the Hinckley Range sequence Cr is near the detection limit.

Troctolitic parental melts

The parent melts to the troctolitic intrusions (e.g., Bell Rock, Jameson Range, and Blackstone Range) were saturated with relatively Fe-rich olivine and sodic plagioclase, and close to magnetite saturation. Silica activity in the melt was low and the bulk SiO_2 content of the fractionating phases (olivine, plagioclase, and magnetite) must have been higher than that of the equilibrium melt. Consequently, there was no SiO_2 enrichment in the melt and no increase in modal orthopyroxene with protracted fractionation upward in the sequence, as confirmed by the scarcity of orthopyroxene in the most Fe-rich cumulates, as well as the most primitive samples. The melt that gave rise to the troctolitic suites must have been enriched

in ferrous iron, resulting in a stable cotectic relationship between Fe-rich olivine and orthopyroxene and between these phases and the melt (Bowen & Schairer 1935). In addition, the magma was low in normative diopside in comparison with the gabbroic and the mafic parental melts, despite clinopyroxene increasing in modal abundance with falling *mg* value (increasing degree of fractionation) in the gabbroic intrusions (Hinckley Range and Latitude Hill).

The low silica activity, high Fe contents, and low normative diopside are chemical characteristics of a melt that experienced extensive fractionation prior to emplacement. The enrichment of the melt in FeO resulted in the equilibrium olivine being no longer in peritectic reaction relationship with its melt (Bowen & Schairer 1935). To derive strongly SiO_2-undersaturated troctolitic melts, the fractionating assemblages must have had a bulk SiO_2 content at least as high as that of their equilibrium melt. As suggested below, this probably resulted from pre-emplacement high-pressure pyroxene fractionation.

Chemical relationships of the parental melts

At first sight, it seems straightforward to derive all parent melt compositions and cumulates from one primitive mantle liquid, by simply fractionating the phase assemblages that occur as cumulate layers in intrusions of the Giles Complex. This model implies that the ultramafic cumulate suites form the basal sequence, the gabbroic intrusions the main section, and the troctolitic intrusions the highly evolved roof section of a single magma chamber (Sprigg & Wilson 1959), and that the complex became dismembered by later thrusting (cf. Harley 1989).

The above model, however, is inconsistent with the behaviour of olivine. Olivine persists as a fractionating phase through a range of cumulates, from Fo_{89} in the Murray Range mafic–ultramafic intrusion down to Fo_{40} in the Blackstone Range troctolite/gabbro intrusion (Fig. 113). The expected trend in a single mafic magma chamber would be that olivine temporarily disappears from the liquidus when the silica activity of the melt exceeds that of the olivine–orthopyroxene peritectic of the melt, to reappear as a fayalite-rich olivine when FeO is high enough so that olivine and orthopyroxene are in a cotectic relationship. A classic example of this is the Bushveld Complex (Willemse 1969). Most Giles Complex intrusions indeed show replacement of olivine by orthopyroxene — at Fo_{78} in the Murray Range and Wingellina Hills sequences, at Fo_{68} in the Latitude Hill intrusion, and at Fo_{59} in the Hinckley Range gabbronorite. However, it is unlikely that olivine could reappear on the liquidus in successive cumulate sequences while *mg* values continued to fall (Fig. 118).

Evidence for high-pressure crystallisation

The trend in Figure 118 suggests derivation from a single parent magma composition, if the fractionating assemblages had bulk MgO, CaO, and SiO_2 contents higher than their equilibrium melts. An elegant way to achieve this is by high-pressure fractionation (Ballhaus & Glikson 1992). At low confining pressures, up to about 8 kb, a tholeiitic melt initially in equilibrium with mantle assemblages will fractionate olivine followed by clinopyroxene and plagioclase (Green & Ringwood 1967a). A typical intrusive cycle within a replenished magma chamber will thus commence with the formation of primitive dunite and peridotite orthocumulates, followed by more fractionated olivine-bearing pyroxenite, pyroxenite, and

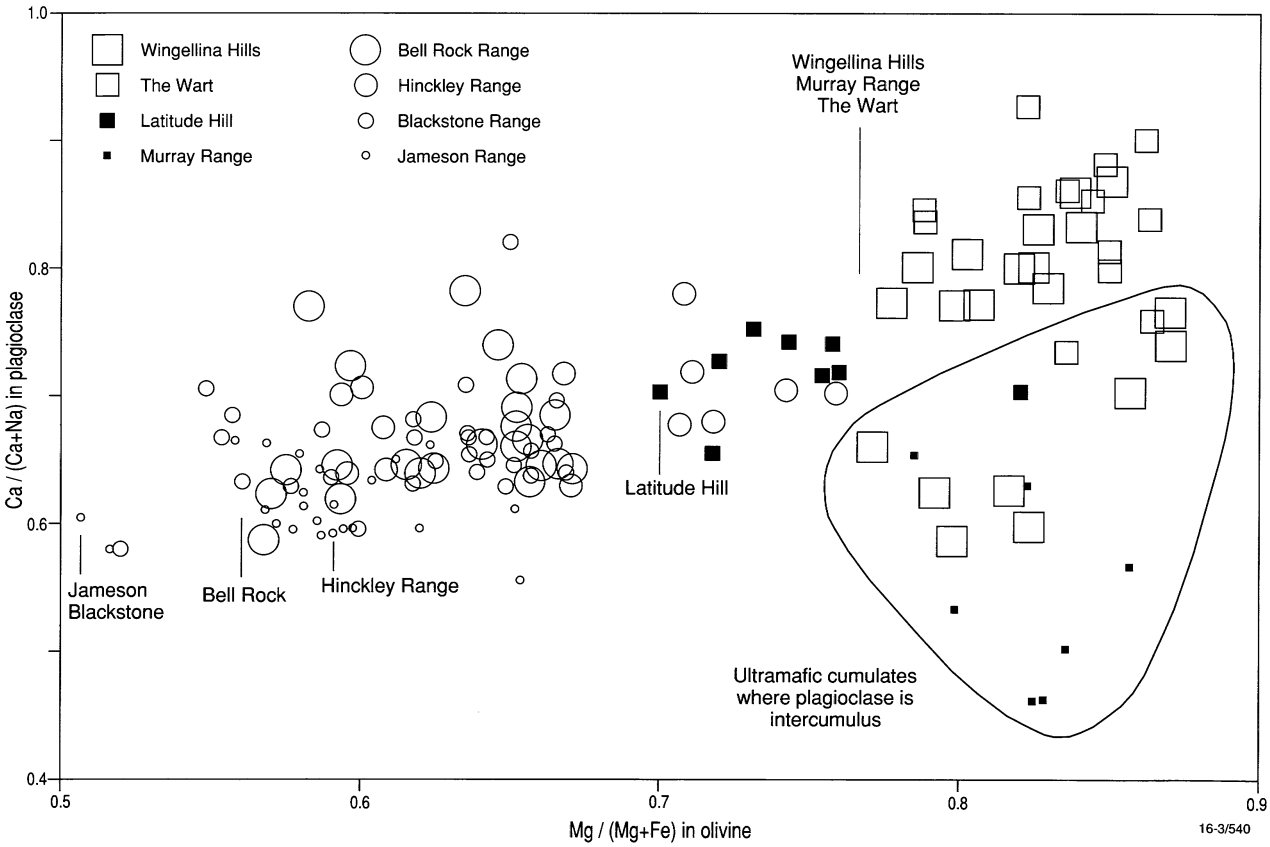

Figure 118. Average compositions of olivine and plagioclase in cumulates of the Giles Complex. Arrows mark the most Fe-rich olivine composition of each cumulate suite. In the ultramafic and gabbroic sequences, the most Fe-rich olivine marks the point in the fractionation history where olivine was replaced by orthopyroxene.

then gabbro (Ballhaus & Glikson 1989). Chemical evolution will be along an olivine control line, whereby *mg* values of the cumulus phases fall and the activity of silica in the equilibrium melt rises. The fractionating mineral assemblages at all times have lower bulk SiO_2 contents than the magma from which they separated. When silica activity exceeds that of the olivine–orthopyroxene peritectic, olivine will be replaced by orthopyroxene and further fractionation will not involve olivine until high FeO terminates the peritectic relationship between olivine and melt.

This scenario changes if crystallisation takes place at higher confining pressures. The olivine–orthopyroxene peritectic shifts toward the olivine stability field until it becomes a cotectic phase boundary. The clinopyroxene and spinel stability fields expand at the expense of the olivine and plagioclase fields until troctolitic assemblages (olivine+plagioclase) become unstable (Green & Ringwood 1967a, b; Presnall et al. 1978). A direct consequence is that the SiO_2 contents of melts along the olivine–orthopyroxene cotectic will be lower than the SiO_2 content of the equilibrium orthopyroxene (Kushiro 1969; Presnall et al. 1978, 1979). Crystal fractionation under such conditions will consist of pyroxene+olivine and will deplete the melt in MgO and CaO relative to FeO and Na_2O without enrichment in SiO_2, because the fractionating phases have bulk SiO_2 contents as high, or higher than, their equilibrium melts.

It is suggested that the fractionation trends observed in the Giles Complex can be explained by high-pressure fractionation followed by low-pressure fractionation. The range in parent melt compositions could have been produced by high-pressure pyroxene±olivine fractionation when olivine and orthopyroxene were in cotectic relationships, preventing an increase in SiO_2 in the melt (Fig. 118). The fractionation trends shown by individual intrusions must have originated at lower pressures, when olivine was in a reaction relationship with the melt. It is envisaged that fractions of the evolving high-pressure melt were periodically squeezed off into shallower magma reservoirs in the crust at various degrees of chemical fractionation. As a result, melts that were fractionating pyroxene±olivine at high pressure experienced a relative compositional shift into the olivine-only stability field when decompression occurred. Further fractionation at low pressure was then dominated by olivine, allowing silica activity to increase as fractionation continued. Depending on the stage in the high-pressure fractionation history at which a derivative melt fraction became squeezed from its high-pressure reservoir, the liquid crystallised to gabbroic or troctolitic cumulates. It is likely that the gabbroic parent magmas had undergone significantly more olivine fractionation and less pyroxene fractionation (to produce a near SiO_2-saturated melt) than the troctolitic parent magmas. This suggests somewhat lower-pressure pre-emplacement fractionation (and possibly a shallower depth of melt segregation: Green & Ringwood 1967a) in the former case.

There is ample evidence to support high-pressure fractionation for parts of the Giles Complex (cf. Goode & Moore 1975):

- In all troctolitic intrusions, clinopyroxene remains a minor phase and appears late (if at all) in the crystallisation sequence. This is only understandable if the parental melts were severely depleted in normative diopside through a prolonged history of high-pressure fractionation, prior to emplacement in their crustal reservoirs.
- The Murray Range sequence includes cumulates where olivine and orthopyroxene coexist as cumulus phases at an olivine composition as primitive as Fo_{88} (Ballhaus 1993). This suggests that both minerals crystallised along a cotectic phase boundary very early in the fractionation history. The minimum pressure to achieve this must have been at least 7 to 8 kb (Green & Ringwood 1967a), assuming that the parental liquid was a tholeiitic low-pressure, moderately olivine-normative mantle melt.
- Plagioclase in the Murray Range sequence is more sodic at any given olivine composition than in other, compositionally similar, sequences of the Giles Complex. This may in part be attributed to the fact that, in the Murray Range intrusion, plagioclase appears later in the crystallisation sequence than olivine and clinopyroxene, i.e., crystallised from a magma that was depleted in CaO and enriched in SiO_2 by olivine–clinopyroxene fractionation. Both factors will tend to stabilise more sodic plagioclase. On the other hand, high pressure will also stabilise clinopyroxene and aluminous spinel relative to anorthite (Green & Ringwood 1967b; Green & Hibberson 1970; Presnall et al. 1979), and thus delay nucleation of plagioclase.
- Pyroxenes are high in Al_2O_3 and other non-quadrilateral components, notably in the ultramafic cumulates of the Murray Range sequence (Ballhaus & Glikson 1995). The primary reason for this must be a high crystallisation temperature; indirectly, however, high temperature may indicate high confining pressure, since increasing pressure displaces the liquidus of a dry basaltic melt to higher temperatures.
- One type of mafic dyke contains partly resorbed orthopyroxene as the only phenocryst generation, in a matrix containing olivine microphenocrysts (Ballhaus 1993). These dykes may represent quenched fractions of a high-pressure mafic melt, tapped from greater depths, that preserved samples of the high-pressure fractionating phase as intratelluric phenocrysts.

An emplacement model for the Giles Complex

The Giles Complex, as well as coeval mafic volcanic rocks of the Tollu Group and mafic dykes, was derived from an enriched source, probably involving subcontinental lithospheric mantle (see mafic dyke section). The estimated Giles Complex parent magma composition is given in Table 6. Magmatism which produced the Giles Complex, as well as associated metamorphism, presumably resulted from a thermal anomaly in the upper mantle below the Musgrave Block (Sun & Sheraton 1992). Emplacement of melts into the crustal reservoirs must have coincided with an extensional period during the prolonged granulite-facies metamorphic event, possibly as a result of lithospheric thinning above the upper mantle thermal anomaly. Some fractions of the primitive mantle-derived magma (or magmas) were emplaced directly into crustal reservoirs where pressures were low enough to allow extensive olivine fractionation, followed by clinopyroxene and plagioclase fractionation. The cumulate sequences derived from these batches of primitive magma comprise the Murray Range, The Wart, Wingellina Hills, Kalka, Ewarara, Gosse Pile, and Claude Hill intrusions (Fig. 47).

Other fractions of the primitive magma must have ponded at greater depths, possibly in reservoirs within the lower crust or even in the shallow subcontinental lithosphere. Owing to higher confining pressure, the stable liquidus phases included orthopyroxene and clinopyroxene in addition to olivine. These melts experienced various degrees of SiO_2 depletion or enrichment with progressive fractionation at a range of depths.

Development of particular tectonic conditions may have resulted in the squeezing of fractions of the evolving high-pressure melts into (secondary) shallower crustal reservoirs. This decompression caused an expansion of the olivine and plagioclase stability fields relative to those of pyroxene and

spinel, and a relative shift in melt composition away from multiple saturation into the olivine stability field. Depending on the stage at which these melts moved from their high-pressure reservoirs, they gave rise to either gabbroic or troctolitic cumulate sequences. Fractionation predominantly of olivine+pyroxene+plagioclase occurred in the gabbroic sequences (Hinckley Range, Michael Hills–Latitude Hill, Mount Davies, Cavenagh Range), whereas olivine+plagioclase-dominated fractionation characterises the troctolitic sequences (Bell Rock, Blackstone Range, Jameson Range).

The ultramafic units intercalated within the gabbro-dominated intrusions do not represent local crystal fractionation of the resident gabbroic magmas within the magma chamber, although some in-situ fractionation is evident from upward iron enrichment, for example in the Hinckley Range intrusion (Fig. 85). Furthermore, the intrusions differ from each other with regard to the degree of fractionation of their parent magmas, as represented by the point at which olivine was replaced on the liquidus by orthopyroxene. Thus, in ultramafic sequences the olivine–melt peritectic occurs at Fo_{78-77}, and in primitive gabbroic bodies at Fo_{67-59}, whereas in the troctolitic intrusions olivine persists to Fo_{56-40} (Fig. 118).

An example of an intrusion representative of much of the Giles Complex is the Wingellina Hills body, which consists of a poorly fractionated sequence of dunite, wehrlite, pyroxenite, gabbro, and gabbronorite (Ballhaus & Glikson 1989). Chemical fractionation is limited; olivine ranges from Fo_{89} to Fo_{77}, below which it is replaced on the liquidus by orthopyroxene. Microprobe data have demonstrated a multiple-intrusive history for this intrusion, with batches of olivine–spinel-saturated parent magma periodically emplaced into cooler and more evolved orthopyroxene–clinopyroxene–plagioclase-saturated resident magma (see below). Intrusive events are recognised by coarse-grained ultramafic orthocumulate horizons resting on partly resorbed fine-grained footwalls of fractionated gabbronoritic adcumulates (Fig. 62). These contacts are marked by sharp reversals in the compositions of olivine, plagioclase, and clinopyroxene.

Some major results of petrological studies of the Giles Complex (Ballhaus & Glikson 1989, 1995; Ballhaus & Berry 1990; Ballhaus 1993) are summarised below:

1. The layered mafic–ultramafic bodies experienced a multiple-intrusive history, as documented in Wingellina Hills, where fractionated gabbronorite resident magma was periodically replenished by batches of more primitive olivine-saturated melt. Similar relationships exist in other bodies with significant ultramafic components, e.g., Murray Range and The Wart.

2. The intrusions crystallised from several distinct parental melts, derived by different degrees of fractionation from a either a single parent magma or, more likely, a range of compositionally similar parent magmas, under a range of P–T conditions prior to emplacement. The *mg* value at which olivine is replaced by orthopyroxene on the liquidus is a function of the silica activity of the melt, which, in turn, reflects the fractionation (and possibly also assimilation) history of the parent magma. The Wingellina Hills, Murray Range, and The Wart intrusions were derived from a near-primitive (i.e., little-fractionated) olivine-normative tholeiitic melt. The Bell Rock, Jameson Range, and Blackstone Range troctolitic bodies were derived from strongly fractionated, relatively silica-undersaturated (strongly olivine-normative, but only slightly hypersthene-normative) melts. The Hinckley Range and Latitude Hill intrusions fall between these extremes, having crystallised from moderately fractionated, near silica-saturated melts.

3. Most of the intrusions display a marked increase in the degrees of fracionation of their cumulus phases within about 200 m of their present upper margins, suggesting that the latter approximate to the original upper intrusive contacts and that each intrusion followed its own liquid line of descent, intermittently interrupted by replenishment.

4. The mafic dyke swarms within the Giles Complex includes compositions that may represent those of the parental precursor and/or derivative magmas of the layered intrusions. Phenocryst compositions and crystallisation sequences in these dykes commonly match those of the host intrusions, although other dykes are clearly unrelated.

5. The intrusions display at least two generations of gabbro: volumetrically minor relict concordant units of microgabbro up to a few metres thick, and massive medium to coarse-grained gabbro. The main intrusive episodes thus appear to have been preceded by small and more rapidly cooled gabbroic pulses.

The above arguments suggest that the present structural pattern of the layered intrusions closely reflects the original distribution of the sill-like magmatic bodies, i.e., they are not tectonic slices of an originally continuous Bushveld-type lopolith. Hence, the present sizes of the intrusions probably roughly corresponds to those of individual middle to upper crustal magma chambers. Their geographical distribution may reflect vertical stacking of individual magma chambers within the Mesoproterozoic crustal section. This distribution may well have been controlled by magma density, i.e., buoyancy differences between the magma and surrounding crust. The parental liquids to the gabbroic and troctolitic sequences would have intruded shallower crustal levels than the denser, primitive mantle-derived liquids, which ponded in deeper levels of the crust. Intrusions with similar parentage tend to occur in belts parallel to the regional layering in the country rocks: (1) peridotite and pyroxenite-dominated intrusions along the north-eastern margin of the Tomkinson Ranges (i.e., Murray Range, Ewarara, Claude Hills, Gosse Pile), (2) gabbro-dominated intrusions with significant to minor pyroxenite located south of the ultramafic bodies (i.e., Kalka, Mount Davies, Wingellina Hills, Hinckley Range, Michael Hills, The Wart), and (3) troctolitic intrusions in the southern and western parts of the western Musgrave Block (i.e., Bell Rock, Blackstone Range, Jameson Range). That the exposed crustal section shallows from the Woodroffe Thrust in the northeast to the southwest is implicit in this model.

A corollary of the high-pressure fractionation model for the Giles Complex is that pyroxene-dominated intrusions may be present at lower crustal levels. Such high-pressure cumulates would be characterised by high modal pyroxene/olivine ratios and high-temperature and pressure crystallisation features, such as high Cr and Al contents in pyroxene and highly aluminous spinel. Plagioclase, if present, would be a minor, comparatively Na-rich phase. The only exposed intrusions which even approach these features are the pyroxenite-rich Murray Range, Ewarara, and Gosse Pile intrusions (Goode & Krieg 1967; Moore 1971a, b; Goode & Moore 1975).

The most significant known mineral deposits in the western Musgrave Block are associated with Giles Complex intrusions. Nickeliferous laterites and ochres occur in shear zones in pyroxenite and dunite near Wingellina (Sprigg & Rochow 1975) and elsewhere, and V-rich titano-magnetite layers, containing from 0.71 to 1.40 precent V_2O_5, occur mainly in the troctolitic bodies, particularly the Jameson Range intrusion (Daniels 1974).

Evaluation of prospects for the Giles Complex having

potential for magmatic chromite–sulphide–PGE (platinum-group elements) mineralisation must await more comprehensive studies of trace elements, including PGE and S. However, such prospects are probably limited, as the Giles Complex has important differences from economically important complexes, such as the Bushveld, Great Dyke, and Stillwater intrusions (cf. Naldrett et al. 1987). Cumulate textures illustrated by Ballhaus (1993) suggest that the Giles Complex intrusions cooled faster than these layered intrusions, giving less scope for efficient accumulation of incompatible elements, such as the PGE (see Morse 1986 for cumulate growth mechanisms). Limited S data suggest that the parent magmas were S-saturated, or nearly so, also restricting the likelihood of significant PGE concentration during fractionation (see economic geology section). Chromitite layers, commonly spatially associated with stratiform sulphide–PGE mineralisation, are rare, probably because the melt was depleted in Cr during early high-pressure clinopyroxene fractionation (cf. Goode & Moore 1975). Any sulphide–PGE mineralisation present in the Giles Complex is likely to be restricted to specific cumulate sequences, in view of the discrete nature of individual intrusive bodies.

Magma mixing in layered intrusions

It is widely accepted that many layered gabbroic intrusions have formed by multiple intrusion of separate magma batches (Irvine et al. 1983; Naldrett et al. 1987). Whereas the precise stratigraphic interval at which new influxes of magma occurred may be difficult to identify because of mixing and/or fractionation effects, such new magma pulses are generally indicated by mineralogical reversals which reflect injection of magma which is less fractionated than the host rocks. Some interlayered cumulate pyroxenite–anorthosite sequences, such as in the Bushveld and Stillwater Complexes, imply derivation by mixing of at least two unrelated magma series (Barnes & Naldrett 1985).

In the Giles Complex, the Wingellina Hills gabbro/pyroxenite intrusion provides a good example of periodic replenishment by a primitive liquid (Ballhaus & Glikson 1989). A wide range of cumulates can be derived by sequential olivine–pyroxene fractionation of a single olivine-saturated parent melt and/or mixing between liquids of different degrees of differentiation. Ultramafic cumulates were derived directly from major influxes of olivine-saturated primitive melt, gradually evolving to wehrlite, olivine gabbro, and fractionated leucocratic gabbronorite. The hybrid gabbronorite–pyroxenite footwall (Fig. 61) suggests that each major pulse of new melt was preceded by a gradually increasing number of small batches until sufficient magma was available to form a laterally continuous ultramafic unit.

Differentiation and mixing paths of resident and replenishing melt components are illustrated in the system olivine–clinopyroxene–plagioclase–quartz (Ol–Cpx–Pl–Qz, Figs 119, 120). The phase boundaries in Figure 119 were extrapolated graphically to complex multicomponent melts from the simple system study of Presnall et al. (1978). Apart from Cr, additional components do not greatly alter the morphology of the phase diagram relative to the simple system, at least at low pressures. The effects of Fe and Na are to suppress spinel and olivine stabilities relative to clinopyroxene and plagioclase (Longhi & Pan 1988). Figure 119 shows two sections through the system at different silica contents, which cover the range of chemical fractionation observed. The melt parental to the gabbroic units, i.e., the resident melt, started to crystallise at position P and gradually evolved towards the Qz apex along a line connecting P and P′, the trace of the Ol(Opx)–Cpx–Pl cotectic. The first cumulates to form were magnesian olivine gabbros (P), and, as the liquid progressed along the Ol(Opx)–Cpx–Pl cotectic, olivine was replaced by orthopyroxene. The most fractionated cumulates separated from a melt (P′) and contain orthopyroxene phenocrysts in a leucocratic matrix of plagioclase and clinopyroxene (gabbronorite).

The composition of the primitive parent melt is less clear. The great abundance of olivine and clinopyroxene in ultramafic cycles suggests a position within the olivine stability field above the trajectory from the Ol apex to P (e.g., position U

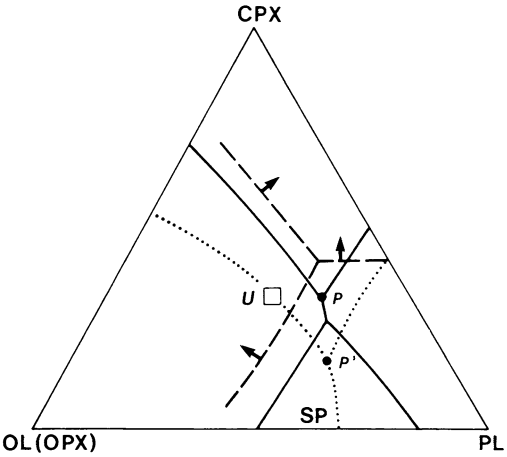

Figure 119. Two sections through the system olivine–clinopyroxene–plagioclase–quartz for different SiO_2 contents (solid and dotted phase boundaries). The solid phase boundaries represent a section close to the plane Ol–Cpx–Pl, to illustrate the position of the parent liquid U and its fractionation path to P; the dotted lines are a section through Opx–Cpx–Plg to show the position of the most fractionated resident liquid P′. The phase boundaries are extrapolated graphically from Presnall et al. (1978), and the effects of iron and sodium are schematically included using the data of Longhi & Pan (1988). The dashed lines are hypothetical phase boundaries illustrating the effect of undercooling on the morphology of the system; the arrows indicate the directions of the phase boundary shift as undercooling increases (after Ballhaus & Glikson 1989).

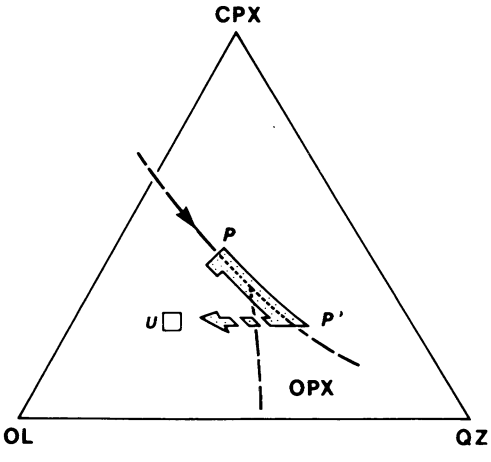

Figure 120. The pseudoternary system olivine–clinopyroxene–quartz after Grove & Kinzler (1986), extrapolated to 5 kb and projected from plagioclase. Liquids in this diagram must be saturated in plagioclase, and the diagram is only strictly applicable to liquids evolving along the Ol(Opx)–Cpx–Pl cotectic (P–P′). The primitive replenishing component U and hybrids between U and P′ are slightly shifted off the plagioclase stability field. The gradual reversal from orthopyroxene to olivine at the base of ultramafic cycles (Fig. 61) is explained by mixing between the most evolved liquid P′ and the added component U (after Ballhaus & Glikson 1989).

in Fig. 119). Fractional crystallisation along an olivine control line would then give the observed cumulate sequence:

(1) olivine cumulates with intercumulus clinopyroxene and plagioclase;
(2) olivine–clinopyroxene cumulates when the fractionation path intersected the cotectic; and
(3) olivine gabbro when the melt reaches position P.

The presence of cumulus spinel in the most refractory olivine cumulates, however, seemingly contrasts with a parental melt of composition U. Where it occurs, cumulus spinel is at least the second phase, and locally the first phase, after olivine. Clinopyroxene is invariably later than spinel. To crystallise spinel after olivine, the parent melt in Figure 119 should be situated below a line connecting the Ol apex with the piercing point Ol–Sp–Pl. However, any such parent is unlikely to yield significant amounts of wehrlite, but would mainly fractionate plagioclase after olivine and spinel. It thus appears that the spinel volume was temporarily expanded so that the Ol–Pl cotectic was replaced by a Cpx–Sp cotectic when the olivine–spinel orthocumulates formed (e.g., dashed lines in Fig. 119). A possible explanation for this effect is metastable spinel nucleation due to undercooling, so that a primitive undercooled melt at U can crystallise spinel after olivine during an initial period of rapid cooling. The metastable spinel largely reacted with the evolving melt and is commonly only preserved within olivine or pyroxene grains (Ballhaus & Glikson 1989).

The basal orthopyroxene-rich pyroxenite units of the Wingellina Hills intrusion cannot have been derived from a liquid of composition U. A parent melt to these cumulates would have to have been of siliceous high magnesian composition to crystallise En_{85} as the first liquidus phase. Goode & Moore (1975) suggested that equivalent rock types at Ewarara and Gosse Pile are high-pressure cumulates, because pressure stabilises orthopyroxene relative to olivine and shifts the reaction relationships to higher *mg* numbers (Green & Ringwood 1967a). However, in the Wingellina Hills intrusion, olivine re-appeared on the liquidus shortly after formation of the basal orthopyroxenites, without a concomitant increase in *mg* number. The local persistence of orthopyroxene to very magnesian compositions is only seen at interfaces between gabbronoritic and ultramafic cumulates, and is more easily explained by localised mixing of the primitive melt layer with highly evolved silica-rich residual melt parental to gabbronorites. This is shown schematically in Figure 120, where the mixing line between U and P′ extends across the orthopyroxene stability field, and the most heavily contaminated melt fractions crystallise orthopyroxene. Any further fresh melt addition progressively dilutes the influence of contaminant P′, and the corresponding cumulates gradually turn into wherlites and finally peridotites.

Similar relationships to those in the Wingellina Hills intrusion can be observed in other layered mafic–ultramafic bodies, such as The Wart and Michael Hills intrusions.

Granitic rocks

A variety of felsic intrusive rocks, ranging from veins and dykes to small plutons, crops out in the western Tomkinson Ranges (Fig. 121). Most are of granitic (s.s.) composition, with subordinate quartz monzodiorite, quartz monzonite, and quartz syenite; granodiorite and tonalite appear to be rare or absent (Tables 6, 7; Sheraton & Sun 1995). Apparent back intrusion relationships and a spatial association with Giles Complex intrusions (Stewart & Glikson 1991; Clarke 1992; Clarke et al. 1995a) suggest that emplacement of some of these granitoids was closely associated with, and followed immediately after, that of the Giles Complex (i.e., they are post-D_2 and pre-D_3). In the western Champ de Mars area (Fig. 122), south of the Hinckley Range, three main varieties — orthopyroxene granite ('charnockite'), rapakivi granite, and porphyritic ('megacrystic') to even-grained granite — were recognised by Clarke (1992), who considered the more melanocratic varieties of orthopyroxene and rapakivi granite to have been derived by contamination of porphyritic granite with mafic material. However, some foliated orthopyroxene granitoids were shown to be of pre-Giles Complex age (post-D_1 and pre-D_2), and many post-D_2 porphyritic to rapakivi granites are also pre-Giles (1188±4 Ma, Sun et al. 1996a). Farther west, south of the Blackstone and Bell Rock Ranges, mostly biotite-bearing granitic rocks form the basement to the mafic to felsic volcanics (and subordinate sedimentary rocks) of the Tollu Group of the Bentley Supergroup. Granitic rocks are

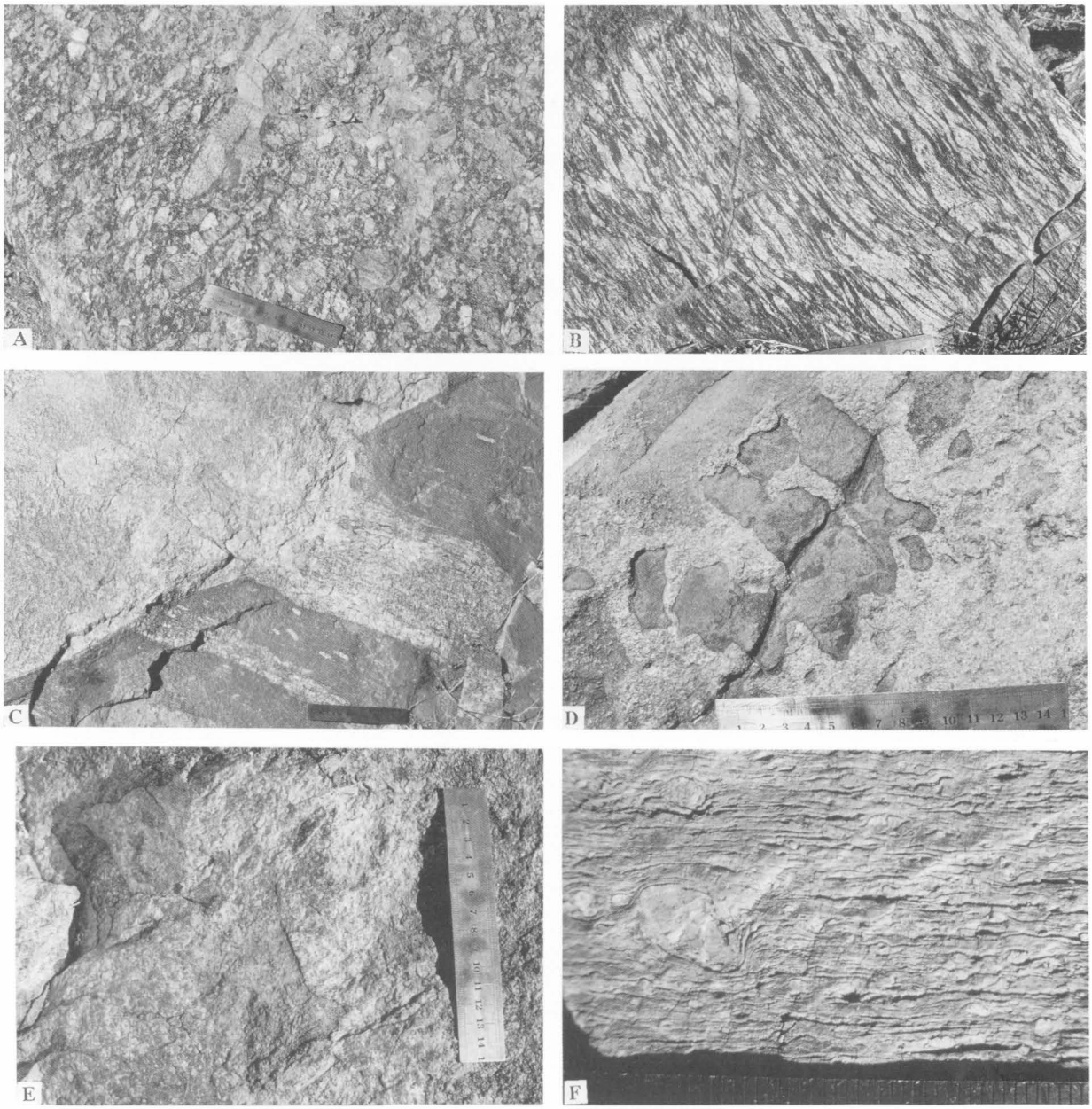

Figure 121. Outcrops of granitoids, western Tomkinson Ranges. (A) Megacrystic (rapakivi) granite, with xenolith of felsic granulite or microgranite, Champ de Mars valley. (B) Intermediate orthogneiss (augen gneiss), basement to Bentley Supergroup, south of Blackstone Range. (C) Layered porphyritic granite and microgranite, intruded by leucogranite (upper left), basement to Bentley Supergroup, south of Blackstone Range. (D) Mafic xenoliths in porphyritic granite, south of Latitude Hill. (E) Xenoliths of quartzite in recrystallised felsic granulite or granite, south of Latitude Hill. (F) Mylonitised granite, south of Latitude Hill.

also common north and west of Mount Aloysius, in the Morgan Range–Mount Fanny–Mount Daisy Bates–Mount Gosse area (Fig. 2), and include rapakivi varieties like those of the Champ de Mars area (Daniels 1972; Stewart 1995b).

In this section, granitic intrusives of the western Musgrave Block are discussed in terms of four major groups: (1) foliated, post-D_1, pre-D_2 orthopyroxene granitoids ('charnockites'), (2) post-D_2 porphyritic and rapakivi hornblende–biotite granitoids, including dykes, of the Hinckley Range area, (3) quartz syenites of Mount Aloysius, and (4) granites of the basement to the Bentley Supergroup.

Pre-D_2 orthopyroxene granitoids

Orthopyroxene-bearing granite, quartz monzonite, and quartz monzodiorite (charnockites of Clarke et al. 1995a) crop out near the Mount Davies and Kalka layered intrusions, in the western Hinckley Range, and in areas flanking the Murray and Blackstone Ranges. Biotite granite gneiss at Minno (about 10 km northwest of Mount Davies), emplaced before D_2 and probably the deformed equivalent of nearby orthopyroxene granite, has given a zircon U–Pb ion microprobe age of 1198±6 Ma (Sun et al. 1996a), within error of the Rb-Sr age (1204±17 Ma, Gray 1978).

In the Charnockite Flats and Champ de Mars areas (west and south of the Hinckley Range, respectively), small, locally discordant pods and larger stocks of foliated, locally porphyritic granite contain up to 3 percent of orthopyroxene, with smaller amounts of reddish-brown biotite and, less commonly, greenish-brown hornblende and clinopyroxene. Perthite is generally more abundant than (commonly antiperthitic) oligoclase–andesine. Accessory minerals comprise Fe–Ti oxides, apatite, and zircon. These pre-D_2 granitoids are petrographically distinct from post-D_2 orthopyroxene granitoids, with more biotite and hornblende, which are spatially associated with, and apparently genetically related to, the rapakivi–porphyritic granitoids (see below). Quartz monzodiorite intruding metamorphics southwest of Mount Davies contains more (5–7%) orthopyroxene and clinopyroxene (up to 3%), and feldspar is predominantly antiperthitic andesine; granophyric intergrowths of quartz and K-feldspar are conspicuous. Orthopyroxene granite in the Murray Range area contains mesoperthite.

All the analysed orthopyroxene granites (Table 6; Fig. 123) are I-type. They are metaluminous or only slightly peraluminous (ASI < 1.1) and define a trend of increasing ASI with SiO_2 (Fig. 124). Most rocks do not show Y (and, by implication, HREE) depletion (Figs 125, 126), and spidergrams are markedly irregular, with negative Nb, Sr, P, and Ti anomalies (Fig. 127). These features are consistent with melting of plagioclase-rich, predominantly felsic crustal rocks (Tarney et al. 1987; Sheraton & Black 1988). In contrast, quartz monzodiorites intruding metamorphic rocks in the Mount Davies area do not have Sr anomalies (Fig. 127), and probably represent new felsic crust derived either directly from the mantle (Stern & Hanson 1991), by fractionation of mantle-derived magma, or by hydrous melting of a plagioclase-poor mafic source (e.g., amphibolite: Sheraton & Black 1983). Most orthopyroxene granites have lower Rb, Th, U, Zr, Nb, La, Ce, Y, and Ga/Al, and higher K/Rb than the rapakivi–porphyritic hornblende–biotite granitoid suite of the Champ

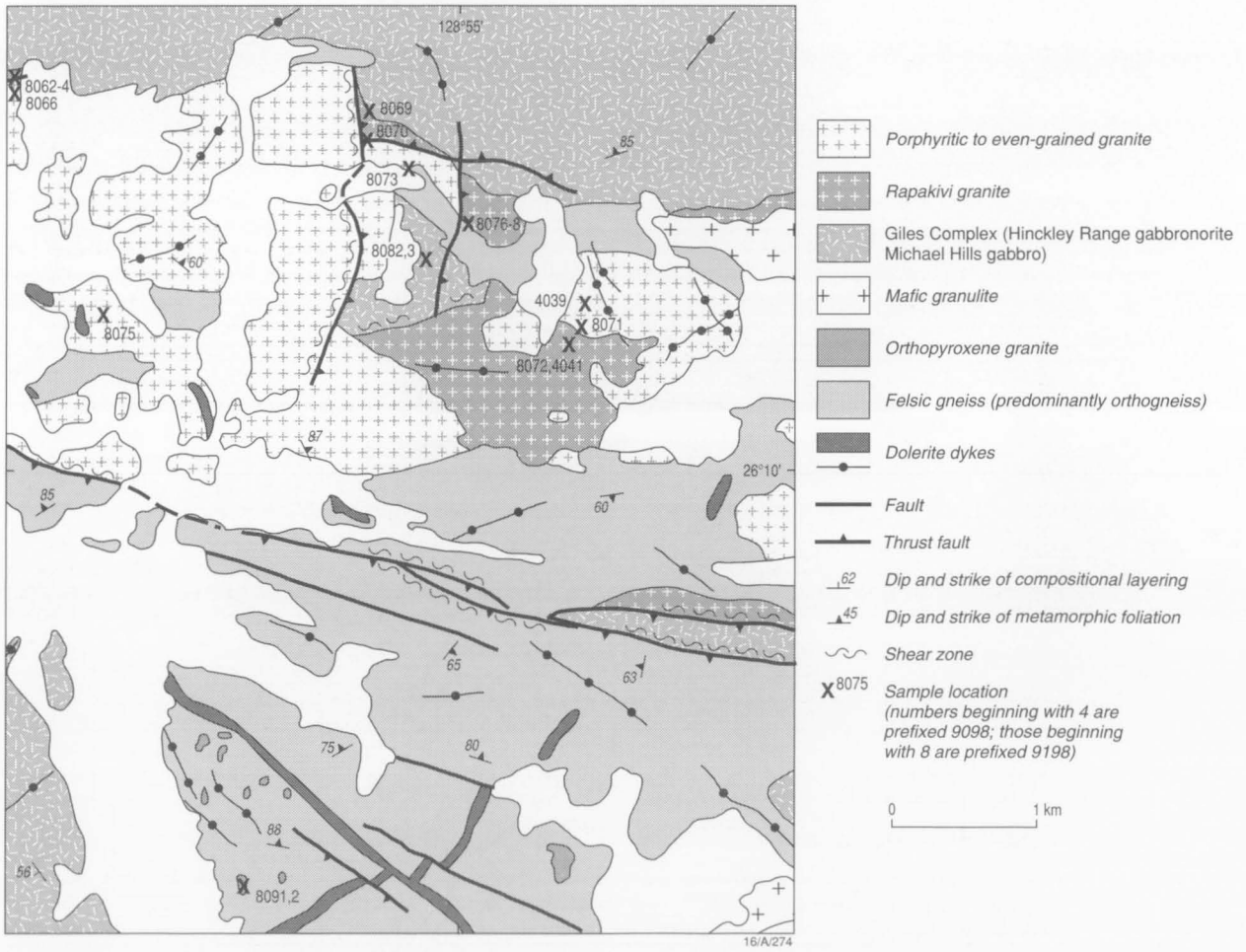

Figure 122. Geological map of the western Champ de Mars area, south of the Hinckley Range, showing sample localities of intrusive rocks.

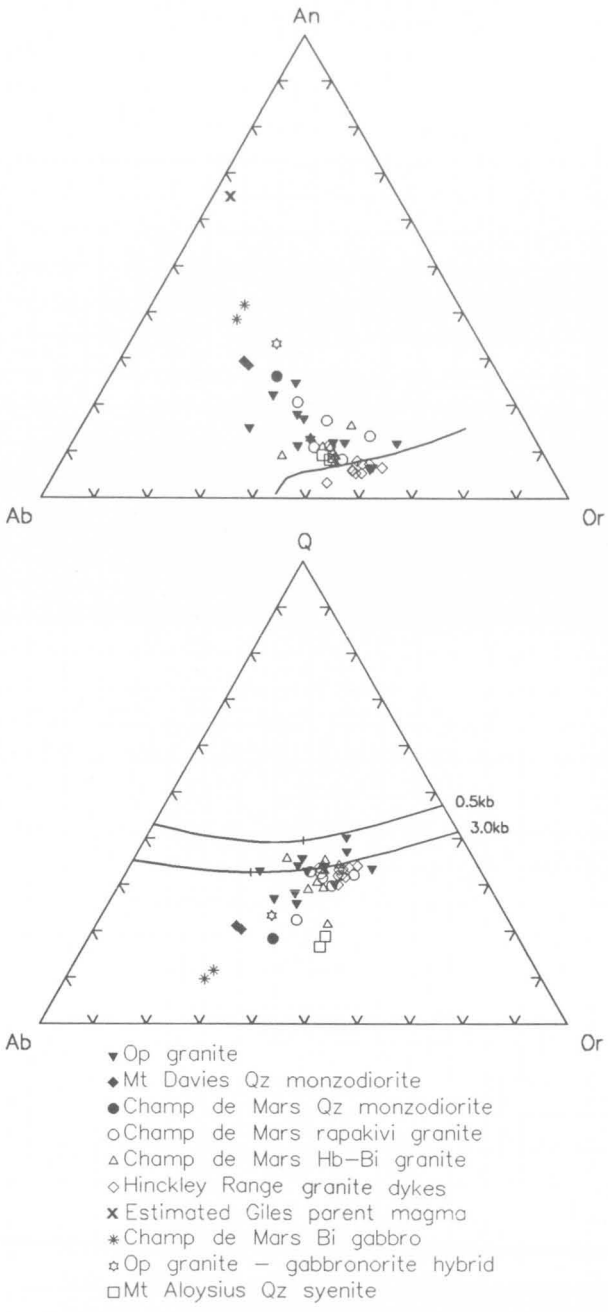

Figure 123. Normative Ab–Or–An and Q–Ab–Or diagrams for granitoids from the western Tomkinson Ranges. The former shows the plagioclase–alkali feldspar field boundary at 1 kbar P_{H2O}, projected onto the Ab–Or–An face of the tetrahedron (after James & Hamilton 1969).

de Mars area (Fig. 125), and are, therefore, unrelated. Indeed, as already pointed out, most or all are significantly older (pre-D_2).

Post-D_2 hornblende–biotite granitoids of the Hinckley Range area

These include the porphyritic and rapakivi granites in the Champ de Mars area, some of charnockitic affinities (Clarke et al. 1995a), as well as granite dykes cutting the western part of the Hinckley Range gabbronorite intrusion. Rapakivi granite (Fig. 121A) forms stocks and dykes, commonly associated

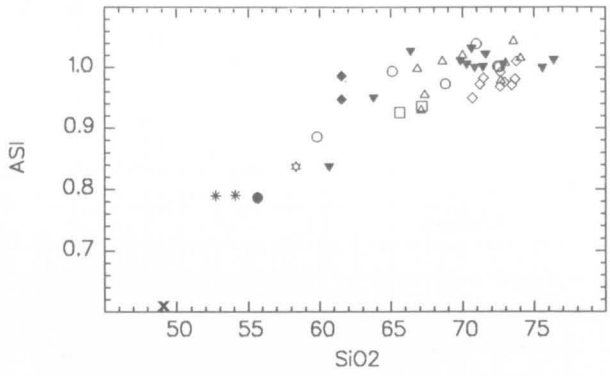

Figure 124. Plot of alumina saturation index against SiO_2 for granitoids from the western Tomkinson Ranges. Symbols as in Figure 123.

with, and gradational into, porphyritic and even-grained granite. This suggests that these petrographically rather diverse rocks are genetically closely related. However, they are not all of the same age. A porphyritic granite (91988071) from the relatively large intrusive body west of Champ de Mars (Fig. 122) has been dated by the U–Pb zircon ion microprobe technique at 1188±4 Ma; in contrast, a rapakivi clinopyroxene–biotite granite dyke (91988064), which clearly intrudes the Giles Complex, is 1068±6 Ma old (Sun et al. 1996a, b). The latter age is only slightly younger than that of the Giles Complex, consistent with formation of these small granitic bodies (mostly dykes and veins) having been related to emplacement of the mafic–ultramafic intrusions.

Rapakivi granite (Figs 121A, 158E) contains corroded megacrysts of perthitic K-feldspar (commonly microcline), rimmed by relatively fine-grained plagioclase, associated with, or including, hornblende, pyroxene, or quartz (Fig. 128). However, the distribution of mantled K-feldspars is markedly irregular, and some K-feldspar grains, as well as oligoclase–andesine phenocrysts, are unmantled. Rapakivi granite, which grades into quartz monzonite, typically contains brownish-green hornblende (up to 10%) and reddish-brown biotite (up to 5%), with clinopyroxene (up to 3%) and minor orthopyroxene in some rocks. Accessories comprise apatite, zircon, Fe–Ti oxides, and ?chevkinite. Most granites were extensively recrystallised during D_3 and later events, more extreme deformation resulting in the formation of augen gneiss. Small amounts of pale golden garnet are widespread in the more deformed rocks, whereas pyroxene appears to be confined to less deformed granitoids. Much, although by no means all, of the biotite and hornblende forms fine-grained aggregates with quartz, presumably replacing pyroxene.

Porphyritic to even-grained granite (Fig. 121D) is petrographically quite similar to the rapakivi granite, apart from the absence of mantled K-feldspars; perthitic K-feldspar phenocrysts are commonly partly resorbed. Up to 4 percent of dark brownish-green primary or paler green secondary hornblende is present in some granites, whereas dark brown to reddish-brown biotite (up to 4%) is ubiquitous; orthopyroxene (up to 2%) and relict clinopyroxene occur in a few rocks. Many granites are much recrystallised and small amounts of secondary garnet are common. Accessory minerals comprise Fe–Ti oxides, apatite, zircon, allanite, and, less commonly, titanite.

Locally porphyritic granite dykes which intrude the Hinckley Range gabbronorite in the western Hinckley Range contain biotite (up to 2%), hornblende (up to 3%), and rare clinopyroxene, as well as accessory Fe–Ti oxides, apatite, zircon, sphene, and rare allanite and ?chevkinite. They may be related to the younger of the hornblende–biotite granitoids, having

Table 6. Chemical analyses of representative gabbroic and granitic rocks from the Tomkinson Ranges. Abbreviations as in Table 5.

Sample no.	*91980267A*	*91985001A*	*91988092*	*91988100*		*91988082*	*91988063*	*91988073*
Locality	*SW of Mount Davies*	*North of Ewarara Range*	*Western Champ de Mars*	*Western Champ de Mars*	*Estimated Giles Complex Parent magma**	*Western Champ de Mars*	*Western Champ de Mars*	*Western Champ de Mars*
Lithology	*Bt-Cp-Op grano-diorite*	*Cp-Op granite gneiss*	*Foliated Op granite*	*Porphyrit. Op granite*		*Cp-Op-Bt-Hb gabbro*	*Granite/ granulite hybrid*	*Op-Bt-Cp quartz monzodior.*
SiO_2	61.54	69.85	75.60	72.85	49.0	52.70	58.33	55.66
TiO_2	0.68	0.42	0.24	0.20	0.8	1.87	1.13	2.38
Al_2O_3	17.20	14.40	12.40	13.75	14.0	15.32	15.44	13.96
Fe_2O_3	2.20	1.48	0.45	1.00	–	2.39	3.43	2.98
FeO	3.00	1.25	0.54	1.14	11.0	8.62	4.91	7.71
MnO	0.07	0.05	0.02	0.05	0.17	0.16	0.12	0.14
MgO	2.35	0.32	0.26	0.30	12.0	5.02	3.39	2.63
CaO	5.04	1.79	0.83	1.59	11.0	7.72	6.14	6.10
Na_2O	3.93	2.95	2.56	3.53	1.6	2.79	2.85	2.96
K_2O	2.85	5.90	6.23	4.74	0.3	1.75	2.95	3.16
P_2O_5	0.23	0.11	0.03	0.07	0.09	0.47	0.25	0.68
LOI	0.44	0.41	0.32	0.35	–	1.15	0.68	0.88
Rest	0.48	0.29	0.18	0.17	–	0.38	0.32	0.46
Total	**100.01**	**99.22**	**99.66**	**99.74**	**–**	**100.34**	**99.94**	**99.70**
O=F,S,Cl	0.04	0.00	0.00	0.00	–	0.03	0.01	0.05
Total	**99.96**	**99.22**	**99.66**	**99.74**	**–**	**100.30**	**99.93**	**99.65**
	C.I.P.W. norms							
Q	13.46	25.90	34.67	30.05	–	4.44	12.67	9.86
C	–	0.17	0.01	0.09	–	–	–	–
Or	16.84	34.86	36.81	28.01	1.8	10.34	17.43	18.67
Ab	33.25	24.96	21.66	29.87	13.5	23.61	24.12	25.05
An	20.87	8.16	3.92	7.43	30.1	24.11	20.62	15.47
Di	2.12	–	–	–	19.3	9.16	6.65	8.62
Hy	7.52	1.27	0.91	1.78	20.0	19.04	9.74	10.27
Ol	–	–	–	–	11.0	–	–	–
Mt	3.19	2.15	0.65	1.45	2.7	3.47	4.97	4.32
Il	1.29	0.80	0.46	0.38	1.5	3.55	2.15	4.52
Ap	0.54	0.26	0.07	0.17	0.2	1.11	0.59	1.61
mg	58.3	31.3	46.2	31.9	69.6	50.9	55.2	37.8
	Trace elements in parts per million							
Ba	1725	1525	723	655	100	637	928	1042
Li	7	2	6	6	–	19	6	1
Rb	73	165	203	190	–	73	67	115
Sr	733	164	161	104	200	293	198	248
Pb	24	28	43	54	–	20	24	32
Th	<2	3	26	9	–	14	5	27
U	<0.5	<0.5	1.0	3.0	–	2.5	<0.5	1.5
Zr	264	349	121	152	70	444	350	491
Hf	6	11	2	3	-	10	9	11
Nb	8	3	6	3	3	19	15	28
Y	31	24	18	45	18	49	60	83
La	43	27	44	50	7	81	64	96
Ce	79	46	78	79	17	148	116	209
Nd	32	19	27	33	10	67	52	97
Pr	5	5	6	8	–	11	12	28
Sc	13	5	3	3	–	30	24	25
V	66	18	8	11	–	197	158	197
Cr	26	3	4	4	–	55	93	11
Ni	22	10	3	1	–	51	59	14
Cu	21	7	<1	<1	–	27	78	16
Zn	76	51	17	49	–	139	90	147
Sn	4	4	3	<2	–	<2	3	2
Ga	21	19	12	19	–	19	20	23
S	900	30	10	10	–	690	200	920
Be	3	1	<1	2	–	2	3	<1

* From Sun & Sheraton (1992); norm calculated assuming $Fe^{2+} = 0.85Fe^{total}$.

Sample no.	*91988064*	*91988072*	*91988076*	*90980506*	*90984039*	*91988070*	*91988060*	*91988044*
Locality	*Western Champ de Mars*	*Western Champ de Mars*	*Western Champ de Mars*	*Champ de Mars*	*Western Champ de Mars*	*Western Champ de Mars*	*West Hinckley Range*	*Mount Aloysius (west)*
Lithology	*Rapakivi Cp-Bt granite*	*Rapakivi Bt-Hb Qz monzonite*	*Rapakivi Cp-Bt-Hb granite*	*Foliated porphyrit. Bt granite*	*Porphyrit. Bt granite*	*Cp-Bt-Hb granite*	*Foliated Bt granite dyke*	*Ol-Hb-Cp quartz syenite*
SiO_2	68.79	59.80	72.57	73.56	70.01	66.86	73.76	65.63
TiO_2	0.68	1.74	0.18	0.23	0.47	0.98	0.39	0.55
Al_2O_3	13.69	14.07	14.21	13.57	14.13	13.21	13.01	15.52
Fe_2O_3	2.77	2.23	0.76	0.55	1.38	3.42	1.44	1.17
FeO	1.40	6.29	0.55	0.85	1.63	2.93	0.63	3.31
MnO	0.06	0.12	0.02	0.02	0.05	0.10	0.02	0.09
MgO	0.74	1.73	0.15	0.28	0.57	0.60	0.30	0.27
CaO	2.17	4.49	1.25	1.23	1.64	2.36	.79	2.28
Na_2O	2.39	3.03	3.22	3.73	3.25	2.44	2.83	3.77
K_2O	6.08	4.04	6.24	4.39	5.37	5.27	6.38	6.22
P_2O_5	0.16	0.68	0.05	0.05	0.12	0.32	0.05	0.13
LOI	0.42	0.96	0.44	0.50	0.46	0.45	0.36	0.34
Rest	0.29	0.49	0.23	0.17	0.35	0.37	0.22	0.45
Total	**99.64**	**99.67**	**99.87**	**99.13**	**99.43**	**99.31**	**100.18**	**99.73**
O=F,S,Cl	0.00	0.00	0.00	0.00	0.00	0.00	0.00	0.01
Total	**99.64**	**99.67**	**99.87**	**99.13**	**99.43**	**99.30**	**100.18**	**99.72**
	C.I.P.W. norms							
Q	26.55	14.29	27.14	31.80	26.00	26.96	30.88	13.72
C	–	–	0.01	0.57	0.28	–	0.13	–
Or	35.93	23.87	36.87	25.94	31.73	31.14	37.70	36.76
Ab	20.22	25.64	27.25	31.56	27.50	20.65	23.95	31.90
An	8.67	12.86	5.87	5.78	7.35	9.53	3.59	7.06
Di	0.82	4.18	-	-	-	0.07	-	2.97
Hy	1.46	9.26	0.50	1.46	2.59	2.58	0.75	3.49
Ol	–	–	–	–	–	–	–	–
Mt	2.73	3.23	1.10	0.80	2.00	4.96	0.96	1.70
Il	1.29	3.30	0.34	0.44	0.89	1.86	0.74	1.04
Ap	0.38	1.61	0.12	0.12	0.28	0.76	0.12	0.31
mg	48.5	32.9	32.7	37.0	38.4	26.7	45.9	12.7
	Trace elements in parts per million							
Ba	1187	1431	791	556	1123	1429	409	1622
Li	6	14	12	39	10	5	10	9
Rb	177	129	273	265	264	186	340	213
Sr	124	257	102	89	166	137	35	141
Pb	39	41	49	48	63	45	44	48
Th	16	16	47	15	158	19	69	25
U	1.0	2.5	2.0	1.0	9.5	1.0	10.5	<0.5
Hf	9	18	4	4	11	13	11	16
Zr	347	777	212	171	401	542	345	712
Nb	12	44	12	11	22	12	25	30
Y	51	122	48	34	83	71	74	100
La	74	172	78	20	106	87	94	136
Ce	136	393	162	39	307	171	170	268
Nd	58	168	67	18	95	81	61	119
Pr	12	37	18	4	22	19	16	27
Sc	8	22	4	2	6	12	5	6
V	36	112	5	8	23	22	12	2
Cr	9	8	<1	3	4	3	4	3
Ni	8	7	2	3	2	5	8	2
Cu	12	13	<1	<1	4	17	5	2
Zn	55	152	31	31	72	120	38	88
Sn	3	2	3	2	3	4	8	4
Ga	17	21	20	20	18	19	16	25
S	70	60	40	20	<100	70	20	180
Be	3	5	4	3	4	4	4	3

given a U-Pb zircon age of 1052±11 Ma (Sun et al. 1996a).

There are no clear chemical differences between the various hornblende–biotite granitoids in the Champ de Mars area (Table 6), even though they include rocks of significantly different ages. Rapakivi and porphyritic to even-grained granites have, with few exceptions, similar ranges of SiO_2 and trace element abundances, although both types are compositionally rather varied. However, as a group, they tend, for a given SiO_2 content, to be more enriched in many incompatible elements (Rb, Th, U, Zr, Nb, La, Ce, and Y) than the pre-D_2 orthopyroxene granites (Fig. 125), which could be explained either by derivation from a different source or by lower degrees of melting of a similar source. Like these orthopyroxene granites, they are metaluminous or slightly peraluminous (I-type, Fig. 124) and show a K-rich trend on an Ab–Or–An diagram (Fig. 123). High HFSE (high field strength elements: Zr, Nb, Y), LREE, and Ga/Al, compared to most granites, suggest A-type ('anorogenic') affinities (Collins et al. 1982; Whalen et al. 1987), in common with other rapakivi granites (Rogers & Greenberg 1990). However, *mg* (atomic 100Mg/(Mg + Fe^{2+})) values (17–48) are not as low as for typical A-types, suggesting that they are not truly anorogenic. Like most rapakivi granites, they are Sr-depleted and Y-undepleted (Fig. 126), and have irregular spidergrams (large negative Nb, Sr, P, and Ti anomalies: Fig. 129), typical of melts derived from felsic crust. Granitic rocks from Mount Daisy Bates and Amy Giles Hill in the Bates 1:100 000 sheet area have very similar chemical features.

Most of these features are explicable in terms of relatively high-temperature partial melting of virtually anhydrous granulite-facies crustal rocks, probably, in some cases, caused by emplacement of Giles Complex mafic–ultramafic intrusions. For example, Zr is relatively soluble in high-temperature melts (Watson & Harrison 1983). Although high Th/U (mostly 10–25) is consistent with melting of a granulite-facies source, absolute abundances of Th and U are much higher than in typical granulite-facies gneisses, ranging up to 158 and 28 ppm, respectively. This feature suggests derivation from a different source (or at least the presence of a distinct ?mantle-derived source component) to that of the orthopyroxene granitoids, because degrees of melting are unlikely to have been significantly lower for these comparatively melanocratic granitoids. Nd isotopic data are consistent with melting of felsic crustal rocks presently exposed in the area, which have similar depleted mantle (DM) model ages (1610–1900 Ma) to those of the granitic rocks (1677–1912 Ma, Table 11; Sun & Sheraton 1992). The relatively potassic compositions of many Hinckley Range granites (Fig. 123) are consistent with the experimental data of Ebadi & Johannes (1991) and Beard et al. (1994), which show that low P_{H2O} melting of felsic crustal rocks produces liquids with high Or/Ab; incorporation of calcic plagioclase (i.e., the An component) into the melt would enhance this effect (James & Hamilton 1969).

Clarke (1992) suggested that the less siliceous rapakivi granitoids were formed by contamination of more felsic magma (which produced the porphyritic granite) by gabbroic material. Nd isotopic data lend some support to this proposal, because the 1188±4 Ma rapakivi granites have slightly younger Nd T_{DM} model ages and higher ε_{Nd} (1781 to 1786, and -2.4 to -2.7, respectively) than porphyritic granites (1877 to 1912, and -3.8, Table 6; Sun & Sheraton 1992). However, apart from the few SiO_2-poor quartz monzonites and quartz monzodiorites, the rapakivi and porphyritic hornblende–biotite granitoids show a wide, but broadly similar, range of SiO_2 content (~65–75%). The two least siliceous (i.e., intermediate) rocks (91988073, an orthopyroxene–biotite–clinopyroxene quartz monzodiorite and 91988072, a rapakivi biotite–hornblende quartz monzonite, Table 6) have abundances of many elements consistent with formation by mixing of mafic and felsic end members, but contents of other elements do not support such a model. In particular, TiO_2, P_2O_5, Zr, Nb, Y, La, and Ce are too high and Al_2O_3, MgO, Cr, and Ni too low for simple mixing. This contrasts with a sample (91988063) of porphyritic gabbronorite containing irregular veins and patches of orthopyroxene granite (i.e., a quartz monzodioritic bulk composition), which has the chemistry (and ε_{Nd} of -1.5) expected of such a hybrid. For example, Cr and Ni are much higher and TiO_2, P_2O_5, Zr, Nb, Y, La, and Ce are lower in this mixed rock than in the other intermediate rocks. A more complex origin for the various intermediate to felsic intrusives is thus indicated.

Spidergrams (Fig. 129) of these two intermediate intrusive rocks (as well as the least siliceous rapakivi granite, 90984041) are quite similar to, although more enriched than, those of two unusually biotite±hornblende-rich gabbronorites (which have similar ε_{Nd} (-2.0) to the rapakivi suite) from a small body about 0.5 km south of the main Hinckley Range gabbronorite intrusion near Champ de Mars (Fig. 122). These biotite–hornblende gabbronorites (91988082, Table 6) are considerably older (1176±5 Ma, S-S. Sun, unpublished data) than the Giles Complex. They are much more enriched than the estimated Giles Complex parent magma (Table 6; Sun & Sheraton 1992), as well as typical non-cumulate samples of Giles gabbronorites, which have much flatter patterns. This might indicate that the biotite-rich gabbronorites and intermediate intrusives (quartz monzonites and quartz monzodiorites) were formed by either progressive contamination (with felsic crustal material) or fractionation of gabbroic magma (cf. Sheraton et al. 1992). Trace element contents and ratios are perhaps more consistent with the latter process, because incompatible element/Zr ratios (e.g., K/Zr, Ba/Zr, Nb/Zr, P/Zr, and Ce/Zr) are essentially constant for the whole range of compositions, whereas at least some of these ratios (e.g., P/Zr) would be expected to decrease upon contamination with felsic crust or a granitic melt. Of the two intermediate rocks, the quartz monzodiorite has a similar S content (920 ppm) to the postulated gabbroic parent, whereas the rapakivi quartz monzonite has much lower S (60 ppm). Unfortunately, without more isotopic data, it is difficult to make more definite correlations between these various rock types.

Although the range of granitic (*s.s.*) rocks could, in theory, have been derived by mixing of an intermediate magma with a felsic end member, this seems unlikely because intermediate compositions are much less common than felsic ones. Moreover, there is some indication of a compositional gap between the intermediate and granitic rocks, and the latter have distinctive, much more irregular, spidergrams with larger Nb anomalies (Fig. 129). Hence, we consider it more likely that most hornblende–biotite granites were derived from a different parent magma (or magmas) to that of the intermediate rocks (quartz monzodiorites and quartz monzonites). Some degree of contamination of felsic magma with mafic material may well have occurred, but much of the chemical variation of the granitic rocks is probably due to other processes, such as crystal fractionation, different extents of melting, cumulate unmixing (Cullers et al. 1993), or combinations of these. The marked decreases of both *mg* and K/Rb with increasing SiO_2 suggest at least some degree of fractional crystallisation.

Biotite–hornblende granite dykes (e.g., 91988060, Table 6) in the western Hinckley Range are quite strongly fractionated (high K_2O, Rb, Th, U, Sn, and Rb/Sr, and low CaO, Na_2O, Ba, Sr, and K/Rb), with highly irregular spidergrams (Fig. 129). Although compositionally similar to the more evolved variants of the Champ de Mars rapakivi and porphyritic granites, they

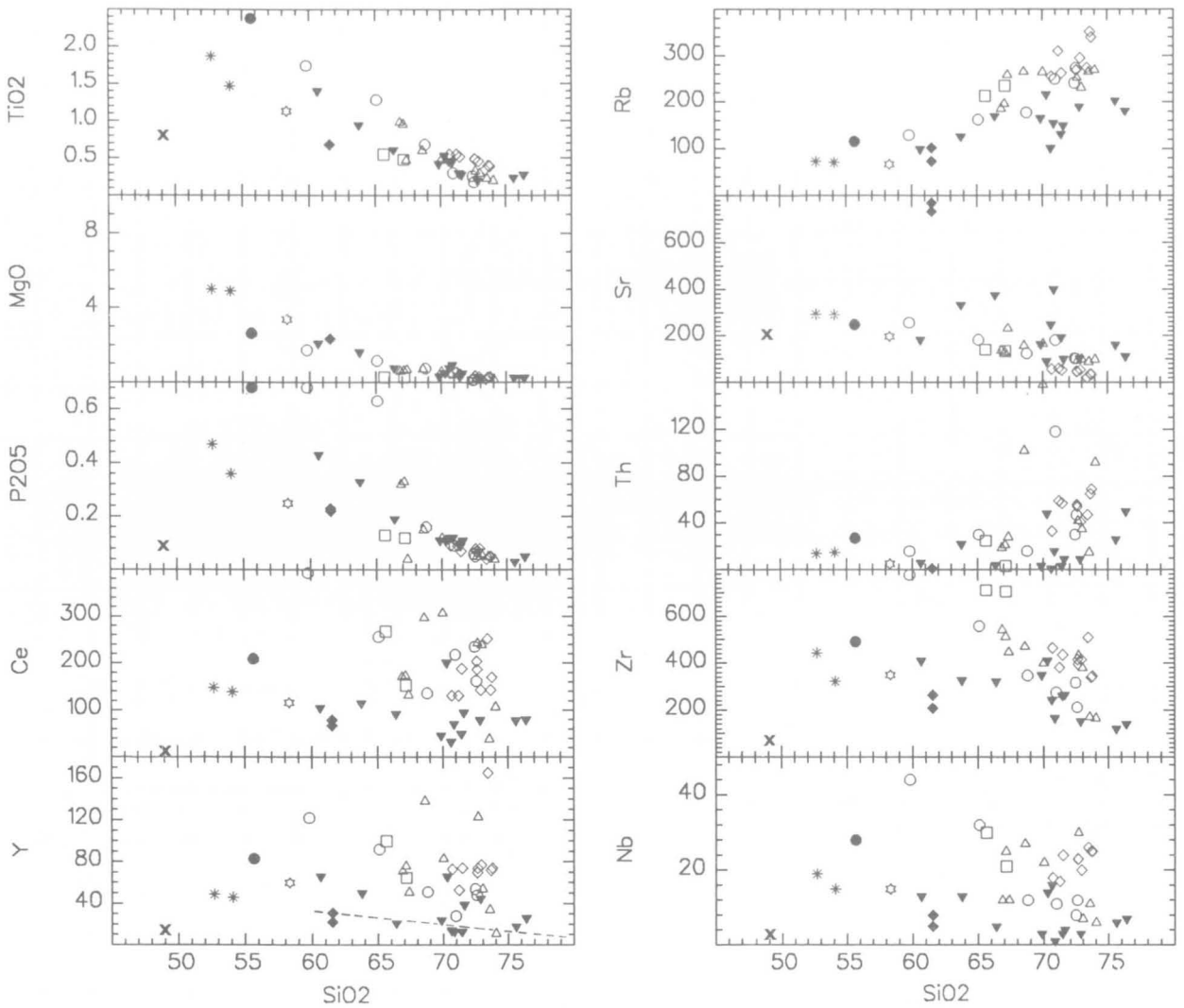

Figure 125. SiO_2 variation diagrams for granitoids from the western Tomkinson Ranges. Symbols as in Figure 123 and boundary between Y-depleted and Y-undepleted orthogneisses from Sheraton & Black (1983).

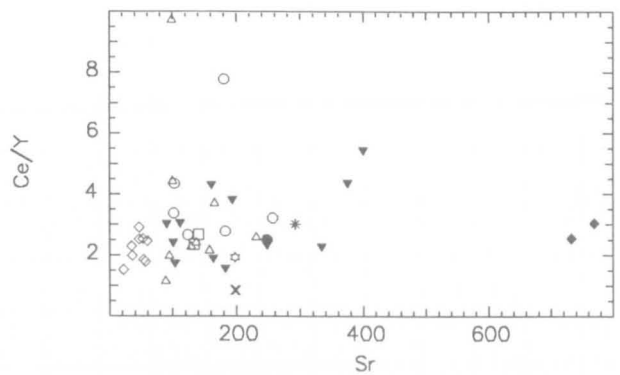

Figure 126. Plot of Ce/Y against Sr for granitoids from the western Tomkinson Ranges. Symbols as in Figure 123.

Figure 127. Spidergrams for orthopyroxene granitoids from the western Tomkinson Ranges.

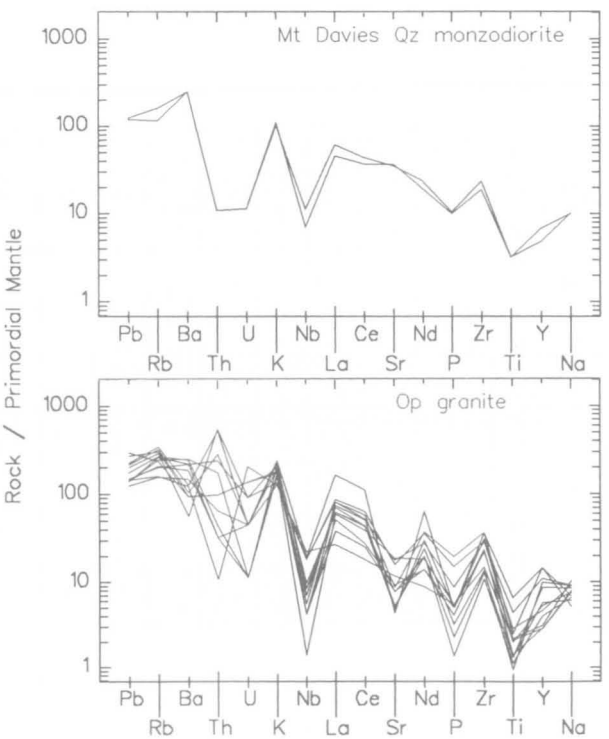

Figure 128. K-feldspar megacryst in rapakivi clinopyroxene–biotite granite dyke, showing irregular overgrowths (right and bottom) and inclusions (top centre) of antiperthitic plagioclase. The K-feldspar has strongly perthitic zones (e.g., left centre). Sample 91988064; western Champ de Mars; crossed polarisers.

have higher Nb, Sn, and ε_{Nd} (-1.8 to -2.5, i.e., 1 to 2 units higher than the latter at 1080 Ma, Table 11), implying the presence of a younger source component.

Quartz syenite of Mount Aloysius

Several small (c. 100 m) stocks of quartz syenite crop out on the western side of Mount Aloysius. The rocks are bluish-grey and unfoliated, and contain clinopyroxene with exsolved blebs and lamellae of orthopyroxene (possibly after pigeonite: ~5%), fayalite (~1%), and minor orthopyroxene, greenish-brown hornblende, and biotite. Orthopyroxene also occurs as granular rims (with clinopyroxene) around primary clinopyroxene. Abundant accessory minerals include Fe–Ti oxides, apatite, zircon, ?chevkinite, and fluorite, and K-feldspar is strongly perthitic. Although there is little evidence of deformation and recrystallisation, the quartz syenite appears to be of similar age (c. 1200 Ma) to the older hornblende–biotite granitoids (S-S. Sun, unpublished data).

The quartz syenites (91988044, Table 6) are highly fractionated (Fig. 130) rocks with high K_2O, Ba, Zr, Nb, Y, La, Ce, and Ga and low MgO, Sr, Cr, Ni, Sc, and V. High HFSE and Ga/Al, and low *mg* (12–13) are all characteristic of A-type granitoids, and are consistent with high-temperature melting of lower crustal granulites (Sheraton & Black 1988), although an origin by fractionation of mafic magma, possibly combined with crustal assimilation, has also been suggested for such syenitic rocks (see various papers in Fitton & Upton 1987; Zhao et al., 1995). Unfortunately, the strong fractionation of the Mount Aloysius quartz syenites complicates attempts to estimate the composition of their parent magma, but the presence of 1300 Ma inherited zircons and ε_{Nd} of -2.0 (similar to those of country rock orthogneisses at 1200 Ma, Table 11) indicates a major crustal component in these rocks. Whatever their origin, the higher Zr (Fig. 125) and much lower *mg* compared to the hornblende–biotite granitoids of the Champ de Mars area implies that they are unrelated.

Granitic rocks of the basement to the Bentley Supergroup

The basement to the predominantly volcanic Bentley Supergroup in the western Musgrave Block consists mainly of biotite granite (Fig. 121B, C). Typical rocks contain dark brown biotite (up to 3%), quartz, slightly perthitic microcline, sericitised oligoclase, and minor Fe–Ti oxides, apatite, zircon, sphene, and, less commonly, allanite, ?chevkinite, and fluorite. Some granites contain K-feldspar phenocrysts and many are foliated. Secondary epidote, chlorite, and muscovite are common. A distinctive fluorite–hornblende granite (91988006), which crops out about 6 km south of Bell Rock, is closely associated with, and may actually intrude (although the contact is not exposed) the Smoke Hill Felsic Volcanics. It contains conspicuous fluorite and is quite strongly foliated, with minor secondary garnet.

In many respects, most of these biotite granites are compositionally similar to the Champ de Mars granitoids (Table 7),

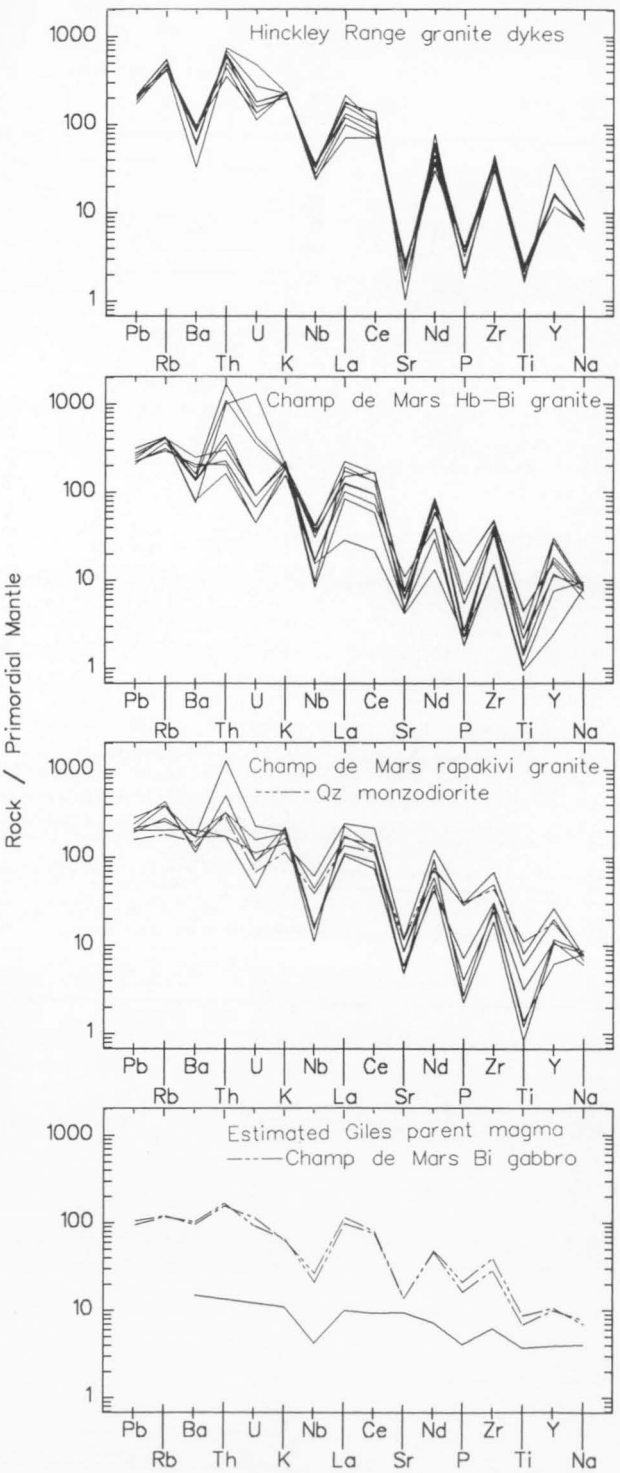

Figure 129. Spidergrams for gabbroic rocks and granitoids from the Hinckley Range area.

Table 7. Chemical analyses of representative granitic rocks from the basement to the Bentley Supergroup in the westernmost Musgrave Block. Abbreviations as in Table 5.

Sample no.	*91988011*	*91989395*	*90984015*	*91988007*	*91988101*	*91988006*
Locality	*McDougall Bluff*	*McDougall Bluff*	*West of Mummawarr. Hill*	*McDougall Bluff*	*West of Bell Rock Range*	*West of Bell Rock Range*
Lithology	*Bt granite*	*Foliated Bt granite*	*Bt granite*	*Slightly porphyrit. Bt granite*	*Porphyrit. Fl-Bt granite*	*Porphyrit. Fl-Hb granite*
Group	*Y-dep.*	*Y-dep.*	*Y-undep.*	*Y-undep.*		
SiO_2	74.37	72.97	74.54	68.00	73.22	72.38
TiO_2	0.18	0.24	0.19	0.62	0.27	0.34
Al_2O_3	13.39	13.45	12.61	14.46	12.57	12.54
Fe_2O_3	0.93	0.81	0.63	1.94	0.84	2.26
FeO	0.15	0.49	1.10	1.16	1.13	1.15
MnO	0.04	0.04	0.04	0.05	0.02	0.05
MgO	0.17	0.32	0.10	0.89	0.22	0.11
CaO	0.99	0.79	0.93	2.34	1.13	1.01
Na_2O	3.74	3.21	2.93	3.54	2.54	4.01
K_2O	4.77	6.06	5.53	4.57	6.28	5.14
P_2O_5	0.05	0.06	0.03	0.22	0.05	0.01
LOI	0.45	0.37	0.79	0.75	0.95	0.42
Rest	0.16	0.19	0.22	0.41	0.37	0.36
Total	**99.39**	**99.00**	**99.64**	**98.95**	**99.59**	**99.78**
O=F,S,Cl	0.00	0.00	0.00	0.02	0.00	0.00
Total	**99.39**	**99.00**	**99.64**	**98.94**	**99.59**	**99.78**
	C.I.P.W. norms					
Q	32.13	29.11	33.70	24.22	31.56	27.93
C	0.39	0.32	0.19	–	–	–
Or	28.19	35.81	32.68	27.01	37.11	30.37
Ab	31.65	27.16	24.79	29.95	21.49	33.93
An	4.58	3.53	4.42	10.07	4.35	1.04
Di	–	–	–	0.08	0.78	0.59
Wo	–	–	–	–	–	1.32
Hy	0.42	0.80	1.51	2.18	1.12	–
Mt	0.09	1.01	0.91	2.10	1.22	2.88
Il	0.34	0.46	0.36	1.18	0.51	0.65
Ap	0.12	0.14	0.07	0.52	0.12	0.02
mg	66.9	53.7	13.9	57.8	25.8	14.6
	Trace elements in parts per million					
Ba	416	681	298	1358	562	680
Li	11	11	46	24	15	1
Rb	237	241	481	269	406	216
Sr	208	243	45	397	93	50
Pb	60	54	69	51	82	9
Th	36	30	131	63	225	49
U	4.0	2.5	14	8.0	37	7.0
Zr	116	138	217	327	330	826
Hf	4	4	5	8	10	19
Nb	9	6	18	24	19	90
Y	10	6	75	58	58	197
La	47	43	108	150	339	153
Ce	65	76	187	216	578	316
Nd	21	17	55	69	177	144
Pr	4	7	18	18	52	37
Sc	2	1	3	6	4	1
V	7	7	<2	33	8	3
Cr	3	3	4	13	<1	2
Ni	2	3	1	6	2	<1
Cu	<1	<1	1	5	<1	3
Zn	28	32	37	78	40	67
Sn	3	6	15	8	14	23
Ga	19	15	21	21	17	37
S	20	20	<100	310	50	<100
Be	5	4	9	5	7	4

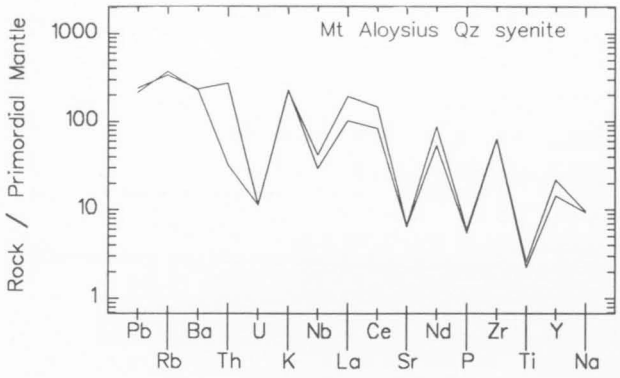

Figure 130. Spidergrams for quartz syenites from Mount Aloysius.

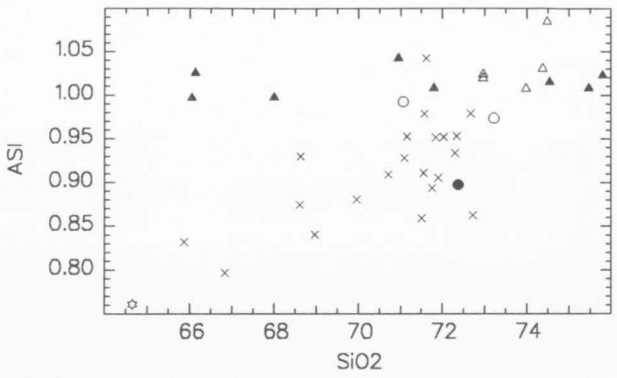

Figure 132. Plot of alumina saturation index against SiO_2 for granitoids and felsic volcanics from the westernmost Musgrave Block. Symbols as in Figure 131.

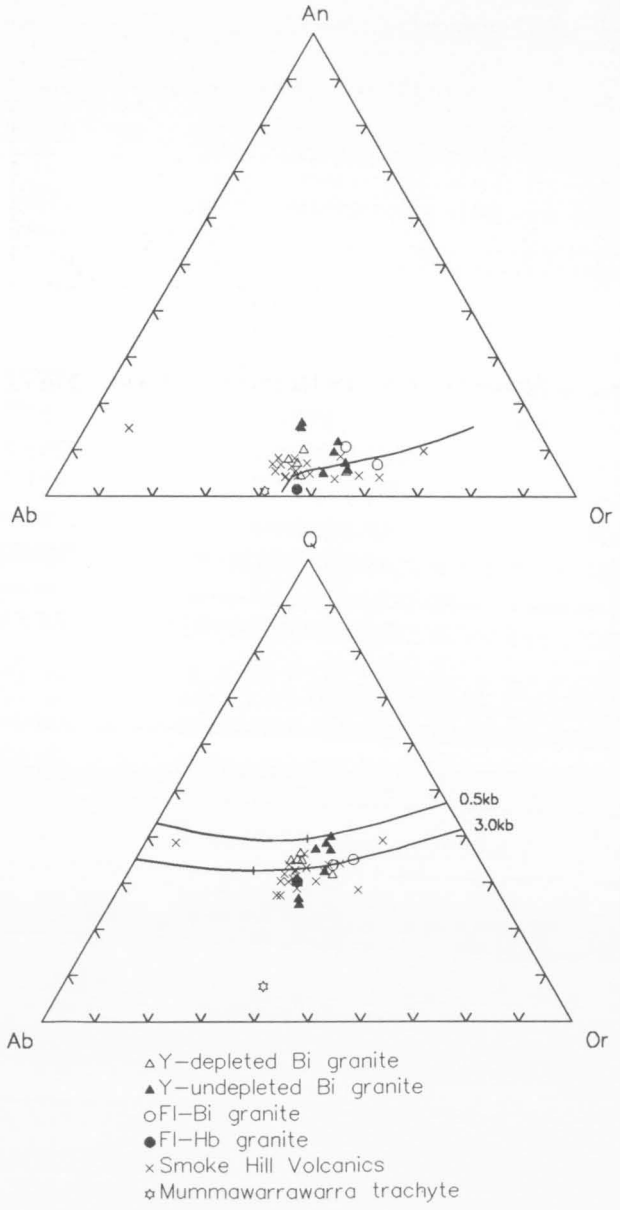

Figure 131. Normative Ab–Or–An and Q–Ab–Or diagrams for granitoids and felsic volcanics from the westernmost Musgrave Block.

but tend to be more siliceous (all analysed samples are granite, *s.s.*: Figs 131, 133). They are also of I-type (Fig. 132) and have the irregular spidergrams typical of intracrustal melts (Fig. 135). However, many rocks, in particular those from MacDougall Bluff, differ in having higher Sr, Be, and Sn. Several of these are characterised by relatively low Zr, Nb, Y, La, and Ce and high Ce/Y (Figs 133, 134); spidergrams show marked Y depletion and only very small negative Sr anomalies (Fig. 135). Hence, although quite siliceous (73.0–74.5% SiO_2), they cannot be related to any of the other Bentley Supergroup basement granites by crystal fractionation processes and were probably derived from a distinct more plagioclase-poor (possibly hornblende±garnet-bearing mafic) source. They are thus equivalent to the Y-depleted suite of Sheraton & Black (1983), and, in contrast to most granitic intrusive rocks in the western Musgrave Block, they may represent new felsic crust.

Two fluorite-bearing biotite granites from southeast of Mummawarrawarra Hill (e.g., 91988101, Table 7) have particularly high K_2O and Rb and low Na_2O, Sr, *mg*, and K/Rb, and were probably derived from a further distinct parent magma. One of these rocks contains accessory allanite and has very high Th, U, La, and Ce. The fluorite–hornblende granite (91988006, Table 7) apparently represents yet another magma type. It has a quite different composition to all other analysed samples: low MgO, P_2O_5, Sr, Ni, Cr, Sc, V, Li, *mg* (15), and Ce/Y and high HFSE (Zr, Nb, Y), LREE, Sn, Ga, Ga/Al, and ε_{Nd} (+0.8 at 1080 Ma: Table 11); the spidergram is particularly irregular (i.e., fractionated; Fig. 135). Such features are characteristic of A-type granitoids and can be explained by high-temperature melting of dry (but possibly F-rich) granulite-facies felsic crustal rocks (Collins et al. 1982; Sheraton & Black 1988). Alternatively, derivation by fractionation of a mafic parent magma is possible. Both models are considered in the discussion of the compositionally and isotopically almost identical rhyolites of the Smoke Hill Felsic Volcanics, which are clearly the extrusive equivalents of this granite (see next section).

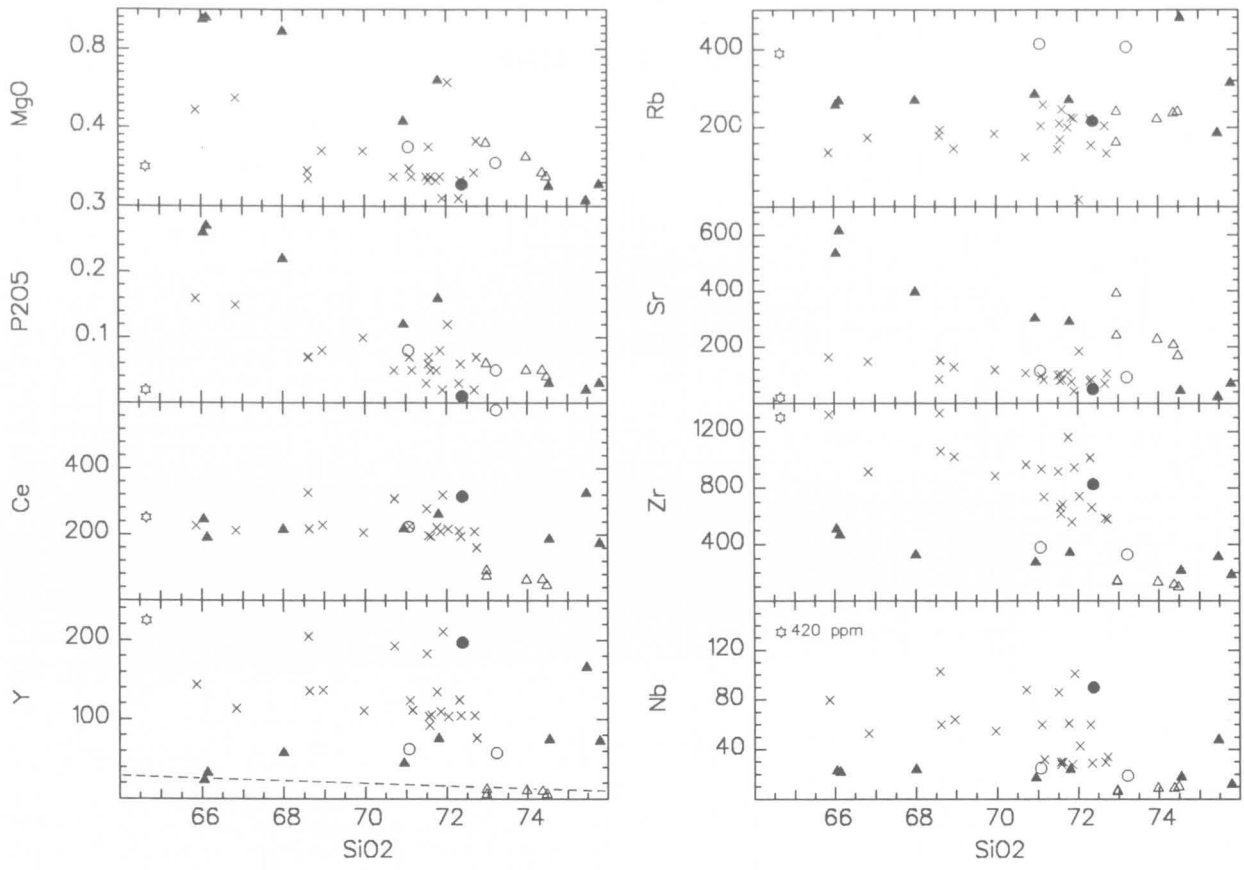

Figure 133. SiO_2 variation diagrams for granitoids and felsic volcanics from the westernmost Musgrave Block. Symbols as in Figure 131.

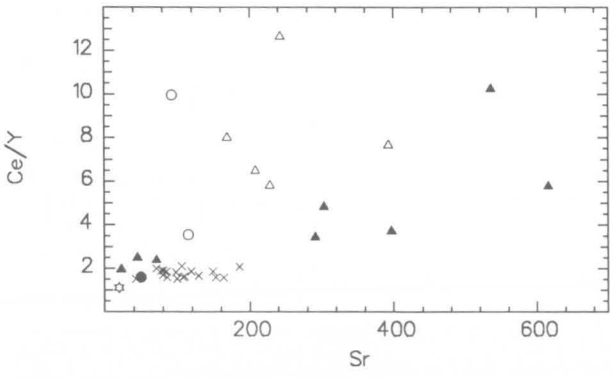

Figure 134. Plot of Ce/Y against Sr for granitoids and felsic volcanics from the westernmost Musgrave Block. Symbols as in Figure 131.

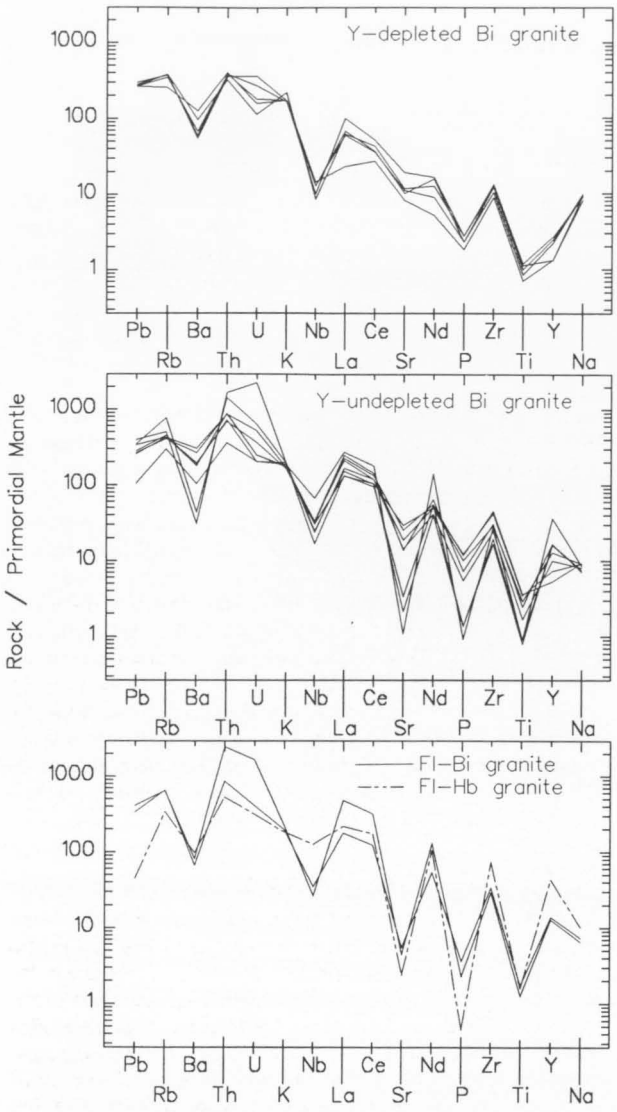

Figure 135. Spidergrams for granitoids from the basement to the Bentley Supergroup, westernmost Musgrave Block.

Tollu Group volcanic rocks

Stratigraphy of the Tollu Group

The Tollu Group is part of the regionally extensive Bentley Supergroup, which also includes several other associations of mainly felsic volcanic rocks, namely the Skirmish Hill volcanic association, southwest of the Bell Rock Range, and the Palgrave and Scamp volcanic associations in the Bentley and Talbot 1:250 000 sheet areas (Fig. 97; Daniels 1970, 1971b). The block west and south of the Bell Rock and Blackstone Range bodies consists of the gently dipping to flat-lying Tollu Group volcanic sequence, which overlies granitic basement rocks through a major unconformity. The unconformity is well exposed along the southwestern flank of MacDougall Bluff, where it is capped by a 15 to 80 m thick basal conglomerate, consisting of well-rounded quartz pebbles in an immature gritstone–arkose matrix (Fig. 136B), defined as the MacDougall Formation (Daniels 1974). The Bell Rock and Blackstone Range intrusions are bounded to the southwest and south by structural discontinuities manifested by magnetic lineaments (Fig. 95), which probably define normal faults along which the Tollu Group rocks were down-faulted. No exposures of this fault zone have been observed, although at one locality felsic volcanic rocks crop out within a few hundred metres of gabbro. The Tollu Group is intruded by stocks and sills of gabbro, e.g., at Tollu Hill, north of the Cavenagh Range, and at Mummawarrawarra Hill. The suggestion that these bodies are equivalents of the Giles Complex (Daniels 1974) is consistent with new isotopic age data. A rhyolite from the Smoke Hill Felsic Volcanics has given a U–Pb zircon age of 1078±5 Ma (Sun et al. 1996a), virtually identical to that of the Giles Complex. This age is generally consistent with the imprecise 1040±140 Ma Rb–Sr isochron age reported by Compston & Nesbitt (1967), refined by Gray (1971) to 1038±35 Ma.

The volcanic sequence of the Tollu Group has been divided into three formations, as follows:

Mummawarrawarra Basalt (BTM). The formation consists of a 240 m thick sequence of amygdaloidal mafic to intermediate flows (Fig. 136A, C, D) and minor pyroclastic rocks. The amygdales are oval to pipe shaped and are typically filled with quartz, chlorite, and epidote, which also occur as alteration veins within massive flows. The basalts are intruded by basaltic dykes and stocks of gabbro in the eastern part of Mummawarrawarra Hill.

Smoke Hill Felsic Volcanics (BTS). This formation, with type localities at Tollu Hill and Mount Maria (Fig. 136E), consists of felsitic even-grained to porphyritic rhyolite, rhyodacite, and dacite flows, felsic pyroclastic rocks, breccia, and minor intermediate to mafic components. Phenocrysts are mainly K–feldspar (perthite) and subordinate albite. The rhyolites locally display well-developed flow banding (Fig. 136F, G, H), and contain perlitic fractured areas suggesting the original occurrence of glass. Near Tollu, these rocks are intruded by gabbro and granophyre, which contains rafts of the felsic volcanics (Daniels 1974).

Hogarth Formation (BTH). This comprises mafic to intermediate volcanic rocks, including amygdaloidal types, tuffs, and agglomerates.

Composition of the Tollu Group

Mummawarrawarra Basalt

The Mummawarrawarra Basalt in the Mummawarrawarra Hill–MacDougall Bluff area includes a variety of fine-grained amygdaloidal basalts and basaltic andesites with textures ranging from hypocrystalline to subophitic. Relict clinopyroxene is rare, mafic phases generally being replaced by chlorite, epidote, and/or amphibole; plagioclase is commonly sericitised or saussuritised. Vesicles contain mixtures of quartz, chlorite, epidote, and zeolites.

Most samples are strongly quartz-normative tholeiites (Table 9), ranging from basalt, through basaltic andesite, to andesite on the alkali–SiO_2 classification of Le Maitre (1989). They are relatively fractionated (mg^* = atomic 100Mg/(Mg + 0.85total Fe) = 47–61) and spidergrams have large negative Nb, Sr, P, and Ti anomalies (Fig. 144). LILE contents, in particular, show considerable variations, probably due to secondary alteration, as well as to the highly vesicular nature of the volcanic rocks. Nevertheless, consistently high LILE/Zr ratios (Fig. 142) and low ε_{Nd} (-1.4) imply derivation from an enriched mantle source region generally similar to those of types A1 and the gabbronorite dykes (see next section). However, S contents (20–120 ppm) are much lower than those of these dykes suites (Figs 143, 146). The petrogenesis of the Mummawarrawarra Basalt, and of associated mafic dykes, is discussed in the section on mafic dykes.

Smoke Hill Felsic Volcanics

The 1078±5 Ma Smoke Hill Felsic Volcanics include subordinate mafic and intermediate rocks and are in places intruded by stocks of gabbro and granite. Rhyolite (defined on the alkali–SiO_2 diagram of Le Maitre 1989), grading into dacite and trachydacite, predominates. Dacitic rocks contain phenocrysts of partly sericitised sodic plagioclase and clinopyroxene (largely altered to amphibole) in a fine-grained quartzo-feldspathic matrix with abudant magnetite (Giles 1981). One dacite contains about 12 percent of epidote. Rhyolites are K-feldspar±plagioclase(albite–oligoclase)±quartz-phyric and contain dark green hornblende (fine-grained aggregates or prismatic crystals: up to 5%), with smaller amounts of dark brown biotite, stilpnomelane (in one sample), opaque minerals, titanite, apatite, zircon, and secondary chlorite, epidote, and garnet. The quartzo-feldspathic groundmass is invariably recrystallised, phenocrysts are commonly broken or partly recrystallised, and many rocks have a strong lamination (probably largely primary, but tectonically modified in some rocks). However, relict eutaxitic structures, devitrification textures, and the presence of intercalated crystal and lithic tuffs attest to a pyroclastic origin for at least some of the volcanic rocks (Giles 1981).

A slightly porphyritic trachyte vein cutting Mummawarrawarra Basalt at MacDougall Bluff comprises rare altered alkali feldspar phenocrysts in a trachytic groundmass with minor quartz, opaque minerals, and fluorite.

The Smoke Hill Felsic Volcanics have typical A-type characteristics: low MgO, P_2O_5, Sr, V, Cr, Ni, *mg* (mostly 6–14), and Ce/Y and high Zr, Nb, Y, La, Ce, Ga, and Ga/Al (Table 8; Figs 133, 134). Spidergrams are highly irregular,

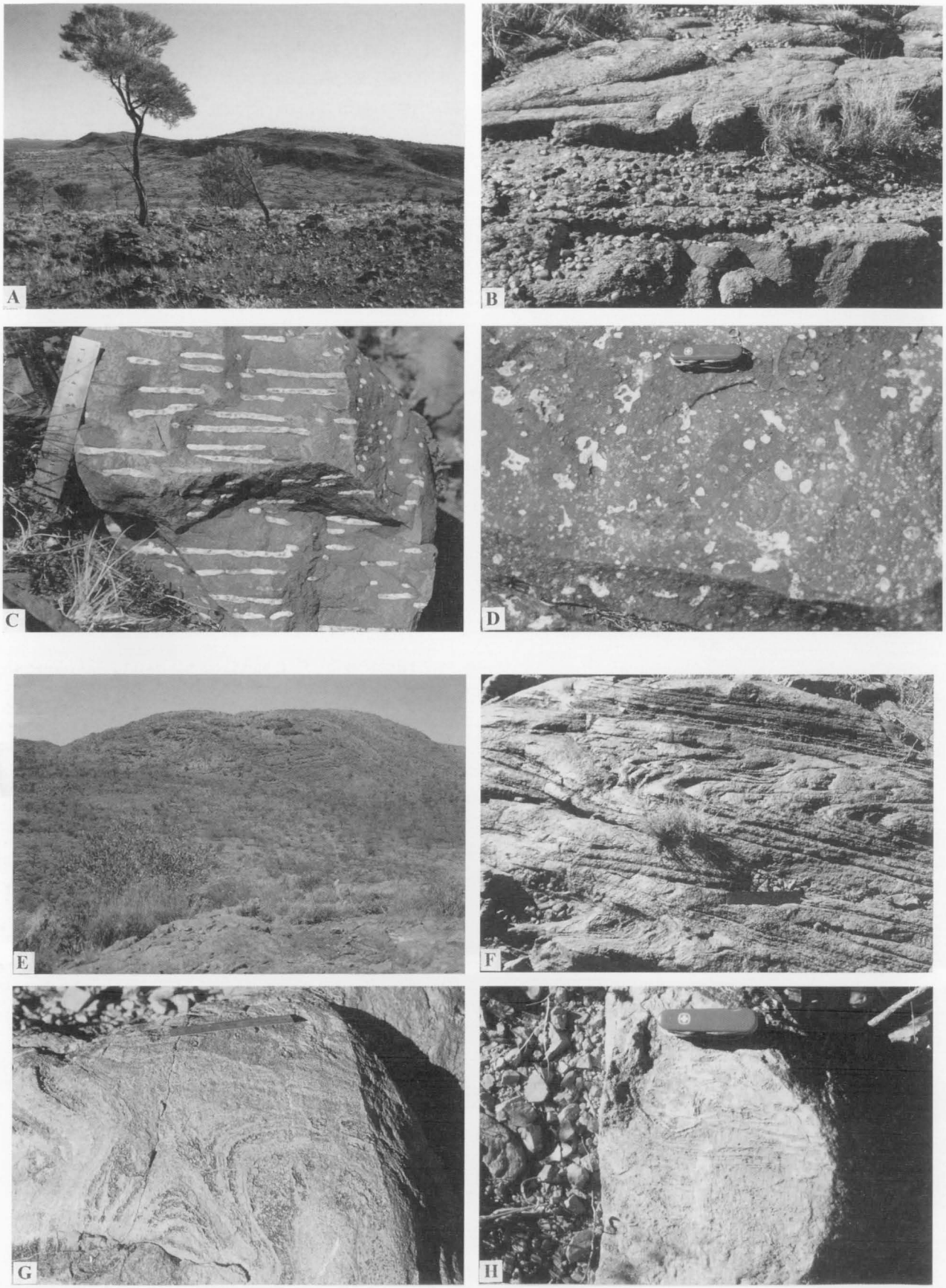

Figure 136. Outcrops of the Tollu Group, south of Blackstone Range. (A) Shallow-dipping sequence of basalt and andesite of the Mummawarrawarra Basalt at MacDougall Bluff. (B) Quartz pebble conglomerate at the base of the MacDougall Formation, MacDougall Bluff. (C) Pipe-structured quartz amygdales in andesite of the Mummawarrawarra Basalt, MacDougall Bluff. (D) Large quartz-filled vugs in andesite of the Mummawarrawarra Basalt, MacDougall Bluff. (E) Smoke Hill Felsic Volcanics at Mount Maria. (F,G) Flow folds in Smoke Hill Felsic Volcanics, Tollu Hill. (H) Flow banding in Smoke Hill felsic pyroclastic rocks, Tollu Hill.

Table 8. Chemical analyses of representative Smoke Hill felsic volcanic rocks (Tollu Group) and related fluorite-hornblende granite from the basement in the westernmost Musgrave Block. Abbreviations as in Table 5.

Sample no.	*91988006*	*91988002*	*91989416*	*91989403*
Locality	*West of Bell Rock Range*	*West of Bell Rock Range*	*Mount Jane*	*McDougall Bluff*
Lithology	*Porphyrit. Fl-Hb granite*	*Slightly porphyrit. rhyolite*	*Porphyrit. rhyolite*	*Porphyrit. trachyte*
SiO_2	72.38	68.61	71.85	64.66
TiO_2	0.34	0.58	0.42	0.07
Al_2O_3	12.54	12.60	12.35	15.71
Fe_2O_3	2.26	3.08	1.82	1.17
FeO	1.15	2.45	1.63	0.27
MnO	0.05	0.06	0.06	0.01
MgO	0.11	0.18	0.15	0.20
CaO	1.01	1.66	0.94	2.93
Na_2O	4.01	3.81	3.27	5.64
K_2O	5.14	4.89	5.62	5.62
P_2O_5	0.01	0.07	0.08	0.02
LOI	0.42	0.63	0.51	2.65
Rest	0.36	0.55	0.37	0.44
Total	**99.78**	**99.17**	**99.07**	**99.39**
O=F,S,Cl	0.00	0.01	0.00	0.01
Total	**99.78**	**99.16**	**99.07**	**99.38**
	C.I.P.W. norms			
Q	27.93	24.67	29.27	6.73
Or	30.37	28.90	33.21	33.21
Ab	33.93	32.24	27.67	47.72
An	1.04	2.84	2.42	0.95
Di	0.59	3.05	1.46	1.07
Wo	1.32	0.57	-	5.04
Hy	-	-	0.53	–
Mt	2.88	4.47	2.64	0.70
Il	0.65	1.10	0.80	0.13
Ap	0.02	0.17	0.19	0.05
mg	14.6	11.6	14.1	56.9
	Trace elements in parts per million			
Ba	680	1404	1388	75
Li	1	3	8	3
Rb	216	179	225	390
Sr	50	86	78	20
Pb	9	21	44	13
Th	49	41	40	82
U	7.0	5.5	4.5	6.5
Zr	826	1329	560	1300
Hf	19	34	15	45
Nb	90	103	28	420
Y	197	205	110	225
La	153	150	114	99
Ce	316	328	210	252
Nd	144	161	90	116
Pr	37	39	22	31
Sc	1	3	5	2
V	3	11	4	8
Cr	2	2	3	3
Ni	<1	2	2	3
Cu	3	30	6	5
Zn	67	160	96	6
Sn	23	16	6	41
Ga	37	38	19	51
S	<100	200	50	250
Be	4	7	5	23

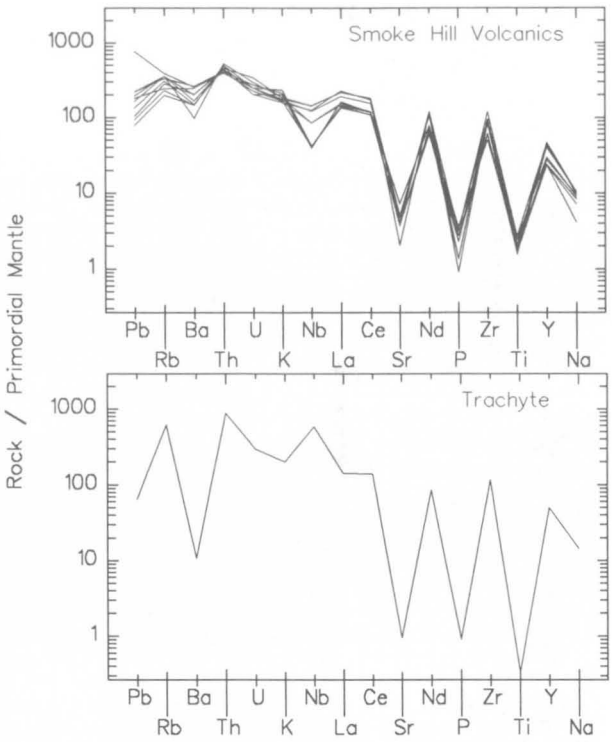

Figure 137. Spidergrams for Smoke Hill Felsic Volcanics and trachyte of the Tollu Group.

with large negative Sr, P, and Ti anomalies (Fig. 137). Virtually all analysed rocks are metaluminous (diopside-normative; Fig. 132). The trachydacites are compositionally similar, but poorer in SiO_2. The epidote-rich dacite has anomalously high CaO and low K_2O, Rb, and Ba, presumably as a result of alteration. The rhyolites show quite wide variations in Na_2O and K_2O contents, probably also resulting from late or post-magmatic redistribution of alkalies (Fig. 131).

The trachyte vein cutting Mummawarrawarra Basalt (91989403, Table 8) has an extremely fractionated composition with, for its SiO_2 content (64.7%), much higher Al_2O_3, Na_2O, Nb, Y, Ga, Sn, and Be and lower TiO_2, FeO, MgO, P_2O_5, Ba, Sr, Sc, and V than the other felsic volcanic rocks (Figs 131, 133, 137). It cannot, therefore, be genetically related to the Smoke Hill Felsic Volcanics.

Giles (1981) carried out least-squares mixing calculations to investigate the possibilty of generation of the felsic volcanic rocks by either fractionation of mafic magma or partial melting of granulite-facies crustal rocks. He concluded that a fractionation model (involving amphibole, plagioclase, clinopyroxene, magnetite, and apatite) could not explain the trace element compositions of the felsic rocks and that the mafic and felsic volcanics are, therefore, unrelated. He further concluded that a source similar to the felsic granulites presently exposed in the Musgrave Block is unlikely because excessive degrees of partial melting would be required to produce a suitable dacitic parent magma and hence the required degrees of enrichment in HFSE could not be attained. Therefore, a mafic–intermediate (possibly residual) source was considered probable.

However, the presently exposed country rocks are not necessarily representative of the presumed lower crustal source, and an intermediate–felsic source would be much less refractory than mafic granulite, which would require an excessive heat input to melt significantly. Experimental data (Beard et al. 1994) show that water-undersaturated melting of a dioritic

source produces siliceous (>72% SiO_2) liquids, even for degrees of melting as high as 50 percent. DePaolo et al. (1992) have shown from Nd isotopic data that crustally-derived granitic magmas are typically melted from intermediate to felsic, rather than mafic, source rocks. An intermediate–felsic source could more easily explain certain trace element data, i.e., strong Sr depletion on the spidergrams, implying a high proportion of residual plagioclase, combined with unfractionated REE patterns (low Ce/Y), implying little or no residual, or fractionating, amphibole or garnet and only relatively minor clinopyroxene. Moreover, there seems to be no compelling reason to assume a refractory residual source for A-type granitoids as suggested by Collins et al. (1982), as even the highest grade metamorphic terranes do not have particularly refractory compositions (Sheraton & Black 1988) and both experimental (Skjerlie & Johnston 1993) and geochemical (Anderson & Morrison 1992) data are more consistent with melting of predominantly felsic igneous (granitic, *s.l.*) rocks. The HFSE contents of A-type granitoids would be enhanced by high F in the parent melt, which increases the solubility of minor phases such as zircon and Fe–Ti oxides (Collins et al. 1982; Keppler 1993). This is certainly the case for some Tollu Group volcanic rocks and associated intrusive rocks, which contain significant amounts of fluorite. However, a significant argument against an intracrustal melting model is the relatively small Nb anomalies of the Smoke Hill Volcanics, which contrast with the much larger anomalies of other granitoids and metamorphic rocks in the area (and indeed most felsic crustal rocks).

The ultimate cause of A-type magmatism was presumably emplacement of mantle-derived magma into the crust. The observed association with mafic volcanic rocks, such as the Mummawarrawarra Basalt, as well as mafic intrusives, is thus significant. In view of the fact that Nd isotopic data (Table 11) are consistent with generation of the Smoke Hill Felsic Volcanics (ε_{Nd} +0.3 to +0.7, compared to -1.4 for the Mummawarrawarra Basalt) by an assimilation–fractional crystallisation (AFC) process (DePaolo 1981) from a basaltic parent magma, and the difficulties with a crustal melting model, this possible alternative origin was examined in more detail. There are, however, also problems with this model. Least-squares mixing calculations for major elements (Wright & Doherty 1970) are broadly consistent with about 90 percent fractionation of clinopyroxene (~20%), orthopyroxene (35%), plagioclase (45%), and minor Ti–magnetite from typical Mummawarrawarra Basalt to give the least siliceous rhyolite. Significant amphibole fractionation would produce a marked increase in Ce/Y and is therefore unlikely. Rayleigh fractionation calculations for many trace elements are compatible with this model, but show that fractionation of K-feldspar would also be necessary to produce the lesser degrees of enrichment shown by K_2O, Ba, and Rb compared to other minor elements; however, the major element modelling program cannot be reconciled with K-feldspar fractionation, and crustal assimilation would be unlikely to produce the observed abundances. It is also difficult to produce the observed degrees of Nb and Y enrichment and Sr depletion. In particular, the felsic rocks have significantly smaller Nb anomalies (Nb/La 0.30–0.65) than the basalts (Nb/La 0.25–0.35). Moreover, there appears to be no suitable intermediate composition and extensive (~90%) fractionation of large quantities of mafic magma would be required to produce the felsic differentiates. The volumetrically minor trachytes within the Mummawarrawarra Basalt are perhaps the most likely products of extensive fractionation of such a basaltic parent magma, but, again, certain element ratios (e.g., extremely high Nb/Zr (0.32) and Nb/La (4.2) and positive Nb anomalies) appear to preclude a direct relationship with the Mummawarrawarra Basalt itself. It is worth pointing out, though, that extreme fractionation of mantle-derived mafic magma through AFC processes was proposed for the economically significant highly Nb-rich (up to 3200 ppm) trachytic volcanic rocks of the Halls Creek Mobile Zone, Western Australia by Taylor et al. (1995). Strong enrichment in Nb can obviously occur in rocks of such extreme composition.

In summary, like the hornblende–biotite granitoids associated with the Giles Complex in the Hinckley Range area, many of the chemical features of the Smoke Hill Felsic Volcanics appear to be generally consistent with partial melting of dry, intermediate to felsic granulite-facies lower crustal rocks (possibly with an additional mantle-derived component: Kerr & Fryer 1993) caused by heating due to emplacement of mantle-derived magma. The somewhat younger Nd T_{DM} model ages and high ε_{Nd} of the Smoke Hill Felsic Volcanics (1543–1549 Ma: Table 11), compared to granulite-facies metamorphics in the western Hinckley Range area (1610–1900 Ma) may be a result of derivation from a relatively young crustal underplate. Indeed, as discussed above, some Y-depleted granitic rocks in the basement to the Bentley Supergroup may represent new felsic crust. On the other hand, generation of the felsic volcanic rocks by direct fractionation of a basaltic magma is also feasible. Although model calculations are not entirely consistent with such an origin, the discrepancies may be due to inappropriate choices of K_d values or parent magma or fractionating mineral compositions. DePaolo et al. (1992) concluded from Nd isotopic data that high silica rhyolitic ignimbrites of the western United States were commonly formed primarily by fractionation of basaltic magma, and a similar origin for A-types was proposed by Javoy & Weis (1987) and Turner et al. (1992). However, because neither the exposed felsic country rocks nor the associated basaltic rocks provide a chemically entirely suitable source for the Smoke Hill Felsic Volcanics, their origin is presently uncertain. Eby (1990) emphasised that A-type granitoids can be produced by a variety of processes, including fractionation of basaltic magma, intracrustal melting, and interaction of mantle-derived magma with continental crust.

Mafic dykes

Regional distribution

Mafic dyke swarms are common throughout the western part of the Musgrave Block, intruding high-grade metamorphic rocks of the Mount Aloysius Complex, granitic rocks, and Giles Complex mafic–ultramafic intrusions (Fig. 138). Such dykes commonly define periods of crustal extension and form useful stratigraphic markers. Dyke compositions provide information about their mantle source regions and the compositional variations of the latter with time.

Three generations of post-Giles Complex mafic dykes (types A, B, and C) were recognised on structural and petrological grounds in the Mount Aloysius and Champ de Mars areas by Clarke (1992) and Clarke et al. (1995a). The oldest (type A) apparently post-dates the Hinckley Range gabbronorite of the Giles Complex and associated granitoids, but is deformed by D_3. Types B and C dolerites post-date D_3. Chemical data support these groupings, but several other chemically distinct

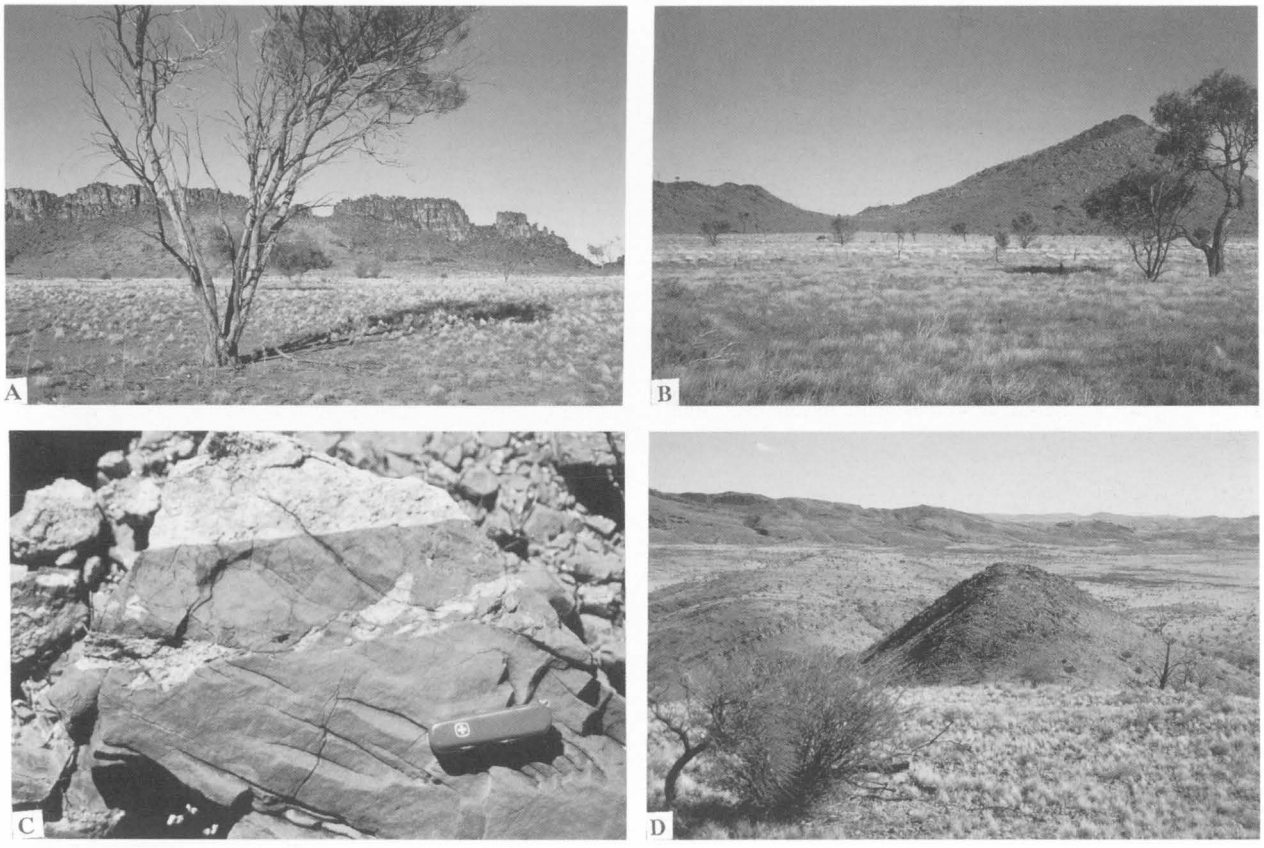

Figure 138. Outcrops of mafic dykes and ultramafic plug. (A) Ridge-forming gabbro dyke in the Charnockite Flats area, west of the Hinckley Range. (B) Shallow-dipping dolerite dyke forming a ridge top to felsic granulite at Mount Aloysius. (C) Mafic dyke cutting anorthosite near Teizi bore. (D) Ultramafic plug intruding felsic granulite, south of Ewarara.

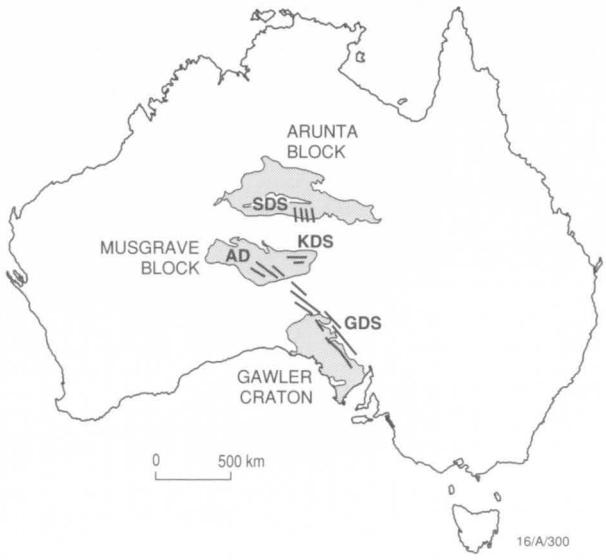

Figure 139. Map showing approximate distribution of dolerite dyke swarms in the Mesoproterozoic Musgrave Block, Palaeoproterozoic Arunta Block, and Archaean–Mesoproterozoic Gawler Craton. KDS, Kulgera dyke swarm; SDS, Stuart dyke swarm; AD, Amata dykes; GDS, Gairdner dyke swarm (after Zhao & McCulloch 1993a).

Table 9. Chemical analyses of representative mafic dykes, sills, and Mummawarrawarra Basalt (Tollu Group) from the western Musgrave Block.

Sample no.	*91988086*	*91989151A*	*91988025*	*91988097*	*90984054*	*90984068*	*91988093*	*91988094*
Locality	*W Champ de Mars*	*N Hinckley Range*	*W Hinckley Range*	*W Champ de Mars*	*W Champ de Mars*	*W Champ de Mars*	*W Champ de Mars*	*W Champ de Mars*
Lithology	*Intergran. dolerite dyke*	*Intergran. dolerite dyke*	*Dolerite dyke*	*Quartz dolerite dyke*	*Olivine dolerite dyke*	*Olivine dolerite dyke*	*Gabbronor–ite dyke margin*	*Gabbronor–ite dyke centre*
Group	*A1*	*A2*	*B*	*B*	*C*	*C*		
SiO_2	49.35	51.91	49.13	50.55	48.59	47.24	51.32	50.77
TiO_2	0.85	1.39	1.56	1.91	1.22	1.35	0.64	0.75
Al_2O_3	14.83	15.77	14.12	13.24	16.14	14.50	16.78	21.03
Fe_2O_3	4.32	1.78	2.07	1.77	3.14	4.18	1.78	1.53
FeO	6.88	8.48	10.25	11.47	7.03	7.35	8.00	7.09
MnO	0.16	0.13	0.17	0.18	0.16	0.16	0.15	0.11
MgO	8.53	6.72	7.58	6.50	9.02	10.90	7.13	3.92
CaO	11.04	8.41	11.43	10.55	10.22	9.93	10.79	10.75
Na_2O	2.34	3.24	2.17	2.23	2.48	2.17	2.35	2.80
K_2O	0.56	0.51	0.26	0.33	0.72	0.76	0.54	0.72
P_2O_5	0.11	0.23	0.13	0.15	0.23	0.18	0.07	0.11
LOI	0.77	0.67	0.73	1.24	0.69	0.88	0.86	0.48
Rest	0.32	0.36	0.24	0.25	0.39	0.43	0.20	0.19
Total	**100.06**	**99.60**	**99.84**	**100.37**	**100.03**	**100.03**	**100.61**	**100.25**
O=F,S,Cl	0.04	0.05	0.01	0.02	0.05	0.06	0.01	0.01
Total	**100.02**	**99.55**	**99.83**	**100.35**	**99.98**	**99.97**	**100.60**	**100.24**
	C.I.P.W. norms							
Q	–	1.01	–	2.93	–	–	0.37	0.29
Or	3.31	3.01	1.54	1.95	4.25	4.49	3.19	4.25
Ab	19.80	27.42	18.36	18.87	20.99	18.36	19.89	23.69
An	28.31	26.98	28.02	25.14	30.78	27.58	33.64	42.69
Di	21.02	10.84	22.85	21.67	14.95	16.61	15.91	8.24
Hy	12.73	23.67	19.95	21.21	9.63	6.86	22.82	16.67
Ol	9.05	–	1.94	–	12.94	18.88	–	–
Mt	2.60	2.44	2.93	3.16	2.38	2.69	2.32	2.05
Il	1.61	2.64	2.96	3.63	2.32	2.56	1.22	1.42
Ap	0.26	0.54	0.31	0.36	0.54	0.43	0.17	0.26
	Trace elements in parts per million							
Ba	264	239	48	41	344	279	214	306
Li	10	5	10	10	6	9	9	8
Rb	15	5	9	11	19	14	12	12
Sr	160	459	176	189	226	346	181	272
Pb	4	<2	3	<2	7	4	4	6
Th	2	<2	<2	<2	<2	<2	3	<2
U	<0.5	<0.5	0.5	<0.5	1.0	<0.5	1.0	<0.5
Zr	86	83	96	125	150	106	49	62
Hf	3	<2	3	<2	4	3	<2	<2
Nb	2	2	5	6	4	6	3	<2
Y	23	20	26	32	30	19	17	19
La	9	11	9	17	20	12	9	11
Ce	26	19	18	29	33	31	17	23
Nd	10	15	12	20	18	9	13	13
Sc	38	24	38	42	39	33	33	25
V	299	228	377	393	223	277	232	172
Cr	384	389	203	176	526	606	189	54
Ni	205	197	135	99	234	329	140	81
Cu	33	112	179	249	86	77	98	69
Zn	80	92	94	115	83	93	72	71
Ga	16	19	19	20	16	18	17	19
As	1.5	1.5	<0.5	1.5	<0.5	<0.5	<0.5	<0.5
S	850	1010	270	310	1060	1180	190	270
*mg**	62.4	58.3	56.8	51.1	65.7	67.3	60.9	49.3
K/Rb	310	847	240	249	315	451	374	498
K/Ba	17.6	17.7	45	67	17.4	23	21	19.5
K/Zr	54	51	22	22	40	60	91	96
Ti/Nb	2500	4200	1900	1900	1800	1300	1300	>2300
Ti/Zr	59	100	97	92	49	76	78	73
P/Zr	5.6	12.1	5.9	5.2	6.7	7.4	6.2	7.7
(Ce/Y)n	2.8	2.4	1.7	2.3	2.8	4.1	2.5	3.0
Sr/Sr*	0.70	2.03	0.89	0.59	0.69	1.39	0.91	1.17
Nb/Nb*	0.17	0.17	0.63	0.47	0.21	0.38	0.26	<0.14

*mg**, atomic 100Mg/(Mg + 0.85total Fe); LOI, loss on ignition.
Ce/Y)n, 2.5Ce/Y; Sr/Sr*, Sr/(5.77Ce + 7.74Nd); Nb/Nb*, Nb/(12.82K2O + 0.507La); i.e., all primordial mantle normalised.

Sample no.	*91989396*	*91989384*	*91988014*	*90980007B*	*90980008*	*88982029*	*88982034*	*91988052*	*91980111*
Locality	*MacDougall Bluff*	*Tollu camp*	*McDougall Bluff*	*Mummawar–rawarra H.*	*Mummawar–rawarra H.*	*SE Bell Rock Ra.*	*SE Bell Rock Ra.*	*W Hinckley Range*	*N Hinckley Range*
Lithology	*Basaltic andesite dyke*	*Basaltic andesite dyke*	*Slightly amygdal. basalt*	*Amygdal. andesite*	*Basaltic andesite*	*Microgabbro sill*	*Microgabbro sill*	*Microgabbronorite*	*Microgabbronorite*
Group			*Tollu*	*Tollu*	*Tollu*	*?Giles*	*?Giles*	*?Giles*	*Giles*
SiO_2	53.92	53.45	50.84	57.90	54.13	48.30	46.78	48.03	50.20
TiO_2	1.74	2.32	1.33	0.76	1.27	0.73	0.87	1.21	1.62
Al_2O_3	14.64	13.39	13.46	15.04	14.15	15.57	18.75	16.34	15.48
Fe_2O_3	4.16	3.09	3.22	3.13	3.23	1.87	1.69	2.45	2.99
FeO	7.71	9.43	8.13	4.11	7.84	8.86	9.30	8.69	8.95
MnO	0.18	0.15	0.15	0.11	0.15	0.16	0.13	0.16	0.17
MgO	3.05	3.25	6.65	3.45	4.22	9.49	8.47	8.47	6.11
CaO	6.78	5.93	8.75	7.64	7.89	11.72	9.83	10.72	8.63
Na_2O	1.72	3.65	2.26	2.33	2.42	1.95	2.51	2.25	2.92
K_2O	0.94	1.54	1.34	3.00	2.00	0.21	0.38	0.45	1.36
P_2O_5	0.12	0.39	0.18	0.17	0.23	0.06	0.12	0.14	0.21
LOI	4.16	2.58	3.33	2.13	1.99	0.69	0.86	0.88	0.68
Rest	0.28	0.29	0.26	0.27	0.30	0.32	0.18	0.32	0.29
Total	**99.40**	**99.46**	**99.90**	**100.04**	**99.82**	**99.93**	**99.87**	**100.11**	**99.61**
O=F,S,Cl	0.02	0.00	0.00	0.00	0.01	0.03	0.01	0.05	0.03
Total	**99.38**	**99.46**	**99.90**	**100.04**	**99.81**	**99.90**	**99.86**	**100.06**	**99.58**
	C.I.P.W. norms								
Q	16.05	6.02	3.95	11.08	7.13	–	–	–	–
Or	5.55	9.10	7.92	17.73	11.82	1.24	2.25	2.66	8.04
Ab	14.55	30.89	19.12	19.72	20.48	16.50	21.24	19.04	24.71
An	29.45	15.60	22.62	21.72	21.84	33.11	38.77	33.16	25.11
Di	2.87	9.49	15.98	12.48	13.18	20.05	7.52	15.59	13.48
Hy	19.90	17.12	19.08	11.20	17.40	13.23	5.36	12.02	15.44
Ol	–	–	–	–	–	10.65	19.15	11.11	5.37
Mt	2.77	2.95	4.67	1.67	2.60	2.55	2.62	2.63	2.81
Il	3.30	4.41	2.53	1.44	2.41	1.39	1.65	2.30	3.08
Ap	0.28	0.92	0.43	0.40	0.54	0.14	0.28	0.33	0.50
	Trace elements in parts per million								
Ba	708	483	369	938	756	75	96	188	563
Li	29	4	14	5	2	3	6	9	5
Rb	38	88	49	58	60	2	9	9	44
Sr	267	211	185	239	215	132	278	229	276
Pb	13	8	9	20	18	<2	<2	3	9
Th	2	14	6	8	8	<2	<2	<2	<2
U	<0.5	1.5	0.5	<0.5	1.0	<0.5	1.0	<0.5	<0.5
Zr	132	416	156	177	286	38	60	73	122
Hf	4	9	<2	5	6	<2	<2	<2	4
Nb	5	29	5	6	9	2	6	4	4
Y	41	65	29	29	45	21	14	24	34
La	21	40	19	22	34	3	7	10	13
Ce	22	78	39	47	75	9	15	16	28
Nd	12	42	22	20	34	6	7	5	14
Sc	31	26	35	25	32	43	20	41	30
V	257	247	261	173	268	262	134	296	265
Cr	21	59	296	128	15	705	63	193	131
Ni	32	41	163	62	85	220	243	236	123
Cu	38	193	115	49	134	148	41	140	48
Zn	120	144	108	71	123	81	86	88	103
Ga	19	23	19	16	19	17	23	18	20
As	1.0	2.0	<0.5	<0.5	1.5	<0.5	<0.5	1.0	<0.5
S	430	10	80	70	120	700	300	1020	520
*mg**	35.8	35.8	55.8	51.1	45.2	65.4	62.1	62.0	52.4
K/Rb	205	145	227	429	277	872	350	415	257
K/Ba	11.0	26	30	27	22	23	33	19.9	20
K/Zr	59	31	71	141	58	46	53	51	93
Ti/Nb	2100	480	1600	760	850	2200	870	1800	2500
Ti/Zr	79	33	51	26	27	115	87	99	80
P/Zr	4.0	4.1	5.0	4.2	3.5	6.9	8.7	8.4	7.5
(Ce/Y)n	1.3	3.0	3.4	4.1	4.2	1.1	2.7	1.7	2.1
Sr/Sr*	1.21	0.27	0.47	0.56	0.31	1.34	1.98	1.75	1.02
Nb/Nb*	0.22	0.72	0.19	0.12	0.21	0.47	0.71	0.37	0.17

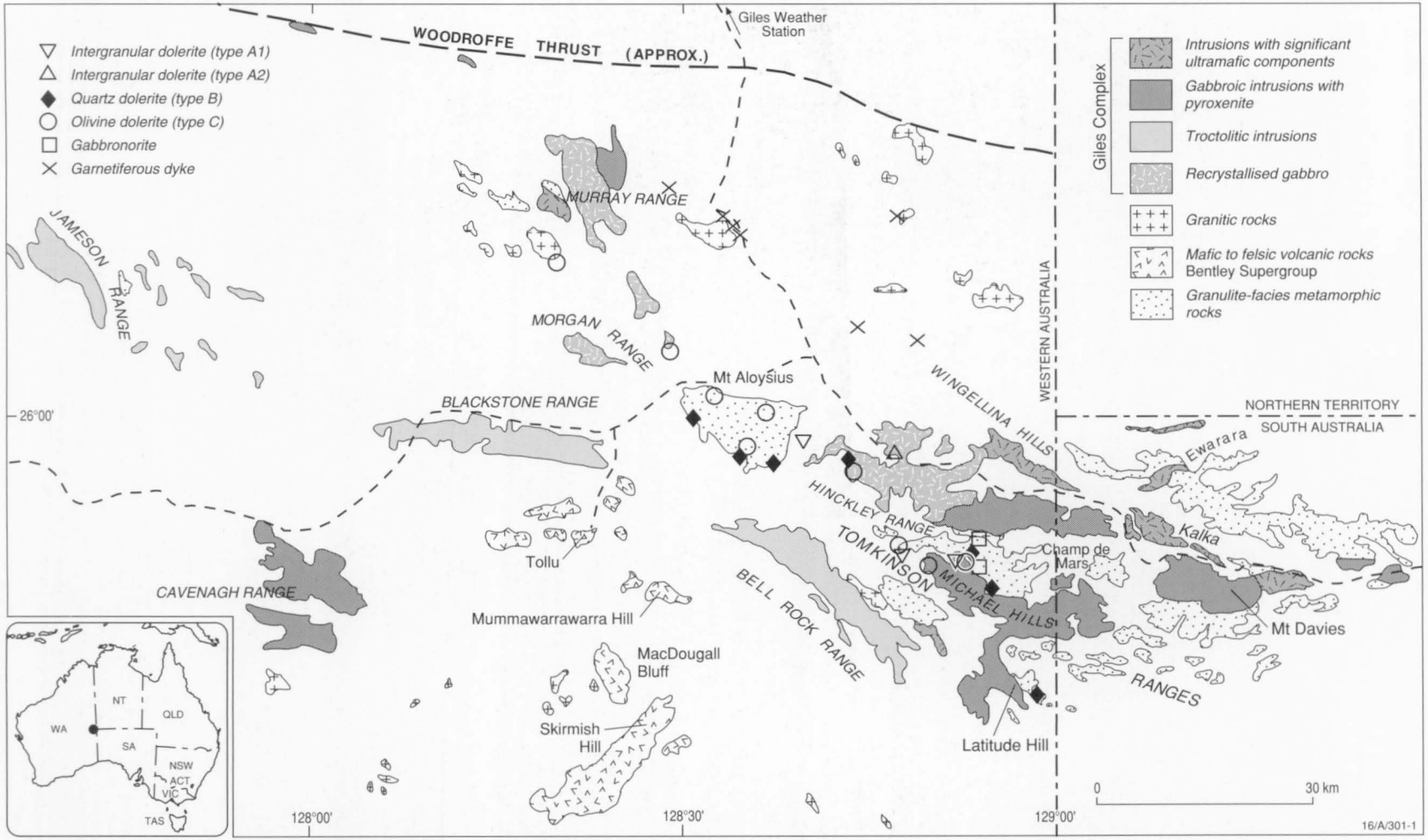

Figure 140. Geological map of the western Musgrave Block, showing major Giles Complex intrusions and locations and chemical groupings of analysed mafic dykes.

types of mafic dyke are also present. Four post-Giles Complex suites of dolerite dykes (A–D) were recognised in the eastern Tomkinson Ranges by Nesbitt et al. (1970).

Dolerite dykes in the central and eastern Musgrave Block have given two distinct Sm–Nd isochron ages: 1090±32 Ma for the Kulgera (also known as the Alcurra) dyke swarm (similar to the age of the Stuart dyke swarm in the Arunta Block, 1076±33 Ma) and 790±40 and 797±49 Ma for dykes at Amata (similar to the age of the Gairdner dyke swarm in the Gawler Craton, 867±47 and 802±35 Ma) (Zhao & McCulloch 1993a; Fig. 139).

The A to C terminology of the three main dyke types recognised by Clarke et al. (1995a) has been retained, even though type B has now been shown to be younger than type C, because it has already been used in a number of papers (e.g., Glikson et al. 1995). The geographical distribution of the various dyke types is shown in Figure 140, and those at Mount Aloysius in Figure 29.

Petrology and geochemistry

Type A intergranular dolerite dykes

These dykes appear to be equivalent, at least in part, to type A

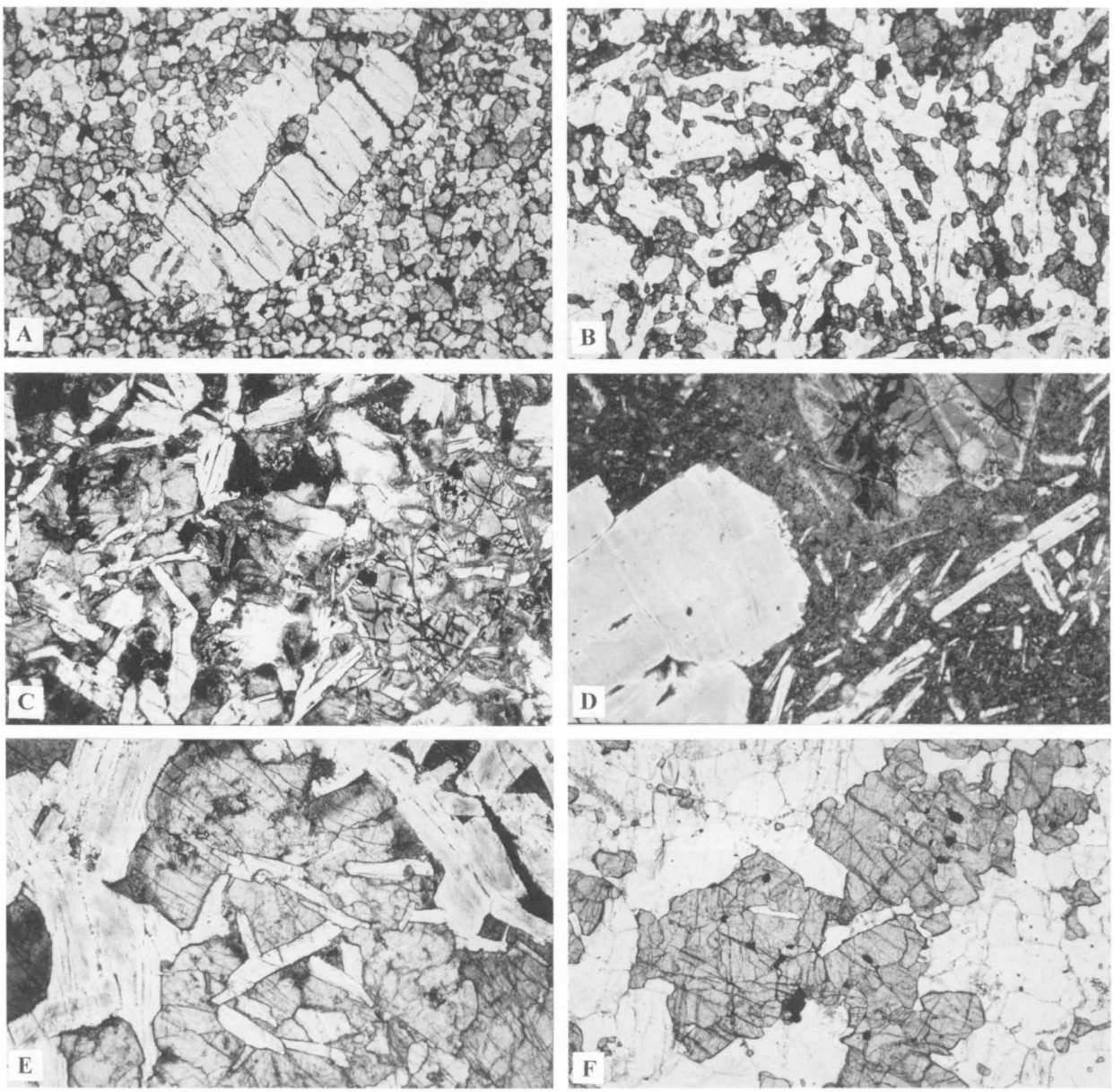

Figure 141. Mafic dyke types. (A) Type A1 intergranular dolerite dyke (91988086), western Champ de Mars. Cracked plagioclase phenocrysts in an intergranular groundmass of clinopyroxene, orthopyroxene, plagioclase, and minor opaque minerals and biotite. (B) Type A2 intergranular dolerite dyke (91989151A), western Hinckley Range. Intergranular clinopyroxene, orthopyroxene, and opaque minerals, with igneous plagioclase laths and a few microphenocrysts. (C) Medium-grained type C olivine dolerite dyke (91988056), western Hinckley Range. Subophitic texture, with clinopyroxene (containing exsolved opaque grains), plagioclase, olivine (right), minor opaque minerals, and secodary amphibole and biotite. (D) Porphyritic type C olivine dolerite dyke (29-168-9), cutting the Bell Rock intrusion. Olivine (top) and plagiocalse phenocrysts in a very fine-grained, altered groundmass, with plagioclase microphenocrysts. (E) Type B dolerite dyke (91988036), south side of Mount Aloysius. Subophitic texture, with clinopyroxene, plagioclase, opaque minerals, and minor secondary amphibole and biotite. (F) Gabbronorite dyke margin (91988096), western Champ de Mars. Gabbroic texture, with clinopyroxene, orthopyroxene, plagioclase, and minor opaque minerals and reddish-brown biotite. Both clinopyroxene and orthopyroxene contain pyroxene exsolution lamellae and blebs.

of Clarke et al. (1995a), although two chemically distinct subgroups (A1 and A2) have been recognised. They are commonly foliated along the margins and have various orientations, but type A1 dykes in the Champ de Mars area are mostly northwest-trending. In the western Champ de Mars, a type A dyke is cut by a type C dolerite.

Type A1 dykes, which crop out in the Champ de Mars area and at Mount Aloysius, have intergranular textures, commonly with zoned plagioclase phenocrysts (Fig. 141A), and are thus texturally distinct from the younger dolerites. Apart from extensive recrystallisation along the margins, the textures are generally primary igneous, rather than metamorphic (i.e., granoblastic). Two aphyric dykes have essentially similar granular textures which may also be of igneous origin, although recrystallisation during deformation cannot be discounted. Intergranular dolerites contain clinopyroxene and orthopyroxene (about 20% each), plagioclase (andesine–labradorite: 55–60%), Fe–Ti oxides (1–5%), and apparently primary reddish-brown biotite (up to 4%). A type A1 dyke has given a Sm–Nd mineral-whole rock isochron age of about 1100 Ma (S-S. Sun, unpublished data). These dykes thus presumably crystallised at considerable crustal depths during the waning stages of high-grade metamorphism and deformation, at about the same time as emplacement of the Giles Complex (i.e., pre to syn-D_3).

Intergranular dolerite dykes (type A2) cutting the northern part of the Hinckley Range gabbronorite intrusion are petrographically similar (Fig. 141B), although there is generally more plagioclase (~65%), less clinopyroxene (~10%), and little or no biotite. Most of these dykes contain plagioclase phenocrysts. They cross cut igneous layering in the gabbronorite (Clarke et al. 1995a), but chemical data suggest that they are genetically related to the latter and are therefore only slightly younger (see below).

Type A1 dolerites are moderately evolved (*mg** = 56–63) olivine or slightly quartz-normative tholeiites (Table 9). LILE (K, Rb, Ba, Pb, Th, and U) and LREE are markedly enriched relative to HFSE (P, Nb, Zr, Ti, etc.), so that LILE/Zr and Ce/Zr ratios are much higher than estimated primordial mantle (Fig. 142); in contrast, P/Zr and Ti/Zr are significantly lower. Sulphur contents are quite high (700–1120 ppm: Fig. 143). Spidergrams show quite fractionated patterns, with large negative Nb anomalies and, for some dykes, small negative Sr anomalies, suggesting some degree of plagioclase fractionation (Fig. 144).

Sheraton et al. (1990) argued that the high LILE contents and Sr and Nd isotopic compositions of many continental tholeiites are better explained by derivation from enriched mantle source regions rather than direct crustal assimilation, although some degree of contamination is quite possible. Ratios of many incompatible elements (LILE, LREE, and some HFSE) are commonly more or less constant (as shown by pairs of elements defining lines of unit slope on logarithmic plots like Fig. 142) and are therefore considered to approximate those of the mantle source. On this basis, the type A1 dolerites were apparently derived from strongly enriched mantle, consistent with relatively low ε_{Nd} (-2.2 for one sample, Table 11).

Type A2 dolerites from the northern Hinckley Range are slightly more evolved (*mg** 49–59) and more strongly quartz-normative than type A1, and have higher Sr, K/Rb, Ti/Zr, and P/Zr, and lower Sc and Rb/Zr (Table 9; Fig. 142). Spidergrams are characterised by the presence of marked positive Sr anomalies (Fig. 144), suggesting some degree of plagioclase accumulation. It is unlikely that the unusually high P/Zr is due to cumulus processes, because P_2O_5 contents are much lower than those required to saturate a mafic melt (Watson 1979). Hence, derivation from an apatite-rich mantle source, such as that postulated to be present beneath southeastern Australia (Menzies & Wass 1983) is probable. Type A2 dykes cannot have been comagmatic with those of type A1, and were presumably derived from a distinct, but similarly-enriched, mantle source region.

Type C olivine dolerite dykes

Olivine dolerite dykes are mostly northeast (rarely northwest) trending, and mostly thinner (1–2 m) and finer grained than those of type B. Textures range from subophitic to porphyritic, with olivine and plagioclase phenocrysts (Fig. 141C). Petrographically very similar dykes cut some of the Giles Complex intrusions (e.g., The Wart, Fig. 67B; Hinckley Range, Fig. 84A; Bell Rock, Figs 92B, 141D). Coarser-grained dykes contain plagioclase (50–60%), clinopyroxene (20–35%), olivine (5-12%), opaque minerals (Fe–Ti oxides and pyrite: 4–6%), and biotite (up to 4%). Olivine is commonly partly serpentinised, and in some dykes clinopyroxene is partly altered. A type C dyke from the western Hinckley Range has given a Sm–Nd mineral-whole rock isochron age of about 1000 Ma (S-S. Sun, unpublished data). Although this is not statistically significantly younger than the type A dolerites, field and petrographic evidence suggest that the type C dykes are post-D_3, and therefore somewhat younger. These dykes may be equivalent to type D olivine dolerites of Nesbitt et al. (1970).

Most type C dolerites are relatively primitive, having high *mg** (58–74), Cr (373–793 ppm), and Ni (202–329 ppm), although two samples are more evolved (*mg** 46 and 48). High S (690–1670 ppm) reflects the presence of late pyrite. Type C dykes are strongly olivine-normative tholeiitic or, rarely, transitional dolerites, with trace element characteristics broadly similar to type A1 dykes, but quite different to type B (Figs 142–144). For example, LILE/Zr and Ce/Zr are higher, whereas Ti/Zr, Nb/Zr, and P/Zr are mostly lower than primordial mantle. Four type C dykes from the Champ de Mars area and western Hinckley Range (e.g., 90984054, Table 9) are characterised by low Ti/Zr, K/Zr, Zn/Zr, and, in particular, Nb/Zr, compared with those from Mount Aloysius. Moreover, the two most evolved (low-*mg**) type C dykes have high P/Zr, and Sr shows much more variation than in the other dyke groups. Type C dykes thus form a chemically quite heterogeneous suite, implying derivation from a hetrogeneous mantle source, and they could be of more than one age. Although their mantle source was generally similar to that of type A1 dykes, their similar incompatible element abundances, coupled with more primitive SiO_2-undersaturated compositions, indicate lower degrees of melting at higher pressures (Green 1973). The two most evolved dykes have similar normative olivine contents to the other type C dykes, suggesting even lower degrees of melting.

There is some geochemical similarity between type C dykes and olivine tholeiites of the Kulgera dyke swarm, eastern Musgrave Block and the Stuart dyke swarm, Arunta Block (Zhao & McCulloch 1993b), but the resemblance is by no means as good as that between the type B and the Amata–Gairdner dykes. For example, most type C dykes have higher P_2O_5 and Zr, and lower Nb/Zr (Figs 142, 144). However, these differences are not surprising in view of the marked heterogeneity within type C in the relatively small area of the western Tomkinson Ranges and their possible differences in age. All type C dykes were apparently derived from a generally similar enriched heterogeneous mantle source to that of the Kulgera and Stuart dykes. The latter have ε_{Nd} of -3.0 to +1.9 and -9.9 to -5.1, respectively (Zhao & McCulloch 1993b), compared to +1.9 for a single (low-K/Zr) type C dyke (Table 11). It is not clear whether the trend of decreasing Nb/Zr with decreasing Nb (Fig. 142) is real or an artefact of the imprecise Nb XRF analyses near the detection limit (2 ppm), but it appears to be supported by spark-source mass spectrometry data for the Kulgera and Stuart dykes (Zhao 1992).

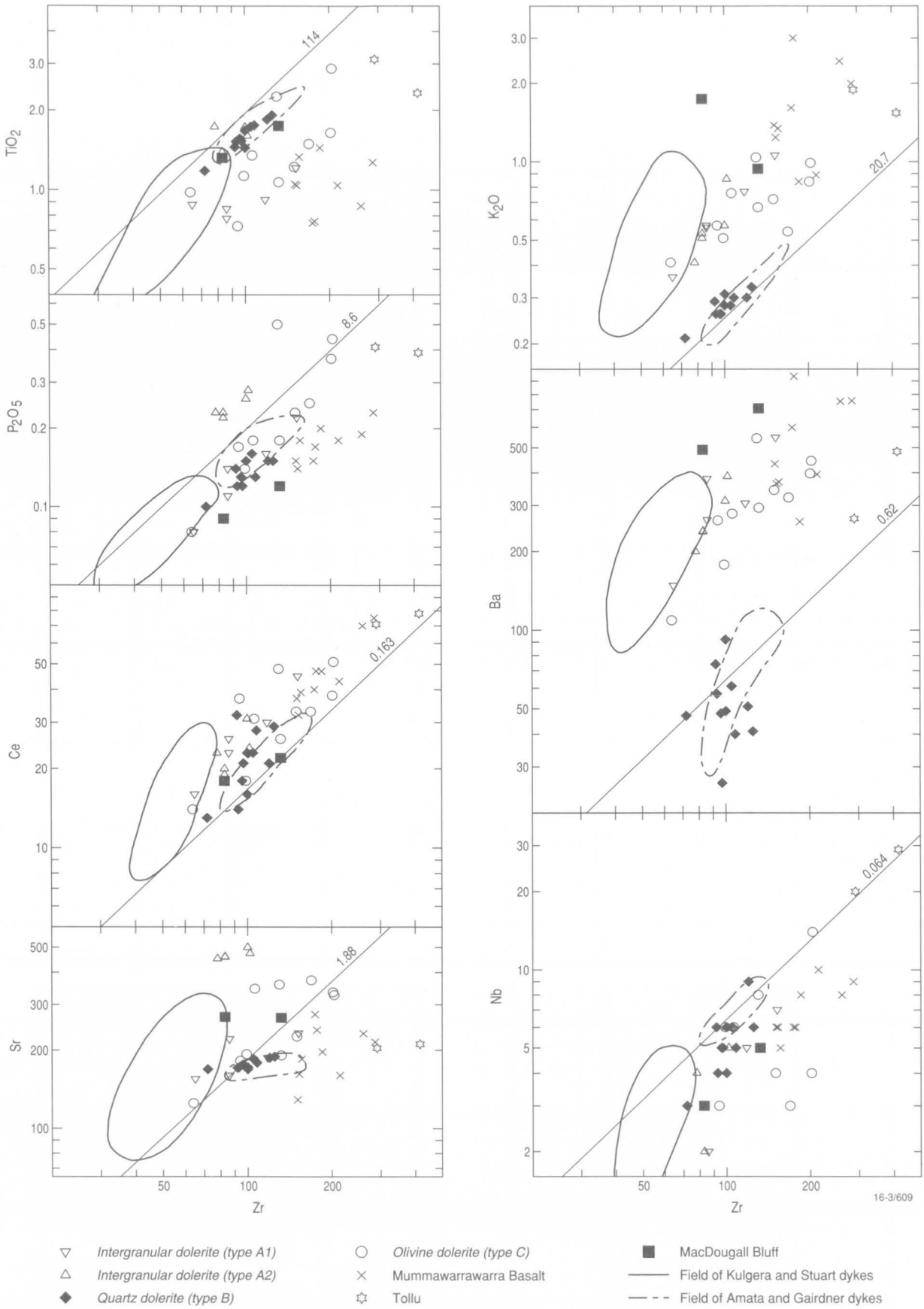

Figure 142. Logarithmic plots of various incompatible elements against Zr for dolerite dykes and Mummawarrawarra Basalt. Fields of Kulgera + Stuart and Amata + Gairdner dykes based on data in Zhao (1992), Zhao et al. (1994), and the AGSO ROCKCHEM database. Lines of unit slope have constant element/Zr ratio, and estimated primordial mantle ratios (after Sun & McDonough 1989) are indicated. Such lines are also those for which the bulk mineral-melt distribution coefficient (K_d) is zero. The K_d value can be estimated using the expression $K_d = 1$ - slope (Allègre et al. 1977), and for some elements it is much higher than zero (e.g., ~0.7–1.0 for Sr in many dyke groups, reflecting plagioclase fractionation).

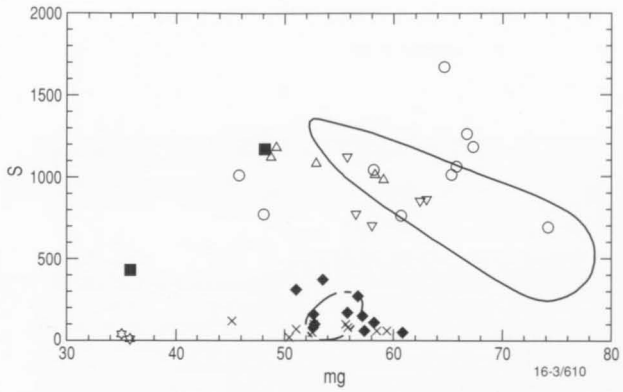

Figure 143. Plot of S against mg* (atomic 100Mg/(Mg + 0.85 total Fe)) for dolerite dykes and Mummawarrawarra Basalt. Symbols as in Figure 142.

Type B quartz dolerite dykes

These are northwest-trending, post-D_3, pre-D_{4-7} dykes, commonly 3 to 5 (but up to 30) metres thick. They have typical medium-grained subophitic textures (Fig. 141E), although some are rather altered and cut by thin mylonite zones. Plagioclase (labradorite: 55–60%), clinopyroxene (35–40%), Fe–Ti oxides (2–4%), and quartz (up to 2%) are the main constituents, but minor biotite and hornblende are commonly present, and in some dykes clinopyroxene is largely uralitised. These dykes have been dated at 824±4 Ma ($^{207}Pb/^{206}Pb$ baddeleyite age: S-S. Sun, unpublished data), similar to the age of the Amata dykes (Zhao & McCulloch 1993a).

Type B dolerites are slightly quartz-normative tholeiites, with *mg** 51–61, but are chemically distinct from any of the types A or C dyke suites (Table 9). In particular, S contents (50–370 ppm) and LILE/Zr ratios are lower, and Cu is higher. Apart from slightly lower P/Zr, incompatible element/Zr ratios are closely comparable with estimated primordial mantle (Sun & McDonough 1989) (Fig. 142). Spidergrams are relatively flat, with smaller Nb anomalies (Fig. 144). These dykes were therefore derived from a much less enriched mantle source, consistent with high ε_{Nd} values (+2.8 to +3.2, Table 11).

Type B dolerites are chemically and isotopically virtually identical to the coeval Amata and Gairdner dykes (Zhao et al. 1994). This is evident from their very similar incompatible element ratios (Fig. 142) and spidergrams (Fig. 144). Even some of the small differences may be more apparent than real, because much of the scatter for elements such as Nb, La, and Ce in type B dykes probably reflects analytical uncertainties near the XRF detection limits. In contrast, the Amata dyke trace element data were obtained by the more precise ICP–MS method. ε_{Nd} values for the Amata and Gairdner dykes are +2.4 to +4.3 and +2.6 to +4.1, respectively (Zhao et al. 1994). There is thus little doubt that type B dolerites, together with the Amata dykes, represent the northwestern extension into the Musgrave Block of the Gairdner dyke swarm in the Gawler Craton and adjacent Stuart Shelf, a correlation supported by their similar northwesterly trends (Fig. 139).

Other mafic dykes in the Hinckley Range area

A 130 metre-thick, northeast-trending gabbronorite dyke in the western Champ de Mars has a gabbroic to subophitic texture and consists of labradorite (60–75%), orthopyroxene (15–24%), clinopyroxene (8–14%), opaque minerals (2%), and minor biotite and apatite (Fig. 141F). It is cut by a type B dolerite and has given a U–Pb zircon age of 1058±14 Ma (S-S. Sun, unpublished data). A petrographically similar gabbronorite dyke occurs near the contact of the Hinckley Range gabbronorite.

The thick gabbronorite dyke is a slightly quartz-normative tholeiite which does not appear to be related to any of the main dyke types, having, for example, different S/Zr, Pb/Zr, and K/Zr ratios. Nevertheless, like types A and C dykes, the gabbronorite was probably derived by melting of relatively enriched mantle with high LILE/Zr and Ce/Zr (Fig. 145), and low ε_{Nd} (-2.3, Table 11). Spidergrams are not unlike those of types A1 and C (Fig. 147), but S is much lower (190–290 ppm: Figs 143, 146). Two samples from the centre of this dyke are relatively fractionated, compared with the margin, with lower *mg** (49–51, compared with 61), FeO, MnO, MgO, Sc, V, Cr, Ni, and Zn, and higher Na_2O, K_2O, Ba, Sr, Pb, La, and Ce; other elements are similar (Table 9). There is little change in most incompatible element ratios, except for P/Zr, which is slightly higher in samples from the dyke centre. The degrees of SiO_2-saturation of these two samples are much the same as those of the marginal samples, suggesting fractionation dominanted by pyroxene, possibly with some plagioclase, but not olivine. The other gabbronorite is olivine-normative (*mg** 57) and has higher Ti/Zr, P/Zr, and Rb/Zr. Hence, although broadly similar in composition, it cannot be directly related.

An unusual orthopyroxene–hornblende-rich dolerite dyke from the western Champ de Mars area contains large poikilitic orthopyroxene and plagioclase 'phenocrysts' in a somwhat foliated intergranular groundmass of hornblende, plagioclase, quartz, opaque minerals, and minor biotite. Compositionally, it is a strongly quartz-normative basaltic andesite, quite similar to mafic dykes in the basement to the Bentley Supergroup (see below), apart from anomalously low Na_2O (0.78%). The reason for this latter feature is unknown, but the hydrous nature of the groundmass and low K/Rb (150) suggest that Na and possibly K may have been lost in a late-magmatic fluid phase. The highly evolved nature of this dyke makes it unlikely to be related to orthopyroxene-phyric dykes in some Giles Complex intrusions (e.g., The Wart, Fig. 67C).

Mafic dykes north of the western Tomkinson Ranges contain high-pressure garnet-bearing assemblages, apparently formed during Cambrian metamorphism and deformation (D_6) associated with development of the Woodroffe Thrust (Clarke et al. 1995a; Stewart 1995b). These generally undeformed dykes contain centimetre-scale garnet-rich aggregates in a fine-grained granoblastic matrix of hornblende, clinopyroxene, plagioclase, and Fe–Ti oxides, so they are difficult to correlate petrographically with unmetamorphosed dykes.

These garnetiferous ('eclogitic') dykes are compositionally varied. Some are virtually identical in composition to type B, indicating that even high-grade metamorphism, with development of quite different mineral assemblages, does not necessarily result in significant chemical changes. Sheraton (1984) showed that deformation is an important factor in determining such changes, although formation of high-pressure garnet-bearing assemblages commonly results in LILE depletion. Other dykes are similar in composition to the gabbronorites, whereas several are more akin to type C olivine dolerites. However, most of the latter have much lower K/Zr, Rb/Zr, Pb/Zr, and Ce/Zr than type C, whereas Ba/Zr is relatively high. These differences may either be due to metamorphism, or else the dykes may not be related to type C dykes to the south. One such metadolerite dyke (91989485A) has ε_{Nd} (at 1000 Ma) of +4.5, significantly higher than that (+1.9) of the only isotopically analysed type C dolerite, and more comparable to the c. 800 Ma type B dykes (Table 11). This dyke has given a Sm–Nd whole rock–clinopyroxene isochron age of 768±110 Ma, consistent with it being of type B, as well as mineral isochron ages of about 530 Ma,

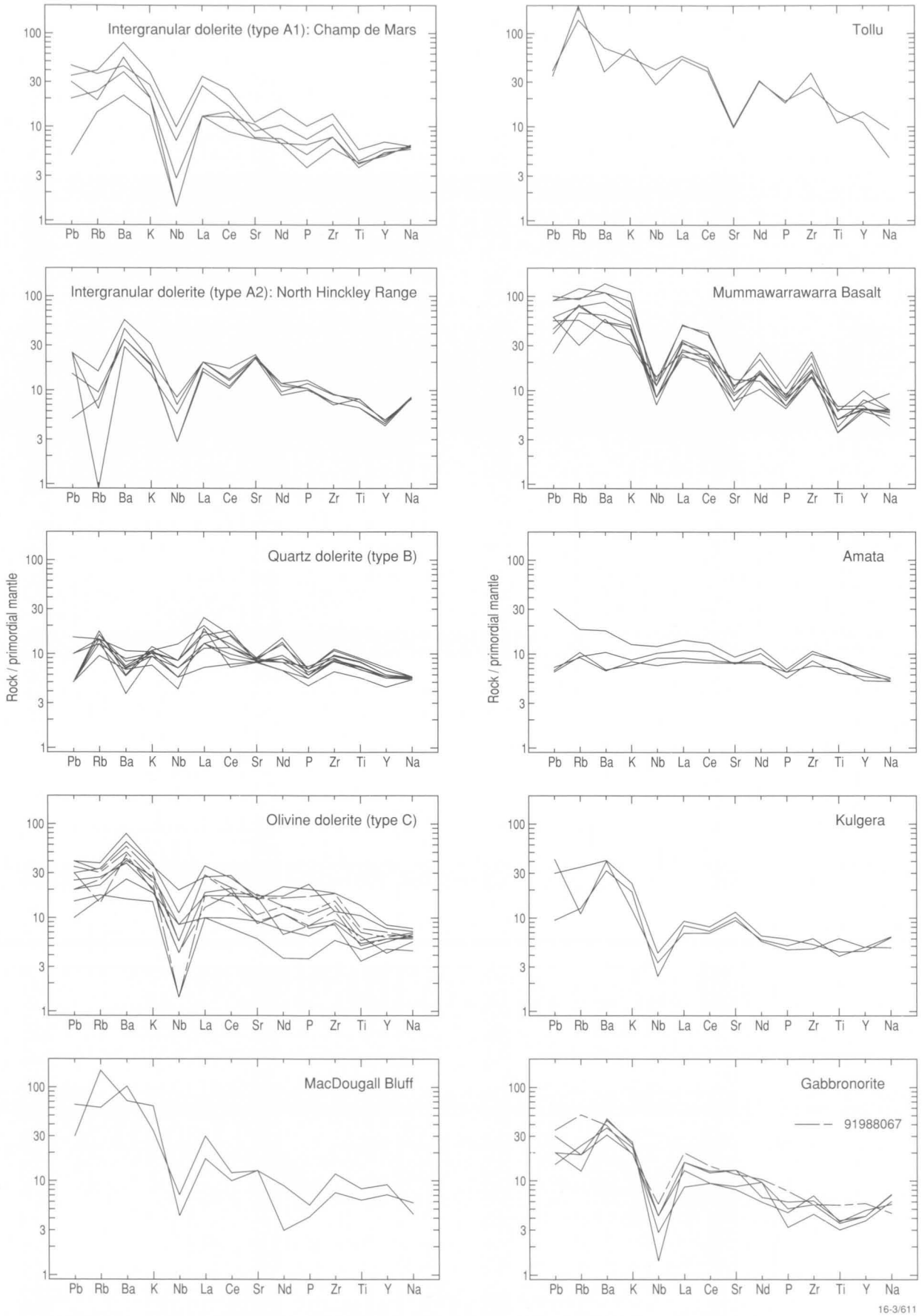

Figure 144. Spidergrams for dolerite and gabbronorite dykes and Mummawarrawarra Basalt. Dot-dashed lines for type C are the low Ti/Zr subgroup. Data for Kulgera and Amata dykes after Zhao (1992) and Zhao et al. (1994), respectively.

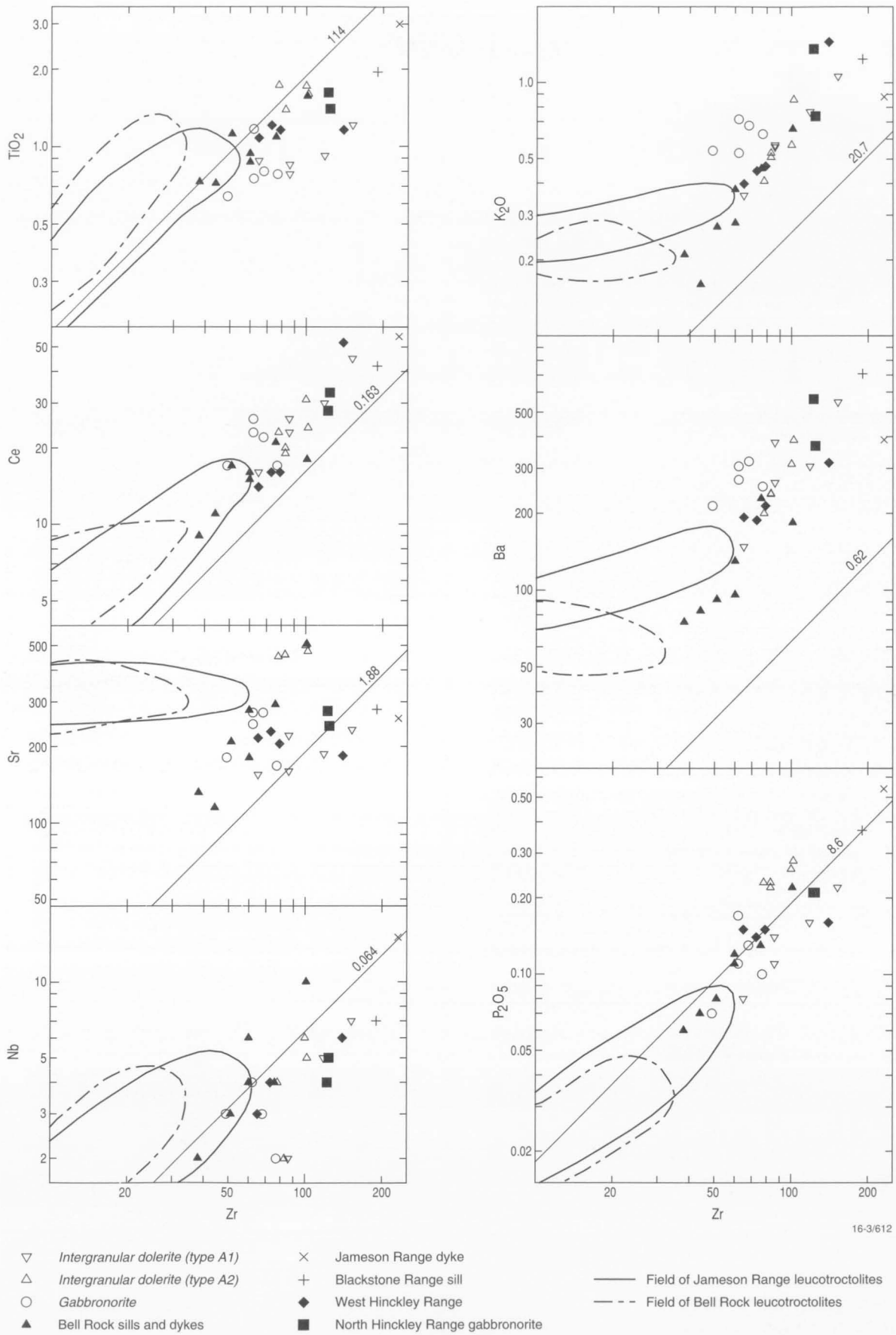

Figure 145. Logarithmic plots of various incompatible elements against Zr for type A1 and gabbronorite dykes, sills and dykes (including type A2) associated with Giles Complex intrusions, and Hinckley Range gabbronorites. Fields of leucotroctolite cumulates from the Bell Rock and Jameson Range intrusions based on data in the AGSO ROCKCHEM database. Note the relatively large K_d values (≤1) for K_2O, Ba, and Sr for the leucotroctolites.

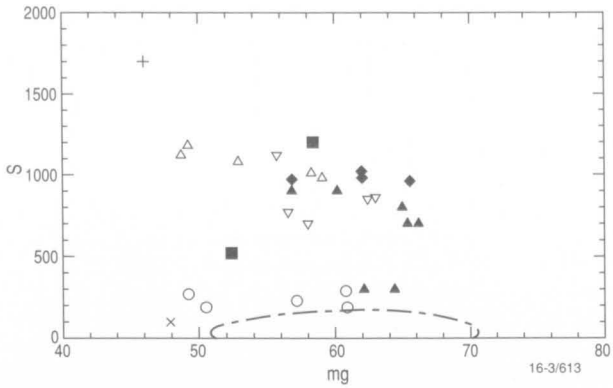

Figure 146. Plot of S against mg for type A1 and gabbronorite dykes, sills and dykes (including type A2) associated with Giles Complex intrusions, and Hinckley Range gabbronorites. Symbols as in Figure 145, except that only the Bell Rock leucotroctolite field is shown.*

consistent with the inferred age of the Woodroffe Thrust (Clarke et al. 1995b and next section).

Mafic dykes in the Tollu Group

Basaltic and basaltic andesite dykes which intrude Tollu Group felsic volcanics near Tollu are fine to medium-grained, and contain abundant amphibole and minor quartz. Petrographically varied dykes in the granitic basement underlying the Tollu Group at MacDougall Bluff include sub-trachytic, relatively quartz-rich basaltic andesite and orthopyroxene-bearing subophitic dolerite. Most of these dykes are east–west-trending.

Basaltic and basaltic andesite (quartz tholeiite) dykes in the Tollu Group felsic volcanic rocks (e.g., 91989384, Table 9) have generally similar compositions to the Mummawarrawarra Basalt (see previous section), although, being more strongly fractionated (*mg** 35–36) than the mafic volcanics, they are unlikely to be direct feeders. Moreover, they have relatively high Nb/Zr and low Ba/Zr, K/Rb, and S (10–40 ppm; Figs 142, 143). Spidergrams show marked negative Sr anomalies, consistent with plagioclase fractionation, but Nb, P, and Ti anomalies are smaller than for the Mummawarrawarra Basalt (Fig. 144). These dykes thus appear to have been derived from a similar mantle source to that of the basalts, but may not be directly related.

Mafic dykes in granitic basement at MacDougall Bluff (e.g., 91989396, Table 9) are also highly evolved quartz tholeiites (*mg** 36–48). However, LREE and HFSE contents are lower, and LILE are similar or even higher than the Tollu dykes, so that LILE/Zr ratios are much higher (Figs 142, 144); S contents (430–1170 ppm) are also much higher (Fig. 143). Hence, although derived from enriched mantle, the MacDougall Bluff dykes do not appear to be closely related to either the Tollu dykes or Mummawarrawarra Basalt or, indeed, to any of the dyke suites in the western Hinckley Range area.

Clarke et al. (1995a) suggested that type A dolerites may represent feeders to the mafic volcanics of the Bentley Supergroup (e.g., Mummawarrawarra Basalt). The much more fractionated compositions of the latter make direct correlations uncertain, but both were derived from very similar mantle source regions and a genetic relationship, if not a strictly comagmatic origin, is quite plausible.

Sills and dykes associated with Giles Complex intrusions

The Bell Rock troctolite/gabbro intrusion contains olivine microgabbro sills and dykes, some of which are clearly intrusive into the cumulates, whereas others appear to be gradational. The latter were apparently emplaced before the host rocks had completely crystallised (Glikson et al. 1995). The microgabbros are commonly fine to medium grained and have similar mineralogy to the host cumulates (Ballhaus 1993; Ballhaus & Glikson 1995). Textures range from cumulus to subophitic or gabbroic, and some have chilled margins. Most are olivine+plagioclase-phyric, and contain interstitial clinopyroxene, Fe–Ti oxides, and, in some rocks, biotite. Ballhaus & Glikson (1995) suggested that such bodies may represent high-pressure fractionated melts similar to those which were parental to the exposed Giles Complex intrusions. A few

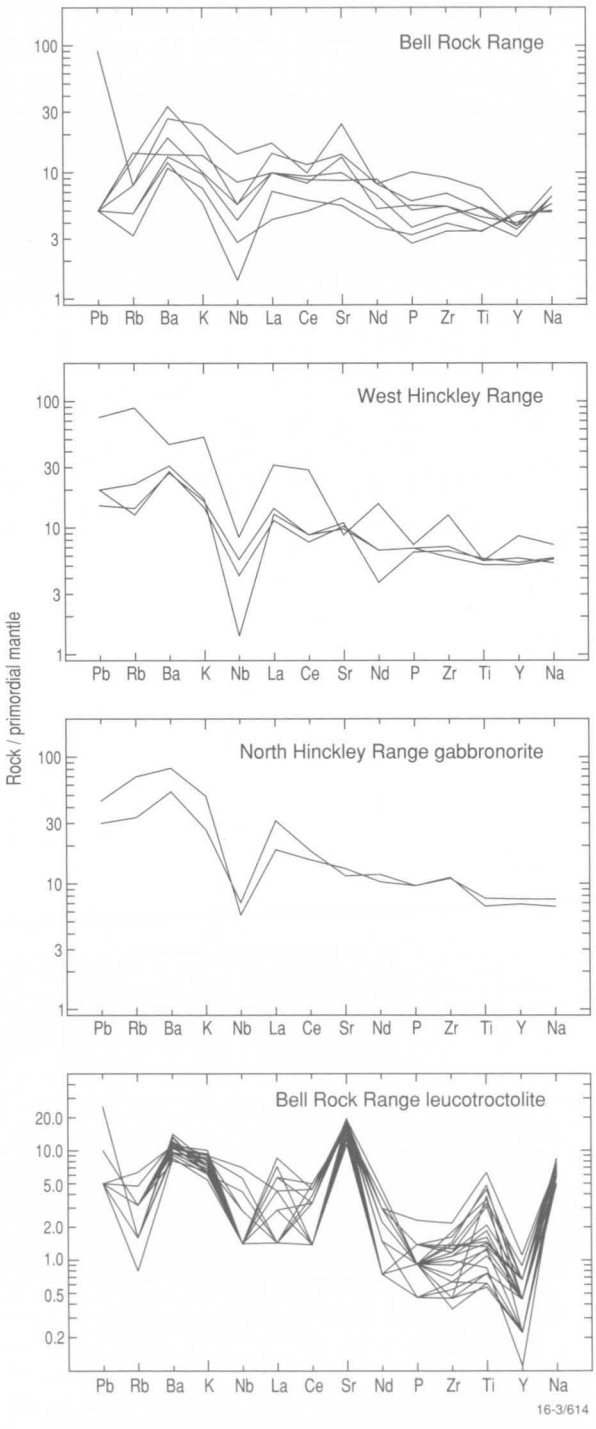

Figure 147. Spidergrams for microgabbro sills and dykes in the Bell Rock intrusion, Hinckley Range gabbroic rocks, and Bell Rock leucotroctolites. Note change of scale for latter.

similar sills and dykes also occur in the Jameson Range and Blackstone Range troctolite/gabbros, although only one was collected from each of the sampling traverses across these bodies. A 25 cm dyke from Jameson Range contains plagioclase and altered ?olivine phenocrysts, whereas a plagioclase-phyric sill from Blackstone Range is olivine-free.

Some of the analysed gabbroic rocks from the western part of the Hinckley Range gabbronorite may also be sills or dykes, but their field relations are unclear, as this part of the intrusion has been extensively recrystallised to mafic granulite. Such rocks range from fresh subophitic olivine dolerite (or microgabbro) to plagioclase-phyric intergranular two-pyroxene dolerite, texturally similar to type A dykes, and show various degrees of recrystallisation to granoblastic textures. The more strongly recrystallised rocks contain abundant brownish-green hornblende and lesser amounts of biotite. Similar conformable layers, sills, and dykes of microgabbro were interpreted by Ballhaus (1993) and Ballhaus & Glikson (1995) as chilled variants of the layered cumulus sequences. One recrystallised sample has given a preliminary U–Pb zircon ion-microprobe age of 1073±5 Ma (Sun et al. 1996b), consistent with this interpretation.

Microgabbro sills and dykes within the Bell Rock intrusion are mostly strongly olivine-normative tholeiites (*mg** 57-66; Table 9), although olivine *mg* values (Ballhaus 1993) suggest that at least some contain cumulus olivine. Like the previously described dyke suites (apart from type B), they are characterised by high LILE/Zr and Ce/Zr, but HFSE/Zr are similar to primordial mantle, rather than being lower (Fig. 145). Sulphur contents (mostly 700–1000 ppm: Fig. 146) and K/Rb ratios (350–1100) also tend to be high. These compositional features are broadly similar to those leucotroctolites and gabbronorites with the least-developed cumulus features in the host intrusions (Fig. 145). Spidergrams show significant positive Sr anomalies, consistent with plagioclase accumulation, whereas the host rocks show much stronger cumulus characteristics, namely marked Sr (plagioclase) and Ti (titanomagnetite) enrichment, relative to other incompatible elements (Fig. 147). In terms of source characteristics, there is a strong similarity to type A2 dykes, although these are more fractionated (quartz-normative, *mg** 49–59) and have slightly higher P/Zr. However, type A2 dykes also show positive Sr anomalies indicative of plagioclase accumulation (Fig. 144).

The Blackstone Range sill and Jameson Range dyke are both olivine-normative tholeiites, but are more evolved in terms of their high incompatible element contents, low *mg** (46–48), and negative Sr anomalies. This may be due to lower degrees of melting of similar mantle sources to the Bell Rock microgabbros, with that for the Jameson Range dyke being somewhat less LILE-enriched (Fig. 145).

Three of the analysed gabbroic rocks in the western part of the Hinckley Range intrusion (e.g., 91988052, Table 9) are olivine tholeiites with relatively high *mg** (62–66) and S (960–1020 ppm). Most incompatible element contents and ratios are indistinguishable from those of the Bell Rock sills and dykes (Fig. 145), but the spidergrams are less irregular, without the cumulus features (Sr enrichment, HFSE depletion) of the latter (Fig. 147). A fourth recrystallised gabbro, which gave the 1073±5 Ma zircon age, is more fractionated (*mg** 57), and has higher Ce/Zr, lower Ti/Zr and P/Zr, and a more irregular spidergram (Figs 145, 147); it may therefore be unrelated to the other west Hinckley Range rocks.

Gabbronorites from the northern Hinckley Range (91980111, Table 9) are compositionally quite similar to those from the west, apart from being more evolved (*mg** 52–58) and having slightly lower Ti/Zr and Nb/Zr (Figs 145, 147). A recrystallised sample has ε_{Nd} of -1.4 at 1080 Ma (S-S. Sun, unpublished data).

Petrogenesis

Relationships between mafic dykes and the Giles Complex

The presence of microgabbro sills and dykes with similar phenocryst assemblages (olivine+plagioclase) to the host cumulates in the Bell Rock and other troctolitic intrusions led Ballhaus (1993) and Ballhaus & Glikson (1995) to suggest that they represent chilled variants of the layered sequences, or were parental to the latter. The lack of precise geochronological data precludes conclusive proof of such relationships, but similar ages of type A1 and gabbronorite dykes to gabbronorites from the western and northern Hinckley Range are consistent with at least some of the dykes being feeders to higher-level Giles Complex intrusions.

As shown above, there are close chemical similarities between microgabbro sills and dykes in the Bell Rock intrusion and gabbroic rocks of the Hinckley Range intrusion. There is also a marked resemblance to type A2 dykes in the northern Hinckley Range, although these have slightly higher P/Zr. These features strongly suggest a common (but not necessarily comagmatic) origin for the dykes and the gabbroic components of the Giles Complex, such as the Hinckley Range body. However, clear relationships with the troctolitic intrusions (Bell Rock, Blackstone Range, and Jameson Range) are more difficult to establish, because there are significant compositional gaps between, for example, the Bell Rock sills and dykes and the host layered sequences (Fig. 145). The latter have strong cumulus features, whereas the microgabbro sills and dykes and type A2 dykes show evidence for only relatively minor plagioclase (and possibly olivine and titanomagnetite) accumulation (Figs 144, 147). Nevertheless, the Bell Rock leucotroctolites were apparently derived from a similarly enriched mantle source to that of the microgabbros. Thus, most incompatible element ratios of Bell Rock samples with the least cumulus features are similar to those of the dykes. Only Sr/Zr, Ti/Zr, and probably Nb/Zr are significantly higher, which can be explained by plagioclase and titanomagnetite accumulation. The Jameson Range leucotroctolites show similar features, and, although LILE contents are somewhat higher, LILE/Zr ratios of the least cumulus samples are similar to those of Bell Rock (Fig. 145).

Assuming that Zr is itself incompatible, logarithmic plots of other incompatible elements against Zr should define lines of unit slope (i.e., lines of constant ratio, corresponding to bulk distribution coefficients, K_d, of zero). Figure 145 shows that K_d values for Ce and P, as well as Y and S (not shown), for the Bell Rock leucotroctolites are close to zero. The K_d for Sr is about 1.0, consistent with plagioclase-dominated accumulation, but K_ds for LILE are much higher (~0.7–1.0) than expected for such a process, suggesting involvement of an additional phase, such as biotite. However, Ballhaus (1993) described biotite as being of late or post-magmatic origin, so possibly the relative LILE enrichment in the cumulates is a deuteric, or even a metamorphic, effect. The K_ds for Ti and Nb are difficult to estimate, but samples with less cumulus characters (higher Zr, etc.) have relatively high Ti/Zr (and possibly Nb/Zr) and may thus be more enriched in Fe–Ti oxides. In other words, there appears to be an inverse correlation between plagioclase and titanomagnetite accumulation. Of the compatible elements (not plotted here), Ni has a K_d of around 2, consistent with olivine accumulation, V shows a similar trend to Ti and Nb, suggesting vanadiferous titanomagnetite accumulation, and Cr shows little correlation with Zr. The estimated K_d for Sc is about 0.7, suggesting some pyroxene control, but petrographic evidence indicates olivine+plagioclase dominated fractionation, so that fractionation of pyroxene may have occurred at an earlier stage of magmatic evolution. Early

clinopyroxene fractionation could also account for the marked Y depletion, relative to other HFSE (Fig. 147). Ballhaus & Glikson (1995) proposed that the parent magmas to the Giles Complex intrusions experienced various degrees of high-pressure (probably >10 kb) orthopyroxene–clinopyroxene±olivine fractionation at significantly greater depths prior to emplacement.

Most of the microgabbro dykes and sills in the troctolitic intrusions thus appear to be more closely related to the gabbroic bodies, like Hinckley Range, than to the troctolitic bodies themselves. They are, in fact, virtually indistinguishable from dykes cutting the gabbros, except that the more evolved microgabbros show some Sr enrichment (plagioclase accumulation) and Y depletion (?clinopyroxene fractionation). S contents are generally comparable, whereas those of most Giles Complex layered sequences are very low (≤ 100 ppm). However, this can be explained, at least to a large extent, by the strongly cumulus nature of the intrusions. As suggested by Ballhaus (1993) and Ballhaus & Glikson (1995), these microgabbros probably represent more fractionated parental liquids derived by high-pressure pyroxene±olivine fractionation of primitive mantle melts. According to these authors, the gabbroic rocks cannot be directly parental to the troctolitic cumulates, which require a more strongly fractionated parental melt, more depleted in normative diopside. Nevertheless, both the gabbroic and troctolitic parent magmas may have separated at different stages from the evolving high-pressure melt(s). Clearly, both were ultimately derived from very similar enriched mantle source regions.

The least fractionated microgabbros in the Bell Rock intrusion may well be representative of such evolved parental magmas to the gabbroic intrusions. Sample 88982029 (Table 9) has a relatively flat, regular spidergram showing only slight Sr enrichment and no Y depletion, i.e., no significant cumulus features. It is broadly similar to Sun & Sheraton's (1992) estimated Giles parent magma (Table 6), but is slightly more evolved and has lower LREE and Zr. Both estimates are characterised by relatively low HFSE, indicating magma generation by large degrees of mantle melting at relatively shallow depths. Unlike the troctolitic rocks, such compositions imply only relatively small degrees of high-pressure fractionation. *mg** values (65 for 88982029) and Cr and Ni contents (705 and 220 ppm, respectively) are not far removed from those of primary olivine tholeiite magmas in equilibrium with mantle pyrolite (Ringwood 1975; Frey et al. 1978).

Nesbitt et al. (1970) proposed that the Tollu Group mafic volcanics may be genetically related to the Giles Complex. However, the compositional relationships between the Giles Complex and its associated dykes and the Mummawarrawarra Basalt are uncertain, because of the degrees of fractionation and alteration and highly vesicular nature of the volcanic rocks. Both the intrusive and extrusive rocks were derived from similar enriched mantle source regions, and are of similar age, so that at least an indirect association is likely. Relatively low P/Zr, Ti/Zr, and Nb/Zr of the basaltic rocks can be attributed to extensive fractionation, but it is not clear that these rocks were derived directly from any of the parent magmas of the Giles intrusions. The low S contents of the Mummawarrawarra Basalt probably reflect loss of S during extrusion (Wallace & Carmichael 1992).

Origin of the c. 1080 Ma magmas

Type A1 dolerites, c. 1080 Ma Giles Complex intrusions and associated dykes and sills, and the Mummawarrawarra Basalt and associated dykes, as well as the somewhat younger (at least in part) type C olivine dolerite dykes, were all derived by melting of an enriched source, probably involving subcontinental lithospheric mantle. This is indicated by LILE/Zr and LREE/Zr ratios much higher than estimated primordial mantle (Sun & McDonough 1989), whereas HFSE/Zr ratios are comparable to, or less than, primordial mantle values. Spidergram patterns are thus moderately to strongly fractionated, and generally have marked negative Nb anomalies, consistent with metasomatic enrichment of the mantle source by a LILE (and LREE) rich fluid or melt, possibly derived by dehydration or partial melting of subducted sediments (Rogers et al. 1987; Nelson & McCulloch 1989). Under hydrous melting conditions, Nb would be retained in residual Ti-oxide minerals (ilmenite, rutile, titanite, or perovskite), which is thought to account for the negative Nb anomalies of island-arc basalts (Saunders et al. 1980; Arculus 1987), and could possibly explain the relatively low Nb/Zr and Ti/Zr of many Musgrave mafic dyke suites (Fig. 142).

Although broadly similar in composition, there are significant chemical differences between the various dyke suites and some (notably type C) are markedly heterogeneous. Some dyke types (A1 and A2, as well as B) show essentially constant ratios of many incompatible elements (i.e., plot on lines of unit slope on Fig. 142). Plots of other elements approximate to lines of lower slope. For example, Sr has a K_d of about 1, indicating fractionation of plagioclase, and trends for Sc (K_d ~1) and Y (K_d ~0.3–0.6, not shown) are consistent with clinopyroxene fractionation. More compatible elements (V, Cr, and Ni) have even higher K_d values. The scatter shown by the Mummawarrawarra Basalt may largely be due to alteration and the presence of abundant amygdales, but for type C dykes, which show relatively large variations in major, as well as trace element compositions, the differences are presumably of primary magmatic origin.

There are several possible explanations for these variations. Some crustal contamination is quite probable, particularly for LILE, although Sheraton et al. (1990) argued that most of the compositional variations of continental tholeiite suites can be explained by partial melting and fractional crystallisation processes, together with derivation from heterogeneous lithospheric mantle sources. Zhao & McCulloch (1993b) also argued against major crustal contamination in formation of the Stuart and Kulgera dyke swarms. Different degrees of melting are implied by the fact that type C olivine tholeiites have similar (or even higher) absolute abudances of most incompatible elements compared to the more evolved (lower *mg**) type A2 and gabbronorite quartz tholeiites. More complex processes, such as dynamic partial melting (Langmuir et al. 1977), RTF (periodically replenished, tapped and fractionated) magma chambers (O'Hara & Mathews 1981; Cox 1988), and possibly disequilibrium melting (Bédard 1989), may also have been important, but would not significantly affect incompatible element, as opposed to compatible/incompatible element, ratios. Chemical and isotopic data for the Stuart dyke swarm (e.g., Ce – Ti/Zr and trace element – initial ε_{Nd} plots) are consistent with a two-component mixing process, possibly between a depleted mantle source and an older slab-derived trondhjemitic melt (J-X. Zhao, personal communication 1995).

Hence, most of the incompatible element heterogeneity shown by the various dyke suites probably reflects mantle source heterogeneity, ultimately caused by subduction processes. For example, type A2 may have been formed by melting of a high-P/Zr (?apatite-rich) source, and type C shows considerable variations in Nb/Zr, Ce/Zr, and Ti/Zr, as well as LILE/Zr. Such heterogeneity appears to have been both lateral (as type C shows significant geographical compositional variations) and vertical (because several chemically distinct suites of similar age crop out in the same area). It is noteworthy that both the Kulgera and Stuart dyke swarms also show considerable heterogeneity, with ε_{Nd} ranging from -9.9 to +1.9 (Zhao & McCulloch 1993b), compared to -2.3 to +1.9 for single samples of types A1 and C, and gabbronorite dykes (Table 11).

Most of the dykes, including those probably genetically related to the Giles Complex gabbroic intrusions, have S contents (700–1200 ppm) typical of those of continental tholeiites (Figs 143, 146). Such S contents are close to saturation levels for mafic magmas (Czamanske & Moore 1977), although type A2 and Bell Rock dykes (as well as the Kulgera and Stuart dykes) show negative correlations with *mg**, suggesting that the magmas may not have been completely saturated in S. If the Giles parent magmas were S-saturated, this would severely restrict their economic potential for platinum group element (PGE) mineralisation (Sun et al. 1991; Wyborn & Sun 1994). Determination of Se (to quantify possible S loss) and PGEs are needed to define this potential. The much lower S of the Mummawarrawarra Basalt (and two high-level dykes near Tollu) can be explained by S loss during ascent and eruption (Wallace & Carmichael 1992).

Zhao & McCulloch (1993b) pointed out that Sm–Nd whole-rock isochron ages and corresponding ε_{Nd} values for the Stuart (1853±189 Ma, ε_{Nd} -4.2±4.2) and Kulgera (1589±165, ε_{Nd} +1.7±3.6) dykes are very similar to those of the associated continental crust. Nd T_{DM} model ages of felsic ortho- and paragneisses in the western Musgrave Block are 1610–1900 Ma and ε_{Nd} values (at c. 1070 Ma) are -2.5 to -4.8 (Table 11). This suggests that metasomatic enrichment of the lithospheric mantle (presumably subduction-related) was coeval with crust formation in the area. Similar correlations between source enrichment and continental crust formation have been demonstrated for many other dyke swarms, including those in the Bunger Hills, East Antarctica (Sheraton et al. 1990).

The ultimate cause of the very extensive mantle melting event which produced the Giles Complex intrusions, dykes, and mafic volcanics at about 1080 Ma is uncertain. Clearly, this magmatism cannot have been the direct cause of the c. 1200 Ma granulite-facies metamorphism in the area, although the latter may also have been associated with at least some mafic magmatism (1176±5 Ma biotite gabbronorite near the Hinckley Range). A major thermal perturbation was clearly necessary to account for the scale of melting involved in formation of the Giles Complex. Zhao & McCulloch (1993b) suggested that the melting temperature would have been significantly lowered if the lithospheric mantle had been hydrated by earlier metasomatism. Subsequent thinning of such hydrous lithosphere could have allowed hot asthenospheric mantle to flow beneath the lithosphere and cause decompression melting, or, alternatively, underplating of refractory mantle diapirs or hot mantle plumes could have caused dehydration melting of the overlying lithosphere.

Origin of the c. 800 Ma magmas

Type B dolerite dykes were derived from a quite different source to the c. 1080 Ma dykes and the Giles Complex. In most respects this source was apparently very similar to estimated primordial mantle (Fig. 142), with ε_{Nd} of +2.8 to +3.2 (Table 11). It was also much more homogeneous than that of the older mafic rocks, particularly as the Amata and Gairdner dykes have virtually identical compositions (ε_{Nd} +2.4 to +4.3: Zhao et al. 1994). This implies a homogeneous mantle source region more than 1000 km across. Only Ba/Zr and possibly Ce/Zr show significant variations which cannot be attributed to analytical uncertainties. These variations are unlikely to be due to crustal assimilation, because other LILE do not show such variations, and presumably characterise the source. In any case, the large-scale compositional homogeneity of the 800 Ma dykes militates against significant crustal assimilation, and suggests an asthenospheric, rather than lithospheric, mantle source. Low Al_2O_3 (13.2–14.8%) is consistent with relatively high-pressure melting. Low S (50–370 ppm) is difficult to explain, even by assuming high degrees of melting at high temperatures (HFSE contents are comparable to those of less fractionated olivine-normative dykes), but may be a result of high oxygen fugacity (Wallace & Carmichael 1992; Carroll & Webster 1994). Alternatively, S loss may have occurred during emplacement at relatively high crustal levels, although emplacement pressures are unknown.

Zhao et al. (1994) postulated that the 800 Ma magmas were derived by decompressional melting of a large-scale asthenospheric mantle plume. This was suggested to have resulted in domal uplift of the overlying crust, followed by rifting, crustal extension, and thinning, and culminated in thermal subsidence and basin formation in central–southern Australia. The northwest-trending dykes were thought to have been emplaced along the axis of the failed arm of a triple junction located above the plume head in the Adelaide Geosyncline. Although such an evolution seems quite plausible, there may be a problem with the timing of these events. In particular, initiation of formation of the Amadeus Basin must have significantly pre-dated the 800 Ma magmatism, particularly if the Bitter Springs Volcanics, which occur near the base of the Amadeus Basin, are the same age as the Amata dykes (Shaw 1991; Shaw et al. 1991), as suggested on chemical grounds by Zhao et al. (1994). Hence, the relationships of the postulated mantle plume activity and associated magmatism to basin formation in central Australia, at least, remain to be clarified.

Geochemical and isotopic evolution

This section summarises whole rock and mineral Sm–Nd isotopic data and SHRIMP ion-microprobe zircon U–Pb ages for the main geological units in the Tomkinson Ranges (Table 10). The full details will be presented in a paper in preparation (Sun et al.). The emphasis of the present study has been on the dating of events which have not previously been well defined by Rb–Sr and K–Ar methods (e.g., Gray & Compston 1978; Webb 1985). In the western Musgrave Block, major tectonothermal events include crust formation at about 1550 and 1300 Ma, and granulite-facies metamorphism and granite emplacement at about 1200 Ma (Gray 1978; Gray & Compston 1978; Maboko et al. 1991; Sun & Sheraton 1992; Sun et al. 1996a, b). The granulite-facies country rocks were intruded by K-feldspar-megacrystic hornblende–biotite granites at 1188±4 Ma (Sun & Sheraton 1992; Sun et al. 1996a, b). A further major tectonothermal event at about 1080 Ma, involved granulite-facies metamorphism and emplacement of the mafic–ultramafic Giles Complex, mafic dykes, and granitic intrusions. In the western part of the Tomkinson Ranges extrusion of contemporaneous, widespread mafic and felsic volcanic rocks of the Tollu Group, occurred about 1050–1080 Ma ago.

The precise emplacement age of the voluminous mafic–ultramafic intrusions of the Giles Complex has been an outstanding issue requiring assessment by the ion-microprobe SHRIMP zircon U–Pb dating method. Selected samples were dated using the SHRIMP 2 at the Research School of Earth Sciences, Australian National University, and the data were processed in a manner similar to those described by Compston et al. (1984, 1986) and Williams & Claesson (1987). The time of emplacement of the Giles Complex has relevance to several important questions: (1) how are the intrusions related to the 1200 Ma high-grade orogenic event, (2) are the spatially associated felsic volcanic rocks of the Tollu Group contemporaneous with, and genetically related to, the Giles Complex, and (3) can this magmatic event be correlated with magmatic activity in other parts of central Australia? A well-defined radiometric age framework is also important for the reconstruction of the pressure–temperature–time (P–T–t) history of the western Musgrave Block, as discussed in the next section.

Neodymium isotopic compositions and Sm and Nd concentrations were determined at the Research School of Earth Sciences, Australian National University, with a multi-collector Finnigan MAT 261 mass spectrometer operated in static multi-collector mode. Chemical separation procedures were similar to those described by Maas & McCulloch (1991). Powdered samples (50–70 mg) were spiked with ^{147}Sm–^{150}Nd tracers and then decomposed with a mixture of HF and HCl in

Table 10. Summary of isotopic age determinations in the western Musgrave Block.

Age (Ma)	*Method*	*Rock type*	*Major geological events*
			D_7 retrograde shear zones
c.530	Sm–Nd mineral isochrons	Garnet-bearing metadolerite dyke	Major ultramylonite–pseudotachylite zones (D_6); N-directed thrusting during Petermann Ranges orogeny; sub-eclogite-facies metamorphism near Woodroffe Thrust
			Ultramylonite zones (D_4, D_5); greenschist to amphibolite-facies metamorphism
824±4	U–Pb baddeleyite ion-probe	Quartz dolerite dyke	Post-D_3 mafic dykes (type B)
c.1000	Sm–Nd mineral isochron	Olivine dolerite dyke	Post-D_3 mafic dykes (type C)
			Granulite-facies metamorphism and regional deformation (D_3)
1052±11	U–Pb zircon ion-microprobe	Porphyritic Hbl–Bt granite dyke	Pre- to syn-D_3 granitic dykes and veins, and mafic dykes (type A)
1068±6	U–Pb zircon ion-microprobe	Rapakivi Cpx–Bt granite dyke	
1058±14	U–Pb zircon ion-microprobe	Gabbronorite dyke	
1078±5	U–Pb zircon ion-microprobe	Rhyolite (Smoke Hill volcanics)	Mafic to felsic volcanism (Tollu Group)
1073±5	U–Pb zircon ion-microprobe	Recrystallised gabbro (Hinckley R)	Giles Complex layered intrusions
1078±3	U–Pb zircon ion-microprobe	Granophyre (Bell Rock intrusion)	
1176±5	U–Pb zircon ion-microprobe	Bt–Hbl gabbronorite	Post-D_2, pre-D_3 Hbl–Bt granitoids and gabbroic rocks
1188±4	U–Pb zircon ion-microprobe	Porphyritic Hbl–Bt granite	
1198±6	U–Pb zircon ion-microprobe	Post-D_1, pre-D_2 Bt granite gneiss (Minno)	Granulite-facies metamorphism; regional penetrative deformation (D_1 and D_2); Post-D_1, pre-D_2 Opx granitoids
1204±17	Rb–Sr isochron		
1305±8	U–Pb zircon ion-microprobe	Protoliths of felsic orthogneiss (S of Hinckley Fault)	
1327±7	Rb–Sr isochron (pooled)		
1564±12	Rb–Sr isochron (pooled)	Protoliths of felsic orthogneiss (N of Hinckley Fault)	

Rb–Sr ages from Gray (1978); U–Pb and Sm–Nd ages from Sun & Sheraton (1992), Sun et al. (1996a, b), and S-S. Sun (unpublished data). Abbreviations as in Table 2.

high-pressure Teflon bombs inside metal jackets. Separation of Sm and Nd was carried out using Kel-F/HDEHP coated ion-exchange columns. For mass fractionation correction, the reported $^{143}Nd/^{144}Nd$ ratios were normalised to $^{146}Nd/^{144}Nd$ of 0.7219. Average $^{143}Nd/^{144}Nd$ values for La Jolla and BCR-1 standards were 0.511872±2 (2σ, n=85) and 0.512653±5 (2σ, n=8), respectively, during this study. The neodymium blank was less than 50 picograms. Reproducibility of $^{143}Nd/^{144}Nd$ values is about 0.002% (i.e., 0.2 ε_{Nd} units); that of $^{147}Sm/^{144}Nd$ for separate decompositions of the same sample is generally better than 0.2%.

The Sm–Nd model age of a felsic igneous rock can provide an estimate of the average crustal residence time of its source rock(s). It is based on the assumption that the major chemical fractionation of Sm and Nd occurs during differentiation of material from the depleted mantle and its incorporation into the crust. There are two schemes used in Australia for calculation of the depleted mantle model age (T_{DM}). Model ages following McCulloch's (1987) approach are calculated assuming that the mantle depletion event occurred at 2750 Ma and the ε_{Nd} value in the depleted mantle increases linearly with time to a present day value of +10. The ε_{Nd} value is defined as $((^{143}Nd/^{144}Nd)_{sample}/(^{143}Nd/^{144}Nd)_{chondrite}-1)\times10^4$ and a present day ε_{Nd} value of +10 corresponds to $^{143}Nd/^{144}Nd$ of 0.51316, relative to an average chondrite value of 0.512653. The other scheme, more commonly used in the literature, assumes that mantle depletion began at about 4560 Ma (the age of the Earth). Model ages calculated for Proterozoic felsic rocks using the scheme of McCulloch (1987) are generally 200–250 Ma younger than values obtained by the other scheme. Table 11 presents Sm–Nd isotope data for representative western Musgrave Block samples and model ages calculated using both schemes. In the following discussion, however, only T_{DM} ages of McCulloch's (1987) scheme are used to allow direct comparison with published data for the Arunta and Gawler Blocks. Sample locations are shown in Figures 28, 148, and 149.

The Mount Aloysius Complex and associated granitoids

T_{DM} model ages for felsic granulites (orthogneisses and paragneisses) from the Mount Aloysius Complex range from 1610–1900 Ma (Table 11). The Musgrave Block rocks generally have T_{DM} model ages more than 300 Ma younger than those (commonly 2100–2300 Ma) of Proterozoic rocks of the Arunta Block to the north and Gawler Block to the south (McCulloch 1987; Sun et al. 1995; Zhao & McCulloch 1995).

Layered granulites, which constitute the oldest recognised unit in the Musgrave Block, were studied at Mount Aloysius by Gray (1978), who reported a pooled Rb–Sr Whole-rock isochron age of 1564±12 Ma, considered to be the protolith age, since confirmed by our U–Pb zircon dating. A similar pooled Rb–Sr whole-rock isochron age of 1327±7 Ma was obtained for felsic granulites from the Bell Rock–Michael Hills area (Gray 1978), very similar to a U–Pb zircon age of 1305±8 Ma for felsic orthogneiss from west of Mount Davies (Sun & Sheraton 1992). According to Gray & Compston (1978), protolith ages of about 1550 Ma appear to predominate north of the latitudinal Hinckley Fault (Fig. 148), whereas c. 1300 Ma ages predominate south of the fault. Although it is probable that these different-aged terranes will be confirmed by further work, the restricted isotopic data presently available cannot be entirely conclusive. Orthogneiss and sillimanite-bearing paragneiss, derived from 1550 Ma old protoliths, at Mount Aloysius contain inherited zircon of about 1650 Ma. Both 1550 and 1300 Ma orthogneisses have high initial ε_{Nd} (about +3 at 1550 Ma and 0 at 1300 Ma) and young Nd T_{DM} model ages (1610–1776 Ma), suggesting formation of juvenile crust from the mantle. Zircons from an Y-depleted orthogneiss (90984024), which has chemical features suggesting an origin by melting of a garnet-bearing mafic source, indicate a protolith age of about 1530 Ma (Sun & Sheraton 1992). Granitic rocks formed between 1200 and 1188 Ma have Nd T_{DM} model ages of 1677 to 1912 Ma and initial ε_{Nd} values of -1.5 to -3.8 (Table 11), consistent with an origin by melting of the 1550–1300 Ma felsic crust (with ε_{Nd} values of -1.2 to -3.6).

The granulite-facies rocks of the Mount Aloysius Complex consist mostly of felsic igneous rocks of primary intrusive or extrusive origin, metasedimentary rocks being relatively scarce. Protoliths of some Y-depleted orthopyroxene-bearing felsic orthogneisses (e.g., 90984024) may represent primary felsic crust derived by partial melting of a hornblende±garnet-bearing, but feldspar-poor, mafic source (such as subducted hydrated oceanic crust). This is consistent with the relatively young Nd T_{DM} model ages of at least some of these rocks. Other orthopyroxene and/or garnet-bearing orthogneisses have geochemical features, notably depletion in Sr but not Y, consistent with intracrustal melting. The geochemical effects of high-grade metamorphism were apparently minor, being mainly confined to loss of U relative to Th (Gray and Oversby 1972; Sheraton & Sun 1995).

Post-D_1, pre-D_2 orthopyroxene granitoids represent intracrustal melts formed during the c. 1200 Ma granulite-facies metamorphism, although minor quartz monzodiorites are likely to have been derived either directly from the mantle, or by hydrous melting of a mafic–intermediate crustal source. An example is the syn-metamorphic Minno augen gneiss, located south of the Kalka intrusion and northwest of Mount Davies (Fig. 148). As shown in Figure 150, igneous zircons yield a concordant zircon U–Pb age of 1198±6 Ma (Sun & Sheraton 1992; Sun et al. 1996b), consistent with a Rb-Sr isochron age of 1204±17 Ma (Gray 1978). Inherited zircon cores indicate an age of 1296±10 Ma for the source rocks. Younger (post-D_2) hornblende–biotite granitoids include rapakivi, porphyritic, and even-grained varieties (Clarke 1992; Clarke et al. 1995a). An example is represented by foliated porphyritic granite in the Champ de Mars area (Fig. 149), which gives a U–Pb zircon age of 1188±4 (Fig. 151; Sun et al. 1996a, b). Inherited zircons are up to 1500 Ma old. Nd isotope data (initial ε_{Nd} = -3.8 and T_{DM} = 1912 Ma) for these granitic rocks are consistent with melting of c. 1550 Ma and, more likely from the inherited zircon ages, c. 1300 Ma felsic granulites in the region (Table 11).

Most of the geochemical features (high HFSE, LREE, and Th/U, and low Sr) of these granitoids, as well as the younger hornblende–biotite granitoids, suggest relatively high-temperature partial melting of near-anhydrous granulite-facies felsic crustal rocks. However, some intermediate rocks, including quartz monzodiorite and quartz monzonite, may have been formed by fractionation of mafic magma or, less likely, by progressive contamination with felsic crustal material. The wide compositional range of the hornblende–biotite granitoids cannot be due entirely to mixing of mafic (or intermediate) and felsic magmas. Much of the variation is probably due to crystal fractionation, different degrees of melting, and/or cumulate unmixing. Quartz syenite of Mount Aloysius represents a distinct magma type with A-type chemical features (high LILE, HFSE, LREE, and Ga, and low *mg* and Sr), derived from a distinct crustal, or possibly mantle, source.

Granitic basement rocks underlying the Bentley Supergroup differ from those in the Hinckley Range area in including a significant proportion of Y-depleted, Sr-undepleted rocks, which may represent juvenile felsic crust. The dominance of biotite–hornblende gneisses in this terrane, and its truncation by the unconformity below the Tollu Group volcanic rocks, absent from the Tomkinson Ranges, suggests that it may have formed at a higher crustal level than the granulite-facies rocks

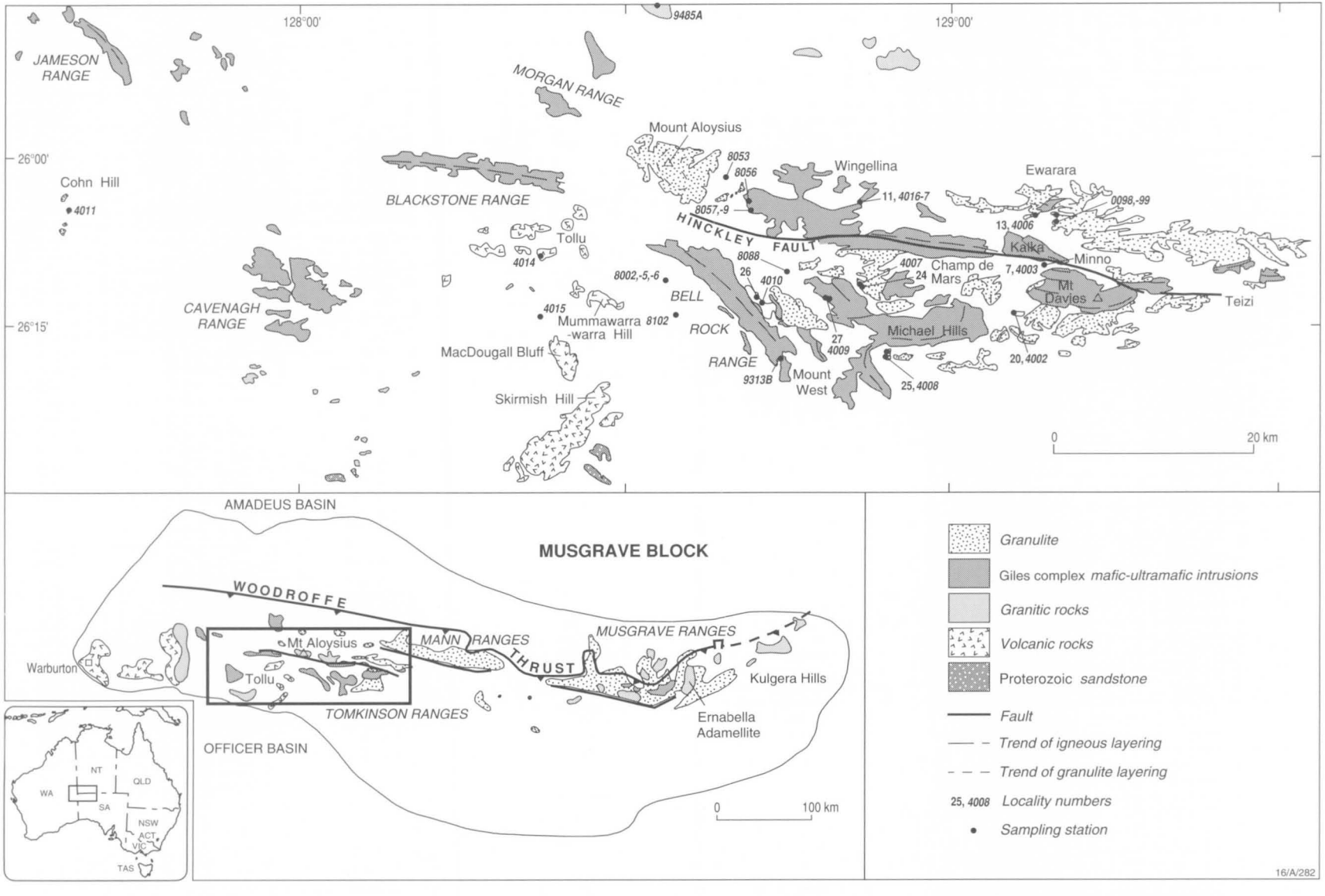

Figure 148. Geological map of the Tomkinson Ranges–Blackstone Range–Jameson Range area, showing locations of SHRIMP zircon U–Pb dated samples. Four digit sample numbers starting with '4' are prefixed '9098', those starting with '0', '8', or '9' are prefixed '9198', and other numbers refer to sample localities of Gray (1978).

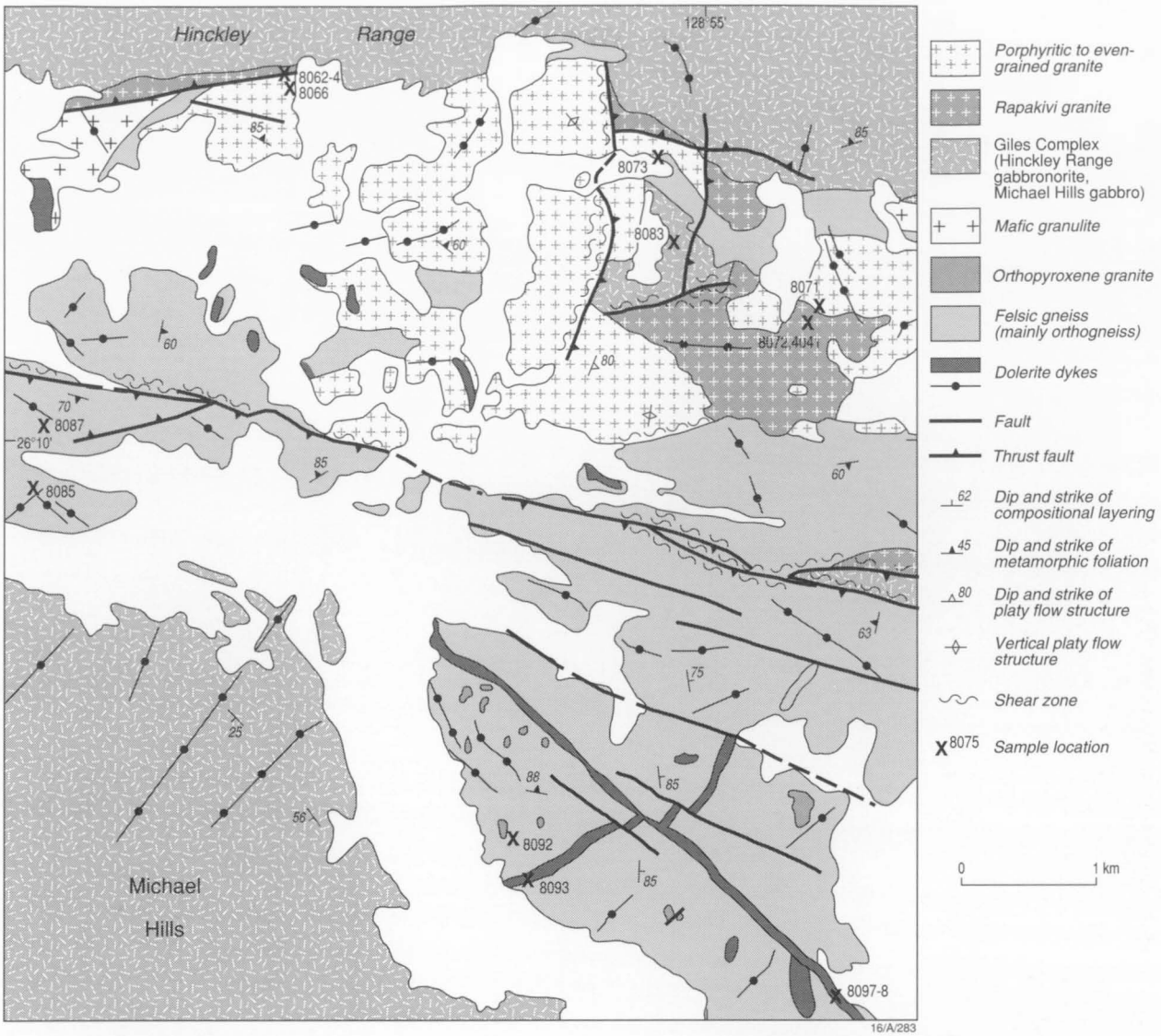

Figure 149. Geological map of the western Champ de Mars area, south of the Hinckley Range, showing field relationships of the Hinckley Range gabbronorite and porphyritic and rapakivi granites. Locations of zircon U–Pb dated samples are shown, all numbers being prefixed '9198'.

to the east. No isotopic studies of rocks from this area have yet been conducted.

The 1050–1080 Ma Giles–Tollu event

The Giles Complex, a suite of large layered mafic–ultramafic intrusions, was emplaced in the western Musgrave Block at deep crustal levels some time after the orogenic event at about 1200 Ma. The magmatism was associated with regional granulite-facies metamorphism, deformation, and generation of syn-metamorphic granites.

In the Champ de Mars area (Fig. 149), small porphyritic and rapakivi hornblende–biotite granite bodies (mostly dykes and veins) locally intruded the southern margin of the Hinckley Range gabbronorite, although, as has been shown, other petrographically similar granites are much older (1188±4 Ma). Some of the type A mafic dykes which intrude the Giles Complex have strong chemical and isotopic similarities to their host rocks, indicating that they are likely to be cogenetic (see mafic dyke section). Granophyre within the Bell Rock intrusion is interpreted to be a late magmatic differentiate of the host troctolitic intrusion. The zircon U–Pb ages of these and other associated igneous rocks can be used to constrain the emplacement age of the Giles Complex.

The results are shown on concordia plots in Figure 152. A granitic dyke (91988059) cutting the western part of the Hinckley Range gabbronorite (Fig. 148) has a $^{207}Pb/^{206}Pb$ age of 1052±11 Ma. A rapakivi-textured felsic dyke (91988064) at the southern margin of the Hinckley Range gabbronorite (Fig. 149), previously thought to be part of the 1188 Ma porphyritic granite to the south, has a concordant U–Pb age of 1068±6 Ma. Thus, this felsic dyke cannot be related to the petrographically and geochemically similar 1188 Ma granites. A rhyolite sample (91988005) of the Smoke Hill Felsic Volcanics of the Tollu Group, has a magmatic $^{207}Pb/^{206}Pb$ age of 1078±5 Ma. A granophyric pegmatite (91989313B) in the Bell Rock troctolitic intrusion contains large, euhedral and simply zoned igneous zircons, which give a concordant U–Pb age of 1078±3 Ma.

Although a range of emplacement ages for different intrusions of the Giles Complex is possible (see section on the

Table 11. Sm–Nd isotopic data, geological ages, and Nd model ages for representative samples from the western Musgrave Block. Locality numbers from Gray (1978). Abbreviations as in Table 2.

Sample	*Sample locality, rock type*	*Sm (ppm)*	*Nd (ppm)*	$^{147}Sm/^{144}Nd$	$^{143}Nd/^{144}Nd$	$\pm 2\sigma$	*T(Ma)*	εNd_i	εNd_{1070}	T_{DM} *(McC)*	T_{DM} *(Ma)*
90984001	Mount Aloysius, felsic Opx orthogneiss	1.233	8.527	0.0874	0.511708	7	1550	3.4	–3.4	1616	1749
90984024	Mount Aloysius, felsic Opx orthogneiss	1.412	9.211	0.0927	0.511739	7	1550	2.9	–3.5	1645	1786
90984005	Mount Aloysius, felsic Opx orthogneiss	3.525	21.13	0.1009	0.511752	5	1550	1.5	–4.4	1737	1898
90984004	Mount Aloysius, Si–Gt gneiss	6.018	29.95	0.1215	0.511875	8	1550	–0.2	–4.8	1901	2118
91988088	Mount Aloysius, Opx leucogneiss	0.891	6.804	0.0792	0.511626	6	1550	3.4	–3.9	1610	1735
90984002	W of Mt Davies (loc. 20), felsic Opx gneiss	3.634	23.94	0.0918	0.511714	7	1300	–0.8	–3.9	1662	1804
90984008	Latitude Hill (locality 25), felsic Hbl gneiss	6.396	31.89	0.1212	0.511958	5	1300	–0.9	–3.2	1776	1977
90984010	Mount West (locality 26), felsic Hbl gneiss	13.66	72.05	0.1146	0.511904	6	1300	–0.9	–3.3	1744	1928
91988016	Mount Aloysius, massive felsic granulite	0.473	3.591	0.0796	0.511612	7	1200	–2.3	–4.2	1629	1756
91988035	Mount Aloysius, felsic Gt granulite (age?)	1.508	12.15	0.0750	0.511578	10	1200	–2.2	–4.3	1615	1736
91988039	Mount Aloysius, Ol–Cpx quartz syenite	15.07	75.30	0.1210	0.511950	6	1200	–2.0	–3.3	1783	1985
90984003	Minno, Bt granite gneiss	5.714	30.91	0.1118	0.511819	6	1200	–3.2	–4.6	1813	2000
91988072	Champ de Mars, rapakivi Bt–Hbl Qz monzonite	30.38	160.5	0.1144	0.511870	7	1188	–2.7	–3.9	1786	1975
91988073	Champ de Mars, rapakivi Cpx Qz monzodiorite	17.88	89.25	0.1211	0.511917	5	1188	–2.8	–4.0		
90984041	Champ de Mars, rapakivi granite	20.54	105.3	0.1179	0.511915	7	1188	–2.4	–3.6	1781	1972
91988071	Champ de Mars, porphyritic granite	10.57	52.65	0.1214	0.511866	6	1188	–3.8	–5.0	1912	2131
91988083	Champ de Mars, Bt gabbronorite	9.810	52.11	0.1138	0.511894	7	1176	–2.3	–3.4		
91988064	Champ de Mars, rapakivi Cpx–Bt granite dyke	10.51	59.55	0.1067	0.511852	6	1068	–3.3	–3.3	1694	1860
91988063	Champ de Mars, rapakivi granite dyke (hybrid)	10.73	53.64	0.1210	0.511984	6	1068	–2.6	–2.6	1733	1929
91988057	Champ de Mars, foliated Bt–Hbl granite dyke	13.71	83.09	0.0997	0.511892	6	1060	–1.6	–1.5	1552	1693
91988059	Champ de Mars, porphyritic Hbl–Bt granite dyke	13.92	76.65	0.1098	0.511923	6	1052	–2.5	–2.3	1646	1811
91988102	W of Bell Rock Range, amygdaloidal basalt	5.203	22.33	0.1409	0.512186	6	1078	–1.4	–1.4		
90984014	Near Bell Rock, Smoke Hill Volcanics rhyolite	21.34	101.4	0.1273	0.512175	8	1078	0.3	0.2	1549	1735
91988005	Tollu, Smoke Hill Volcanics rhyolite	31.38	144.0	0.1318	0.512225	7	1078	0.7	0.6	1543	1738
90984015	W of Mummawarrawarra Hill, granite	11.81	73.52	0.0971	0.511851	6	1078	–1.8	–1.9	1569	1709
91988006	Near Bell Rock, Fl–Hbl granite	34.89	160.1	0.1317	0.512238	7	1078	0.9	0.9	1520	1712
91989313	Bell Rock intrusion, granophyre	7.75	43.01	0.1089	0.511951	5	1078	–1.5	–1.6	1597	1756
91988085	Champ de Mars, dolerite dyke (type A)	4.194	18.38	0.1380	0.512131	6	1060	–2.2	–2.1		
91988093	Champ de Mars, gabbronorite dyke	2.082	8.260	0.1524	0.512223	6	1058	–2.3	–2.3		
91988056	W Hinckley Range, dolerite dyke (type C)	4.701	18.94	0.1501	0.512441	6	1000	1.9	2.1		
91988097	Champ de Mars, dolerite dyke (type B)	4.595	16.70	0.1664	0.512652	7	820	3.2	4.2		
91988098	Champ de Mars, dolerite dyke (type B)	4.339	15.65	0.1676	0.512639	6	820	2.8	3.8		
91989485A	Mt Fanny, western Woodroffe Thrust, metadolerite	1.73	5.08	0.2057	0.512937	6	800	4.7			

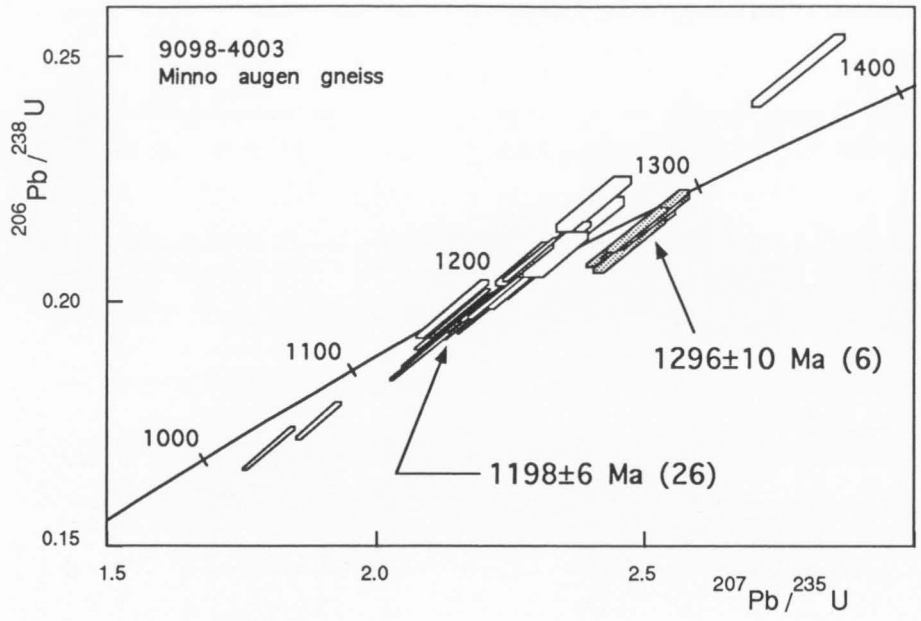

Figure 150. Concordia plot for Minno augen gneiss (90984003), a syn-metamorphic foliated granite from south of the Kalka intrusion near Mount Davies, which has well-zoned, slender igneous zircons defining a concordant zircon U–Pb SHRIMP age of 1198±6 Ma. This emplacement age is consistent with a previous Rb–Sr whole rock isochron age of 1204±17 Ma (Gray 1978). Inherited zircon cores indicate an age of 1296±10 Ma for the source rock.

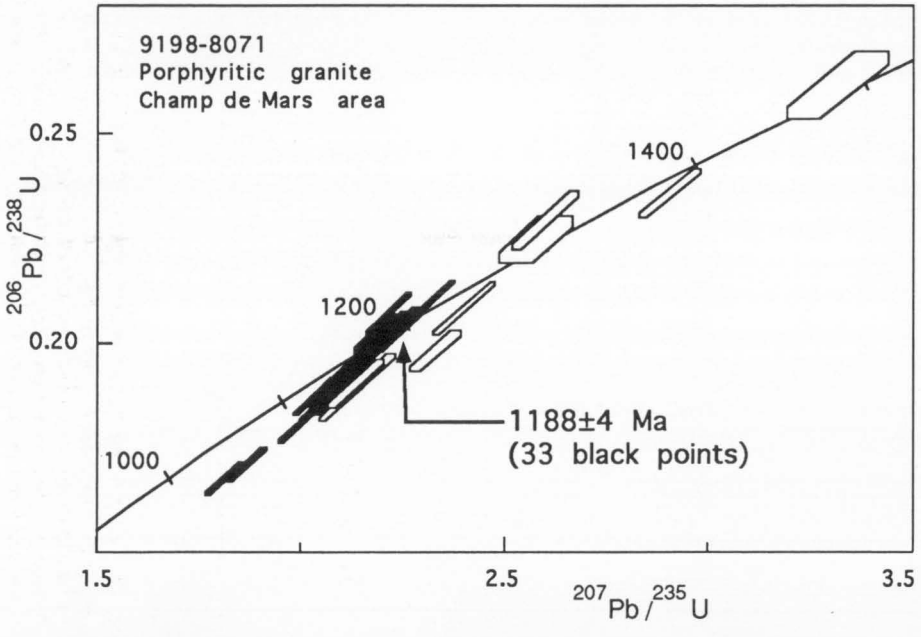

Figure 151. Concordia plot for porphyritic granite (91988071) from south of the Hinckley Range intrusion, which contains abundant igneous zircons giving a well-defined age of 1188±4 Ma. Minor amounts of inherited zircon give ages up to about 1500 Ma. Neodymium isotope data for this granite are consistent with melting of felsic country rocks dated at c. 1550 Ma and c. 1300 Ma.

granulites of the Ewarara area), we tentatively regard the well-defined age of 1078±3 Ma for granophyre from the Bell Rock troctolite/gabbro intrusion as the most probable age of the Giles Complex. This supersedes the 1200–1185 Ma age bracket previously suggested by Sun & Sheraton (1992), based on the 1188±4 age of the porphyritic granite, which was originally correlated with similar granite which clearly intrudes the margin of the Hinckley Range intrusion. The younger age is supported by a preliminary zircon U-Pb age of 1073±5 Ma (based on six grains only) of a 'chilled' phase (or possibly a type A dyke) from the Hinckley Range gabbronorite. It is further supported by data for two leucogabbro samples from the Wingellina Hills intrusion (Fig. 148), emplaced at depths of about 20 km (Ballhaus & Berry 1991), that yield 3-point (clinopyroxene, plagioclase, and whole rock) Sm–Nd isochrons of 1047±28 Ma and 1077±32 Ma. These samples contain olivine, and have igneous textures showing only minor recrystallisation, suggesting that metamorphic overprinting is minimal and that the ages are close to the emplacement age.

Our results support an earlier suggestion, made by Nesbitt et al. (1970), that felsic volcanic rocks of the Tollu Group and back-intruded felsic dykes and granophyres associated with the layered intrusions are all genetically related to the Giles Complex.

This major magmatic event between about 1050 and 1080 Ma in the western Musgrave Block has profound implications for the post-1200 Ma, second episode of granulite-facies metamorphism described by Clarke et al. (1995a). It is clearly distinct from the 1200 Ma high-grade metamorphism. Emplacement of large volumes of high-temperature (1200–1300°C) tholeiitic magma into deep crustal levels is believed to have increased the lithostatic pressure and induced granulite-facies metamorphism and crustal melting, resulting in bimodal mafic and felsic plutonic and volcanic igneous activity. The range of initial ε_{Nd} values (+0.9 to -2.5, Table 11) and the chemistry of 1050–1080 Ma felsic rocks are consistent with magma generation through processes ranging from crustal melting (with ε_{Nd} of -2.5 to -4.8 for 1550–1300 Ma felsic

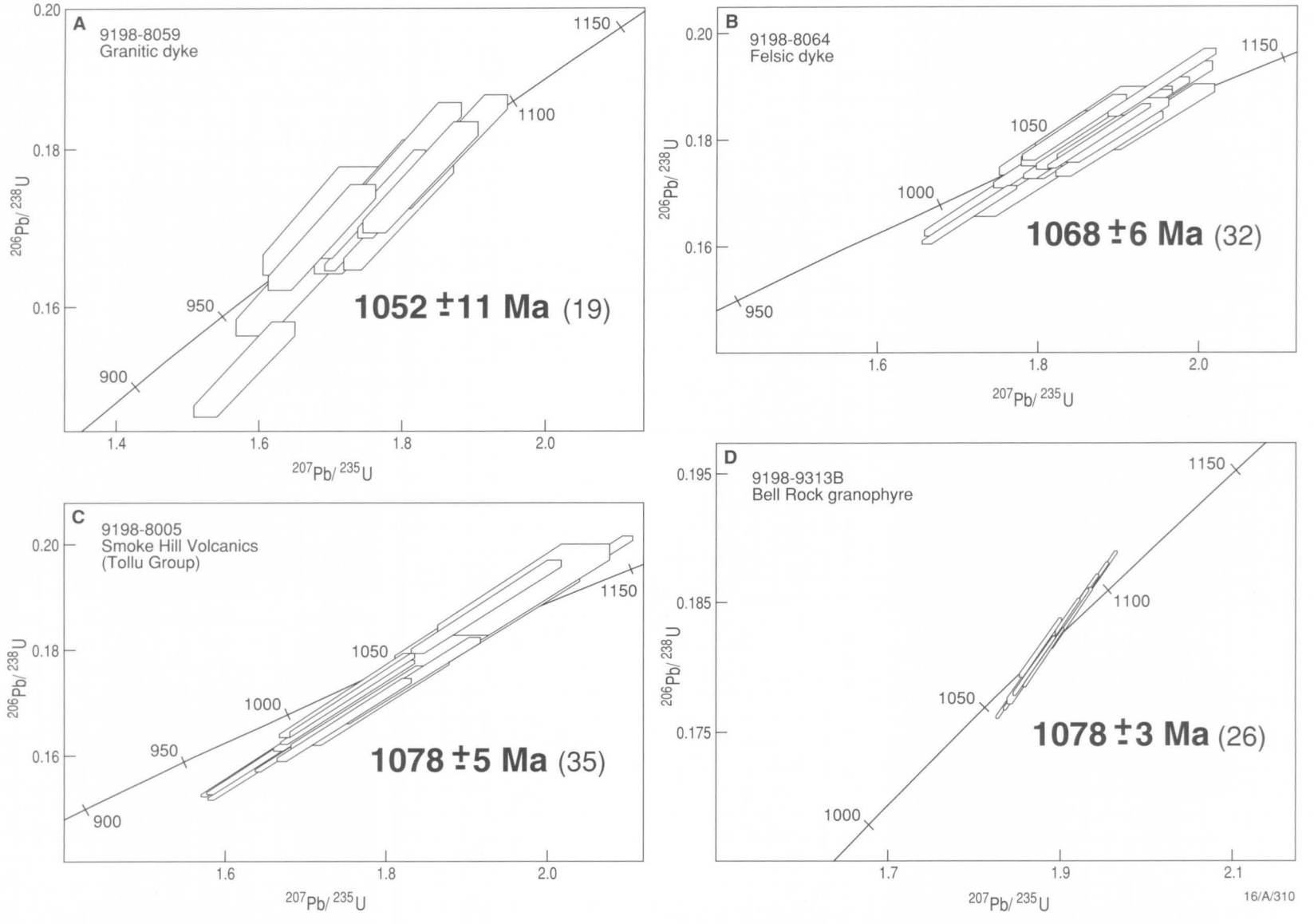

Figure 152. Concordia plots for samples associated with the Giles Complex. (A) A granitic dyke (91988059) cutting the western part of the Hinckley Range intrusion contains squat igneous zircon grains, most with rounded prisms, igneous zoning, and inclusions. They give a $^{207}Pb/^{206}Pb$ age of 1052±11 Ma. (B) A rapakivi-textured granite dyke (91988064) intruding the southern margin of the Hinckley Range intrusion contains mostly clear and euhedral zircon grains, with variable igneous zoning. They give a $^{207}Pb/^{206}Pb$ age of 1068±6 Ma. (C) Rhyolite (91988005) of the Smoke Hill Felsic Volcanics, Tollu Group, contains simply-zoned igneous zircons, which give a magmatic $^{207}Pb/^{206}Pb$ age of 1078±5 Ma. (D) Zircon grains in a granophyric pegmatite (91989313B) in the Bell Rock intrusion are large, euhedral and simply zoned with very high U contents (~4000 ppm). They give a concordant U–Pb age of 1078±3 Ma.

granulite-facies country rocks at 1070 Ma) to derivation from mafic magmas through extensive crustal assimilation coupled with fractional crystallisation.

The 1078±5 Ma Smoke Hill Felsic Volcanics of the Tollu Group have typical A-type compositions (high HFSE, LREE, and Ga, and low *mg*; Sheraton & Sun, 1995). Like the hornblende–biotite granitoids of the Champ de Mars area, these features may be due to partial melting of granulite-facies lower crustal rocks during emplacement of mantle-derived magma (e.g., the Mummawarrawarra Basalt). Alternatively, generation of the felsic volcanic rocks by assimilation–fractional crystallisation of basaltic magma is possible, although petrogenetic modelling is not consistent with a parent magma similar to the Mummawarrawarra Basalt. In particular, the relatively small negative Nb anomalies of the felsic volcanic rocks are difficult to explain by either model, and imply a source different from either the exposed felsic crustal rocks or the mafic volcanic rocks. This lack of major Nb depletion is perhaps more consistent with a mafic, rather than a felsic, crustal source, as continental crustal rocks typically have large negative Nb anomalies. The somewhat younger Nd T_{DM} model ages of the Smoke Hill Felsic Volcanics and genetically related granite (1520–1569 Ma), compared to the granulite-facies metamorphics of the Tomkinson Ranges (1610–1900 Ma), may reflect derivation of the former either from a relatively young crustal underplate or directly from mantle-derived magma.

Both episodes of felsic magmatism, at c. 1190 Ma (porphyritic granite in the Champ de Mars area) and c. 1080 Ma (Smoke Hill Felsic Volcanics), were associated with mafic magmatism. In the first case, at least, the relationship appears to have been indirect, in that the mafic magmas were the cause of intracrustal melting, rather than being parental to the felsic magmas. Both felsic suites display affinities to A-type granitoids, although only the younger appears to be truly anorogenic in its tectonic setting. Granitoids with A-type geochemical characteristics are thus not necessarily confined to anorogenic settings, but may form in any environment in which emplacement of mantle-derived magma provides enough heat to cause high-temperature intracrustal melting, with or without significant mixing of the mantle and crustal components. Nevertheless, only the Smoke Hill Felsic Volcanics (and the Mummawarrawarra trachyte dyke) have the high Nb typical of intraplate granitoids (Pearce et al. 1984). Most other granitoids in the area have high the LILE/HFSE ratios and large negative Nb anomalies characteristic of subduction-related magmatism, including typical continental crust derived directly or indirectly from enriched lithospheric mantle (Brown et al. 1984).

In view of the large scale of mafic–ultramafic magmatism represented by the Giles Complex, it is surprising that intracrustal melting was not more extensive, particularly as many of the granitoids in the Champ de Mars area, at least, are much older. It is possible that much of the granitic magma was emplaced at higher crustal levels, now removed by erosion. The relatively poorly exposed basement to the Bentley Supergroup consists largely of biotite granite and may represent such a higher crustal level, but neither the age nor the tectonic relationships of these rocks with those of the Tomkinson Ranges have yet been established. Extensive granitic rocks, including rapakivi types, in the Bates 1:100 000 sheet area are another possible example of associated felsic magmatism, but their chemical and petrographic similarities with 1188±4 Ma granitic rocks in the Hinckley Range area suggest that they may be older. The dry nature of the granulite-facies country rocks would, of course, limit the extent of melting, although the hornblende–biotite granitoids clearly represent 'wetter' magmas than the older orthopyroxene granitoids. If the country rocks were not the source of the water in these magmas, it was presumably derived either directly from mafic magma (including the Giles Complex) or as a hydrous fluid associated with emplacement of the latter. Either way, it was presumably mantle derived.

The major 1050–1080 Ma magmatic event in the western Musgrave Block can be correlated with emplacement of coeval dolerite dykes more than 400 km to the east in the Kulgera region of the eastern Musgrave Block (Fig. 148), as well as the Stuart dyke swarm in the southern Arunta Block (Zhao & McCulloch 1993a, b). A period of intraplate lithospheric extension and generation of tholeiitic magma at about 1080 Ma in a very wide area covering the Musgrave Block and southern Arunta Inlier is thus indicated.

Age of the Woodroffe Thrust

North–south convergence is recorded in large D_6 mylonite–pseudotachylite fault zones that cut the Musgrave Block and are spatially associated with the development of garnet–clinopyroxene–rutile–plagioclase–hornblende–quartz±kyanite assemblages in dolerite dykes (Clarke et al. 1995a). These assemblages reflect metamorphic conditions of P=14±1 kb and T=700–750°C (Ellis & Maboko 1992; Clarke et al. 1995a). The initial ε_{Nd} value (+4.7 at 800 Ma) and chemistry of a metadolerite dyke (91989485A, Table 11) from Mount Fanny on the western extension of the Woodroffe Thrust (Stewart 1995b) suggest that this is an 800 Ma type B dyke, although the data are somewhat equivocal (Sheraton & Sun in press). Mineral separates of clinopyroxene, plagioclase, hornblende, and garnet, and whole rock samples were analysed for Sm and Nd, but no isochron was obtained due to isotopic disequilibrium (Fig. 153; Clarke et al. 1995b). Diopside has a closure temperature for Sm diffusion (>850°C, Becker 1993) that is higher than temperature estimates obtained for the D_6 event (Clarke et al. 1995a). Accordingly, a two point line connecting the Sm–Nd isotopic ratios of the whole rock and clinopyroxene that gives an age of 768±110 Ma (Fig. 153) is inferred to be close to the emplacement age, consistent with the U–Pb baddeleyite age of 824±4 Ma for a fresh type B dyke (S-S. Sun unpublished data). Sm–Nd data for garnet and plagioclase give a two point line that defines an age of 536±16 Ma (after Ludwig 1990), and the hornblende–clinopyroxene pair gives an age of 533±16 Ma. These 'ages' are consistent with the c. 530–550 Ma age inferred for the Woodroffe

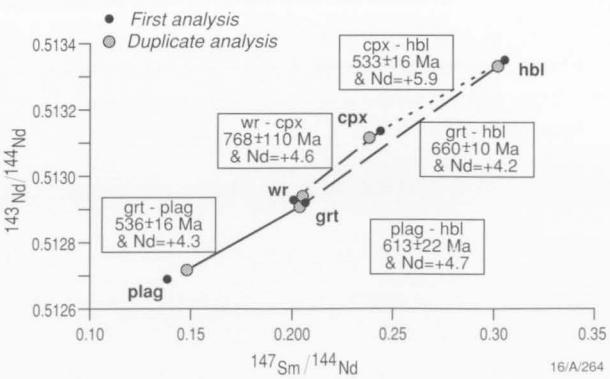

Figure 153. Plot of $^{143}Nd/^{144}Nd$ against $^{147}Sm/^{144}Nd$ for mineral separates and a whole rock sample (91989485A) of a metamorphosed, probably type B, dolerite dyke from north of Mount Fanny (data from Clarke et al. 1995b). As discussed in the text, no isochron was obtained due incomplete isotopic equilibration. The two point ages were obtained following the procedure of Ludwig (1990), and their significance is also discussed in the text.

Thrust, 200 km farther east (Maboko et al. 1992; Camacho & Fanning 1995) and can be correlated with a widespread unconformity which marks the onset of Cambrian sedimentation in the Amadeus Basin (Shaw 1991). A possible explanation for agreement of these c. 530 Ma ages is isotopic inheritance from precusor minereals, i.e., garnet inherited the Nd isotopic composition of its precusor mineral plagioclase, whereas hornblende inherited the Nd isotopic composition of its precusor clinopyroxene. The non-radiogenic Nd isotopic composition and low Sm/Nd of the garnet, in contrast to its normal compositional characteristics (e.g., Jagoutz 1994), are consistent with its derivation from plagioclase. Following this line of reasoning, the garnet–hornblende and plagioclase–hornblende pairs would have been out of isotopic equilibrium at the time of metamorphism, and therefore give geologically meaningless ages (660±10 and 613±22 Ma, respectively).

Metamorphic and structural history

Previous interpretations

Nesbitt et al. (1970) recognised two generations of folding in the felsic granulites of the Musgrave Block. Pre-Giles Complex F_1 folds are intrafolial folds developed within the compositional layering. Post-Giles Complex F_2 folds are more open and associated with only a weak axial-plane foliation. Moore & Goode (1978) estimated that the felsic granulites formed at about 1000°C and 10–11 kb, equivalent to about 30 to 35 km depth. Curvilinear deformation zones, such as the Numbunja and west Kalka gneissic belts, transect the Kalka intrusion and contain blastomylonitic fabrics (Goode 1978). The mafic and ultramafic blastomylonites were considered to have developed soon after crystallisation of the intrusion under lower crustal metamorphic conditions (Goode & Moore 1975), and may be restricted to the higher-pressure parts of the terrane (Goode 1978). The maximum principal elongation occurred parallel to the lineation, apparently while the foliation was almost horizontal (Goode 1978), locally producing up to 400 percent elongation of plagioclase inclusions within orthopyroxene. The effect of this high-temperature deformation was to disrupt the layered bodies soon after their emplacement. According to Nesbitt et al. (1970) and Goode (1978) the east–west-trending modified concentric folds post-date emplacement of most of the Giles Complex intrusions. Many of these bodies display megascopic folding of the igneous layering, e.g., in the eastern part of the Michael Hills (Nesbitt & Talbot 1966), The Wart, and Latitude Hill intrusions (Plate 1), which Nesbitt et al. (1970) attributed to a third phase of folding.

Nesbitt et al. (1970) considered that the Skirmish Hill volcanic rocks, probably equivalent to the Tollu Group, are genetically related to the Giles Complex, and comprise evolved lavas fed from open-system, deeper-level crustal magma chambers of the latter. Nesbitt & Talbot (1966) suggested that the Bell Rock, Blackstone Range, and Cavenagh Range intrusions are part of one large sheet, which forms a synform with the Skirmish Hill volcanic rocks in its core. The age of this folding was presumed to be the same as the regional-scale folding (F_2) found at lower crustal levels. On the other hand, Daniels (1971a, 1974) suggested that the Tollu Group volcanic rocks at Mummawarrawarra Hill are older than, and intruded and contact-metamorphosed by, small high-level dolerite dykes which were correlated with the Giles Complex.

Structural evolution and metamorphic assemblages

The field relations, structure, and petrology of the various stratigraphic units in the western Musgrave Block have been described in previous sections of this Bulletin and are summarised in Table 14. This section concentrates on the metamorphic mineral assemblages and, in particular, on the petrographic effects of the various structural and metamorphic events and their relevance for geothermometry and geobarometry. It is largely based on the detailed maping of Clarke (1992) and Clarke et al. (1995a) in the western Hinckley Range (Fig. 154) and Champ de Mars (Fig. 155) areas. Most of the western Musgrave Block is characterised by granulite-facies metamorphic rocks, but to the north, in the Bates 1:100 000 sheet area, there is evidence of a widespread, late, high-temperature sub-eclogite-facies metamorphism, the effects of which are less clear in the Tomkinson Ranges.

Metamorphism under granulite-facies conditions produced orthopyroxene±garnet-bearing felsic gneiss and rare garnet+sillimanite-bearing metapelitic rocks (Gray 1978; Moore & Goode 1978). High-grade metamorphism was synchronous with two deformation events (D_1 and D_2) and granitic magmatism, with pre-S_1 felsic orthogneiss, mafic granulite, and metasediments, and post-S_1, pre-S_2 foliated orthopyroxene granitoids (Clarke 1992; Clarke et al. 1995a). A penetrative S_1 gneissosity, defined by alternations in the proportions of felsic and mafic minerals, is deformed by isoclinal F_2 folds (Fig. 158A). Except in F_2 fold hinges, S_1 has been rotated into parallelism with S_2. Due to intense recrystallisation during D_2, only rarely can isoclinal F_1 folds be identified (Figs 31, 32). Where unaffected by subsequent deformation, D_2 is characterised by mesoscopic to macroscopic, tight to isoclinal reclined F_2 folds with east to east-southeast-trending axes and an axial-planar foliation, S_2, which is the pervasive gneissosity in the resultant shallowly dipping recumbent granulite terrane (Figs 32, 34, 35). Whereas an S_1–S_2 intersection lineation is common, mesoscopic F_2 folds are not associated with a mineral stretching lineation, implying deformation dominated by pure shear, with only a small component of rotational strain. S_1–S_2 fabrics typically comprise granoblastic interlocking mineral assemblages, in contrast to later mylonitic foliations (S_3, etc.) enveloping relict S_1–S_2 minerals.

Intrusions of the Giles Complex, as well as roughly coeval granitoids and mafic dykes, were deformed by another major phase of deformation (D_3), resulting in locally extensive recrystallisation of gabbro to mafic granulite (Glikson 1990). D_3 produced upright to reclined, open or, more commonly, tight to isoclinal, mesoscopic F_3 folds (Figs 34, 36), with amplitudes and wavelengths from metres to tens of metres (Nesbitt et al. 1970; Gray 1971; Clarke 1992). The steeply dipping southeast-trending S_3 axial plane mylonitic foliation is present throughout much of the western Musgrave Block. In felsic granulite, D_3 resulted in widespread rotation to sub-parallelism of earlier S_1–S_2 granoblastic assemblages, producing S_3–L_3 mylonitic fabrics (Fig. 159D). These fabrics consist of a steeply southwest-plunging L_3 stretching lineation within the predominantly south-dipping S_3 foliation, suggesting southwest-directed compression and recrystallisation under conditions of dominantly simple (rotational) shear. The intensisty of recrystallisation during D_3 is quite variable on a centimetre to metre scale, but many of the granitoids contain a pervasive S_3 foliation. In general, D_3 is difficult to detect in massive gabbro. However, in felsic vein-injected mafic granulite, derived by recrystallisation of gabbro, S_3–L_3 fabrics are dominant, and include penetrative rodding of felsic stringers related to simple shear rotation. Type A dykes display marginal to complete recrystallisation of primary igneous textures to granulite-facies S_3 assemblages; their trend results from D_3 folding and is mostly aligned with the southeast-trending S_3 foliation. On the basis of mineral assemblages in metapelitic rocks from Cohn Hill on the western part of the Cooper 1:250 000 sheet area, Clarke & Powell (1991) inferred a syn-S_3 decompressional P–T path for that part of the Musgrave Block, which is consistent with the P–T path derived from mineral assemblages in mafic dykes near Amata in the eastern part of the Musgrave Block (Maboko et al. 1991).

Both the c. 1000 Ma type C olivine dolerite dykes and c. 800 Ma type B quartz dolerite dykes post-date D_3, but are cut by steep mylonite and ultramylonite zones. The latter were divided into four discrete deformation events ($D_{4\text{-}7}$) by Clarke (1992), although it is probable that they represent a single evolving orogen. It is also likely that later generations of mylonite zone tend to overprint earlier ones. Northeast to southeast-trending, but commonly east to east-northeast-trending, D_4 amphibolite-facies ultramylonites deform the bounda-

ries of the Hinckley Range gabbronorite (Fig. 83). Most dip steeply northwards and have a reverse sense of movement, but some show normal movement. A steeply northwest-plunging mineral and stretching lineation (L_4) indicates (reverse) southeast-directed movement. D_4 ultramylonites are typically 10 to 100 m thick, with throws of similar magnitude, although those cutting gabbroic rocks are commonly much thinner. They are cut by steep, mainly north-trending (east in the western Hinckley Range) D_5 ultramylonites that dip steeply eastwards and show an apparent dextral sense of shear. They commonly contain greenschist-facies (chlorite–sericite–calcite) assemblages. An L_5 mineral and stretching lineation, which plunges obliquely with a trend of 25 to 40°, indicates a southwest-directed reverse throw of a few hundred metres. Displacements of up to several hundred metres for both D_4 and D_5 ultramylonite zones imply significant uplift and/or dissection of the terrane.

East-trending D_6 ultramylonite–pseudotachylite zones are the most prominent of all shear zones (Clarke 1992) and are best developed on the Bates 1:100 000 sheet area, where they represent the western extension (Stewart 1995b; Figs 11–15) of the Woodroffe Thrust (Forman 1965). The Champ de Mars

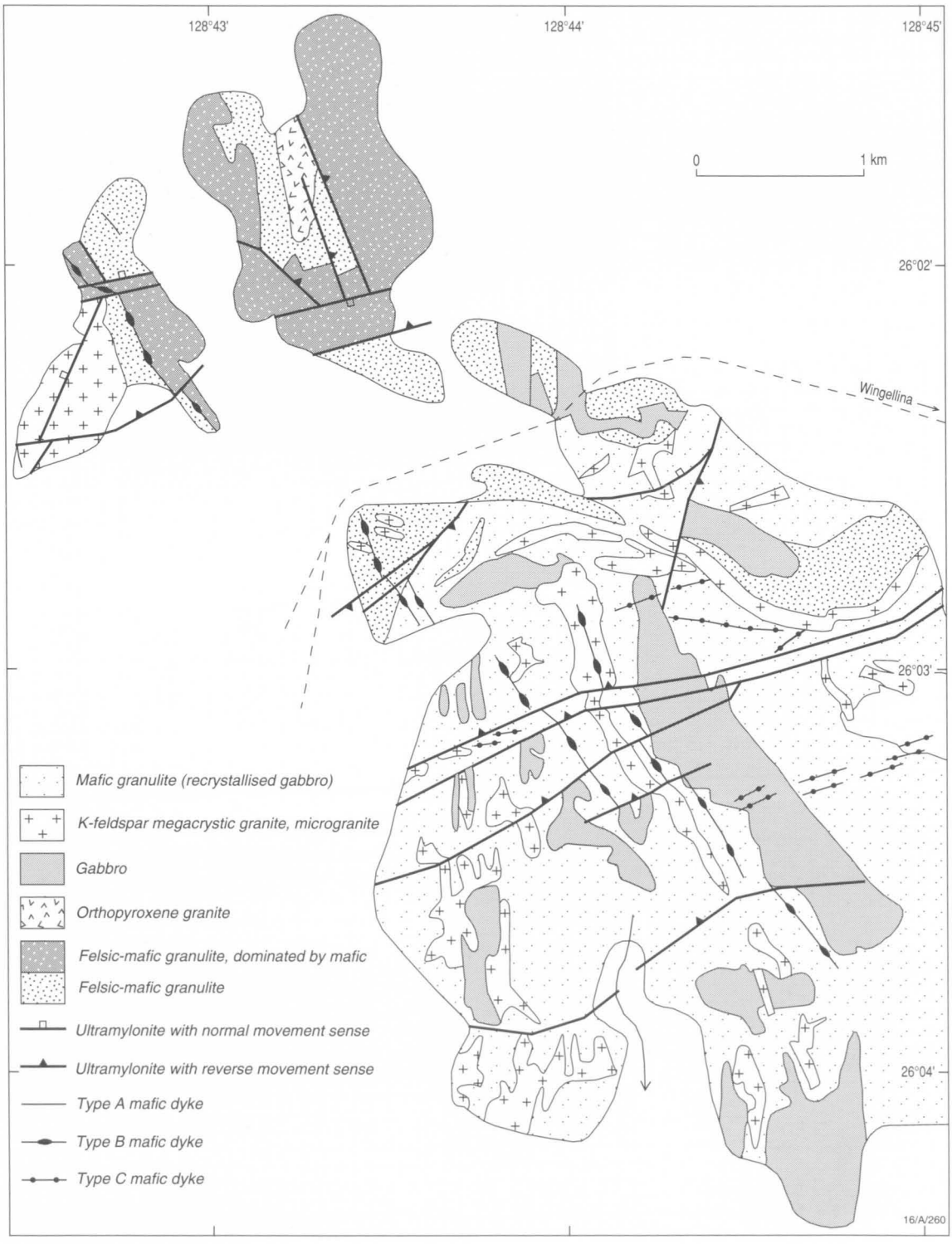

Figure 154. Geological sketch map of the western Hinckley Range.

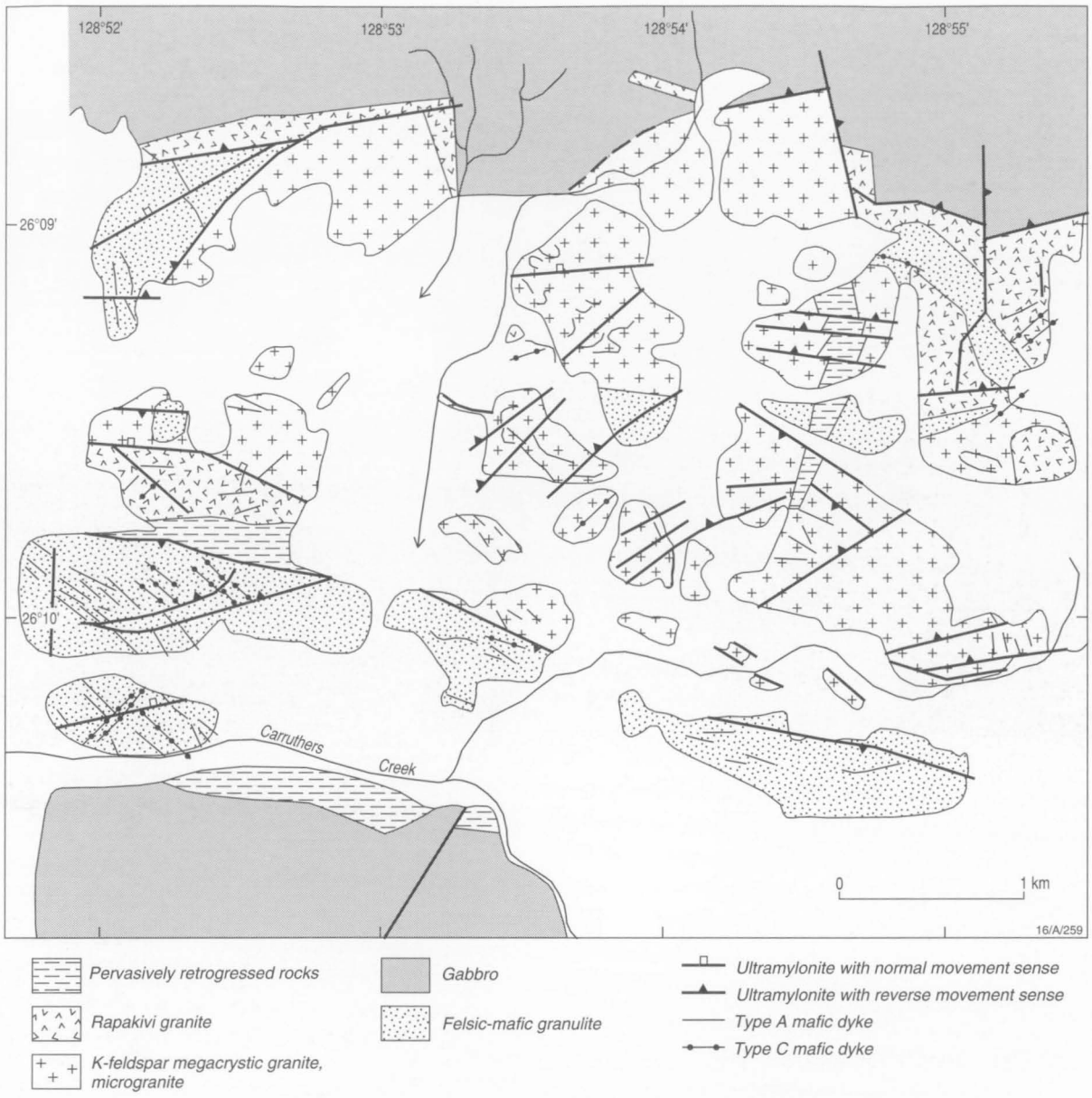

Figure 155. Geological sketch map of the western Champ de Mars area.

Fault, another example of a D_6 structure, consists of a steeply south-dipping zone of S_6 quartzo-feldspathic mylonite to ultramylonite, which passes into the footwall of a pseudotachylite zone within the Hinckley Range gabbronorite (Clarke 1992). The zone of pervasive D_6 recrystallisation is up to 500 m wide where felsic rocks are affected, but less than 150 m wide in gabbro; mylonite in gabbroic rocks is imprinted by extensive pseudotachylite (Figs 83, 156, 157; Glikson & Mernagh, 1990). An intense L_6 mineral and stretching lineation plunges steeply to the south, and, as for the Woodroffe Thrust, movement appears to have involved north-directed thrusting. These major thrusts were generated during the Neoproterozoic to Cambrian Petermann Ranges orogeny, which resulted in north-verging folds, thrusts, and metamorphism in cover rocks (Forman 1965; Forman & Shaw 1973), and produced the overall easterly trend of the Musgrave Block. High-pressure garnet+clinopyroxene-bearing assemblages occur in ultramylonites a few kilometres south of the south-dipping Woodroffe Thrust in the Bates 1:100 000 sheet area, oriented at acute to obtuse angles to this structure (Stewart 1995b; Fig. 1).

D_6 ultramylonite zones contain abundant concordant pseudotachylite veinlets and lenses, which are distinct from pseudotachylite vein–breccia networks in more brittle domains, although both modes of occurrence are largely confined to gabbro, anorthosite, and dolerite dykes (Figs 83, 157; Glikson & Mernagh 1990). Pseudotachylite is developed mainly in deformed and mylonite-intersected intrusions of the central and eastern Tomkinson Ranges, and is rare in the shallow-dipping to flat-lying western intrusions (Blackstone Range, Cavenagh Range, and Jameson Range). It is not clear to what extent melting occurred during ductile deformation at middle crustal levels or upon fault reactivation at brittle higher crustal levels. The limited degree of recrystallisation of pseudotachylite and the occurrence of glass, identified by laser Raman microprobe studies (Glikson & Mernagh 1990), suggest a relatively high-level crustal setting. On the other hand, the preferential concentration of pseudotachylite in the more deformed mylonite-truncated zones favours a genetic relationship between the mylonitic deformation and seismically triggered pseudotachylite formation at middle crustal levels. In terms of this interpretation, the limited recrystallisation of the glass may be due to the dry nature of the mafic host rocks.

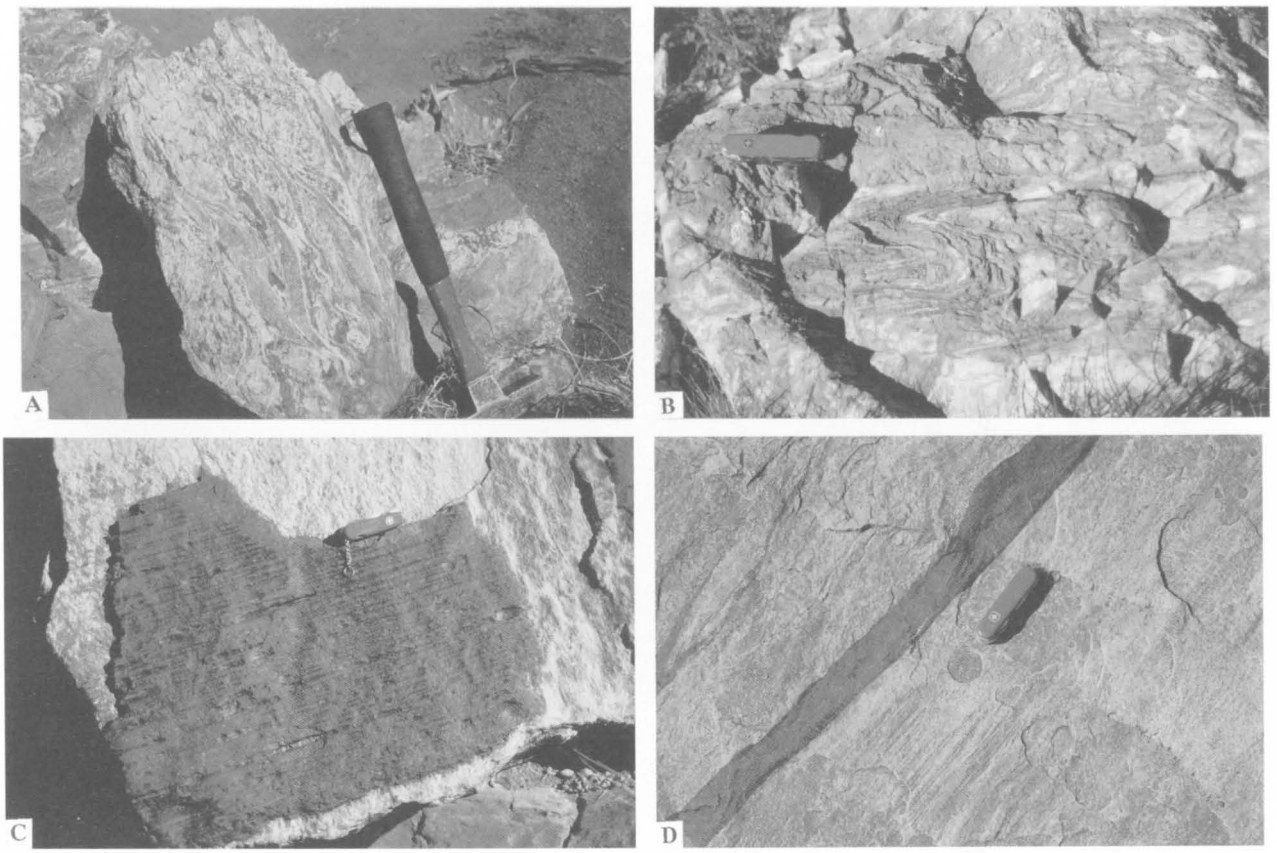

Figure 156. Outcrops of mylonite zones. (A) Folded mylonite in shear zone, southeastern tip of Bell Rock. (B) Mylonitic crush zone, Blackstone Range. (C) Lineations on pseudotachylite vein, Bell Rock Range. (D) Ultramylonite shear cutting granite, Mount West.

Poorly exposed east-trending D_7 retrograde shear zones dip north and preserve a reverse sense of movement, e.g., west of Champ de Mars. They form broad biotite+muscovite-rich 'crush zones'.

Layered felsic and mafic granulites. The oldest rocks in the Tomkinson Ranges are well-layered felsic and mafic granulites (Fig. 158A) that preserve evidence of one or two early deformation events, D_1 and D_2. Metasedimentary gneiss and orthogneiss that were minimally affected by D_3 can be distinguished on textural grounds from those that were intensely recrystallised during D_3: the composite S_1 and S_2 foliation is granoblastic with interlocking coarse-grained minerals, whereas S_3 is a fine-grained mylonitic foliation, typically with quartz ribbons enveloping relict S_2 mineral grains (Fig. 158B, C). This distinction becomes critical in the interpretation of parageneses, and is corroborated by differences in mineral chemistry between S_2 and S_3 grains in individual samples. The rare metasedimentary gneisses are most useful in constraining the metamorphic history, since they commonly contain garnet. Granulite-facies metapelites with pristine S_1 assemblages have coarse-grained poikiloblastic garnet (at least 5 mm diameter), intergrown with, and wrapped round by, a granoblastic S_2 foliation comprising sillimanite, quartz, K-feldspar, plagioclase, and ilmenite. Garnet locally has inclusions of sillimanite that are oriented at an angle to the enveloping S_2 foliation, consistent with the presence of an earlier S_1 foliation. The metapelites are commonly interlayered with garnet+orthopyroxene-bearing gneiss, which may be metapsammites or metamorphosed felsic igneous rocks (Gray 1978). Coarse-grained (up to 5mm diameter) granoblastic garnet, orthopyroxene, plagioclase, quartz, and ilmenite, with or without K-feldspar or perthite, define a pervasive foliation that is most probably a composite of S_1 and S_2. Calc-silicate gneiss has only a weak foliation and contains granoblastic garnet, clinopyroxene, plagioclase, quartz, ilmenite, allanite, and titanite. The mafic and felsic granulites comprise orthopyroxene, clinopyroxene, plagioclase, quartz, and opaque minerals, with or without orthoclase, biotite, and amphibole. Mafic minerals have modal abundances from less than 5 percent to more than 40 percent, and there is a continuum between felsic and mafic granulite. Whereas orthopyroxene is usually present in greater abundance than clinopyroxene in felsic granulite, mafic granulite lacks K-feldspar, and clinopyroxene is usually present in greater abundance than orthopyroxene. Large, zoned and simply twinned plagioclase grains, and large pyroxene grains that contain abundant fine-grained inclusions aligned along cleavages are common in the mafic granulite layers, suggesting that many of these were derived from recrystallised gabbroic rocks.

In the western Hinckley Range area, foliated orthopyroxene granite ('charnockite') and associated dykes cut S_1 in adjacent layered granulites, but contain S_2 (Clarke 1992). The absence of the intense S_1 gneissosity gives the rocks a massive outcrop habit. Apophyses and dykes of the granite pervasively intrude adjacent layered granulite, with the numerous narrow veins giving the composite rocks a migmatitic appearance. Small xenoliths in these veins preserve an S_1 foliation, which is truncated at the margins of the xenoliths.

Garnet+orthopyroxene-bearing gneiss at Mount Aloysius that was partly recrystallised during D_3 is of two types. In the first type, S_2 orthopyroxene and ilmenite are enveloped and partially replaced by S_3 amphibole and hematite. Garnet, plagioclase, K-feldspar, biotite, and quartz were extensively recrystallised during development of the mylonitic S_3 foliation (Fig. 158C), and large garnet grains are strongly zoned. The

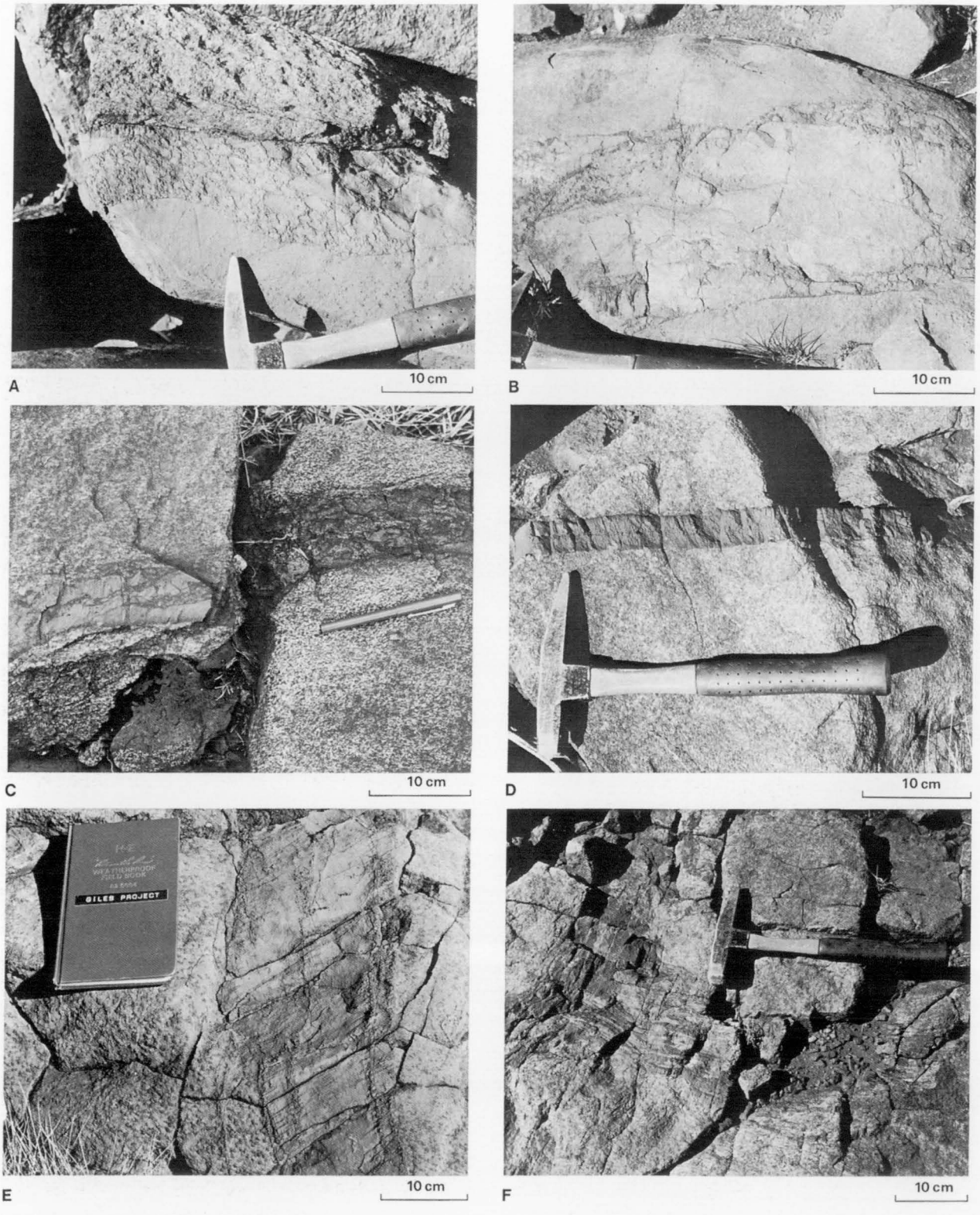

Figure 157. Outcrops of pseudotachylite. (A) Reticulated pseudotachylite–breccia vein between gabbro (above) and dolerite dyke (below) and containing rounded enclaves of dolerite, central Hinckley Range. (B) Thin veinlets of pseudotachylite, showing irregular emplacement into fractures, resulting in angular breccia, central Hinckley Range. (C) Pseudotachylite–breccia vein in gabbro, comprising gabbro enclaves mixed with pseudotachylite zones, central Hinckley Range. (D) Pseudotachylite vein intruding gabbro, showing chilled margins and small fragments of gabbro, eastern Hinckley Range. (E) Concordant to near concordant pseudotachylite veinlets in a dolerite dyke intruding gabbro, Wingellina Hills. (F) Ductile shear zone of intrafolial mylonitised gabbro and pseudotachylite laminae and lenses, intersected by another shear zone; eastern Hinckley Range.

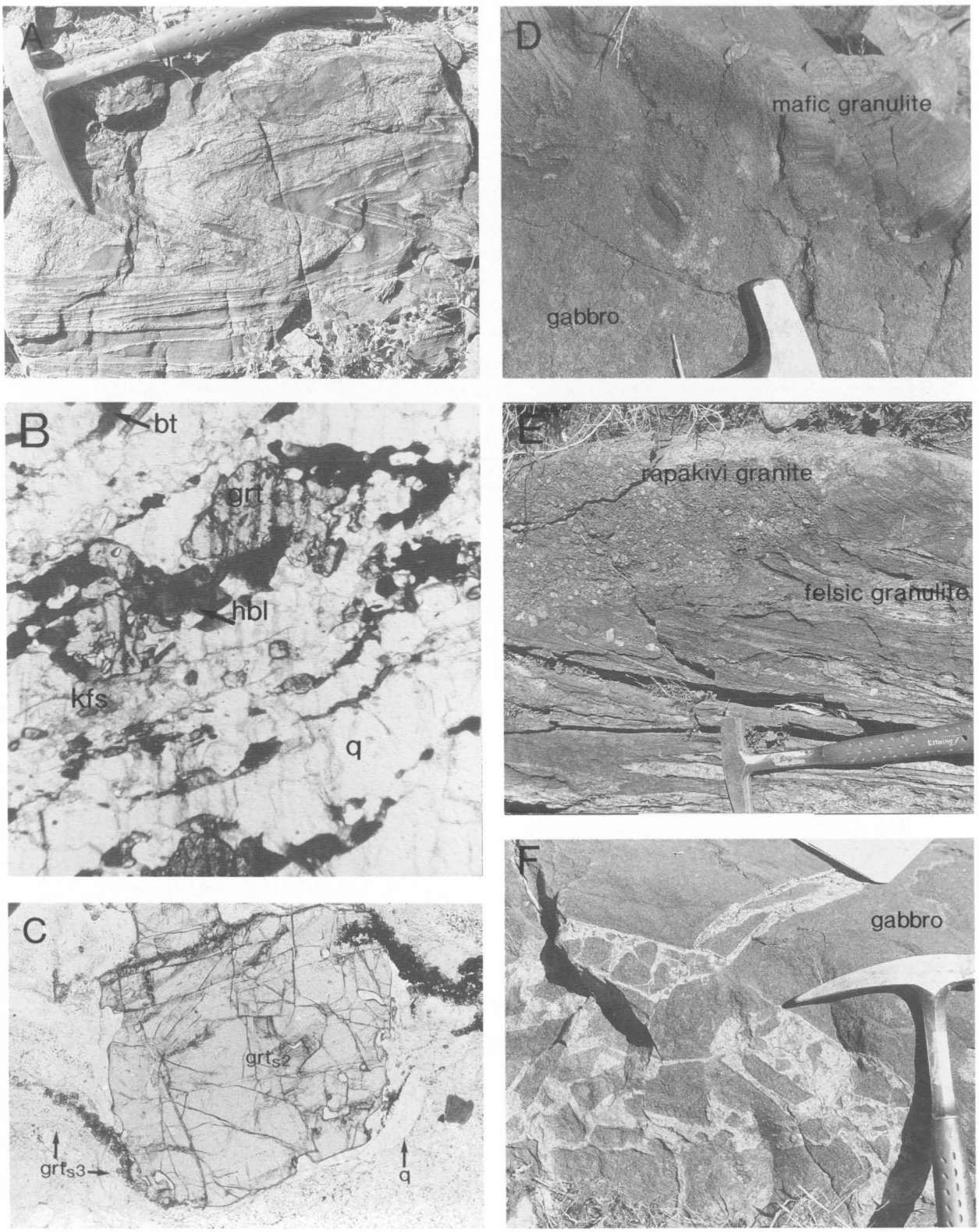

Figure 158. Structural and textural features of rocks from the Mount Fanny and western Hinckley Range areas. (A) F_2 folds refolding F_1 in interlayered felsic and mafic granulite, Charnockite Flats, west of the Hinckley Range. The felsic layers tend to be discontinuous and the complex fabric is interpreted as having been formed by felsic veins derived from a post-S_1, pre-S_2 orthopyroxene granite that injected mafic granulite. (B) Mylonitic S_3 foliation in intermediate gneiss (91989455), defined by garnet (grt), hornblende (hbl), biotite (bt), quartz (q), and alkali feldspar (kfs). Plane-polarised light; width of field: 4 mm. (C) Mylonitic S_3 foliation in intermediate gneiss (91989567B), defined by quartz (q), biotite (bt), and fine-grained garnet (grts3). The S_3 foliation wraps around a porphyroclast of S_2 garnet (grts2). S_2 and S_3 garnet has distinctly different compositions, as discussed in the text. Plane-polarised light; width of field: about 4 mm. (D) Gabbro intruding layered mafic granulite, Charnockite Flats area. Although the mafic rocks in this area are extensively disrupted by felsic intrusions and shear zones, this appears to be a rare example of an intrusive contact between the Hinckley Range gabbronorite and surrounding layered granulite. (E) Xenoliths of felsic granulite in rapakivi granite, with megacrysts of K-feldspar, Champ de Mars area. (F) Felsic dyke containing xenoliths of gabbro and recrystallised gabbro, Charnockite Flats area.

second type involves patchy recrystallisation of the granoblastic S_2 grains, with the effects of D_3 being mostly restricted to narrow (<2 mm wide) S_3 shear zones that are mostly defined by recrystallised feldspar and quartz. Random, fine-grained symplectites of orthopyroxene, plagioclase, and biotite, with or without garnet, partly replace large S_2 garnet grains, and symplectites of garnet and quartz partly to completely enclose S_2 orthopyroxene. Garnet occurs in two forms in the symplectites that enclose the S_2 garnet grains: (1) grains interspersed with, and of similar size to, the symplectic orthopyroxene and plagioclase grains, and (2) as very narrow grains enclosing, and being at least an order of magnitude smaller than, the symplectic orthopyroxene. Whereas the first type is probably relict S_2 garnet, incompletely consumed by S_3 orthopyroxene and plagioclase (see below), the significantly finer-grained garnet may represent the effects of recrystallisation during D_6 (R.W. White & G.L. Clarke, personal communication 1995). The symplectites are drawn into the S_3 foliation and are cut by the narrow shear zones. Syn-S_3 to late-S_3 corona textures are also present in metapelitic gneiss from near Cohn Hill, approximately 100 km west of the Tomkinson Ranges. These contains large grains of garnet (up to 5 mm) and sillimanite (up to 2 mm), enveloped by a mylonitic S_3 foliation, comprising fine-grained (typically <0.5 mm) quartz, K-feldspar, biotite, cordierite, ilmenite, and hercynitic spinel. Well-developed coronas separate garnet and sillimanite from each other, and from the matrix S_2 minerals. Most of the minerals defining the coronas are elongated in S_3, but some also appear to transect S_3. These coronas have been described in detail by Clarke & Powell (1991), and similar textures are present in metapelitic rocks of the Tomkinson Ranges and adjacent areas (Moore 1969).

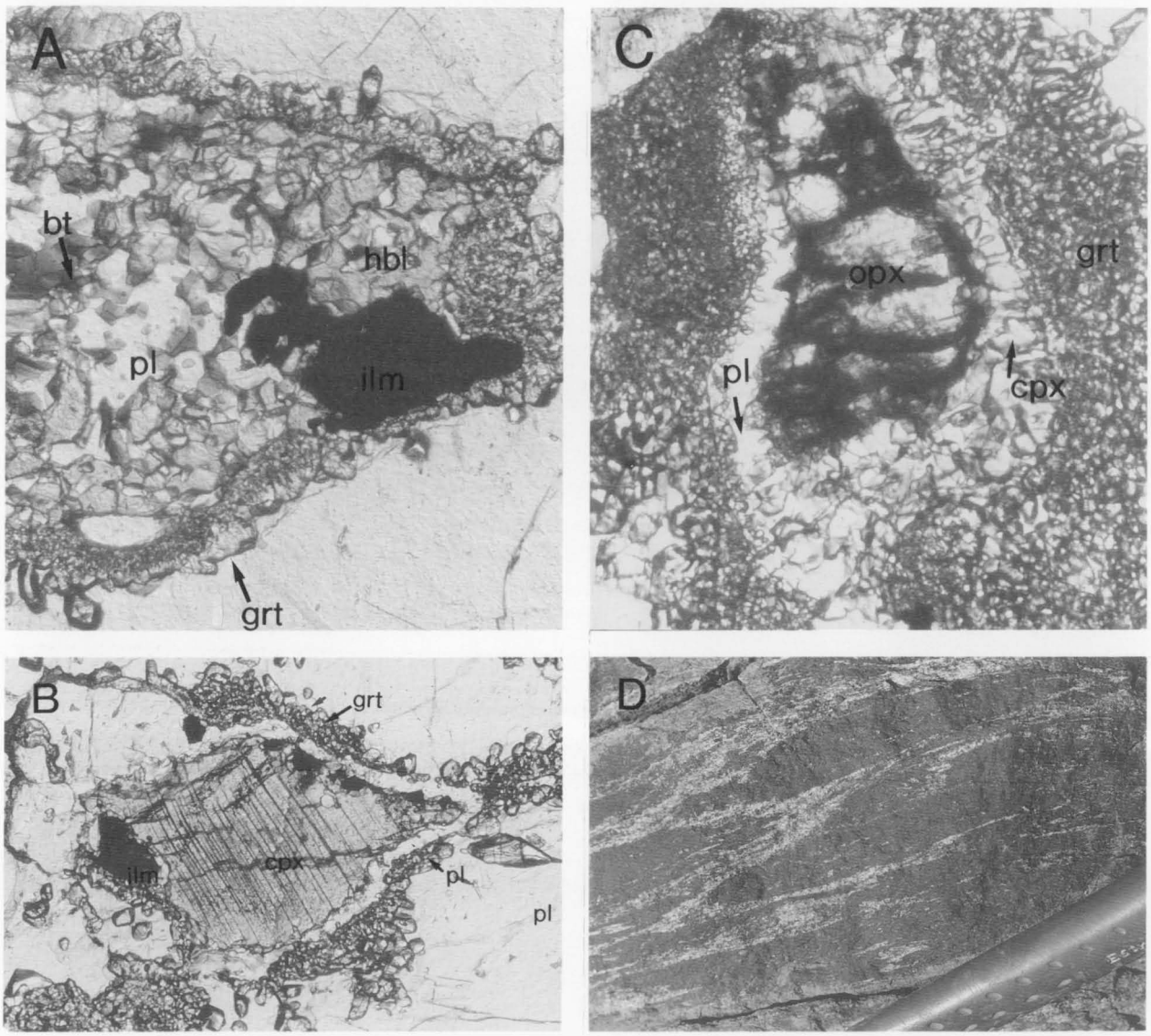

Figure 159. Textural features of rocks from the Mount Daisy Bates and western Hinckley Range areas. (A) Orthopyroxene granite (91989445B), showing corona of garnet (grt) enclosing a symplectite of hornblende (hbl), biotite (bt), plagioclase (pl), and ilmenite (ilm), which is inferred to replace magmatic clinopyroxene. Plane-polarised light; width of field: 2 mm. (B) Orthopyroxene granite (91989445B), showing corona of plagioclase (pl) and garnet (grt) surrounding magmatic clinopyroxene (cpx) and ilmenite (ilm). Note that the garnet corona continues away from clinopyroxene, along old plagioclase grain boundaries. Plane-polarised light; width of field: 2 mm. (C) Orthopyroxene granite (91989458), showing relict magmatic orthopyroxene (opx) surrounded by a structured corona comprising an inner zone of symplectitic clinopyroxene (cpx) and plagioclase (pl), with or without biotite, and an outer corona of garnet (grt) against groundmass plagioclase. Plane-polarised light; width of field: 2 mm. (D) Close-up of S_3 foliation in mafic granulite (recrystallised gabbro), showing the discontinuous nature of the felsic layers, which contrasts with the more laterally persistent felsic layers in the older layered felsic–mafic granulite in Figure 158A).

Granitic rocks. Hornblende–biotite granitoids, including rapakivi types (Figs 121A, 158E), are widespread near the southern margin of the Hinckley Range gabbronorite in the Champ de Mars area (Fig. 155). Some (c. 1070 Ma) clearly intrude the mafic body, whereas others are older (c. 1190 Ma). However, it is commonly difficult to distinguish between them on the basis of field relations, since they are petrographically similar and both are post-S_2 and pre-S_3. Many granitoids were pervasively recrystallised during D_3, and they typically contain K-feldspar and subordinate plagioclase megacrysts enveloped by a mylonitic S_3 foliation defined by K-feldspar, plagioclase, quartz, amphibole, and hematite, with or without garnet, biotite, and ilmenite. Microgranitoids commonly comprise S_3 quartz, antiperthite, perthite, orthopyroxene, and ilmenite, with minor biotite and/or garnet.

Some less deformed, generally more mafic varieties (quartz monzodiorite and quartz monzonite) contain large igneous clinopyroxene, orthopyroxene, and perthite grains in a fine-grained groundmass of quartz, microcline, plagioclase, amphibole, biotite, and ilmenite. Orthoclase megacrysts have plagioclase rims, and hornblende partly pseudomorphs magmatic pyroxene grains and encloses ilmenite. Orthopyroxene is commonly largely or wholly pseudomorphed by biotite, suggesting a high solidus temperature. Coarse-grained symplectites of amphibole, plagioclase, orthopyroxene, clinopyroxene, and magnetite (3 cm diameter) are probably related to hydration of magmatic pyroxene grains. Narrow garnet coronas enclose magmatic clinopyroxene, orthopyroxene, and/or magnetite in these symplectites (Fig. 159A–C), and garnet and biotite symplectites separate amphibole from K-feldspar. The mineral assemblages in these coronas and symplectites may either be equivalent to similar assemblages that define S_3 in the more deformed granitic rocks, or they may correlate with much later garnet-bearing assemblages (attributed to D_6) that occur in post-S_3 mafic dykes.

Hinckley Range gabbronorite. Much of the Hinckley Range gabbronorite intrusion (Fig. 158D), particularly in its northwestern section, is cut by abundant dykes and small stocks of c. 1050–1070 Ma (Sun et al. 1996a) K-feldspar megacrystic granite and microgranite, and is pervasively recrystallised (Glikson 1990; Clarke 1992). This heterogeneous unit is mapped as mafic granulite, and comprises granite-veined mafic granulite that envelopes bodies of gabbro, amphibolite, and foliated granite (Fig. 159D). It has a banded, streaky expression on colour aerial photographs, owing to the intense development of the S_3 foliation. Compositional variations occur on a scale of 1 to 100 m. Larger granite dykes (5 m wide) commonly contain angular xenoliths of foliated amphibolite, derived from recrystallised gabbro (Fig. 158F). Numerous smaller granite dykes and veins range from outcrop scale to hand-specimen scale; most granite was intensely recrystallised during the development of S_3. The mafic granulite is significantly finer grained than the older layered felsic to mafic granulite country rocks, and does not generally have a well-developed compositional layering.

Pods of gabbro may retain coarse-grained igneous textures that are cut by undeformed K-feldspar-rich veins and stringers, surrounded by narrow zones of alteration and recrystallisation. The granite veins contain quartz and microcline (with myrmekite), and have distinct angular margins without selvedges. Poikiloblastic plates of orthopyroxene and clinopyroxene, together with interdigitating plagioclase laths, preserve the igneous fabric of the gabbro. However, aggregates of amphibole, ilmenite (with minor hematite exsolution), and secondary orthopyroxene replace some clinopyroxene grains, and randomly-orientated grains of biotite and amphibole partly replace some pyroxene grains. The pseudomorphous textures and effects of recrystallisation increase in intensity towards the margins of the granite veins. The effects are present at several scales: the size and density of the feldspathic stringers increase towards the margins of the gabbro bodies, with a concomitant increase in the intensity of the S_3 fabric (Fig. 159D), until the gabbro is totally recrystallised to mafic granulite. Similarly, granite veins and sheets may show gradational contacts with mafic granulite, with a discontinuous S_3 layering developed in the mafic granulite by alternations of mafic and felsic rock. The mafic granulite commonly consists of a fine-grained (~0.5 mm) recrystallised assemblage of orthopyroxene, clinopyroxene, plagioclase, biotite, hematite, and quartz, which defines a mylonitic S_3 foliation and envelops coarse-grained (2 mm) igneous porphyroclasts of orthopyroxene, clinopyroxene, and plagioclase. The pyroxene porphyroclasts have rutile and opaque minerals aligned in cleavage traces, and are distinct from the S_3 pyroxene grains.

Mafic dykes. Type A dolerite dykes typically have a porphyritic intergranular texture, involving orthopyroxene, clinopyroxene, plagioclase, ilmenite, and hematite, with or without amphibole or biotite. The cores of the dykes commonly preserve a coarse-grained igneous texture with randomly orientated, zoned, simply twinned plagioclase laths and interstitial aggregates of orthopyroxene and clinopyroxene (commonly rimmed by biotite), and plagioclase. Although there is no penetrative foliation in the cores of such dykes, a recrystallised mylonitic S_3 foliation, which contains clinopyroxene, orthopyroxene, plagioclase, biotite, quartz and hematite, occurs along their margins. Dykes that intrude granitic rocks are commonly recrystallised to amphibolite; they contain S_3 amphibole, plagioclase, ilmenite, and, in some dykes, quartz. Dykes cutting gabbro appear to have been protected from recrystallisation during D_3 and primary igneous features are well preserved. This may be because D_3 conditions in the gabbroic bodies involved lower water activities than those in the surrounding gneiss.

Post-S_3 mafic dykes that occur near near D_6 ultramylonites on the Bates 1:100 000 sheet (Fig. 11), include olivine+plagioclase-bearing dykes, which are probably of type C, and others geochemically virtually identical to type B dykes in the Tomkinson Ranges (see mafic dyke section and Sheraton & Sun in press). Such dykes are partly to completely recrystallised to garnet+clinopyroxene-bearing assemblages. Intensely recrystallised dykes contain amphibole, garnet, plagioclase, scapolite, clinopyroxene, clinozoisite, rutile, and quartz, with or without kyanite, that define a pervasive S_6 foliation (Figs 160A–D). Large clinopyroxene grains in these rocks include igneous porphyroclasts enveloped by amphibole, but small neoblastic clinopyroxene grains indicate partial recrystalliation (Fig. 160B). Kyanite, when present, is fine-grained and intergrown with garnet and rutile. Dykes that were less affected by shearing preserve subophitic textures defined by intermeshing plagioclase, clinopyroxene, and ilmenite grains, with or without olivine and/or orthopyroxene. Orthopyroxene, clinopyroxene, and ilmenite are partly to completely replaced by symplectites of secondary clinopyroxene, plagioclase, amphibole, and rutile, with or without biotite (Fig. 160B, C). The symplectites and phenocrysts are surrounded by structured mineral coronas, containing an inner rim of quartz±plagioclase, a rarely developed intermediate rim of rutile, and an outer rim of garnet, which embays plagioclase±clinozoisite. Ilmenite grains are commonly enclosed by coronas involving an inner discontinuous rim of clinopyroxene+plagioclase, and an outer rim of garnet or garnet+quartz symplectite. In dykes with primary olivine, olivine and plagioclase are separated by coronas involving metamorphic orthopyroxene adjacent to olivine, and garnet adjacent to plagioclase (Fig. 160E). Similarly, igneous orthopyroxene and plagioclase are separated by coronas involving

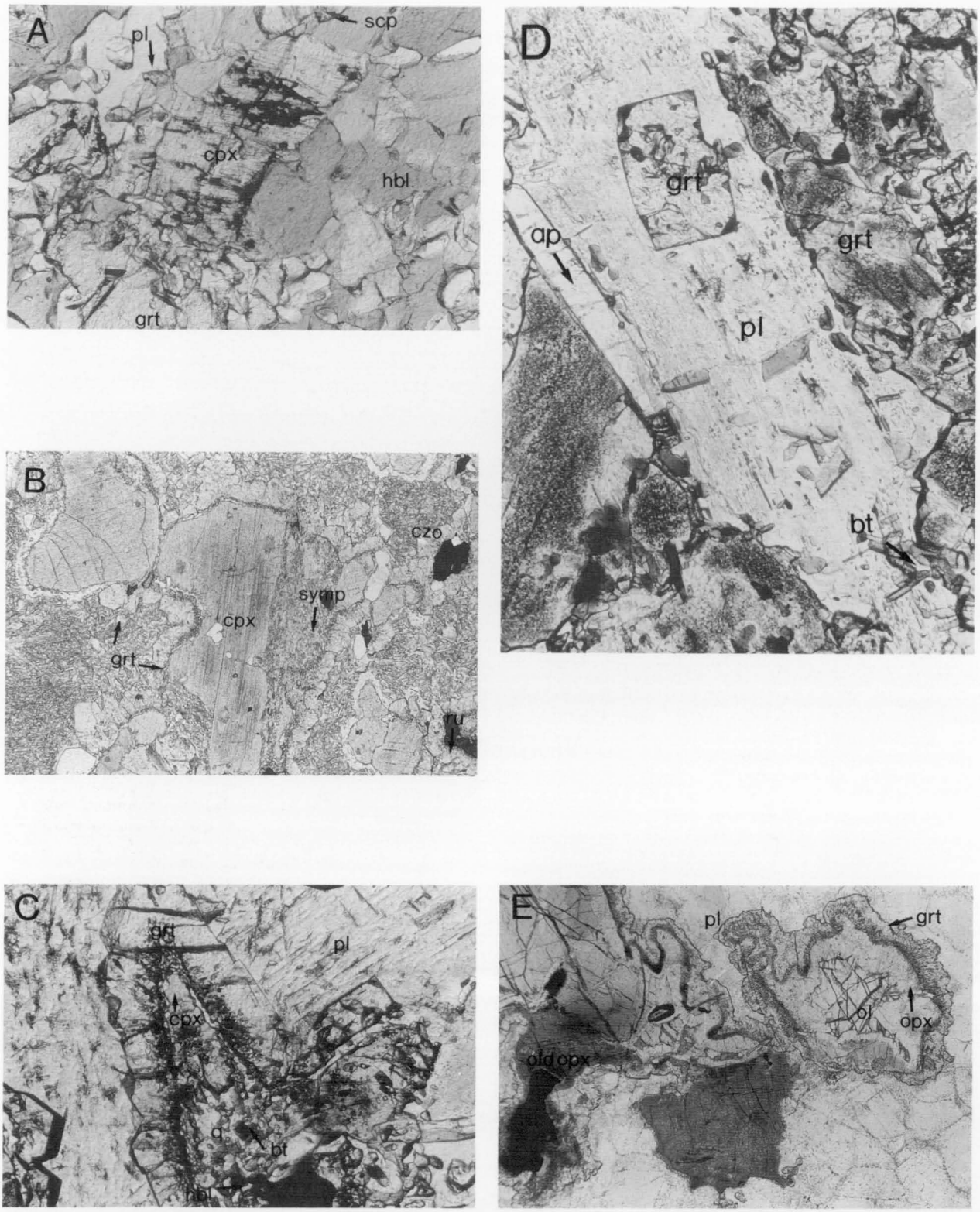

Figure 160. D_6 assemblages in metadolerite dykes from the Bates 1:100 000 sheet area. (A) Sub-eclogite-facies assemblage, comprising intergrown garnet (grt), scapolite (scp), hornblende (hbl), and plagioclase (pl), which enclose relict igneous clinopyroxene (cpx). 91989453; plane-polarised light; width of field: about 2 mm. (B) Sub-eclogite-facies assemblage, in which the original magmatic clinopyroxene (cpx) has been partly replaced by garnet (grt) and symplectites (symp) of clinopyroxene, hornblende, and plagioclase, whereas magmatic calcic plagioclase has been replaced by acicular needles of clinozoisite (czo) in a matrix of sodic plagioclase. The groundmass also contains rutile. 91989569D; plane-polarised light; width of field: 1.8 mm. (C) Structured D_6 coronas, comprising an inner symplectite of neoblastic clinopyroxene (cpx), quartz (q), hornblende (hbl), plagioclase (pl), and biotite (bt), inferred as being after magmatic clinopyroxene, and an outer corona of garnet (grt). 91989442; plane-polarised light; width of field: about 2 mm. (D) Magmatic plagioclase (pl), with interstital clinopyroxene, replaced along its margin by high-relief garnet (grt). Plagioclase contains inclusions of biotite (bt), and is bordered on one side by prismatic apatite (ap). 91989442; plane-polarised light; width of field: about 2 mm. (E) Metamorphosed type C olivine dolerite with structured D_6 coronas, comprising an inner zone of orthopyroxene (opx) mantling igneous olivine (ol), and an outer zone of garnet (grt) mantling igneous plagioclase (pl). Garnet also mantles igneous orthopyroxene (old opx). 91989550C; plane-polarised light.

metamorphic clinopyroxene adjacent to orthopyroxene, and amphibole adjacent to plagioclase. Garnet has also formed along plagioclase–plagioclase grain boundaries.

Mineral chemistry

Representative analyses of minerals from S_2, S_3, and S_6 assemblages are given in Table 12, and the major features of the mineral chemistry for samples used for thermobarometry in Table 13.

S_2 garnets in garnet+orthopyroxene-bearing gneiss from Mount Aloysius are grossular-poor and mostly spessartine-poor almandines, with a variable proportion of pyrope. X_{Fe} (atomic Fe/(Fe+Mg)) in the core of large garnet grains is 0.76 in sample 91989117 and 0.81 in sample 91989082. Whereas garnet in samples 91989117 and 91989082 has less than 2 weight percent MnO, garnet in sample 91989407A contains up to 10 percent MnO. Garnet in rocks that show minimal effects of D_3 have a minor rimward increase in almandine, whereas garnet in rocks recrystallised during the development of S_3 are commonly strongly zoned in grossular content. For example, sample 91989082 contains S_2 garnet and orthoproxene, with S_2 orthopyroxene enveloped and partly pseudomorphed by S_3 amphibole. Garnet in this rock shows an appreciable rimward increase in grossular content (X_{gross} = atomic Ca/(Fe+Mn+Mg+Ca) = 0.12–0.25) at the expense of almandine and pyrope contents (Fig. 161). S_2 garnet (X_{gross} = 0.07–0.09) and orthopyroxene in sample 91989567B form porphyroclasts that are wrapped in a foliation defined by clusters of fine-grained S_3 garnet (X_{gross} = 0.20–0.23; Fig. 161). Garnet in garnet+orthopyroxene+plagioclase symplectites enclosing S_2 garnet in sample 91989117 has similar grossular and almandine contents to the S_2 grains. S_3 garnet in garnet–amphibole gneiss (recrystallised granitic rocks) is essentially

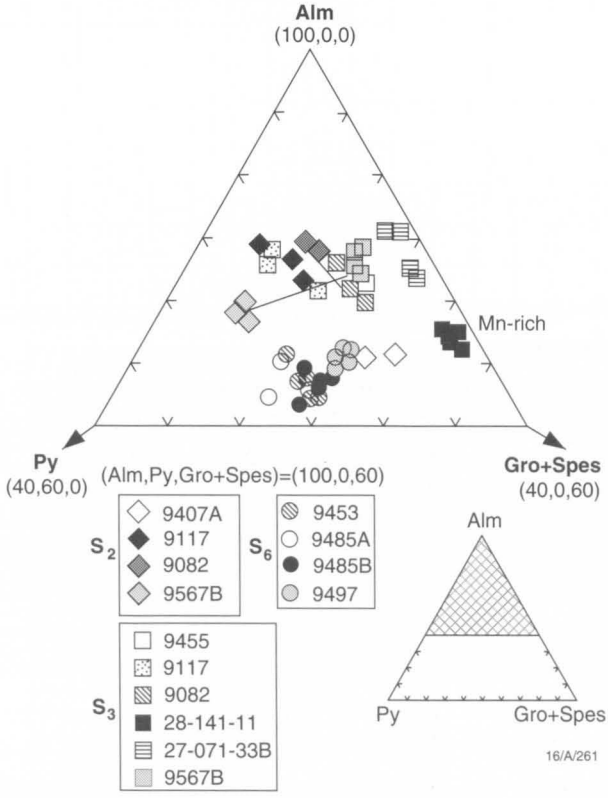

Figure 161. Compositional trends in representative garnets from the western Hinckley Range area, plotted in the ternary diagram almandine–pyrope–(grossular+spessartine). Sample numbers beginning with '9' are prefixed '9198'.

mixtures of almandine and grossular. X_{Fe} and X_{gross} of garnet in sample 91989455 are 0.87 and 0.25, respectively, and in sample 28–141–11 are 0.95 and 0.31. S_6 garnet in ultramylonites and recrystallised mafic dykes are mixtures of almandine, grossular, and pyrope. X_{Fe} and X_{gross} of garnet in recrystallised dyke 91989453 are 0.63 and 0.26, in recrystallised dyke 91989480 are 0.60–0.65 and 0.22–0.29, and in ultramylonite 91989435A are 0.80 and 0.28, respectively. S_6 garnet in recrystallised dyke 91989485B ranges from X_{Fe} = 0.59, X_{gross} = 0.27 to X_{Fe} = 0. 69, X_{gross} = 0.30, with pyrope and grossular contents varying antithetically. S_6 garnet in coronas developed around pyroxene and ilmenite in partly recrystallised dykes is also a mixture of almandine, pyrope, and grossular, and shows a restricted range of composition in individual samples. In sample 91989497, garnet coronas around ilmenite tend to be slightly richer in almandine and poorer in grossular (X_{Fe} = 0. 74, X_{gross} = 0.20) than garnet in coronas to clinopyroxene or along plagioclase–plagioclase grain boundaries (X_{Fe} = 0.70, X_{gross} = 0.27–0.30). These variations in S_6 garnet composition within individual samples are interpreted as reflecting variations in chemistry of the local equilibration volumes that controlled garnet growth.

S_2 orthopyroxene in garnet–orthopyroxene gneiss straddles the hypersthene–ferrosillite boundary, with X_{Fe} 0.51 to 0.55 in sample 91989407A, 0.46 to 0.49 in sample 91989117, and 0.49 to 0.51 in sample 91989082. S_2 orthopyroxene is characterised by low (0.89–1.02 wt % in sample 91989407A) to moderate (1.53–2.54 wt % in sample 91989117) Al_2O_3 contents. In sample 91989117, Al_2O_3 content increases from orthopyroxene cores to rims. S_6 clinopyroxene has Ca contents close to the top of the augite field, X_{Fe} ranging from 0.21 to 0.45, with up to 14 percent jadeite content. As for garnet, there is some variation in clinopyroxene composition within samples, depending on the textural context.

Whereas S_2 biotite has X_{Fe} ranging from 0.3 to 0.45, S_3 biotite has X_{Fe} from 0.45 to 0.7. S_3 amphibole is commonly pargasite, with X_{Fe} from 0.6 to 0.8, and variable but significant contents of both K and Na (Table 12). S_6 amphibole shows a range in composition that straddles the edenite–pargasite–hornblende–tschermakite join, but has a restricted range in X_{Fe} from 0.31 to 0.35. It is Na poor, and in rocks that contain S_6 scapolite has very low Na contents.

S_2 plagioclase in garnet–orthopyroxene gneiss is labradorite in samples 91989082 (An_{55-58}) and 91989117 (An_{55-69}), and bytownite in sample 91989407A (An_{84-90}). Symplectitic S_3 plagioclase in sample 91989117 is richer in Ca than large S_2 plagioclase grains (An_{69} vs An_{55}). S_3 plagioclase in garnet–amphibole gneiss (recrystallised granitoids) is oligoclase in samples 28–141–11 (An_{25}) and 91989455 (An_{19-29}). Plagioclase shows a large range in composition in recrystallised mafic dykes, which is interpreted as representing the partial recrystallisation of igneous plagioclase grains. In dykes 91989485A and B, plagioclase ranges from andesine to bytownite (An_{34-83}). Sample 91989497 contains oligoclase–andesine (An_{17-39}), with Na-rich plagioclase occurring in coronas around clinopyroxene phenocrysts.

D_6 scapolite in mafic dyke 91989453 is close to mizzonite in composition (Eq_{An} = 62–70, where Eq_{An} = atomic 100(Al-3)/3 for Al + Si = 12, Evans et al. 1969)), is fully carbonated, and coexists with D_6 plagioclase (An_{42-47}). Dyke 91989485A also contains coexisting D_6 intermediate scapolite (Eq_{An} 65–67) and plagioclase (An_{30-40}). D_6 clinozoisite in recrystallised mafic dykes is an epidote–clinozoisite solid solution, with about 35 to 40 molecular percent of the epidote end member. The ilmenite end member in ilmenite ranges from 0.87 to 1.0. Hematite is mostly pure. Kyanite may contain up 1 percent Fe_2O_3, but the proportion of Mn_2O_3 is negligible.

Table 12. Representative analyses of minerals from S_2, S_3, and S_6 assemblages. Mineral abbreviations as in Table 2. Sample numbers are prefixed '9198'.

Mineral	*Gt*	*Gt*	*Opx*	*Bt*	*Gt*	*Gt*	*Opx*	*Bt*	*Hbl*	*Gt*	*Hbl*	*Bt*	*Gt*	*Gt*	*Bt*	*Cpx*	*Hbl*	*Gt*	*Gt*	*Ky*	*Pl*
Sample	*9117*	*9117*	*9117*	*9117*	*9082*	*9082*	*9082*	*9082*	*9082*	*9455*	*9455*	*9455*	*9445B*	*9445B*	*9445B*	*9445B*	*9485B*	*9485B*	*9485B*	*9485B*	*9485B*
Paragenesis	*S_2 rim*	*S_3 symp*	*S_2 core*	*S_2 in Gt*	*S_2*	*S_3*	*S_2*	*S_3*	*S_3*	*S_3*	*S_3*	*S_3*	*S_6 with Pl*	*S_6 symp*	*S_6 symp*	*S_6 symp*	*S_6*	*S_6*	*S_6*	*S_6*	*S_6*
SiO_2	38.27	35.45	50.79	37.64	38.61	42.52	50.50	36.78	40.97	38.21	40.34	36.66	38.22	37.90	37.34	51.48	44.28	38.57	39.07	36.67	57.91
TiO_2	0.06	3.36	0.04	6.55	0.12	0.05		5.50		0.10	1.83	4.92	0.01	0.05	5.75	0.14	0.72	0.03	0.03	0.00	0.02
Al_2O_3	21.60	21.09	1.53	14.13	21.44	20.67	1.62	14.27	14.15	20.78	12.13	13.28	21.45	20.86	12.99	2.03	13.36	22.18	22.16	63.19	26.26
Cr_2O_3	0.07																0.00	0.00	0.00	0.04	0.00
FeO	28.92	28.88	28.74	12.90	31.34	24.43	30.00	17.65	16.33	28.25	20.90	20.95	28.74	29.75	17.67	13.52	10.90	23.25	21.23	0.96	0.28
MnO	1.19	0.98	0.28	0.20	1.70	1.51	0.42	0.09	0.22	1.84	0.20	0.05	1.27	1.51	0.05	0.23	0.08	0.65	0.57	0.08	0.04
MgO	5.15	5.08	18.64	14.27	3.86	3.15	16.69	12.23	9.08	2.22	7.54	10.39	2.88	3.40	12.27	10.52	13.82	9.35	7.57	0.02	0.00
CaO	5.45	6.76	0.30	0.30	4.66	8.50	0.53		11.56	9.47	1.10		8.26	6.59	0.00	21.12	12.06	5.89	9.26	0.07	7.85
Na_2O			0.01	0.17				0.11	1.40		1.94	0.14			0.01	1.19	1.59	0.01	0.02	0.03	7.01
K_2O				8.34				9.82	2.27		1.99	9.53			9.61		0.57	0.00	0.02	0.02	0.15
Total	**100.71**	**101.60**	**100.33**	**94.50**	**101.73**	**100.83**	**99.76**	**96.45**	**95.98**	**100.87**	**97.97**	**95.92**	**100.83**	**100.06**	**95.69**	**100.23**	**97.37**	**99.94**	**99.94**	**101.07**	**99.52**
O	12	12	6	22	12	12	6	22	23	12	23	22	12	12	22	6	23	12	12	5	8
Si	2.99	2.78	1.95	5.59	3.01	3.24	1.95	5.52	6.26	3.02	6.24	5.62	3.01	3.01	5.65	1.96	6.451	2.954	2.989	0.985	2.605
Ti	0.00	0.19	0.00	0.73	0.01	0.00		0.62		0.01	0.21	0.57	0.00	0.00	0.65	0.00	0.079	0.002	0.001	0.000	0.000
Al	1.99	1.95	0.07	2.47	1.97	1.86	0.07	2.52	2.58	1.93	2.21	2.40	1.99	1.95	2.31	0.09	2.294	2.003	1.999	2.001	1.392
Cr	0.00																0.000	0.000	0.000	0.000	0.000
Fe	1.89	1.89	0.92	1.60	2.05	1.56	0.97	2.22	2.11	1.87	2.70	2.69	1.89	1.98	2.23	0.43	1.328	1.489	1.359	0.021	0.010
Mn	0.08	0.07	0.01	0.02	0.11	0.10	0.01	0.01	0.03	0.12	0.03	0.01	0.08	0.10	0.01	0.01	0.009	0.042	0.037	0.002	0.002
Mg	0.60	0.59	1.06	3.16	0.45	0.36	0.96	2.73	2.09	0.26	1.74	2.37	0.34	0.40	2.76	0.60	3.001	1.067	0.863	0.000	0.000
Ca	0.46	0.57	0.01	0.05	0.40	0.69	0.02		1.91	0.80	1.84		0.70	0.56	0.00	0.86	1.883	0.483	0.759	0.002	0.378
Na			0.00	0.05				0.03	0.42		0.58	0.04			0.00	0.09	0.448	0.001	0.003	0.002	0.612
K				1.58				1.88	0.45		0.39	1.86			1.85		0.106	0.000	0.002	0.000	0.009
Total	**8.01**	**8.04**	**4.02**	**15.25**	**8.00**	**7.81**	**3.98**	**15.53**	**15.85**	**8.01**	**15.94**	**15.56**	**8.01**	**8.00**	**15.46**	**4.04**	**15.599**	**8.043**	**8.013**	**3.015**	**5.008**
X_{Fe}	0.76	0.76	0.46	0.34	0.82	0.81	0.50	0.45	0.50	0.88	0.61	0.53	0.85	0.83	0.45	0.42	0.31	0.58	0.61		
X_{gross}	0.15	0.18			0.13	0.25				0.26			0.23	0.18				0.16	0.25		

Pressure–temperature conditions

The mineral assemblages described above have considerable potential for the estimation of pressure and temperature conditions, using a variety of directly calibrated geothermometers and geobarometers, as well as the average pressure approach of Powell & Holland (1988) with the expanded, internally consistent dataset of Holland & Powell (1990). The essence of the latter approach is the combination of the pressures, calculated for each reaction in an independent set at an estimated temperature, involving *all* the mineral end members shared between an (equilibrium) mineral assemblage and the dataset. In this way, the calculations maximize the information available from a given mineral assemblage. The application of the average pressure approach to the Musgrave Block rocks is complicated by problems involving garnet and plagioclase composition–activity relations. However, due to the complex history and range in P–T conditions experienced by the Musgrave Block, the diverse mineral assemblages give an indication of the suitability of composition–activity models to various conditions. The results of the application of various geothermometers and barometers are summarised in Table 13, and the suggested P–T–time history in Figure 162.

Peak temperatures associated with the development of S_2 were at least 750°C on the basis of core analyses and garnet–orthopyroxene geothermometry (Harley 1984) using mineral core analyses for samples 91989117, 91989407A, and 91989082 (Table 13). The 873°C estimate for sample 91989407A is unreliable, given the high MnO content of both garnet and orthopyroxene in this rock. However, garnet–clinopyroxene geothermometry (Ellis & Green 1979) for sample 28–142–25C, a calc-silicate gneiss, also gives a high estimate of 909°C. Pressure estimates for the development of S_2 can be made using a variety of methods, assuming a temperature of 750°C. Garnet–plagioclase–clinopyroxene–quartz exchange equilibria give an estimate of 5.1 kb for sample 28–142–25C, following the method of Eckert et al. (1991), with the plagioclase activity model corrected after Newton & Perkins (1982). This estimate is confirmed using garnet–orthopyroxene–plagioclase–quartz exchange equilibria for sample 91989117, following the methods of Perkins & Chipera (1985), Eckert et al. (1991), and Bohlen et al. (1983), all of which give results of about 5.0 kb (Table 13). These estimates are consistent with those obtained using the average pressure approach of Powell & Holland (1988), assuming ideal mixing on sites, which gives an estimate of 5.0±1.0 kb for sample 91989117 using the assemblage garnet–orthopyroxene–plagioclase–quartz–biotite. An inconsistent estimate of 8.6±1.7 kb is produced by the average pressure approach of Powell & Holland (1988), with garnet A–X relations corrected after Berman (1990). This inconsistency suggests that for almandine-rich, grossular-poor garnets, like those defining S_2, the average pressure method gives the best results assuming ideal mixing on sites. Calculations for samples 91989407A and 91989082 give estimates of about 5 kb for S_2 conditions (Table 13), which is considerably lower than those inferred by earlier workers (Nesbitt et al. 1970; Goode & Moore 1975). The somewhat varied results obtained for sample 91989082 (Table 13) probably reflect the effects of incomplete recrystallisation during the development of S_3, which involves S_2 orthopyroxene pseudomorphed by S_3 hornblende and strongly zoned garnet. Garnet core compositions were used for estimates of S_2 conditions, and rim compositions used for estimates of S_3 conditions.

Goode & Moore (1975) estimated high confining pressures of 10–12 kb for crystallisation of the Ewarara, Kalka, and Gosse Pile layered mafic–ultramafic intrusions of the Giles Complex, on the basis of subsolidus reactions between (1) olivine and plagioclase reacting to produce orthopyroxene, clinopyroxene, spinel, and Ca-poor plagioclase, (2) orthopyroxene and plagioclase reacting to produce garnet, and (3) spinel and orthopyroxene reacting to produce garnet. More recent studies on the Wingellina Hills gabbro/pyroxenite intrusion (Ballhaus & Berry 1991) indicated cooling of this body from 1150°C to 750°C at pressures of 6±1 kb, based on the reaction of olivine and plagioclase to produce symplectites of orthopyroxene–clinopyroxene–spinel, olivine–spinel, and spinel–clinopyroxene. As discussed further below, different intrusion depths could be expected, because the intrusions are diverse in composition, and hence density (Ballhaus 1993), and the currently exposed structural level of the Musgrave Block was being pushed to still greater crustal depths at about the same time as emplacement of the Giles Complex. However, some of the garnet coronas may be completely unrelated to isobaric cooling of the Giles Complex.

Temperatures associated with the development of S_3 can be estimated using garnet–amphibole geothermometry on recrystallised granitoids, since both garnet and amphibole are entirely metamorphic phases. Estimates of approximately 700°C are obtained for samples 91989455 and 28–141–11, using the method of Graham & Powell (1984). Garnet in S_3 orthopyroxene–plagioclase symplectites in sample 91989117 also gives an estimate of 700°C (after Harley 1984), but this garnet is probably a relict S_2 phase.

Two very different sets of pressure estimates have been obtained for D_3. Assuming a temperature of 700°C, the method of Kohn & Spear (1990) gives pressure estimates for S_3 of about 9 kb for sample 91989082, compared with an estimate of about 13 kb suggested by average pressure calculations (Powell & Holland 1988), using the assemblage garnet–hornblende–plagioclase–quartz–biotite. Although these estimates suggest a significant increase in pressure, their reliability is uncertain due to possible incomplete chemical re-equilibration during the development of S_3. Similar high pressures were given by sample 91989455, a recrystallised granitoid from the Bates 1:100 000 sheet area, although this sample was collected 38 km northeast of Mount Aloysius and only 12 km south of the Woodroffe Thrust, so the possibility that its assemblages formed during D_6, rather than D_3, cannot be discounted. The minerals garnet, hornblende, plagioclase, and quartz, interpreted as an S_3 assemblage by Clarke et al. (1995a), give a pressure estimate of about 12 kb, following the method of Kohn & Spear (1990), and 13.6±3.1 kb, using the average pressure method of (Powell & Holland 1988). The average pressure result is improved to 13.8±2.4 kb when the garnet activity is modified after Berman (1990). Although this refinement is generally suitable for average pressure estimates using high-pressure granulite-facies assemblages, the trend does not hold for the sub-eclogite-facies assemblages discussed below. However, further evidence for high pressures (c. 11 kb) during D_3 were obtained for sample 28–141–11, a recrystallised granite from Champ de Mars, using the method of Kohn & Spear (1990). In contrast, there appears to be no evidence for such high pressures inferred for D_3 (or D_6) at Mount West, about 20 km west-southwest of Champ de Mars (R.W. White, personal comunication 1996). The extent and significance of this early D_3 compression thus remain to be clarified.

Significantly lower pressure estimates of 4 to 6 kb for S_3 were obtained using orthopyroxene–plagioclase–quartz symplectites enclosing S_2 garnet in sample 91989117. These results cannot imply different metamorphic histories for different crustal blocks, since both high-pressure (91989082) and low-pressure (91989117) estimates are obtained from Mount Aloysius samples that are not separated by major faults. Since significant isothermal, syn-S_3 decompression of at least parts of the western Musgrave Block was inferred on the basis of cordierite+hercynitic spinel coronas on garnet (Clarke & Powell 1991), the simplest explanation would be that the garnet–or-

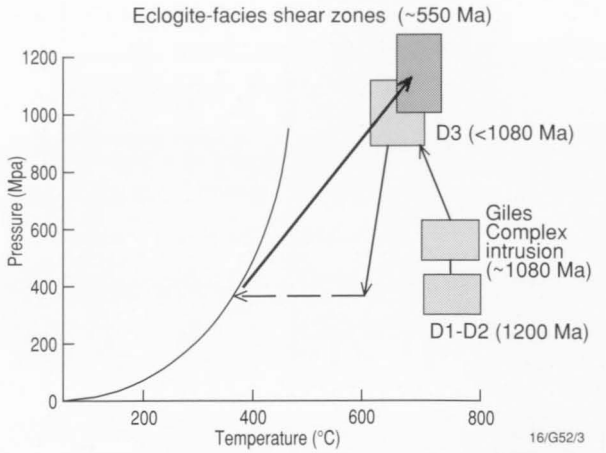

Figure 162. Interpreted pressure–temperature–time history of the western Tomkinson Ranges area (after Clarke et al. 1993).

thopyroxene–plagioclase symplectites formed late in D_3. Whereas the cordierite moats on garnet are not abundant, and it could be argued that they are not representative of widespread decompression, S_3 is cut by abundant and terrane-wide type C olivine+plagioclase-bearing dolerite dykes that do imply decompression from maximum D_3 pressures (Green & Ringwood 1967b; Banno & Green 1968).

Zones of intense D_6 recrystallisation involved minimum temperatures of 750°C on the basis of garnet–hornblende (Graham & Powell 1984) and garnet–clinopyroxene (Ellis & Green 1979) geothermometry on recrystallised mafic dykes and felsic gneiss. Consistent estimates (within 10°C) obtained using the two methods on individual samples suggests chemical re-equilibration of neoblastic clinopyroxene in at least some rocks. Pressure estimates for S_6 range from 11 to 15 kb (Table 13). Calculations made using the assemblage garnet–hornblende–plagioclase–quartz in sample 91989480, following the method of Kohn & Spear (1990), give 12.4–12.7 kb (Table 13); a lower pressure estimate of 11.1 kb is obtained using the assemblage garnet–clinopyroxene–plagioclase–quartz for sample 91989480 after Eckert et al. (1991). Average pressure calculations made using the assemblage garnet–hornblende–plagioclase–quartz–clinopyroxene–clinozoisite in sample 91989480 give 14.1±1.9 kb, which is consistent with the result following the method of Kohn & Spear (1990). The results of the average pressure calculation range from 13.2 to 15.0 kb for T=700 to 800°C, which change only slightly to 14.4±1.7 kb when garnet end member activities are corrected following Berman (1990). A more precise result of 14.0±1.1 kb is obtained for the assemblage garnet–hornblende–plagioclase–kyanite–quartz in sample 91989485B, using the average pressure method of Powell & Holland (1988). The pressure estimate for this sample ranges from 12.9 to 15.0 kb for T=700-800°C. Changing the garnet activity according to Berman (1990) does not improve the results for average pressure calculations using these sub-eclogite-facies assemblages.

Whereas temperature and pressure estimates can be made using symplectite assemblages for the less intensely recrystallised dykes (Table 13), they are of questionable significance since they involve complexities of limited diffusion and arrested reaction. Nonetheless, using complex symplectites and analyses of adjacent grains, identical conditions are implied for D_6 in samples from the Bates 1:100 000 sheet area (e.g., 91989497, Table 13).

It is noteworthy that pressure estimates for S_6 overlap with some of those for S_3. Nevertheless there are significant differences in mineral assemblages formed during these two events. Whereas S_3 assemblages involve hematite, ilmenite, garnet, and hornblende, S_6 assemblages involve rutile, more Na-rich plagioclase, clinozoisite, and commonly more Ca-rich garnet. Such distinctions are consistent with D_6 having occurred under conditions transitional between the granulite and eclogite facies (see Green & Ringwood 1967b; Banno & Green 1968) and S_3 under high-temperature medium-pressure granulite-facies conditions. The occurrence of S_6 plagioclase precludes the assemblages being true eclogites (Carswell 1990). The changes in mineral chemistry are consistent with S_3 conditions having involved somewhat lower pressures than those for S_6, but we cannot exclude the possibility that S_3 conditions were simply significantly more oxidising. Moreover, the distinction between S_6 and S_3 assemblages is not always clear. For example, several rocks from Champ de Mars contain symplectitic assemblages that are similar to D_6 symplectites in recrystallised dykes from the Bates 1: 100 000 sheet area (e.g., samples 27–074–33B (orthopyroxene granitoid) and 28–142–15A (mafic granulite), Table 13). The Champ de Mars symplectites imply cooler conditions and lower pressures of 6–8 kb (Table 13) than those obtained from D_6 assemblages in the Bates samples. If these symplectites did indeed form during D_6, then the lower-pressure estimates are consistent with a shallowing in the structural level with distance south of the Woodroffe Thrust, as suggested by Ballhaus (1993). Alternatively, the assemblages may have formed during D_3. Without clear timing relationships between the development of these assemblages and S_3, it is not possible to assess the significance of the lower P–T estimates from the Champ de Mars symplectites.

Tectonic and metamorphic evolution

The western Musgrave Block has undergone a complex metamorphic and magmatic history spanning at least 1000 Ma (Table 14; Figs 162, 164). Granulite-facies metamorphism and D_{1-2} deformation occurred about 1200 Ma ago at more than 750°C and 5±1.0 kb (Clarke et al. 1995a). Such low-pressure granulite-facies metamorphism could have been related to an asthenospheric thermal perturbation, accounting for the high geothermal gradient implied by the peak metamorphic conditions (Sandiford et al. 1991). If so, evidence for an extensive magmatic flux contemporary with the peak conditions would be expected, although such evidence is limited. Some foliated orthopyroxene granitoids cut S_1, but are affected by S_2, indicating at least some felsic magmatism between D_1 and D_2. Other, mainly hornblende–biotite granitoids are of similar age (c. 1190 Ma). Chemically similar (high Zr, Nb, Y, and LREE), voluminous granitic rocks, including rapakivi types, in the Bates 1:100 000 sheet area may be of similar age, although they have not yet been dated. There is also evidence for mafic magmatism soon after this metamorphism: a small (about 1 km across) body of biotite leucogabbronorite in the western Champ de Mars has given a U-Pb zircon age of 1176±5 Ma (S-S. Sun, unpublished data). Thus, the high-grade metamorphism may have resulted from mafic underplating at that time.

The very extensive mantle melting event which produced the Giles Complex intrusions post-dates the peak (in terms of formation of the regional foliation) of the 1200 Ma granulite-facies metamorphism in the area by more than 100 Ma. Hence, the Giles Complex magmatism cannot have been the direct cause of this event. The ultimate cause of this magmatism, which also produced mafic dyke swarms and mafic volcanics at about 1080 Ma, is far from clear, although a major thermal perturbation of the lithospheric mantle was clearly necessary to account for the scale of melting involved. Zhao & McCulloch (1993b) suggested that either lithospheric thinning allowed

hot asthenospheric mantle to flow beneath the metasomatised subcontinental lithosphere and cause decompression melting, or underplating of mantle diapirs or hot mantle plumes caused dehydration melting of such lithosphere. Mathur & Shaw (1982) envisaged the intracratonic Musgrave mobile belt to have begun as a zone of incipient crustal fracture or rifting, accompanied by voluminous mafic–ultramafic magmatism.

The country rocks were still deep in the crust when the Giles Complex was emplaced. The Giles Complex has, in fact, long been recognised as an example of mafic magma emplaced into lower to middle crustal levels, on the basis of pressures calculated from subsolidus reactions between (1) olivine and plagioclase reacting to produce orthopyroxene, clinopyroxene, spinel, and Ca-poor plagioclase, (2) orthopyroxene and plagioclase reacting to produce garnet, and (3) spinel and orthopyroxene reacting to produce garnet (Goode & Moore 1975). Clinopyroxene and orthopyroxene are enriched in Ca–Al and Mg–Al Tschermak's components. Ballhaus & Berry (1991) undertook thermobarometric studies of the Wingellina Hills intrusion, where orthopyroxene–clinopyroxene–spinel symplectites between olivine and plagioclase indicate a medium-pressure near-isobaric cooling path of 1150–750°C at 6.5–6.2 kb. Some ultramafic cumulates contain highly potassic calcic antiperthite ($An_{75}Ab_5Or_{20}$) which indicates temperatures as high as 1200°C based on the An–Or solvus (Morse 1968). The thin nature of rare chilled margins is consistent with the country rocks having been at temperatures well above the stable continental geotherm.

High-pressure features have previously been recorded only in layered intrusions north of the Hinckley Fault, including the Wingellina Hills, Kalka, Ewarara, Gosse Pile, Teizi, and possibly Claude Hills intrusions (Fig. 4). In other intrusions, olivine and plagioclase are in stable coexistence, except for rare amphibole–spinel coronas at olivine–plagioclase contacts in altered units in the The Wart layered intrusion (Fig. 66 F, G). Consequently, it has been postulated that intrusions south of the Hinckley Fault and west of the Tomkinson Ranges (the Blackstone Range, Cavenagh Range, and Jameson Range intrusions, Fig. 47) were emplaced at shallower crustal levels (Nesbitt et al. 1970; Goode & Moore 1975). This view is consistent with the general shallowing in crustal level southwards and westwards postulated from increased magmatic fractionation of layered intrusions in this direction (Ballhaus & Glikson 1995; Glikson et al. 1995), as well as the occurrence of coeval Tollu Group mafic and felsic volcanic rocks in the same area.

Intrusion of the Giles Complex magmas caused at least localised intracrustal melting which produced a variety of granitic bodies, including rapakivi granites, some of which show back-intrusion relationships (Sheraton & Sun 1995). However, the apparently more voluminous rapakivi granitoids south of the Hinckley Range are considerably older (1188±4 Ma, Sun et al. 1996a, b). There is some evidence, albeit somewhat equivocal, for a large pressure increase to about 11 kb at 650–700°C early in D_3 in the Hinckley Range area and elsewhere during or soon after emplacement of the Giles Complex (Fig. 162; Clarke et al. 1995a; R.W. White, personal communication 1995), possibly at least partly as a result of the significant crustal thickening involved. D_3 is constrained to the time interval between 1080 Ma, the age of the Giles Complex and Tollu Group, and 1000 Ma, the (imprecise) age of the type C dykes. It resulted in the development of an impersistent, steep southeast-trending mylonitic S_3 foliation. Generally, the layered intrusions of the Giles Complex were not exposed to hydrous conditions during D_3, except along shear zones. Parts of the Hinckley Range gabbronorite and Michael Hills gabbro were extensively intruded by c. 1060 Ma granite dykes. In these areas, D_3 resulted in extensive recrystallisation of the gabbro to mafic granulite, possibly aided by introduced volatiles (Daniels 1974; Glikson et al. 1990b; Stewart & Glikson 1991).

Near-isothermal decompression of the granulites to pressures of about 4 to 5 kb is inferred to have occurred at Cohn Hill, south of the Jameson Range (Fig. 97), late in D_3, on the basis of syn-S_3 cordierite coronas around garnet (Fig. 162; Clarke & Powell 1991). The presence of post-S_3 olivine–plagioclase-bearing type C mafic dykes in the western Tomkinson Ranges is also consistent with such uplift.

The geothermal pulse associated with emplacement of voluminous mafic–ultramafic bodies of the Giles Complex may have resulted in thermal weakening of the crust and consequent extensional collapse, possibly involving large detachments and rapid exhumation (Lister & Baldwin 1993). However, as the Tollu Group volcanic rocks and the Giles Complex are coeval, the part of the Musgrave Block west of the Bell Rock Range and south of the Blackstone Range must have already undergone uplift and erosion before 1080 Ma. The basement to the Tollu Group consists mainly of granitic rocks of somewhat different composition to those farther east. Unfortunately, significant dislocation of the Musgrave Block during D_6 would probably have disrupted any pattern of D_{1-3} isograds, thus complicating elucidation of the tectonic history. The Tollu Group is overlain by the Townsend Quartzite, which forms a possible equivalent of the areally extensive Heavitree Quartzite, located at the base of the Neoproterozoic to Palaeozoic Amadeus Basin (Forman 1965). The Musgrave Block thus formed a basement to, and a source of sediments for, the Amadeus Basin.

The tectonic significance of the 800 Ma type B dolerite dykes is unclear. They were derived from a much less enriched source than the 1080 Ma magmas, possibly a large-scale asthenospheric mantle plume (Zhao et al. 1994).

North of the Tomkinson Ranges (in the Bates 1:100 000 sheet area), the 800 Ma dykes, together with their host rocks, were recrystallised by a second high-pressure event (D_6) during the 550 Ma Petermann Ranges orogeny (Forman 1965; Maboko et al. 1992) under conditions of T>750° and P = 14±1 kb. In this area, the effects of high-pressure shearing and recrystallisation are extensive (Stewart 1993, 1995b; Clarke et al. 1995a). Northwest overthrusting of a crustal section more than 25 km thick during D_6 resulted in major decompression (uplift) of rocks of the southern granulite-facies block. Corona textures in rocks in other parts of the western Musgrave Block that may have developed during this event, though widespread, are less well developed and cannot be unambiguously constrained to be post-S_3. Some of the garnet-bearing corona textures within Giles Complex intrusions are similar to those in some, less thoroughly recrystallised post-S_3 dykes, and may thus be related to the 550 Ma sub-eclogite event rather than to post-intrusion cooling (Clarke et al. 1995a).

Similar high-temperature sub-eclogite-facies assemblages have been reported from large ultramylonite zones farther east in the Musgrave Block (Ellis & Maboko 1992). In this area, the southern granulite-facies Musgrave Block was thrust over the amphibolite-facies Olia Gneiss terrane along the Woodroffe Thrust (Figs 1, 163; Forman 1965; Maboko et al. 1992). Northward thrusting of the Musgrave Block over Neoproterozoic cover rocks of the Amadeus Basin occurred along shears that contain kyanite+muscovite±staurolite assemblages (Forman 1965). Whereas the earlier tectonothermal events (D_{1-3}) were associated with major heat inputs in the form of magmatic fluxes, the P–T conditions recorded by the 550 Ma D_6 event are interpreted in terms of both tectonic burial and exhumation. Large thrust faults, such as the Woodroffe Thrust, the Bell Rock–Blackstone Thrust, and the Officer Basin Thrust Fault, could represent re-activated late-D_3 detachment faults. The structural significance of these late thrust faults has been recognised for some time, and the Woodroffe Thrust has been

Table 13. Summary of results from the application of geothermometers and geobarometers (after Clarke et al. 1995a).

Sample	*Rock type (Location)*	*Foliation*	*Assemblage*	*Assumed*	*T °C*	*P kbar*	*Method*
28-142-25C	Calc-silicate (Charnockite Flats)	S_2	$Gr_{80}Alm_{20}$–$Woll_{50}Hed_{78}$–An_{97}–Qz	P=4	909		1
			$Gr_{80}Alm_{20}$–Hed_{78}–An_{97}–Qz	T=750		5.1	2
91989117	Mafic Gt-Opx granulite (1 km W of Mount Aloysius)	S_2	$Alm_{67}Py_{20}Gr_{10}$–Fs_{49}	P=4 cores	780		3
			$Alm_{67}Py_{20}Gr_{10}$–Fs_{49}–An_{78}–Qz	T=750 cores		P_{Fe}= 6.1	4
						4.9	5
						5.2	6
						5.5	7
			$Alm_{67}Py_{20}Gr_{10}$–Fs_{49}–An_{78}–Ann_{30}			5.0±1.0	8
						8.6±1.7	9
91989407A	Felsic Gt-Opx gneiss (10 km S of Latitude Hill)	S_2	$Alm_{57}Py_{18}Gr_{15}$–Fs_{55}	P=4 cores	873		3
			$Alm_{54}Py_{11}Gr_{16}$–Fs_{56}	rims	641		3
			$Alm_{57}Py_{18}Gr_{15}$–Fs_{55} (Mn-rich garnet)	T=750		P_{Fe}=5.5	4
						6.7	5
						4.0	6
						5.6	7
						3.8±1.1	8
						4.8±1.0	9
91989082	Mafic Gt-Opx granulite (5 km WNW of Mount Aloysius)	S_2	$Alm_{69}Py_{16}Gr_{12}$–Fs_{49}–An_{55}–Qz	T=750 cores		P_{Mg}=6.8 P_{Fe}=6.3	4
						2.9	5
						5.5	6
						6.2	7
						6.0±1.3	8
						6.4±1.2	9
		S_3	$Alm_{56}Py_{18}Gr_{25}$–Parg–An_{55}–Qz	T=700 rims		P_{Mg}=8.8 P_{Fe}=8.3	10
			$Alm_{56}Py_{18}Gr_{25}$–Parg–An_{55}–Qz–Ann_{45}			13.0±2.4	8
						13.5±1.7	9
91989455	Gt-Am metagranite (6 km ESE of Mount Daisy Bates)	S_3	$Alm_{62}Py_{10}Gr_{25}$–Parg		699		11
			$Alm_{62}Py_{10}Gr_{25}$–Parg–An_{29}–Qz	T=700		P_{Mg}=11.9 P_{Fe}=12.1	10
						13.6±3.0	8
						13.8±2.4	9
28-141-11	Gt-Am metagranite (Champ de Mars)	S_3	$Alm_{57}Py_3Gr_{32}$–Parg		670–754		11
			$Alm_{57}Py_3Gr_{32}$–Parg–An_{25}–Qz	T=700		P_{Mg}=11.1 P_{Fe}=11.2	10
			$Alm_{57}Py_3Gr_{32}$–Parg–An_{25}–Qz–Ksp_{90}–Ann_{70}	T=700		9.8±2.5	8

Sample	*Rock type (Location)*	*Foliation*	*Assemblage*	*Assumed*		*T °C*	*P kbar*	*Method*
91989480	Metadolerite dyke	S_6	$Alm_{46}Py_{24}Gr_{28}$–$Woll_{47}Hed_{18}$	P=12		764		1
	(11 km N of Mount		$Alm_{46}Py_{24}Gr_{28}$–Parg			762		11
	Fanny)		$Alm_{46}Py_{24}Gr_{28}$–Parg–An_{30}–Qz	T=700			P_{Mg}=12.7 P_{Fe}=12.4	10
			$Alm_{46}Py_{24}Gr_{28}$–Parg–An_{30}–Qz–$Cz_{64}Ep_{36}$				14.1±1.9	8
							14.4±1.7	9
91989435A	Mylonite (14 km NNE	S_6	$Alm_{57}Py_{14}Gr_{29}$–$Woll_{42}Aug_{45}$	P=12		875		1
	of Mount Gosse)							
91989453	Metadolerite dyke	S_6	$Alm_{45}Py_{26}Gr_{29}$–Parg			811		11
	(1 km SW of Mount		$Alm_{45}Py_{26}Gr_{29}$–$Woll_{46}Hed_{22}$	P=14		821		1
	Daisy Bates)		$Alm_{45}Py_{26}Gr_{29}$–$Woll_{46}Hed_{22}$–An_{43}–Qz	T=750			9.7	2
			$Alm_{45}Py_{26}Gr_{29}$–$Woll_{46}Hed_{22}$–An_{43}–Qz–Parg				12.2±2.2	8
							12.9±1.9	9
91989485A	Metadolerite dyke	S_6	$Alm_{47}Py_{32}Gr_{22}$–Parg			731		11
	(3 km NNW of Mount		$Alm_{47}Py_{32}Gr_{22}$–Parg–An38–Qz	T=750			P_{Mg}=11.7 P_{Fe}=11.8	10
	Fanny)		$Alm_{47}Py_{32}Gr_{22}$–Parg–An_{38}–Qz–Ky				14.0±1.1	8
							14.3±1.2	9
91989485B	Metadolerite dyke	S_6	$Alm_{45}Py_{29}Gr_{26}$–Parg			738		11
	(3 km NNW of Mount		$Alm_{45}Py_{29}Gr_{26}$–Parg–An_{35}–Qz	T=750			P_{Mg}=11.0 P_{Fe}=10.8	10
	Fanny)		$Alm_{45}Py_{29}Gr_{26}$–Parg–An_{35}–Qz–Ky				13.7±1.6	8
							14.3±1.6	9
91989497	Metadolerite dyke	S_6	$Alm_{49}Py_{23}Gr_{28}$–$Woll_{42}Aug_{39}$	P=14	corona to S_3 hematite	708		1
	(3 km E of Mount		$Alm_{49}Py_{23}Gr_{28}$–$Woll_{42}Aug_{39}$–An_{17}–Qz	T=750	corona to Cpx_{ig}		12.5	2
	Fanny)		$Alm_{49}Py_{23}Gr_{28}$–Parg–An_{17}–Qz	T=750	corona to Cpx_{ig}		P_{Mg}=14.0 P_{Fe}=13.5	10
27-071-33B	Orthopyroxene granite	S_6	$Alm_{63}Py_3Gr_{30}$–Parg	P=14	sympl	591		11
	(Champ de Mars)		$Alm_{63}Py_4Gr_{23}$–$Woll_{43}Aug_{69}$		sympl	501		1
			$Alm_{63}Py_4Gr_{23}$–Parg–An_{26}–Qz	T=750	sympl		P_{Mg}=6.3 P_{Fe}=8.4	10
28-142-15A	Mafic granulite	S_6	$Alm_{66}Py_4Gr_{30}$–Parg		sympl	568		
	(Champ de Mars)		$Alm_{66}Py_4Gr_{30}$–Parg–An_{33}–Qz	T=750	sympl		P_{Mg}=6.8 P_{Fe}=8.7	10
				T=650			P_{Mg}=6.7 P_{Fe}=8.0	10

Methods: 1, Ellis & Green (1979); 2, Eckert et al. (1991), corrected plagioclase model after Newton & Perkins (1982); 3, Harley (1984); 4, Perkins & Chipera (1985), after Ganguly & Saxena (1984); 5, Eckert et al. (1991), corrected plagioclase model after Newton & Perkins (1982); 6, Bohlen et al. (1983), with garnet A–X after Ganguly & Saxena (1984); 7, Bohlen et al. (1983,) with garnet A–X after Newton & Perkins (1982); 8, Powell & Holland (1988), assuming ideal mixing on sites; 9, Powell & Holland (1988), with garnet A–X after Berman (1990); 10, Kohn & Spear (1990); 11, Graham & Powell (1984).

Abbreviations: Alm (almandine) = Fe/(Fe+Mn+Mg+Ca); Py (pyrope) = Mg/(Fe+Mn+Mg+Ca); and Gr (grossular) = Ca/(Fe+Mn+Mg+Ca) in garnet. Hed = Fe/(Fe+Mg) in hedenbergite; Aug = Fe/(Fe+Mg) in augite; Woll (wollastonite) = Ca/2 in clinopyroxene. An = Ca/(Ca+Na+K) in plagioclase. Fs (ferrosilite) = Fe/(Fe+Mg) in orthopyroxene. Ann (annite) = Fe/(Fe+Mg) in biotite. Cz (clinozoisite) = (Al-2)/((Al-2)+Fe) and Ep = Fe/((Al-2)+Fe) in epidote. Other abbreviations as in Table 2.

Table 14. Summary of the tectonic, igneous, and metamorphic history of the western Musgrave Block. Typical foliation dips and lineation plunges are given for the various deformation events.

Age (Ma)	*Structural events*	*Igneous events*	*Metamorphic conditions*
<550	D_7 retrograde shear zones; E-trending; foliation 030°/80°; lineation 030°/80°		Contain muscovite and biotite
c.550	Major D_6 ultramylonite–pseudotachylite zones; E-trending, N-directed thrusting (e.g., Woodroffe and Champ de Mars Thrust Faults); foliation 190°/80°, 355°/60°; lineation 175°/80° (reverse), 350°/60° (normal)		Uplift and erosion of the high-grade terrane during the Petermann Ranges orogeny; sub-eclogite facies near sole of Woodroffe Thrust: P=14.0±1.1 kb; T>750°C
	D_5 mylonite–ultramylonite zones; mainly N-trending; SW thrusting; foliation 070°/80°; lineation 025°/50° (reverse movement)		Greenschist facies
	D_4 ultramylonite zones; mainly E to ENE-trending; SE thrusting; foliation 005°/65°; lineation 325°/40° (reverse movement)		Amphibolite facies
820	Post-D_3	Type B quartz dolerite dykes	
c.1000	Post-D_3	Type C olivine dolerite dykes	
	D_3 penetrative simple shear deformation; upright open to isoclinal F_3 folds; mainly SE-trending mylonitic foliation 045°/80°; lineation 025°/80°		Granulite facies; P=4.5±1.1 kb (late) and possibly up to 11 kb (early); T=650–700°C
1050–1080	Pre- to syn-D_3	Hbl–Bt granite veins and dykes (including rapakavi varieties); type A intergranular dolerite dykes	
1080		Felsic and mafic volcanism (Tollu Group, west of Tomkinson Ranges)	Lower greenschist facies; show little evidence for D_3
1080	Post-D_2, pre-D_3	Emplacement of Giles Complex	Wingellina Hills intrusion emplaced at P=6±1 kb; near-isobaric cooling from 1050° to 750°C; lower pressures to SW
1190	Post-D_2, pre-D_3	Porphyritic and rapakivi Hbl–Bt granitoids and gabbronorite (Champ de Mars); syenite (Mt Aloysius)	
	D_2 penetrative pure shear deformation; recumbent isoclinal folds; lineation 105°/15°		Granulite facies; P=5±1 kb; T>750°; S_{1-2} is the pervasive foliation
1200	Post-D_1, pre-D_2	Opx granitoids (e.g., Minno)	
	D_1 layer parallel foliation, reoriented during D_2; isoclinal folds rarely preserved		Granulite facies
c.1300		Protoliths of felsic orthogneiss (S of Hinckley Fault)	
c.1550		Protoliths of felsic orthogneiss (probably both intrusive and extrusive; N of Hinckley Fault); ages of protoliths of mafic granulite and metasedimentary rocks unknown	

interpreted as the root zone of the Petermann Ranges Nappe at the southwest margin of the Amadeus Basin (Forman & Shaw, 1973; Bell 1978). Polymictic boulder beds and matrix-supported, poorly sorted conglomeratic sandstones of the Olgas Range probably represent molasse derived from eroding thrust scarps (Sweet & Crick 1992). Thus, the Woodroffe Thrust forms a crustal suture that controlled the 550 Ma old north–south convergence of the Musgrave Block and Amadeus Basin. The lateral extent of the crustal overthickening involved and the extension of the Woodroffe Thrust into the Paterson Province (Fig. 163) in northwestern Australia (Horowitz & Daniels 1966; Myers 1990) remain subjects for further field work in the westernmost Musgrave Block.

Economic geology

There has been little mining activity to date in the Musgrave Block. The most significant identified deposits are all associated with Giles Complex mafic–ultramafic intrusions. They include several subeconomic deposits of nickel, some with chrysoprase, associated with lateritised ultramafic rocks, as well as vanadiferous titano-magnetite seams within troctolitic intrusions. In addition, minor copper and lead mineralisation occurs in volcanic rocks of the Bentley Supergroup. Comprehensive stream sediment geochemical surveys, geophysical surveys, limited geological mapping, and shallow drilling were carried out in the Tomkinson Ranges and surrounding area during the late 1960s and early 1970s by Southwestern Mining Company Limited (SMC). Exploration was also conducted by Westfields Minerals NL. In the Mount Woodroffe area of the central Musgrave Block, a geochemical stream sediment study (Cu, Pb, Zn, Co, Ni, Cr, V, Mn, Pt, Os, Ir) of the Giles Complex was carried out by the South Australia Department of Mines (SADME). Results are available on microfiche reports archived with the Geological Survey of Western Australia and SADME. A review of mineral deposits and prospects in the Musgrave Block in Western Australia, as known up to the early 1970s, is given by Daniels (1974), and summarised by Daniels (1975). Tonkin (1991) reviewed the known mineral occurrences of the Musgrave Block in South Australia. The present NGMA project did not include systematic studies of mineralisation, as this was a condition of access into the Aboriginal reserves.

Lateritic nickel

The Wingellina (Irrunitju) nickeliferous laterite and ochre deposits are confined to shear zones in pyroxenite and dunite of the Wingellina Hills layered gabbro/pyroxenite intrusion (Sprigg & Rochow 1975). The deeply weathered lateritic profile is interspersed with less-weathered mafic and ultramafic rocks displaying shear and fold structures interpreted by Daniels (1974) as having allowed active ground water circulation which enhanced the development of laterite. Leaching of SiO_2 and MgO and concentration of residual Al_2O_3 and Fe_2O_3 was accompanied by supergene enrichment of trace metals, including Ni, in the deposits, which overlie the magnesium-rich ultramafic rocks; in many areas, the laterite is cut by veinlets of chrysoprase. Extensive drilling by SMC at Wingellina has proved a resource of about 61 million tonnes (Mt) at 1.32% Ni, with a possible additional 41 Mt (Daniels 1974). Co and Cr are minor components of the deposits. The nickeliferous laterite consists of goethite, kaolin, minor manganese oxide and ilmenite, and rare gibbsite. Similar deposits occur north and east of the Kalka norite/pyroxenite intrusion (Thomson 1963, 1965b) and around the Claude Hills peridotite/gabbro intrusion (Miller 1969). The estimated reserve in the latter area is 4.5 Mt at 1.5% Ni, and the nickeliferous laterite deposits occur in palaeodepressions overlying peridotite and pyroxenite (Turner 1968).

Vanadiferous titano-magnetite units

Vanadium-bearing titano-magnetite layers and lenses occur in troctolitic intrusions of the Giles Complex — Bell Rock, Blackstone Range, and, in particular, Jameson Range. Titano-magnetite layers in the Jameson Range troctolite/gabbro intrusion contain from 0.71 to 1.40% V_2O_5 (Daniels 1974), consistent with the three new analyses of this study which range from 1.06 to 1.30% V_2O_5. Thin (<30 cm) vanadiferous titano-magnetite layers also occur in the northern part of the Bell Rock intrusion (Daniels 1974), as well as in some of the Giles Complex intrusions in South Australia (Hiern 1975). The latter include small deposits at the western end of the Kalka intrusion (up to 1.28% V_2O_5) and in the Caroline intrusion, 150 km farther east (up to 0.54% V_2O_5; Miller 1969).

Magnetite-rich units in the Jameson Range intrusion and environs occur mainly in poorly exposed plains, where they can be traced through their iron oxide-rich weathering products, which show, for example, high 5/4, 7/4, and 3/1 band ratios on Landsat-5 TM images (see Appendix I).

Daniels (1974) divided the Jameson Range troctolite/gabbro sequence into four zones, with vanadiferous units occurring mainly in zones 2 and 4. Two components can be distinguished in outcrops of the oxide-rich layers: ilmenite, which has a metallic lustre, and a reddish-brown oxidised magnetite component. Primary ilmenite grains are aligned parallel to the igneous layering. Zone 2 is a 300 m-thick sequence dominated by lherzolite, which crops out for about 13 km along strike on the northeastern side of the Jameson Range intrusion. Oxides form up to 50 percent of the rocks, and three analyses of lherzolite average 0.68% V_2O_5. Vanadiferous titano-magnetite layers contain 17.2 to 21.0% TiO_2 and 1.11 to 1.40% V_2O_5. Two samples of the lateritic weathering products of these rocks contain 0.39% and 0.46% V_2O_5 (Daniels 1974).

The 3000 m-thick zone 4, on the southwestern side of the Jameson Range, consists mainly of troctolite and gabbro and contains a higher concentration of titano-magnetite layers than zone 2. Near the base of this zone is a 19 km-long titano-magnetite unit, with an exposed thickness of up to 15 m. TiO_2 contents average 23.4% and V_2O_5 contents average 1.20% (1.33% near the base of the unit). Higher in zone 4, discontinuous magnetite layers occur over a strike distance of about 37 km from northwest to southeast, with thicknesses ranging up to 61 m over short sections. V_2O_5 contents (average 0.79%) are lower than in the basal magnetite unit, probably because the magma was progressively depleted in V by magnetite fractionation (Daniels 1974).

Platinum-group elements

Evaluation of the potential for stratabound PGE-enriched sulphide concentrations in layered mafic–ultramafic intrusions can be made using S abundances in the host rocks. Conditions favourable for the accumulation of PGE-bearing sulphides occur when a PGE-rich S-undersaturated ultramafic magma interacts with S-rich material, such as a new pulse of a high-S mafic magma or through assimilation of sedimentary country rocks. Economic mineralisation is thus likely to occur either along mixing zones of ultramafic and mafic magma, as in the Merensky Reef (Bushveld Complex), J-M Reef (Stillwater Complex), Great Dyke, and the Munni Munni intrusion, or at the basal contacts of the intrusions (commonly Ni–Cu–Co–PGE sulphide mineralisation), as at Sudbury and Radio Hill (see Hoatson et al. 1992 for further discussion). For layered intrusions derived from S-undersaturated parent magmas, fractionation processes would allow efficient concentration of PGE prior to their precipitation when S-saturation was attained, due to the extremely high sulphide/melt partition coefficients for PGE (Sun et al. 1991; Wyborn & Sun 1994). In contrast, intrusions derived from S-saturated magmas will have much more restricted potential for stratabound PGE mineralisation, but may still have potential for the basal contact type.

Estimates of S abundances in the Giles Complex magmas are critically dependant on estimates of the amount of intercumulus material in the layered sequences (Hoatson & Keays 1989). However, limited S data, combined with relatively high S/Zr ratios (commonly around 10), for the Wingellina

Hills, Michael Hills, Murray Range, Bell Rock, Blackstone Range, and Jameson Range intrusions suggest that the magmas were either S-saturated or close to saturation. The widely disseminated sulphides in the Wingellina Hills ultramafic cumulates also suggest that the most primitive derivatives of the parent magmas were S-saturated when emplaced. Similarly, mafic dykes considered to be related to Giles Complex intrusions have S contents (700–1200 ppm) typical of those of continental tholeiites and probably close to saturation levels for mafic magmas (Czamanske & Moore 1977). Nevertheless, some mafic dykes in the Bell Rock intrusion show a negative correlation of S with *mg*, suggesting that this particular magma type may not have been completely S-saturated. Determination of Se, which is positively correlated with S in mafic magmas but is less susceptible to secondary mobilisation (Hoatson & Keays 1989), is needed in order to better estimate original S contents.

Several other factors restrict the prospectivity for economic PGE mineralisation in the Giles Complex intrusions, which have significant differences from the economically important PGE-rich intrusive complexes, such as the Bushveld Complex (northern Transvaal), Great Dyke (Zimbabwe), and Stillwater Complex (Montana) (cf. Naldrett et al. 1987). For example, the Giles Complex consists of a number of spatially distinct sills and lopoliths emplaced at middle crustal levels (probably within the 4–7 kb range), rather than constituting faulted segments of an originally continuous Bushveld-type lopolith (Ballhaus 1993; Ballhaus & Glikson, 1995). This conclusion is supported by the discrete fractionation sequences within individual layered intrusions, e.g., Bell Rock, Blackstone Range, and Michael Hills. Any stratabound sulphide–PGE mineralisation in the Giles Complex is therefore likely to be restricted to specific cumulate sequences, in view of the discrete nature of individual intrusive bodies.

Textural features (Ballhaus 1993) suggest that the Giles Complex cumulates cooled much faster than these other layered intrusions, giving less scope for efficient concentration of incompatible elements, such as PGE, and precipitation of sulphides (see Morse 1986 for cumulate growth mechanisms). Such high cooling rates are reflected in the abundance of intercumulus material, representing trapped melt, in the ultramafic and mafic rocks, namely, a prevalence of orthocumulates as compared to adcumulates. No sulphide-rich stratabound layers nor chromitite layers (see below) have been identified in the Giles Complex, and no basal sulphide mineralisation of the Sudbury type has yet been found.

Preliminary PGE (Pt, Pd, Ir, and Ru) analyses for the Wingellina Hills intrusion have been conducted by R.R. Keays (University of Melbourne, now at Laurentian University, Sudbury, Ontario) and C.G. Ballhaus (personal communication 1993). The highest values (30 ppb of combined Pd and Pt) occur in the most primitive ultramafic units just above the levels of magma replenishment; PGE contents drop rapidly to about 3 ppb in the more fractionated gabbroic cumulates. This militates against concentration of PGE during crystal fractionation, at least in the sampled parts of this intrusion. A more detailed evaluation of PGE prospectivity must await more comprehensive studies of trace element geochemistry, particularly PGE, S, and Se, but the present, admittedly very limited, data suggest that the economic potential of the Giles Complex may not be high. Nevertheless, it is worth pointing out that, for example, it took more than 20 years of intensive exploration to define the J-M Reef of the Stillwater Complex (D.M. Hoatson personal communication 1996).

Chromite

Rare occurrences of chromite in the Giles Complex include a 1.5 cm-thick layer of chromitite at Mount Davies (Coats 1956) and chromite grains in pegmatoid pyroxenite in the Wingellina Hills intrusion (Ballhaus & Glikson 1989). The overall scarcity of chromite in the Giles Complex can be attributed to depletion of the parental melts in Cr by early high-pressure fractional crystallisation of clinopyroxene (cf. Goode & Moore 1975; Ballhaus & Glikson 1995). Such high-pressure fractionation of pyroxene is consistent with the relatively silica-undersaturated compositions of the troctolitic rocks of the Bell Rock, Blackstone Range, and Jameson Range intrusions. Low oxygen fugacities may also have inhibited crystallisation of chromite (Nesbitt et al. 1970).

Other minerals

Small stratabound units of copper sulphides in granulite-facies gneisses of possibly primary volcanogenic origin in parts of the central Musgrave Block suggest a potential for Broken Hill style mineralisation (Tonkin 1991). Minor Cu and Cu–Pb mineralisation occurs in felsic volcanic rocks of the Palgrave volcanic association of the Bentley Supergroup near Mount Palgrave and Mount Eliza (Daniels 1974, 1975). Subeconomic Cu mineralisation is also present in Mission Group sedimentary rocks and basalt near the top of the Bentley Supergroup in the Warburton Mission area, and in Smoke Hill Felsic Volcanics near Tollu (Daniels 1974). Small lenses of fluorite occur in brecciated felsic volcanic rocks of the Scamp volcanic association near Mount Elvire (Daniels 1974). Most of these occurrences are in the Talbot 1:250 000 sheet area to the west of the present study area. The Blackstone Range–Rawlinson Range region has been considered in connection with the search for the fabled Lasseter's Reef, although no significant traces of gold have yet been discovered.

Regional correlations

Correlations within the Musgrave Block

The Woodroffe Thrust juxtaposes the major southern granulite-facies-dominated terrane of the Musgrave Block with a northern amphibolite-facies terrane containing the older Olia Gneiss (Figs 1, 163, 164). In the eastern Musgrave Block, the southern and northern terranes are termed the Fregon (or Kulgera) terrane and the Mulga Park terrane, respectively (Edgoose et al. 1993; Major & Conor 1993). The Fregon terrane comprises granulite-facies gneisses that lie above the Woodroffe Thrust and are thus broadly equivalent to the southern terrane in the western Musgrave Block. Like the latter, they were derived from protoliths up to 1550 Ma old, and were deformed and metamorphosed at about 1200 Ma (Rb–Sr isochron ages, Gray 1978). Amphibolite-facies rocks below the Woodroffe Thrust in the Mulga Park terrane include the older Olia Gneiss (Forman 1972), an orthogneiss which apparently underwent amphibolite-facies metamorphism at 1607±14 Ma and possibly a second metamorphic event at about 1400 Ma (U–Pb zircon ion-microprobe ages, Maboko et al. 1991). However, Camacho & Fanning (1995) suggested that the two terranes may be essentially equivalent, apart from differences in metamorphic grade, as orthogneisses from both give U–Pb zircon ion-microprobe ages of about 1550 Ma. Thus, the significance and distribution of the pre-1600 Ma Olia Gneiss component remain to be clarified. Emplacement of the LILE-rich (C.M. Gray, personal communication 1994) Kulgera and Ayers Ranges granites occurred in the Fregon terrane about 1150 Ma ago, based on U-Pb zircon ion-microprobe dating (Camacho & Fanning 1995). Movement along the Woodroffe Thrust is constrained to have occurred between 560 and 520 Ma by K–Ar and Rb–Sr ages of syn-kinematic muscovite and biotite (Camacho & Fanning 1995), consistent with Sm–Nd data for a recrystallised dolerite dyke (Clarke et al. 1995b).

Mafic igneous events in the central and eastern Musgrave Block which are roughly contemporaneous with the Giles–Tollu event are represented by the Kulgera (or Alcurra) dyke swarm (Rb–Sr age of 1054±14 Ma, Camacho et al. 1991; Sm–Nd age of 1090±32 Ma, Zhao & McCulloch 1993a). Equivalent dykes in the southern Arunta Block, north of the Amadeus Basin (Fig. 139), are termed the Stuart dyke swarm (1076±33 Ma Sm–Nd age, Zhao & McCulloch 1993a). The post-D_3 800 Ma type B dykes in the western Musgrave Block are probably correlated with the 790±40 Ma Amata dyke swarm in the central Musgrave Block, as well as the 802±35 Ma Gairdner dyke swarm of the Gawler Craton and Stuart Shelf (Sm–Nd ages, Zhao et al. 1994). Park et al. (1995) suggested that the Gairdner dyke swarm may represent part of a giant radiating dyke swarm which also included dykes of western North America and was emplaced into a Neoproterozoic supercontinent. However, the North American dykes may be significantly younger (U–Pb and $^{40}Ar/^{39}Ar$ ages are c. 780 Ma) than the Australian examples.

The Dean and Townsend Quartzites that unconformably overlie the Musgrave Block form the basal units of the southwestern Amadeus Basin and northern Officer Basin, respectively, and may be correlatives of the Heavitree Quartzite of the northern and eastern Amadeus Basin (Fig. 164; Forman 1965; Daniels 1974). Mafic volcanic rocks in the Bitter Springs Formation, which overlies the Heavitree Quartzite in the northern Amadeus Basin, may be correlatives of the Amata dykes (Zhao et al. 1994), in which case basin formation would be older than 800 Ma. If so, it would be difficult to correlate basin formation directly with the somewhat younger mantle plume activity which gave rise to the magmatism (Zhao et al. 1994). The Amadeus Basin contains several unconformities and Neoproterozoic glacigene sequences (Sturtian, Marinoan) which can be correlated over wide areas of Australia (Shaw et al. 1991). Initial deposition resulted in areally extensive sheets of the basal Heavitree Quartzite and equivalents, followed by the development of a large asymmetric east–west sub-basin in the southern part of the Amadeus Basin, separated by a narrow arch from a shallower sub-basin to the north (Shaw et al. 1991). A profound change in basin morphology occurred near the end of the Proterozoic, when the main axis of deposition shifted northwards due to north–south compression during the Petermann Ranges orogeny. This resulted in northward movement of the Musgrave Block along the Woodroffe Thrust and the formation of nappes in the southern part of the Amadeus Basin (Forman 1965; Forman & Shaw 1973). The consequent crustal overthickening is reflected in the formation of the syn-tectonic early Cambrian Mount Currie Conglomerate in the central part of the basin (Shaw et al. 1991) and the Sir Frederick Conglomerate in the western part (Grey 1990). These deposits consist of thick, poorly sorted conglomerate and boulder lenses, with clasts up to 1 m across (Sweet & Crick 1992), and unconformably overlie equivalents of the 670 Ma Marinoan glacigene sediments of the Amadeus Basin (Grey 1990). The conglomerate interfingers with sandstone further north. In contrast, the effects of the Petermann Ranges orogeny have not been recognised in the northern Amadeus Basin, where pre and post-Cambrian sediments were deposited with apparent conformity (Korsch & Lindsay 1989; Shaw et al. 1991).

Inter-province correlations

Magmatic and metamorphic events broadly contemporaneous (1300–1050 Ma) with those in the Musgrave Block have been reported for the Albany–Fraser Province of southwestern Australia, and the Bunger Hills and Windmill Islands areas of the East Antarctic Shield (Figs 163, 164). The Albany–Fraser Province, on the southern boundary of the Archaean Yilgarn Block, consists of a western terrane, and an eastern terrane which comprises the Biranup Complex (including the mafic Fraser Complex) and the Nornalup Complex to its southeast (Myers 1990). Protolith ages in the western section are not well established, but tonalite emplacement occurred at 1289±10 Ma (U–Pb zircon age, Pidgeon 1990), and granulite-facies metamorphism at about 1190 Ma (U–Pb zircon ion-microprobe ages, Black et al. 1992). Reported protolith ages for the Biranup Complex include 1600 to 1700 Ma for granitoid emplacement (U±Pb zircon ages, Nelson et al. 1995) and crystallisation of gabbro in the Fraser Complex at 1291±21 Ma (Sm–Nd mineral age, Fletcher et al. 1991). Both the Biranup and Nornalup Complexes underwent granulite-facies metamorphism about 1300 Ma ago (Rb–Sr isochron ages, Bunting et al. 1976; U–Pb zircon ages, Nelson et al. 1995), and granite emplacement occurred between about 1190 and 1130 Ma (Nelson et al. 1995).

Granulite-facies metamorphism of virtually identical age (1190±15 Ma U–Pb zircon ion-microprobe age) to that in the western Musgrave Block occurred in the Bunger Hills area of Antarctica (Sheraton et al. 1993). Protoliths of granodioritic orthogneisses were emplaced between 1700 and 1500 Ma. Metamorphism was closely followed by emplacement of voluminous, largely mantle-derived plutonic rocks, ranging from gabbro to granite (1170–1150 Ma) and abundant dolerite dykes (c. 1140 Ma). In the Windmill Islands, emplacement of felsic

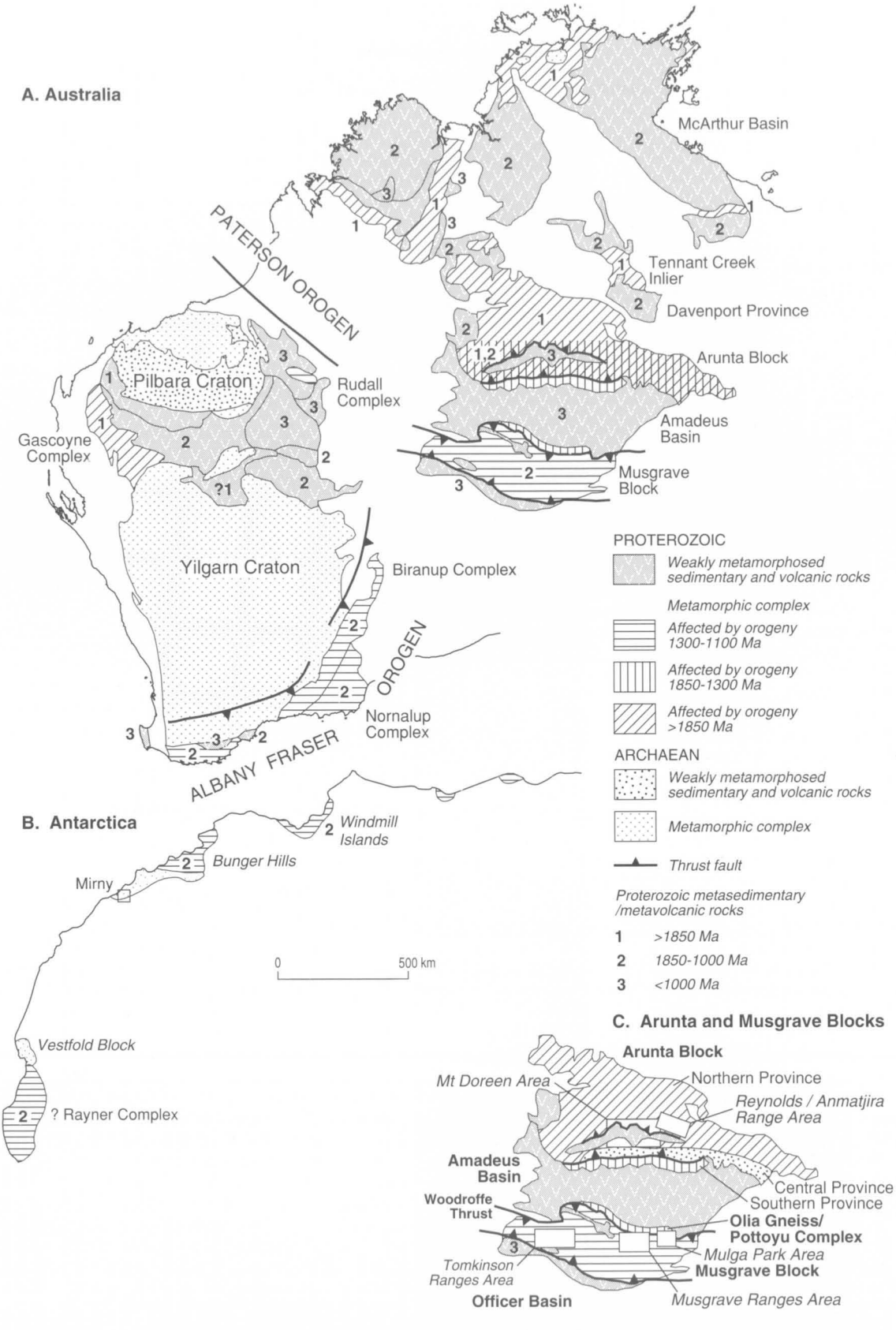

Figure 163. Geological map showing Precambrian rocks of (A) northern and western Australia (after Palfreyman et al. 1976; Myers & Hocking 1988) and (B) once adjacent parts of East Antarctica (after Sheraton et al. 1993) using the Gondwana reconstruction of Veevers & Eittreim (1988). The subdivision of Proterozoic rocks is based on that proposed by Dunn et al. (1966) and refined by Plumb (1985) and Page (1988). The age of high-grade metamorphic rocks near Mirny, Antarctica, is poorly constrained. They are at least partly Archaean, but with a major 'Pan-African' (c. 500 Ma) overprint. The inset (C) shows the geological setting of the Musgrave and Arunta Blocks, with locations of areas and geological features discussed in the text.

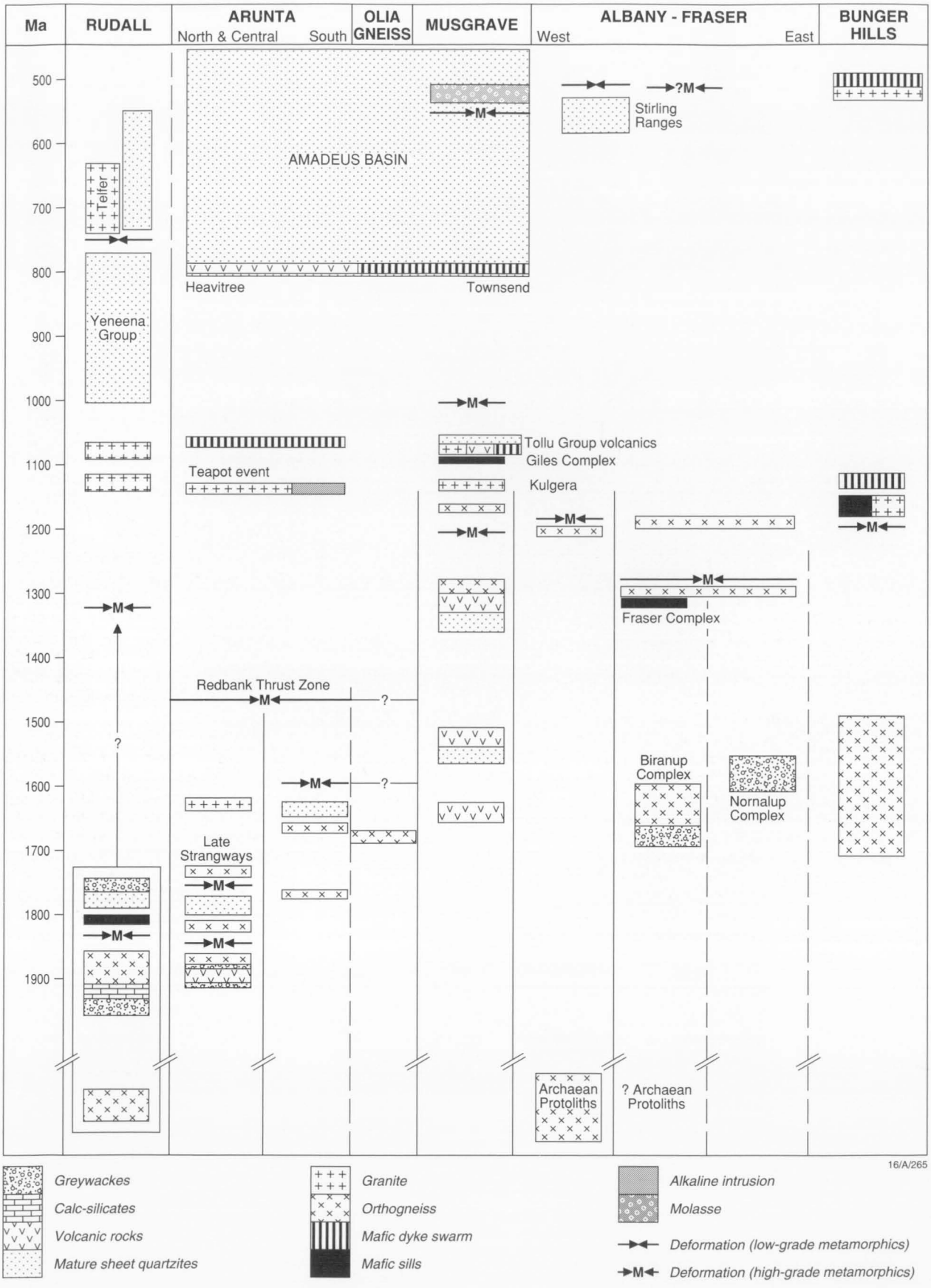

Figure 164. Time–space diagram summarising the geological evolution of the Proterozoic terranes discussed in the text. The thick vertical lines represent terrane distinctions; the lines end where terrane boundaries are transgressed by a magmatic, tectonic, or sedimentary event that joins two or more terranes. As described in the text, note the close correlation of the c. 1200 Ma magmatic and metamorphic event through the Musgrave Block, Albany–Fraser Province, Bunger Hills, and possibly the Windmill Islands (not shown). It is likely that incompatible element-rich granitoids that intruded both the Arunta and Musgrave Blocks at about 1150 Ma represent a late stage of this event.

igneous rocks was apparently coeval with high-grade metamorphism about 1500 Ma ago (Williams et al. 1983). However, it is probable that metamorphism continued at least until (or also occurred at) about 1200 Ma, as the Ardery Charnockite was emplaced at about that time (Rb–Sr isochron age of 1172±28 Ma, Tingey 1991), and possibly as late as 1070±36 Ma (Rb–Sr isochron age of Ford Granite).

On the basis of these geochronological similarities, Sheraton et al. (1993) suggested that the 1190 Ma metamorphism in the Bunger Hills resulted from collision between the Yilgarn Block and an Antarctic Archaean craton. However, the Bunger Hills metamorphism and associated mantle-derived magmatism was considered to have occurred in a continental arc tectonic setting, with the actual collision zone situated to the east and involving the Albany–Fraser Province and Windmill Islands. Whatever the details, the geological similarities strongly support the juxtaposition of the Albany–Fraser, Bunger Hills, and Windmill Island terranes in Gondwana reconstructions. Indeed, Moores (1991) proposed that these terranes may be parts of a global-scale Grenvillean belt which extended from eastern North America, through Antarctica into Australia. Nevertheless, there are sufficient geological complexities to caution against too sweeping correlations. For example, in Antarctica the continuation of the mobile belt to the west of the Bunger Hills includes the Denman Glacier region, in which no evidence for a Mesoproterozoic metamorphism has so far been found, although there is evidence for extensive 'Pan-African' (c. 500 Ma) magmatism. Moreover, the high-grade Rayner Complex, still further west in the sector 45° to 75° E, was apparently metamorphosed about 1000 Ma ago (Sheraton et al. 1993). On the other hand, the c. 1300 Ma events reported in the both parts of the Albany–Fraser Province are similar in age to the formation of some orthogneiss protoliths in the Musgrave Block. Whereas the Musgrave Block clearly experienced metamorphic and magmatic activity broadly contemporaneous with those in the Albany–Fraser Province, the extensive intervening cover rocks make it difficult to assess the relative positions of these terranes at 1200 Ma. In contrast to the Albany–Fraser and Antarctic terranes, for which a continental margin setting is likely, the Musgrave Block had probably evolved to an intraplate setting by 1200 Ma. This does not preclude the presence of an active continental margin earlier in the block's Proterozoic evolution, as the composition of many Y-depleted orthogneisses suggests an ultimate derivation by melting of subducted oceanic crust. Moores (1991) shows his postulated Grenvillean mobile belt passing south of the Musgrave Block, under cover rocks of the Officer Basin. Moreover, both gravity and magnetic data suggest that the east to east-southeast trend of the Musgrave Block is discordant to the northeast trend of the Fraser terrane, rather than curving into it (Wellman 1976; Shaw et al. 1995), although it is possible that the former trend at least partly resulted from younger (D_3–D_6) events.

The northern and central provinces of the Arunta Block (Fig. 163) show similarities to Proterozoic terranes in northern Australia (Page 1988). They include metasedimentary sequences, intruded by 1880 to 1590 Ma granitic rocks, and show widespread effects of the 1780 to 1730 Ma Strangways orogeny (Black & Shaw 1992; Collins & Shaw 1995). In contrast, the southern province, which is separated from the other two provinces by the Redbank Thrust Zone (Glikson 1986, 1987; Shaw & Black 1991), is apparently a distinct, somewhat younger terrane, dominated by orthogneiss which crystallised about 1660 Ma ago (U–Pb zircon ion-microprobe ages, Black & Shaw 1992; Collins et al. 1995) and was susequently deformed during the c. 1600 Ma Chewings orogeny (Collins & Shaw 1995); this orthogneiss has no known equivalents in the northern provinces. Large-scale thrusting assembled the three provinces as the Arunta Block by about 1500 to 1400 Ma (Shaw & Black 1991). Emplacement of the c. 1150 Ma intraplate Kulgera and Ayers Ranges granites, on the northern margin of the Musgrave Block, was contemporaneous with the 'enriched' intraplate magmatism of the Teapot thermal event in the southern province of the Arunta Block (1136±6 Ma U–Pb zircon ion-microprobe age, Black & Shaw 1995). Both the Olia Gneiss and the southern Arunta province are extensively intruded by dolerite dykes (the Kulgera and Stuart dykes, respectively), which are probably part of the same swarm. Palaeomagnetic evidence for these dykes (Camacho et al. 1991; Zhao & McCulloch 1993a) show that the Arunta and Musgrave Blocks were in their present relative positions by the time of the 1080 Ma Giles Complex–Tollu Group magmatism.

Metamorphic rocks of broadly similar age to the above terranes crop out in the Rudall Complex of the Paterson Province in northern Western Australia (Fig. 163). Here, amphibolite-facies metamorphism occurred 1333±44 Ma ago, during the Watrara orogeny, and biotite monzogranite was emplaced at 1080 Ma (Rb–Sr isochron ages, Chin & de Laeter 1981). The relationship of these rocks to the Musgrave Block is uncertain, as they are also separated by cover rocks of the northwestern Officer Basin. However, geophysical data suggest a structural, if not a lithological, connection (Wellman 1976; Shaw et al. 1995).

Conclusions

On the basis of the NGMA Musgrave Project, as well as earlier studies, the following sequence of events is proposed for the western Musgrave Block (Table 14):

- C. 1550 Ma and c. 1300 Ma felsic igneous rocks, including some which probably represent new felsic crust, together with subordinate sedimentary and mafic igneous rocks, form protoliths of the high-grade metamorphic Mount Aloysius Complex.
- Granulite-facies metamorphism and deformation about 1200 Ma ago involved mostly penetrative pure shear during D_1 and D_2 at >750°C and 5±1 kb. Metamorphism was associated with emplacement of post-D_1, pre-D_2 orthopyroxene granites ('charnockites') and post-D_2 granitoids, including rapakivi types (1188±4 Ma) and syenites. Leuconorite was emplaced at 1176±5 Ma.
- Emplacement of voluminous mafic–ultramafic magmas of the Giles Complex occurred 1078±3 Ma ago, with near-isobaric cooling from 1150° to 750°C at 6±1 kb (estimated for the Wingellina Hills intrusion). Troctolite–gabbro bodies in the southwestern part of the area were emplaced at lower pressures of about 4 kb at higher crustal levels. Pervasive granite veining, probably representing back intrusion of crustal melts, was associated with recrystallisation to mafic granulite of marginal parts of the Giles Complex (probably during D_3), particularly in the western Hinckley Range. Extrusion of the bimodal Tollu Group volcanic rocks onto an uplifted and eroded basement of amphibolite-facies granitic gneiss was coeval with the Giles magmatism. The basement was apparently metamorphosed at shallower crustal levels than the granulite-facies gneisses into which the Giles Complex was emplaced, and may, in part, represent younger felsic crust. Some type A dolerite dykes (e.g., type A2) may well have been feeders to Giles Complex intrusions.
- Penetrative simple shear deformation (D_3) produced near-vertical high-strain zones, apparently under high-pressure conditions (650–700°C, ~11 kb). This may reflect increased lithostatic pressures associated with emplacement of the thick (>10 km in total) mafic–ultramafic sills and lopoliths of the Giles Complex. It was apparently followed by near-isothermal decompression, associated with major uplift and erosion of more than 12 km of crust, to about 4 to 5 kb.
- Post-D_3 type C olivine dolerite dykes were emplaced about 1000 Ma ago, although their age is not well constrained. They are chemically and isotopically similar to the slightly older (~1080 Ma) Kulgera (eastern Musgrave Block) and Stuart (Arunta Block) dyke swarms.
- Type B quartz dolerite dykes were emplaced about 800 Ma ago. They are chemically and isotopically equivalent to the Amata dykes (eastern Musgrave Block) and the Gairdner dyke swarm (Gawler Craton), and so form part of a very extensive swarm.
- At least four phases of mylonite and ultramylonite zone formation (D_{4-7}) post-date type B dykes. The c. 550 Ma east–west-trending D_6 ultramylonite–pseudotachylite zones are the largest, and were formed during major northward thrusting of the Giles Complex and host gneisses in the Petermann Ranges orogeny (Forman & Shaw 1973). They are best developed in the Bates 1:100 000 sheet area, where they form the western extension of the Woodroffe Thrust, and formed at elevated pressures (>750°C, 14.0±1.1 kb) along the sole of the thrust; sub-eclogite-facies garnet–clinopyroxene-bearing assemblages were formed. Other major thrusts include the marginal thrust of the Officer Basin and the Bell Rock–Blackstone Range thrust fault, which led to the erosional removal of the Tollu Volcanic rocks from the Tomkinson Ranges and eastern parts of the Musgrave Block.

At least seven phases of deformation have thus been recognised in the western Tomkinson Ranges: (1) pure shear deformation (D_{1-2}), which formed the dominant foliation in the Mount Aloysius Complex, (2) mylonitic simple shear deformation (D_3), and (3) younger mylonite, ultramylonite, and retrograde shear zones (D_{4-7}). However, correlations of these various deformation events (especially D_{4-7}) over the whole area have proved difficult, perhaps because their orientations are quite variable. The Giles Complex is constrained by structural and metamorphic studies to be post-D_2, and pre-D_3. Although a range of ages is possible for individual intrusions, we tentatively regard the well-defined U–Pb zircon age of 1078±3 Ma for granophyre from the Bell Rock intrusion as the emplacement age of the Giles Complex. It is supported by a preliminary U–Pb zircon age of 1073±5 Ma for a microgabbronorite (or possibly a type A dyke) in the Hinckley Range intrusion, as well as Sm–Nd mineral–whole-rock isochron ages (1077±32 and 1047±28 Ma) for leucogabbro in the Wingellina Hills intrusion (Sun et al. 1996b). The estimated age of the Smoke Hills Felsic Volcanics (1078±5 Ma U–Pb zircon age for rhyolite) is within error of most of these ages (Sun et al. 1996a, b). Emplacement of the Giles Complex more than 100 Ma after the peak (in terms of formation of the regional foliation) of the granulite-facies metamorphism means that the Giles magmatism cannot have been the direct cause of this Grenvillean-age event.

The extensive recrystallisation and felsic veining of the Giles Complex in the western Hinckley Range and parts of the Michael Hills and other intrusions were interpreted by Daniels (1974) as due to marginal contamination of the gabbro. However, evidence for the intrusion of veins and stocks of granite into fractured, consolidated gabbro, and the common occurrence of angular mafic xenoliths within the granites suggest back intrusion of felsic magma, roughly coeval with emplacement of the mafic bodies, but when the latter were at subsolidus temperatures (Moore 1971a, b; Glikson et al. 1990b). As the recrystallisation was associated with formation of a superposed S_3 foliation, it is likely that D_3 occurred very soon after emplacement of the Giles Complex. Derivation of the post-D_3 type C olivine dolerite dykes from a similar mantle source to those of both the Giles Complex and c. 1080 Ma Kulgera dyke swarm would also be consistent with a broadly similar age for all these mafic intrusives.

The present study suggests that the Mesoproterozoic mafic–ultramafic Giles Complex forms a suite of discrete major sill-like bodies preserved in near-original form, rather than tectonic slices of an originally contiguous Bushveld-type lopolith. Their present dimensions are therefore thought to approximate the original sizes of individual middle to upper crustal magma chambers. The various intrusions cannot be related to a single liquid line of descent of a single continuously fractionating parent magma, but crystallised from separate batches of variably fractionated parent melts (cf. Nesbitt et al. 1970; Daniels 1974). Phase equilibrium considerations show that at least three parent magmas (primitive, gabbroic, and troctolitic) were involved. These parent melt compositions can be related chemically to a primitive mantle-derived parental liquid or liquids by various degrees of polybaric pyroxene± olivine fractionation. The Giles Complex is thus a series of spatially and compositionally discrete coeval intrusions,

including sills and associated feeder dykes, related through a common, or very similar, magma parentage.

The geographical distribution of the intrusions probably reflects vertical stacking of discrete magma chambers within the Mesoproterozoic crustal section. The ratio of mafic to ultramafic components of the Giles Complex intrusions increases south-southwestwards with progressively shallower crustal levels from the Woodroffe Thrust, reflecting density and buoyancy controls on the emplacement levels of the rising magmas:

- peridotite and pyroxenite-dominated intrusions along the northeastern margin of the Tomkinson Ranges (e.g., Ewarara, Claude Hills, Gosse Pile);
- gabbro-dominated intrusions with significant to minor pyroxenite located south of the ultramafic bodies (e.g., Kalka, Mount Davies, Wingellina Hills, Hinckley Range, Michael Hills);
- troctolitic intrusions in the southern and west parts of the western Musgrave Block (e.g., Bell Rock, Blackstone Range, Jameson Range).

Evidence for a multiple-intrusive history includes (1) the presence of chemically varied primitive, gabbroic, and troctolitic intrusions, (2) emplacement of pulses of primitive olivine–spinel-saturated magma into more evolved gabbroic orthopyroxene–clinopyroxene–plagioclase-saturated magma, and (3) emplacement of numerous small pulses of microgabbro into still hot and plastic host intrusions.

Prospects for the Giles Complex having potential for magmatic chromite–sulphide–PGE mineralisation must await more comprehensive studies of trace elements, including S and Se to assess degrees of S-saturation. However, the Giles Complex has important differences from economically important complexes, such as the Bushveld, Great Dyke, and Stillwater intrusions (cf. Naldrett et al. 1987). Cumulate textures suggest that the Giles Complex intrusions cooled faster than these layered intrusions, giving less scope for efficient accumulation of incompatible elements, such as the PGE. Chromitite layers, commonly spatially associated with stratiform sulphide–PGE mineralisation, are rare, probably because the melt was depleted in Cr during high-pressure clinopyroxene fractionation. Sulphide–PGE mineralisation may therefore be restricted to specific cumulate sequences, in view of the discrete nature of individual intrusive bodies. Vanadiferous titano-magnetite layers in troctoitic intrusions, such as Jameson Range, contain up to 1.4 percent V_2O_5.

The Giles Complex, together with coeval mafic volcanic rocks of the Tollu Group (Mummawarrawarra Basalt) and mafic dykes, was derived by melting of an enriched source, probably involving subcontinental lithospheric mantle. A major thermal perturbation, perhaps resulting from lithospheric thinning associated with crustal extension, or mantle plume activity, was clearly necessary to account for the scale of melting involved. Thermal and magmatic modelling of deep-seated mafic intrusions (Campbell & Turner 1987; Huppert & Sparks 1988) emphasises the extremely efficient convective heat transfer and resultant intracrustal melting in and above the roof zones of large magma chambers. At crustal levels of around 20 km and deeper, melting of roof rocks, already at near-solidus temperatures under the attendant geotherm, would give rise to extensive crustal melting and high rates of cooling. This contrasts with the lower degrees of crustal melting, and thereby of heat loss, in the roof zones of shallower crustal magma chambers in colder country rocks, where heat transfer would take place mainly by conduction. High-temperature melting of near-anhydrous granulite-facies country rocks commonly produces A-type granitoids rich in Zr, Nb, Y, and LREE like those associated with the Giles Complex in the western Musgrave Block.

The emplacement of large volumes of mafic–ultramafic magma, with associated felsic plutonic and volcanic activity in the western Musgrave Block at 1080 Ma is a classic example of coeval mafic plutonism and crustal anatexis in pre-existing sialic crust. The range of initial ε_{Nd} values (+0.9 to -2.5) of the c. 1050–1080 Ma felsic igneous rocks is consistent with a wide spectrum of processes, from mantle derivation to crustal anatexis. That these events encompassed much of central Australia is indicated by the extensive coeval Kulgera dyke swarm in the central and eastern Musgrave Block and the Stuart dyke swarm in the Arunta Block.

The 800 Ma dolerite dykes were derived from a much less enriched source than the 1080 Ma magmas, possibly an asthenospheric mantle plume (Zhao et al. 1994). This magmatism was even more widespread than the earlier, as dykes of similar age and composition crop out near Amata, in the eastern Musgrave Block, and in the Gawler Craton (the Gairdner dyke swarm).

Acknowledgements

The study of the Giles Complex intrusions was originally suggested by John Ferguson, former chief of the Division of Petrology and Geochemistry, Bureau of Mineral Resources. The authors are grateful to members, field guides, and advisers of the Ngaanyatjarra Aboriginal communities in Western Australia, in particular, Irrunitju (Wingellina), Blackstone, and Jameson, and to members of the Pitjantjatjarra Aboriginal community of Pipalyatjarra in South Australia, for their co-operation, help, and friendship. We particularly wish to thank Rob Shelton, former community adviser, Irrunitju, for invaluable support in the field. We are also grateful to Ruth Raintree, Murray Wells, and Diana James for helping us communicate with the Aboriginal people. We are indebted to John Vickers, Erwin Feeken, Neil Holzapfel, and Geoff Windsor for able field assistance during several trips. Acknowledgments are also due to our geological colleagues Nigel Duncan, Tim Pharaoh, and John Myers for their field contributions, and Ken Barrett for cartographic assistance. Andrew Glikson acknowledges patient supervision by John Creasey and helpful advice on image-processing techniques by Phil Bierwirth, Taro Macias, and Matt Peljo.

Tim Bell, Phil Bierwirth, Lance Black, Richard Blewett, Ian Buick, Alfredo Camacho, David Champion, Nigel Duncan, John Foden, Chris Gray, Dean Hoatson, Lynton Jaques, Taro Macias, Ken Plumb, Mike Rickard, Russell Shaw, Peter Stuart-Smith, Gladys Warren, Alan Whitaker, Richard White, Peter Williams, and Jian-Xin Zhao all made useful comments on various parts of the manuscript. Many of the Figures were drafted by AGSO's Cartographic Services Unit.

References

Allègre, C.J., Treuill, M., Minster, J-F., Minster, B. & Albarede, F., 1977. Systematic use of trace elements in igneous processes. Part 1: Fractional crystallisation processes in volcanic suites. Contributions to Mineralogy and Petrology, 60, 57–75.

Anderson, J.L. & Morrison, J., 1992. The role of anorogenic granites in the Proterozoic crustal development of North America. In: Condie, K.C. (editor), Proterozoic crustal evolution. Elsevier, Amsterdam, 263–299.

Arculus, R.J., 1987. The significance of source versus process in the tectonic control of magma genesis. Journal of Volcanology and Geothermal Research, 32, 1–12.

Arriens, P.A. & Lambert, I.B., 1969. On the age and strontium isotopic geochemistry of granulite facies rocks from the Fraser Range, Western Australia, and the Musgrave Ranges, central Australia. Geological Society of Australia, Special Publication 2, 377–388.

Ballhaus, C.G., 1993. Petrology of the layered mafic/ultramfic Giles Complex, western Musgrave Block, Western Australia. Australian Geological Survey Organisation Record 1992/73.

Ballhaus, C.G. & Berry, R.F., 1991. Crystallization pressure and cooling history of the Giles layered igneous complex, central Australia. Journal of Petrology, 32, 1–28.

Ballhaus, C.G. & Glikson, A.Y., 1989. Magma mixing and intraplutonic quenching in the Wingellina Hills intrusion, Giles Complex, central Australia. Journal of Petrology, 30, 1443–1469.

Ballhaus, C.G. & Glikson, A.Y., 1992. Magmatic and metamorphic evolution and economic potential of the mafic/ultramafic Giles Complex, western Musgrave Block, W.A. BMR Research Newsletter, 16, 6–9.

Ballhaus, C.G. & Glikson, A.Y., 1995. The petrology of layered mafic–ultramafic intrusions of the Giles Complex, western Musgrave Block, Western Australia. AGSO Journal of Australian Geology and Geophysics, 16, 69–89.

Banno, S. & Green, D.H., 1968. Experimental studies on eclogites: the roles of magnetite and acmite in eclogite assemblages. Chemical Geology, 3, 21–32.

Barker, F., 1979. Trondhjemite: definition, environment and hypotheses of origin. In Barker, F. (editor), Trondhjemites, dacites, and related rocks. Elsevier, Amsterdam, 1–12.

Barnes, S.J. & Naldrett, A.J., 1985. Geochemistry of the J–M reef of the Stillwater complex, Minneapolis adit area. II. Silicate mineral chemistry and petrogenesis. Journal of Petrology, 27, 791–825.

Bates, R.L. & Jackson, J.A., 1987. Glossary of geology. American Geological Institute, Alexandria, Virginia.

Beard, J.S., Lofgren, G.E., Sinha, A.K. & Tollo, R.P., 1994. Partial melting of apatite-bearing charnockite, granulite, and diorite: melt compositions, restite mineralogy, and petrologic implications. Journal of Geophysical Research, 99, 21591–21603.

Becker, H., 1993. Garnet peridotite and eclogite Sm–Nd mineral ages from the Lepontine dome (Swiss Alps): new evidence for Eocene high-pressure metamorphism in the central Alps. Geology, 21, 599–602.

Bédard, J.H., 1989. Disequilibrium mantle melting. Earth and Planetary Science Letters, 91, 359–366.

Bell, T.H., 1978. Progressive deformation and reorientation of fold axes in a ductile mylonite zone: the Woodroffe thrust. Tectonophysics, 44, 283–320.

Berman, R.G., 1990. Mixing properties of Ca–Mg–Fe–Mn garnets. American Mineralogist, 75, 328–344.

Bierwirth, P.N., 1990. Mineral mapping and vegetation removal via data-calibrated pixel unmixing, using multispectral images. International Journal of Remote Sensing, 11, 1999–2017.

Black, L.P. & Shaw, R.D., 1992. U–Pb zircon chronology of prograde Proterozoic events in the central and southern provinces of the Arunta Block, central Australia. Australian Journal of Earth Sciences, 39, 153–171.

Black, L.P. & Shaw, R.D., 1995. An assessment, based on U–Pb zircon data, of Rb–Sr dating in the Arunta Inlier, central Australia. Precambrian Research. 71, 3–15.

Black, L.P., Harris, L.B. & Delor, C.P., 1992. Reworking of Archaean and early Proterozoic components during a progressive, middle Proterozoic tectonothermal event in the Albany Mobile Belt, Western Australia. Precambrian Research, 59, 95–123.

Bohlen, S.R., Wall, V.J. & Boettcher, A.L., 1983. Experimental investigation and application of garnet granulite equilibria. Contributions to Mineralogy and Petrology, 83, 52–61.

Boudreau, A.E., 1987. Pattern formation during crystallization and the formation of fine-scale layering. In: Parsons, I. (editor), Origins of igneous layering. D. Reidel, Dordrecht, pp 453–471.

Bowen, N.L. & Schairer, J.F., 1935. The system MgO–FeO–SiO_2. American Journal of Science, 29, 151–217.

Brown, G.C., Thorpe, R.S. & Webb, P.C., 1984. The geochemical characteristics of granitoids in contrasting arcs and comments on magma sources. Journal of the Geological Society of London, 141, 413–426.

Bunting, J.A., de Laeter, J.R. & Libby, W.G., 1976. Tectonic subdivisions and geochronology of the northeastern part of the Albany–Fraser Province, Western Australia. Geological Survey of Western Australia, Annual Report, 1975, 117–126.

Camacho, A. & Fanning, C.M., 1995. Some isotopic constraints on the evolution of the granulite and upper amphibolite facies terranes in the eastern Musgrave Block, central Australia. Precambrian Research, 71, 155–181.

Camacho, A., Simons, B. & Schmidt, P.W., 1991. Geological and palaeomagnetic significance of the Kulgera dyke swarm, Musgrave Block, N.T., Australia. Geophysical Journal, 107, 37–45.

Campbell, I.H., 1987. Distribution of orthocumulate textures in the Jimberlana intrusion. Journal of Geology, 95, 35–54.

Campbell, I.H. & Turner, J.S., 1987. A laboratory investigation of assimilation at the top of a basaltic magma chamber. Journal of Geology, 95, 155–173.

Carroll, M.R. & Webster, J.D., 1994. Solubilities of sulfur, noble gases, nitrogen, chlorine, and fluorine in magmas. In Carroll, M.R. & Holloway, J.R. (editors), Volatiles in magmas. Reviews in Mineralogy, Mineralogical Society of America, 30, 231–279.

Carswell, D.A., 1990. Eclogites and the eclogite facies: definitions and classification. In: Carswell, D.A. (editor), Eclogite facies rocks. Blackie, London, pp 1–13.

Chappell, B.W. & White, A.J.R., 1974. Two contrasting granite types. Pacific Geology, 8, 173–174.

Chin, R.J. & de Laeter J.R., 1981. The relationship of new Rb–Sr isotopic dates from the Rudall Metamorphic Complex to the geology of the Paterson Province. Geological Survey of Western Australia, Annual Report, 1980, 80–87.

Clarke, G.L., 1992. Field relationships and tectonic history of the Hinckley gabbro, felsic to mafic granulites and granitoids, west Hinckley Range and Champ de Mars areas, Tomkinson Ranges, Musgrave Block, WA. Australian Geological Survey Organisation Record 1992/33.

Clarke, G.L. & Powell, R., 1991. Decompressional coronas and symplectites in granulites of the Musgrave Block, central Australia. Journal of Metamorphic Geology, 9, 441–450.

Clarke, G.L., Buick, I.S. & Glikson, A.Y., 1992. Contact relationships and structure of the Hinckley gabbro and environs, Giles Complex, western Musgrave Block, W.A. AGSO Research Newsletter, 17, 6–8.

Clarke, G.L, Stewart, A.J. & Glikson, A.Y., 1993. High pressure granulite to eclogite-facies metamorphism in the western Musgrave Block, central Australia. AGSO Research Newsletter, 18, 6–7.

Clarke, G.L., Buick, I.S., Glikson, A.Y. & Stewart, A.J., 1995a. Structural and pressure–temperature evolution of host rocks of the Giles Complex, western Musgrave Block, central Australia: evidence for multiple high-pressure

events. AGSO Journal of Australian Geology and Geophysics, 16, 127–146.
Clarke, G.L., Sun, S-S. & White, R.W., 1995b. Grenville-age belts and associated older terranes in Australia and Antarctica. AGSO Journal of Australian Geology and Geophysics, 16, 25–39.
Coats, R.P., 1956. Occurrence of chromite at Mount Davies, Tomkinson Ranges. Mining Review, Adelaide, 101, 46.
Collerson, K.D., Oliver, R.L. & Rutland, R.W.R., 1972. An example of structural and metamorphic relationships in the Musgrave Orogenic Belt, central Australia. Journal of the Geological Society of Australia, 18, 379–393.
Collins, W.J. & Shaw, R.D., 1995. Geochronological constraints on orogenic events in the Arunta Inlier. Precambrian Research, 71, 315–346.
Collins, W.J., Beams, S.D., White, A.J.R. & Chappell, B.W., 1982. Nature and origin of A-type granites with particular reference to southeastern Australia. Contributions to Mineralogy and Petrology, 80, 189–200.
Collins, W.J., Williams, I.S., Shaw, S.E. & McLaughlin, N.A., 1995. The age of the Ormiston Pound Granite: implications for Mesoproterozoic evolution of the Arunta Inlier, central Australia. Precambrian Research, 71, 91–105.
Compston, W. & Nesbitt, R.W., 1967. Isotopic age of the Tollu volcanics, Western Australia. Journal of the Geological Society of Australia, 14, 235–238.
Compston, W., Williams, I.S. & Meyer, C., 1984. U–Pb geochronology of zircons from lunar breccia 73217 using a sensitive high-resolution ion-microprobe. Proceedings of the 14th Lunar Science Conference, Journal of Geophysical Research, 89, B525–534.
Compston, W., Kinny, P.D., Williams, I.S. & Foster, J., 1986. The age and Pb loss behaviour of zircons from the Isua supracrustal belt as determined by ion-microprobe. Earth and Planetary Science Letters, 80, 71–81.
Cox, K.G., 1988. Numerical modelling of a randomized RTF magma chamber: a comparison with continental flood basalt sequences. Journal of Petrology, 29, 681–697.
Cruikshank, B.I. & Pyke, J.G., 1993. Analytical methods used in Mineral and Land Use Program's geochemical laboratory. Australian Geological Survey Organisation Record 1993/26.
Cullers, R.L., Stone, J., Anderson, L., Sassarini, N. & Bickford, M.E., 1993. Petrogenesis of Mesoproterozoic Oak Creek and West McCoy Gulch plutons, Colorado: an example of cumulate unmixing of a mid-crustal, two-mica granite of anorogenic affinity. Precambrian Research, 62, 139–169.
Czamanske, G.K. & Moore, J.G., 1977. Composition and phase chemistry of sulfide globules in basalt from the Mid-Atlantic Ridge rift valley near 37°N lat. Geological Society of America Bulletin, 88, 587–599.
D'Addario, G.W., Wilford, G.E., Fetherston, J.M., Cameron, R.L. & Wedgebrow, J.M., 1976. Geology of the Northern Territory, 1:2 500 000 geological map. Bureau of Mineral Resources, Canberra, Australia.
Daniels, J.L., 1970. Bentley, Western Australia, 1:250 000 geological sheet and explanatory notes, Geological Survey of Western Australia.
Daniels, J.L., 1971a. Cooper, Western Australia, 1:250 000 geological sheet and explanatory notes, Geological Survey of Western Australia.
Daniels, J.L., 1971b. Talbot, Western Australia, 1:250 000 geological sheet and explanatory notes, Geological Survey of Western Australia.
Daniels, J.L., 1972. Scott, Western Australia, 1:250 000 geological sheet and explanatory notes, Geological Survey of Western Australia.
Daniels, J.L., 1974. The geology of the Blackstone region, Western Australia. Geological Survey of Western Australia, Bulletin 123.
Daniels, J.L., 1975. Musgrave Block — sundry mineralization. A. Western Australia. In: Knight, C.L. (editor), Economic geology of Australia and Papua New Guinea. 1. Metals. The Australian Institute of Mining and Metallurgy, Monograph 5, 455–457.
DePaolo, D.J., 1981. Trace element and isotopic effects of combined wallrock assimilation and fractional crystallisation. Earth and Planetary Science Letters, 53, 189–202.
DePaolo, D.J., Perry, F.V. & Baldridge, W.S., 1992. Crustal versus mantle sources of granitic magmas: a two-parameter model based on Nd isotopic studies. Transactions of the Royal Society of Edinburgh: Earth Sciences, 83, 439–446.
Dunn, P.R., Plumb, K.A. & Roberts, H.G., 1966. A proposal for time-stratigraphic subdivision of the Australian Precambrian. Journal of the Geological Society of Australia, 13, 593–608.
Ebadi, A. & Johannes, W., 1991. Beginning of melting and composition of first melts in the system Qz–Ab–Or–H_2O–CO_2. Contributions to Mineralogy and Petrology, 106, 286–295.
Eby, G.N., 1990. The A-type granitoids: a review of their occurrence and chemical characteristics and speculations on their petrogenesis. Lithos, 26, 115–134.
Eckert, J.O., Newton, R.C. & Kleppa, O.J. 1991. The ΔH of reaction and recalibration of garnet–pyroxene–plagioclase–quartz geobarometers in the CMAS system by solution calorimetry. American Mineralogist, 76, 148–160.
Edgoose, C.J., Camacho, A., Wakelin-King, G.A. & Simons, B.A., 1993. Kulgera 1:250 000 geological sheet and explanatory notes. Northern Territory Geological Survey, Darwin, Australia.
Ellis, D.J. & Green, D.H., 1979. An experimental study of the effect of Ca upon garnet–clinopyroxene Fe–Mg exchange equilibria. Contributions to Mineralogy and Petrology, 71, 13–22.
Ellis, D.J. & Maboko, M.A.H., 1992. Precambrian tectonics and the physicochemical evolution of the continental crust. I. The gabbro–eclogite transition revisited. Precambrian Research, 55, 491–506.
Evans, B.W., Shaw, D.M. & Houghton, D.R., 1969. Scapolite stoichiometry. Contributions to Mineralogy and Petrology, 24, 293–305.
Feeken, E.H.J., 1992. Notes on the 1:100 000 environmental map of the Tomkinson Ranges, western Musgrave Block, central Australia. Australian Geological Survey Organisation Record 1992/34.
Feeken, E.H.J., Glikson, A.Y. & Stewart, A.J., 1991. Environmental mapping in BMR: Cainozoic deposits, landforms, and vegetation in the Tomkinson Ranges. BMR Research Newsletter, 14, 7–8.
Fitton, J.G. & Upton, B.G.J., 1987. Alkaline igneous rocks. Geological Society of London, Special Publication 30.
Fletcher, I.R., Myers, J.S. & Ahmat, A.L., 1991. Isotopoic evidence on the age and origin of the Fraser Complex, Western Australia: a sample of mid-Proterozoic lower crust. Chemical Geology, 87, 197–216.
Fleuty, M.J., 1964. The description of folds. Proceedings of the Geologists Association, 75, 461–492.
Forman, D.J., 1965. Ayers Rock, Northern Territory, 1:250 000 geological sheet and explanatory notes. Bureau of Mineral Resources, Canberra, Australia.
Forman, D.J., 1972. Petermann Ranges, Northern Territory, 1:250 000 geological sheet and explanatory notes. Bureau of Mineral Resources, Canberra, Australia.
Forman, D.J. & Shaw, R.D., 1973. Deformation of crust and mantle in central Australia. Bureau of Mineral Resources, Australia, Bulletin 144.
Fraser, S.J. & Green, A.A., 1987. A software defoliant for geological analysis of band ratios. International Journal of Remote Sensing, 8, 525–532.
Frey, F.A., Green, D.H. & Roy, S.D., 1978. Integrated models of basalt petrogenesis: a study of quartz tholeiites to olivine melilitites from southeastern Australia utilizing geochemical and experimental petrological data. Journal of Petrology, 19, 463–513.
Ganguly, J. & Saxena, S.K., 1984. Mixing properties of aluminosilicate garnets: constraints from natural and experimental data and application to geothermobarometry. American Mineralogist, 69, 88–97.
Giles, C.W., 1981. A comparative study of Archaean and Proterozoic felsic volcanic associations in southern Australia. Ph.D. Thesis, University of Adelaide (unpublished).
Glikson, A.Y., 1986. An upthrusted early Proterozoic basic granulite–anorthosite suite and anatectic gneisses, southwest

Arunta block, central Australia: evidence on the nature of the lower crust. Transactions of the Geological Society of South Africa, 89, 263–283.
Glikson, A.Y., 1987. Regional structure and evolution of the Redbank–Mount Zeil thrust zone: a major lineament in the Arunta inlier, central Australia. BMR Journal of Australian Geology and Geophysics, 10, 89–107.
Glikson, A.Y., 1993. Landsat Thematic Mapper image correlations: application to NGMA mapping of the western Musgrave Block, central Australia. 7th Australasian Remote Sensing Conference, Melbourne, Poster Volume, pp 73–78.
Glikson, A.Y., 1994. Landsat-5 thematic mapper image correlations: application to NGMA mapping of the western Musgrave Block, central Australia. Australian Geological Survey Organisation Record 1994/17.
Glikson, A.Y. & Ballhaus, C.G., 1989. Significance of ultrabasic components of the Giles Complex, central Australia. BMR Research Newsletter, 10, 4–6.
Glikson, A.Y. & Creasey, J.W., 1995. Application of Landsat-5 TM imagery to mapping of the Giles Complex and associated granulites, Tomkinson Ranges, western Musgrave Block, central Australia. AGSO Journal of Australian Geology and Geophysics, 16, 173–193.
Glikson, A.Y. & Mernagh, T.P., 1990. Significance of pseudotachylite vein systems, Giles basic/ultrabasic complex, Tomkinson Ranges, western Musgrave Block, central Australia. BMR Journal of Australian Geology and Geophysics, 11, 509–519.
Glikson, A.Y. & Stewart, A.J., 1992. Mapping in high grade terrains: use of remotely sensed data and airborne geophysics. BMR Research Newsletter, 16, 22–23.
Glikson, A.Y., Ballhaus, C.G., Goleby, B.R. & Shaw, R.D., 1990a. Major thrust faults and the crustal zonation of the middle to upper Proterozoic crust in central Australia. In: Salisbury, M.H. & Fountain, D.M. (editors), Exposed cross-sections of the continental crust. Kluwer Academic Publishers, Netherlands, pp 285–304.
Glikson, A.Y., Ballhaus, C.G. & Pharaoh, T.C., 1990b. The Giles Complex, central Australia: new insights into tectonics and metamorphism. BMR Research Newsletter, 12, 18–20
Glikson, A.Y., Stewart, A.J. & Ballhaus, C.G., 1991. Layered basic/ultrabasic intrusions and the deep-seated Proterozoic crust of central Australia (abstract). Geological Society of America Annual Convention, Abstracts with Programs, 1991, A60.
Glikson, A.Y., Ballhaus, C.G., Clarke, G.L., Sheraton, J.W., Stewart, A.J. & Sun, S-S., 1995. Geological framework and crustal evolution of the Giles mafic–ultramafic complex and environs, western Musgrave Block, central Australia. AGSO Journal of Australian Geology and Geophysics, 16, 41–67.
Goleby, B.R., Wright, C., Collins, C.D.N. & Kennet, B.L.N., 1988. Seismic reflection and refraction profiling across the Arunta Block and the Ngalia and Amadeus Basins. Australian Journal of Earth Sciences, 35, 275–294.
Goode, A.D.T., 1970. The petrology and structure of the Kalka and Ewarara layered basic intrusions, Giles Complex, central Australia. Ph.D. Thesis, University of Adelaide (unpublished).
Goode, A.D.T., 1975. A transgressive picrite suite from the western Musgrave Block, central Australia. Journal of the Geological Society of Australia, 22, 187–194.
Goode, A.D.T., 1976. Small-scale primary cumulus igneous layering in the Kalka layered intrusion, Giles Complex, central Australia. Journal of Petrology, 17, 379–397.
Goode, A.D.T., 1977. Intercumulus igneous layering in the Kalka layered intrusion, central Australia. Geological Magazine, 114, 215–218.
Goode, A.D.T., 1978. High temperature, high strain rate deformation in the lower crustal Kalka intrusion, central Australia. Contributions to Mineralogy and Petrology, 66, 137–148.
Goode, A.D.T. & Krieg, G.W., 1967. The geology of the Ewarara intrusion, Giles Complex, central Australia. Journal of the Geological Society of Australia, 14, 185–194.
Goode, A.D.T. & Moore, A.C., 1975. High pressure crystallisation of the Ewarara, Kalka and Gosse Pile intrusions, Giles Complex, central Australia. Contributions to Mineralogy and Petrology, 51, 77–97.
Graham, C.M. & Powell, R., 1984. A garnet–hornblende geothermometer: calibration, testing, and application to the Pelona Schist, Southern California. Journal of Metamorphic Geology, 2, 13–31.
Gray, C.M., 1967. The geology, petrology and geochemistry of the Teizi anorthosite. B.Sc. Honours Thesis, University of Adelaide (unpublished).
Gray, C.M., 1971. Strontium isotopic studies on granulites. Ph.D. Thesis, Australian National University, Canberra (unpublished).
Gray, C.M., 1977. The geochemistry of central Australian granulites in relation to the chemical and isotopic effects of granulite facies metamorphism. Contributions to Mineralogy and Petrology, 65, 79–89.
Gray, C.M., 1978. Geochronology of granulite-facies gneisses in the western Musgrave block, central Australia. Journal of the Geological Society of Australia, 25, 403–414.
Gray, C.M. & Compston, W., 1978. A Rb–Sr chronology of the metamorphism and prehistory of central Australian granulites. Geochimica et Cosmochimica Acta, 42, 1735–1748.
Gray, C.M. & Goode, A.D.T., 1981. Strontium isotopic resolution of magma dynamics in a layered intrusion. Nature, 294, 155–158.
Gray, C.M. & Goode, A.D.T., 1989. The Kalka layered intrusion, central Australia. A strontium isotopic history of contamination and magma dynamics. Contributions to Mineralogy and Petrology, 103, 35–43.
Gray, C.M. & Oversby, V.M., 1972. The behaviour of lead isotopes during granulite facies metamorphism. Geochimica et Cosmochimica Acta, 36, 939–952.
Green, A.A. & Craig, M.D., 1985. Analysis of aircraft spectrometer data with logarithmic residuals. Passadena Jet Propulsion Laboratory Publication 85-41, 111–119.
Green, D.H., 1973. Experimental melting studies on a model upper mantle composition at high pressure under water-saturated and water-undersaturated conditions. Earth and Planetary Science Letters, 19, 37–53.
Green, D.H. & Hibberson, W., 1970. The instability of plagioclase in peridotite at high pressure. Lithos, 3, 209–221.
Green, D.H. & Ringwood, A.E., 1967a. The genesis of basaltic magmas. Contributions to Mineralogy and Petrology, 15, 103–190.
Green, D.H. & Ringwood, A.E., 1967b. An experimental investigation of the gabbro to eclogite transformation and its petrological application. Geochimica et Cosmochimica Acta, 31, 767–833.
Grey, K., 1990. Amadeus Basin. In: Trendall, A. (editor), Geology and mineral resources of Western Australia. Geological Survey of Western Australia Memoir 3, 335–348.
Grove, T.L. & Kinzler, R.J., 1986. Crystallisation kinetics in a multiply saturated basalt magma: an experimental study of Luna 24 ferrobasalt. Proceedings of the Lunar and Planetary Science Conference, 10, 439–478.
Harley, S.L., 1984. An experimental study of the partitioning of Fe and Mg between garnet and orthopyroxene. Contributions to Mineralogy and Petrology, 86, 359–373.
Harley, S.L., 1989. The origins of granulites: a metamorphic perspective. Geological Magazine, 126, 215–247.
Henderson, P., 1982. Inorganic geochemistry. Pergamon Press, Oxford.
Hiern, M.N., 1975. Musgrave Block — sundry mineralization. B. South Australia. In: Knight, C.L. (editor), Economic geology of Australia and Papua New Guinea. 1. Metals. The Australian Institute of Mining and Metallurgy, Monograph 5, 457–459.
Hirschmann, M.M. & Ghiorso, M.S., 1994. Activities of nickel, cobalt, and manganese silicates in magmatic liquids and applications to olivine/liquid and to silicate/metal partitioning. Geochimica et Cosmochimica Acta, 58, 4109–4126.
Hoatson, D.M. & Keays, R.R., 1989. Formation of platiniferous sulfide horizons by crystal fractionation and magma mixing in the Munni Munni layered intrusion, west Pilbara Block, Western Australia. Economic Geology, 84, 1775–1804.

Hoatson, D.M., Wallace, D.A., Sun, S-S., Macias, L.F., Simpson, C.J. & Keays, R.R., 1992. Petrology and platinum-group element geochemistry of Archaean layered mafic–ultramafic intrusions, west Pilbara Block, Western Australia. Australian Geological Survey Organisation, Bulletin 242.

Holland, T.J.B. & Powell, R., 1990. An enlarged and updated internally consistent dataset with uncertainties and correlations: the system K_2O–Na_2O–CaO–MgO–MnO–FeO–Fe_2O_3–Al_2O_3–TiO_2–SiO_2–C–H_2–O_2. Journal of Metamorphic Geology, 8, 89–124.

Honey, F.R. & Daniels, J.L., 1985. Application of Carr Boyd Minerals Limited airborne multispectral scanner to spectral discrimination of hydrothermally altered areas. In: 4th Thematic Conference on Remote Sensing for Exploration Geology, San Francisco, California.

Honey, F.R. & Daniels, J.L., 1986. Rock discrimination and alteration mapping for mineral exploration using the Carr Boyd/Geoscan airborne multispectral scanner. In: 5th Thematic Conference on Remote Sensing for Exploration Geology, Reno, Nevada.

Horwitz, R.C. & Daniels, J.D., 1966. A late Precambrian belt of volcanicity in central Australia. Geological Survey of Western Australia, Annual Report, 1966, 50–53.

Huppert, H.E. & Sparks, S.J., 1988. The generation of granitic magmas by intrusion of basalt into continental crust. Journal of Petrology, 29, 599–624.

Irvine, T.N., 1980. Magmatic infiltration metasomatism, double-diffusive fractional crystallization, and adcumulus growth in the Muskox Intrusion and other layered intrusions. In: Hargraves, R.B. (editor), Physics of magmatic processes. Princeton University Press, Princeton, pp 325–385.

Irvine, T.N., 1982. Terminology for layered intrusions. Journal of Petrology, 23, 127–162.

Irvine, T.N., Keith, D.W. & Todd, S.G., 1983. The J–M platinum-palladium reef of the Stillwater complex, Montana. II. Origin by double diffusive convection magma mixing and implications for the Bushveld complex. Economic Geology, 78, 1287–1334.

Jagoutz, E., 1994. Isotopic systematics of metamorphic rocks. In: Lanphere, M.A., Dalrymple, G.B. & Turrin, B.D. (editors), Abstracts of the Eighth International Conference on Geochronology, Cosmochronology, and Isotope Geology. United States Geological Survey, Circular 1107, 156.

James, R.S. & Hamilton, D.L., 1969. Phase relations in the system $NaAlSi_3O_8$–$KAlSi_3O_8$–$CaAl_2Si_2O_8$–SiO_2 at 1 kilobar water vapour pressure. Contributions to Mineralogy and Petrology, 21, 111–141.

Jaques, A.L. & Green, D.H., 1980. Anhydrous melting of peridotite at 0–15 kbar pressure and the genesis of tholeiitic basalts. Contributions to Mineralogy and Petrology, 73, 287–310.

Javoy, M. & Weis, D., 1987. Oxygen isotopic composition of alkaline anorogenic granites as a clue to their origin: the problem of crustal oxygen. Earth and Planetary Science Letters, 84, 415–422.

Keppler, H., 1993. Influence of fluorine on the enrichment of high field strength trace elements in granitic rocks. Contributions to Mineralogy and Petrology, 114, 479–488.

Kerr, A. & Fryer, B.J., 1993. Nd isotope evidence for crust–mantle interaction in the generation of A-type granitoid suites in Labrador, Canada. Chemical Geology, 104, 39–60.

Kohn, M.J. & Spear, F.S., 1990. Two new geobarometers for garnet amphibolites, with applications to southeastern Vermont. American Mineralogist, 75, 89–96.

Korsch, R.J. & Lindsay, J.F., 1989. Relationship between deformation and basin evolution in the intracratonic Amadeus Basin, central Australia. Tectonophysics, 158, 5–22.

Kushiro, I., 1969. The system forsterite–diopside–silica with and without water at high pressures. American Journal of Science, 267A, 269–294.

Lambeck, K. & Burgess, G., 1992. Deep crustal structures of the Musgrave Block, central Australia: results from teleseismic travel time anomalies. Australian Journal of Earth Sciences, 39, 1–19.

Langmuir, C.H., Bender, J.F., Bence, A.E. & Hanson, G.N., 1977. Petrogenesis of basalts from the FAMOUS area: Mid-Atlantic Ridge. Earth and Planetary Science Letters, 36, 403–414.

Laut, P., 1977. Environments of South Australia: Province 8 — Northern Arid. CSIRO Division of Land Research, Canberra.

Laws, A.T., 1982. Hydrology report No. 2466. Geological Survey of Western Australia (unpublished).

LeMaitre, R.W., 1989. A classification of igneous rocks and glossary of terms. Blackwell Scientific Publications, Oxford.

Leven, J.H. & Lindsay, J.F., 1995. A geophysical investigation of the southern margin of the Musgrave Block, South Australia. AGSO Journal of Australian Geology and Geophysics, 16, 155–161.

Lindsay, J.F. (editor), 1995. Geological atlas of the Officer Basin, South Australia. Australian Geological Survey Organisation and Mines and Energy South Australia, 30 plates.

Lister, G.S. & Baldwin, S.L., 1993. Plutonism and the origin of metamorphic core complexes. Geology, 21, 607–610.

Longhi, J. & Pan, V., 1988. A reconnaissance study of phase boundaries in low alkali basaltic liquid. Journal of Petrology, 29, 115–147.

Ludwig, K.R., 1990. ISOPLOT — a plotting and regression program for radiogenic-isotope data for IBM-PC compatible computers, version 2.11. United States Geological Survey, Open File Report 88-557, Revision of August 7, 1990.

Maas, R. & McCulloch, M.T., 1991. The provenance of Archaean clastic sediments in the Narryer Gneiss Complex, Western Australia: trace element geochemistry, Nd isotopes and U–Pb ages from detrital zircons. Geochimica et Cosmochimica Acta, 55, 1915–1932.

Maboko, M.A.H., Williams, I.S. & Compston, W., 1991. Zircon U–Pb chronometry of the pressure and temperature history of granulites in the Musgrave Ranges, central Australia. Journal of Geology, 99, 675–697.

Maboko, M.A.H., Williams, I.S. & Compston W., 1992. Geochronological evidence for ~530–550 Ma juxtaposition of two Proterozoic metamorphic terranes in the Musgrave Ranges, central Australia. Australian Journal of Earth Sciences, 39, 457–471.

Major, R.B. & Conor, C.H.H., 1993. Musgrave Block. In: Drexel, J.F., Preiss, W.V. & Parker, A.J. (editors), The Geology of South Australia. Geological Survey of South Australia Bulletin 54, 156–167.

Marsh, B.D., 1988. Crystal size distribution in rocks and kinetics and dynamics of crystallisation. Contributions to Mineralogy and Petrology, 99, 277–291.

Mathur, S.P. & Shaw, R.D., 1982. Australian orogenic belts: evidence for evolving plate tectonics. Earth Evolution Sciences, 2, 281–308.

McCulloch, M.T., 1987. Sm–Nd isotopic constraints on the evolution of Precambrian crust in the Australian continent. In: Kröner, A. (editor), Proterozoic lithospheric evolution. American Geophysical Union Geodynamic Series, 17, 115–130

Menzies, M.A. & Wass, S.Y., 1983. CO_2 and LREE-rich mantle below eastern Australia: a REE and isotopic study of alkaline magmas and apatite-rich mantle xenoliths from the Southern Highlands Province, Australia. Earth and Planetary Science Letters, 65, 287–302.

Miller, P.G., 1969. Final report on nickel investigations, northwest province 1953–1967. South Australia Department of Mines, Report Book 68/95.

Milton, B.E. & Parker, A.J., 1973. An interpretation of geophysical observations on the northern margin of the eastern Officer Basin. Quarterly Notes of the South Australia Geological Survey, 46, 10–14.

Moore, A.C., 1969. Corona textures in granulites from the Tomkinson Ranges, central Australia. Geological Society of Australia, Special Publication 2, 361–366.

Moore, A.C., 1971a. Some aspects of the geology of the Gosse Pile ultramafic intrusion, central Australia. Journal of the Geological Society of Australia, 18, 69–80.

Moore, A.C., 1971b. The mineralogy of the Gosse Pile ultramafic intrusion, central Australia. II. Pyroxenes. Contri-

butions to Mineralogy and Petrology, 18, 243–258.
Moore, A.C. & Goode, A.D.T., 1978. Petrography and origin of granulite-facies rocks in the western Musgrave Block, central Australia. Journal of the Geological Society of Australia, 25, 341–358.
Moores, E.M., 1991. Southwest U.S.–east Antarctic (SWEAT) connection: a hypothesis. Geology, 19, 425–428.
Morse, S.A., 1968. Feldspars. Yearbook of the Carnegie Institute, Washington, 67, 120–126.
Morse, S.A., 1986. Convection in aid of adcumulus growth. Journal of Petrology, 27, 1183–1214.
Mutton, A.J., Shaw, R.D. & Wilkes, P., 1983. Analysis of geological, geophysical and physical property data from the southwest Arunta Block, Northern Territory. Bureau of Mineral Resources, Australia, Record 1983/1.
Myers, J.S., 1990. Precambian tectonic evolution of part of Gondwana, southwestern Australia. Geology, 18, 537–540.
Myers, J.S. & Hocking, R.M., 1988. 1:2 500 000 geological map of Western Australia and explanatory notes. Geological Survey of Western Australia.
Naldrett, A.J., Cameron, G., Von Gruenewaldt, G. & Sharpe, M.R., 1987. The formation of stratiform PGE deposits in layered intrusions. In: Parsons, I. (editor), Origins of igneous layering. D. Reidel, Dordrecht, pp 313–397.
Nelson, D.R. & McCulloch, M.T., 1989. Enriched mantle components and mantle recycling of sediments. In Ross, J. (editor). Kimberlites and related rocks. Volume 1: their composition, occurrence, origin and emplacement. Geological Society of Australia, Special Publication 14, 560–570.
Nelson, D.R., Myers, J.S. & Nutman, A.P. 1995. Chronology and evolution of the middle Proterozoic Albany–Fraser Orogen, Western Australia. Australian Journal of Earth Sciences, 42, 481–495.
Nesbitt, R.W. & Kleeman, A.W., 1964. Layered intrusions of the Giles Complex, central Australia. Nature, 203, 391–393.
Nesbitt, R.W & Talbot, J.L., 1966. The layered basic and ultrabasic intrusives of the Giles Complex, central Australia. Contributions to Mineralogy and Petrology, 13, 1–11.
Nesbitt, R.W., Goode, A.D.T., Moore, A.C. & Hopwood, T.P., 1970. The Giles Complex, central Australia: a stratified sequence of mafic and ultramafic intrusions. Geological Society of South Africa, Special Publication 1, 547–564.
Newton, R.C. & Perkins, D., 1982. Thermodynamic calibration of geobarometers based on the assemblages garnet–plagioclase–orthopyroxene (clinopyroxene)–quartz. American Mineralogist, 67, 203–222.
Norrish, K. & Chappell, B.W., 1977. X-ray fluorescence spectrometry. In Zussman, J. (editor), Physical methods in determinative mineralogy. Academic Press, London, pp 201–272.
Norrish, K. & Hutton, J.T., 1969. An accurate X-ray spectrographic method for the analysis of a wide range of geological samples. Geochimica et Cosmochimica Acta, 33, 431–453.
O'Hara, M.J. & Mathews, R.E., 1981. Geochemical evolution in an advancing, periodically replenished, continuously fractionated magma chamber. Journal of the Geological Society of London, 138, 237–277.
Page, R.W., 1988. Geochronology of early to middle Proterozoic fold belts in northern Australia: a review. Precambrian Research, 40/41, 1–19.
Palfreyman, W.D., D'Addario, G.W., Swoboda, R.A., Bultitude, J.M. & Lamberts, I.T., 1976. Geology of Australia, 1:2 500 000 map. Bureau of Mineral Resources, Canberra.
Park, J.K., Buchan, K.L. & Harlan, S.S., 1995. A proposed giant radiating dyke swarm fragmented by the separation of Laurentia and Australia based on paleomagnetism of ca. 780 Ma mafic intrusions in western North America. Earth and Planetary Science Letters, 132, 129–139.
Pearce, J.A., Harris, N.B.W. & Tindle, A.G., 1984. Trace element discrimination diagrams for the tectonic interpretation of granitic rocks. Journal of Petrology, 25, 956–983.
Perkins, D. & Chipera, S.J., 1985. Garnet–orthopyroxene–plagioclase–quartz barometry: refinement and application to the English River subprovince and the Minnesota River Valley. Contributions to Mineralogy and Petrology, 89, 69–80.
Pharaoh, T.C., 1990. Aspects of structural geology of the Giles layered mafic/ultramafic complex, Tomkinson Ranges, Musgrave Block, central Australia. Bureau of Mineral Resources, Australia, Record 1990/6.
Philpotts, A.R., 1990. Principles of igneous and metamorphic petrology. Prentice Hall, New Jersey.
Pidgeon, R.T., 1990. Timing of plutonism in the Proterozoic Albany Mobile Belt, southwestern Australia. Precambrian Research, 47, 157–167.
Plumb, K.A., 1985. Sub-division and correlation of late Precambrian sequences in Australia. Precambrian Research, 29, 303–329.
Powell, R. & Holland, T.J.B., 1988. An internally consistent dataset with uncertainties and correlations. 3. Applications to geobarometry, worked examples and a computer program. Journal of Metamorphic Geology, 6, 173–204.
Presnall, D.C., Dixon, S.A., Dixon, J.R., O'Donnell, T.H., Brenner, N.L., Schrock, R.L. & Dykus, D.W., 1978. Liquidus phase relations on the join diopside–forsterite–anorthite from 1 atm to 20 kbar: their bearing on the generation and crystallization of basaltic magma. Contributions to Mineralogy and Petrology, 66, 203–220.
Presnall, D.C., Dixon, J.R., O'Donnell, T.H. & Dixon, S.A., 1979. Generation of mid-ocean ridge tholeiites. Journal of Petrology, 20, 3–36.
Ramsay, J.G., 1967. Folding and fracturing of rocks. McGraw Hill, New York.
Ringwood, A.E., 1975. Composition and petrology of the Earth's mantle. McGraw-Hill, New York.
Roeder, P.L. & Emslie, R.F., 1970. Olivine–liquid equilibrium. Contributions to Mineralogy and Petrology, 29, 275–289.
Rogers, J.J.W. & Greenberg, J.K., 1990. Late-orogenic, post-orogenic, and anorogenic granites: distinction by major-element and trace-element chemistry and possible origins. Journal of Geology, 98, 291–309.
Rogers, N.W., Hawkesworth, C.J., Mattey, D.P., & Harmon, R.S., 1987. Sediment subduction and the source of potassium in orogenic leucitites. Geology, 15, 451–453.
Sandiford, M., Martin, N., Zhou, S. & Fraser, G., 1991. Mechanical consequences of granite emplacement during high-T, low-P metamorphism and the origin of 'anticlockwise' PT paths. Earth and Planetary Science Letters, 107, 164–172.
Saunders, A.D., Tarney, J. & Weaver, S.D., 1980. Transverse geochemical variations across the Antarctic Peninsula: implications for the generation of calc-alkaline magmas. Earth and Planetary Science Letters, 46, 344–360.
Shaw, R.D., 1991. The tectonic development of the Amadeus Basin, central Australia. In Korsch, R.J. & Kennard, J.M. (editors), Geological and geophysical studies in the Amadeus Basin, central Australia. Bureau of Mineral Resources, Australia, Bulletin 236, 429–461.
Shaw, R.D. & Black, L.P., 1991. The history and tectonic implications of the Redbank thrust zone, central Australia, based on structural, metamorphic and Rb–Sr isotopic evidence. Australian Journal of Earth Sciences, 38, 307–332.
Shaw, R.D., Etheridge, M.A. & Lambeck, K., 1991. Development of the Late Proterozoic to Mid-Palaeozoic, intracratonic Amadeus Basin in central Australia: a key to understanding tectonic forces in plate interiors. Tectonics, 10, 688–721.
Shaw, R.D., Gunn, P., Wellman, P. & Whitaker, A., 1995. Australian crustal elements based on the distribution of geophysical domains, 1:5 000 000 map. Australian Geological Survey Organisation, Canberra.
Sheraton, J.W., 1984. Chemical changes associated with high-grade metamorphism of mafic rocks in the East Antarctic Shield. Chemical Geology, 47, 135–157.
Sheraton, J.W. & Black, L.P., 1983. Geochemistry of Precambrian gneisses: relevance for the evolution of the East Antarctic Shield. Lithos, 16, 273–296.
Sheraton, J.W. & Black, L.P., 1988. Chemical evolution of granitic rocks in the East Antarctic Shield, with particular reference to post-orogenic granites. Lithos, 21, 37–52.
Sheraton, J.W. & Sun, S-S., 1995. Geochemistry and origin of felsic igneous rocks of the western Musgrave Block.

AGSO Journal of Australian Geology and Geophysics, 16, 107–125.

Sheraton, J.W. & Sun, S-S., in press. Mafic dyke swarms of the western Musgrave Block, central Australia: their geochemistry, origin, and relationships to the Giles Complex. AGSO Journal of Australian Geology and Geophysics.

Sheraton, J.W., Black, L.P., McCulloch, M.T. & Oliver, R.L., 1990. Age and origin of a compositionally varied mafic dyke swarm in the Bunger Hills, East Antarctica. Chemical Geology, 85, 215–246.

Sheraton, J.W., Black, L.P. & Tindle, A.G., 1992. Petrogenesis of plutonic rocks in a Proterozoic granulite-facies terrane — the Bunger Hills, East Antarctica. Chemical Geology, 97, 163–198.

Sheraton, J.W., Tingey, R.J., Black, L.P. & Oliver, R.L., 1993. Geology of the Bunger Hills area, Antarctica: implications for Gondwana correlations. Antarctic Science, 5, 85–102.

Skjerlie, K.P. & Johnston, A.D., 1993. Fluid-absent melting behavior of an F-rich tonalitic gneiss at mid-crustal pressures: implications for the generation of anorogenic granites. Journal of Petrology, 34, 785–815.

Sprigg, R.C. & Rochow, K., 1975. Nickeliferous ochres in the Hinckley (W.A.) and Tomkinson (S.A.) Ranges ("Daisy Bates" – Wingellina field). In: Knight, C.L. (editor), Economic geology of Australia and Papua New Guinea. 1. Metals. The Australian Institute of Mining and Metallurgy, Monograph 5, pp 1008–1009.

Sprigg, R.C. & Wilson, R.B., 1959. The Musgrave mountain belt in South Australia. Geological Rundschau, 47, 531–542.

Stern, R.A. & Hanson, G.N., 1991. Archean high-Mg granodiorite: a derivative of light rare earth element-enriched monzodiorite of mantle origin. Journal of Petrology, 32, 201–238.

Stewart, A.J., 1993. Extension of the Woodroffe Thrust, Musgrave Block, into Western Australia. AGSO Research Newsletter, 18, 5–6.

Stewart, A.J., 1995a. Resolution of conflicting structures and deformation history of the Mount Aloysius granulite massif, western Musgrave Block, central Australia. AGSO Journal of Australian Geology and Geophysics, 16, 91–105.

Stewart, A.J., 1995b. Western extension of the Woodroffe Thrust, Musgrave Block, central Australia. AGSO Journal of Australian Geology and Geophysics, 16, 147–153.

Stewart, A.J. & Glikson, A.Y., 1991. The felsic metamorphic/igneous core complexes hosting the Giles Complex. BMR Research Newsletter, 14, 6–16.

Streckeisen, A., 1976. To each plutonic rock its proper name. Earth-Science Reviews, 12, 1–33.

Sun, S-S. & McDonough, W.F., 1989. Chemical and isotopic systematics of oceanic basalts: implications for mantle composition and processes. In: Saunders, A.D. & Norry, M.J. (editors), Magmatism in ocean basins. Geological Society of London, Special Publication 42, 313–345.

Sun, S-S. & Sheraton, J.W., 1992. Zircon U/Pb chronology, tectono-thermal and crust-forming events in the Tomkinson Ranges, Musgrave Block, central Australia. ASGO Research Newsletter, 17, 9–11.

Sun, S-S., Wallace, D.A., Hoatson, D.M., Glikson, A.Y. & Keays, R.R., 1991. Use of geochemistry as a guide to platinum group element potential of mafic–ultramafic rocks: examples from the west Pilbara Block and Halls Creek Mobile Zone, Western Australia. Precambrian Research, 50, 1–35.

Sun, S-S., Warren, R.G. & Shaw, R.D., 1995. Nd isotope study of granites from the Arunta Inlier, central Australia: constraints on geological models and limitation of the method. Precambrian Research, 71, 301–314.

Sun, S-S., Sheraton, J.W., Glikson, A.Y. & Stewart, A.J., 1996a. A major magmatic event during 1050–1080 in central Australia and an emplacement age for the Giles Complex. Geological Society of Australia, Abstracts, 41, 423.

Sun, S-S., Sheraton, J.W., Glikson, A.Y. & Stewart, A.J., 1996b. A major magmatic event during 1050–1080 in central Australia and an emplacement age for the Giles Complex. AGSO Research Newsletter, 24, 13–15.

Sweet, I.P. & Crick, I.H., 1992. Uluru and Kata Tjuta: a geological history. Australian Geological Survey Organisation, Canberra.

Tarlowski, C. & Simonis, F., 1992. 1:5 000 000 total magnetic intensity map of Australia. Australian Geological Survey Organisation, Canberra.

Tarney, J. & Windley, B.F., 1977. Chemistry, thermal gradients and evolution of the lower continental crust. Journal of the Geological Society of London, 134, 153–172.

Tarney, J., Skinner, A.C. & Sheraton, J.W., 1972. A geochemical comparison of major Archaean gneiss units from northern Scotland and east Greenland. 24th International Geological Congress, Section 1, 162–174.

Tarney, J., Wyborn, L.A.I., Sheraton, J.W. & Wyborn, D., 1987. Trace element differences between Archaean, Proterozoic and Phanerozoic crustal components — implications for crustal growth processes. In: Ashwal, L.D. (editor), Workshop on the growth of continental crust. Lunar and Planetary Institute, Technical Report 88.02, 139–140.

Taylor, S.R. & McLennan, S.M., 1985. The continental crust: its composition and evolution. Blackwell, Oxford.

Taylor, W.R., Esslemont, G. & Sun, S-S., 1995. Geology of the volcanic-hosted Brockman rare-metals deposit, Halls Creek Mobile Zone, northwest Australia. II. Geochemistry and petrogenesis of the Brockman volcanics. Mineralogy and Petrology, 52, 231–255.

Thomson, B.P., 1963. Nickel mineralization in the Giles Complex in the Tomkinson Ranges, South Australia. South Australia Geological Survey, Quarterly Notes, 8, 2–3.

Thomson, B.P., 1965a. Geological atlas of South Australia, Davies sheet, 1:63 360 series. South Australia Department of Mines and Energy.

Thomson, B.P., 1965b. Weathering and related mineralization, Mt Davies area. South Australia Geological Survey, Quarterly Notes, 16, 6–8.

Thomson, B.P., 1975. Musgrave Block — regional geology. In: Knight, C.L. (editor), Economic geology of Australia and Papua New Guinea. 1. Metals. The Australian Institute of Mining and Metallurgy, Monograph 5, pp 451–454.

Thomson, B.P., 1980. 1:1 000 000 geological map of South Australia. South Australia Department of Mines and Energy.

Thomson, B.P., Miriams, R.C. & Johnson, J., 1962. Mann, South Australia, 1:250 000 geological sheet and explanatory notes. South Australia Department of Mines and Energy.

Tingey, R.J., 1991. The regional geology of Archaean and Proterozoic rocks in Antarctica. In: Tingey, R.J. (editor), The geology of Antarctica. Clarendon Press, Oxford, 1–73.

Tonkin, D.J., 1991. The geology and mineral potential of the Pitjantjatjarra lands, South Australia. South Australia Department of Mines and Energy, Report Book 91/103.

Turner, A.R., 1968. The distribution and association of nickel in the ferruginous zones of the laterites of the Giles Complex. AMDEL Bulletin, 5, 76–93.

Turner, S.P., Foden, J.D. & Morrison, R.S., 1992. Derivation of some A-type magmas by fractionation of basaltic magma: an example from the Padthaway Ridge, South Australia. Lithos, 28, 151–179.

Tuttle, O.F. & Bowen, N.L., 1958. Origin of granite in the light of experimental studies in the system $NaAlSi_3O_8$–$KAlSi_3O_8$–SiO_2–H_2O. Geological Society of America Memoir 74.

Veevers, J.J. & Eittreim, S.L., 1988. Reconstruction of Antarctica and Australia at breakup (95±5 Ma) and before rifting (160 Ma). Australian Journal of Earth Sciences, 35, 355–362.

Wallace, P. & Carmichael, I.S.E., 1992. Sulfur in basaltic magmas. Geochimica et Cosmochimica Acta, 56, 1863–1874.

Watson, E.B., 1979. Apatite saturation in basic to intermediate magmas. Geophysical Research Letters, 6, 937–940.

Watson, E.B. & Harrison, T.M., 1983. Zircon saturation revisited: temperature and composition effects in a variety of crustal magma types. Earth and Planetary Science Letters, 64, 295–304.

Webb, A.W., 1985. Geochronology of the Musgrave Block. Mineral Resources Review, South Australia Department of Mines and Energy, 23–37.

Wellman, P., 1976. Gravity trends and the growth of Australia:

a tentative correlation. Journal of the Geological Society of Australia, 23, 11–14.

Whalen, J.B., Currie, K.L. & Chappell, B.W., 1987. A-type granites: geochemical characteristics, discrimination and petrogenesis. Contributions to Mineralogy and Petrology, 95, 407–419.

Willemse, J., 1969. The geology of the Bushveld Igneous Complex, the largest repository of magmatic ore deposits in the world. In: Wilson, H.D.B. (editor), Magmatic ore deposits: a symposium. Economic Geology Monograph 4, 187–208.

Williams, I.S. & Claesson, S., 1987. Isotopic evidence for the Precambrian provenance and Caledonian metamorphism of high grade paragneisses from the Seve Nappes, Scandinavian Caledonides, II. Ion microprobe zircon U–Th–Pb. Contributions to Mineralogy and Petrology, 97, 205–217.

Williams, I.S., Compston, W., Collerson, K.D., Arriens, P.A. & Lovering, J.F., 1983. A reassessment of the age of the Windmill Metamorphics, Casey area. In: Oliver, R.L., James, P.R. & Jago, J.B. (editors), Antarctic earth science. Australian Academy of Sciences, Canberra, 73–76.

Wilson, A.F., Compston, W., Jeffery, P.M. & Riley, G.H. 1960. Radiometric ages from the Precambrian rocks in Australia. Journal of the Geological Society of Australia, 6, 179–195.

Wright, T.L. & Doherty, P.C., 1970. A linear programming and least squares computer method for solving petrologic mixing programs. Geological Society of America Bulletin, 81, 1995–2008.

Wyborn, D. & Sun, S-S., 1994. Sulphur-undersaturated magmatism — a key factor for generating magma-related copper–gold deposits. AGSO Research Newsletter, 21, 7–8.

Zhao, J-X, 1992. Proterozoic crust–mantle evolution in central Australia: geochemical and isotopic constraints. PhD Thesis, Australian National University, Canberra (unpublished).

Zhao, J-X. & McCulloch, M.T., 1993a. Sm–Nd isochron ages of Late Proterozoic dyke swarms in Australia: evidence for two distinctive events of mafic magmatism and crustal extension. Chemical Geology (Isotope Geoscience Section), 109, 341–354.

Zhao, J-X. & McCulloch, M.T., 1993b. Melting of a subduction-modified continental lithospheric mantle: evidence from Late Proterozoic mafic dike swarms in central Australia. Geology, 21, 463–466.

Zhao, J-X. & McCulloch, M.T., 1995. Geochemical and Nd isotope systematics of granites from the Arunta Inlier, central Australia: implications for Proterozoic crustal evolutiuon. Precambrian Research, 71, 265–299.

Zhao, J-X., McCulloch, M.T. & Korsch, R.J., 1994. Characterisation of a plume-related ~800 Ma magmatic event and its implications for basin formation in central–southern Australia. Earth and Planetary Science Letters, 121, 349–367.

Zhao, J-X., Shiraishi. K., Ellis, D.J. & Sheraton, J.W., 1995. Geochemical and isotopic studies of syenites from the Yamato Mountains, East Antarctica: implications for the origin of syenitic magmas. Geochimica et Cosmochimica Acta, 59, 1363–1382.

Appendix I: Image processing methodology and remotely sensed correlations

Logarithmic residual images

Significant enhancement of Landsat data can be obtained by the application of the logarithmic residuals method. This approach represents both within-pixel spectral relations and the relations between individual pixels and the entire scene. Images produced by this method are less affected by topographic shade, as this can be separated as a distinct component, although shade still affects ratios, especially in the visible range. Consequently, the method is relatively independent of overall atmospheric and gain corrections that apply uniformly to all the pixels of any particular scene.

Logarithmic residual (LR) images help to identify the significance of any single within-pixel band digital number (DN) value relative to the within-pixel bands mean and relative to the entire image pixels mean (Green & Craig 1985). Each LR DN in band i represents the radiance value of a particular band of a single pixel (R_{bp}) divided by the within-band mean value (R_{bmp}), and further divided by the mean of the entire image (R_{mmi}):

$$\text{LR DN(i) value} = R_{bp(i)} / R_{bmp} / R_{mmi}$$

This normalisation procedure cancels out multiplicative effects, such as atmospheric absorption, solar illumination, and sensor gains, all of which effect all the pixels of a scene scanned at a particular time. The log residual program separates a shadow component, which can subsequently be recombined with LR bands or with dark pixel-corrected radiance bands in any particular image in order to enhance topography and structure. Inverted log residual (ILR) DN values assign high DN values to, and therefore highlight, distinct spectral absorption features.

Lithological correlations of Landsat-5 TM images

Visible Range (VIS, bands 1–3). For green vegetation, reflectance in band 2 forms a small peak relative to bands 1 and 3. In contrast, clay minerals reflect strongly, whereas iron oxide absorbs in the VIS, allowing a useful distinction between materials with different proportions of clay and iron oxide. Silica and free quartz reflect more strongly in all spectral bands than other materials, and can be identified by the combination (addition) of bands (e.g., bands 1+3+5+7 or 1+7). Combined quartz and clay-bearing weathering products of felsic rocks have stronger reflectance in the VIS, compared to iron oxide and clay-bearing weathered mafic bedrock surfaces. Iron oxide-rich materials, including laterite, weathering crusts of ferrogabbro, and iron-rich pyroxenite and their derived detritus, show low reflectance in the visible range, owing to absorption by iron oxide.

Near Infrared Range (NIR, band 4). The NIR band 4 is characterised by strong reflectance of green and dry vegetation, carbonate, and clay minerals, whereas the iron oxide reflectance is somewhat subdued. Although calibrated reflectances of end members (clay, hematite, carbonate, goethite) are closely grouped in band 4, Landsat-5 TM data are capable of distinguishing between high-reflectance felsic granulite, lower reflectance mafic rocks, and lowest reflectance pyroxenite and their derived detritus. The differences between the weathering crusts of mafic rocks and orthopyroxene-rich ultramafic rocks represent the different proportions of clay and iron oxide in these materials. The reflectance of dry vegetation exceeds that of green vegetation, allowing their discrimination.

Short Wave Infrared Range (SWIR, bands 5 and 7). Landsat-5 TM SWIR bands display high reflectance of iron oxide, allowing the effective discrimination of ferruginous materials (laterite and weathering surfaces of ferrogabbro and some pyroxenite) from clay-rich weathering crusts of mafic components of the layered intrusions (gabbro, gabbronorite, norite, anorthosite). Although quartz in felsic rocks is partly coated by clay and iron oxide films, it results in a higher reflectance of these rocks in the SWIR relative to mafic rocks, owing to the absorption effect of clay-rich weathering crusts of the latter. For band 5, the high reflectance of silica and, to a lesser extent, carbonate results in a higher albedo for silcrete and calcrete relative to laterite.

The combination of single bands is particularly useful for discriminating a range of topographic and lithological features. An example is offered by red–green–blue (RGB) 7:4:1 images, which emphasise the role of iron oxide in band 7 (R), the role of vegetation in band 4 (G) and the role of clay and/or carbonate in band 1 (B). Consequently, 7:4:1 and 5:4:1 RGB images show gabbroic rocks in blue–black (kaolinite ± carbonate-bearing weathering crusts), anorthosite in bright cyan (clay and carbonate-rich weathering of plagioclase in bands 1 and 4), felsic granulite and granite in purple (clay, showing in blue in band 1, combined with a contribution from iron oxide detritus derived from mafic dykes, showing in red in band 7), calcrete in light blue (band 1), iron oxide-rich pediments and laterite in red (band 7), vegetated areas in green, and alluvial plains in yellow (representing the combined effects of silica, iron oxide (R) and vegetation (G)). The composition of alluvial–pediment collars around or along unidentified bedrock outcrops can be usefully applied to the regional mapping of remote or inaccessible inselbergs. These outcrops may be too small for the identification of their bedrock spectra and the spectral characteristics of their surrounding alluvial material provides a clue to the source composition. As a rule, mafic outcrops are mostly surrounded by iron oxide-rich detritus (red collars on 7:4:1 RGB images), whereas felsic outcrops are associated with quartz and clay-rich detritus (light cyan collars on 7:4:1 RGB images).

Spectral data for dark pixel-corrected images indicate that, in general, orthopyroxene-rich rocks, clinopyroxene-rich rocks, gabbroic rocks, and anorthosite display an increasing reflectance in the visible and short-wave infrared bands, in that order, owing to an increasing abundance of carbonate–clay weathering crusts with higher abundances of clinopyroxene and plagioclase. Characterisation of generally altered peridotitic rocks is complicated, as weathering surfaces may be dominated by carbonate (magnesite), hydrated magnesium silicates, and iron oxide. Orthopyroxene-rich (calcium-poor) rocks may have low reflectance DN values in the visible range, a result of absorption by iron oxide coatings which characterise their weathering surfaces. In contrast, clinopyroxene-bearing websterite shows higher reflectance, owing to higher Ca and Al-rich weathering products. For these reasons, mafic igneous rocks, including gabbro, gabbronorite, norite, anorthosite, and ferrogabbro, are characterised by generally higher reflectance than pyroxenite. Anorthosite shows a high reflectance in the lower visible band, owing to high clay and carbonate contents of their weathering surfaces, resulting in bright cyan on 7:4:1 RGB images, compared to the darker blue of gabbro. Felsic

granulite and granitoids, which show higher reflectance than mafic materials in the infrared range, are not readily distinguished from the latter in the visible range.

LR and ILR images offer lithological discriminations that are better pronounced than those shown by single band or band ratio images. For each pixel, the log residual program calculates the band mean (average brightness or albedo), which is included in the output as an additional spectral band, allowing the creation of an image representing the topographic and structural characteristics of the area. This image can be usefully combined with other LR and ILR images, as well as images of any other type. Clay and/or carbonate are represented by either high LR DN values in band 1 or high ILR DN values in band 7. Green vegetation is represented by high LR band 4 (LR–4) DN values or by inversion of the band 3 absorption feature, namely high ILR–3 DN values. Iron oxide is represented by either high LR–7 DN values or by high ILR–1 DN values. Because laterite and gullies that cut mafic rocks are commonly covered by relatively dense green vegetation, some of their spectral features are similar.

Orthopyroxene-dominated rocks and ferrogabbro display high LR–7 DN values and low LR–4 and LR–3 DN values, compared to norite and gabbro, reflecting the high iron oxide and low clay components of weathering crusts of these feldspar-poor ultramafic rocks. These variations are clearly shown on log residual 7:4:1 RGB images by high LR–5 and LR–7 of pyroxenite and ferrogabbro. The signatures of clay (±carbonate)-rich weathering crusts of anorthosite and leucogabbro are broadly similar to those of gabbro, showing high LR–3 and LR–4 DN values and higher ILR–7 DN values, including clay-rich arenaceous girdles around outcrops of felsic granulite and calcrete along creeks. Higher abundances of calcic plagioclase and its clay weathering products over anorthosite result in a stronger reflectance in LR–4 and a resulting cyan colour on LR–7:4:1 RGB images. A similar effect is imparted by deep weathering profiles on gabbro, representing the combined effects of clay and vegetation. Anorthosite interlayered with felsic granulite is distinguished from the latter by its higher LR–4 and lower LR–7 and ILR–1 DN values. Mafic granulite of the western Hinckley Range shows significantly higher LR–5 and LR–7 DN values than gabbro and lower LR–7 DN values relative to the iron-rich weathering crusts of pyroxenite and ferrogabbro. This distinction stands out, for example, on LR–7:4:1 RGB images (mafic granulite in red, gabbro in cyan), allowing the discrimination of little-recrystallised relict bodies of gabbro from mafic granulite in the western Hinckley Range (Glikson 1994). The spectral differences between gabbro and mafic granulite, which have near-identical mineralogy and chemistry, are attributable to the more silica-rich weathering crusts on granulite outcrops which are related to penetrative intrusion by granitic veins. This is contrasted with the clay–carbonate-rich weathering crusts on little-recrystallised coarser-grained gabbro. Another factor contributing to the different spectral characteristics of gabbro and mafic granulite is the finer-grained texture of the latter.

Log residual images allow effective discrimination between gabbroic rocks and felsic igneous and metamorphic rocks on the basis of differences in LR–5, which displays higher DN values for felsic rocks, owing to greater abundances of iron oxide in their weathering crusts. Consequently, images such as LR–7:5:4 RGB commonly display iron-rich pyroxenite in red (LR–7), felsic materials in shades of green (LR–5), and gabbro in dark blue (LR–4). Emplacement of mafic dykes into felsic rocks enhances the iron oxide signature of the latter due to scattered mafic detritus. Weathered felsic rocks at topographically high positions below uplifted early erosion surfaces (peneplains) display higher DN values in LR–3 and LR–4, owing to clay and associated green vegetation, represented on LR–7:4:1 RGB images by green (LR–4), e.g., at Mount Aloysius, Mount West, and the Ewarara area. Felsic and mafic granulites have similar DN values in LR–7 and LR–5, and appear in similar colours on LR–7:5:4 and LR–7:4:1 RGB images. Mafic granulite has somewhat lower DN values than felsic granulite on LR–3 and LR–4 images.

The spectral response of laterite is similar to that of ferrogabbro in LR–7, LR–5, and LR–4, representing the high abundance of iron oxide in these materials. On LR–7:5:4 RGB images, the high DN values in LR–5 results in a characteristic deep apple-green colour for laterite. Calcrete deposits associated with creeks are distinguished by high DN values in LR–3 and LR–1, similar to anorthosite and gabbro, where clay (±carbonate) coatings may be important. On LR–7:4:1 RGB images, calcrete shows in cyan, but is difficult to discriminate from silcrete, a feature related to local mixtures of these components.

Alluvial deposits derived from specific bedrock types are closely related to their source composition. Thus, oxidised colluvium and alluvium derived from mafic rocks display higher DN values in LR–7 (iron oxide-dominated) than debris derived from felsic rocks. Alluvial deposits derived from the felsic rocks have generally higher DN values in LR–5 and LR–4, the latter representing green vegetation supported by the arenaceous material shed from felsic sources. Such alluvial collars fringe outcrops of felsic granulite, as displayed on LR–7:4:1 RGB images in cyan (vegetation on clay-rich soil; Glikson 1994). Alluvial deposits derived from mixed sources display intermediate effects. Dunes show little difference from mixed-source alluvial deposits, and display generally high reflectance related to the effect of abraded free quartz. Some silt–clay deposits display lower DN value in LR–5 and high DN values in LR–3 and LR–1, representing lower iron oxide and higher clay components relative to coarser-grained alluvial deposits.

Fireburn effects in alluvial and dune areas are manifested by higher LR–4 DN values, representing young green vegetation, relative to old growth dominated by high LR–7 DN values that represent dry vegetation. On LR–7:4:1 RGB images, fireburns are displayed in mixtures of bands LR–4 and LR–7 (yellow), whereas old growth areas are displayed by high LR–7 DN values (red). Fireburnt gabbro outcrops reflect more strongly in LR–4 and LR–3 and less in LR–7, as compared to old growth areas dominated by high LR–7 and LR–1 DN values. Consequently, on LR–7:4:1 RGB images, mafic fireburn areas show in cyan and old growth in purple.

Log residual images are significantly enhanced by the application of AMSS Geoscan Mark-1 images. For example, an LR–9:4:1 RGB image of the Wingellina Hills area allows discrimination between weathered gabbro and laterite. The weathered gabbro shows high reflectance by clay in band LR–1 and high absorption DN values in ILR–9 and ILR–4, and is consequently displayed in red and green (yellow). In contrast, the bush-covered laterite reflects strongly in LR–4 and, to a lesser extent, LR–9, showing high absorption in bands ILR–1 and, to a lesser extent, ILR–9, resulting in a purple colour (Glikson 1994).

Landsat-5 TM band ratio images

Given the limited number of bands and the broad wavelength spectrum covered by Landsat-5 TM bands, the identification of surface types is complicated by spectral superposition. Landsat-5 TM spectra allow identification of iron oxide (hematite, high 3/1, 5/4, and 5/3), clay + dry vegetation (high 5/7), green vegetation (high 4/3), and quartz–silica (bands 1+3+5+7). Since the 3/1 band ratio is also representative of green vegetation spectra, iron oxide is better discriminated by the 5/4 and 7/4 band ratios. Thus, the 5/4:4/3:5/7 RGB image is

useful for distinction of iron oxide, green vegetation, and clay, in that order. In this image, a partial green vegetation cover over clay–carbonate bedrock displays in cyan, whereas fireburn areas show in a dark brownish colour. However, spectral overlaps occur, for example, between (1) clay and carbonate, (2) the 5/7 ratio of clay and dry vegetation, and (3) goethite and hematite. The effects of histogram stretching, maximising the range of DN values for each of the ratios on RGB images, complicates comparisons between band ratios. Examination of Landsat-5 TM spectral patterns for training areas in the Tomkinson Ranges indicates systematic differences between some of the principal ratios, which are summarised below.

Laterite, characterised by high reflectance in band 7 owing to its iron oxide-rich nature, displays high 5/4 ratio DN values (~2.7) and high 5/1 ratio DN values (~4.6–5.1), but does not display high 3/1 ratios relative to other less-ferruginous materials. Clay pans and dry lakes (Champ de Mars, Lake Wilson) do not display the high 5/7 band ratio DN values expected for clay, suggesting they may consist principally of silt. The bed of Lake Wilson is characterised by a high 5/4 band ratio (~2.6), signifying iron oxide-rich detritus. Weathered clay-rich felsic granulite and anorthosite have relatively high 5/7 band ratio DN values (~1.4) due to clay (±carbonate) enrichment, as does calcrete. The high 5/7 ratios of silcrete suggest silica–carbonate mixtures. The masking effects of dry and green vegetation are partly overcome by calculating the band ratios of devegetated images, using a pixel-unmixing program that subtracts the green vegetation end member from the bands (Bierwirth 1990; Glikson 1994). The results of this analysis indicate consistent lowering of the 5/7 and 5/4 band ratios and increases in the 3/1 and 5/1 band ratios in green vegetation-free images, compared to mixed mineral–vegetation images. In the following, the characteristics of individual band ratio images are described.

5/4 band ratio images. This band ratio is extremely useful for the discrimination of hematite and goethite, since the other common components — clay, carbonate, silica, and green and dry vegetation — have significantly lower ratios. High 5/4 DN values are typical of laterite, iron-rich pyroxenite, and oxidised mafic-derived pediment and colluvium deposits. In contrast, the 3/1 band ratio of hematite and goethite is partly overlapped by the spectral patterns of dry vegetation, yielding a poorly defined image, which shows only a weak expression of iron oxide-rich units, including dry vegetation patterns corresponding to fireburns. Felsic rocks are characterised by higher 5/4 ratios than gabbroic rocks, confirming the higher iron oxide contents of their weathering crusts and presence of material from mafic dykes. In mafic terranes, fireburn areas show lower 5/4 ratios than old vegetated areas.

5/7 band ratio images. This band ratio is diagnostic of clay minerals, but it is overlapped by the 5/7 band ratio of dry vegetation. Felsic rocks show higher DN values than mafic rocks. Surface types displaying very high 5/7 band ratio DN values in the Kalka–Mount Davies area include (1) clay-rich alluvial girdles around isolated outcrops of felsic granulite, (2) carbonate-rich weathering zones overlying peridotitic rocks at the centre of the Mount Davies range, (3) calcrete along creeks, and (4) very low 5/7 band ratios typical of vegetated shaded southern slopes, e.g., Mount Davies, Kalka, the Hinckley Fault scarp, and ridges southeast of Ewarara. Patchy zones of high 5/7 band ratio DN values also occur over gabbroic bedrock surfaces, representing combinations of clay-rich areas and dry vegetation.

4/3 band ratio images. DN values of this ratio representing green vegetation are markedly higher than for areas covered by dry vegetation and/or iron oxide. High 4/3 band ratio DN values occur along gullies, creeks, strike depressions over pyroxenite near Mount Davies, parts of the southern shaded and better-vegetated slopes of Mount Davies, and the eastern extension of the Ewarara ridge. High 4/3 band ratio DN value zones may coincide with regrowth of green vegetation in recent fireburn areas.

Principal component analysis

Principal component analysis of single bands

The generally high correlation between bands of common materials in natural terrains requires a method of discriminating spectral patterns which departs from the general norm. Principal component (PC) analysis measures the correlation between band reflectance DN values in each pixel and the mean spectral pattern of the total pixel array. The method quantifies the proximity of each reflectance value to best-fit variance axes in N-dimensional space, the number of axes equalling the number of spectral channels. The highest principal component (PC1) represents best-correlated band DN values, whereas lower PCs represent increasingly less-correlated spectra of potential interest. Each PC is influenced by all six Landsat-5 TM bands. Particular PCs are influenced by particular surface types, although such correlations may vary within and between images.

Eigen vectors weighting the effect of each of the 6 spectral bands in each of the 6 PCs (based on bands 1,2,3,4,5, and 7, excluding the thermal band 6) are tabulated in Glikson (1994). In general, the PC analysis of Landsat-5 TM data in the Tomkinson Ranges suggests correlations of low-order least-well correlated PCs with vegetation types and fireburn patterns. Thus, whereas RGB images of PCs 1, 2, and 3 outline geological and structural elements, RGB images of PCs 3, 4, and 5 display the distribution of vegetation and fireburn areas. PCs 3 and 4 contain information on the distribution of free quartz in alluvial and dune deposits, in contrast to weathering product-coated quartz in bedrock and silcrete.

Single principal component images display the following features:

- PC–1 is dominated by bands 2, 3, and 7, i.e., clay, carbonate, and iron oxide. Both mafic and felsic rock types display high DN values. Gabbro and pyroxenite display high to very high DN values, as do felsic granulite and granite. However, whereas mafic source-derived alluvium reflects with intermediate DN values, felsic source-derived alluvium and dune crests have very low DN values. This difference is interpreted in terms of (1) high correlations of bands representing clay–carbonate–iron oxide-dominated weathering crusts in a compositionally wide range of bedrock types, and (2) low correlations of bands representing free quartz-dominated felsic source-derived alluvium and dunes. The relatively low quartz expression in the felsic rocks themselves is attributed to their coating by weathering products such as clay and iron oxide. Calcrete and silcrete show very low correlations of bands in PC–1. Fireburns are displayed by the somewhat higher DN values of old growth, and shade is represented by lower DN values.
- PC–2 shows a strong negative correlation with band 7 (iron oxide), allowing discrimination between iron oxide-rich materials (pyroxenite, ferrogabbro, and laterite) of intermediate to high DN and anorthositic to gabbroic rocks of low DN. Felsic granulite and granite display intermediate to high DN values. Fireburn areas on gabbro show lower DN values compared to old growth. Calcrete and silcrete may show low DN values and felsic-derived alluvium and

dunes show in black, representing the low correlation of bands representing free quartz. Green vegetation, and therefore creeks, show as low-DN dark zones.

- PC–3 is influenced by bands 2 and 5 (clay, iron oxide), and appears to be dominated by free quartz, as suggested by very high DN values of felsic-derived alluvial materials and of dunes. The role of quartz is confirmed by the high negative Eigen vector value of the thermal band (6) in the original Landsat-5 TM image (Glikson 1994). Interpretations of band 6 are complicated by its sensitivity to atmospheric conditions. The PC–3 image is useful for discrimination of fireburns, thanks to significantly higher DN values in fireburn areas over bedrock and alluvial deposits. Calcrete and silcrete duricrusts show low DN values. PC–3 images show little discrimination between other surface types.
- PC–4 shows a strong negative correlation with bands 5 and 3 and displays high DN values for iron oxide and fireburn areas. The DN values of the latter are inversely proportional to their age, i.e., young fireburns display higher DN values. PC–4 gives good discrimination between gabbro and mafic granulite, the latter displaying higher DN values. Felsic materials show lower DN values than mafic materials, and free quartz-bearing felsic alluvium shows as black areas.
- PC–5 shows a negative correlation with band 1 and a positive correlation with band 4, which represents green vegetation which occurs mainly along creeks and depressions, in agreement with the high Eigen vectors in band 4. Little contrast is shown between mafic and felsic lithologies.
- PC–6 is dominated by negative correlations in bands 4 and 1. The images are very 'noisy' and show faint outlines which cannot be correlated with geological features, possibly reflecting old fireburn patterns and dry vegetation patterns.

Directed principal component analysis of band ratios

Application of directed principal component analysis to band ratios allows discrimination of materials with partly overlapping spectral patterns (Fraser & Green 1987). High 4/3 band ratio DN values pertain to both iron oxide and green vegetation, and high 5/7 ratio DN values pertain to both clay and vegetation. However, iron oxide can be distinguished from vegetation by much lower 5/7 ratio DN values. Likewise, clay can be distinguished from vegetation by much lower 4/3 ratios. These discriminations can be made using principal component analysis of pairs of ratios. For vegetation and clay the difference is expressed by principal component analysis of bands 4/3 and 5/7, namely, pc2(4/3;5/7). The discriminative principal component can be combined with band ratios in RGB images to display a range of clay–iron oxide variations along with a separate vegetation component.

The colour composite image, pc2(clay-dominated)–5/4 (iron oxide)–4/3 (green vegetation), displayed as RGB, has been found to allow direct comparisons between the ratios of clay–carbonate, iron oxide, and green vegetation. In this type of image, the visually sensitive red and green colours represent lithological variations and the visually less sensitive blue colour represents vegetation. Comparisons between lithological correlations allowed by this image and correlations suggested by log residual images, band ratio images, and pixel-unmixed images suggest superior resolution of surface types, as follows:

- Old growth-covered gabbro: red and purple, representing clay–carbonate weathering crusts and dry vegetation, green vegetation being particularly dense in shaded southward slopes that show in deep purple.
- Fireburn over gabbro: dark brown to red, representing low DN values of clay-covered weathering surfaces.
- Ferrogabbro: bright apple green, representing iron oxide.
- Pyroxenite: green-dominated, commonly ranging to cyan, representing strong effects of iron oxide, e.g., northern Kalka, Ewarara, Latitude Hill, Gosse Pile, merging into cyan where vegetation is important, e.g., southern shaded slopes of the Gosse Pile intrusion.
- Felsic granulite and granitic gneiss: mostly yellow (clay–iron oxide red–green mixtures) covered in places by blue (vegetation on southern slopes) and red where weathered to clay. Strong sub-peneplain clay weathering is conspicuous at high levels on Mount Aloysius.
- Laterite: marked apple green (iron oxide) to yellow (iron oxide–clay mixtures), e.g., east of Kalka and Poonawarra, and cyan, where laterite is covered by dense mulga bush, e.g., around Wingellina.
- Calcrete: orange red, e.g., along creeks and locally over peridotite.
- Silcrete: bright red.
- Mafic source-derived alluvium: shades of light green to light orange, representing the importance of iron oxide and clay.
- Felsic source-derived alluvium: light red to purple, commonly forming collars around outcrops of felsic granulite, representing the importance of clay and vegetation.
- Silt and claypans: light orange to red (Champ de Mars clay pan) and green (Lake Wilson), the latter suggesting suspended iron oxide–clay mixtures.

An equally effective RGB image combines pc2(4/3;5/7)[red], 5/4 band ratio [green], and bands (1+3+5+7)[blue], the latter representing the high albedo of free quartz.

Discussion

The results of the image analysis methods discussed above are summarised here in relation to the identification of specific surface material types.

Iron oxide. Hematite shows a good correlation with the 5/4 and 7/4 band ratio images, thanks to the uniquely high DN values for iron oxide compared to other materials. Surface types identified in this way include lateritic deposits, iron oxide-impregnated weathering crusts of pyroxenite and ferrogabbro, oxidised mafic debris in strike valleys that overlie pyroxenite units and in creeks, and, to a lesser extent, iron oxide-bearing weathering products of felsic granulite transected by mafic dykes. The low 5/4 band ratio DN values of gabbroic rock surfaces represent the dominance of clay in their weathering products. Low 5/4 band ratios of tracks represent the winnowing away of fine iron oxide dust from quartz-rich sand. A distinction between hematite and goethite may be possible where iron oxide-rich material has low 5/4 band ratio DN values. Other iron oxide correlations, such as the 3/1 band ratio, are largely masked by high 3/1 band ratio DN values of dry grass.

Clay and carbonate. Traditionally, 5/7 band ratio DN values are used as an effective discriminant of clay components, although similar criteria apply to carbonates and dry vegetation. 5/7 band ratio DN values in the Kalka–Mount Davies area represent the relative abundance of clay components in the weathering products of gabbroic rocks, carbonate weathering of peridotite, and calcrete deposits. The second principal component of the combined band ratios (4/3;5/7) allows the separation of the clay component from the vegetation com-

ponent. The inverted log residual ILR–7 image, which represents strong absorption of band 7 owing to clay minerals, indicates clay–carbonate weathering of gabbroic rocks as high DN values, but depicts clay components shed from felsic granulite to a lesser extent.

Quartz–silica. The uniformly high reflectance of quartz and silica in all bands can be used to separate these components by adding the DN values of several spectral bands, e.g., bands (1+3+5+7) or bands (1+7), resulting in high combined reflectance values compared to other materials. The identified quartz–silica component can be combined with clay–carbonate and iron oxide, forming a diagnostic three-mineral component RGB image, e.g., pc2(4/3;5/7) : 5/4 : (1+3+5+7), representing clay+carbonate – iron oxide – quartz+silica.

Green vegetation. 4/3 band ratio DN values effectively discriminate green vegetation, which under the arid conditions of the Tomkinson Ranges is concentrated along creeks, southern slopes, strike valley depressions, alluvial collars around felsic rock outcrops, vegetation-fringed tracks, and airstrips. In view of the strong absorption by the chlorophyll of green vegetation in band 3, an inverted log residual image of this band (ILR–3) is also useful in discriminating green vegetation, which yields high DN values. However, vegetated alluvial collars around felsic rock outcrops are only weakly displayed on this image, possibly owing to variations in the type of plants.

Other image-processing methods

Pixel-unmixing and vegetation-screening analysis

Pixel-unmixing analysis (Bierwirth 1990; P.N. Bierwirth, personal communication 1994) depends on a choice of realistic spectrally distinct end members identified in the field. Similar spectral patterns are difficult to separate, e.g., distinctions between clay and carbonate and between hematite and goethite are not readily obtained on Landsat-5 TM images. Model end members can include dry vegetation and green vegetation (higher 4/3 and 2/3 band ratios than dry vegetation). The number of end members cannot exceed the number of bands, namely up to six bands in Landsat-5 TM images (excluding the thermal band 6). Modelling of end member abundances by pixel unmixing allows subtraction of the reflectance effects of dry and/or green vegetation end members in each band from the primary (radiance-corrected) Landsat-5 TM band DN value in order to obtain the devegetated images.

In the present study (Glikson 1994), the following field-measured end member spectra were selected: (1) kaolinite, (2) calcite, (3) hematite, (4) goethite, (5) silica, (6) eucalyptus green vegetation, (7) dry vegetation, and (8) spinifex vegetation (similar to green vegetation). Comparisons between pixel-unmixed model images and selected band ratio images confirm the unmixing model with regard to (1) the unmixed clay component, which correlates with 5/7 band ratio images, (2) the unmixed iron oxide component, correlated with band ratio 5/4 images, and (3) the unmixed green vegetation component, correlated with 4/3 band ratio images. On the other hand, no discriminations of clay from carbonate or of hematite from goethite have proved possible. Kaolinite, representative of clays in general, is suggested in the weathered surfaces of felsic igneous and metamorphic rocks and derived alluvial materials, the latter forming distinct rings and fringes around felsic igneous and metamorphic rock outcrops. Clay–carbonate mixtures are suggested in the weathering surfaces of gabbroic igneous rocks. Carbonate and carbonate–silica mixtures are represented by calcrete along creeks and by calcrete rises beneath alluvial surfaces. Hematite and/or goethite dominate outcrops of orthopyroxenite, ferrogabbro, lateritic deposits, and iron oxide-rich alluvial deposits derived from mafic igneous rocks. Attempts to model goethite were unsuccessful, in part due to its spectral overlap with vegetation. Silica is not discriminated, except as generally high to very high reflectance areas, e.g., in silcrete open cuts near Wingellina and Pipalyatjarra. Green vegetation is well represented along creeks and in fireburn areas covered by young green spinifex regrowth, allowing discrimination of fireburn outlines. These areas offer geological 'windows' through which the spectral patterns of mineral components are better manifested than in old growth areas covered by highly reflective dry vegetation.

In view of the near overlap between the 5/7 band ratio of dry vegetation and clay, removal of the dry vegetation component in the unmixing analysis may result in loss of information with regard to the clay component, as indicated by comparisons between the original data and devegetated images with log residual images. Comparisons between single-band pixel-unmixed images and band ratio images show the following similarities and differences (Glikson 1994). The hematite end member band of the pixel-unmixed image has important features in common with the 5/4 band ratio image. Both images show very high reflectance for laterite and for oxidised mafic-derived colluvium, intermediate reflectance for felsic granulite, and low reflectance for clay–carbonate weathered mafic rocks and for clay and quartz-rich girdles around felsic outcrops. The correlation between the clay end member band of the pixel-unmixed image and the 5/7 band ratio image is not as good, although clay–carbonate-rich areas at the centre of Mount Davies and clay–quartz-rich alluvial girdles around felsic granulite outcrops are expressed by high DN values in both types of image. The otherwise poor correlation is due to superposition of vegetation on the 5/7 band ratio, requiring comparisons with devegetated images. A close similarity is shown between the green vegetation end member in the pixel-unmixing image and the 4/3 band ratio image. Both images display the greater concentration of green vegetation in creeks, strike-parallel depressions of less resistant lithologies, and some southern slopes, e.g., Gosse Pile.

In attempting to produce devegetated images by pixel-unmixing analysis, it is evident that, since field-measured spectra indicate a close coincidence between the 5/7 ratios of dry vegetation and clay, a significant loss of mineral-related data occurs upon subtraction of the dry vegetation end member. For this reason, only green vegetation subtraction was applied to the Tomkinson Ranges scene. The comparison between original (dark pixel-corrected) images and devegetated images (Glikson 1994) shows (1) a consistent reduction in the 4/5 and 5/7 band ratios of the devegetated spectra, due to the removal of the positive 5/7 and 5/4 ratios of green vegetation, (2) a consistent decrease in the 4/3 band ratio of the devegetated spectra, due to the removal of the high 4/3 band ratio of green vegetation, and (3) a lowering of the 2/1 and 2/3 band ratios, which are high in green vegetation. Devegetated images of the Tomkinson Ranges show that, whereas sharpening of the images and good definition of some lithological units are obtained, much of the detail shown in the original images and in log residual images and ratio images is lost. This may indicate that green vegetation concentrations help to define surface mineral types.

Unsupervised image classification

Unsupervised image classification involves comparisons between nearest-neighbour pixels, calculation of mid points, and migration of means by an iterative process — grouping analogous spectra into a user-specified number of classes. The method differs from supervised classification in which specified spectral types are derived from training areas, a process involving *a priori* categorisation of the classes, or subjective selection. Unsupervised classification can be performed either

on raw spectral data, corrected spectral data, or processed images. On classified images, each spectral group is given a separate colour, allowing its visual distinction. In this study, unsupervised classification images produced on the I^2S image-processing system, using 20 and 30 class selections allowed the following correlations:

- A 20-class image differentiates between the following surface types:
  1. gabbro.
  2. ferrogabbro and pyroxenite.
  3. felsic granulite and granite.
  4. quartz-rich alluvial deposits.
  5. weathered felsic granulite.
  6. vegetated dune areas.
- A 30-class images differentiates between the following surface types:
  1. mafic and ultramafic rocks.
  2. felsic granulite and granite.
  3. quartz-rich alluvium.
  4. vegetated dunes.

The above suggests that an increase in the number of classes may result in subdivisions whose significance in terms of correlation with surface types is unclear. In view of the limited resolution of classified raw data images, unsupervised classification was performed on geologically particularly useful images, for example the pc2(4/3;5/7):5/4:4/3 RGB image. The classification process results in image degradation due to the averaging of pixel arrays, generally diminishing the resolution of individual surface types. Thus, whereas the classified image still allows discrimination between gabbro, iron oxide-rich ferrogabbro–pyroxenite–laterite, felsic granulite, and weathered felsic granulite, its spatial resolution is distinctly inferior to that of the unclassified image.

AMSS Geoscan Mark-I image correlations

Two runs of AMSS Geoscan 13-band 10 meter-pixel Mark-I imagery flown over the Tomkinson Ranges was provided by Geoscan, through the courtesy of Dr J.L. Daniels, for lithological comparisons. The two runs, covering 5 km-wide east–west and north–south strips, allow further discrimination because of the smaller pixel size as well as additional information derived from bands in the thermal range. The data allow correlations with surface types not readily identified by Landsat-5 TM data, as follows (Honey & Daniels 1985, 1986):

6/7 band ratio: highlights kaolin-rich areas.
6/8 band ratio: highlights sericite and smectite-rich areas.
6/9 band ratio: highlights carbonate-rich areas
7/8 band ratio: positive discrimination of smectite.
8/7 band ratio: highlights alunite-rich areas.
11/10 band ratio: highlights areas of high free silica.

Comparisons between ratio RGB images of the above bands (6/8:6/9:5/4, 6/8:6/9:11/10, 10:11:12) for the Tomkinson Ranges area allow the following observations and correlations:

1. The 6/8 band ratio discriminates clay–arkose-rich pediments which fringe felsic granulite and granite outcrops, and shows a patchy pattern over weathered clay-bearing outcrops of felsic granulite and over calcrete.

2. The 6/9 band ratio discriminates outcrops of gabbro of the Giles Complex.

3. The 5/4 band ratio discriminates gabbro of the Giles Complex and, more strongly, oxidised mafic detritus and alluvium derived from mafic sources, due to iron oxide, although the AMSS Geoscan band 5 is different from the Landsat-5 TM band 5 interval.

4. The 11/10 band ratio discriminates quartz-rich alluvial material derived from felsic sources and also over silcrete.

AMSS Geoscan Mark-I log residual images help to accentuate lithological distinctions. For example, a log residual 9:4:1 RGB image of the Wingellina area clearly shows the difference between weathered outcrops of gabbro and laterite. Further processing of AMSS Geoscan Mark-I images will be reported elsewhere.

Appendix II: Petrography of samples from cross sections through selected Giles Complex intrusions

Detailed sampling traverses were made across seven of the Giles Complex intrusions, namely, The Wart gabbro/pyroxenite, Latitude Hill gabbro/pyroxenite, Hinckley Range gabbronorite, Bell Rock gabbro/troctolite, Murray Range peridotite/pyroxenite/gabbro, Blackstone Range troctolite/gabbro, and Jameson Range troctolite/gabbro (Fig. 47). Analyses of minerals from these intrusions are listed in Ballhaus (1993). Most of the samples from the last four of these intrusions were chemically analysed, and the results are contained in the AGSO ROCKCHEM database.

Field No. / AGSO No. / Stratigraphic level / Petrography

The Wart gabbro/pyroxenite intrusion

32/50-12 88981034 1840m – olivine-bearing feldspathic clinopyroxenite orthocumulate to melagabbro. Olivine and clinopyroxene are cumulus; plagioclase is intercumulus, but near to a cumulus phase. Clinopyroxene is in places rich in exsolved spinel, and brownish exsolved spinel granules are common. Olivine–plagioclase contacts locally have pyroxene–spinel symplectites. Some interstitial orthopyroxene.

32/50-15 88981035 1680m – olivine melagabbro. Olivine, clinopyroxene, and plagioclase are cumulus, and plagioclase is texturally close to intercumulus. Orthopyroxene rims olivine, and locally grades into intercumulus. Columnar orthopyroxene and greenish spinel symplectites occur at olivine–plagioclase contacts.

32/50-16 88981036 1208m – Coarse-grained olivine–plagioclase-phyric cross-cutting dyke. Large roundish olivine and elongated euhedral plagioclase are phenocrysts, in a groundmass largely composed of biotite and oxides. Clinopyroxene interstitial to plagioclase. Probably not related to The Wart cumulates due to differences in crystallisation sequence.

32/50-17A 88981037 1102m – fine-grained plagioclase–clinopyroxene-phyric dyke. Large euhedral plagioclase laths and euhedral clinopyroxene phenocrysts, in a matrix of plagioclase microphenocrysts and brownish (biotite-rich?) hydrated groundmass. Intrudes gabbro and shows well-developed chilled margins.

32/50-17B 88981038 1120m – annealed pyroxenite adcumulate. Clinopyroxene, locally with cores rich in exsolved spinel and interlocked at grain boundaries, is cumulus. Antiperthite forms rare interstitial material. Presence of cumulus orthopyroxene uncertain.

32/50-18A 88981039 1002m – olivine-bearing gabbro. Clinopyroxene, minor olivine, and plagioclase are cumulus. Olivine is surrounded by narrow orthopyroxene rims, and, where in contact with plagioclase, by an additional outer layer of pyroxene–spinel symplectite. Shows alternating olivine-rich and plagioclase-rich units in outcrop.

32/50-18B 88981040 1007m – annealed clinopyroxenite adcumulate. Clinopyroxene is cumulus, with rare interstitial plagioclase. Clinopyroxene is interlocked at grains boundaries.

32/50-18C 88981041 1012m – annealed olivine-bearing (feldspathic) clinopyroxenite adcumulate. Olivine and clinopyroxene are cumulus; rare plagioclase (locally antiperthitic) is interstitial. Rare orthopyroxene is intercumulus, associated with olivine. Some clinopyroxene cores are rich in exsolved spinel.

32/50-18D 88981042 1017m – annealed olivine-bearing clinopyroxenite adcumulate. Clinopyroxene (moderately rich in exsolved spinel) and slightly altered olivine are cumulus. Neither plagioclase nor orthopyroxene observed.

32/50-19A 88981043 970m – annealed olivine-bearing clinopyroxenite adcumulate (similar to 18D). Clinopyroxene and highly altered olivine are cumulus. Some clinopyroxene cores are very rich in exsolved spinel. Neither plagioclase nor orthopyroxene observed.

32/50-19B 88981044 975m – peridotite orthocumulate. Slightly altered rounded olivine (serpentinisation along cracks) is cumulus, clinopyroxene is cumulus to intercumulus, and plagioclase always interstitial. Poikilitic orthopyroxene is rare. No cumulus spinel observed. Soft zones with preferential weathering.

32/50-20 88981045 950m – orthopyroxene-phyric dyke. Euhedral orthopyroxene and some augite phenocrysts, in a fine-grained matrix of plagioclase and pyroxene microphenocrysts and oxides. Olivine not positively identified; a few elongated laths of a highly birefringent phase are present. Possibly a dyke with high-pressure phenocrysts.

32/50-21A 88981046 900m – coarse-grained banded wehrlite orthocumulate, locally grading into olivine-rich melagabbro and peridotite–dunite. Rounded olivine and clinopyroxene are cumulus; plagioclase is mostly intercumulus, but locally has euhedral shapes (where modal plagioclase content is high). Orthopyroxene is a poikilitic phase around olivine. Olivine grains that are in contact with plagioclase are surrounded by columnar orthopyroxene rims, and, in places, by an additional outer layer of fine-grained 'dirty' pyroxene–spinel symplectite.

32/50-21B 88981047 905m – annealed clinopyroxenite. Clinopyroxene is apparently the only cumulus phase, as cumulus orthopyroxene was not positively identified. Interstitial plagioclase is rare. Grains are interlocked at contacts.

32/50-21C 88981048 910m – annealed olivine-bearing clinopyroxenite. Clinopyroxene and slightly altered olivine are cumulus, but cumulus orthopyroxene was not verified. Interstitial plagioclase and possibly orthopyroxene are rare. Grains are interlocked at contacts.

32/50-22A 88981049 785m – olivine gabbro. Slightly altered olivine, plagioclase, and clinopyroxene are cumulus. Olivine is surrounded by orthopyroxene rims, which, in contact with plagioclase, is columnar with an additional outer pyroxene–spinel symplectite layer. Sample from a well-layered graded unit with a dunitic base and olivine gabbro towards the top.

32/50-22B 88981050 790m – olivine-bearing melagabbro(norite), locally feldspathic pyroxenite. Minor olivine, clinopyroxene, orthopyroxene(?), and small elongated plagioclase laths are cumulus. Pyroxene/plagioclase modal ratio is more typical of a feldspathic pyroxenite orthocumulate. Olivine in contact with plagioclase is surrounded by columnar orthopyroxene rims and outer pyroxene–spinel symplectite layers.

32/50-22C 88981051 795m – olivine-bearing melagabbro(norite). Similar to 22B, but lower pyroxene/plagioclase modal ratio.

32/50-23 88981052 1234m – olivine gabbro. Olivine, clinopyroxene, and plagioclase are cumulus, orthopyroxene apparently occurs only as rims around olivine. Clinopyroxene has vermicular exsolved orthopyroxene. Olivine in contact with plagioclase is surrounded by columnar orthopyroxene

rims and pyroxene–spinel symplectite.

32/50-24 88981053 1312m – olivine gabbro. Similar to 23, but slightly coarser-grained and olivine more altered.

32/51-14A 88981001A 1065m – olivine-bearing gabbro. Plagioclase and clinopyroxene are the main cumulus phases. A few cumulus olivine relics, some of which are replaced by hydrous silicates. Columnar orthopyroxene rims olivine, with pyroxene–spinel symplectites in contact with plagioclase grains. Western contact of layered suite, forming a massive ridge.

32/51-14B 88981002 1070m – annealed clinopyroxenite adcumulate. Clinopyroxene, with vermicular exsolved orthopyroxene, and lesser orthopyroxene(?) are cumulus, and interlocked along grain boundaries. Very rare interstitial plagioclase.

32/51-15 88981003 1048m – same as 14B (but presence of orthopyroxene uncertain). Between 14B and 15 are multiple repetitions of gabbro and pyroxenite.

32/51-16A 88981004 1028m – coarse-grained olivine-rich gabbronorite to gabbronoritic troctolite. Rounded altered olivine, plagioclase, orthopyroxene (to some extent), and clinopyroxene are cumulus. Columnar orthopyroxene rims olivine, with, where in contact with plagioclase, an additional pyroxene–spinel 'cauliflower' symplectite rim.

32/51-16B 88981005 1033m – olivine-bearing (feldspathic) pyroxenite, locally wehrlite. Clinopyroxene, olivine, and possibly orthopyroxene are cumulus. Rare patches of feldspathic mesocumulate occur where cumulus clinopyroxene grains are finer-grained and embedded in interstitial plagioclase. Intruded by pseudotachylite veinlets.

32/51-16C 88981006 1038m – plagioclase-phyric sill. Elongated euhedral plagioclase phenocrysts, minor olivine microphenocrysts, and isolated clinopyroxene phenocrysts, in a dirty oxide-rich matrix. Large opaque relics, with radial overgrowth rims, may be an early generation of olivine phenocrysts.

32/51-17A 88981007 990m – annealed clinopyroxenite adcumulate (alternating with gabbroic cumulates, see 17B). Clinopyroxene, with vermicular exsolved orthopyroxene, is cumulus, interlocked along grain boundaries. Very rare interstitial plagioclase.

32/51-17B 88981008 995m – olivine gabbro. Plagioclase, olivine and clinopyroxene are cumulus phases; orthopyroxene not positively identified. Columnar orthopyroxene forms overgrowths on olivine, with pyroxene–spinel 'cauliflower' symplectites at olivine–plagioclase contacts. Abundant clinopyroxene neoblasts are present in plagioclase.

32/51-18 88981009 956m – olivine melagabbro, generally similar 17B. Multiply layered suite, gabbro alternating with pyroxenite.

32/51-19A 88981010 920m – olivine gabbronorite. Plagioclase, olivine, clinopyroxene, and abundant orthopyroxene are cumulus. Columnar orthopyroxene overgrowths on olivine, and narrow fine-grained pyroxene–spinel symplectites at olivine–plagioclase contacts.

32/51-19B 88981011 925m – annealed clinopyroxenite adcumulate. Clinopyroxene, with vermicular exsolved orthopyroxene, is cumulus, interlocked along grain boundaries. Very rare interstitial plagioclase. Pyroxenite interlayered with olivine gabbro.

32/51-20 88981012 866m – annealed olivine-bearing clinopyroxenite adcumulate. Olivine, exsolved clinopyroxene, and possibly some orthopyroxene are cumulus, interlocked along grain boundaries. Very rare interstitial plagioclase (calcic antiperthite with exsolved K-feldspar).

32/51-21 88981013 812m – olivine gabbro. Plagioclase, clinopyroxene, olivine, and possibly some minor orthopyroxene are cumulus. Columnar orthopyroxene and very fine-grained brownish pyroxene–spinel symplectites rim olivine. Interlayered with pyroxenite.

32/51-22 88981014 780m – similar to 21.

32/51-23A 88981015 750m – olivine-bearing feldspathic clinopyroxenite mesocumulate. Rare irregular, slightly altered olivine, clinopyroxene, and possibly some orthopyroxene are cumulus. Rare plagioclase is intercumulus, locally concentrated up to an orthocumulate texture. Pyroxene–spinel symplectites present at olivine–plagioclase contacts.

32/51-23B 88981016 755m – olivine-bearing melagabbro. Clinopyroxene, small plagioclase laths, and rare olivine relics are cumulus. Modal pyroxene/plagioclase ratio more like feldspathic pyroxenite, but plagioclase is a cumulus phase throughout. Interlayered with pyroxenite.

32/51-24 88981017 686m – olivine-bearing feldspathic clinopyroxenite meso- to adcumulate. Olivine (relict only) and clinopyroxene are cumulus; plagioclase is locally intercumulus. Distribution of intercumulus plagioclase is irregular, variable on thin section scale. Clinopyroxene is interlocked at grain boundaries. Pyroxenite is the major rock type in outcrop.

32/51-25 88981018 632m – olivine-bearing feldspathic clinopyroxenite meso- to adcumulate. A few olivine grains and clinopyroxene are cumulus, and sparse plagioclase (calcic antiperthite) are intercumulus. Clinopyroxene is interlocked at grain boundaries.

32/51-26 88981019 584m – feldspathic wehrlite orthocumulate. Rounded olivine grains and anhedral clinopyroxene are cumulus, and altered zoned plagioclase is interstitial. Columnar orthopyroxene occurs at olivine–plagioclase contacts. In outcrop, wehrlite alternates with peridotite and olivine-bearing pyroxenite, commonly with a patchy distribution.

32/51-27 88981020 559m – clinopyroxenite adcumulate. One relict olivine grain, wholly replaced by hydrous phases, and clinopyroxene are cumulus; plagioclase not observed.

32/51-28A 88981021 534m – clinopyroxenite adcumulate. Rounded clinopyroxene grains, slightly annealed and interlocked at grain boundaries, are cumulus. Very rare plagioclase is interstitial.

32/51-28B 88981022A 538m – very coarse-grained feldspathic clinopyroxenite mesocumulate. Clinopyroxene in a range of grain sizes is cumulus, and plagioclase is interstitial. Presence of cumulus orthopyroxene uncertain, but exsolved orthopyroxene present. Sample from a cyclic unit of peridotite, wehrlite, pyroxenite, gabbro, and gabbronorite.

32/51-29 88981022B 456m – feldspathic wehrlite mesocumulate. Rounded olivine and clinopyroxene are cumulus, and plagioclase is interstitial. Fine-grained inclusions in plagioclase comprise exsolved K-feldspar, clinopyroxene neoblasts, and symplectitic colourless spinel due to reaction with olivine. In outcrop, olivine/clinopyroxene ratios vary on a small scale.

32/51-30 88981023 394m – slightly altered sheared clinopyroxenite adcumulate. Clinopyroxene is cumulus; rare plagioclase is interstitial.

32/51-31 88981024 350m – clinopyroxenite adcumulate. A few altered olivine relics (wholly replaced by hydrous phases) and clinopyroxene are cumulus, and rare plagioclase is interstitial. Fine-grained inclusions in plagioclase are either exsolved K-feldspar (calcic antiperthite), clinopyroxene neoblasts, or symplectitic colourless spinel formed by reaction with olivine.

32/51-32 88981025 284m – annealed clinopyroxenite adcumulate. Clinopyroxene is the only cumulus phase, annealed

and interlocked at grain contacts. Clinopyroxene is present in a bimodal size distribution—a few large elongated clinopyroxene laths in finer-grained matrix of equigranular rounded clinopyroxene. Posibly a rapid-cooling texture.

32/51-33 88981026 240m – altered olivine-bearing feldspathic clinopyroxenite mesocumulate. Olivine and clinopyroxene are cumulus, and plagioclase is interstitial and locally enriched to an orthocumulate texture. There is a marked bimodal clinopyroxene size distribution. A small shear zone shows evidence for fluid infiltration.

32/51-34A 88981027 220m – annealed olivine-bearing feldspathic clinopyroxenite adcumulate. Minor olivine and clinopyroxene are cumulus, whereas rare antiperthitic plagioclase is intercumulus. Has a contact with microgabbro, possibly a sill.

32/51-34B 88981028A 225m – olivine-bearing melagabbro. Clinopyroxene and small plagioclase laths are cumulus. Modal pyroxene/plagioclase ratio more like feldspathic pyroxenite, but plagioclase is a cumulus phase throughout. Unusual texture with very abundant clinopyroxene.

32/51-35 88981028B 190m – annealed feldspathic clinopyroxenite adcumulate. Clinopyroxene (and orthopyroxene?) are cumulus, and minor antiperthitic plagioclase is interstitial. One relict altered olivine grain present. Sample from a patchy footwall with intermingled pyroxenite and gabbro.

32/51-36 88981029 152m – olivine-bearing clinopyroxenite meso- to orthocumulate from a thick pyroxenite zone. A few altered olivine relics and clinopyroxene are cumulus, and plagioclase is intercumulus. Columnar orthopyroxene rims olivine. Clinopyroxene is extremely rich in exsolved spinel, suggesting an intraplutonic quenching zone.

32/51-37 88981030 108m – poikilitic feldspathic wehrlite meso- to orthocumulate, from a pyroxenite zone. Rounded to euhedral olivine and locally euhedral clinopyroxene are cumulus. Large poikilitic clinopyroxene grains contain trapped olivine and clinopyroxene(?) in different optical orientations. Clinopyroxene is rich in exsolved spinel. The presence of orthopyroxene, other than as columnar overgrowths on olivine, is doubtful. Between 36 and 37 are some minor wehrlite intercalations.

32/51-38A 88981031 76m – olivine-bearing clinopyroxenite meso- to orthocumulate. Rounded olivine grains and clinopyroxene, rich in exsolved spinel, are cumulus; plagioclase is intercumulus. Columnar orthopyroxene rims olivine, with some small pyroxene–spinel symplectites at olivine-plagioclase contacts. Granule exsolution of greenish spinel.

32/51-38B 88981032 81m – clinopyroxenite mesocumulate. Clinopyroxene and a few relict olivine grains, totally replaced by hydrous silicates, are cumulus, and antiperthite is interstitial. Exsolved spinel in clinopyroxene is less abundant.

32/51-39 88981033 40m – olivine-bearing feldspathic clinopyroxenite orthocumulate. A few olivine grains and clinopyroxene are cumulus, and plagioclase is interstitial. Clinopyroxene has very abundant exsolved spinel, and plagioclase has minor exsolved K-feldspar (despite high modal plagioclase contents). Sample is from contact with a granite.

Latitude Hill gabbro/pyroxenite intrusion

34/124-1 88983001 5163m – 'doleritic-textured' fine-grained noritic gabbro to melagabbro. Clinopyroxene and elongated plagioclase laths are cumulus phases, orthopyroxene is rarely cumulus, but more commonly poikilitic (later in sequence than clinopyroxene).

34/124-2 88983002 5333m – coarse-grained 'doleritic-textured' gabbronorite. Brownish clinopyroxene and plagioclase are cumulus, and grayish orthopyroxene is also cumulus, but slightly later than clinopyroxene. Plagioclase has abundant minute brownish exsolved grains. Intercalated with feldspathic pyroxenite.

34/124-4 88983003 5603m – coarse-grained 'doleritic-textured' gabbronorite. Clinopyroxene, large orthopyroxene, and elongated brownish plagioclase laths are cumulus phases. All phases are dusted with submicroscopic inclusions, in plagioclase locally recrystallised to minute clinopyroxene neoblasts.

34/124-6 88983004 5693m – coarse-grained 'doleritic-textured' gabbronorite. Clinopyroxene, large orthopyroxene, and large elongated brown plagioclase grains are cumulus phases. All phases are dusted with submicroscopic inclusions, in plagioclase locally recrystallised to minute clinopyroxene neoblasts.

34/124-7 5843m – 'doleritic-textured' gabbro.

34/124-8 5891m – 'doleritic-textured' gabbro.

34/124-9 5979m – pyroxenite to 'doleritic-textured' melagabbro.

34/124-10 88983005 6003m – gabbroic cataclasite. Clinopyroxene is altered to green actinolitic amphibole, whereas cumulus plagioclase relics are preserved. Fine-grained groundmass largely consists of actinolitic amphibole.

34/124-11A 88983006A 6033m – formerly olivine-bearing gabbronorite. Olivine relics (largely replaced by opaques and hydroxides), orthopyroxene, clinopyroxene, and elongated plagioclase laths are cumulus phases. Preferential orientation of plagioclase defines a weak igneous lamination. All phases except olivine are strongly dusted by brownish submicroscopic inclusions, masking birefringence colours in clinopyroxene. Brownish inclusions are recrystallised to clinopyroxene neoblasts along plagioclase–plagioclase grain boundaries. Beautiful textures, possibly indicating rapid cooling conditions.

34/124-11B 88983006B 6037m – olivine-bearing pyroxenite adcumulate. Euhedral olivine and small orthopyroxene cumulus crystals in a matrix of larger and more abundant cumulus clinopyroxene. No peritectic reaction relationships evident between olivine and melt (olivine and orthopyroxene cotectic). Plagioclase not observed. All phases except olivine are dusted with minute brownish submicroscopic inclusions or exsolutions.

34/124-12 88983007 6143m – gabbronorite. Clinopyroxene, coarse orthopyroxene, and elongated laths of plagioclase are cumulus phases. Submicroscopic inclusions occur in all phases, in clinopyroxene masking birefringence colours, and in plagioclase recrystallised to clinopyroxene and clearing toward grain contacts. In outcrop, melagabbro–pyroxenite is intruded by felsic veins.

34/124-14 88983008 6265m – olivine-bearing 'doleritic-textured' gabbronorite. Sparse olivine, and coarse orthopyroxene, clinopyroxene, and plagioclase are all cumulus. Plagioclase has submicroscopic brownish inclusions that tend to clear and recrystallise toward plagioclase–plagioclase grain boundaries. Beautiful fine-grained pyroxene–(spinel?) 'cauliflower' symplectites at olivine–plagioclase contacts. Some pyroxenite rubble in the valley.

34/124-15A 88983009A 6307m – very fine-grained olivine gabbronorite (according to field relations, a cross-cutting dyke). Olivine is surrounded by amphibole alteration rims; orthopyroxene, clinopyroxene, and plagioclase are cumulus phases. Clinopyroxene has brownish submicroscopic inclusions masking birefringence colours. Fine exsolutions in plagioclase tend to coarsen toward grain boundaries and are locally recrystallised to small clinopyroxene neoblasts.

34/124-15B 88983009B 6311m – gabbronorite. Large orthopyroxene, smaller clinopyroxene, and elongated plagioclase laths are cumulus phases, orthopyroxene locally tending to a poikilitic texture. All phases have finely dispersed inclusions, which, at plagioclase grain contacts, are locally recrystallised to vermicular clinopyroxene.

34/124-16A 88983010A 6377m – very coarse-grained pyroxenite adcumulate. Both orthopyroxene and clinopyroxene are cumulus phases, with a bimodal grain size distribution; plagioclase was not observed. Some minor hydrous alteration and recrystallisation along small cracks. Pyroxenite is intercalated with gabbro.

34/124-16B 88983010B 6381m – olivine gabbronorite with a conformable microgabbro pod in gabbro. Olivine, larger orthopyroxene, clinopyroxene, and elongated plagioclase laths are cumulus phases. Plagioclase has a preferential orientation defining an igneous lamination. Olivine has reaction rims of columnar orthopyroxene and opaque phases, probably magnetite. Plagioclase and clinopyroxene are dusted with minute brownish inclusions. In plagioclase these tend to be recrystallised to small neoblasts along grain boundaries and cracks, in clinopyroxene they are concentrated along orthopyroxene exsolution lamellae. Beautiful textures! Sample from a well-layered sequence of pyroxenite alternating with gabbroic rocks.

34/124-17A 88983011A 6435m – 'dirty' anorthosite adcumulate with rare interstitial clinopyroxene. Small clinopyroxene needles in plagioclase may be equivalent to the much finer-grained inclusions in less fractionated samples.

34/124-17B 88983011B 6439m – olivine-bearing feldspathic pyroxenite orthocumulate. Sparse olivine, large orthopyroxene, and medium-sized clinopyroxene are cumulus phases; plagioclase is interstitial. Fine-grained orthocumulate zones contain cumulus clinopyroxene and orthopyroxene as rims around clinopyroxene. These orthocumulate zones are irregularly distributed in a matrix of coarser pyroxenite mesocumulate with abundant early cumulus orthopyroxene. Localised hydrous alteration occurs along well-defined cracks. Gullies coincide with well layered gabbro–-pyroxenite sequences, and ridges with massive gabbro.

34/124-18 88983012 6415m – sheared altered gabbro (protocataclasite). Relict cumulus plagioclase, rare relict clinopyroxene, and actinolite (probably replacing cumulus clinopyroxene) occur in a fine-grained post-deformational matrix of actinolitic amphibole.

34/124-19 88983013 6440m – olivine-bearing gabbronorite. Altered olivine with narrow moats of columnar orthopyroxene, clinopyroxene, rare large orthopyroxene grains, and plagioclase are cumulus phases. Clinopyroxene neoblasts occur along plagioclase grain boundaries, and 'cauliflower' pyroxene–(spinel?) symplectites in plagioclase, especially in contact with olivine.

34/124-20 88983014 6523m – olivine-bearing gabbronorite. Olivine (rimmed by columnar orthopyroxene and a hydrous alteration moat), clinopyroxene, orthopyroxene, and elongated laths of plagioclase are cumulus phases. 'Cauliflower' pyroxene–(spinel?) symplectites occur in plagioclase, especially adjacent to olivine. Intercalated with pyroxenite.

34/124-21A 88983015A 6599m – olivine-bearing gabbronorite. Altered olivine relics, orthopyroxene, clinopyroxene, and plagioclase are cumulus phases. All phases except olivine are dusted with tiny brownish inclusions. Clinopyroxene neoblasts are present along plagioclase–plagioclase grain boundaries (Fe–Mg grain boundary diffusion).

34/124-21B 88983015B 6603m – pyroxenite adcumulate with local feldspathic orthocumulate pockets. Brownish orthopyroxene and clinopyroxene are cumulus phases. Plagioclase is absent except in local orthocumulate pockets where it forms well defined poikilitic (optically continuous) crystals with small euhedral clinopyroxene inclusions. Sample 21A between points 20 and 21.

34/124-22 88983016 6747m – feldspathic pyroxenite orthocumulate. Clinopyroxene and much larger orthopyroxene are cumulus (orthopyroxene locally poikilitic). Plagioclase forms large poikilitic crystals that are optically continuous over wide areas.

34/124-23 88983017 6815m – poikilitic olivine-bearing feldspathic pyroxenite orthocumulate. Large altered olivine, large orthopyroxene, and small grains of clinopyroxene are cumulus phases, and plagioclase is poikilitic, forming large optically continuous grains. Locally advanced alteration and incipient uralitisation of clinopyroxene to greenish actinolitic amphibole. Small abundant clinopyroxene neoblasts occur in plagioclase, particularly in contact with olivine, locally recrystallised to vermicular grains. Sample is from a well-layered sequence of alternating pyroxenite and olivine-rich units.

34/124-24 88983018 6845m – gabbronorite. Clinopyroxene, orthopyroxene, and plagioclase are cumulus phases. Forms massive ridge and is intercalated with pyroxenite.

34/124-25A 88983019 6875m – gabbronorite. Large orthopyroxene grains, smaller plagioclase, and clinopyroxene are cumulus. Euhedral plagioclase laths are included in orthopyroxene, which tends towards a poikilitic texture. Plagioclase is dusted with minute birefringent inclusions. Cut by an epidote-bearing vein.

34/124-25B 6879m – mylonite. No thin section available.

34/124-26A 88983020A 6983m – gabbronorite. Large orthopyroxene and plagioclase are early cumulus phases, and clinopyroxene is texturally slightly later. Brownish plagioclase has abundant minute exsolved grains. Small clinopyroxene neoblasts trace grain boundaries in plagioclase-rich portions, suggesting grain boundary diffusion of Fe and Mg; alternatively may be due to granule exsolution of submicroscopic impurities in plagioclase.

34/124-26B 88983020B 6987m – sheared granitoid. Fine-grained recrystallized quartz, K-feldspar, possibly albitic plagioclase, and abundant zircon. Hill between 25 and 26 is composed mainly of gabbroic rocks.

34/124-26C 88983020C 6991m – gabbronorite. Clinopyroxene and elongated plagioclase are cumulus phases; coarse orthopyroxene is cumulus to poikilitic. Plagioclase is dusted by submicroscopic inclusions, coarsening and clearing toward grain contacts.

34/124-27 7109m – shear zone within gabbro and pyroxenite. No sample taken.

34/124-28 88983021 7181m – olivine-bearing gabbronorite. Rare olivine relics in a matrix of finer-grained cumulus clinopyroxene, orthopyroxene, and plagioclase. Orthopyroxene is locally poikilitic. Plagioclase is dusted with small inclusions, locally recrystallised to larger neoblasts in contact with olivine.

34/124-29A 88983022A 7287m – strongly recrystallised granitic vein. Quartz, K-feldspar, albitic plagioclase, abundant recrystallised zircon, minor altered clinopyroxene, and euhedral oxides.

34/124-29B 88983022B 7291m – gabbronorite. Clinopyroxene, large orthopyroxene grains, and elongated plagioclase are cumulus phases. All phases contain minute inclusions, possibly due to exsolution; those in plagioclase are recrystallised to clinopyroxene. Clinopyroxene neoblasts trace grain boundaries between plagioclase (Fe–Mg grain boundary dif-

fusion).

34/124-30 88983023 7329m – very fine-grained olivine gabbronorite. Olivine, clinopyroxene, and elongated laths of plagioclase are cumulus phases; larger orthopyroxene grains are poikilitic. All phases except olivine are rich in submicroscopic brownish inclusions. Apparently a sill or a dyke, in two-dimensional outcrop appearing to parallel the magmatic layering.

34/124-31 88983024 7211m – coarse-grained pyroxenite adcumulate. Large orthopyroxene cumulus grains and smaller cumulus clinopyroxene, with rare interstitial plagioclase. All phases are rich in minute brownish inclusions. Rock has a highly varied grain size: a coarse-grained pod in a finer-grained matrix.

34/124-32 88983025 7275m – gabbronorite. Large orthopyroxene and plagioclase are cumulus phases; clinopyroxene is cumulus, but tends towards a poikilitic texture (i.e., contemporaneous with, but also later than, plagioclase and orthopyroxene). Plagioclase has abundant minute brownish exsolved grains.

34/124-33 88983026 7325m – 'doleritic-textured' noritic gabbro. Clinopyroxene and elongated plagioclase laths are cumulus, and large sparse cumulus orthopyroxene crystals tend to poikilitic textures at grain contacts. Plagioclase is dusted with brownish submicroscopic inclusions. Possibly a rapid crystallisation texture. Interlayered with minor gabbro.

34/124-34 88983027 7437m – 'doleritic-textured' gabbro. Clinopyroxene and elongated aligned plagioclase laths are cumulus; rare orthopyroxene occurs in small grains along grain boundaries. Clinopyroxene neoblasts along grain boundaries between plagioclase and along cracks in plagioclase are probably due to Fe–Mg diffusion.

34/124-35 88983028 7535m – 'doleritic-textured' noritic gabbro. Clinopyroxene and elongated plagioclase laths are cumulus phases, and sparse orthopyroxene occurs mainly as rims around clinopyroxene. Plagioclase is dusted with minute inclusions (exsolution or neoblasts resulting from subsolidus Fe–Mg diffusion). Clinopyroxene forms tiny neoblasts along plagioclase–plagioclase grain boundaries (Fe–Mg grain boundary diffusion). Texture is reminiscent of a coarse-grained dyke, although sample is part of the magmatic stratigraphy; may be a rapid cooling texture close to a chilled margin.

34/124-36 88983029 7615m – coarse-grained 'doleritic-textured' noritic gabbro. Clinopyroxene and large strongly elongated plagioclase laths are cumulus, and orthopyroxene forms moats around clinopyroxene. Plagioclase is dusted by inclusions. May be a rapid cooling texture close to a chilled margin.

34/125-1 88983030 3582m – strongly sheared gabbro cut by thin near-opaque pseudotachylite veinlets. Clinopyroxene is recrystallised and oxidised along minute cracks. Minor pyroxenite intercalations.

34/125-2 88983031 3692m – undeformed fresh gabbroic rock. Clinopyroxene is partly recrystallised, with ilmenite and other opaque exsolution lamellae possibly due to oxidation. A coarse-grained cross-cutting dyke intruding deformed gabbroic rocks like 34/125-1.

34/125-3 88983032 3772m – strongly sheared leucogabbro, infiltrated by abundant pseudotachylite veinlets. Clinopyroxene is entirely recrystallised and oxidised by fluid infiltration; plagioclase is zoned and has undulous extinction.

34/125-5A 88983033A 3885m – same as 3.

34/125-5B 88983033B 3889m – porphyroclastic anorthositic mylonite. Rare clinopyroxene relics are poorly preserved. Syn-deformational Fe oxide impregnation and silification.

34/125-6 88983033C 3955m – slightly sheared recrystallised gabbro. Clinopyroxene is dusted with finely-dispersed oxides due to limited fluid infiltration and partial recrystallisation.

34/125-8A 88983034A 4199m – coarse-grained altered leucogabbro. Shows fluid infiltration along fine cracks, recrystallisation and oxidation of clinopyroxene, and precipitation of Fe oxide along grain boundaries and cracks.

34/125-8B 88983034B 4203m –layered felsic granulite from a cataclastic quartzo-feldspathic zone. Quartz, feldspar, pyroxene, and oxides.

34/125-9 88983035 4255m – anorthositic to gabbroic mylonite. Relict cumulus plagioclase and clinopyroxene porphyroclasts in a finer-grained plagioclase–quartz(?) matrix. Clinopyroxene is strongly altered, oxidised, and forms layers. From a major mylonite zone with abundant pseudotachylite.

34/125-11 88983036 – recrystallised, slightly deformed quartzo-feldspathic rock. Quartz, K-feldspar, dark brown biotite, dark green amphibole, and common apatite, associated with hydrous silicates. Relatively abundant large euhedral zircon crystals. Origin unclear; may be a granitic rock or a granophyric differentiate of the host cumulates.

34/127-1 88983039 210m – 'doleritic-textured' gabbro. Large elongated oriented cumulus plagioclase laths, with clinopyroxene tending towards interstitial. Possibly a rapidly crystallised rock.

34/127-3 88983040 368m – coarse-grained clinopyroxenite adcumulate. Orthopyroxene is rare, mainly forming moats around clinopyroxene. Plagioclase not observed.

34/127-5A 88983041A 20m – fine-grained microgabbro. Plagioclase forms euhedral laths, and clinopyroxene and orthopyroxene smaller rounded cumulus crystals. Contains coarse-grained K-feldspar–quartz myrmekite. May be a rapidly quenched gabbroic marginal facies with internal differentiation and/or mobilisation of felsic differentiates, or the segregations may be due to back intrusion of felsic material. Sample is from the contact between gabbro and felsic granulite.

34/127-5B 88983041B 20m – same as 5A.

34/127-8 88983042 – sheared gabbro (proto-mylonite). Cumulus plagioclase and clinopyroxene show mylonitisation along grain boundaries. Sample is from a mafic sliver outside the magmatic sequence that may predate emplacement of the Latitude Hill intrusion.

34/127-13A 88983043A 590m – annealed pyroxenite adcumulate with rare interstitial plagioclase. Large cumulus clinopyroxene grains; orthopyroxene mainly forms moats around clinopyroxene, but is locally poikilitic. Intermingled with gabbroic rocks.

34/127-13B 88983043B 594m – sheared pyroxenite adcumulate with local finer-grained feldspathic orthocumulate patches. Large kinked orthopyroxene grains predominate over clinopyroxene. Local mylonite zone with tendency toward pseudotachylite. Extensively altered sample from a patchy orthopyroxene-rich footwall.

34/127-14A 88983044A 600m – coarse-grained pyroxenite adcumulate, with local finer-grained feldspathic orthocumulate zones. Clinopyroxene predominates over orthopyroxene as cumulus phases; orthopyroxene also forms moats around clinopyroxene. Patchy mixed rock, taken from a mixing zone (patchy footwall) of 'partly resorbed' gabbro.

34/127-14B 88983044B 604m – same as 14A.

34/127-15A 88983045A 610m – feldspathic peridotite, locally sheared and altered. Olivine, orthopyroxene, clinopyroxene, and spinel are cumulus phases, and zoned altered

plagioclase is interstitial. Spinel has partly equilibrated by Al transfer from plagioclase and pyroxene, and in contact with plagioclase is surrounded by clinopyroxene–spinel symplectite. Forms base of peridotite in pyroxenite, and shows some intermingling with gabbro.

34/127-15B 88983045B 614m – deformed clinopyroxenite adcumulate. Recrystallisation along grain boundaries has produced a proto-mylonitic texture. Interstitial plagioclase is rare. Interlayered with gabbroic rocks.

34/127-16A 88983046A 620m – annealed pyroxenite adcumulate. Clinopyroxene predominates over orthopyroxene, with exsolved ilmenite. Very rare interstitial plagioclase. Sample from a patchy mixing zone with intermingled gabbroic material.

34/127-16B 88983046B 624m – coarse-grained annealed pyroxenite adcumulate. Large, slightly bent exsolved clinopyroxene is cumulus, whereas orthopyroxene occurs mainly as narrow rims, and occasionally as oikocrysts and as exsolved granules. Plagioclase not observed. Between sampling points 15 and 16 are several peridotite units.

34/127-17A 88983047A 630m – noritic gabbro. Clinopyroxene and plagioclase are cumulus phases, and orthopyroxene is present as narrow moats around clinopyroxene. Small gabbroic remnant within patchy pyroxenite.

34/127-17B 88983047B 634m – clinopyroxenite adcumulate. Orthopyroxene occurs mainly as exsolved grains and rims around clinopyroxene. Plagioclase is a rare interstitial phase. From a zone of intermingling between gabbro and pyroxenite.

34/127-18 – mylonite zone.

34/127-18 – mylonite zone (285°/75°).

34/127-20 88983048 715m – fresh gabbro. Plagioclase and clinopyroxene are cumulus.

34/127-21 88983049 793m – slightly deformed leucogabbro. Some recrystallisation along grain boundaries. Between 20 and 21 is a mylonitic shear zone.

34/127-22 88983050 833m – pyroxenite adcumulate. Orthopyroxene and clinopyroxene are cumulus and present in equal proportions. No plagioclase observed.

34/127-23 88983051 915m – fine-grained orthopyroxenite orthocumulate. Euhedral cumulus orthopyroxene in a matrix of intercumulus plagioclase. Cumulus clinopyroxene is rare. There is a bimodal grain-size distribution, suggesting a zone of rapid cooling.

34/127-24 959m – pyroxenite from a mixed cumulate with some gabbroic patches. No sample taken.

34/127-25 88983052 1141m – slightly altered pyroxenite adcumulate. Evidence for fluid infiltration along fine parallel cracks, possibly in the vicinity of a pseudotachylite or mylonite zone. Pyroxene grain margins zoned, possibly due to fluid-enhanced subsolidus equilibration.

34/127-25B 88983037 – granular oxide-rich felsic granulite.

34/127-26 88983053 1179m – melagabbro. Clinopyroxene and plagioclase are cumulus phases, and minor orthopyroxene forms moats around clinopyroxene. Appears to be close to a shear zone.

34/127-27 88983054 1257m – altered sheared feldspathic clinopyroxenite with local orthocumulate pockets. Clinopyroxene is the only cumulus phase, and rare orthopyroxene occurs as reaction(?) moats around clinopyroxene. Interstitial plagioclase occurs only in orthocumulate pockets. Fluid infiltration along shear zones caused oxidation of pyroxene (finely dispersed opaques). Sample presumably from the vicinity of a pseudotachylite or mylonite zone.

34/127-28 1305m – gabbro. No sample taken.

34/127-29 1327m – pyroxenite. No sample taken.

34/127-30 88983055 1357m – slightly deformed gabbronorite. Orthopyroxene forms large 'kinked' grains in a finer-grained matrix of deformed cumulus clinopyroxene and plagioclase. Minor recrystallisation along grain boundaries is due to deformation.

34/127-31 1370m – ridge of pyroxenite. No sample taken.

34/127-32 1444m – gabbro in creek bed. No sample taken.

34/127-33 88983056 1606m – pyroxenite adcumulate. Clinopyroxene is cumulus, and sparse orthopyroxene forms rims around clinopyroxene and occurs as oikocrysts. Between 32 and 33, pyroxenite alternates with gabbroic layers.

34/127-34 1610m – pyroxenite. Distinctly porphyritic and alternating with locally pegmatoidal orthocumulates. No sample taken.

34/127-35 88983057 1635m – pyroxenite adcumulate with sparse, small feldspathic orthocumulate pockets. Cumulus clinopyroxene predominates over orthopyroxene, and plagioclase is absent except in orthocumulate pockets.

34/127-36 88983058 1653m – melagabbronorite. Large orthopyroxene, smaller clinopyroxene, and elongated plagioclase laths are cumulus phases; orthopyroxene locally tends to a poikilitic texture. Intercalated with pyroxenite.

34/127-37 88983059 1683m – feldspathic orthopyroxenite mesocumulate, locally with orthocumulate pockets. Orthopyroxene is a cumulus phase, clinopyroxene is poikilitic, and plagioclase is interstitial. Forms a ridge.

34/127-38 88983060 1833m – feldspathic pyroxenite orthocumulate. Clinopyroxene is cumulus, orthopyroxene is poikilitic and forms narrow rims around clinopyroxene, and plagioclase is a later poikilitic intercumulus phase. Plagioclase occurs only in local orthocumulate patches. Porphyritic in outcrop.

34/127-39 88983061 1913m – strongly sheared gabbronorite proto-mylonite. Plagioclase, orthopyroxene, and rare clinopyroxene are cumulus relics, with fine-grained clinopyroxene fragments and neoblasts along sheared grain boundaries. Some minor hydrous alteration along cracks.

34/127-40 88983062 1953m – feldspathic pyroxenite orthocumulate. Clinopyroxene is cumulus, and orthopyroxene forms large poikilitic crystals ranging from near-cumulus to intercumulus. Plagioclase is interstitial, but optically continuous over large areas. Porphyritic in outcrop.

34/127-41 88983063 2021m – porphyroclastic gabbronorite mylonite. Deformed plagioclase, orthopyroxene, and rare clinopyroxene cumulus relics in a fine-grained, partly recrystallised anhydrous matrix of plagioclase and clinopyroxene neoblasts.

34/127-42 88983064 2084m – very coarse-grained pyroxenite adcumulate with fine-grained granular pyroxenite adcumulate zones. Pronounced bimodal size distribution of cumulus phases. Both orthopyroxene and clinopyroxene are cumulus; plagioclase was not observed.

34/127-43 88983065 2137m – very coarse-grained annealed pyroxenite adcumulate. Cumulus clinopyroxene grains with interlocked grain boundaries; orthopyroxene apparently rare.

34/127-44A 88983066A 2235m – fine-grained 'doleritic-textured' gabbronorite. Elongated euhedral plagioclase laths with subhedral clinopyroxene between plagioclase laths. Orthopyroxene forms poikilitic grains and rims around clinopyroxene grains. Possibly a rapid cooling texture.

34/127-44B 88983066B 2239m – melagabbro. Cumulus clinopyroxene rimmed by orthopyroxene; small elongated cumulus plagioclase laths are interstitial to clinopyroxene. Texture is quite unlike that of a typical cumulate, since pyroxene/plagioclase ratios are too high for plagioclase to be a cumulus phase. Texture may be due to rapid cooling. Interlayered with orthopyroxenite adcumulates.

34/127-44C 88983066C 2243m – porphyroclastic pyroxenite mylonite. Large pyroxene cumulus relics in a fine-grained granular matrix composed mainly of clinopyroxene.

34/127-45 2315m – pyroxenite.

34/127-46 88983067 2377m – slightly altered coarse-grained pyroxenite. Clinopyroxene and orthopyroxene are cumulus phases, with a bimodal size distribution. No plagioclase observed. Fine-grained opaques along grain boundaries suugest oxidation or alteration. Some gabbronorite present between 45 and 46.

34/127-47 2440m – pyroxenite.

34/127-48 88983068 2510m – slightly deformed feldspathic pyroxenite mesocumulate. Coarse-grained clinopyroxene and orthopyroxene are cumulus phases, locally with strained recrystallised grain boundaries. Interstitial to the cumulus grains are local feldspathic orthocumulate pockets where smaller euhedral cumulus pyroxene grains are embedded in poikilitic plagioclase.

34/127-49 88983069 2558m – coarse-grained pyroxenite adcumulate with abundant feldspathic pyroxenite orthocumulate pockets. Large clinopyroxene and orthopyroxene grains with incipient stress-induced recrystallisation along mutual grain boundaries in adcumulate portions. In orthocumulate pockets, small euhedral clinopyroxene is rimmed by orthopyroxene, and included in large poikilitic plagioclase. Sample from a mixing zone where pyroxenite is intermingled with gabbroic rocks.

34/127-50 88983070 2620m – altered feldspathic pyroxenite orthocumulate. Clinopyroxene is cumulus, orthopyroxene cumulus to poikilitic, and plagioclase a late poikilitic intercumulus phase. Several small shear cracks and thin pseudotachylite veinlets are present.

34/127-51 88983071 2672m – very coarse-grained deformed pyroxenite adcumulate. Cracks and advanced alteration and oxidation of pyroxene due to fluid infiltration.

34/127-52 2776m – mixed unit of gabbro and pyroxenite. No sample taken.

34/127-53 2894m – gabbro with some pyroxenite and pseudotachylite veining. No sample taken.

34/127-54 88983072 2974m – sheared mylonitic uralitised melagabbro. Intense pseudotachylite veining, oxidation during shearing and fluid infiltration. Contains a granitic vein.

34/127-55 3134m – recrystallised gabbro with abundant pseudotachylite veins (similar to 56). No sample taken.

34/127-56A 88983073 3282m – sheared altered mylonitic gabbro with pseudotachylite veinlets. Finely dispersed opaques throughout; fluid infiltration during shearing has caused oxidation of pyroxene.

34/127-56B 88983074 3286m – coarse-grained deformed and altered gabbro. Clinopyroxene oxidised, with finely dispersed opaques along cracks and grain boundaries; plagioclase is altered and zoned. Locally proto-mylonitic texture.

34/127-57 88983038 – plagioclase-phyric dyke. Amphibole and biotite are present in the groundmass.

Hinckley Range gabbronorite intrusion

26/30-1 87980001 5380m – recrystallised anorthositic gabbronorite. Large plagioclase cumulus grains are recrystallised along grain boundaries. Clinopyroxene, rich in exsolved opaque oxide and brown ilmenite platelets, is largely interstitial, but locally recrystallised to smaller granular mosaic grains with rounded oxide grains (recrystallised exsolved grains). Orthopyroxene forms smaller grains in recrystallised zones, possibly at former olivine positions or resulting from granule exsolution from clinopyroxene. Olivine not observed.

26/30-3 87980002 5552m – deformed altered troctolite. Plagioclase, altered olivine relics, and rare irregular opaque oxides are cumulus; orthopyroxene forms large aggregates in vermicular intergrowths with magnetite. Clinopyroxene rims olivine, and amphibole and biotite rim oxide grains. Extensive pseudotachylite infiltration and alteration.

26/30-5 87980003 5514m – olivine-bearing gabbronorite. Plagioclase, exsolved oxide-rich clinopyroxene, orthopyroxene, and a few olivine grains are cumulus. Orthopyroxene also forms vermicular intergrowths with magnetite. Abundant cumulus and intercumulus opaque oxides. Narrow columnar orthopyroxene overgrowths occur around olivine.

26/30-6 87980004 5756m – olivine gabbronorite with a weak lamination. Partly recrystallised plagioclase, olivine, exsolved oxide-rich clinopyroxene, and orthopyroxene are cumulus. Fe–Mg silicates layers define an igneous(?) lamination. Cumulate texture is partly recrystallised. Very fine-grained submicroscopic greenish reaction rims between olivine and plagioclase may be symplectites. Amphibole and biotite quite common around Fe–Mg silicates.

26/30-7A 87980005A 5622m – olivine gabbronorite. Plagioclase and olivine, locally altered, are cumulus, and clinopyroxene is cumulus, grading into poikilitic to interstitial (later than olivine). Orthopyroxene forms rims around olivine, columnar overgrowths, and symplectitic intergrowths with magnetite. Abundant biotite and green–brown amphibole are present. Locally magnetite-rich pegmatoidal varieties conspicuous in outcrop.

26/30-7B 87980005B 5622m – olivine-phyric cross-cutting dyke. Olivine phenocrysts with euhedral spinel inclusions, plagioclase microphenocrysts, and clinopyroxene interstitial to plagioclase, in a fine-grained oxide- bearing matrix. Possible parent to the primitive olivine gabbros and plagioclase-bearing ultramafics of the Wingellina Hills intrusion, or perhaps the more fractionated olivine gabbros of the Hinckley Range intrusion.

26/30-8A 87980006A 5576m – coarse-grained altered poikilitic olivine gabbro. Plagioclase and altered olivine are cumulus, but large exsolved oxide-rich poikilitic clinopyroxene is the volumetrically dominant phase. Orthopyroxene forms wide columnar greenish overgrowths on olivine and symplectitic intergrowths with magnetite. Sheared and altered by fluid infiltration. There is an alternation of fine-grained and coarse-grained pegmatoidal varieties.

26/30-8B 87980006B 5576m – coarse-grained granitoid or granophyre of the Giles Complex. Quartz and K-feldspar occur in graphic intergrowths.

26/30-12 87980007 5336m – olivine–plagioclase-phyric dyke, coarser-grained than 7B. Plagioclase laths, small rounded olivine, and opaque oxides are phenocrysts, and clinopyroxene is interstitial to plagioclase laths and contains olivine inclusions. Clinopyroxene with exsolved oxides is similar to cumulates from the Hinckley Range and elsewhere (e.g., sample 26/30-5). Beautiful texture illustrating an intermediate stage between a

dyke and a 'doleritic-textured' cumulate (e.g., Latitude Hill).

26/30-14 87980008 5100m – gabbronorite. Clinopyroxene, with exsolved oxides, and plagioclase are cumulus phases, partially recrystallised along grain boundaries. Oxide granules occur in recrystallised clinopyroxene aggregates, and there are a few irregular magmatic oxide grains. Intercalated with coarser-grained varieties.

26/30-15 87980009 5074m – gabbronorite. Plagioclase, clinopyroxene, with exsolved oxides, and orthopyroxene are cumulus. A few irregular magmatic oxide grains are largely intercumulus.

26/30-16 87980010 4932m – gabbronorite. Similar to 14 and 15, but slightly more deformed and recrystallised along grain boundaries. Small vermicular clinopyroxene crystallites along boundaries between plagioclase grains suggest Fe–Mg grain boundary diffusion. Cut by a mafic dyke.

26/30-18 87980011 4786m – gabbronorite. Cumulus relics of plagioclase, orthopyroxene, and clinopyroxene in a finer-grained matrix of granular mosaic pyroxene and plagioclase grains. Clinopyroxene is locally poikilitic. Oxide granules associated with recrystallised pyroxene.

26/30-20 87980012 4084m – olivine gabbro. Plagioclase, olivine, and large clinopyroxene, with oxide lamellae, are cumulus; orthopyroxene is slightly later and rims olivine and clinopyroxene. Amphibole forms rims around Fe–Mg minerals, those around olivine apparently in fibrous intergrowth with columnar orthopyroxene. Intercumulus oxides are rimmed by amphibole and minor biotite. Cut by mafic dykes.

26/30-20A 87980013 4084m – olivine-phyric dyke. Olivine and plagioclase form microphenocrysts. Clinopyroxene tends to interstitial, and oxides and some biotite comprise the dirty groundmass. Olivine contains small euhedral spinel inclusions, possibly Cr–Al spinel. A relatively primitive dyke composition.

26/30-22 87980014 3720m – olivine-bearing noritic gabbro. Plagioclase, minor olivine, and clinopyroxene, with abundant exsolved oxides, are cumulus; orthopyroxene occurs as smaller grains mostly attached to clinopyroxene or olivine. Some lamination due to concentration of mafic minerals in layers. Moderately recrystallised, with oxide granules in recrystallised pyroxene-rich layers. Minor amphibole occurs along grain boundaries.

26/30-23 87980015 3548m – olivine-bearing leucogabbronorite. Similar to 22, but more plagioclase and more extensive recrystallisation.

26/30-24 87980016 3448m – gabbroic granulite. Equigranular plagioclase, clinopyroxene, orthopyroxene, and smaller rounded oxide grains. A recrystallised gabbroic cumulate in which exsolved oxide grains have been recrystallised to rounded oxide granules. Similar oxide/pyroxene ratio to partly recrystallised magmatic clinopyroxene aggregates.

27/76-1 87980017 520m – fine-grained gabbroic chilled margin(?) cumulate. Granular rounded clinopyroxene and slightly larger elongated orthopyroxene, with interstitial laths of variably sized zoned brownish plagioclase with submicroscopic inclusions. There are a few large poikilitic euhedral plagioclase grains with numerous pyroxene inclusions. Both irregular magmatic oxide grains and smaller rounded oxide grains, probably due to granule exsolution, are present. Possibly a coarser-grained equivalent to 26/30-12. Interpreted as a marginal recrystallised facies.

27/76-3 87980018 465m – very similar to 1, but slightly coarser-grained.

27/76-4 87980019 488m – coarse-grained plagioclase–olivine-phyric chilled marginal(?) cumulate or marginal facies (cf. 27/76-1). Large rounded to irregular olivine phenocrysts and elongated brownish 'dirty' euhedral plagioclase laths penetrating olivine. Abundant interstitial oxides with some biotite. Columnar orthopyroxene rims olivine, possibly with some fine-grained greenish spinel (olivine and plagioclase in reaction relationship?). Alternation of fine-grained and coarser-grained material in outcrop.

27/76-5 87980020 510m – very similar to 1.

27/76-6A 87980021A 470m – gabbro to gabbroic granulite(?). Gabbroic patches where plagioclase and exsolved oxide-rich clinopyroxene are cumulus and magmatic oxides are intercumulus. These patches are embedded in a much finer-grained equigranular mosaic matrix consisting of neoblastic plagioclase, clinopyroxene, orthopyroxene, and rounded oxide grains. Enigmatic rock type, in which the fine-grained matrix may be due either to partial high-temperature recrystallisation or various cooling rates (no deformation was observed in the coarse-grained gabbroic domains). Most probably represents very high-temperature recrystallisation.

27/76-6B 87980021B 470m – very similar to 1 and 5.

27/76-9 87980022 625m – coarse-grained gabbroic dyke or chilled margin (coarser-grained variety of 1 and 5). Euhedral laths of brownish zoned plagioclase, and smaller clinopyroxene grains interstitial to plagioclase laths. Abundant interstitial magmatic oxide grains, with some rounded oxides due to granule exsolution. Locally close to a genuine cumulate texture.

27/76-10A 87980023A 610m – flow-textured plagioclase-phyric dyke or thick pseudotachylite vein. Undeformed plagioclase phenocrysts in a fine-grained oxide-bearing matrix.

27/76-10B 87980023B 596m – 'doleritic-textured' gabbroic cumulate. Elongated brownish euhedral zoned 'cumulus' plagioclase, with slightly later clinopyroxene locally grading into a poikilitic texture. A few large interstitial oxide aggregates. Sample cut by a pseudotachylite veinlet.

27/76-11A 87980024A 752m – olivine–plagioclase-phyric dyke, locally grading into a sill. Similar in mineralogy to 27/76-4, but much finer-grained. Rounded olivine grains and smaller brownish plagioclase laths are phenocryst phases. Abundant oxides in a fine-grained groundmass may partly result from subsolidus reactions between olivine, plagioclase, and matrix. Columnar orthopyroxene rims olivine.

27/76-11B 87980024B 752m – primitive olivine-phyric dyke. Olivine phenocrysts with euhedral Cr–Al spinel inclusions in a very fine-grained plagioclase–oxide-phyric matrix. Columnar orthopyroxene rims olivine phenocrysts. Plausible parental melt to ultramafic units and gabbroic cumulates of the Wingellina Hills and related intrusions, and ultramafic plugs near Ewarara.

27/76-12 87980025 826m – olivine–plagioclase-phyric sill. Irregular olivine phenocrysts and smaller euhedral brownish plagioclase laths in a fine-grained groundmass, showing advanced hydrous alteration. Microgabbro unit interpreted as recrystallised microgabbro conformable with coarser-grained gabbro.

27/76-14 87980026 1160m – coarse-grained gabbroic troctolite to olivine gabbro. Olivine and plagioclase are cumulus, and olivine is embedded in large poikilitic clinopyroxene grains. Thee are orthopyroxene–magnetite symplectites and columnar orthopyroxene occurs between olivine and plagioclase.

27/76-15 87980027 1428m – troctolite. Plagioclase and olivine are cumulus, and clinopyroxene is poikilitic to intercumulus. Locally wide orthopyroxene rims surround olivine, in places with magnetite symplectites. Indeterminate reaction rims between olivine and plagioclase.

27/76-17 87980028 3258m – deformed altered olivine gabbro to gabbroic troctolite. Granular plagioclase, olivine, and clinopyroxene. The original magmatic cumulate texture is largely obliterated by recrystallisation. Hydrous alteration and local mylonitisation along shear planes. Interlayered with some anorthositic rocks.

27/76-19 87980029 2914m – well layered gabbronorite with graded layering. Plagioclase, orthopyroxene, and exsolved oxide-rich clinopyroxene are cumulus. Local oxide grains formed by granule exsolution.

27/76-23 87980030 2460m – deformed altered olivine gabbro. Olivine, plagioclase, and clinopyroxene are cumulus, clinopyroxene locally grading into intercumulus. Abundant oriented clinopyroxene neoblasts within plagioclase. Several small shear zones, with associated fluid infiltration (oxidation of Fe–Mg silicates).

27/76-26 87980031 2140m – sheared recrystallised olivine gabbro to gabbroic troctolite. Original magmatic texture largely obliterated by shearing and oxidation due to fluid infiltration. Numerous shear zones.

27/76-28 87980032 1946m – gabbroic mylonite with massive pseudotachylite, in places several metres thick.

27/76-29 87980033 2040m – deformed altered olivine gabbro. The original magmatic texture is largely obliterated by shearing and oxidation due to fluid infiltration. Numerous dark oxide/hydroxide-rich shear zones. Gradations between sheared gabbro and pseudotachylite in outcrop.

27/76-30A 87980034A 2060m – same as 29. Several dark pseudotachylite veinlets within a shear zone.

27/76-30B 87980034B 2060m – massive oxide-rich layer or lens in deformed gabbro.

27/76-40 87980035 1640m – deformed altered gabbroic troctolite to olivine gabbro. Olivine and plagioclase are cumulus, and clinopyroxene is interstitial. Wide columnar orthopyroxene rims around olivine, possibly containing another phase (spinel?). Several small mylonite zones grade into pseudotachylite.

Bell Rock troctolite/gabbro intrusion

29/168-1 88982001 3556m – troctolite. Plagioclase, olivine, and rounded oxide grains are cumulus; orthopyroxene, with numerous small olivine inclusions, and less abundant clinopyroxene are poikilitic to interstitial phases. Fine-grained 'cauliflower' symplectites occur in plagioclase at olivine–plagioclase contacts.

29/168-2 88982002 3530m – troctolite. Plagioclase, olivine, and rounded oxides are cumulus. Orthopyroxene forms wide poikilitic rims around some olivine grains, and columnar overgrowths on others. Clinopyroxene is interstitial and less common than orthopyroxene. Fine-grained 'cauliflower' symplectites occur in plagioclase and at olivine–plagioclase contacts.

29/168-3 88982003 3453m – troctolite. Similar to 2, but slightly higher olivine/plagioclase ratio and more pyroxene.

29/168-5 88982004 3337m – troctolite. Plagioclase, olivine, and rounded opaque oxides are cumulus phases. Olivine forms large aggregates, embedded in poikilitic orthopyroxene and, less commonly, clinopyroxene. Columnar orthopyroxene rims most olivine grains, and fine-grained 'cauliflower' symplectites in plagioclase occur at olivine–plagioclase contacts.

29/168-6 88982005 3280m – troctolite. Similar to 5, but almost no primary magmatic oxides. Contains orthopyroxene–magnetite symplectites. A weak pyroxene–plagioclase layering is present.

29/168-8 88982006 3177m – olivine-bearing anorthosite. Plagioclase and a few oxide grains are cumulus, and minor irregular olivine is cumulus to interstitial. Orthopyroxene forms wide rims around olivine, commonly grading into poikilitic grains, narrow columnar overgrowths, and symplectites with magnetite. Clinopyroxene is interstitial, and also forms narrow rims around olivine. Fine-grained 'cauliflower' symplectites occur in plagioclase and at olivine–plagioclase contacts.

29/168-9 88982007 3130m – very fine-grained plagioclase–olivine-phyric dykelet, in contact with altered anorthosite. The dyke has a phenocryst mineralogy resembling in detail the cumulus mineralogy of the fractionated troctolitic intrusions of the Giles Complex (Bell Rock and Blackstone). The host cumulates are locally pegmatoidal.

29/168-11 88982008 3042m – altered sheared anorthosite. Plagioclase and rare euhedral oxides are cumulus, and minor clinopyroxene is poikilitic to interstitial. No olivine observed.

29/168-13 88982009 2948m – anorthositic troctolite. Plagioclase, a few oxide grains, and irregular olivine are cumulus, whereas orthopyroxene and clinopyroxene are poikilitic to interstitial, especially in olivine-rich aggregates. Some minor biotite occurs around oxides. Very minor fine-grained 'cauliflower' symplectites occur in plagioclase and at olivine–plagioclase contacts.

29/168-14A 88982010A 2885m – altered deformed troctolite. Plagioclase, a few oxide grains, and altered olivine are cumulus, and orthopyroxene and clinopyroxene intercumulus. All olivine and some oxide grains are surrounded by fine-grained 'cauliflower' symplectites, enhanced by fluid infiltration. Sample shows shearing and minor pseudotachylite veining.

29/168-14B 88982010B 2885m – fine-grained olivine–plagioclase-phyric sill, in contact with altered sheared anorthosite. Same phenocryst population as the cumulus phases in the Bell Rock cumulates; probably one of the parental magmas of the intrusion.

29/168-15 88982011 2876m – troctolite. Plagioclase, opaque oxides, and olivine are cumulus, and orthopyroxene is poikilitic and grown around olivine; clinopyroxene forms narrow rims around olivine. Some Fe–Mg minerals are rimmed by amphibole and biotite.

29/168-16 88982012 2833m – troctolite. Olivine, opaque oxides, and plagioclase are cumulus; clinopyroxene, with exsolved oxides, and less common orthopyroxene are poikilitic phases.

29/168-17 88982013 2731m – troctolite. Plagioclase and small rounded olivine grains are cumulus, and orthopyroxene forms rims around olivine and intergrowths with magnetite, grading into poikilitic grains.

29/168-18 88982014 2700m – gabbroic troctolite. Olivine, a few oxide grains, and plagioclase are cumulus, and clinopyroxene (rich in exsolved oxides) and orthopyroxene form large poikilitic grains. Oxide grains mainly represent granule exsolution from recrystallised clinopyroxene, but orthopyroxene–magnetite symplectites are also present. Biotite rims Fe–Mg silicates.

29/168-19B 88982015 2684m – anorthosite. Rare altered cumulus olivine relics, mantled by orthopyroxene, and rare clinopyroxene interstitial to cumulus plagioclase.

29/168-20 88982016 2621m – olivine-phyric sill. Abundant plagioclase microphenocrysts, with some clinopyroxene and euhedral oxides in a dark, oxide-rich groundmass. Locally glomerophyric phenocryst accumulations and pseudotachylite veinlets. Possibly a parental magma to the Bell Rock intrusion.

29/168-21A 88982017A 2504m – troctolite. Olivine, a few large oxide grains, and plagioclase are cumulus; rare orthopyroxene forms rims around olivine and symplectitic intergrowths with magnetite.

29/168-21B 88982017B 2504m – plagioclase-phyric dyke. Brownish inclusion-rich dirty plagioclase microphenocrysts and a few large phenocrysts in an oxide-rich groundmass. Minor clinopyroxene is interstitial to plagioclase laths. Another possible parental magma to the Bell Rock intrusion.

29/168-24A 88982018A 2149m – fine-grained troctolite. Rounded olivine and plagioclase are cumulus, clinopyroxene is poikilitic, and orthopyroxene is mainly in symplectitic intergrowths with magnetite. Oxide grains are mostly derived from recrystallised clinopyroxene. Cut by a mafic dyke.

29/168-24B 88982018B 2149m – coarse-grained olivine-plagioclase-phyric dyke. Large 'cumulus' olivine, dirty brownish plagioclase laths (cf. plagioclase in the rapidly cooled Latitude Hill intrusion), and 'interstitial' clinopyroxene similar to a poikilitic texture. Very close to a genuine cumulus texture.

29/168-25A 88982019A 1973m – coarse-grained anorthositic to gabbroic troctolite. Plagioclase and large irregular olivine are cumulus phases, clinopyroxene (exsolved oxide-rich) forms large poikilitic crystals, and opaque oxides are interstitial. Narrow orthopyroxene rims occur around olivine.

29/168-25B 88982019B 1973m – weakly layered massive opaque oxide unit with some green exsolved spinel or intergrowths.

29/168-27 88982020 1778m – altered sheared troctolite. Olivine and plagioclase are cumulus, and opaque oxides intercumulus. Massive fluid infiltration along cracks with associated hydrous alteration. Pseudotachylite veinlets present.

29/168-28 88982021 1693m – altered oxide-rich troctolite. Olivine and plagioclase are cumulus, and opaque oxides surround altered rounded olivine grains. Local shearing and hydrous alteration.

29/168-29 88982022 1623m – altered troctolite. Olivine and plagioclase, both highly altered and deformed, are cumulus phases. Pseudotachylite veins present.

29/168-31 88982023 3575m – troctolite. Olivine, plagioclase, and a few rounded oxide grains are cumulus, and clinopyroxene with exsolved oxide lamellae are poikilitic. Orthopyroxene forms rims around olivine and symplectitic intergrowths with magnetite. Rare biotite flakes are associated with magmatic oxide grains, and fine-grained 'cauliflower' symplectites occur in plagioclase at olivine–plagioclase contacts.

29/169-2 88982024 55m – coarse-grained plagioclase–olivine-phyric sill or pod of microgabbro within coarser-grained gabbroic cumulates. Olivine and euhedral brownish plagioclase laths (rich in submicroscopic inclusions) are phenocrysts, with a second generation of plagioclase microphenocrysts. Groundmass contains fine-grained clinopyroxene, oxides, and biotite. Phenocryst mineralogy resembles the cumulus mineralogy in the Bell Rock troctolites.

29/169-5 88982025 280m – olivine gabbronorite. Plagioclase, minor altered olivine, and a few opaque oxide grains are cumulus, with abundant large poikilitic grains of exsolution-rich clinopyroxene. Minor orthopyroxene occurs mainly around olivine and intergrown with vermicular magnetite.

29/169-6 88982026 412m – similar to 5, but more plagioclase-rich.

29/169-7A 88982027A 451m – troctolite. Plagioclase, olivine, and opaque oxides are cumulus, and exsolution-rich clinopyroxene is poikilitic to interstitial. Large irregular magmatic oxide grains are associated with biotite, whereas small rounded oxide grains result from exsolution from clinopyroxene.

29/169-7B 88982027B 451m – olivine gabbro to gabbroic troctolite. Plagioclase, opaque oxides, and large olivine grains are cumulus, and abundant exsolution-rich clinopyroxene and orthopyroxene are poikilitic, locally grading into cumulus textures. Biotite flakes are attached to magmatic oxides, and small rounded oxide blebs represent granule exsolution from recrystallised clinopyroxene.

29/169-9 88982028 590m – troctolitic anorthosite. Plagioclase is cumulus, and olivine cumulus, locally grading into intercumulus. Magmatic oxides form large poikilitic grains; clinopyroxene is intercumulus. Minor orthopyroxene is mainly attached to olivine.

29/169-9B 88982029 590m – olivine–plagioclase–oxide-phyric sill. Moderately abundant olivine phenocrysts, abundant plagioclase microphenocrysts, and rounded oxide grains with minor biotite are set in a fine-grained groundmass of clinopyroxene, oxides, and hydrous silicates. Phenocryst mineralogy resembles the crystallisation sequence in the troctolitic cumulates. A 2 metre-thick sill of microgabbro, with a coarser-grained central zone and fine-grained chilled margins.

29/169-11 88982030 1138m – anorthosite. Minor interstitial clinopyroxene and magmatic opaque oxides, but no olivine observed.

29/169-12 88982031 1191m – same as 9B. Pseudotachylite veinlet at the contact between sheared altered gabbroic anorthosite cumulate and a sill.

29/169-13 88982032 1296m – recrystallised olivine gabbronorite. Olivine and opaque oxides are cumulus; plagioclase is entirely and clinopyroxene partly recrystallised to an equigranular medium-grained metamorphic texture. Gabbro and microgabbro are conformably interlayered.

29/169-14 8982033 1386m – pegmatoidal gabbronorite. Large plagioclase grains, clinopyroxene with dense exsolved opaque oxides and ilmenite platelets, orthopyroxene with fewer exsolution lamellae, and minor interstitial oxides.

29/169-15 88982034 1458m – fine-grained clinopyroxene-phyric sill, chilled against altered troctolite. Clinopyroxene phenocrysts and plagioclase microphenocrysts are set in a dark matrix. The troctolite contains cumulus olivine and plagioclase, minor intercumulus clinopyroxene and orthopyroxene associated with olivine. Narrow columnar orthopyroxene rims surround olivine grains.

29/169-16 88982035 1488m – altered recrystallised feldspathic dunite. Rounded olivine and minor plagioclase. The original magmatic texture is largely obliterated, being recrystallised to a granoblastic fabric.

29/169-17 88982036 1514 – anorthositic troctolite. Plagioclase, olivine, and rare magmatic oxides are cumulus. Orthopyroxene and clinopyroxene are interstitial, commonly growing around olivine grains. Intruded by felsic veins.

Murray Range pyroxenite/peridotite/gabbro intrusion

17/34-1A 88980001 2580m – slightly annealed fine-grained feldspathic pyroxenite mesocumulate, locally adcumulate and orthocumulate zones. Clinopyroxene and orthopyroxene are cumulus; intercumulus feldspar tends to be antiperthitic in mesocumulate to adcumulate sections.

17/34-2A 88980002 2570m – fresh feldspathic peridotite. Cumulus olivine and cumulus spinel are surrounded by poikilitic and interstitial orthopyroxene and clinopyroxene. Clinopy-

roxene is dark brown due to abundant exsolved spinel. Columnar orthopyroxene overgrows olivine. Intercumulus plagioclase is zoned in contact with Fe–Mg silicates, particularly near olivine. Locally near-opaque cumulus chromite is concentrated in poikilitic clinopyroxene and intercumulus spaces. Red–brown biotite is commonly associated with oxides. Clinopyroxene–spinel symplectites occur at spinel–plagioclase contacts and olivine–clinopyroxene–spinel symplectites at olivine contacts; spinel in these symplectites is brownish to greenish, well equilibrated and crystallised.

17/34-2B 88980003 2566m – pegmatoidal feldspathic clinopyroxenite, locally with quartz–orthoclase–apatite–biotite segregations (good sample to search for zircon). Clinopyroxene with abundant exsolved spinel is cumulus, and abundant plagioclase is intercumulus. Incipient recrystallisation has occurred along grains boundaries. This rock may have crystallised from a fractionated 'squeezed' intercumulus melt derived from more ultramafic cumulates, such as 2A.

17/34-3 88980004 2560m – feldspathic pyroxenite, locally with an orthocumulate texture. Clinopyroxene and orthopyroxene are cumulus, and plagioclase poikilitic to intercumulus. Pyroxene has a distinctly bimodal size distribution. Rock is intensely fractured and slightly altered due to fluid infiltration. Interlayered fine-grained and coarse-grained porphyritic pyroxenite.

17/34-4A 88980005 2472m – laminated to massive leucogabbronorite. Plagioclase, large orthopyroxene grains, and clinopyroxene are cumulus, with clinopyroxene locally intercumulus and recrystallised to small neoblasts. Orthopyroxene contains exsolved ilmenite, and abundant small opaque oxide (?magnetite and ilmenite) neoblasts are due to granule exsolution from clinopyroxene.

17/34-4B 88980006 2468m – strained leucogabbronorite with proto-mylonitic texture. Plagioclase and orthopyroxene are cumulus; clinopyroxene is largely recrystallised to interstitial neoblasts and fragments. Porphyroblastic orthopyroxene is largely undeformed. Small clinopyroxene needles in plagioclase may be recrystallised impurities trapped in plagioclase due to rapid growth. Interlayered with porphyritic pyroxenite and cut by quartzo-feldspathic veins.

17/34-4C 88980007 2464m – amphibolite. Recrystallised anorthositic gabbro in which clinopyroxene is completely altered to blue–green (sodic?) amphibole and epidote. Relict cumulus texture.

17/34-4D 88980009 2462m – fresh feldspathic wehrlite orthocumulate. Olivine, rare opaque spinel, and clinopyroxene are cumulus, and plagioclase is intercumulus; clinopyroxene locally grades into poikilitic grains with rounded cores extremely rich in exsolved brownish spinel (an early clinopyroxene generation?). Orthopyroxene forms wide columnar overgrowths on olivine, locally with spinel symplectites. Greenish spinel is common at contacts between Fe–Mg silicates and plagioclase. Rare chromite inclusions occur in clinopyroxene.

17/34-5 88980010 2442m – feldspathic harzburgite orthocumulate. Olivine, chromite, and orthopyroxene are cumulus, whereas clinopyroxene is mostly poikilitic. Orthopyroxene is commonly included in poikilitic clinopyroxene, in places forming large elongated crystals, possibly due to rapid growth. Zoned plagioclase is a minor intercumulus phase. Localised orthocumulate pockets have orthopyroxene and chromite as the main cumulus phases, with interstitial plagioclase. Cumulus chromite is in reaction relationship with plagioclase.

17/34-6 88980011 2354m – primitive serpentinised olivine-rich poikilitic dunite orthocumulate. Olivine and chromite are cumulus, clinopyroxene is poikilitic, and altered plagioclase is intercumulus. Very little orthopyroxene identified. Extensive alteration.

17/34-8 88980012 2426m – fine-grained feldspathic orthopyroxenite orthocumulate. Orthopyroxene is cumulus, clinopyroxene poikilitic, and plagioclase intercumulus and locally antiperthitic. Some orthopyroxene grains are distinctly elongated and rich in exsolved spinel, possibly rapid growth features. No olivine observed.

17/34-9A 88980013 2376m – slightly deformed altered coarse-grained gabbronorite. Clinopyroxene, orthopyroxene, and commonly zoned plagioclase are cumulus. Abundant spinel neoblasts represent granule exsolution from pyroxene.

17/34-9B 88980014 2372m – amphibolite (relict gabbro). Clinopyroxene is entirely replaced by large euhedral grains of green–blue (sodic?) amphibole. Magmatic plagioclase is preserved.

17/34-10 88980015 2280m – fine-grained recrystallised gabbronorite. Small orthopyroxene, clinopyroxene, and locally elongated plagioclase are cumulus. Abundant neoblasts form inclusions in plagioclase, probably recrystallised impurities.

17/34-11A 88980016 2272m – gabbronorite. Large orthopyroxene porphyroblasts and plagioclase, in a matrix of small clinopyroxene and plagioclase neoblasts. Sharp contact between a very fine-grained variety and a coarser-grained unit.

17/34-11B 88980017 2268m – orthopyroxenite orthocumulate. Orthopyroxene, locally as distinctly elongated grains, is cumulus. Clinopyroxene, rich in brownish exsolved spinel, is poikilitic, grading to intercumulus; rare plagioclase is intercumulus. Orthopyroxene grains in poikilitic clinopyroxene are marginally resorbed. Brownish spinel neoblasts along grain boundaries. No olivine observed.

17/34-12A 88980018 2182m – coarse-grained pegmatoidal feldspathic clinopyroxenite orthocumulate, recrystallised and fragmented along grain boundaries. Large clinopyroxene grains are rich in exsolved spinel and ilmenite. Plagioclase contains abundant very fine-grained impurities (?clinopyroxene).

17/34-12B 88980019 2178m – feldspathic orthopyroxenite mesocumulate. Euhedral orthopyroxene is cumulus, and plagioclase and clinopyroxene are interstitial. Clinopyroxene locally grades into a poikilitic texture. Both pyroxenes, particularly clinopyroxene, are rich in exsolved spinel,.

17/34-13 88980020 2172m – pegmatoidal feldspathic clinopyroxenite orthocumulate. Clinopyroxene, locally rich in exsolved spinel and ilmenite, is cumulus; zoned plagioclase is cumulus to intercumulus.

17/34-14A 88980021 2144m – coarse-grained altered feldspathic pyroxenite orthocumulate. Clinopyroxene and orthopyroxene are cumulus, and altered zoned plagioclase is intercumulus. Primary phases are locally wholly replaced by hydrous minerals.

17/34-14B 88980022 2140m – coarse-grained feldspathic orthopyroxenite orthocumulate. Euhedral orthopyroxene is cumulus, rare clinopyroxene poikilitic, and plagioclase intercumulus. Plagioclase contains very fine-grained impurities, possibly a rapid crystallisation feature. Plagioclase too abundant to be an intercumulus phase. These orthopyroxenite cumulates may have formed under conditions of rapid crystallisation where fresh hot magma mixed with a cooler and more siliceous fractionated melt, and where trapped liquid could not escape by compaction due to rapid solidification.

17/34-15 88980023 2082m – weakly layered recrystallised annealed orthopyroxenite adcumulate. Orthopyroxene is a cumulus phase, and very rare plagioclase is intercumulus. No olivine observed. Brown spinel granules have exsolved from

orthopyroxene and concentrated along grain boundaries.

17/34-16 88980024 2062m – coarse-grained pyroxenite adcumulate. Large orthopyroxene and lesser clinopyroxene are cumulus phases, and minor to rare plagioclase is intercumulus. Highly altered brownish rounded relics of olivine are present.

17/34-18A 88980025 1992m – coarse-grained, locally pegmatoidal olivine-bearing pyroxenite. Orthopyroxene, rounded olivine grains, and euhedral spinel are cumulus, orthopyroxene and clinopyroxene are poikilitic, and plagioclase is intercumulus. In one place, cumulus orthopyroxene is surrounded by olivine. There is a distinctly bimodal size distribution, with some large elongated orthopyroxene grains. Exsolved spinel in pyroxene is locally recrystallised to granules.

17/34-18B 88980026 1988m – feldspathic pyroxenite orthocumulate, locally grading into melagabbro. Large elongated clinopyroxene is the main cumulus phase; plagioclase is intercumulus, locally approaching cumulus textures. Cumulus clinopyroxene is locally recrystallised to small neoblasts. Rock has a pegmatoidal appearance in outcrop.

17/34-18C 88980027 1984m – pegmatoidal olivine-bearing pyroxenite orthocumulate. Large orthopyroxene and clinopyroxene cumulus crystals have inclusions of altered olivine. Olivine in contact with plagioclase is surrounded by columnar orthopyroxene. All pyroxenes are rich in exsolved spinel. Intercumulus plagioclase is locally highly altered.

17/34-19A 88980028 1956m – pyroxenite adcumulate. Orthopyroxene and clinopyroxene are cumulus, with orthopyroxene predominating over clinopyroxene. Plagioclase is a rare intercumulus phase.

17/34-19B 88980029 1952m – olivine-bearing pyroxenite adcumulate, locally grading into peridotite. Olivine, euhedral opaque spinel, and orthopyroxene are cumulus. Orthopyroxene locally grades into a poikilitic texture relative to olivine, and clinopyroxene tends towards interstitial positions. All pyroxenes are rich in exsolved spinel, clinopyroxene more so than orthopyroxene. Intercumulus plagioclase is altered and very rare.

17/34-20A 88980030 1898m – highly altered serpentinised dunitic orthocumulate. Olivine and rare brown spinel are cumulus phases. Dark brown clinopyroxene (rich in exsolved spinel) and brownish orthopyroxene are intercumulus, and locally poikilitic. No plagioclase observed.

17/34-20B 88980031 1894m – same as 20A.

17/34-20C 88980032 1890m – amphibolite, possibly derived from an ultramafic dunitic orthocumulate (cf. 20A). There is a relict cumulus texture.

17/34-21 88980033 1810m – olivine-bearing orthopyroxenite adcumulate. Minor olivine and abundant orthopyroxene are cumulus, and brown spinel-rich clinopyroxene is intercumulus. Olivine and orthopyroxene are apparently cotectic. All pyroxenes are rich in exsolved spinel granules, interstitial clinopyroxene more so than orthopyroxene. No plagioclase found.

17/34-22 88980034 1770m – orthopyroxenite adcumulate. Large elongated orthopyroxene and rare olivine relics are cumulus; intercumulus clinopyroxene is rich in exsolved spinel. Olivine is commonly replaced by mosaic orthopyroxene granules. Granules of exsolved brown spinel in pyroxene are concentrated along grain boundaries. No plagioclase found.

17/34-24A 88980035 1636m – amphibolite. Strongly recrystallised magmatic plagioclase and greenish-bluish amphibole are the main constituents. There is a relict cumulus texture of a strained gabbro to anorthosite, with a local proto-mylonitic texture. A sheared hydrated ultramafic rock with some chrysoprase veins.

17/34-24B 88980036 1632m – olivine-bearing orthopyroxenite adcumulate to mesocumulate, grading into harzburgite cumulate. Olivine and orthopyroxene are cumulus, i.e., not in a peritectic reaction relationship with melt. Euhedral opaque spinel is a minor cumulus phase. Clinopyroxene is intercumulus, and all pyroxenes are rich in exsolved spinel, clinopyroxene more so than orthopyroxene. Exsolved granular spinel occurs along grain boundaries. The cumulus phases have a bimodal size distribution.

17/34-27 88980037 1506m – amphibolite. No relict cumulus texture nor primary magmatic phase is preserved.

17/34-28 88980038 1489m – mafic dyke. A fine-grained biotite-rich mafic rock with a few large orthopyroxene grains rich in exsolved opaque grains (oxidation?). A mafic dyke that has apparently been partly recrystallised.

17/34-29 88980039 1417m – wehrlite adcumulate. Olivine, clinopyroxene, and opaque spinel are cumulus; orthopyroxene is intercumulus, and also occurs as exsolution lamellae in clinopyroxene, and as reaction rims around olivine. Clinopyroxene is somewhat recrystallised and exsolved, spinel granules occur along grain boundaries. All pyroxenes are rich in exsolved spinel, clinopyroxene more so than orthopyroxene.

17/34-30A 88980040 1355m – wehrlite adcumulate. Olivine and clinopyroxene are cumulus, but no cumulus spinel was found. Clinopyroxene is strongly annealed and exsolved, and orthopyroxene occurs only as exsolved grains within and between clinopyroxene, and as reaction rims around olivine. Spinel and orthopyroxene granules are concentrated along grain boundaries.

17/34-30B 88980041 1351m – coarse-grained olivine-bearing feldspathic orthopyroxenite mesocumulate. Large orthopyroxene, minor olivine, and rare euhedral opaque spinel are cumulus, and minor clinopyroxene between cumulus and interstitial. No peritectic reaction relationship apparent between olivine, orthopyroxene, and melt. Plagioclase is intercumulus.

17/34-31 88980042 1463m – wehrlite adcumulate. Olivine and clinopyroxene are cumulus phases, and orthopyroxene is present only as exsolution lamellae in clinopyroxene and as reaction moats around olivine. Clinopyroxene is extremely rich in exsolved brown spinel granules. No plagioclase observed.

17/34-32 88980043 1319m – same as 31.

17/34-33A 88980044 1249m – wehrlite adcumulate (similar to 31). Olivine and exsolution-rich clinopyroxene are cumulus phases. Orthopyroxene is present as exsolution lamellae, as reaction rims around olivine, and as a rare intercumulus phase. Clinopyroxene is extremely rich in exsolved brown spinel granules. No plagioclase observed, but plagioclase-rich lithologies are present in outcrop.

17/34-33B 88980045 1245m – altered wehrlite adcumulate, with dunitic patches alternating with wehrlite. Partially serpentinised olivine, clinopyroxene, and opaque spinel are cumulus phases, and orthopyroxene is poikilitic to interstitial. Clinopyroxene is extremely rich in brown exsolved spinel. No plagioclase observed.

17/34-33C 88980046 1241m – amphibolite. Plagioclase is partly preserved, with a relict gabbroic texture.

17/34-34A 88980047 1195m – olivine-bearing pyroxenite adcumulate. Clinopyroxene (rich in exsolved spinel), minor olivine, and orthopyroxene are cumulus. Orthopyroxene also occurs as exsolution lamellae in clinopyroxene, as granules along grain boundaries, and as reaction moats around olivine. Both pyroxenes are rich in exsolved brownish spinel, clinopyroxene more so than orthopyroxene. No plagioclase observed.

17/34-34B 88980048 1191m – deformed gabbronorite. Plagioclase and orthopyroxene are cumulus, with large deformed kinked orthopyroxene phenocrysts. Clinopyroxene tends towards interstitial positions and is preferentially recrystallised and locally replaced by greenish sodic amphibole. Proto-mylonitic texture.

17/34-35 88980049 1157m – same as 34B

17/34-36A 88980050 1215m – altered serpentinised coarse-grained wehrlite adcumulate. Partly serpentinised olivine, clinopyroxene, and minor orthopyroxene are cumulus. No cumulus spinel or plagioclase observed. There is extensive alteration along one prominent veinlet. Clinopyroxene is extremely rich in exsolved brown spinel and orthopyroxene granules. Possible cross-cutting relationships suggest that the rock may be a dyke.

17/34-36B 88980051 1211m – sheared, strongly altered gabbroic dyke cutting peridotite. Proto-mylonitic texture.

17/34-37 88980052 1119m – olivine-bearing clinopyroxenite with ad- to mesocumulate texture. Rare olivine and exsolved brown spinel-rich clinopyroxene are cumulus phases; orthopyroxene is interstitial, and also forms exsolved grains and reaction moats around olivine. No plagioclase observed. Granule exsolution of spinel and orthopyroxene, with concentration of granules along grain boundaries.

17/34-38 88980053 1041m – annealed pyroxenite adcumulate. Clinopyroxene and tabular elongated orthopyroxene are cumulus. No plagioclase observed.

17/34-39 88980054 1006m – strongly deformed gabbro. Pyroxene is largely broken up into small fragments (proto-cataclasite to proto-mylonite). Adjacent to pyroxenite unit.

17/34-40 88980055 950m – deformed leucogabbronorite, with a proto-mylonitic to cataclastic texture. Cumulus clinopyroxene is largely broken up and/or recrystallised, but magmatic orthopyroxene is preserved. There are abundant small clinopyroxene inclusions in plagioclase. Part of a narrow mylonite zone.

17/34-41A 88980056 900m – strongly sheared leucogabbronorite (proto-)mylonite. Relict clinopyroxene and plagioclase are set in a fine-grained recrystallised matrix of plagioclase and clinopyroxene. Orthopyroxene is largely preserved. Locally replaced by amphibolite in outcrop.

17/34-41B 88980057 896m – amphibolite. Plagioclase relics set in a matrix of fine-grained greenish-bluish amphibole. Possibly a more altered proto-mylonite, similar to 41A, but no pyroxene is preserved.

17/34-42A 88980058 844m – strongly sheared gabbronorite (proto-cataclasite). Fragments of pyroxene and plagioclase in a fine-grained groundmass. Sample from a gabbro–pyroxenite contact.

17/34-42B 88980059 840m – coarse-grained orthopyroxenite adcumulate. Orthopyroxene and possibly relict olivine are cumulus. Interstitial clinopyroxene and plagioclase are rare. Ultramafic patches in predominantly leucocratic material.

17/34-42C 88980060A 836m – leucogabbronorite proto-cataclasite. Plagioclase, clinopyroxene, and orthopyroxene are cumulus. Clinopyroxene is broken up into small fragments, but orthopyroxene and plagioclase are largely preserved. There are abundant small clinopyroxene inclusions in plagioclase.

17/34-43 88980060B 798m – annealed pyroxenite. Clinopyroxene, lesser orthopyroxene, and one orthopyroxene–magnetite symplectite pseudomorph after olivine are cumulus. No plagioclase observed. Minor granule exsolution of spinel.

17/34-44 88980060C 770m – gabbroic/amphibolitic mylonite to cataclasite. Porphyroclastic 'augen' of clinopyroxene, plagioclase, and brown–green hornblende (after clinopyroxene?) are set in a fine-grained fragmental matrix of plagioclase, post-deformational actinolitic amphibole, and some biotite. Part of a major mylonite zone with numerous felsic veins.

17/34-45 88980061A 714m – coarse-grained pyroxenite adcumulate. Clinopyroxene and orthopyroxene are cumulus and rich in exsolved spinel. There is incipient recrystallisation and cataclasis along grain boundaries, but little grain deformation. Sample apparently close to a major mylonite zone.

17/34-46 88980061B 30m – gabbronorite. No sample taken. Weakly layered gabbro, with some siliceous veins.

17/34-47 95m – aplitic vein or aphanitic siliceous plug. No sample taken.

17/34-48 105m – gabbronorite. Possibly similar to 49.

17/34-49 88980061C 90m – deformed leucogabbronorite. Plagioclase, clinopyroxene, and orthopyroxene are cumulus. Clinopyroxene is partly recrystallised to smaller grain aggregates. Pyroxenes are rich in exsolved magnetite and ilmenite, with oxidation during deformation evident. There is incipient mylonitisation along grain boundaries. Intruded by a felsic vein.

17/34-50 – granitic pegmatite vein.

17/34-51A 88980062 118m – deformed leucogabbronorite (similar to 49). Plagioclase and pyroxene are cumulus, with pyroxenes rich in exsolved opaque grains, including ilmenite, due to syn-deformational oxidation. The proto- mylonitic texture is more advanced than in 49.

17/34-51B 88980063 114m – granitic pegmatite. Contains coarse-grained post-deformational muscovite.

17/34-52A 88980064 140m – felsic mylonite with secondary post-deformational silification.

17/34-52B 88980065 136m – strongly deformed gabbronorite cataclasite. Large cumulus orthopyroxene relics, with exsolved ilmenite, and fragments of cumulus plagioclase, are set in a fragmental matrix of clinopyroxene and plagioclase.

17/34-54 300m – pyroxenite, patchy footwall contact with gabbroic material. No sample taken.

17/34-55A 88980066 398m – undeformed annealed pyroxenite adcumulate. Clinopyroxene and orthopyroxene are cumulus, with rare interstitial plagioclase. No exsolved spinel in pyroxene.

17/34-55B 88980067 394m – strongly deformed feldspathic pyroxenite. Large fragments of clinopyroxene and orthopyroxene in a matrix of pyroxene fragments and neoblasts and rare interstitial plagioclase. Proto-mylonite, locally grading into mylonite or cataclasite. Between 54 and 55 is some minor gabbroic material. Part of a mylonite zone.

17/34-56 600m – apparently a shear zone within a layered pyroxenite–gabbro sequence. Some granitic pegmatite is present. No sample taken due to poor outcrop.

17/34-57A 88980068 654m – deformed gabbronorite. Plagioclase, clinopyroxene, and orthopyroxene are cumulus. There are abundant clinopyroxene inclusions in plagioclase. Proto-mylonitic texture. Contact with pyroxenite (sample 57B).

17/34-57B 88980069 650m – deformed pyroxenite. Large cumulus orthopyroxene relics in a matrix of finer-grained and deformed clinopyroxene. Very minor recrystallisation along grain boundaries, so not quite a proto-mylonite. No plagioclase observed.

17/34-58 88980070 548m – silicified, carbonated, ferruginous ultramafic cumulate. Goethite pseudomorphs after olivine

in a matrix of chlorite and quartz. Quartz veins present throughout the rock.

17/36-1 – coarse-grained holocrystalline plagioclase–clinopyroxene-phyric dyke. Elongated plagioclase, rich in impurities, is the main phenocryst phase. Interstitial to plagioclase laths are granular greenish clinopyroxene–oxide aggregates with some biotite. The dyke may be equivalent to fractionated gabbronorite units in which clinopyroxene is close to becoming intercumulus, is rich in exsolved oxides, and commonly forms grain aggregates rather than single grains (e.g., in the Hinckley Range intrusion).

Blackstone Range troctolite/gabbro intrusion

22/12-1 90980132 1778m – anorthositic troctolite. Olivine, rare opaque oxides, and abundant plagioclase are cumulus, whereas clinopyroxene with exsolved oxide lamellae is poikilitic to interstitial. Some olivine and clinopyroxene grains are rimmed by brown amphibole.

22/12-2 90980133 1873m – altered troctolite. Olivine, rare opaque oxides, and plagioclase are cumulus, and clinopyroxene with exsolved oxide lamellae is interstitial. There is actinolitic alteration along grain boundaries, and brown amphibole rims some clinopyroxene and olivine grains. Interlayerrd magnetite-bearing troctolite and gneissose anorthosite.

22/12-3 90980134 1960m – well-layered fine-grained amphibolite. Sample from a folded mylonite zone with some pseudotachylite.

22/12-4 90980135 2014m – anorthositic to gabbroic troctolite. Plagioclase and rare opaque oxides are cumulus, and olivine is cumulus, grading to intercumulus. Abundant clinopyroxene is poikilitic to interstitial; some orthopyroxene is attached to olivine or intergrown with magnetite in symplectites.

22/12-5 90980136 2105m – troctolitic to gabbroic anorthosite. Plagioclase and sparse small olivine grains are cumulus, abundant coarse-grained clinopyroxene is poikilitic to intercumulus, and orthopyroxene and opaque oxides are intercumulus. Very fine-grained 'cauliflower' symplectites, possibly involving colourless spinel, occur at olivine–plagioclase and oxide–plagioclase contacts. Biotite is associated with opaque oxides. Some pegmatitic pockets are apparent in outcrop.

22/12-6 90980137 2183m – anorthositic troctolite. Plagioclase and very rare opaque oxide grains are cumulus, and small rounded olivine grains are cumulus to intercumulus. Minor clinopyroxene is poikilitic to intercumulus. Narrow columnar orthopyroxene moats surround most olivine grains.

22/12-7 90980138 2228m – gabbroic troctolite. Plagioclase and irregular olivine are cumulus, and abundant clinopyroxene and opaque oxides are poikilitic phases. Orthopyroxene forms wide rims around some olivine grains, locally grading into a poikilitic texture.

22/12-8 90980139 2342m – olivine gabbronorite. Plagioclase and small rounded olivine grains are cumulus, whereas clinopyroxene, opaque oxides, and orthopyroxene are poikilitic to interstitial. Some biotite is intergrown with oxides.

22/12-9 90980140 2454m – very similar to 8, but slightly more pyroxene and olivine.

22/12-10 90980141 2748m –olivine-bearing gabbroic anorthosite. Plagioclase, olivine, and opaque oxides are cumulus, and clinopyroxene is poikilitic to interstitial. Orthopyroxene is intergrown with stubby and vermicular oxide grains.

22/12-11 90980142 2806m – anorthositic troctolite. Plagioclase, olivine, and opaque oxides are cumulus, olivine being concentrated in layers. Interstitial clinopyroxene is associated with small rounded olivine grains and oxides; orthopyroxene is intercumulus and associated with oxides in wide rims around olivine grains. Minor biotite present.

22/12-12 90980143 2842m – coarse-grained plagioclase-phyric sill. Elongated plagioclase laths form phenocrysts; fine-grained masses of clinopyroxene, hydrous minerals, and oxides are interstitial phases. Plagioclase is dusted with submicroscopic inclusions, clearing toward grain boundaries. No olivine observed. Texture not unlike the 'doleritic-textured' cumulates of the Latitude Hill intrusion.

22/12-13 90980144 2918m – gabbroic troctolite. Plagioclase and small rounded olivine grains are cumulus, and clinopyroxene, with exsolved oxide lamellae, is poikilitic to intercumulus. Narrow columnar orthopyroxene rims surround olivine. Opaque oxide grains are mainly associated with clinopyroxene. Small pyroxene-rich symplectites occur in plagioclase, mainly along grain boundaries. Minor pargasitic amphibole is present.

22/12-14 90980145 3000m – coarse-grained olivine gabbro. Plagioclase and small olivine grains are cumulus, and abundant clinopyroxene is cumulus, tending to poikilitic. Exsolved opaque minerals in clinopyroxene are locally recrystallised to granular clinopyroxene–oxide aggregates. Orthopyroxene is mainly associated with olivine. Biotite is rare.

22/12-15 90980146 3142m – recrystallised olivine gabbro. Elongated plagioclase laths and olivine are cumulus, and clinopyroxene, with exsolved oxides, and orthopyroxene form large interstitial grains. Other interstitial phases are oxides, with green spinel inclusions, and minor biotite. There is incipient recrystallisation along grain boundaries.

22/12-16 90980147 3431m – fine-grained recrystallised gabbro (marginal recrystallised facies). Comprises equigranular mosaic plagioclase, clinopyroxene, orthopyroxene, and opaque oxides, the latter probably derived from oxides exsolved from clinopyroxene. Fully recrystallised gabbroic cumulate (cf. partly recrystallised sample 13).

22/12-17 90980148 3318m – olivine gabbro (marginal recrystallised facies). Elongated plagioclase and a few larger olivine grains are cumulus; small recrystallised rounded olivine grains and clinopyroxene are intercumulus. Columnar orthopyroxene rims olivine. Small oxide grains associated with clinopyroxene result from recrystallisation of exsolution lamellae.

22/12-18A 90980149 3597m – fine-grained oxide-rich gabbroic granulite. Recrystallised gabbroic cumulate with granular mosaic plagioclase, clinopyroxene, rounded oxide blebs, and biotite flakes.

22/12-18B 90980150 3597m – recrystallised gabbro. Cumulus plagioclase and clinopyroxene, but apparently little orthopyroxene. Extensive recrystallisation, and granular exsolved oxides.

22/12-18C 90980151 3597m – oxide-rich gabbroic granulite. Zones of fine-grained equigranular plagioclase, clinopyroxene, rounded oxide grains, and biotite flakes, alternate with coarser-grained zones in which a relict cumulus texture is still recognisable.

24/166-1 90980164 9m – troctolite. Cumulus phases are plagioclase and olivine. Clinopyroxene forms poikilitic to interstitial grains, and rare orthopyroxene is mainly in symplectitic intergrowths with magnetite. Minor biotite is associated with oxide grains. Intruded by quartz veins.

24/166-2 90980165 158m – gabbroic oxide-rich troctolite. Sparse olivine and abundant plagioclase are cumulus phases, and abundant clinopyroxene forms large poikilitic crystals. Irregular oxide grains contain rare green spinel. Plagioclase contains very fine-grained needles, and very fine-grained symplectites, possibly involving colourless spinel, occur at

some olivine–plagioclase contacts.

24/166-3A 90980166 240m – layered troctolite (pyroxene–plagioclase phase layering). Coarse-grained olivine and plagioclase are cumulus, and brownish clinopyroxene is poikilitic. Orthopyroxene is apparently very rare. Irregular opaque oxide aggregates contain inclusions of dark green spinel and are commonly surrounded by biotite and small olivine crystallites. Very fine-grained symplectites occur at olivine–plagioclase and oxide–plagioclase contacts.

24/166-3B 90980167 240m – gabbroic troctolite. Small rounded olivine grains and plagioclase are cumulus, whereas clinopyroxene, with oxide exsolution lamellae and ilmenite platelets, is poikilitic. Orthopyroxene forms rare moats around olivine, and intergrowths with magnetite. Irregular oxides grains are locally associated with biotite.

24/166-4 90980168 287m – troctolite. Olivine, plagioclase, and rare subhedral opaque oxides are cumulus phases, and sparse brown clinopyroxene, with oxide exsolution lamellae is poikilitic. Olivine is concentrated in layers, which define a weak lamination.

24/166-5A 90980169 325m – troctolite. Subhedral mosaic grains of olivine and plagioclase are cumulus and concentrated in layers. Sparse clinopyroxene ranges from cumulus to intercumulus. Rare cumulus to intercumulus oxides are associated with biotite.

24/166-5B 90980170 325m – altered olivine-rich cumulate. Cumulus olivine relics are set in a matrix of small euhedral laths of actinolitic amphibole. Relict oxide grains are marginally corroded. Alteration was above the stability limit of serpentine.

24/166-5D 90980171 325m – dunite. Comprises cumulus olivine and marginally corroded opaque oxides. Any former interstitial phases are entirely replaced by actinolitic amphibole.

24/166-6A 90980172 381m – sheared granitoid. Large relict quartz and K-feldspar grains are set in a fine-grained recrystallised matrix. Syn-deformational biotite occurs along shear zones. Proto-mylonitic texture. Interpreted as a granophyre vein cutting through the magnetite-bearing cumulates.

24/166-6B 90980173 381m – coarse-grained gabbroic troctolite to olivine gabbro. Euhedral plagioclase is cumulus, and large irregular grains of olivine are cumulus to interstitial. Large grains of clinopyroxene range from cumulus to intercumulus. Narrow orthopyroxene reaction rims surround olivine. Irregular oxides are commonly overgrown by olivine and associated with biotite flakes.

24/166-7 90980174 467m – altered anorthosite. Plagioclase is the only cumulus phase. Actinolitic amphibole occurs along grain boundaries, as well as replacing former interstitial material (?clinopyroxene). Relict magmatic opaque oxides are rare.

24/166-8A 90980175 628m – troctolitic anorthosite. Plagioclase is the predominant cumulus phase, whereas small rounded olivine grains and opaque oxides are cumulus phases interstitial to larger plagioclase laths. Clinopyroxene is a poikilitic intercumulus phase. Rare biotite is associated with oxides. Rare orthopyroxene is intergrown with magnetite.

24/166-8B 90980176 628m – troctolite to troctolitic anorthosite, with cm-scale lamination. Plagioclase and olivine are cumulus phases, and rare clinopyroxene occurs mainly as moats around olivine. Orthopyroxene forms symplectitic intergrowths with magnetite. Irregular opaque oxide grains are rare.

24/166-9 90980177 690m – sheared granitoid vein. Contains with large quartz and K-feldspar relics in a mylonitic matrix. Vein cross cuts layered troctolitic cumulates.

24/166-10A 90980178 793m – layered troctolite. Plagioclase and olivine are cumulus phases, with olivine locally interstitial to plagioclase. Sparse clinopyroxene is interstitial, rare orthopyroxene is intergrown with magnetite, and rare opaque oxides are associated with biotite. Layering is on a cm scale.

24/166-10B 90980179 793m –coarse-grained layered troctolite. Large irregular olivine grains and plagioclase are cumulus phases. Clinopyroxene is interstitial as well as rimming olivine. Rare orthopyroxene moats surround olivine. Irregular opaque oxides are associated with small biotite flakes. Layering is on a cm scale.

24/166-11 90987501 812m – altered troctolite. Very large olivine grains and plagioclase are cumulus phases, and clinopyroxene is interstitial. Orthopyroxene forms narrow rims around olivine and rare intergrowths with magnetite. Abundant fine-grained 'cauliflower' symplectites, possibly involving colourless spinel, occur along cracks in plagioclase, along plagioclase grain boundaries, and at olivine–plagioclase grain contacts. Symplectite formation by Fe–Mg diffusion along grain boundaries and reaction with plagioclase was apparently enhanced by fluid infiltration, with much hydrous alteration.

24/166-12 90987502 923m – troctolitic anorthosite. Plagioclase is cumulus, and olivine cumulus to intercumulus. Rare clinopyroxene forms narrow rims around olivine, and orthopyroxene occurs as rims around olivine and symplectitic intergrowths with magnetite.

24/166-13A 90987503 1097m – anorthositic troctolite. Plagioclase and olivine are cumulus, and clinopyroxene is interstitial and forms rims around olivine. Some olivine grains have orthopyroxene moats. Magmatic opaque oxides are very rare.

24/166-13B 90987504 1097m – troctolitic anorthosite. Plagioclase is a cumulus phase, and olivine is cumulus to intercumulus. Orthopyroxene and rare clinopyroxene mostly occur as rims around olivine. A few magmatic oxide grains are associated with biotite. There is less olivine than 12A.

24/166-14 90987505 1127m – anorthositic troctolite. Plagioclase and olivine are cumulus phases, with olivine tending to interstitial. Clinopyroxene and opaque oxides form large poikilitic crystals, the oxides with amphibole rims. Abundant orthopyroxene is largely associated with oxide grains. Green spinel forms inclusions in opaque oxides.

24/166-15 90987506 1205m – troctolitic anorthosite. Plagioclase is cumulus, and small olivine grains are cumulus to interstitial. Interstitial clinopyroxene is rare. Interstitial oxides are rimmed by pargasitic amphibole and commonly associated with orthopyroxene–oxide intergrowths.

24/166-16 90987507 1333m – anorthositic troctolite. Plagioclase, olivine, and opaque oxides are cumulus phases, and orthopyroxene and rare clinopyroxene occur mostly as rims around olivine. Interstitial oxides are surrounded by pargasitic amphibole rims and associated with biotite flakes.

24/166-17 90987508 1378m – oxide-rich troctolite. Olivine, plagioclase, and opaque oxides are cumulus phases, and sparse clinopyroxene is interstitial or forms rims around olivine. Some oxide grains, especially those in interstitial positions, are surrounded by biotite.

24/166-18 90987509 1474m – oxide-rich troctolite. Olivine, plagioclase, and some opaque oxides are cumulus phases, whereas clinopyroxene and most of the oxides are interstitial. Oxides are commonly rimmed by brown amphibole, and, where in contact with plagioclase, have reacted to fine-grained symplectites. Outcrops consist of thin pure magnetite layers, with abundant massive magnetite float.

24/166-19a 90987510 1494m – highly altered troctolitic to gabbroic anorthosite. Aggregates of altered cumulus olivine

are associated with, and surrounded by, poikilitic to interstitial pyroxene. Plagioclase is the most common cumulus phase. One large alteration vein consists of fine-grained hydrous silicates.

24/166-19B 90987511 1494m – troctolitic anorthosite. Plagioclase, euhedral opaque oxides, and irregular olivine are cumulus, and minor orthopyroxene and rare clinopyroxene are interstitial. Some olivine grains are rimmed by orthopyroxene and oxides, and olivine is commonly rimmed by biotite. Outcrop contains veins of pseudotachylite.

24/166-20 90987512 1588 – coarse-grained troctolitic anorthosite. Plagioclase and one large olivine grain are cumulus, and minor clinopyroxene and rare orthopyroxene are interstitial. There are orthopyroxene–magnetite symplectites, and 'cauliflower' symplectites occur in plagioclase near olivine grains and rarely along plagioclase grain boundaries away from olivine (Fe–Mg grain-boundary diffusion).

24/166-21 90987513 1627m – anorthositic troctolite. Plagioclase and olivine are cumulus, and some olivine and rare orthopyroxene are interstitial. Minor clinopyroxene is attached to, and occurs as rims around, olivine.

24/166-22 90987514 1674m – amphibolite, with proto-mylonitic texture. Deformed cumulus plagioclase relics with interstitial aggregates of greenish-bluish amphibole.

Jameson Range troctolite/gabbro intrusion

3/98-1 90980019 10m – finely layered recrystallised leucotroctolite. A few large deformed cumulus plagioclase relics are set in a recrystallised fine-grained granular matrix of plagioclase, clinopyroxene, and olivine. Olivine and plagioclase are concentrated in diffuse layers. It is not clear whether this layering is primary magmatic or due to deformation.

3/98-2B 90980021 31m – recrystallised troctolite. Large deformed cumulus plagioclase relics, with largely recrystallised olivine and minor clinopyroxene and orthopyroxene. Olivine and plagioclase are concentrated in layers (as in 1). Primary magmatic lamination and some modal grading is apparent in outcrop.

3/98-3 90980022 49m – layered altered recrystallised troctolitic anorthosite. A few large deformed cumulus plagioclase relics in a recrystallised fine-grained granular matrix of plagioclase. Minor clinopyroxene and olivine tend to form layers. There is some alteration, mainly of Fe–Mg silicates.

3/98-4 90980023 58m – weakly laminated recrystallised gabbroic troctolite. A few large deformed cumulus plagioclase and olivine relics are set in a recrystallised fine-grained granular matrix of plagioclase, clinopyroxene, and olivine. Layering of Fe–Mg silicates may be due to deformation. Interstitial opaque oxides and biotite flakes are mainly associated with olivine.

3/98-6 90980025 140m – recrystallised troctolitic anorthosite. Large deformed cumulus plagioclase and a few olivine relics occur in a matrix of granular plagioclase, with minor olivine and clinopyroxene. Olivine and clinopyroxene are concentrated in microlenses, defining a weak lamination.

3/98-8A1 90980026 220m – anorthositic troctolite. Large deformed cumulus plagioclase relics and aggregates of cumulus olivine define a weak lamination. The recrystallised matrix consists of plagioclase, olivine, and clinopyroxene, with discrete layers of biotite.

3/98-8A2 90980027 220m – deformed troctolite. Similar to 8A, but distinctly more olivine.

3/98-8B 90980028 220m – deformed gabbroic troctolite. Contains deformed cumulus plagioclase relics, coarse-grained flattened olivine grains, and formerly interstitial clinopyroxene, rich in exsolved oxides. There is incipient recrystallisation along grain boundaries.

3/98-9 90980029 258m – recrystallised deformed gabbroic troctolite. A few large deformed cumulus plagioclase and olivine relics occur in a matrix of granular plagioclase, olivine, and clinopyroxene, in which the Fe–Mg silicates are concentrated in discrete layers. Olivine has kink banding. Abundant rounded oxide grains represent granule exsolution. The outcrop shows that a flaser gneissose texture is superimposed on the magmatic layering.

3/98-10 90980030 275m – weakly layered recrystallised gabbroic anorthosite. A few lenses, rich in recrystallised clinopyroxene and rounded oxide blebs, occur in a matrix of recrystallised plagioclase. No olivine observed.

3/98-11 90980031 328m – gneissose recrystallised gabbroic troctolite. A few large deformed cumulus plagioclase and kinked olivine relics in a recrystallised fine-grained granular matrix of plagioclase, clinopyroxene, and olivine. The Fe–Mg silicates tend to form layers, possibly due to deformation. Interstitial opaque oxides and deformed biotite flakes are mainly associated with olivine-rich layers.

3/98-12 90980032 339m – plagioclase–(olivine)-phyric dyke. Large elongated euhedral plagioclase laths and olivine pseudomorphs (hydrous silicates) are phenocrysts, set in a fine-grained matrix consisting of plagioclase microphenocrysts and oxides. Dyke is about 25 cm thick.

3/98-13 90980033 362m – recrystallised laminated to rhythmically layered troctolitic anorthosite. Large deformed cumulus plagioclase relics in a matrix of granular plagioclase, olivine, and clinopyroxene. Olivine and clinopyroxene are concentrated in thin layers, defining a lamination in hand specimen and thin section.

3/98-14 90980034 433m – recrystallised deformed massive gabbroic troctolite. A few large deformed cumulus plagioclase relics and kink-banded olivine grains are set in a matrix of granular plagioclase, olivine, and clinopyroxene. Fe–Mg silicates are concentrated in layers. Magmatic oxides are interstitial.

3/98-15 90980035 487m – recrystallised deformed troctolitic anorthosite. A few large deformed cumulus plagioclase relics occur in a matrix of granular plagioclase, olivine, and clinopyroxene. Fe–Mg silicates are concentrated in thin layers. A few interstitial magmatic oxide grains are associated with biotite flakes. Displays a gneissose texture in outcrop.

3/98-16 90980036 517m – deformed coarse-grained gabbro. Comprises large deformed cumulus plagioclase relics, large exsolved oxide-rich intercumulus clinopyroxene grains, and rare magmatic oxide grains. No olivine observed. There is extensive recrystallisation along grain boundaries.

3/98-17A 90980037 568m – recrystallised troctolitic anorthosite. A few large cumulus plagioclase relics are set in a matrix of recrystallised plagioclase. Altered olivine grains, clinopyroxene, some orthopyroxene, and interstitial oxides are arranged in layers, which define a weak lamination.

3/98-17B 90980038 568m – deformed altered troctolite. Consists of deformed cumulus plagioclase relics, large kinked olivine grains, large deformed exsolution-rich clinopyroxene grains, and rare interstitial oxide grains. There is some recrystallisation along grain boundaries.

3/98-18 90980039 593m – recrystallised gabbroic troctolite. There are large cumulus plagioclase relics, but the rock is otherwise largely recrystallised. Olivine, clinopyroxene, interstitial oxides, and possibly some orthopyroxene are concentrated in layers, defining a weak lamination in hand specimen.

3/98-19 90980040 650m – same as 18.

3/98-20 90980041 625m – recrystallised troctolitic anorthosite. A few large cumulus plagioclase relics survive. Minor olivine, clinopyroxene, and interstitial oxides are concentrated in layers, defining a weak lamination in hand specimen.

3/100-1A 90980042 2495m – coarse-grained anorthosite. Cumulus plagioclase relics are recrystallised along grain boundaries. Olivine and clinopyroxene are minor phases. A few granular olivine–clinopyroxeneorthopyroxene aggregates occur where olivine is slightly altered.

3/100-1B 90980043 2495m – troctolitic to gabbroic anorthosite. Contains recrystallised plagioclase, aggregates of olivine, clinopyroxene, orthopyroxene, and minor interstitial oxides. There are large cumulus plagioclase relics.

3/100-2A 90980044 1825m – gabbroic to troctolitic anorthosite. Coarse-grained recrystallised plagioclase, with aggregates of olivine, clinopyroxene, minor orthopyroxene, and interstitial oxides. Rare biotite flakes are mainly associated with oxides. Some rounded oxide grains in clinopyroxene-rich aggregates represent granule exsolution.

3/100-2B 90980045 1825m – recrystallised troctolite. The matrix is recrystallised plagioclase, alternating with olivine-rich layers. Clinopyroxene and orthopyroxene are minor phases. Abundant interstitial oxides show some textural preference for olivine-rich patches.

3/100-3A 90980046 1510m – massive oxide layer. Some staining by secondary copper minerals.

3/100-3B 90980047 1510m – massive oxide layer. Contains isolated olivine relics, totally replaced by hydrous silicates.

3/100-4 90980048 1425m – massive oxide layer.

3/100-5A 90980049 1295m – recrystallised troctolitic anorthosite. Mainly recrystallised plagioclase, with isolated mafic patches and lenses consisting of granular olivine, minor clinopyroxene, and some orthopyroxene. Interstitial oxides are minor.

3/100-5B 90980050 1295m – recrystallised anorthositic troctolite. Comprises large deformed cumulus plagioclase relics, with small olivine grains, clinopyroxene, and minor orthopyroxene concentrated in layers. Some interstitial oxides are associated with olivine. Gneissose appearance in outcrop.

3/100-6A 90980051 995m – recrystallised troctolitic anorthosite. Consists of recrystallised plagioclase, with thin, laterally discontinuous layers of granular altered olivine, minor clinopyroxene, and some orthopyroxene. Interstitial oxides are minor.

3/100-6B 90980052 995m – recrystallised anorthositic to gabbroic troctolite. Recrystallised plagioclase contains layers of granular olivine, alternating with more clinopyroxene-rich layers. Clinopyroxene locally contains oxide exsolution lamellae, but is mostly recrystallised to a granular fabric with rounded oxide blebs. Some interstitial oxide grains are preferentially associated with olivine.

Appendix III: Chemically analysed rocks from the western Musgrave Block

excluding samples of the Giles Complex listed in Appendix II. Mineral abbreviations as in Table 2.

Sample	*Lat. S*	*Long. E*	*Rock type*	*Locality*
Mount Aloysius Complex				
90984001	26.035	128.582	Felsic Opx gneiss	Mount Aloysius (west side)
90984002	26.230	129.131	Felsic Opx gneiss	NW of Pulalpulal
90984004	25.995	128.596	Si-Gt-Kfs-Qz pelite	Mount Aloysius (NW side)
90984005	26.024	128.619	Felsic gneiss	Mount Aloysius (central)
90984006	26.087	129.183	Felsic Gt-Opx gneiss	North of Kalka
90984007	26.188	128.899	Felsic Bt-Hbl-Opx gneiss	Western Champ de Mars
90984008	26.291	128.960	Sheared felsic Hbl gneiss	South of Michael Hills
90984009	26.203	128.811	Felsic Opx gneiss	Mount West
90984010	26.208	128.760	Sheared felsic Hbl gneiss	Mount West NW
90984011	26.058	127.626	Felsic Gt gneiss	North of Cohn Hill
90984019	26.022	128.617	Felsic Opx-Gt gneiss	Mount Aloysius (central)
90984020	26.022	128.617	Felsic Gt-Opx gneiss	Mount Aloysius (central)
90984022	26.081	129.121	Sheared felsic Opx gneiss	NW of Kalka
90984024	26.048	128.599	Felsic Opx gneiss	Mount Aloysius (central)
90984057	26.195	128.905	Felsic Bt-Hbl gneiss	Western Champ de Mars
91980098	26.094	129.197	Kfs quartzite	South of Ewarara Range
91980099	26.094	129.197	Sheared felsic Gt gneiss	South of Ewarara Range
91980105	26.094	129.197	Sheared felsic Gt gneiss	South of Ewarara Range
91980266B	26.220	129.170	Felsic Opx gneiss	SW side of Mount Davies
91988015	26.017	128.664	Felsic Opx-Cpx gneiss	Mount Aloysius (east side)
91988016	26.017	128.664	Felsic gneiss	Mount Aloysius (east side)
91988017	26.017	128.664	Hbl-Bt-Cpx-Opx-Kfs-Pl gneiss	Mount Aloysius (east side)
91988018	26.017	128.664	Felsic Bt-Opx gneiss	Mount Aloysius (east side)
91988020	26.005	128.669	Felsic Bt-Opx gneiss	Mount Aloysius (east side)
91988023	26.050	128.728	Felsic Bt-Cpx-Opx gneiss (xenolith)	Western Hinckley Range
91988030	26.022	128.644	Felsic Gt gneiss	Mount Aloysius (east side)
91988031	26.022	128.644	Felsic Gt gneiss	Mount Aloysius (east side)
91988032	26.057	128.614	Felsic Opx-Gt gneiss	Mount Aloysius (south side)
91988033	26.057	128.614	Felsic Bt-Gt gneiss	Mount Aloysius (south side)
91988034	26.057	128.601	Felsic Opx-Mt gneiss	Mount Aloysius (south side)
91988035	26.057	128.601	Felsic Gt gneiss	Mount Aloysius (south side)
91988037	26.046	128.589	Felsic Gt-Opx gneiss	Mount Aloysius (south side)
91988038	26.046	128.589	Felsic Opx-Hbl gneiss	Mount Aloysius (south side)
91988041	26.021	128.549	Tit-Opx-Cpx-Pl quartzite	Mount Aloysius (west side)
91988045	26.050	128.582	Felsic Opx gneiss	Mount Aloysius (west side)
91988046	26.050	128.582	Felsic Hbl gneiss	Mount Aloysius (west side)
91988048	26.064	128.639	Felsic Opx gneiss	Mount Aloysius (south side)
91988074	26.149	128.917	Felsic Gt-Bt gneiss	Western Champ de Mars
91988087	26.165	128.867	Felsic Bt-Opx gneiss	Western Champ de Mars
91988088	26.164	128.803	Felsic Opx gneiss	Western Champ de Mars
91988090	26.190	128.900	Felsic Bt-Opx gneiss	Western Champ de Mars
91989009	25.782	128.312	Felsic Bt-Opx gneiss	Murray Range
91989056	25.980	128.575	Felsic Bt-Cpx gneiss	Mount Aloysius (NW side)
91989059	25.973	128.557	Sheared felsic Gt gneiss	Mount Aloysius (NW side)
91989075	25.995	128.560	Sheared felsic All-Cpx gneiss	Mount Aloysius (NW side)
91989106	26.007	128.578	Felsic All-Cpx gneiss	Mount Aloysius (NW side)
91989327A	26.322	128.971	Gt psammite	Latitude Hill
91989331	26.332	128.976	Felsic Gt gneiss	Latitude Hill
91989436D	25.736	128.934	Felsic Gt-Hbl gneiss	East of Mount Daisy Bates
91989462	25.779	128.756	Felsic gneiss	SW of Mount Daisy Bates
91989464B	25.767	128.698	Felsic Opx gneiss	East of Mount Fanny
91989465A	25.784	128.669	Porphyroblastic felsic gneiss	East of Mount Fanny
91989499A	25.801	128.604	Felsic gneiss	SE of Mount Fanny
91989540	25.837	128.911	Felsic Cpx-Bt-Gt gneiss	West of Mount Gosse
91989563	25.953	128.963	Felsic Gt gneiss	South of Mount Gosse
91989571	25.928	128.746	Felsic Gt-Cpx gneiss	NE of Mount Aloysius
90984018	26.018	128.664	Bt-Cpx-Opx-Pl granulite	Mount Aloysius (east side)

Sample	*Lat. S*	*Long. E*	*Rock type*	*Locality*
90984021	26.072	129.196	Bt-Cpx-Opx-Pl granulite	Ewarara Range
90984023	26.020	128.599	Hbl-Cpx-Opx-Pl granulite	Mount Aloysius (central)
90984025	26.019	128.602	Hbl-Cpx-Opx-Pl granulite	Mount Aloysius (central)
90984067	26.158	128.821	Cpx-Opx-Pl granulite	Western Champ de Mars
90984084	26.088	129.149	Opx-Cpx-Pl granulite (?calc-silicate)	South of Ewarara Range
90984088	26.002	128.669	All-Cpx-Pl granulite (?calc-silicate)	Mount Aloysius (east side)
90984090	26.000	128.669	Gt-Cpx-Pl granulite (calc-silicate)	Mount Aloysius (east side)
91988019	26.005	128.669	Tit-Cpx-Pl granulite (calc-silicate)	Mount Aloysius (east side)
91988026	26.031	128.725	Bt-Opx-Cpx-Pl granulite	Western Hinckley Range
91988042	26.050	128.582	Bt-Cpx-Kfs-Qz-Opx-Pl granulite	Mount Aloysius (west side)
91988043	26.050	128.582	Bt-Cpx-Kfs-Qz-Opx-Pl granulite	Mount Aloysius (west side)
91989060	25.973	128.537	Sheared Gt-Cpx-Opx-Pl granulite	Mount Aloysius (NW side)
91989117	25.999	128.587	Mafic granulite	Mount Aloysius (NW side)
91989370A	26.394	128.960	Cpx-Qz-Lab granulite (calc-silicate)	South of Latitude Hill
91989373	26.386	128.976	Bt-Opx-Cpx-pl granulite	South of Latitude Hill
91989407A	26.429	128.967	Gt granulite	South of Latitude Hill
91989410B	26.397	128.970	Tit-Qz-Pl-Cpx granulite (calc-silicate)	South of Latitude Hill
91989442B	25.713	128.825	Gt-Hbl-Pl granulite	NE of Mount Daisy Bates
91989474	25.736	128.517	Ep-Tit-Pl-Cpx granulite (calc-silicate)	NW of Mount Fanny
91989480A	25.692	128.560	Mafic Gt granulite	North of Mount Fanny
91989487	25.746	128.622	Opx-Cpx-Hbl-Pl granulite	NE of Mount Fanny
91989488B	25.760	128.637	Mafic Gt granulite	NE of Mount Fanny
91989536C	25.838	128.911	Mafic granulite	West of Mount Gosse
91989569D	25.941	128.780	Cpx-Gt-Pl granulite (calc-silicate)	WSW of Mount Gosse
91989580A	25.943	128.550	Mt-Cpx-Qz-Pl granulite (calc-silicate, Qz blebs)	SE of Amy Giles Hill
Giles Complex				
90980001	25.823	127.688	Bt-Ol leucogabbronorite (JTG)	North of Jameson camp
90980003	25.823	127.688	Cpx-Hbl leucogabbro (JTG)	North of Jameson camp
90984016	26.068	128.891	Recrystallised gabbronorite (HRG)	3 km west of Wingellina
90984026	26.022	128.244	Leucotroctolite (BTG)	Central Blackstone Range
90984030	26.138	128.953	Granoblastic microgabbronorite (HRG)	Western Champ de Mars
90984035	26.157	128.934	Xenolithic Hbl-Bt microgabbronorite (HRG)	Western Champ de Mars
90984075	26.078	129.153	Recrystallised Ol gabbronorite (EWP)	Ewarara Range, north of Kalka
91980097	26.094	129.197	Sp-Gt pyroxenite (EWP)	South of Ewarara Range
91980102B	26.101	129.190	Pl-Ol websterite plug (EWP)	Ewarara Range, north of Kalka
91980104A	26.101	129.190	l gabbronorite plug (EWP)	Ewarara Range, north of Kalka
91980104B	26.101	129.190	Ol gabbronorite plug (EWP)	Ewarara Range, north of Kalka
91980107D	26.086	129.142	Gabbronorite plug (EWP)	Ewarara Range, north of Kalka
91980111	26.112	128.777	Bt microgabbronorite (HRG)	Western Hinckley Range
91985001B	26.078	129.164	Bt gabbronorite (EWP)	Ewarara Range, north of Kalka
91985001C	26.078	129.164	Gabbronorite (EWP)	Ewarara Range, north of Kalka
91985001D	26.078	129.164	Pl websterite (EWP)	Ewarara Range, north of Kalka
91985001E	26.078	129.164	Sp-Ol websterite (chilled margin) (EWP)	Ewarara Range, north of Kalka
91985005	26.078	129.164	Sp-Pl-Ol websterite (EWP)	Ewarara Range, north of Kalka
91985006	26.078	129.164	Pl websterite (chilled margin) (EWP)	Ewarara Range, north of Kalka
91985007	26.078	129.164	Leucogabbronorite (chilled margin) (EWP)	Ewarara Range, north of Kalka
91985008	26.078	129.164	Leucogabbronorite (chilled margin) (EWP)	Ewarara Range, north of Kalka
91988051	26.058	128.733	Bt-Hbl-Ol microgabbro (HRG)	Western Hinckley Range
91988052	26.058	128.733	Intergranular Bt-Hbl microgabbronorite (HRG)	Western Hinckley Range
91988053	26.058	128.733	Recrystallised Bt gabbronorite (HRG)	Western Hinckley Range
91988054	26.058	128.733	Intergranular Hbl gabbronorite (HRG)	Western Hinckley Range
91988110	26.079	128.990	Pegmatitic gabbro (WGP)	Wingellina Hills
91989209	26.177	128.830	Ol gabbronorite (MHG)	Carruthers Creek
91989211	26.192	128.885	Gabbronorite (MHG)	Carruthers Creek
91989212	26.192	128.885	Microgabbronorite (MHG)	Carruthers Creek
91989213	26.192	128.885	Granoblastic gabbronorite (MHG)	Carruthers Creek
91989216	26.192	128.885	Websterite (MHG)	Carruthers Creek
91989245	26.248	128.893	Granoblastic gabbronorite (MHG)	Carruthers Creek
91989247	26.248	128.893	Granoblastic-poikilitic gabbronorite (MHG)	Carruthers Creek
91989338	26.329	128.949	Norite (LHGP)	Latitude Hill
91989358	26.369	129.006	Gabbronorite (LHGP)	SE of Latitude Hill
91989374	26.386	128.976	Ol-Hbl gabbro (LHGP)	South of Latitude Hill
91989476D	25.725	128.512	Gabbronorite	NW of Mount Fanny
91989517B	25.842	128.778	Gabbro	SSE of Mount Daisy Bates

Sample	Lat. S	Long. E	Rock type	Locality
Granitic rocks				
90980098A	25.988	128.377	Hbl-Bt-Cpx-Opx granite	North of Blackstone Range
90980098B	25.988	128.377	Bt-Opx granite	North of Blackstone Range
90980180	26.050	128.785	Foliated Cpx-Hbl granite vein	Western Hinckley Range
90980506	26.175	128.968	Foliated porphyritic Bt granite	Champ de Mars
90984003	26.168	129.168	Bt granite gneiss	Minno Hill
90984015	26.220	128.350	Mt-Bt granite	West of Mummawarrawarra Hill
90984017	26.068	128.891	?Cpx granite gneiss	3 km west of Wingellina
90984034	26.159	128.930	Hbl-Bt granite dyke	Western Champ de Mars
90984039	26.159	128.923	Porphyritic Bt granite	Western Champ de Mars
90984041	26.161	128.922	Rapakivi Bt granite	Western Champ de Mars
90984064	26.148	128.840	Hbl granite gneiss	Western Champ de Mars
90984070	26.179	128.813	Hbl-Bt-Opx granite	Western Champ de Mars
91980110	26.112	128.777	Bt-Hbl granite vein	Western Hinckley Range
91980112	26.112	128.777	Bt-Cpx granite vein	Western Hinckley Range
91980182	26.165	129.160	Porphyritic Bt-Hbl-Opx granite	Near Mount Davies Camp
91980267A	26.224	129.171	Bt-Cpx-Opx granodiorite	SW contact of Mt Davies Intrusion
91980267B	26.224	129.171	Bt-Opx granodiorite	SW contact of Mt Davies Intrusion
91980302	26.246	128.572	Porphyritic Fl-Bt granite	West of Bell Rock Range
91985001A	26.078	129.164	Cpx-Opx granite gneiss	Ewarara Range, north of Kalka
91988006	26.179	128.581	Sheared porphyritic Fl-Hbl granite	West of Bell Rock Range
91988007	26.300	128.400	Slightly porphyritic Bt granite	MacDougall Bluff
91988008	26.300	128.400	Bt granite	MacDougall Bluff
91988009	26.300	128.400	Bt granite	MacDougall Bluff
91988010	26.300	128.400	Foliated Bt granite	MacDougall Bluff
91988011	26.300	128.400	Bt granite (rusty blebs)	MacDougall Bluff
91988022	26.050	128.728	Foliated Opx granite	Western Hinckley Range
91988027	26.031	128.725	Cpx granite dyke	Western Hinckley Range
91988028	26.031	128.725	Opx granite dyke	Western Hinckley Range
91988039	26.036	128.585	Ol-Cpx quartz syenite	Mount Aloysius (west side)
91988044	26.050	128.582	Ol-Hbl-Cpx quartz syenite	Mount Aloysius (west side)
91988055	26.058	128.733	Foliated Cpx-Mt-Hbl granite dyke	Western Hinckley Range
91988057	26.075	128.739	Foliated Bt-Hbl granite dyke	Western Hinckley Range
91988058	26.075	128.739	Foliated Bt-Hbl granite dyke	Western Hinckley Range
91988059	26.075	128.739	Porphyritic HblL-Bt granite dyke	Western Hinckley Range
91988060	26.075	128.739	Foliated Bt granite dyke	Western Hinckley Range
91988061	26.075	128.739	Foliated Hbl-Bt granite dyke	Western Hinckley Range
91988062	26.144	128.886	Foliated rapakivi Bt granite dyke	Western Champ de Mars
91988063	26.144	128.886	Mafic granulite/Opx granite vein (hybrid)	Western Champ de Mars
91988064	26.144	128.886	Rapakivi Cpx-Bt granite dyke	Western Champ de Mars
91988065	26.144	128.886	Foliated Bt granite dyke	Western Champ de Mars
91988066	26.144	128.886	Porphyritic Opx-Bt granite	Western Champ de Mars
91988069	26.144	128.910	Cpx-Bt-Opx-Hbl granite	Western Champ de Mars
91988070	26.144	128.910	Cpx-Bt-Hbl granite	Western Champ de Mars
91988071	26.156	128.924	Porphyritic granite	Western Champ de Mars
91988072	26.156	128.924	Rapakivi Bt-Hbl quartz monzonite	Western Champ de Mars
91988073	26.149	128.917	Opx-Bt-Cpx quartz monzodiorite	Western Champ de Mars
91988075	26.158	128.892	Foliated Bt-Hbl granite	Western Champ de Mars
91988076	26.153	128.918	Rapakivi Cpx-Bt-Hbl granite	Western Champ de Mars
91988077	26.153	128.918	Porphyritic Hbl-Bt granite	Western Champ de Mars
91988078	26.153	128.918	Porphyritic Bt-Hbl granite	Western Champ de Mars
91988080	26.154	128.914	Foliated Gt-Bt granite	Western Champ de Mars
91988081	26.154	128.914	Foliated porphyritic Gt-Bt granite	Western Champ de Mars
91988091	26.190	128.900	Foliated ?Opx granite	Western Champ de Mars
91988092	26.190	128.900	Foliated Opx granite	Western Champ de Mars
91988099	26.203	128.965	Opx granite	Western Champ de Mars
91988100	26.203	128.965	Porphyritic Opx granite	Western Champ de Mars
91988101	26.246	128.572	Porphyritic Fl-Bt granite	West of Bell Rock Range
91989030	25.807	128.337	Opx granite (mesoperthite)	Murray Range
91989156	26.045	128.710	Hbl-Cpx-Opx granite	Charnockite Flats
91989219	26.218	128.773	Bt granite gneiss	Mount West
91989313A	26.296	128.774	Granophyric leucogranite	Boundary Peak, Bell Rock intrusion
91989313B	26.296	128.774	Granophyric leucogranite	Boundary Peak, Bell Rock intrusion
91989364	26.374	128.948	Opx granite	South of Latitude Hill
91989393A	26.300	128.400	Foliated Tit-Bt granite	MacDougall Bluff
91989393B	26.300	128.400	Foliated Bt granite	MacDougall Bluff
91989393C	26.300	128.400	Foliated porphyritic Bt granite	MacDougall Bluff

Sample	*Lat. S*	*Long. E*	*Rock type*	*Locality*
91989394	26.300	128.400	Bt granite	MacDougall Bluff
91989395	26.300	128.400	Foliated Bt granite	MacDougall Bluff
91989397A	26.300	128.400	Bt granite gneiss	MacDougall Bluff
91989406C	26.423	128.958	Granitic augen gneiss	South of Latitude Hill
91989409E	26.400	128.964	Opx granite	South of Latitude Hill
91989418	25.648	128.752	Gt-Hbl granite	NW of Mount Daisy Bates
91989421	25.638	128.802	Bt granitic gneiss	North of Mount Daisy Bates
91989422	25.641	128.807	Hbl-Tit granitic gneiss	North of Mount Daisy Bates
91989425A	25.650	128.826	Bt granitic gneiss	North of Mount Daisy Bates
91989435	25.724	128.988	Gt-Hbl granite	NE of Mount Daisy Bates
91989440	25.708	128.830	Bt-Gt-Hbl granite	North of Mount Daisy Bates
91989443B	25.728	128.814	Rapakivi Gt granite	Mount Daisy Bates
91989444	25.734	128.802	Gt-Hbl granite	Mount Daisy Bates
91989445B	25.745	128.795	Gt-Hbl granite	Mount Daisy Bates
91989448	25.744	128.835	Gt-Hbl granite	Mount Daisy Bates
91989451	25.750	128.814	Gt-Hbl granite	Mount Daisy Bates
91989454	25.756	128.805	Gt-Hbl granite	Mount Daisy Bates
91989455	25.773	128.868	Gt-Hbl granite gneiss	SE of Mount Daisy Bates
91989458	25.744	128.724	Porphyritic quartz monzonite	West of Mount Daisy Bates
91989460A	25.753	128.758	Bt-Gt-Cpx-Opx granite	West of Mount Daisy Bates
91989460B	25.753	128.758	Bt-Opx granite	West of Mount Daisy Bates
91989460E	25.753	128.758	Microgranite vein	West of Mount Daisy Bates
91989466	25.782	128.668	Bt-Gt-Cpx-Opx quartz monzonite	East of Mount Fanny
91989473	25.737	128.515	Gt-Bt-Hbl granite	NW of Mount Fanny
91989475	25.735	128.521	Sheared porphyritic Gt-Hbl-Bt granite	NW of Mount Fanny
91989498	25.776	128.606	Opx granite	Mount Fanny
91989528C	25.865	128.853	Bt-Hbl granite	SSW of Mount Daisy Bates
91989535B	25.813	128.907	Gt-Hbl granite	NW of Mount Gosse
91989542	25.810	128.982	Granitic augen gneiss	NE of Mount Gosse
91989544A	25.880	128.984	Sheared Bt-Gt granite	SE of Mount Gosse
91989558C	25.940	128.922	Gt-Hbl granite	SSW of Mount Gosse
91989578	25.946	128.571	Gt-Bt-Hbl granite	SE of Amy Giles Hill
91989585A	25.894	128.523	Bt-Opx granite	NE of Amy Giles Hill
Tollu Group				
Mummawarrawarra Basalt				
90980004	26.197	128.428	Amygdaloidal basalt	Mummawarrawarra Hill
90980007A	26.197	128.428	Amygdaloidal basalt	Mummawarrawarra Hill
90980007B	26.197	128.428	Amygdaloidal basalt	Mummawarrawarra Hill
90980008	26.197	128.428	Basalt	Mummawarrawarra Hill
90980009	26.197	128.428	Amygdaloidal basalt	Mummawarrawarra Hill
91988014	26.300	128.400	Slightly amygdaloidal basalt	MacDougall Bluff
91988102	26.238	128.575	Amygdaloidal basalt	West of Bell Rock Range
91988103	26.238	128.575	Amygdaloidal basalt	West of Bell Rock Range
91989399	26.300	128.400	Amygdaloidal basalt	MacDougall Bluff
Smoke Hill Felsic Volcanics				
90984014	26.155	128.368	Rhyolite	Tollu Mining Centre
91988001	26.179	128.581	Dacite	West of Bell Rock Range
91988002	26.179	128.581	Slightly porphyritic rhyolite	West of Bell Rock Range
91988003	26.179	128.581	Slightly porphyritic rhyolite	West of Bell Rock Range
91988004	26.179	128.581	Rhyolite	West of Bell Rock Range
91988005	26.179	128.581	Rhyolite	West of Bell Rock Range
91989381	26.139	128.325	Rhyodacite	Tollu Camp
91989386	26.139	128.325	Porphyritic rhyolite	Tollu Camp
91989414	26.082	128.430	Porphyritic rhyolite	Mount Jane
91989415	26.082	128.430	Porphyritic rhyolite	Mount Jane
91989416	26.082	128.430	Porphyritic rhyolite	Mount Jane
MacDougall Formation				
91988013	26.300	128.400	Feldspathic sandstone	MacDougall Bluff
91989397B	26.300	128.400	Feldspathic sandstone	MacDougall Bluff
Mafic dykes, etc.				
90984047A	26.158	128.896	Dolerite dyke (type B)	Western Champ de Mars
90984047B	26.158	128.896	Dolerite dyke (type B)	Western Champ de Mars
90984053	26.170	128.866	Intergranular dolerite dyke (type A1)	Western Champ de Mars
90984054	26.170	128.866	Ol dolerite dyke (type C)	Western Champ de Mars
90984068	26.161	128.802	Ol dolerite dyke (chilled margin)	Western Champ de Mars

Sample	Lat. S	Long. E	Rock type	Locality
91988012	26.300	128.400	Opx dolerite dyke	MacDougall Bluff
91988021	26.017	128.664	Intergranular dolerite dyke (type A1)	Mount Aloysius (east side)
91988024	26.050	128.728	Dolerite dyke (type B)	Western Hinckley Range
91988025	26.050	128.728	Dolerite dyke (type B)	Western Hinckley Range
91988029	26.031	128.725	Bt-Opx-Cpx-Pl granulite sill	Western Hinckley Range
91988036	26.046	128.589	Dolerite dyke (type B)	Mount Aloysius (south side)
91988040	26.036	128.585	Ol dolerite dyke (type C)	Mount Aloysius (west side)
91988047	26.064	128.639	Qz dolerite dyke (type B)	Mount Aloysius (south side)
91988049	26.064	128.639	Qz dolerite dyke (margin) (type B)	Mount Aloysius (south side)
91988050	26.064	128.639	Qz dolerite dyke (centre) (type B)	Mount Aloysius (south side)
91988056	26.061	128.744	Ol dolerite dyke (type C)	Western Hinckley Range
91988067	26.144	128.910	Gabbronorite dyke (or xenolith)	Western Champ de Mars
91988068	26.144	128.910	Sheared Mt-Cpx-Opx-Pl granulite ?dyke	Western Champ de Mars
91988079	26.153	128.918	Poikilitic Hbl-Opx dolerite dyke	Western Champ de Mars
91988082	26.154	128.914	Cpx-Opx-Bt-Hbl gabbro (pre-Giles)	Western Champ de Mars
91988083	26.154	128.914	Opx-Cpx-Bt gabbro (pre-Giles)	Western Champ de Mars
91988084	26.167	128.867	Ol dolerite dyke (type C)	Western Champ de Mars
91988085	26.167	128.867	Intergranular dolerite dyke (type A1)	Western Champ de Mars
91988086	26.167	128.867	Intergranular dolerite dyke (type A1)	Western Champ de Mars
91988089	26.164	128.803	Intergranular dolerite dyke (type A1)	Western Champ de Mars
91988093	26.190	128.900	Gabbronorite dyke (margin)	Western Champ de Mars
91988094	26.190	128.900	Gabbronorite dyke (centre)	Western Champ de Mars
91988095	26.190	128.900	Gabbronorite dyke (centre)	Western Champ de Mars
91988096	26.190	128.900	Gabbronorite dyke (margin)	Western Champ de Mars
91988097	26.207	128.929	Altered Qz dolerite dyke (margin) (type B)	Western Champ de Mars
91988098	26.207	128.929	Altered Qz dolerite dyke (centre) (type B)	Western Champ de Mars
91989031	25.807	128.337	Bt-Ol dolerite dyke (type C)	Murray Range
91989053	25.970	128.551	Dolerite dyke (type C)	Mount Aloysius (NW side)
91989068	25.997	128.525	Recrystallised dolerite dyke (type B)	Mount Aloysius (NW side)
91989110B	25.991	128.622	Dolerite dyke (type C)	Mount Aloysius (N side)
91989111	25.993	128.622	Opx dolerite dyke	Mount Aloysius (N side)
91989112	25.995	128.625	Sheared dolerite dyke margin	Mount Aloysius (N side)
91989147	26.030	128.800	Intergranular dolerite dyke (Type A2)	Western Hinckley Range
91989148	26.030	128.800	Intergranular dolerite dyke (Type A2)	Western Hinckley Range
91989150	26.030	128.800	Intergranular dolerite dyke (Type A2)	Western Hinckley Range
91989151A	26.020	128.790	Intergranular dolerite dyke (Type A2)	Western Hinckley Range
91989151B	26.020	128.790	Intergranular dolerite dyke (Type A2)	Western Hinckley Range
91989208	26.177	128.830	Ol dolerite dyke (type C)	Carruthers Creek
91989329	26.327	128.968	Metadolerite dyke (granulite)	Latitude Hill
91989348	26.336	128.969	Recrystallised dolerite dyke (type B)	Latitude Hill
91989382	26.139	128.325	Altered basalt dyke	Tollu Camp
91989384	26.139	128.325	Altered basaltic andesite dyke	Tollu Camp
91989396	26.300	128.400	Basaltic andesite dyke	MacDougall Bluff
91989403	26.300	128.400	Porphyritic trachyte dyke	MacDougall Bluff
91989404	26.395	128.964	Hbl norite dyke	South of Latitude Hill
91989453	25.755	128.807	Gt metadolerite dyke	Mount Daisy Bates
91989476B	25.725	128.512	Dolerite plug	NW of Mount Fanny
91989476C	25.725	128.512	Gt metadolerite dyke	NW of Mount Fanny
91989485A	25.753	128.567	Gt metadolerite dyke	North of Mount Fanny
91989496B	25.773	128.602	Gt metadolerite dyke	Mount Fanny
91989497	25.776	128.605	Gt metadolerite dyke	Mount Fanny
91989500C	25.833	128.566	Dolerite dyke	South of Mount Fanny
91989504	25.776	128.547	Pyroxenite dyke	West of Mount Fanny
91989550C	25.915	128.839	Gt metadolerite dyke	SW of Mount Gosse
91989574	25.901	128.750	Gt metadolerite dyke	NE of Mount Aloysius
91989581C	25.927	128.503	Subophitic gabbronorite dyke	Amy Giles Hill
91989583A	25.909	128.503	Ol dolerite dyke (type C)	Amy Giles Hill
91989590A	25.965	128.652	Dolerite dyke	NE of Mount Aloysius

Appendix IV: Stratigraphic definition of the Mount Aloysius Complex

Proposer. A.J.Stewart.

Derivation of name. Mount Aloysius, latitude 26.00076°S, longitude 128.59631°E, Cooper 1:250 000 sheet area, Western Australia.

Distribution. Exposed over about 4000 km^2 in the Tomkinson Ranges of Western Australia and South Australia; extends from Mount Aloysius in the Bell Rock 1:100 000 sheet (4645) in the west to Teizi Hill in the Davies 1:100 000 sheet (4745) in the east, and south to Latitude Hill in the Bell Rock 1:100 000 sheet; also extends into the southwestern corner of the Bates 1:100 000 sheet (4646).

Type area. The range of hills around and including Mount Aloysius (982 m asl), termed the Mount Aloysius massif, is the type area. A reference section from GR 570210 (lat. 26.0292°S, long. 128.5702°E) to 590225 (lat. 26.0157°S, long. 128.5903°E) is representative of much of the complex, and exposes (from southwest to northeast) leucofelsic granulite (unit *fnk*), interlayered felsic to mafic granulite (*fn,mn*) and felsic granulite (*fn*), felsic garnet granulite (*fg*), and sillimanite–garnet granulite (*fns*). A second reference section from GR 628237 (lat. 26.005°S, long. 128.6283°E) to 610230 (lat. 26.0113°S, long. 128.6103°E) exposes weakly layered to massive intermediate granulite (*fna*), and a third reference section from GR 557258 (lat. 25.9858°S, long. 128.5574°E) to 559250 (lat. 25.9931°S, long. 128.5594°E) exposes mafic granulite (*mn*).

Lithology. Felsic, intermediate, and mafic granulite of both igneous and sedimentary origin are interlayered on scales ranging from centimetres to hundreds of metres.

Component units. The following units have been mapped:

fns. Sillimanite–garnet granulite (metasediment); crops out near the centre of the Mount Aloysius massif.

fg. Felsic garnet granulite, metasedimentary in part; crops out in the central part of the Mount Aloysius massif, and near Ewarara.

fna. Weakly layered to massive felsic to intermediate granulite (orthogneiss); makes up most of the eastern part of the Mount Aloysius massif, and is also exposed near Champ de Mars and Ewarara.

fn,mn. Composite unit of strongly layered felsic granulite (mainly orthogneiss), with numerous mafic granulite interlayers and rare calc-silicate and quartzite; forms the bulk of the Mount Aloysius massif, and also crops out elsewhere.

fn. Massive felsic granulite (orthogneiss); forms disrupted layers at Mount Aloysius, and is one of the main components of the Mount Aloysius Complex elsewhere in the Tomkinson Ranges.

fnk. Massive leucofelsic granulite (orthogneiss); forms discrete bodies at Mount Aloysius, and is widespread elsewhere, particularly near Ewarara and Mount Davies.

fni. Intermediate granulite (orthogneiss); widespread, but volumetricaly minor, unit interlayered with massive felsic granulite.

mn. Mafic granulite of mainly igneous origin; widespread unit, commonly forming discrete layers. Much larger, but younger and unrelated, bodies of mafic granulite represent recrystallised gabbroic rocks of the Giles Complex.

fnm. Homogeneous intermediate to mafic granulite; commonly forms discrete layers, e.g., near Ewarara.

fnq. Quartz-rich felsic granulite; minor metasedimentary unit which crops out near Teizi Hill and Mount West.

fnv. Garnetiferous granulite; minor unit, probably in part of sedimentary orign, which crops out near the Gosse Pile intrusion.

No stratigraphic facing is preserved in the granulites, and so the stratigraphic order is unknown.

Relationships. No older rocks are known. The Mount Aloysius Complex is intruded by a variety of granitic and syenitic rocks, ranging from dykes and veins to small plutons, abundant dolerite dykes, and major layered mafic to ultramafic bodies of the Giles Complex.

Age. A pooled Rb–Sr whole-rock isochron age of 1564±12 Ma (Gray 1978, Gray & Compston 1978) for felsic granulite samples is interpreted as a protolith age because individual isochrons (1) describe large bodies of rock or entire lithological units, (2) possess a large spread in Rb/Sr ratio, and (3) most are precise. In addition, initial ratios of felsic granulite layers are quite distinct from those of interlayered mafic granulite units. A similar pooled Rb–Sr whole-rock isochron age of 1327±7 Ma was obtained for felsic granulites from south of the Hinckley Fault (Gray 1978). These results have been confirmed by SHRIMP ion-microprobe U–Pb zircon ages of about 1550 Ma and 1305±8 Ma on felsic orthogneisses (Sun & Sheraton 1992). The time of granulite-facies metamorphism was reported by Gray (1978) and Gray & Compston (1978) on the basis of Rb–Sr data to be about 1200 Ma, the best estimate of 1204±7 Ma being obtained for a probable post-D_1, pre-D_2 granitic gneiss at Minno. The age for the latter sample has also been confirmed by a SHRIMP U–Pb zircon age of 1198±6 Ma (Sun & Sheraton 1992).

Synonomy. None.

GEOLOGY OF THE GILES COMPLEX AND ENVIRONS

WESTERN MUSGRAVE BLOCK

GEOLOGY AND SURFACE DEPOSITS OF THE TOMKINSON RANGE

WESTERN AUSTRALIA/SOUTH AUSTRALIA

PLATE 1 OF 3

by A.Y. Glikson, A. J. Stewart and E.H.J. Feeken 1995

BENTLEY SUPERGROUP [BS]

Tollu Group (TG):

BTH *Hogarth Formation: mafic volcanics*
BTS *Smoke Hill Felsic Volcanics: rhyolite*
BTM *Mummaweerawarra Basalt: amygdaloidal basalts and tuff*
BTD *Masdougal Formation: basal quartz-pebble conglomerate interbedded with cross bedded arkose and sandstone*

MAFIC DYKES

DC *Dyke swarm C (c. 1000 Ma, ormetamorphosed, post-D3)*
DB *Dyke swarm B (c. 800 Ma, post-D3)*
DA *Dyke swarm A (c. 1100 Ma, metamorphosed, post-D2 pre-D3)*

GRANITOIDS AND GRANITIC GNEISSES

GT *Felsite, granite and pegmatite veins and dykes (c. 1060 Ma, ≈m-Tollu Group, pre-D3)*
GP *Porphyritic and rapakivi granite gneiss and associated felsite, granite and pegmatite veins (c. 1188 Ma, pre-D2)*
GCH *Charnockite pods within felsic granulites (post-D2 pre-D3, pre-Giles Complex, possibly c. 1200 Ma)*

GILES COMPLEX LAYERED MAFIC/ULTRAMAFIC INTRUSIONS [GC]
(c. 1060 Ma):

HRG *Hinckley Range gabbronorite intrusion ≈~6000m–Olivine gabbro, gabbronorite, troctolite, anorthosite, pyroxenite, marginal microgabbro, olivine-spinel basic dykes. The western part of the HRG is extensively recrystallised to mafic granulites intruded by felsic veins dated as c.1060 Ga= old contemporaneous with volcanics of the Tollu Group).*
BRTG *Bell Rock troctolite/gabbro intrusion≈c.3600m–troctolite, gabbroic troctolite, anorthosite, gabbro, microgabbro, minor dunite, magnetite-rich troctolite, pods and lenses of cumulate magnetite.*
TWGP *Tingwell Gabbro intrusion≈2000m–gabbro, leucocratic olivinegabbronorite, olivinepyroxenite, wehrlite, peridotite, olivine melagabbro, basic dykes. Possibly a basal segment of the Bell Rock Troctolite Gabbro.*
MHG *Michael Hills gabbro intrusion≈>8000m–gabbro, orthopyroxenites, olivine-bearing ultramafic cumulates, abundant late sills of microgabbro.*
LHGP *Latitude Hill gabbronorite intrusion≈>8000m–a segment of the Michael Hills gabbro intrusion)–dolerite-textured gabbronorite, pyroxenite, feldspathic peridotite, gabbro, anorthosite marginal microgabbro.*
MDGP *Mount Denison gabbro/pyroxenite intrusion~>7000m–gabbro, gabbronorite, pyroxenite, peridotite.*
KNP *Kenmark pyroxenite intrusion~>8000m–including norite, anorthosite, olivine gabbro, olivine websterite and peridotite.*
GPP *Giasse Pile pyroxenite intrusion ≈2000m–orthopyroxenite, olivine orthopyroxenite, websterite, peridotite, norite.*
EVIP *Everarre pyroxenite intrusion~>500m–bronzitite, harzburgite, pyroxenite, melagabbro.*
WGP *Wingellina gabbro/pyroxenite intrusion~>1800m–gabbro, gabbronorite, olivine gabbro, clinopyroxenite, wehrlite, minor peridotite.*
CHPG *Claude Hill peridotite/gabbro intrusive–poorly exposed thin sill/er of olivine gabbro, gabbronorite, peridotite.*
MPG *Mann Range gabbro/peridotite/gabbro intrusion≈c.2600m–deformed pyroxenite, peridotite, harzburgite, dunite, gabbro, gabbronorite.*
UP *Ultramafic Pugs and Stocks-pyroxenite, peridotite, dunite– mainly in the Everarre area and probably related to the Everarre Pyroxenite.*
BTG *Blacksterne Range troctolite/gabbro intrusion~c.3600m–little-deformed troctolite, olivine gabbro, anorthosite.*
CG *Cavanagh gabbro intrusion: flat-lying gabbro and gabbronorite intruded by a network of mafic dykes on a dense scale (75-150m)*
JTG *Jameson Range troctolite/gabbro intrusion~c.2560m–low-dipping troctolite, gabbroic troctolite, anorthosite, monzonitic/felsic veins/leuco-magnetite units.*

GRANULITE FACIES PARAGNEISS AND ORTHOGNEISS

MAC *Mount Aloysius Complex (c. 1600 Myr and c.1300 Myr precursors, c. 1200 Myr metamorphic ages)–mainly felsic facies felsic gneisses, intermediate gneisses and minor mafic granulite interlayered on asbke ranging from centimetres to hundreds of metres. The granulites are intruded by a few small bodies of granite, syenite and pegmatite and include quartz-garnet and sillimanite-bearing varieties. Lithological types inoiude: fna, fg, fna, fn, nm, fns. Deformed by D1, D2 and D3. Intruded by mafic dykes.*

Units equivalent to the MAC:

MWG *Gneiss at Mount West-dominated by granitic orthogneiss and including units/arrcivcs of paragneiss and locally mica schist.*
ETG *Granulites of the Everarre-Tekl Range dominated by paragneiss, including interlayered felsic granulite, porphyroblastic orthogneiss, minor mafic granulite, anorthosite, quartzite, garnet and sillimanite-bearing granulite and marble.*
WG *Granulites at Wanidu-Hijiata-dominated by layered felsic granulites, including minor quartzose granulites, garnet-sillimanite granulite, and mafic granulite.*

SUMMARY OF THE GEOLOGICAL EVOLUTION OF THE WESTERN MUSGRAVE BLOCK

AGE (Ma)	EVENT	METAMORPHIC CONDITIONS		FOLDS	STRUCTURAL FABRICS: DOMINANT FOLIATION	STRUCTURAL FABRICS: LINEATION, DOMINANT MOVEMENT
1550 [1]	Protolith of felsic granulites (N of Hinckley Fault)					
1300 [1]	Protolith of felsic granulites (S of Hinckley Fault)	MAC	MWG, ETG, WG			
	D_1			Rarely preserved	Layered parallel S_1, reoriented during D_2	None observed
1200 [1]	Intrusion of charnockite D_2	P=5-11 kbar, T>750°C P_f fluids, oriented parallel to L_2		Reclined isoclinal 330/18 NE	Pervasive S_2 gneissosity L_2 18->106	Pervasive intersection
1188 [2,4]	Intrusion of fine grained granite and K-feldspar mega-crystic granitoids		GP			
1100 [5]	Intrusion of mafic dykes Type A		DA			
1080 [5]	Intrusion of Giles Complex	P=6-11 kbar; uplift, erosion; extrusion of Tollu Group volcanics	GC			
			BTH, BTS, BTM, BTD			
			TG			
1060 [5]	D_3 early	P=11 kbar, T=650-700°C	GT	Open to isoclinal Upright F_3 folds	135/80NE	Down-dip mineral and stretching 80->025
	late	P=4.5-11 kbar				
1000 [5]	Intrusion of mafic dykes Type C (including ophites= plagioclase dykes)		DC			
800 Ma [3]	Intrusion of mafic dykes Type B		DB			
	D_4 Ultramylonite (SE transport):	Amphibolite facies		095/65N		42->325 Reverse
	D_5 mylonite/ultramylonite (SW/transport)	Greenschist facies		160/80E	80->025 common fracture cleavage	Reverse
550 Ma [4,5]	D_6 Petermann Orogeny: Ultramylonite with mylonite zones. Mesh-directed thrusting: e.g. Champe de Mar Fault, Woodroffe Thrust	P=14.0/11.1 kbar, T=750°C		Large shear zones with associated mesoscopic tecrrtites	150/80E 085/80N	80->175 Reverse 80->350 Normal
	Dy=trogenic shear zones	Contain muscovite and biotite		Broad "crush" zones		80->030

[1] Rb-Sr whole rock isochrons, Gray (1971, 1977); [2] U-Pb on zircons, Maboko (1988); [3] U-Pb on zircons, Sun and Sheraton (1992); [4] $^{40}Ar/^{39}Ar$ Maboko (1988); [5]Sun and Clarke, unpublished data

LITHOLOGY

Granulite facies gneisses (including orthogneiss and paragneiss):

- fg *Garnet felsic granulite*
- fn *Felsic granulite*
- fna *Felsic granulite, massive to weakly layered, approaches granitic texture in places, layering may be interrupted, discontinuous or irregular*
- fwg *Quartzite felsic granulite*
- fnt *Intermediate granulite*
- fnv *Garnet/fenous granulite*
- eg *Kymatite*
- peg *Pegmatite*
- fna *Leucofelsic granulite*
- fns *Metasedimentary felsic granulite*
- fnm *Homogeneous granulite of intermediate to mafic composition*
- mn *Mafic granulite*

Metasediments:

- mm *Marble*
- qt *Quartzite*
- grq *Garnet quartzite*

Felsic Igneous rocks:

- gr *Granite*
- grh *Granitic gneiss*
- grm *Microgranite*
- gp *Porphyritic granite*
- gr *Rapakivi granite*
- mt *Migmatite/leukmatite*
- mtb *K-feldspar-rich migmatite*
- my *Mylonite*
- sy *Syenite*
- dr *Dionite*

Ultramafic Igneous rocks:

- um *Ultramafic rock*
- px *Pyroxenite*
- uno *Orthopyroxenite*
- uoco *Olivine orthopyroxenite*
- uwe *Websterite*
- up *Peridotite*

Mafic Igneous rocks:

- gb *Gabbro*
- gbm *Melagabbro*
- gbn *Norite*
- gd *Dolerite-textured gabbro*
- gba *Anorthosite*
- gbat *Anorthositic troctolite*
- gbt *Troctolitic gabbro*
- gbam *Amphibole-bearing gabbro*
- gbf *Ferrogabbro*
- gbo *Olivine gabbro*
- dl *Dolerite*

Tollu Group Volcanics

- v *Volcanics*

SURFACE DEPOSITS AND LANDFORMS

	DEPOSIT	LANDFORM
Ay	*Greasy or gritty clay; silt: claypan*	Floodplain, alluvial plain, sandplain
Asy	*Sand, silt, clay*	Floodplain
Asy	*Gravel, sand, silt, clay*	Floodplain
Asy	*Silt, clay, sand, red loam*	Alluvial plain
Asy	*Gravel, silt, clay, sand*	Alluvial plain
Af	*Coarse to fine sand, silt*	Alluvial fan
A	*Grading from coarse sand to clay*	Ancient channel
Dp	*Coarse to medium sand, often with magnetite grains*	Sandplain, and predominantly longitudinal dune fields
Dr	*Coarse to fine sand, often with fine magnetite grains*	Isolated, more or less circular dunes in the sandplains, or dunes attached to minor well-weathered outcrop
Dr	*Very fine to fine sand, gravelly in places*	Pediment
D	*Fine to coarse sand, at times rich in magnetite, gravelly to pebbly in places; occasional ferruginous rubble with magnetite grains*	Predominantly colluvial and alluvial valley floor deposits
fs	*Ferricrete outcrops, minor calcrete interbeds, weathered ferruginous gravel, minor mottled zone, magnetitic gravel in places*	Near margins of ultramafic rock, forming low rises
Ks	*Calcrete, minor ferricrete; weathered calcrete cobbles, pebbles and gravels; minor silcrete interbeds*	Forming very low rises in plains, also flanking some major stream beds
Rky	*Silcrete outcrops, boulders, pebbles and gravels*	Occurring in association with calcrete, ferricrete
Rky	*Undivided duricrust*	See fs, ftr, Rky

SCALE 1:100 000

1 0 1 2 3 4 5 6 7 8 9 10 Kilometres

UNIVERSAL TRANSVERSE MERCATOR PROJECTION, AUSTRALIAN MAP GRID, ZONE 52

LATITUDE OF ORIGIN : 0°, LONGITUDE OF ORIGIN : 129°

- *Geological boundary with lithology letter symbol*
- *Lithology marker bed*
- *Surface deposit boundary with letter symbol*
- *Fault*
- *Fault showing relative horizontal displacement*
- *Low-angle normal fault. Scuare on downfaulted rocks*
- *Thrust-fault. Triangle on up-thrusted rocks*
- *Shear zone*
- *Dyke or vein: g-granite, peg-pegmatite, q-quartz Unlabded dykes are dolerite*
- *Syncline showing plunge*
- *Antiform showing plunge*
- *Synform showing plunge*
- *Overturned antiform*

Where location of boundaries, faults and folds is approximate, line is broken; where inferred quarried; where concealed, boundaries and folds are dashed, faults are shown by short dashes

- *Minor anticline showing plunge*
- *Minor synciine showing plunge*
- *Minor fold showing plunge*
- *Asymmetrical minor fold showing plunge*
- *Vergence to left in upright horizontal fold*
- *Vergence to right in upright plunging fold*
- *Strike and dip of strata*
- *Vertical strata*
- *Strike and dip of strata, facing not known*
- *Strike and dip of strata. Dot indicates proved direction of facing*
- *Facing of beds*
- *Strike and dip of strata, dip 15 to 45*
- *Strike and dip of strata, dip greater than 45*
- *Trend of primary layering*
- *Trend of foliation/gneissosity*
- *Lineament*
- *Joint pattern*
- *Strike and dip of foliation*
- *Vertical foliation*
- *Strike and dip of cleavage*
- *Plunge of lineation*
- *Plunge of mineral elongation*
- *Specimen locality with reference number A - 9799, B - 9899, C - 9996, D - 9098, E - 9198, F - 9298*
- *Measured section with reference number*
- *Abandoned mine or open cut, Cr. - Chrysoprase*

Alphoto interpretation

- *Bore with windpump*
- *Sand dunes*
- *Scarp*
- *Road*
- *Vehicle track*
- *Landing ground*
- *Building*
- *Trigonometrical station*
- *Elevation in metres*

ROCK UNIT RELATIONSHIP DIAGRAM

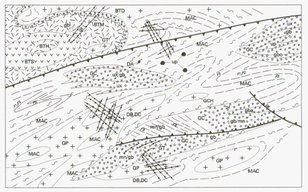

F1, F2, F3 refer to D symbols in Time/Tectonic/Stratigraphic Table

- *Thrust fault Triangle on older rocks*
- *Shear zone*
- *Felsic volcanics*
- *Mafic volcanics*
- *Conglomerate*
- *Unconformity, Top of U towards younger rocks*
- *Mafic-ultramafic intrusions*
- *Granitoids*
- *Felsic granulites and granitic gneiss*

GEOLOGICAL SKETCH MAP OF THE MUSGRAVE BLOCK

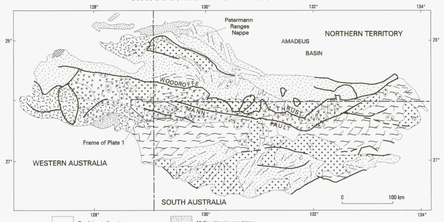

- *Overlying sediments*
- *Granite*
- *Mafic and anorthosite intrusions*
- *Quartzite*
- *Felsic volcanics, granophyre*
- *Mafic volcanics, sandstone*
- *Schist, gneissose granite (greenschist facies)*
- *Schist, gneiss, gneissose granite (amphibolite facies)*
- *Gneiss (transitional amphibolite-granulite facies ; sedimentary)*
- *Felsic & mafic granulites (metavolcanic= metasedimentary)*

TOTAL MAGNETIC INTENSITY AND GRAVITY SECTION

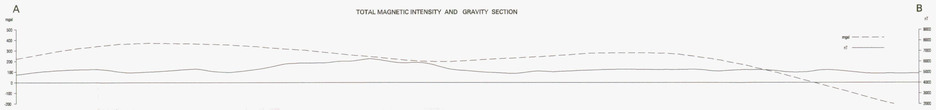

SCHEMATIC TOPOGRAPHIC AND GEOLOGICAL SECTION

Scale: $\frac{V}{H}$=5

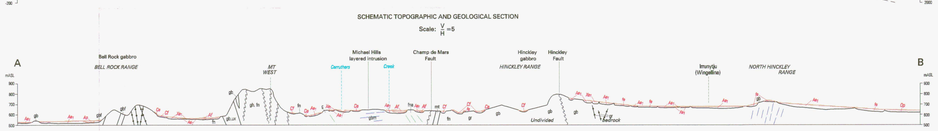

TOTAL MAGNETIC INTENSITY AND GRAVITY SECTION

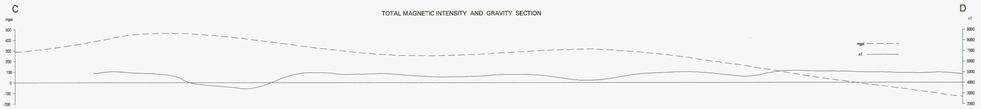

SCHEMATIC TOPOGRAPHIC AND GEOLOGICAL SECTION

Scale: $\frac{V}{H}$=5

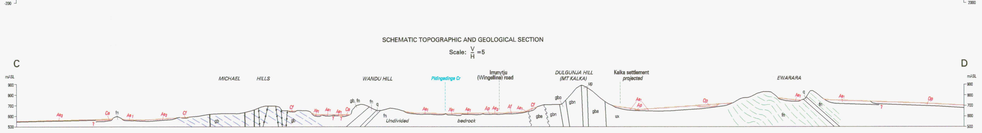

GRAVITY

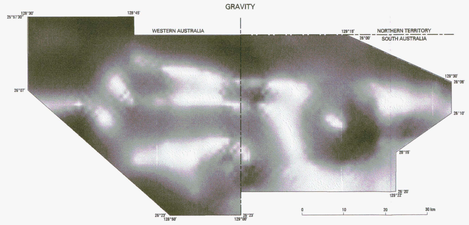

TOTAL MAGNETIC INTENSITY

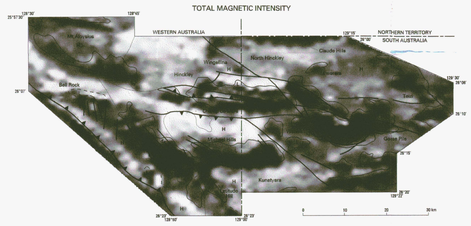

SOLID GEOLOGY SKETCH MAP

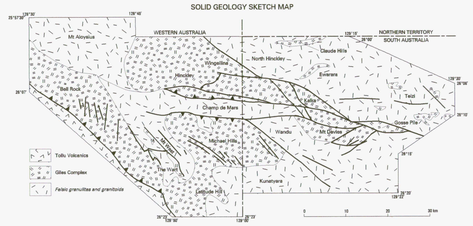

Geology 1994 by B.P. Thomson (South Australia Department of Mines, SADME) and by Southwestern Mining Pty Ltd
1995-1997 by J.L. Glikson, R.C. Horwitz, J.B. Kriewaldt, J.J.G. Doepel, R.A.Fairbridge (Geological Survey of Western Australia, GSWA)
1998-1999 by A.D.T. Smith, M.E. Grey, A.C. Moore, R.N.W. Haeldtl GSWA, of Adelaide.
1997 by A.Y. Glikson, C.J. Simpson (Australian Geological Survey Organisation, AGSO), C.G. Belbhaus (UNIv., of Tasmania)
1998 by A.Y. Glikson (AGSO), C.G. Belbhaus (Univ. of Tasmania), T.C. Pharaoh (British Geological Survey), J.S. Myers (GSWA)
1999 by A.Y. Glikson, A.J. Stewart, E.H.J. Feeken
(AGSO)
1991 by A.Y. Glikson, A.J. Stewart, J.W. Sheraton, E.H.J. Sun (AGSO), C. Clarke (Univ. of Sydney), S.A. Wilde (Curtin University of Technology)

Compiled 1993-1998 by A.Y. Glikson, A.J. Stewart, E.H.J. Feeken and D.A. Fillinger

Cartography by N. Jeffery, AGSO
Edited by A.T. Gibbons, D.M. Whipper
Produced by AGSO Cartographic Services Unit using Intergraph graphics applications.

Published by the Australian Geological Survey Organisation, Department of Primary Industries and Energy, Canberra, Australia. Geology and surface deposits mapped by Mineral Mapping Section and Energy Base map compiled by AGSO from 1: 100 000 scale topographic maps supplied by the Australian Surveying and Land Information Group, Department of Administrative Services
Topographic base information © AUSLIG 1994

This map is accompanied by a text publication:
Glikson, A.Y., Stewart, A. J., Belbhaus, C. G., Clarke, G. L., Sheraton, J. W., Sun, G. S. and E. H. J. Feeken, *Geology of the Giles Complex and environs, Western Musgrave Block, Central Australia*

It is recommended that this map be referred to as:
GLIKSON, A.Y., et al 1995,
Geology of the Giles Complex, and Environs, Western Musgrave Block, Central Australia (1: 100 000 scale map) Australian Geological Survey Organisation, Canberra

Copies of this map and the accompanying Record may be obtained from:

AGSO Sales Centre
GPO Box 378
Canberra ACT 2601
Phone (06) 2488519 Facsimile (06) 2489982

The digital data for this map were compiled on the AGSO Intergraph system and may be suitable for transfer to other digital systems. Detailed site data are stored in the Oracle NORA Field Database. Information on formats, release conditions, and costs are available from AGSO Sales Centre

GRAVITY
Image generated by A. Murrer from the Gravity Anomaly Grid of Australia (1.0°), 1994

MAGNETICS
Image generated by T. Mackey, P. Milligan and C. Tarlowski from the Magnetic Anomaly Grid of Australia, 1993

The digital magnetic/gamma-ray/gravity data on which this interpretation is based may be obtained from the Geophysical Mapping Section, AGSO Phone (06) 2489233 Facsimile (06) 2489983

UNIVERSAL GRID REFERENCE

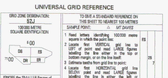

MAP LOCALITY

INDEX TO 1:100 000 MAPS

1:250 000 maps shown in blue

NGMA
Product of the National Geoscience Mapping Accord

AGSO
AUSTRALIAN GEOLOGICAL SURVEY ORGANISATION

GEOLOGY OF THE GILES COMPLEX AND ENVIRONS

WESTERN MUSGRAVE BLOCK

GEOLOGY AND SURFACE DEPOSITS OF THE TOMKINSON RANGE

WESTERN AUSTRALIA/SOUTH AUSTRALIA

PRELIMINARY EDITION

PLATE 1 OF 3

/usr2/nsapi/gmn/dvg/plates/1tgmproc1.dgn

29-FEB-1996

mbl

GEOLOGY OF THE GILES COMPLEX AND ENVIRONS

WESTERN MUSGRAVE BLOCK

ENLARGEMENTS OF SELECTED AREAS OF THE TOMKINSON RANGE

WESTERN AUSTRALIA/SOUTH AUSTRALIA

PLATE 2 OF 3

by A.Y. Glikson, A. J. Stewart, C.G. Ballhaus, G.L. Clarke and E.H.J. Feeken, 1995

SCALE 1:50 000

1 0 1 2 3 4 5 Kilometres

UNIVERSAL TRANSVERSE MERCATOR PROJECTION, AUSTRALIAN MAP GRID, ZONE 52
LATITUDE OF ORIGIN : 0°, LONGITUDE OF ORIGIN : 129°

A GEOLOGICAL SKETCH MAP SHOWING THE LOCALITIES OF ENLARGED AREAS

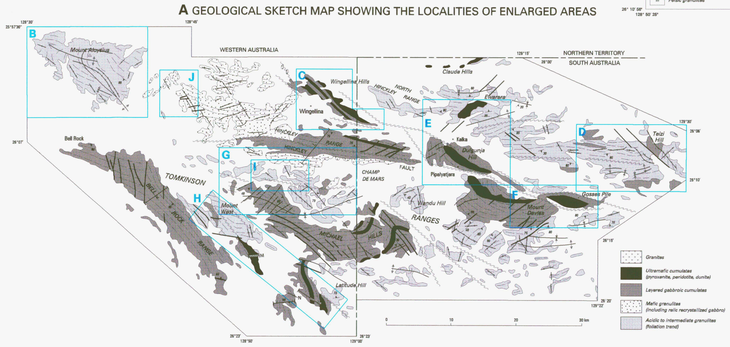

B MOUNT ALOYSIUS

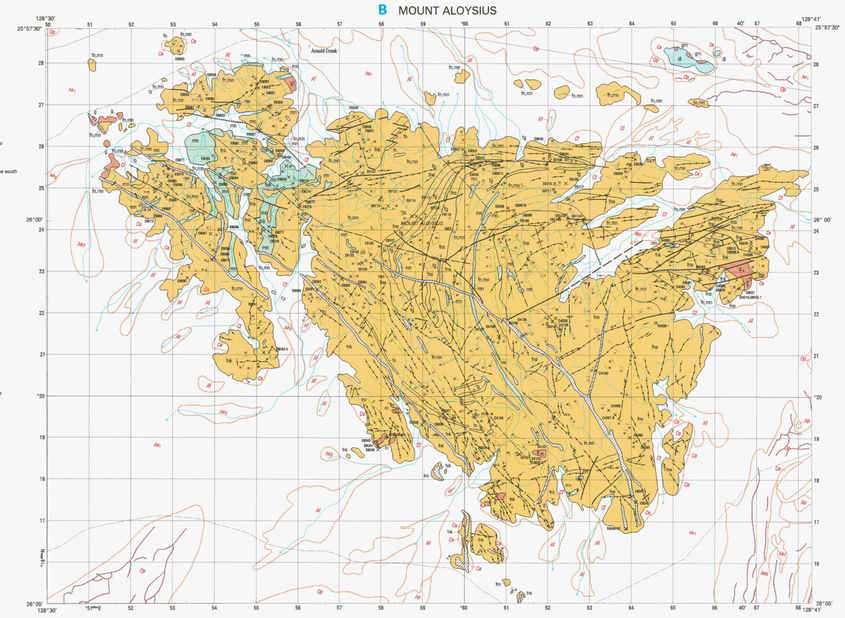

C WINGELLINA HILLS

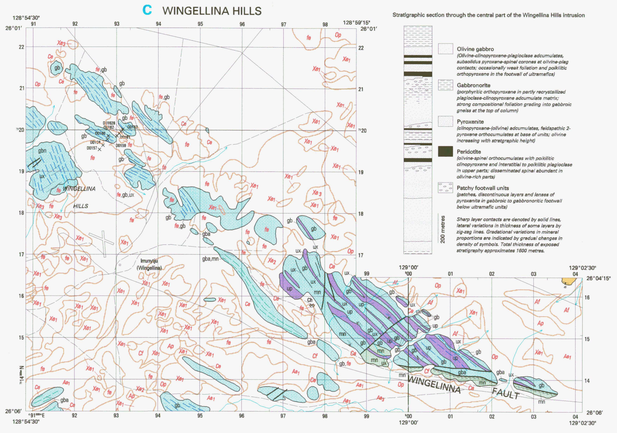

Stratigraphic section through the central part of the Wingellina Hills Intrusion

D TEIZI HILL AREA

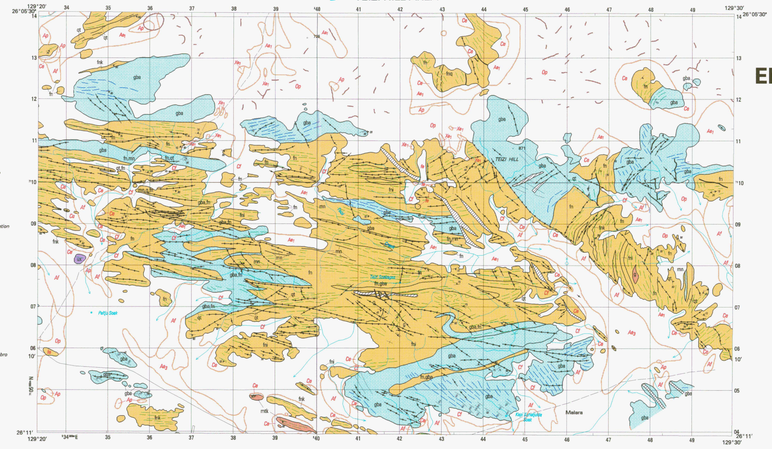

E KALKA AND EWARARA INTRUSIONS

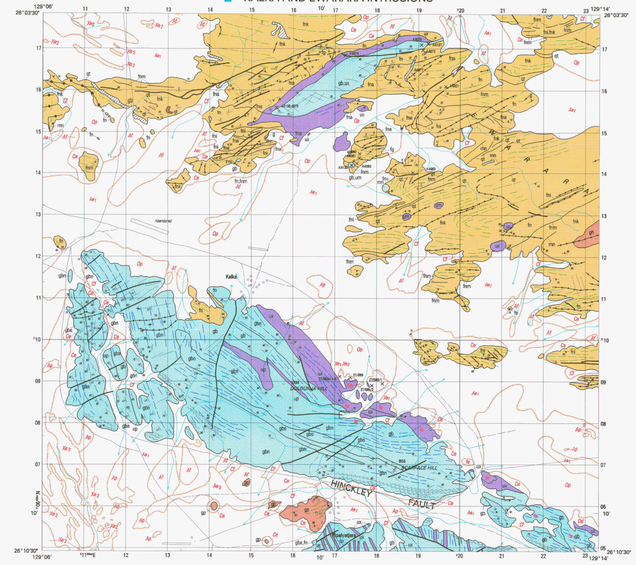

F GOSSE PILE INTRUSION AND EASTERN PART OF THE MOUNT DAVIES INTRUSION

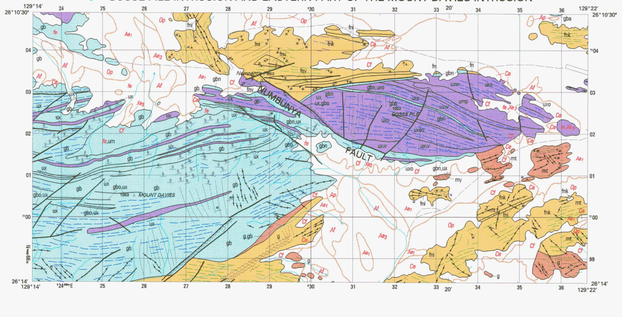

G CHAMP DE MARS AREA

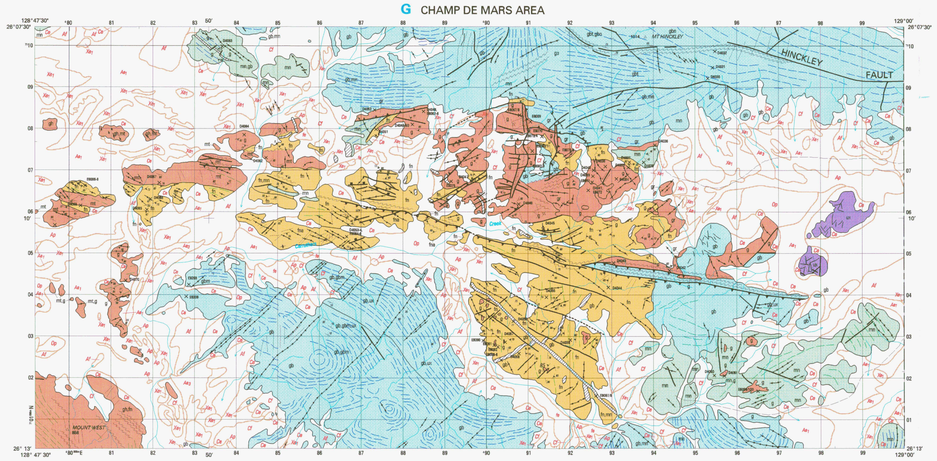

H MOUNT WEST TO LATITUDE HILL AREA

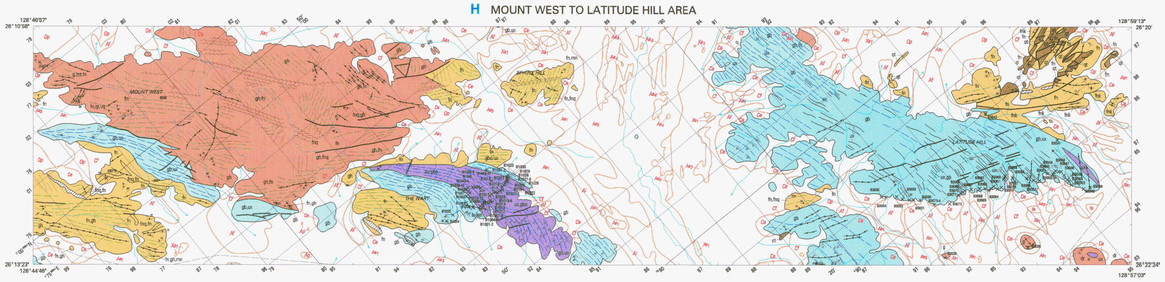

I STRUCTURAL GEOLOGY OF THE CHAMP DE MARS AREA

J STRUCTURAL GEOLOGY OF THE WESTERN HINCKLEY RANGE AREA

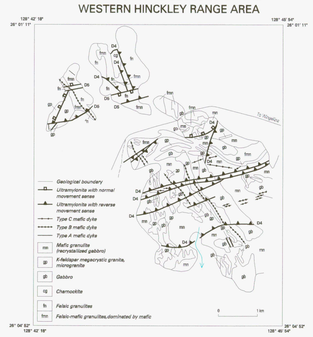

K BELL ROCK TROCTOLITE/GABBRO INTRUSION

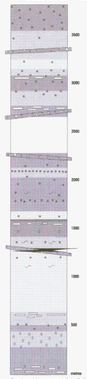

Stratigraphic sequence of the Bell Rock Range intrusion. Variable olivine:plagioclase modal ratios are depicted by variable grey shades. The sequence includes several sills and intrapolutonic quenching horizons (open rectangles). Disseminated oxides are signified by filled dots, the presence of clinopyroxene is illustrated by small open diamonds. The sequence is cut by numerous olivine plagioclase-phyric dykes that are similar in mineralogy to the cumulates.

L HINCKLEY RANGE GABBRONORITE/TROCTOLITE INTRUSION

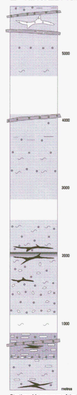

Stratigraphic sequence of the Hinckley Range intrusion. The sequence is predominantly ironstaltic until about the 2000m elevation, and above that level predominantly gabbroic. Rapidly crystallized units occur at the base of the intrusion (open triangles). The layered sequence is cut by several olivine and olivine-plagioclase-phyric dykes. Major pseudotachylyte veining (shown by schematic black veins) occurs near the Hinckley thrust fault and along the inferred bottom contact of the intrusion.

M THE WART GABBRO/PYROXENITE INTRUSION

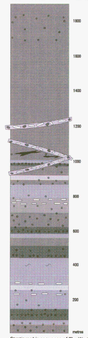

Stratigraphic sequence of The Wart intrusion. The sequence is predominantly clinopyroxenitic with variable olivine:pyroxene:plagioclase ratios (illustrated by variable grey shades). The presence of olivine is denoted by black dots, inferred roof cooling textures and stratigraphic positions where intrapolutonic quenching may have occurred by open rectangles.

N LATITUDE HILL GABBRO/PYROXENITE INTRUSION (segment of the Michael Hills gabbro)

Magmatic stratigraphy of the Latitude Hill intrusion. Predominantly gabbro with several pyroxenite intersections (darker shading). Olivine (black dots) is common in the upper part of the sequence, and 'diorite-textured' gabbro (open triangles) occurs at several elevations. The central units are highly deformed and veined by pseudotachylyte (black veins).

SUMMARY OF THE GEOLOGICAL EVOLUTION OF THE WESTERN MUSGRAVE BLOCK

AGE (Ma)	EVENT	METAMORPHIC CONDITIONS	STRUCTURAL FABRICS: FOLDS	STRUCTURAL FABRICS: DOMINANT FOLIATION	STRUCTURAL FABRICS: LINEATION, DOMINANT MOVEMENT
1550[7]	Protolith of felsic granulites (N of Hinckley Fault)				
1300[7]	Protolith of felsic granulites (S of Hinckley Fault)				
	D_1		Rarely preserved	Layered parallel S_0, reoriented during D_2	None observed
1200[7]	Intrusion of charnockite				
	D_2	P=5±1 kbar,T>750°C F_2 folds, oriented parallel to L_2	Recliined isoclinal 335/15 NE	Pervasive S_2-gneissosity L_2/S>105	Pervasive intersection
1188±4[8]	Intrusion of fine grained granite and K-feldspar megacrystic granitoids				
1100[5]	Intrusion of mafic dykes Type A				
1080[3]	Intrusion of Giles Complex				
	D_3 early	P=6±1 kbar; uplift, erosion; extrusion of Tollu Group volcanics			
1060[3]	D_3 late	P=11 kbar, T=.650-700°C P=4.8-11 kbar	Open to isoclinal Upright F_3folds	135/90NE	Down-dip mineral and stretching: 80->225
1000[5]	Intrusion of mafic dykes Type C (including olivine-clinopyroxenite)				
800 Ma[3]	Intrusion of mafic dykes Type B				
	D_4 ultramylonite (SE transport)	Amphibolite facies	090/65NE		42->325 Reverse
	D_5 mylonite,ultramylonite (SW/transport)	Greenschist facies	160/80E	SS->325 common fracture cleavage	Reverse
550 Ma[4,6]	D_6 Petermann Orogeny Ultramylonite with pseudotachylite north-directed thrusting e.g. Champs de Mar Fault, Woodroffe Thrust	P=14.0±1.1 kbar,T=.750°C	Large shear zones extensive pseudotachylite	100/80S 085/80N	80->175 Reverse 80->360 Normal
	D_7 greenschist-facies shear zones	Contain mascovite and biotite	Broad "crush" zones		80->030

[3]Rb-Sr whole rock isochrons, Gray (1971, 1977); [4]U-Pb on zircons, Maboko (1988); [5]U-Pb on zircons, Sun and Sheraton (1992); [6]^{40}Ar-^{39}Ar, Maboko (1988);[8] Sun and Clarke, unpublished data

NGMA

Product of the National Geoscience Mapping Accord

AGSO AUSTRALIAN GEOLOGICAL SURVEY ORGANISATION

GEOLOGY OF THE GILES COMPLEX AND ENVIRONS
WESTERN MUSGRAVE BLOCK
ENLARGEMENTS OF SELECTED AREAS OF THE TOMKINSON RANGE
WESTERN AUSTRALIA/SOUTH AUSTRALIA

PRELIMINARY EDITION

PLATE 2 OF 3

Jun23\maps\mrinfo\plates\tom2\tgmap02.cdr

24 FEB 1996

GEOLOGY OF THE GILES COMPLEX AND ENVIRONS
WESTERN MUSGRAVE BLOCK

GEOLOGY OF THE BLACKSTONE - JAMESON REGION

WESTERN AUSTRALIA/SOUTH AUSTRALIA
PLATE 3 OF 3
by A.Y. Glikson, A. J. Stewart and E.H.J. Feeken 1995

SCALE 1:100 000
1 0 1 2 3 4 5 6 7 8 9 10 Kilometres
UNIVERSAL TRANSVERSE MERCATOR PROJECTION, AUSTRALIAN MAP GRID, ZONE 52
LATITUDE OF ORIGIN : 0°, LONGITUDE OF ORIGIN : 129°

NOTE: FOR LITHOLOGICAL REFERENCE SEE PLATE 1

S1 BLACKSTONE RANGE TROCTOLITE/GABBRO

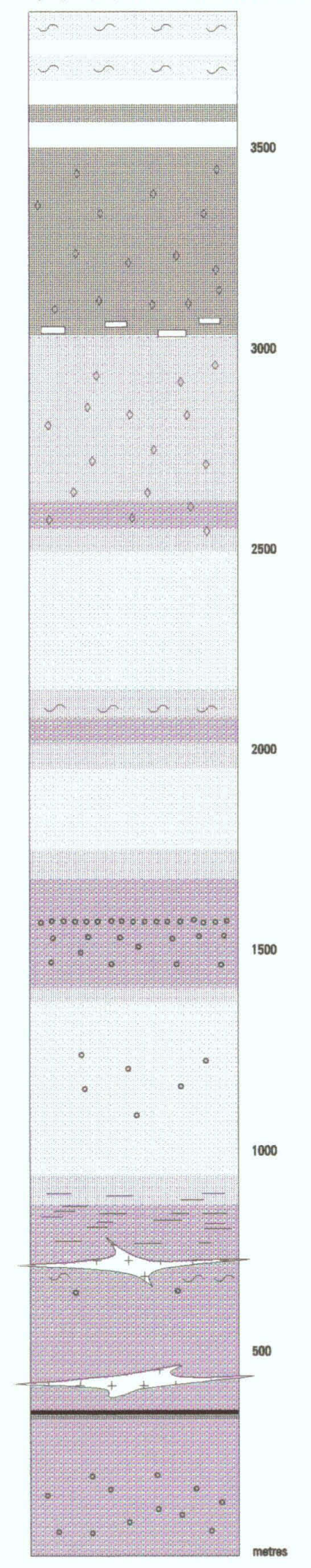

90980149-151	*Mafic granulite*
147-48	*Mafic granulite*
145-46	*Olivine gabbro*
142-44	*F.g. olivine-plg-phyric sill or quench of ol gabbro*
141	*Ol-bearing gabbroic anorthosite*
140	*Olivine gabbronorite*
139	*Olivine gabbronorite*
137-38	*Anorthositic troctolite*
136	*Troctolitic to gabbroic anorthosite*
135	*Anorthositic to gabbroic troctolite*
134	*Troctolite and amphibolite*
133	*Altered troctolite*
132	*Anorthositic troctolite*
90987514	*Anorthositic troctlite and amphibolite*
512-513	*C.g. troctolitic anorthosite*
509-511	*Magnetite-rich troctolite, magnetite layers*
507-508	*Magnetite-rich troctolite*
503-506	*Troctolitic anorthosite*
502	*Troctolitic anorthosite*
501	*Altered troctolite*
90980178-179	*Inch-layered troctolite*
177	*Cross cutting granitic vein and mylonite*
175-176	*Troctolitic anorthosite*
172-174	*Cross-cutting sheared granitoid*
168-171	*Thin dunite horizons*
168	*Magnetite-rich troctolite*
166-167	*Troctolite*
165	*Oxide-rich troctolite*
164	*Troctolite*

S2 JAMESON RANGE TROCTOLITE/GABBRO

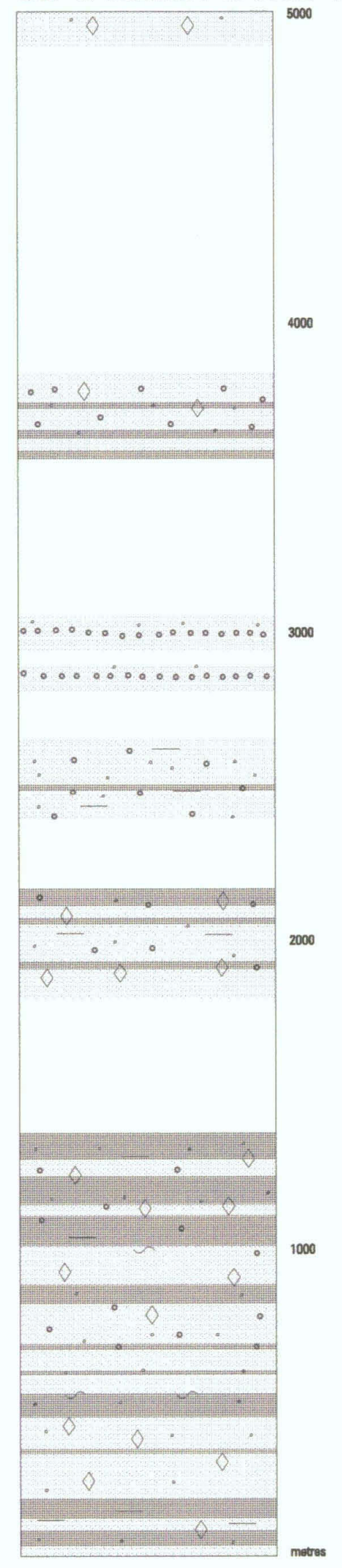

90980042-43	*C.g. recrystallized olivine-bearing gabbroic anorthosite*
44-45	*Olivine anorthosite with interstital oxides, troctolite and garrbo layers*
46-47	*Massive Fe-Ti oxide layers in anorthosite and troctolite*
48	*Massive Fe-Ti oxide layers in anorthosite and troctolite*
49-50	*Recrystallized anorthositic troctolite, troctolite, interstitial oxides*
51-52	*Recrystallized anorthositic to gabbroic troctolite*
37-39	*Troctolite, anorthosite, gabbro, interstitial magmatic oxides*
36	*C.g. deformed gabbro*
35	*Recrystallized deformed troctolitic anorthosite*
34	*Troctolite, interstitial oxides*
33	*Recrystallized troctolitic anorthosite*
31-32	*Anorthosite, minor troctolite*
29-30	*Troctolite, minor gabbro*
26-28	*Deformed troctolite*
25	*Recrystallized troctolitic anorthosite*
21-23	*Weakly laminated anorthosite*
19	*Recrystallized leucotroctolite*

S3 MURRAY RANGE PYROXENITE/PERIDOTITE

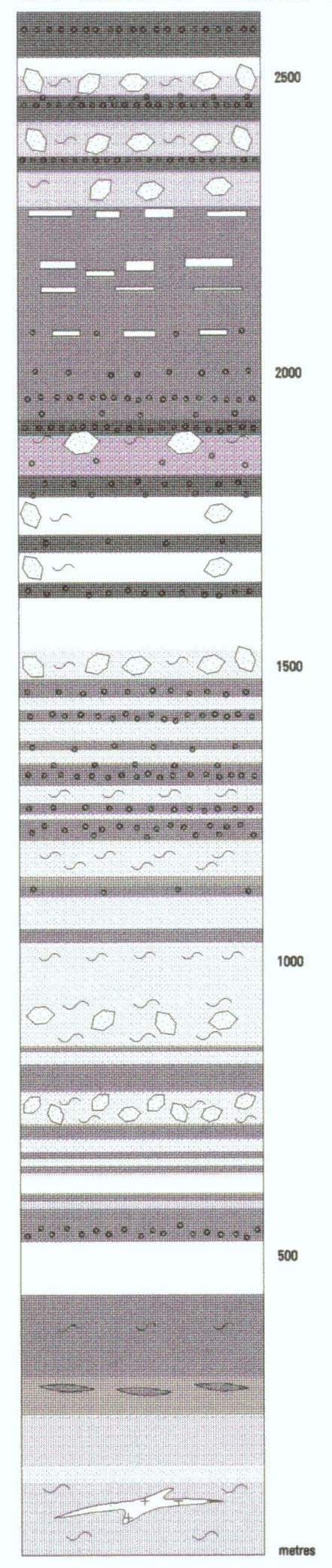

88980001-3	*Annealed pyroxenite, peridotitic layers*
5-9	*Amphibolite, relic gabbro*
10	*Feldspapthic harzburgite to wehrlite*
12-14	*Amphibolite after gabbro*
11	*Dunite orthocumulate layer in amphibolite*
15-17	*Amphibolite after gabbronorite; orthopyroxenite*
18-22	*Orthocumulate (porphyritic) orthopyroxenite*
23-24	*Orthocumulate (porphyritic) orthopyroxenite*
25-27	*Olivine pyroxenite*
28-29	*Olivine pyroxenite, peridotite*
30-32	*Serpentinized dunite orthocumulate, olivine pyroxenite, amphibolite*
33-34	*Olivine orthopyroxenite*
35-36	*Olivine orthopyroxenite, harzburgite, cut by mylonite*
37-38	*Amphibolite, mafic granulite*
42	*Wehrlite adcumulate*
39	*Wehrilite cumulate alternating with gabbro*
40-41	*Feldspathic orthopyroxenite*
43	*Shear zone through gabbronorite*
44-46	*Wehrlite and olivine pyroxenite, sheared gabbro*
47-51	*Variably deformed gabbro to gabbronorite*
52	*Olivine clinopyroxenite*
53	*Gabbro and pyroxenite*
54	*Deformed gabbronorite, mylonite*
55	*Deformed and amphibolized gabbro*
57-59	*Pyroxenite and gabbronorite*
60b,c	*Gabbroic to amphibolitic mylonite*
61a,68,69	*Gabbro, gabbronorite, pyroxenite*
70	*Silicified pyroxenite*
66-67	*Recrystallized pyroxenite, minor gabbro*
62,64,61b,c	*Deformed gabbronorite intruded by granitic veins*

D JAMESON RANGE TROCTOLITE/GABBRO INTRUSION

See Section S2

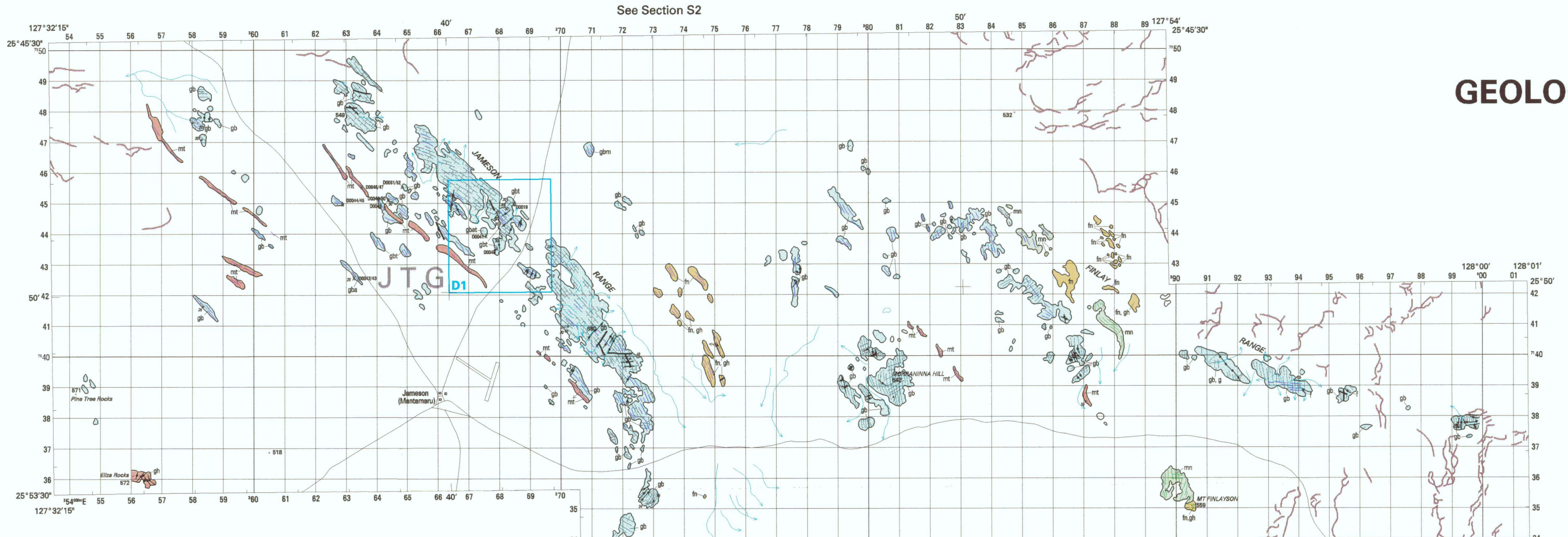

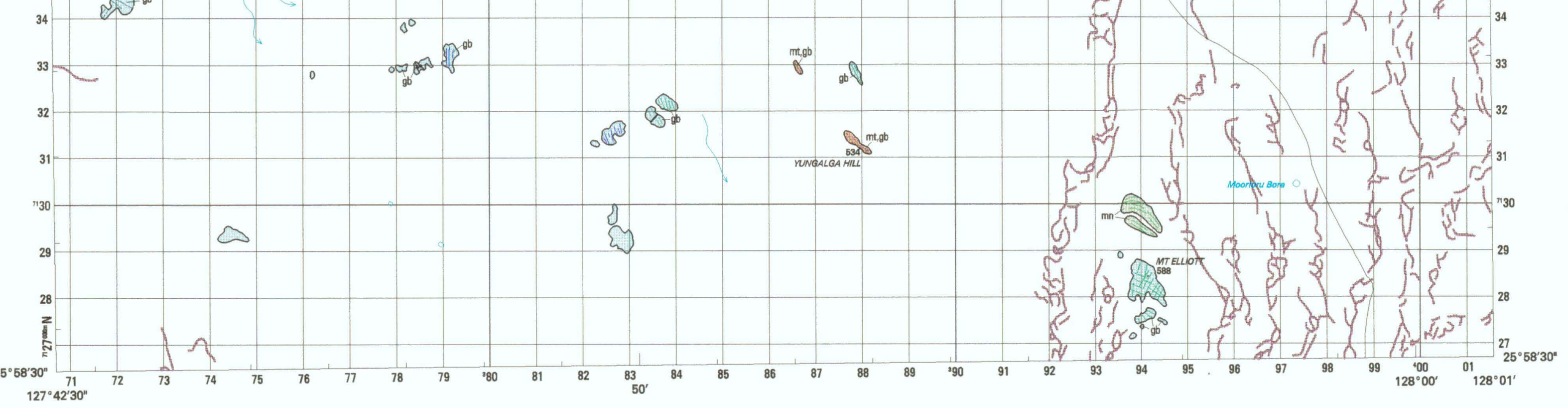

D1 JAMESON RANGE TROCTOLITE/GABBRO INTRUSION (1:50 000)

See Section S2

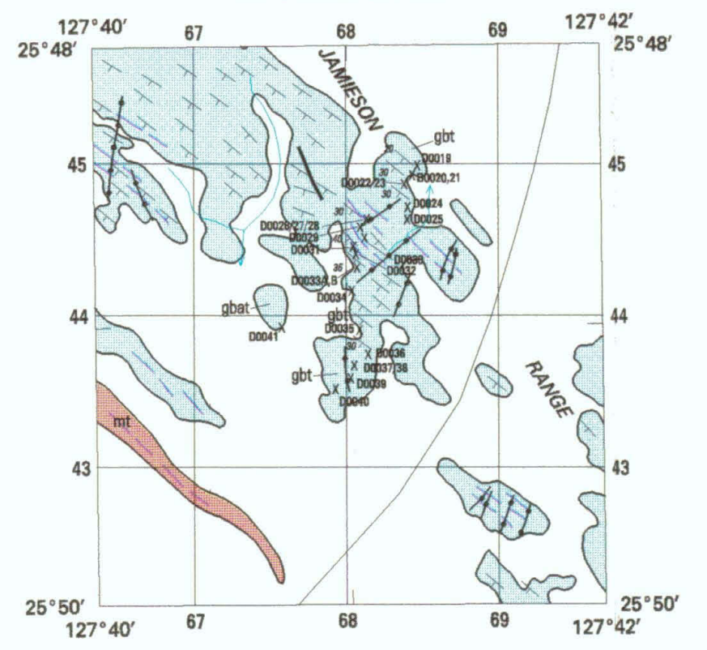

TOTAL MAGNETIC INTENSITY

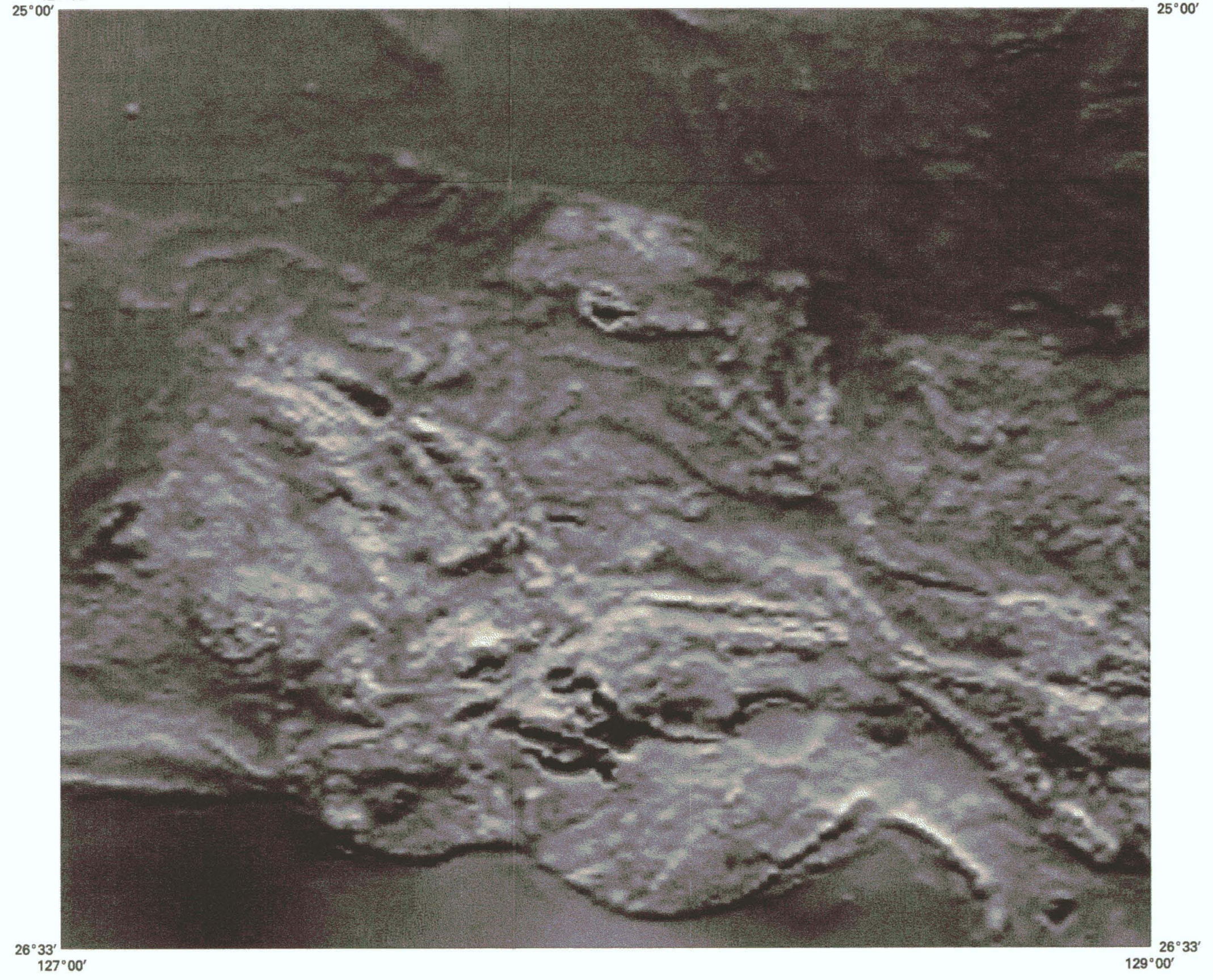

GRAVITY

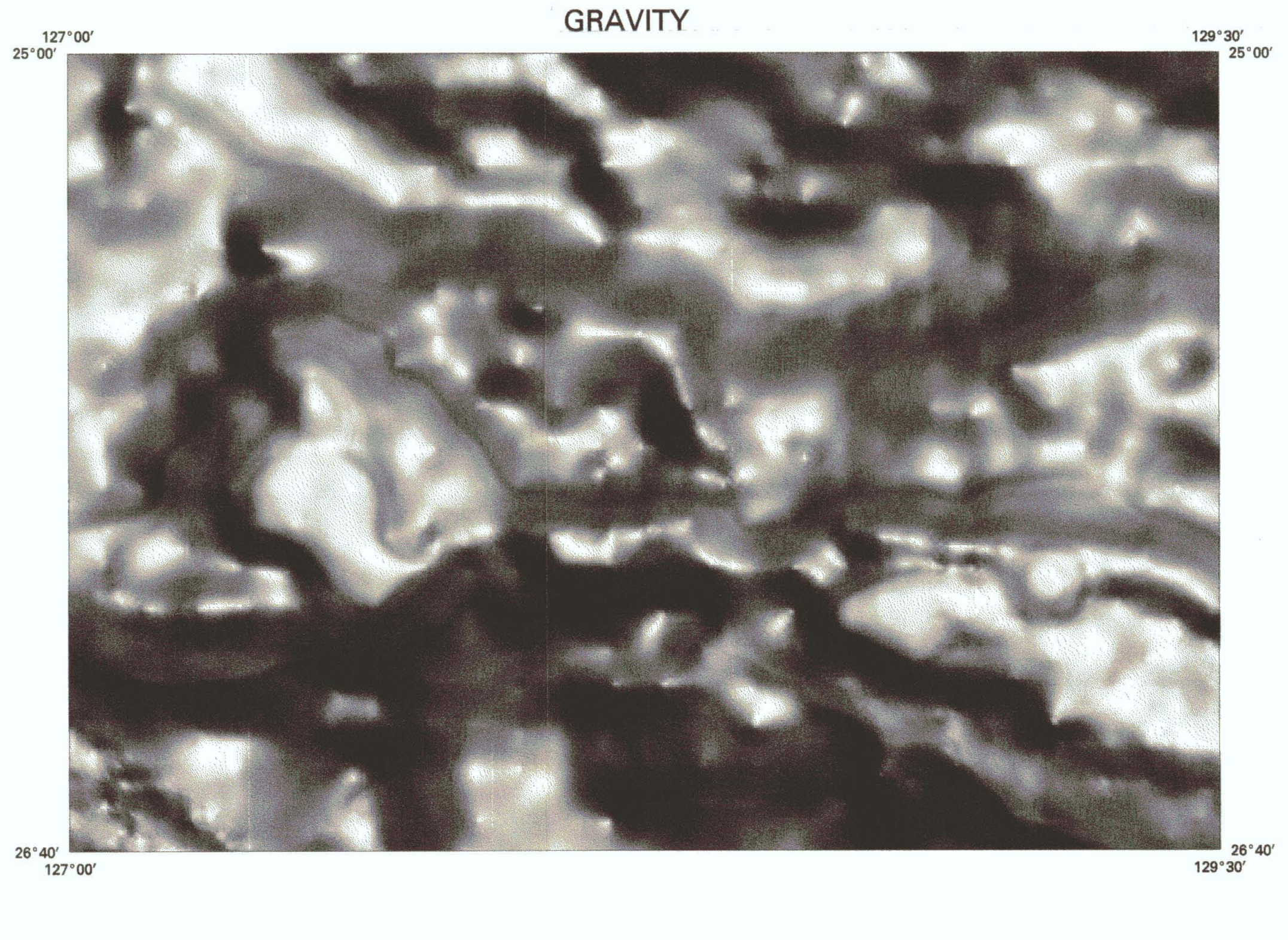

GEOLOGICAL SKETCH MAP SHOWING THE LOCALITIES OF ENLARGED AREAS

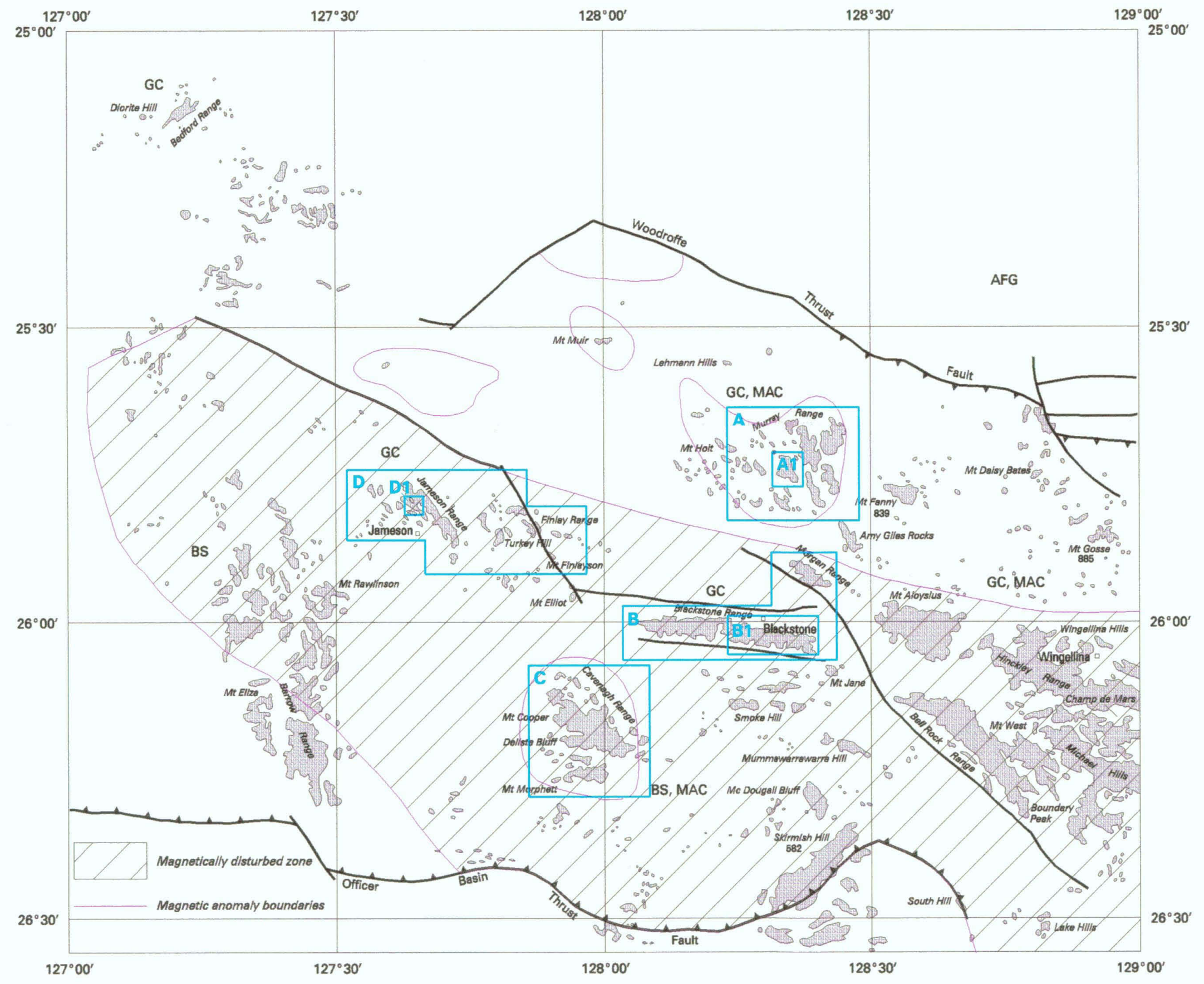

C CAVENAGH RANGE GABBRO INTRUSION

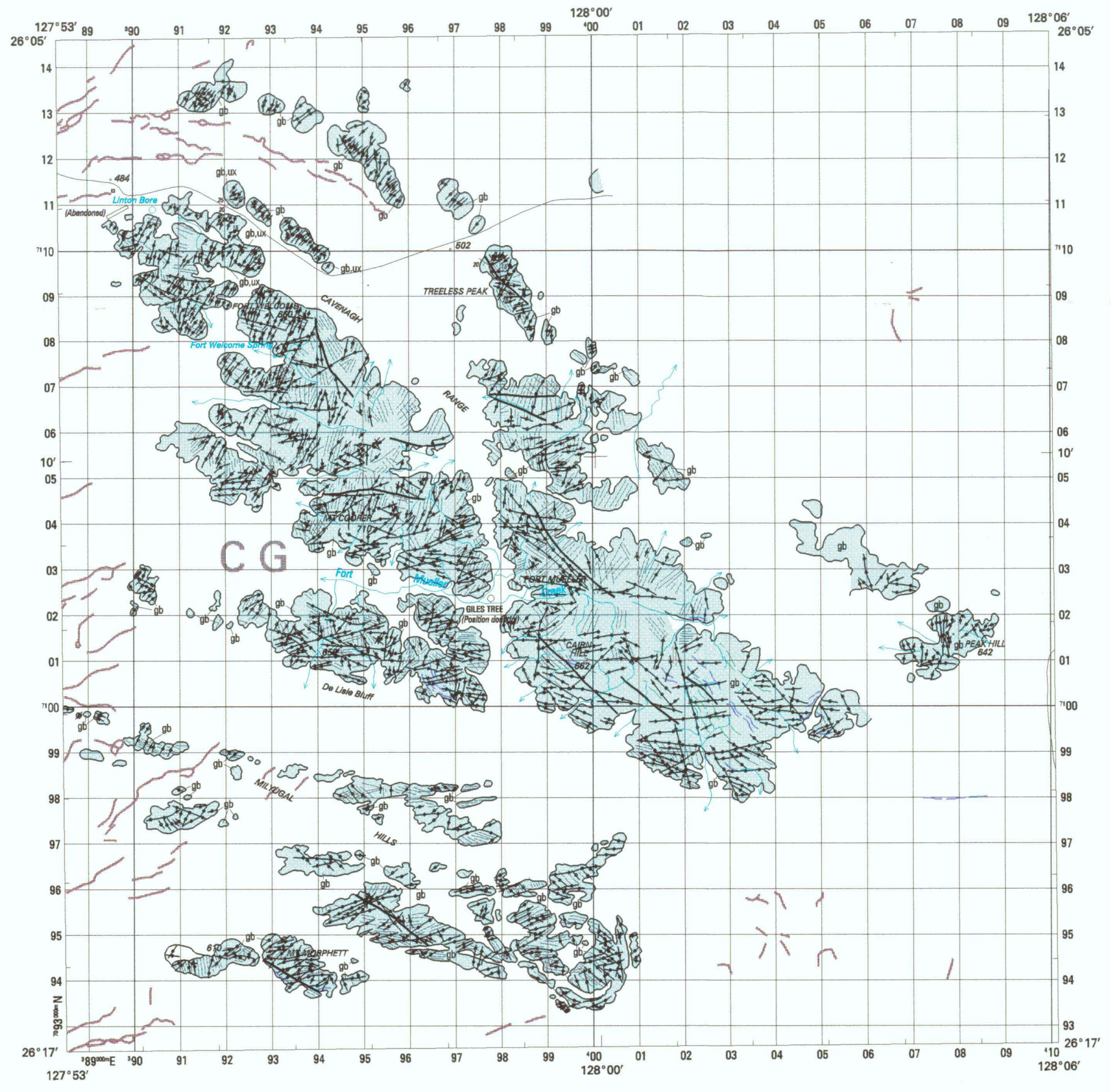

B BLACKSTONE RANGE

See Section S1

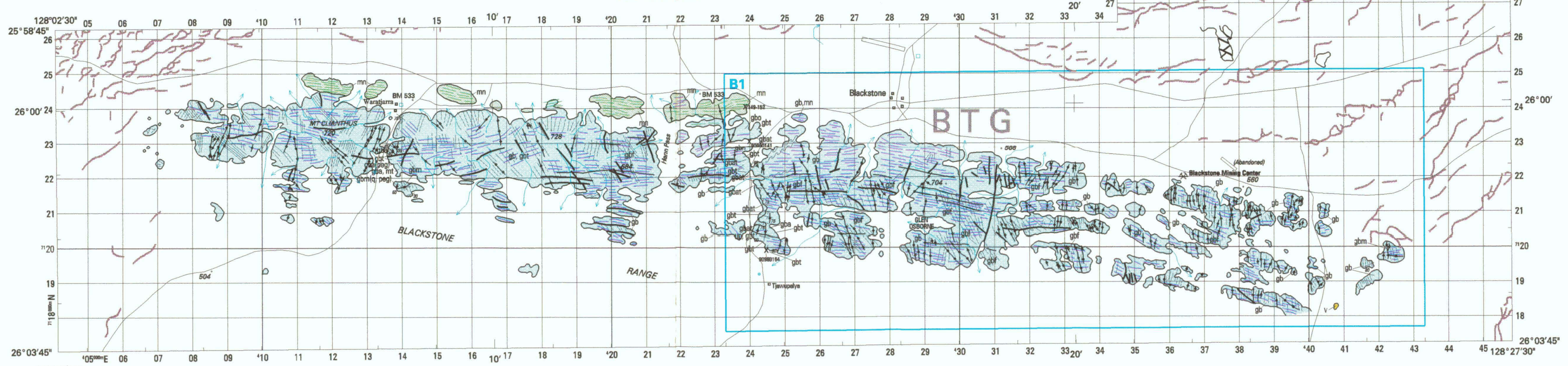

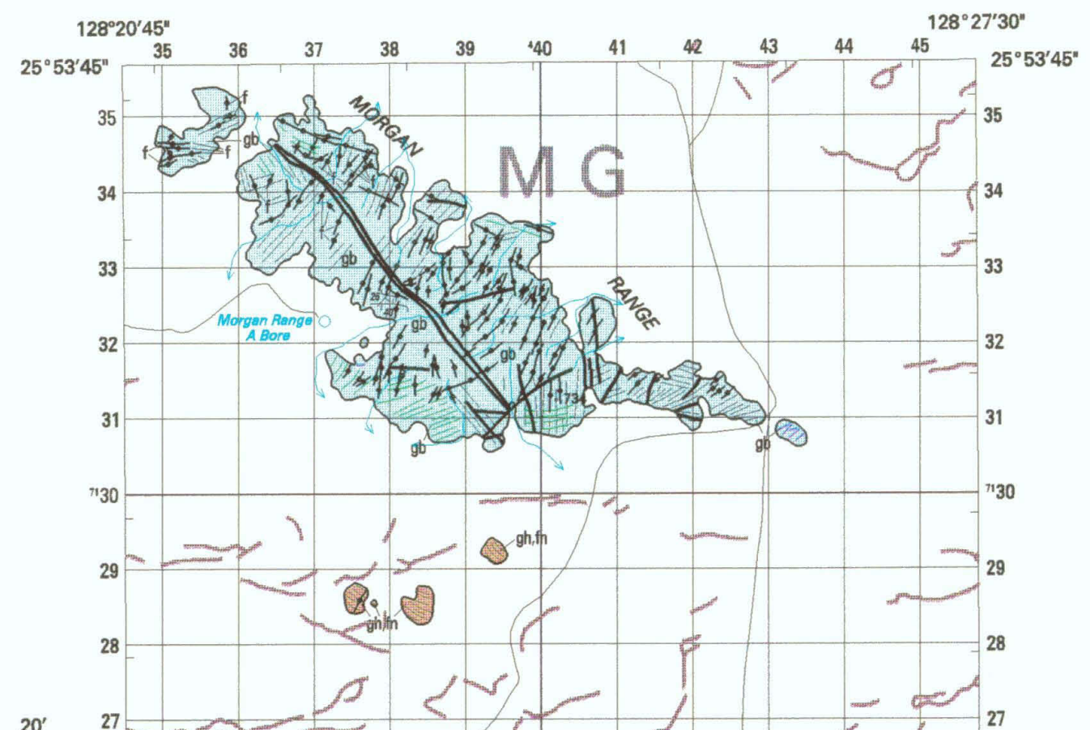

B1 BLACKSTONE RANGE TROCTOLITE/GABBRO INTRUSION (1:50 000)

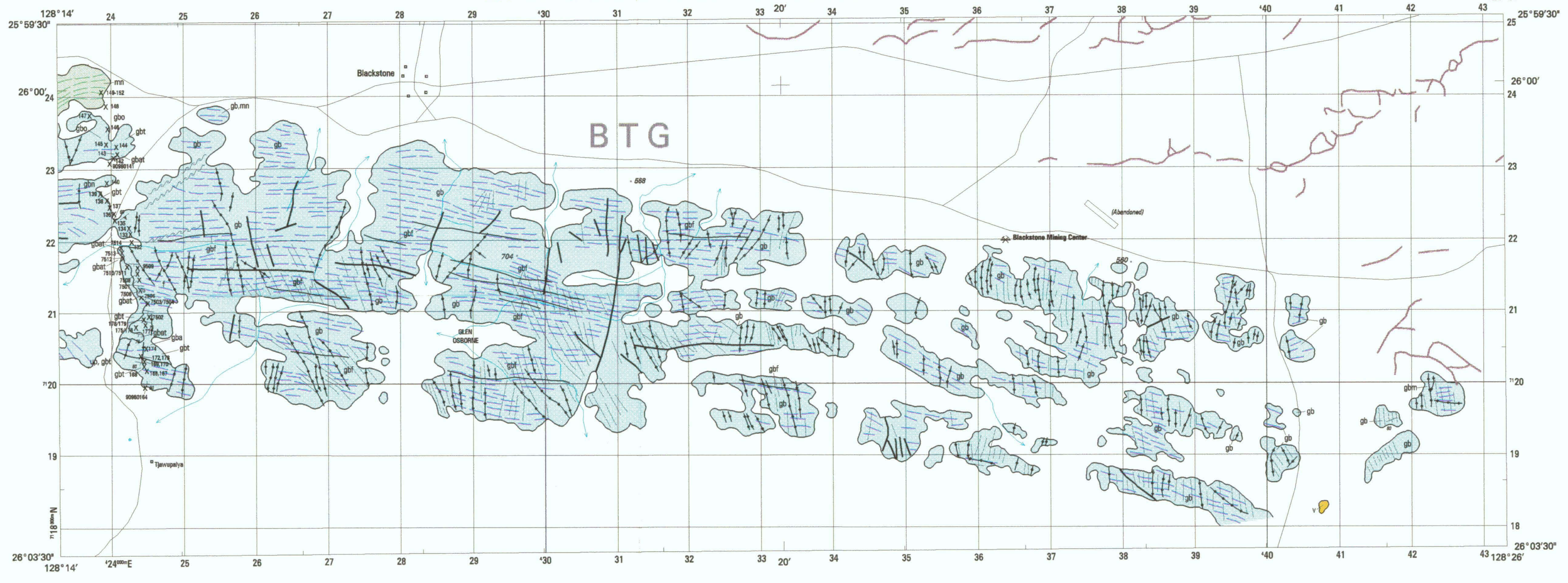

A MURRAY RANGE

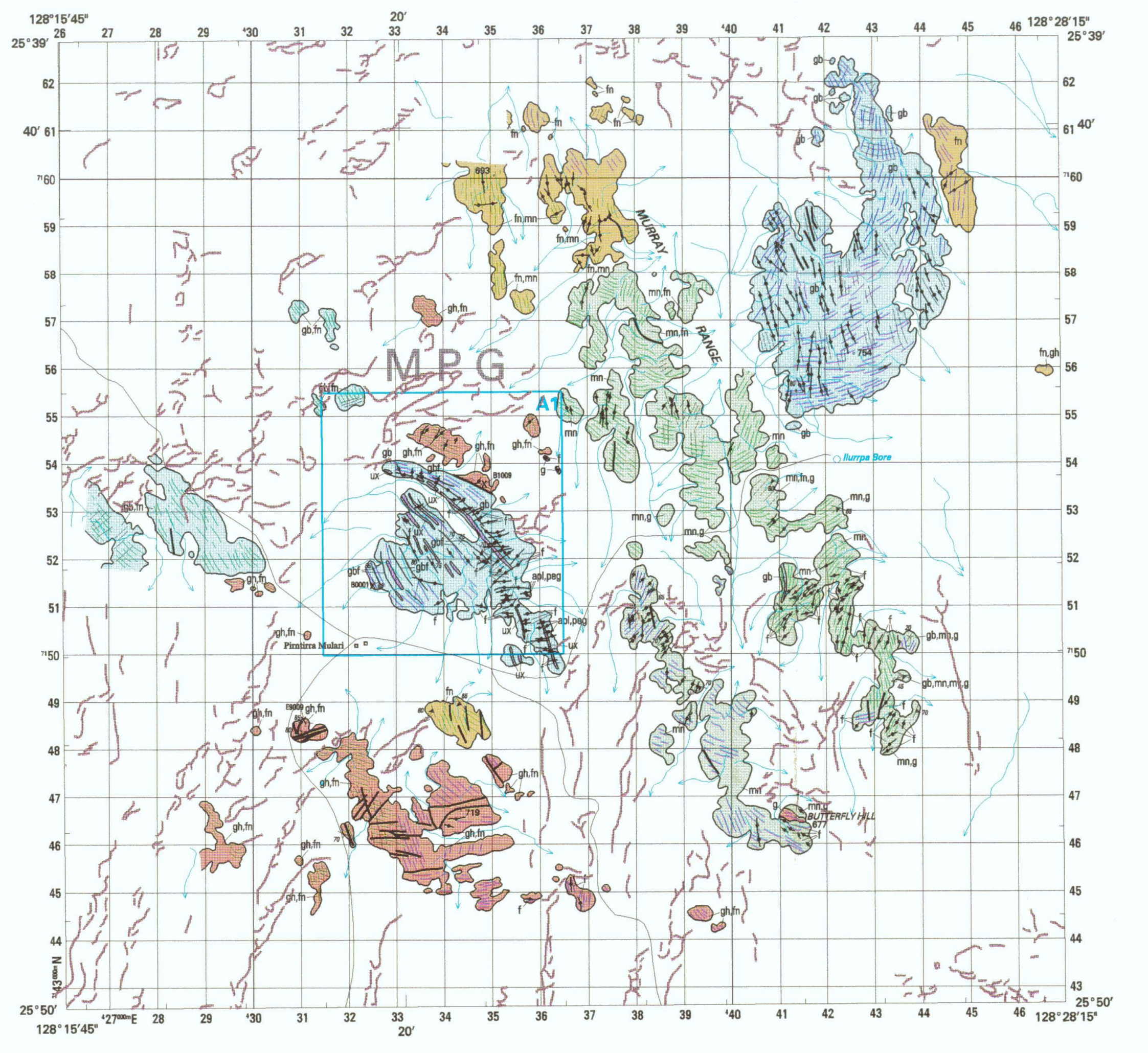

A1 MURRAY RANGE PYROXENITE/PERIDOTITE/GABBRO INTRUSION (1:50 000)

See Section S3

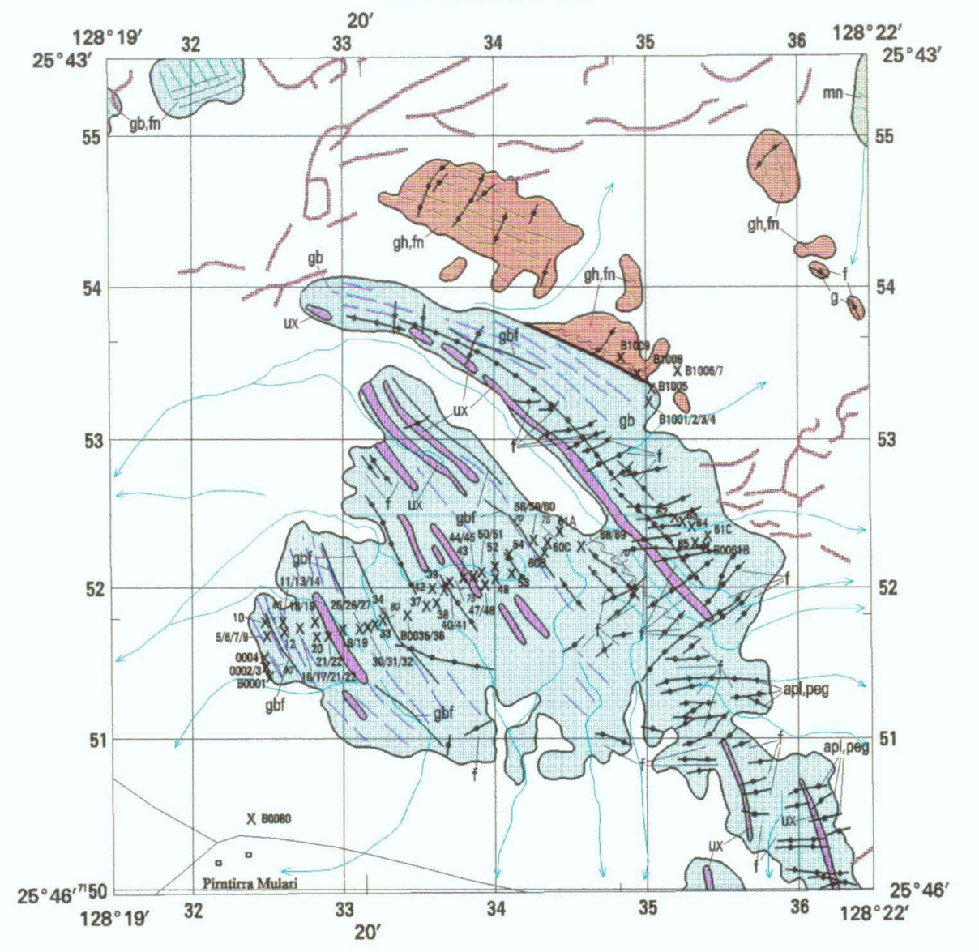

NGMA

Product of the National Geoscience Mapping Accord

AUSTRALIAN GEOLOGICAL SURVEY ORGANISATION

GEOLOGY OF THE GILES COMPLEX AND ENVIRONS
WESTERN MUSGRAVE BLOCK
GEOLOGY OF THE BLACKSTONE - JAMESON REGION
WESTERN AUSTRALIA/SOUTH AUSTRALIA
PRELIMINARY EDITION
PLATE 3 OF 3

/usr2/map/rgm/mb/giles/plate3/trgmpol3.dgn 29-FEB-1996 rhill